ISBN 978-80-969-672-5-4

Institute of Measurement Science
Slovak Academy of Sciences
Dúbravská cesta 9
841 04 Bratislava, Slovakia

MEASUREMENT 2013

MEASUREMENT
2013

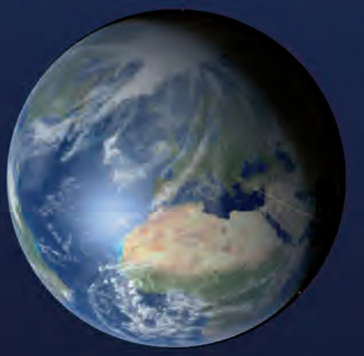

9th International Conference on Measurement

Smolenice, Slovakia
May 27 - 30, 2013

Proceedings

The 9th International Conference MEASUREMENT 2013 was organized by the Institute of Measurement Science, Slovak Academy of Sciences, Bratislava, Slovakia.

MEASUREMENT 2013

Proceedings of the
9th International Conference on Measurement

Congress center of the Slovak Academy of Sciences
Smolenice castle, Slovakia
May 27-30, 2013

MEASUREMENT 2013

Editors: Ján Maňka, Milan Tyšler, Viktor Witkovský, Ivan Frollo
Publisher: Institute of Measurement Science
Slovak Academy of Sciences
Dúbravská cesta 9, 841 04 Bratislava
Slovakia

ISBN 978-80-969-672-5-4

Printed in Slovakia
by VEDA, Publishing House of the Slovak Academy of Sciences

MEASUREMENT 2013

Editors: Ján Maňka, Milan Tyšler, Viktor Witkovský, Ivan Frollo
Publisher: Institute of Measurement Science
Slovak Academy of Sciences
Dúbravská cesta 9, 841 04 Bratislava
Slovakia

ISBN 978-80-969-672-5-4

Printed in Slovakia
by VEDA, Publishing House of the Slovak Academy of Sciences

ORGANIZATION OF THE CONFERENCE

Organizer
Institute of Measurement Science, Slovak Academy of Sciences, Bratislava, Slovakia

Co-organizers
Technical University Vienna, Wien, Austria
Faculty of Mechatronics and Machine Building, Kielce University of Technology, Kielce, Poland
Faculty of Biomedical Engineering, Czech Technical University in Prague, Kladno, Czech Republic
Faculty of Electrical Engineering and Information Technology, Slovak University of Technology, Bratislava, Slovakia
Faculty of Electrical Engineering, University of Žilina, Slovakia
Faculty of Mechanical Engineering, Technical University Košice, Slovakia

Technical sponsorship
Slovak National Committee IMEKO, TC7 and TC13 committees,
Slovak Metrological Society
Slovak National Committee U.R.S.I.
Slovak Society of Biomedical Engineering and Medical Informatics

Conference Chairman
M. Tyšler, Slovakia

International Advisory Board
I. Frollo, Slovakia, chairman
S. Adamczak, Poland
M.N. Durakbasa, Austria
M. Dado, Slovakia
V. Havlíček, Czech Republic
G. Juhás, Slovakia
P.P.L. Regtien, The Netherlands
J. Rosina, Czech Republic
T. Švantner, Slovakia
S. Trattnig, Austria
J. Živčák, Slovakia

Local Organizing Committee
V. Witkovský
P. Andris
M. Hain
E. Bukovenová
A. Dvurečenskij
S. Fialová
D. Gogola
V. Juráš
R. Ševčík
M. Škrátek
M. Teplan

International Program Committee
J. Maňka, Slovakia, Chairman
I. Bajla, Slovakia
V. Boháč, Slovakia
E. Cocherová, Slovakia
D. Eidukas, Lithuania
R. Harťanský, Slovakia
M. Horacek, Canada
R. Hudák, Slovakia
Y. V. Chugui, Russia
E. Kawate, Japan
P. Kneppo, Czech Republic
R. Köning, Germany
G. Kozmann, Hungary
L. Laurinavičius, Lithuania
F. Lehocki, Slovakia
L. Lhotská, Czech Republic
R. Maniewski, Poland
K. Meigas, Estonia
L. Michaeli, Slovakia
V. Mlynarik, Switzerland
K. Roubík, Czech Republic
V. Smieško, Slovakia
D. Šimšík, Slovakia
M. Štork, Czech Republic
S. Takayama, Japan
M. Tarata, Romania
E. Tkacz, Poland
I. Van Driessche, Belgium
G. Wimmer, Slovakia
V. Witkovský, Slovakia
J. Zakrzewski, Poland

Preface

One accurate measurement is worth a thousand expert opinions.

Grace Murray Hopper (1906 – 1992)

The words of the American computer scientist and US Navy Rear Admiral who came with the idea of machine-independent programming languages and developed the first compiler underscore the importance of measurement in research, engineering, society and decision making in general. We all are aware of the fact that development of measurement and measuring methods open new ways for technology advances and represent a prominent instrument on the way to major revelations. In a bit joky way the role of measurement expressed also Enrico Fermi, Italian theoretical and experimental physicist (1901 – 1954) saying *"There are two possible outcomes: If the result confirms the hypothesis, then you've made a measurement. If the result is contrary to the hypothesis, then you've made a discovery"*.

However, to play this serious role, each measurement has to fulfill at least two conditions: proper measuring method, yielding values of desired quantity has to be used and the measured values have to be properly interpreted. Measurement science investigates both these aspects of measurement. In this sense also the MEASUREMENT conferences are focused on new developments in measurement theory, evaluation of measured data and estimation of their uncertainty as well as on advances in measuring methods and their applications in two specific areas: biomedicine and physics. Every two years since 1997, the Smolenice castle offers the conferences its comfortable environment for scientific talks, informal working discussions and friendly relaxation moments.

Continuing this tradition, also the 9th International Conference MEASUREMENT 2013 is devoted to theoretical problems of measurement, measurements in biomedicine and measurements of physical quantities. It includes actual themes of modeling of measured objects and development of new imaging techniques. The mission of the Conference is passing and exchanging of new ideas among specialists in measurement science but also education of young students and investigators and their competition for the Young Investigator Award that is sponsored by the conference organizers.

The conference is organized by the Institute of Measurement Science, Slovak Academy of Sciences in collaboration with several co-organizers and technical sponsors that substantially contribute to preparation of the conference program. This year the conference has a special flavor. As the Institute celebrates its 60th anniversary, this event is a good opportunity to summarize its achievements and to indicate future perspective areas of research.

I wish that the 9th international conference on measurement will become both, a high quality scientific meeting and an enjoyable social event allowing the participants from many countries to exchange new information but also mutually learn about their cultural specificity. Together with the editors of these proceedings I also hope that the book will give some insight into the high professional level of the conference, will be a useful source of information for those who were not able to participate personally and will become a quoted reference in measurement science and technology.

Milan Tyšler
Conference Chairman

CONTENTS

Invited Papers

Uncertainty Evaluation for Quality Tracking in Natural Gas Grids

R. Kessel, K. D. Sommer

Physikalisch-Technische Bundesanstalt (PTB), Braunschweig, Germany
Email: ruediger.kessel@ptb.de

Abstract. *Simulation tools are in used to manage the grids by allowing the reconstruction of the state of the grid (flows and pressures). This allows tracking of the gas properties while the gas is transported by the grid. In practice often only rough estimates of the momentary consumption by the end users are available creating uncertainty about the value calculated from the reconstruction of the state and therefore in the tracking of the transported gas properties. We present an approach based on the Guide to the Expression of Uncertainty in Measurement (GUM) Supplement 1 to evaluate the uncertainty involved with the state reconstruction and property tracking. In future, gas grids will transport gasses with a wider range of calorific values at the same time which complicates the correct billing of the delivered energy. We show how the uncertainty involved with the state reconstruction and the property tracking can be used to monitor the validity of a quality tracking system for natural gas grids.*

Keywords: Natural Gas Grids, Uncertainty Evaluation, Monte Carlo Simulation

1. Introduction

Natural gas grids are an important infrastructure in Germany since a significant fraction (about 30%, 2005) of the energy consummated today is generated using natural gas. Distributed natural gas grids can transport and store significant amounts of energy equivalents. Therefore gas grids will play an important role in solving problems with the energy supply in future by complementing the electrical grids.

In Germany, natural gas from 8 major origins is distributed through the transport grids. The composition of the gas is mainly dependent on its origin and for some sources it also has some time dependency. Table 1 lists the major natural gas sources for Germany together with some important properties. The calorific value is varying between 10.6 kWh/m^3 and 12.9 kWh/m^3. The maximal variability is about 20 %. The CO_2 fraction varies between 0 % for liquefied natural gas (LNG) and 2.9 % for bio-gas.

Table 1. Summary of natural gas sources for Germany with their main properties [1].

		Russia	North Sea	Denmark	Libya LNG	Nigeria LNG	Egypt LNG	Bio-gas	Bio-gas + LPG
Calorific value	kWh/m^3	11.2	11.6	12.1	12.9	12.2	11.3	10.6	11.6
Difference to ref. 11.6		-3.4 %	0	+4.3 %	+11.2 %	+5.2 %	-2.6 %	-8.6 %	0
CO_2	Mol %	0.18	1.94	0.60				2.90	2.68

The most important property of natural gas is its calorific value. For industrial users the CO_2 content is important, too because it might affect their CO_2 balance.

The calorific value of natural gas can be measured with standard calorimeters or gas chromatography. But measuring equipment is expensive to install and to operate. Therefore in

Germany most transport grids are equipped with gas quality tracking systems since several decades.

Transport grids have a structure with a few input and output nodes all equipped with flow meters and long distance pipelines connecting them. Their nominal pressures are between 70 and 100 bar. Reliable quality tracking is relatively easy for transport grids.

Recent liberalisations in the market for natural gas and the introduction of bio-gas have lead to increased variability of the natural gas quality in the distribution grids. Distribution grids are operated with a nominal pressure between 10 bar and 25 bar. They are connecting the customers to the transport grids. Distribution grids have usually an intermeshed structure with several connections to different transport grids. The measurement infrastructure is often incomplete so that some output flows cannot be measured. Quality tracking for distribution grids is therefore challenging. But the concepts of uncertainty in measurement introduced by the Guide to the Expression of Uncertainty in Measurement (GUM) [2] and especially its Supplement 1 [3] can be used to manage the challenge.

2. Tracking Gas Qualities in Distribution Grid for Natural Gas

Quality tracking systems for transport grids and distribution grids can be decomposed in two parts (Fig. 1). The reconstruction of state calculates the internal (not measured) flow rates and pressures based on the grid topology and the measured input and output flows, the grid pressure and the temperature. A gas transport model evaluates the gas quality of the output flows based on the internal flows and the gas qualities of the input flows.

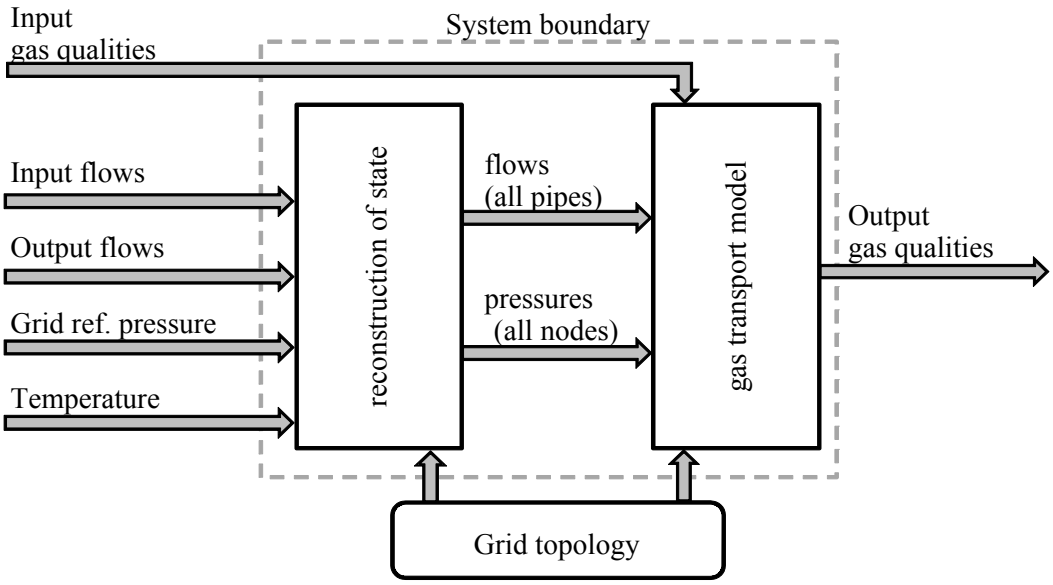

Fig. 1. Structure of the flow of information in a gas quality tracking system.

The reconstruction of state and the gas transport model are realized by complex software systems involving heavy numerical calculations and the solution of a system of differential equations. For the evaluation of uncertainty the calculations inside the reconstruction of state and the gas transport model can be treated as a black box.

3. Model of Evaluation

The reconstruction of state and the gas transport model are treated as the model function or model of evaluation. Input gas quality, input flows, output flows, grid pressure, temperature

and output gas qualities are time series data. Every point in the time series is an individual input or output quantity. The time resolution should be one value per hour or better and the evaluation period is usually one month or more. This results in a system of a very large number of input and output quantities. For our studies we have used the small distribution grid simulation developed at the TU Clausthal [4]. The topology of the distribution grid is shown in Fig. 2. It is a small grid with 4 input nodes (K000, K002, K004 and K006), 25 output nodes and the time resolution is 12 min, but the model for the uncertainty evaluation has about 30000 input quantities and about 20000 result quantities.

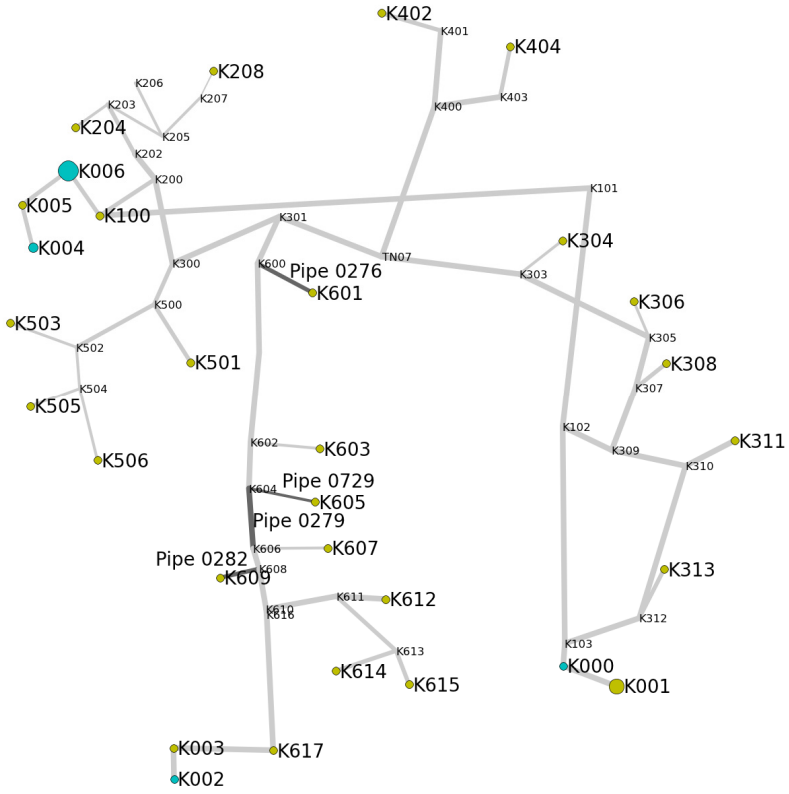

Fig. 2. Topology of the grid under investigation with 4 input node (K000, K002, K004 and K006) and 25 output nodes.

Table 2. Secification of the knowledge about the input quantities for the uncertainty evaluation.

Input quantity		Knowledge	Distribution
Calorific value of the gas sources		≤ 1 %	normal
Source (input) flow rate		≤ 2 %	rectangular
Drain (output) flow rate	online	≤ 2 %	rectangular
	load profile	30 %	normal
Grid reference pressure		≤ 5 %	rectangular
Temperature		0 °C – 15 °C	rectangular
Grid topology	length of pipes	≤ 10 %	rectangular
	diameter	≤ 5 %	rectangular
	roughness	≤ 50 %	rectangular

The available knowledge about the input quantities is summarized in Table 2. It should be noted that the output flow rates for 15 nodes out of the 25 nodes are actually not measured but estimated based on load profiles representing the typical customer consumption. This leads to the relative large uncertainties for these flow rates of 30 %. The specified knowledge in Table 2 represents the typical accuracy with which data can be made available for distribution grids.

4. Uncertainty Calculation

For the uncertainty calculation we have chosen the Monte Carlo (MC) simulation as described in GUM Supplement 1. Even if an evaluation model of this size would be semi-linear it is a huge effort to propagate all variances. The numerical calculation of the sensitivity coefficients would require at least 30000 complete calculations of the evaluation model which in this case is very demanding in respect to computational effort. If the number of Monte Carlo trails can be limited then MC is more economic.

With the assumption that the variances of the MC results are converging, the number of MC trails needed to achieve the required relative accuracy r can be calculated [5] using

$$n = \frac{1}{r^2} \times \mathrm{norm}\left(1 - \frac{1-p}{2}\right)^2 \qquad (1)$$

where n is the number of MC trails, p is a chosen probability for the accuracy interval and norm() is the quantile of the normal distribution. We choose a relative accuracy for the uncertainty of 5% (r=0.05) with a probability of 95 % (p=0.95) which leads to 1600 MC trails.

For our studies we have developed a Python script which generates for each run a set of random factors with expectation value of 1.0 and distribution based on the specification in Table 2 for all input quantities. For each MC run the original input data is multiplied with a set of factors and the reconstruction of state and the gas transport model are calculated. The uncertainties were calculated from the standard deviation of the results from all runs. Since we could only perform a limited number of MC trails a coverage interval based on spread of results would not be reliable. Therefore we chose a fixed coverage factor of k=2 to arrive at an expanded uncertainty statement which covers a large fraction of possible result values.

5. Monte Carlo Simulation Results

Since we are mainly interested in studying the uncertainties introduced by the limited knowledge about the transport process through the grid, we have treated the calorific values as perfectly known with no uncertainties during our simulations. The uncertainties introduced by the grid transport and the uncertainties associated with the calorific values of the gas sources are uncorrelated and the variances can simply be added to get the combined uncertainty of the calorific values of the output flows.

For the discussion we use simulation results from a period of 160 h while the calorific values of the sources were varying between 10.7 kWh/m^3 and 11.2 kWh/m^3.

In our simulations we found that the uncertainties associated with the reconstruction of the internal flow rates are time dependent and are varying a lot between different pipelines. Some internal flow rates can be reconstructed accurately with an uncertainty better than 2.5 % (see Fig. 3. For many internal flow rates the uncertainty of the reconstruction is about 30 %, but for some flow rates the uncertainty is 300 % and more (e.g. pipeline 0279, Fig. 4). It can be observed that the uncertainties are larger if the flow rates are small in respect to diameter of the pipelines.

Although it is useful to analyse the uncertainties associated with the reconstruction of the internal flow rates, the final quantities of interest are the calorific values and their associated uncertainties. Since the calorific values are only varying by about 5 % during our simulation period, the effect of the limited knowledge of the transport process on the gas transport model

calculation can be expected to be significantly smaller than the uncertainty associated with the reconstruction of state.

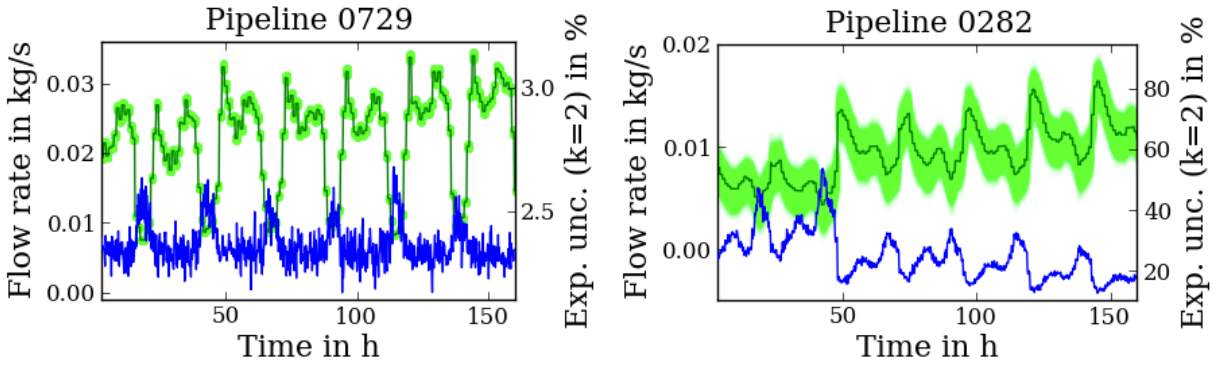

Fig. 3. Simulation results for the flow rate in pipeline 0729 and pipeline 0282. The top graph shows the flow rate and the bottom graph shows the relative expanded uncertainty (k=2).

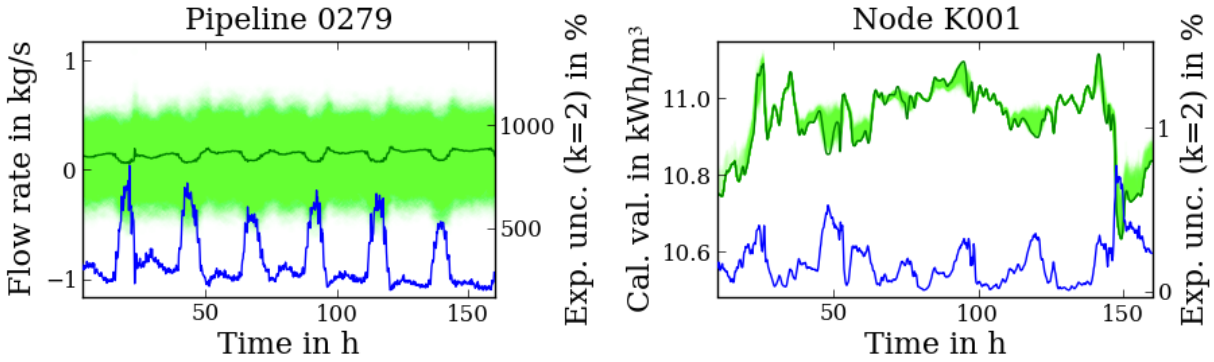

Fig. 4. Simulation results for the flow rate in pipeline 0279 and the calorific value for node K001. The top graph shows the flow rate or the calorific value and the bottom graph shows the relative expanded uncertainty (k=2).

In our study we found that the uncertainties of the calorific values are also time dependent and they are varying between output nodes. Fig. 4 shows the calorific value at node K001 which has the largest consumption during the investigated period. The uncertainty is most of the time well below 0.5% with one peak up to 0.8 %.

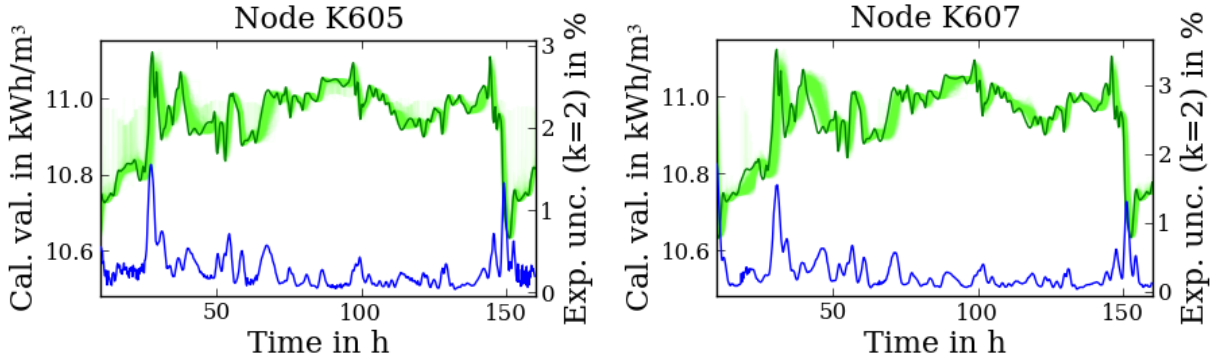

Fig. 5. Simulation results for the calorific value for node K605 and node K607. The top graph shows the calorific value and the bottom graph show the relative expanded uncertainty (k=2).

It can be observed that rapid changes over time of the calorific value are correlated with an increase in the uncertainty of the calorific value. This can be explained by the fact that the

reconstruction of the internal grid state is used by the gas transport model to calculate the throughput time of the gas. Uncertainties in the reconstruction of the internal flow rates lead to uncertainties in the calculated throughput time. The effect on the calorific value is therefore dependant on how rapidly the calorific value is changing in time.

Output node K605 and K607 are connected via pipeline 0279 (see Fig. 2). The associated uncertainty with the reconstructed flow for this pipeline is as large as 700 %. As shown in Fig. 5, the calorific value of the nodes can still be reconstructed relatively well with a peak uncertainty of 1.4 %. The uncertainty is 0.5 % or less most of the time. This demonstrates that good quality tracking is possible even if the knowledge about the internal state of the grid is rather limited. As expected the calorific values and the uncertainties for node K605 and K607 are very similar. The signal at K607 is a bit shifted in time since the distance to the major source at K006 is larger.

For billing purposes often an average calorific value for a longer period (1 month or 1 year) is of interest. It is possible to calculate the uncertainty of average value by including the averaging in the model used by the MC calculations.

6. Conclusions

Uncertainty evaluation according to GUM Supplement 1 is a useful addition to quality tracking systems for natural gas grids. Especially for distribution grids where some of the output flow rates cannot be measured and are only estimated by load profiles, it is difficult to ensure that the calculated calorific values are reliable under all possible operating conditions without evaluating uncertainties.

Providing a complete result including measurement uncertainty for all calorific values characterising the reliability of the gas transport model and the reconstruction of state supports the decision that the results are ‘fit for its intended use’.

The uncertainty evaluation is not replacing a validation of the simulation model by real measurements. The uncertainty statement is not covering for differences between the model and the real system. It is a statement about the reliable of the results under the assumption that the model is correct. An evaluation of uncertainty is complementing the ongoing operation of quality tracking system, ensuring that all the results are meaningful over time.

References

[1] Altfeld, Klaus; Schley, Peter: Entwicklung der Erdgasbeschaffenheiten in Europa, *gwf Das Gas- und Wasserfach, Gas - Erdgas,* Jg.: 152, Nr.9, page 544-550, 2011.

[2] Guide to the Expression of Uncertainty in Measurement, International Organization for Standardization, 1995.

[3] Guide to the Expression of Uncertainty in Measurement Supplement 1: Propagation of distributions using a Monte Carlo method, JCGM 101:2008.

[4] Cathrin Schröder: Prozessbegleitende Simulation von regionalen Gasverteilnetzen mit unvollständiger Messinfrastruktur durch Einsatz eines Knotenlastbeobachters, Dissertation, TU Clausthal, Germany, 2009, ISBN 978-3-89720-998-5.

[5] Kessel, Rüdiger; Kacker, Raghu: Improved adaptive procedure to determine the necessary number of Monte Carlo trials to achieve the required numerical tolerance, International Conference on Advanced Mathematical and Computational Tools in Metrology and Testing IX, 2011.

Advanced MR Methods at Ultra-high Field (7 Tesla) for Clinical Musculoskeletal Applications

[1]S. Trattnig, [1]S. Zbyn, [1]B. Schmitt, [1]K. Friedrich, [1,2]V. Juras, [1,2]P. Szomolanyi, [1]W. Bogner

[1]MR Center of Excellence - High field MR, Department of Radiology, Medical University of Vienna/Vienna General Hospital, Vienna, Austria,
[2]Department of Imaging Methods, Institute of Measurement Science, Slovak Academy of Sciences, Bratislava, Slovakia
Email: siegfried.trattnig@meduniwien.ac.at

Abstract. *This presentation provides an overview of the initial clinical results of musculoskeletal studies performed at 7 Tesla, with special focus on sodium imaging, new techniques such as chemical exchange saturation transfer (CEST) and T_2* imaging, and multinuclear MR spectroscopy. Sodium imaging was clinically used at 7 Tesla in the evaluation of patients after cartilage repair procedures because it enables to monitor the GAG content, which is crucial for cartilage function, in non-invasive fashion. Sodium imaging and T_2* mapping allow insights into the ultra-structural composition of the Achilles tendon and help detect early stages of disease. Chemical exchange saturation transfer was, for the first time, successfully applied in the clinical set-up at 7 Tesla in patients after cartilage repair surgery. The potential of phosphorus MR spectroscopy in muscle was demonstrated in a comparison study between 3 and 7 Tesla, with higher spectral resolution and significantly shorter data acquisition times at 7 Tesla. Presented initial clinical studies demonstrate the potential of ultra-high field MR at 7 Tesla, with the advantage of significantly improved sensitivity for other nuclei, such as ^{23}Na (sodium) and ^{31}P (phosphorus). The application of non-proton imaging and spectroscopy provides new insights into physiology of healthy and diseased musculoskeletal tissues, particularly cartilage, tendons, and muscles.*

Keywords: 7 Tesla, Sodium MRI, gagCEST, T_2 Mapping, Phosphorus MR Spectroscopy, Musculoskeletal Radiology, MR Clinical Studies*

1. Introduction

By the end of the 1990s, high-field MRI at 3 Tesla had become the benchmark for routine clinical applications, as well as for clinical MRI research. The next important step was taken in the early 2000s and involved increasing the MRI field strength by another factor of approximately two, up to the 7 Tesla. During the last several years, the number of finalized installations or installations under preparation has increased to about 40 (0.2% of the currently installed MR systems). This rapid increase indicates the growing interest in ultra-high-field MRI in the bio-imaging community, brought to the fore by promising results with regard to morphological detail, as well as functional imaging capability.

Most clinical MR research centers operating at 7 Tesla primarily focus on neuroradiological applications, with only a few sites performing whole-body clinical research at 7 Tesla. This is because of the limited availability of suitable transmit/receive coils for 7 Tesla, the higher B_0 and B_1 heterogeneity related to the ultra-high field, as well as safety issues, particularly about 22 times higher specific absorption rate at 7 Tesla compared to 3 Tesla.

This presentation provides an overview of the initial clinical results of musculoskeletal studies performed at 7 Tesla, with a special focus on sodium imaging, new techniques such as

chemical exchange saturation transfer (CEST) and T_2* imaging, as well as multinuclear metabolic imaging or MR spectroscopy (MRS) in tissues such as cartilage, tendons, and muscles.

2. Subject and Methods

Sodium MRI at 7 Tesla - Sodium Imaging of Cartilage and Cartilage Repair

Proton MRI at ultra-high-field (7 Tesla and above) MR systems poses various challenges, including radiofrequency power deposition, increased chemical shift, susceptibility artifacts, homogeneity of RF coils, and changes in relaxation times, compared to lower-field clinical MR systems. These problems are much less pronounced in nuclei with a low gyromagnetic ratio, such as sodium (^{23}Na). However, a 3.8-fold smaller gyromagnetic ratio, a lower resonance frequency (^{23}Na: 78.6 MHz vs. ^{1}H: 297.2 MHz), a significantly shorter T_2 relaxation time, and a lower concentration of sodium nuclei (^{23}Na: 300 mM vs. ^{1}H: 110 M) result in sodium MR signal in articular cartilage that is 1/4,000–1/5,000 smaller than the proton MR signal. In order to achieve sufficiently high SNR (SNR>15), sodium MRI requires longer measurement times (15–40 min) and results in low-resolution images. Ultra-high-field MR systems can provide higher intrinsic ^{23}Na SNR and/or higher spatial/temporal resolution and improved contrast in the image [1, 2]. The MR relaxation properties of sodium nuclei in biological systems are dominated by quadrupolar interactions and result in very short longitudinal (T_1) and transverse relaxation (T_2) times. Due to the short T_1 of sodium, rapid averaging can be used in sodium MRI in order to improve the SNR in image. Many recent studies on sodium MRI of articular cartilage at 7 Tesla have used MR techniques with non-Cartesian k-space trajectories, such as 3D radial [3-7] or 3D cones [2], which enable ultra-short echo time (UTE) acquisition.

Sodium MRI offers many potential clinical applications. Sodium content measured by ^{23}Na MRI has been shown to be proportional to glycosaminoglycan (GAG) content in articular cartilage [8, 9]. Sodium MRI can be used to detect early signs of cartilage degeneration or injury before morphological changes can be detected by proton MRI [10]. Sodium MRI may enable the noninvasive in vivo evaluation of disease-modifying treatments for osteoarthritis (OA) and methods for cartilage repair. Affecting millions of people, OA is the most common degenerative disease of the musculoskeletal system

Sodium Imaging of Tendons

Degeneration of the Achilles tendon leads to thickening of the tendon [11]. Tendinopathy is also accompanied by disaggregation of the microfibrillar bundles due to the greater quantities of water and proteoglycan [12]. Almost double the GAG content was observed in pathologic tendons in studies using biochemical assays [13]. In a study by Juras et al., the feasibility of sodium magnetic resonance imaging for the diagnosis of Achilles tendinopathy was investigated at ultra-high field [14]. Their cohort comprised 20 healthy volunteers with no history of pain in the Achilles tendon and 8 patients with clinical findings of chronic Achilles tendinopathy. The study found that the mean bulk sodium SNR in Achilles tendon was 4.9±2.1 in healthy control subjects and 9.3±2.3 in patients with Achilles tendinopathy. This study not only showed a statistically significant increase in sodium SNR in patients with Achilles tendinopathy, compared with healthy tendons, but also revealed abnormal sodium signal values in the whole tendon, as well as morphologically focal abnormalities with focal thickening. Sodium signal values may correspond to GAG content in the Achilles tendon, which, as shown in in vitro studies, is increased with tendinopathy.

T_2 Mapping of the Achilles Tendon at 7 Tesla*

MRI is quite frequently used for morphological evaluation of the Achilles tendon (AT). It was successfully employed to detect partial or total tendon rupture or even the degenerative

processes in the tendon tissue. Most imaging findings are related to the pathologic processes of tendon degeneration and repair progression [15]. In addition to the morphological MRI evaluation (imaged predominantly by T_2*-weighted sequences), the quantitative MRI analysis of tendon tissue may be helpful in identifying the early pathological changes in the tissue. Quantitative analysis of the relaxation or diffusion constants [such as T_1, T_2*, $T_1\rho$, and apparent diffusion coefficient (ADC)] of the AT may provide additional information about the overall condition of the tendon. On conventional high-field MR systems (1.5–3 Tesla), several parameters have been investigated as prospective markers for Achilles tendon degeneration, such as T_2* [16], $T_1\rho$ [17], ADC [18], magnetisation transfer [19], or spectroscopically, even T_2 [20]. Using spectroscopic methods, it was shown that the T_2* decay in the Achilles tendon is a multicomponent process [21]. However, with clinical sequences, it is difficult to acquire signal from the second, third, and fourth components, since these have a small component ratio. The first component has the largest ratio, but it is in the submillisecond range, and thus, can barely be acquired with conventional sequences. In general, MR imaging of rapidly relaxing tissues, such as tendons, menisci, ligaments, and bones, is rather difficult with clinical sequences. Recent developments in new hardware and sequence design allow the acquisition of a signal directly from these tissues. Moreover, ultra-high field provides a substantial increase in the SNR [1]. The 3D-UTE sequence provides the ability to detect MR signal from a large variety of rapidly relaxing tissues and materials, including tendons. Juras et al. used a 3D-UTE sequence at 7 Tesla to estimate T_2* in tendons in order to investigate the potential feasibility of using this parameter as a marker for Achilles tendinopathy [22].

Chemical Exchange Saturation Transfer (CEST) at 7 Tesla

Saturation transfer (ST) is a commonly used technique in nuclear magnetic resonance (NMR) [23] and has been proposed as a method for the direct detection of chemical exchange between bulk water protons and protons bound to solutes [24]. The resultant MR imaging scheme is referred to as CEST MRI [25, 26]. The basic principle of CEST imaging is a reduction in bulk water MR signal after off-resonant spins are selectively pre-saturated by radiofrequency (RF) irradiation and then undergo chemical exchange with bulk water protons [27]. The hydroxyl and amide protons of glycosaminoglycans (GAG) provide exchange properties that render them principally suited for CEST experiments [28]. In vitro experiments at 11.7 Tesla demonstrated that CEST imaging can be used as a biomarker for cartilage GAG content (gagCEST) in bovine cartilage samples [29, 30]. However, GAG–OH protons resonate at frequency offsets ($\Delta\omega$) of only 1 and 1.5–2 ppm downfield from bulk water, and rate constants of chemical exchange (k) can be on the order of 1,000 s^{-1} [30]. At a magnetic field strength of 3.0 T, the $\Delta\omega$ of hydroxyl protons corresponds to a separation from bulk water of 128 Hz and 192–256 Hz in frequency units. As a consequence, radiofrequency power intended to selectively saturate –OH resonances simultaneously attenuates the bulk water signal (RF spillover), which impairs quantification of the CEST effect at 3.0 T. At higher fields, i.e., with increasing frequency differences, the RF spillover decreases, making ultra-highfield strengths, such as 7.0 T, ultimately favorable for CEST experiments.

After the introduction of the gagCEST approach, further studies have been performed with animals and humans to assess the feasibility of gagCEST imaging in vivo [31-33], and several imaging sequences for fast and reliable detection of gagCEST effects have been proposed [31, 34-36]. Most techniques are based on multiple image acquisition with pre-saturation at different offset frequencies ($\Delta\omega$). The remaining bulk water signal (MSat), normalised to a reference (MRef), is then plotted against the RF presaturation offset (z-spectrum).

Despite the requirements mentioned above, gagCEST imaging is a valuable tool for the non-invasive assessment of GAG content in vivo. A recent study demonstrated that gagCEST can

be used to reliably detect GAG in the knee cartilage of patients who had undergone cartilage repair surgery [37]. This study was conducted at 7.0 T with a 3D GRE-based measurement technique, and ^{23}Na MRI was used as a reference for GAG measurements. Moreover, the potential of gagCEST for GAG evaluation in intervertebral discs at 3.0 T has been demonstrated [38, 39]. Given the results from the latter studies, it seems possible that gagCEST can also be used to detect cartilage GAG content at 3 Tesla, which indicates the potential of this approach for use in the clinical routine. The main strength of gagCEST compared to other GAG-sensitive imaging techniques, such as dGEMRIC and sodium imaging, is the relatively short acquisition time, which covers the entire volume of a knee joint in approximately 10 min [37], and gagCEST does not require administration of contrast agent and can easily be implemented into a standard imaging protocol.

Metabolic Imaging of Muscles at 7 Tesla

Another MR method that has the potential to become increasingly important in clinical musculoskeletal MR at 7 Tesla is metabolic imaging or MR spectroscopy (MRS). MRS is a powerful noninvasive tool for the investigation of metabolite concentrations and studies of bioenergetics that could otherwise only be assessed by invasive muscle biopsies [40]. MRS provides information on a cellular level beyond the anatomical information assessed by standard imaging methods and aids in the understanding of various lesions [40-42], clinical diagnosis [42, 43], and treatment monitoring [44, 45].

The availability of fast and robust MRS methods at 7 Tesla will provide new opportunities for imaging a large clinical spectrum of musculoskeletal diseases, such as mitochondrial disorders [46, 47], glycolytic defects [48], systemic diseases affecting muscle metabolism [42], muscle injury [49], or diabetes [50, 51], for diagnostic use [42, 43], therapy monitoring [44, 45], and clinical research [42].

3. Conclusions

In conclusion, initial clinical studies demonstrate the potential of ultra-high-field MR at 7 Tesla, with the advantage of significantly improved sensitivity for other nuclei, such as ^{23}Na (sodium) and ^{31}P (phosphorus). This will provide new insights into physiology of healthy and diseased musculoskeletal tissues and the metabolism of muscle, and will, therefore, provide new in vivo clinical applications.

Acknowledgements

Funding for this study was provided by Vienna Spots of Excellence des Wiener Wissenschafts- und Technologie-Fonds (WWTF) and Vienna Advanced Imaging Center; grant sponsor: VIACLIC and the Slovak Scientific Grant Agency VEGA; grant number: 2/0090/11.

References

[1] Regatte RR, Schweitzer ME. Ultra-high-field MRI of the musculoskeletal system at 7.0T. *J Magn Reson Imaging*. 2007;25:262-9.

[2] Staroswiecki E, Bangerter NK, Gurney PT, et al. In vivo sodium imaging of human patellar cartilage with a 3D cones sequence at 3 T and 7 T. *J Magn Reson Imaging*. 2010;32:446-51.

[3] Wang L, Wu Y, Chang G, et al. Rapid isotropic 3D-sodium MRI of the knee joint in vivo at 7T. *J Magn Reson Imaging*. 2009;30:606-14.

[4] Madelin G, Lee JS, Inati S, et al. Sodium inversion recovery MRI of the knee joint in vivo at 7T. *Journal of Magnetic Resonance*. 2010;207:42-52.

[5] Madelin G, Chang G, Otazo R, et al. Compressed sensing sodium MRI of cartilage at 7T: Preliminary study. *J Magn Reson*. 2011; 214: 360-5.

[6] Madelin G, Babb JS, Xia D, et al. Reproducibility and repeatability of quantitative sodium magnetic resonance imaging in vivo in articular cartilage at 3 T and 7 T. *Magn Reson Med*. 2012; 68: 841-849.

[7] Madelin G, Jerschow A, Regatte RR. Sodium relaxation times in the knee joint in vivo at 7T. *NMR Biomed*. 2012; 25: 530-537.

[8] Wheaton AJ, Borthakur A, Dodge GR, et al. Sodium magnetic resonance imaging of proteoglycan depletion in an in vivo model of osteoarthritis. *Acad Radiol*. 2004; 11: 21-28.

[9] Shapiro EM, Borthakur A, Gougoutas A, et al. 23Na MRI accurately measures fixed charge density in articular cartilage. *Magn Reson Med*. 2002; 47: 284-91.

[10] Reddy R, Insko EK, Noyszewski EA, et al. Sodium MRI of human articular cartilage in vivo. *Magn Reson Med.* 1998; 39: 697-701.

[11] Schweitzer ME, Karasick D. MR imaging of disorders of the Achilles tendon. *American Journal of Roentgenology*. 2000; 175: 613-625.

[12] Samiric T, Parkinson J, Ilic MZ, et al. Changes in the composition of the extracellular matrix in patellar tendinopathy. *Matrix Biology*. 2009; 28: 230-236.

[13] Fu SC, Chan KM, Rolf CG. Increased deposition of sulfated glycosaminoglycans in human patellar tendinopathy. *Clinical Journal of Sport Medicine*. 2007; 17: 129-134.

[14] Juras V, Zbyn S, Pressl C, et al. Sodium MR Imaging of Achilles Tendinopathy at 7 T: Preliminary Results. *Radiology*. 2012; 262: 199-205.

[15] Gelberman RH, Manske PR, Vande Berg JS, et al. Flexor tendon repair in vitro: a comparative histologic study of the rabbit, chicken, dog, and monkey. *J Orthop Res*. 1984; 2: 39-48.

[16] Robson MD, Benjamin M, Gishen P, et al. Magnetic resonance imaging of the Achilles tendon using ultrashort TE (UTE) pulse sequences. *Clin Radiol.* 2004; 59: 727-35.

[17] Du J, Carl M, Diaz E, et al. Ultrashort TE T1rho (UTE T1rho) imaging of the Achilles tendon and meniscus. *Magn Reson Med*. 2010; 64: 834-42.

[18] Fechete R, Demco DE, Eliav U, et al. Self-diffusion anisotropy of water in sheep Achilles tendon. *NMR Biomed.* 2005; 18: 577-86.

[19] Hodgson RJ, Evans R, Wright P, et al. Quantitative magnetization transfer ultrashort echo time imaging of the Achilles tendon. *Magn Reson Med.* 2011; 65: 1372-6.

[20] Henkelman RM, Stanisz GJ, Kim JK, et al. Anisotropy of NMR properties of tissues. *Magn Reson Med*. 1994; 32: 592-601.

[21] Peto S, Gillis P. Fiber-to-field angle dependence of proton nuclear magnetic relaxation in collagen. *Magn Reson Imaging.* 1990; 8: 705-12.

[22] Juras V, Zbyn S, Pressl C, et al. Regional variations of T 2* in healthy and pathologic achilles tendon in vivo at 7 Tesla: Preliminary results. *Magnetic Resonance in Medicine.* 2012; 68: 1607-1613.

[23] Forsen S, Hoffman RA. Study of Moderately Rapid Chemical Exchange Reactions by Means of Nuclear Magnetic Double Resonance. *Journal of Chemical Physics*. 1963; 39: 2892.

[24] Guivel-Scharen V, Sinnwell T, Wolff SD, et al. Detection of proton chemical exchange between metabolites and water in biological tissues. *Journal of Magnetic Resonance*. 1998; 133: 36-45.

[25] Ward KM, Aletras AH, Balaban RS. A new class of contrast agents for MRI based on proton chemical exchange dependent saturation transfer (CEST). *Journal of Magnetic Resonance*. 2000; 143:79-87.

[26] Ward KM, Balaban RS. Determination of pH using water protons and chemical exchange dependent saturation transfer (CEST). *Magnetic Resonance in Medicine*. 2000; 44: 799-802.

[27] Zhou JY, van Zijl PCM. Chemical exchange saturation transfer imaging and spectroscopy. *Progress in Nuclear Magnetic Resonance Spectroscopy*. 2006; 48: 109-136.

[28] Ling W, Regatte RR, Schweitzer ME, et al. Characterization of bovine patellar cartilage by NMR. Nmr in Biomedicine. 2008; 21: 289-295.

[29] Ling W, Eliav U, Navon G, et al. Chemical exchange saturation transfer by intermolecular double-quantum coherence. *Journal of Magnetic Resonance.* 2008; 194: 29-32.

[30] Ling W, Regatte RR, Navon G, et al. Assessment of glycosaminoglycan concentration in vivo by chemical exchange-dependent saturation transfer (gagCEST). Proceedings of the National Academy of Sciences of the United States of America. 2008; 105: 2266-2270.

[31] Schmitt B, Bock M, Stieltjes B, et al. A new, 3D GRE based CEST imaging method for clinical application and verification with gagCEST in articular cartilage. Proceedings 18th Scientific Meeting, International Society for Magnetic Resonance in Medicine, Stockholm. 2010: 6237.

[32] Vinogradov E, Ivanishev A, Grant AK, et al. CEST and Sodium Imaging of Glycosaminoglycans in-vivo in the 3T: Preliminary Results. Proceedings 18th Scientific Meeting, International Society for Magnetic Resonance in Medicine, Stockholm. 2010:5900.

[33] Fenty M, Kassey V, Kogan F, et al. Feasibility of CEST imaging on the guinea pig stifle at 9.4 T. Proceedings 19th Scientific Meeting, International Society for Magnetic Resonance in Medicine, Montreal. 2011: 2766.

[34] Vinogradov E, Lenkinski RE. Detection of Glycosaminoglycans using Positive CEST approach. Proceedings 18th Scientific Meeting, International Society for Magnetic Resonance in Medicine, Stockholm. 2010: 5404.

[35] Varma G, Alsop DC, Lenkinski RE, et al. Optimization of pulsed-gagCEST at 3.0T. Proceedings 19th Scientific Meeting, International Society for Magnetic Resonance in Medicine, Montreal. 2011: 2770.

[36] Varma G, Lenkinski RE, Vinogradov E. Keyhole Chemical Exchange Saturation Transfer. Proceedings 19th Scientific Meeting, International Society for Magnetic Resonance in Medicine, Montreal. 2011: 2775.

[37] Schmitt B, Zbyn S, Stelzeneder D, et al. Cartilage Quality Assessment by Using Glycosaminoglycan Chemical Exchange Saturation Transfer and (23)Na MR Imaging at 7 T. Radiology. 2011; 260: 257-264.

[38] Ling W, Saar G, Regatte R, et al. Assessing the Inververtebral Disc via gagCEST. Proceedings 17th Scientific Meeting, International Society for Magnetic Resonance in Medicine, Honolulu. 2009: 293.

[39] Kim M, Chan Q, Anthony MP, et al. Assessment of glycosaminoglycan distribution in human lumbar intervertebral discs using chemical exchange saturation transfer at 3 T: feasibility and initial experience. *NMR in Biomedicine*. 2011; 24: 1137-1144.

[40] Boesch C. Musculoskeletal spectroscopy. *Journal of Magnetic Resonance Imaging*. 2007; 25: 321-338.

[41] Lindquist D. What can 31P MR spectroscopy tell us about muscle disease? *Radiology*. 2008; 247: 1-2.

[42] Taylor DJ. Clinical utility of muscle MR spectroscopy. *Semin Musculoskelet Radiol.* 2000; 4: 481-502.

[43] Ko SF, Huang CC, Hsieh MJ, et al. 31P MR spectroscopic assessment of muscle in patients with myasthenia gravis before and after thymectomy: initial experience. *Radiology*. 2008; 247: 162-169.

[44] Taivassalo T, Matthews PM, DeStefano N, et al. Combined aerobic training and dichloroacetate improve exercise capacity and indices of aerobic metabolism in muscle cytochrome oxidase deficiency. *Neurology*. 1996; 47: 529-534.

[45] Lodi R, Hart PE, Rajagopalan B, et al. Antioxidant treatment improves in vivo cardiac and skeletal muscle bioenergetics in patients with Friedreich's ataxia. *Annals of Neurology*. 2001; 49: 590-596.

[46] Kuhl CK, Layer G, Traber F, et al. Mitochondrial Encephalomyopathy - Correlation of P-31 Exercise Mr Spectroscopy with Clinical Findings. *Radiology*. 1994; 192: 223-230.

[47] Taylor DJ, Kemp GJ, Radda GK. Bioenergetics of Skeletal-Muscle in Mitochondrial Myopathy. Journal of the Neurological Sciences. 1994; 127: 198-206.

[48] Duboc D, Jehenson P, Dinh ST, et al. Phosphorus Nmr-Spectroscopy Study of Muscular Enzyme Deficiencies Involving Glycogenolysis and Glycolysis. *Neurology*. 1987; 37: 663-671.

[49] Mccully KK, Argov Z, Boden BP, et al. Detection of Muscle Injury in Humans with 31-P Magnetic-Resonance Spectroscopy. Muscle & Nerve. 1988; 11: 212-216.

[50] Szendroedi J, Schmid AI, Meyerspeer M, et al. Impaired Mitochondrial Function and Insulin Resistance of Skeletal Muscle in Mitochondrial Diabetes. *Diabetes Care*. 2009; 32: 677-679.

[51] Phielix E, Mensink M. Type 2 diabetes mellitus and skeletal muscle metabolic function. *Physiology & Behavior*. 2008; 94: 252-258.

Theoretical Problems of Mesurement

Tail Probability Calculator by Characteristic Function Inversion

[1]T. Duby, [2]G. Wimmer, [3]V. Witkovský

[1]Agilent Technologies Ltd, Yarnton, Oxford, Great Britain,
[2]Institute of Mathematics and Statistics, Masaryk University, Brno, Czech Republic,
Mathematical Institute, Slovak Academy of Sciences, Bratislava, Slovakia,
Faculty of Natural Sciences, Matej Bel University, Banská Bystrica, Slovakia,
[3]Institute of Measurement Science, Slovak Academy of Sciences, Bratislava, Slovakia,
Email: tomy@duby.co.uk

Abstract. *We are developing a computer program to calculate tail probabilities of random variables from their characteristic functions. This code written in Matlab and is an implementation of method described in [1]. We present some practical results. The need for such calculations appears naturally e.g. in metrology: in the problem of calibration [2] and/or in determination of the reference values in interlaboratory comparisons [3]. Currently, as suggested by GUM and its Supplement 1 [4], such problems are typically solved by propagation of distributions using a Monte Carlo method.*

Keywords: Characteristic Function, Inversion of Characteristic Function Tail Probability Calculation

1. Introduction

In advanced statistical analysis there is sometimes the need to deal with linear combination of *N* independent random variables. If these have probability density functions, pdf's, then the pdf of the linear combination is the convolution of the individual pdf's. This may be a computationally intensive task as it requires evaluation of an $N-1$ dimensional integral. And the evaluation of tail probability adds on top of this one more integration. (If $F_X(x)$ is the cumulative distribution function, cdf, of random variable *X*, then its tail probability is defined as $1-F_X(x)$.) Similarly, the Monte Carlo method [4, page 27] is computationally demanding.

Using characteristic functions of random variables to calculate the tail probability eliminates the need for numerical evaluation of an *n*-dimensional integral. The calculation reduces to evaluation of a single integral. Though it involves integrating of an oscillatory integrand over the whole real line, which has its own difficulties, in certain cases this evaluation can be efficiently performed.

In this paper we present the first results obtained from a computer program developed for efficient calculation of tail probabilities of a linear combination of continuous random variables.

2. Subject and Methods

Linear Combination of Random Variables

The following property of characteristic function makes it attractive for above mentioned calculations: Let $X_i, i=1,\dots,N$ be independent random variables with characteristic functions $\varphi_{X_i}(t)$. Then the characteristic function of random variable Z, $\varphi_Z(t)$, defined as the linear combination of random variables X_i with real constant coefficients a_i, that is

$$Z=\sum_{i=1}^{N} a_i X_i, \tag{1}$$

is given by

$$\varphi_Z(t)=\prod_{i=1}^{N} \varphi_{X_i}(a_i t). \tag{2}$$

Inversion of the Characteristic Function

Over the years a number of methods were developed to obtain the cdf (or tail probability) from the characteristic function. Gil-Pelaez's inversion formula from 1951, [5] looks simple

$$F_X(x) = \frac{1}{2} - \frac{1}{\pi} \int_0^\infty \frac{\Im\left(e^{-itx}\varphi_X(t)\right)}{t}\, dt \tag{3}$$

where $\Im(\cdot)$ is the imaginary part. As the above integral is an improper one, its numerical evaluation is the source of two kinds of errors: error due to truncation, ϵ_t, and error due numerical approximation of the truncated integral, ϵ_a. Experience has shown that extended (or compound) trapezoidal rule "tends to work well for oscillating integrals because the errors tend to cancel" [3, page 18]. This is the formula for extended trapezoidal rule

$$\int_a^b f(x)dx = h\left[\frac{f(a)}{2} + f(a+h) + \cdots f(a+(N-1)h) + \frac{f(b)}{2}\right] + \epsilon_a \tag{4}$$

where N is the number of intervals into which the original (finite) integration range is subdivided, $h = (b-a)/N$ is the step size. The error due to numerical approximation is

$$e_a = -\frac{(b-a)\,h^2}{12}\, f''(\xi),\ \ a < \xi < b, \tag{5}$$

provided the second derivative of function f exist.

R. Strawderman, [1] applied the theory of F. Stenger to evaluate of the integral in equation (3): Under certain conditions [7] when the integrand is analytic in a strip containing the path of integration, the error due to numerical approximation decreases exponentially with the step size h. Specifically, when function $g(z)$ is analytic on strip $D = \{z \in \mathbb{C}: |\Im(z)| < \pi/2\}$ then

$$\int_{-\infty}^{+\infty} g(x)dx = h \sum_{m=-\infty}^{+\infty} g(mh) + \epsilon_a \tag{6}$$[1]

where

$$|\epsilon_a| < N_D(g)e^{-\frac{\pi^2}{h}} \tag{7}$$

and $N_D(g)$ is some number depending on function g [7, equation 1.8]. This method is applicable for those random variables for which the moment generating function exists on an analytic strip $[c, d]$, where $-\infty \le c < 0 < d \le +\infty$.

Method

We are developing a computer program called TPC for **T**ail **P**robability **C**alculator for efficient and high precision calculation of cumulative distribution function, cdf (or tail probability) of arbitrary continuous random variable. It is written in Matlab [8] as its *anonymous function* feature allows the user to his / hers function and pass it name as an argument.

TPC requires the following mandatory inputs:

1. The characteristic function of the random variable as an anonymous function
2. Values of x (scalar of vector) for which to calculate the cdf / tail probability.

The following inputs are optional

1. Width of the analytic strip as a vector of length 2. If the user does not provide it the program attempts to find it.
2. Expected accuracy of the tail probability calculation. Default is 10^{-8}.

[1] Note that though the integral in the left hand side is an improper one we cannot avoid the truncation error as the summation in the right hand side needs to be truncated.

The simplified flowchart of the TCP program is shown in Figure 1

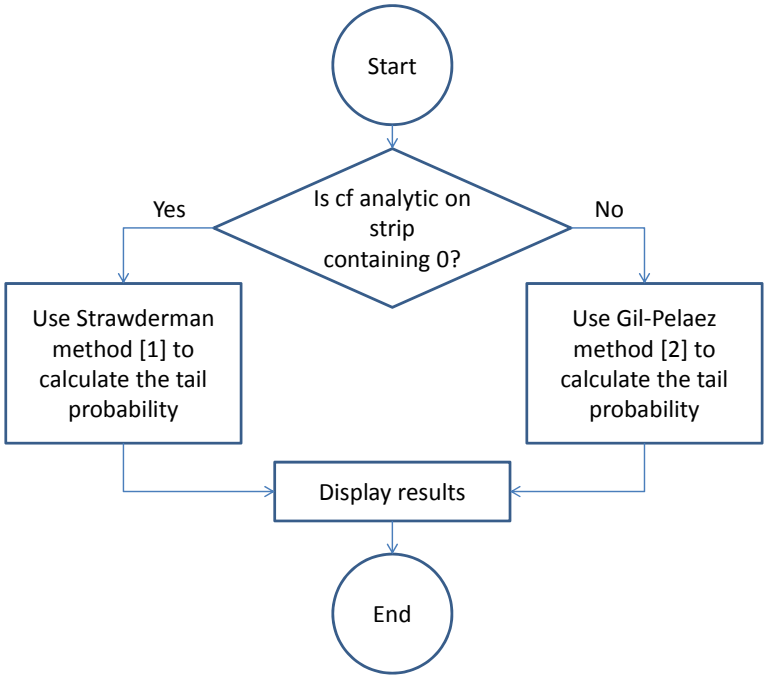

Figure 1: Overall flowchart of the TPC program.

3. Results

χ_1^2 distribution turned is a good case for testing this program: (1) its cdf is known in a closed formula, (2) its analytic strip is $[-\infty, 1/2]$, and (3) its characteristic function decays to zero as $t^{-\frac{1}{2}}$. Numerical results are presented in Table 1.

Table 1: Results of cumulative distribution function calculations of χ_1^2.

x	cdf of $\chi_1^2(x)$	Absolute error	No. of integrand subintervals
3	0.916735483336450	-4.4409e-16	243
10	0.998434597741998	-1.1102e-16	89
15	0.999892488823271	-1.1102e-16	58

A more complicated example can be found in [4, section 9.2.3]. Here the random variable X is the sum of four uniform random variables of unit standard deviation. In language of Matlab the characteristic function of X is defined as the anonymous function `fun923`:

```
bb = sqrt(3);
fun923 = @(t)cf_uniform(t,-bb,bb).^4;
```

where `cf_uniform(t,a,b)` is the author's Matlab function for cf of uniform distribution with limits `a` and `b`.[2] For this distribution the 95% coverage is known analytically [4, Appen-

[2] The standard deviation of uniform distribution with limits $[-a, a]$ is $\sigma = a/\sqrt{3}$.

dix E]. TPC gives for $x = 2\sqrt{3}\left[2 - \left(\frac{3}{5}\right)^{\frac{1}{4}}\right] = 3.879406741347821$ the tail probability is 0.025000000000001 giving a coverage of 94.9999999999998%.

4. Discussion

The computer program presented here based on [1] provides an efficient method to calculate tail probabilities by inversion of characteristic functions. For the sake of completeness the completed program will include methods that will calculate the tail probability in cases when assumptions of [1] do not hold: the random variable does not have a moment generating function.

Acknowledgements

The work was supported by the Slovak Research and Development Agency, grant APVV-0096-10.

References

[1] Strawderman R. Computing tail probabilities by numerical Fourier inversion: the absolutely continuous case. *Statistica Sinica*, 14: 175–201, 2004.

[2] Wimmer G, and Witkovský V. New procedure for calculating the uncertainty of one output quantity in calibration certificates. In *MEASUREMENT 2013, Proceedings of the 9th International Conference on Measurement 2013*. Smolenice, Slovakia, May 27−30, 2013. Submitted.

[3] Witkovský V, and Wimmer G. Method for evaluation of the key comparison reference value and its expanded uncertainty based on metrological approach. In *MEASUREMENT 2007, Proceedings of the 6th International Conference on Measurement 2007*. Smolenice, Slovakia, May 20−24, 2007, 26−29.

[4] Evaluation of measurement data — Supplement 1 to the "Guide to the expression of uncertainty in measurement" — Propagation of distributions using a Monte Carlo method, JCGM 101:2008.

[5] Gil-Pelaez J. Note on the inversion theorem, Biometrika, 38 (3/4): 481–482, 1951.

[6] Abate J and Whitt W, The Fourier-series method for inverting transforms of probability functions. *Queuing Systems*, 10: 5-88, 1992.

[7] Stenger F. Integration Formulae Based on the Trapezoidal Formula, *J. Inst. Maths Appliecs* 12: 103−114 1973.

[8] MathWorks, Inc., Natick, Massachusetts, U.S.A.

A Performance Comparison of HTM and DBN Models Applied to Visual Object Classification

[1,2]K. Valentín, [1]I. Bajla, [3,1]S. Štolc

[1]Institute of Measurement Science, Department of Theoretical Methods, Slovak Academy of Sciences, Bratislava, Slovakia
[2]Faculty of Mathematics, Physics, and Informatics, Department of Applied Informatics, Comenius University in Bratislava, Slovakia
[3]Austrian Institute of Technology, GmbH, Seibersdorf, Austria
Email: kristian.valentin@fmph.uniba.sk

Abstract. *In the paper we compare the performance of two Deep architecture models – Hierarchical Temporal memory (HTM) and Deep Belief Network (DBN) in the task of visual object classification. Both models utilize k-Nearest Neighbor classifier for the final object classification. We conduct two experiments in order to study invariance properties of the models with respect to object's rotation and scaling using image database of tree leaves containing 11 categories. Obtained results show that the HTM model outperforms the DBN model in both types of experiments.*

Keywords: Hierarchical Temporal Memory (HTM), Deep Belief Network (DBN), Visual Object Classification, Rotational and Scaling Invariance

1. Introduction

Both Hierarchical Temporal Memory (HTM) and Deep Belief Network (DBN) models can be framed into Deep architectures [1,2] which attracted attention of the computational neuroscience in the recent years. They are inspired by basic principles of information processing in the neocortex, but their structure, learning and inference algorithms differ in several aspects. They both aspire to solve problems of visual object classification, however, no comparative analysis of their performance in this area has been published yet. Therefore, the goal of this paper is to evaluate the performance of the HTM and DBN models on appropriate benchmark experiments. In particular, we are interested in how they tackle problems of the visual object classification invariant against scale and rotation geometrical transformations.

2. Description of Deep Architecture Models

Hierarchical Temporal Memory

Structurally, HTM [3,4] is a multi-layered hierarchical network. The hierarchy has a tree-shaped structure consisting of a set of basic computational units, called nodes. The nodes have receptive fields that are reflected in a way that nodes in the given layer are connected only to a subset of nodes in the previous layer. By ascending the hierarchy, the nodes "see" gradually growing portion of the network's input. Each node uses the very same learning and inference algorithm. Unlike many other methods, HTM combines spatial and temporal learning. For the temporal learning, a sequence of input data is needed. The sequence can be either natural (e.g., video stream) or it must be generated from a still image. The first step in learning a layer of nodes is spatial learning which produces a lossy compression in the spatial domain using vector quantization. Then the temporal learning takes the result of the spatial learning and by

exploiting the learned sequences it creates a spatio-temporal representation of the input data. The representation is stored in a hierarchy that is organized in such a way that the higher levels of the hierarchy cover larger parts of the input space and they correspond to longer durations of time. This all is done in semi-unsupervised manner. The only "teacher" is time that is based on assumption that patterns occurring close in time are mutually related. The inference is based on Bayesian belief propagation.

Deep Belief Network

Deep Belief Network (DBN) is a graphical probabilistic generative model composed of multiple layers of stochastic, latent variables [5]. The latent variables, often called hidden units or feature detectors, have usually binary values. The structure of DBN can be seen as a stack of restricted type of Boltzmann machines (RBM) [6]. Each RBM contains a layer of visible units that represent the data and a layer of hidden units that learn to represent features which capture higher-order correlations in data. The two layers are connected by a matrix of symmetrically weighted connections. There are no lateral connections between units in a layer. When two RBMs are to form a DBN, the layer with hidden units of the first RBM is linked with the layer with visible units of the second RBM. The top two layers form RBM. DBN trains one layer at a time starting from the bottom one. The values of the hidden units in one layer, when they are being inferred from data, are treated as the data for training the next layer. The training is based on the stochastic gradient descent method and uses contrastive divergence algorithm to approximate the maximum log-likelihood. The common way of how to use DBN for image classification tasks is a combination of unsupervised pre-training and subsequent supervised fine-tuning. This discriminative fine-tuning can be performed by adding a final layer of variables that represent the desired outputs and back-propagating error derivatives.

3. Comparison of HTM and DBN in a classification task of visual objects

In order to create a model of input data, HTM uses the "time as a teacher" concept, whereby the time is not inherently used in DBN, even if it can be adapted to learn sequences. This leads to a different learning procedure for HTM, where a learning sequence has to be generated from still input images, e.g., by moving an object smoothly within the field of view of the network. Designing an optimal HTM architecture with optimal values of the parameters is a non-trivial task, although, there is graceful performance degradation when parameters are set suboptimally. In the HTM networks, the node-sharing mode during learning with a combination of pooling algorithms, supports certain invariance to position, rotation and scale, whereas in the DBN networks, there is no such architectural or learning predetermination.

4. Experiments

Data

Based on preliminary tests carried out separately with DBN on a dataset of tree leaves, we have decided to use the same dataset for our comparative analysis. This dataset consists of 11 categories of five gray-scale images of size 64×64 pixels. Within each image there is always one object – a leaf – centered on the black background. The most important information for classification of the tree leaves is contained in their shape. In order to extract such a type of information regardless from the object's absolute brightness, we decided for using a well-known edge detection method – Canny edge detector (lower threshold=100, upper threshold=200). In the first step, we applied the edge detector to all original images, afterwards, the resulting contour images were used as equivalent inputs for both the HTM and DBN models.

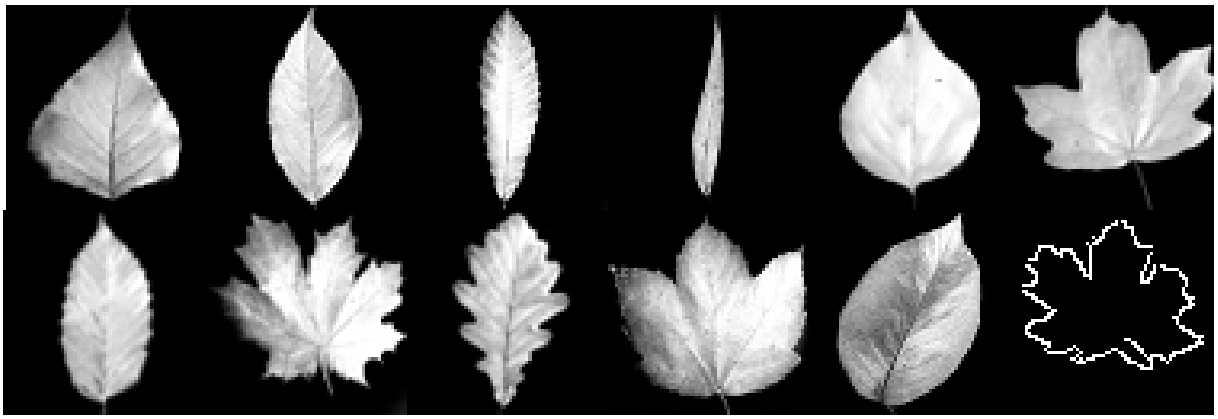

Fig. 1. Examples of 11 tree categories form the database leaves used. The bottom-right image shows the actual network's input obtained from the gray-scale image by application of the Canny edge detector.

To test the both network models in the task of invariant object classification, we conducted two types of experiments. The aim of Experiment 1 was to test the rotational invariance. The original images were rotated 12 times by 30 degrees which resulted altogether in 660 images. The aim of Experiment 2 was to test the invariance to scale of the objects within images. Leaves in original images were scaled randomly 5 times with scaling factor ranging between 0.5 and 1. The size of the dataset for this experiment was 275 images.

Set-up

In order to make the training conditions for both networks equivalent, we decided to require the same number of image pixels to be used for training. To satisfy this requirement, we adjusted the number of epochs in the case of DBN and the length of training sequences in the case of HTM. The other parameters were tuned empirically for the best results for these particular classification tasks and data. Moreover, the same classifier was used for both models, namely k-Nearest Neighbor (k-NN) with k=1.

The DBN network consisted of two hidden layers having 512 and 200 neurons. The learning rate for the training was set to 0.1, the batch size was set to 10, and the number of training epochs was set to 600.

The HTM network contained two levels of nodes. The nodes in 1st level were arranged to cover 8×8 pixels image regions. At 2nd level, the nodes formed 2×2 regions. The training sequence was generated using the random sweep explorer with 5000 iterations. The node-sharing mode was chosen for both levels. The values for 3 parameters of the spatial pooler and 2 parameters of the temporal pooler are listed in Table 1.

Table 1. *Parameters of the HTM network.*

Level	Spatial pooler			Temporal pooler	
	maxDistance	*sigma*	*maxCoincidenceCount*	*transitionMemory*	*maxTemporalGroupCount*
1	0.01	1.5	400	6	64
2	0.20	1.5	500	12	128

5. Results

Overall results of the two experiments are summarized in Table 2. The performance has been analyzed with respect to the perceptual split between data used for training and testing (i.e., 20:80, 30:70, 40:60, and 50:50). That gave us a clearer picture about inherent capabilities of each tested model regarding generalization and learned invariances. As a baseline, we provide

also performance of the k-NN (k=1) classifier applied to the original input data (edge images). Each experiment has been performed 20 times for each split factor to allow for calculating averaged classification accuracy values and associated standard deviations.

Table 2. *The average classification accuracy values in % and associated standard deviations obtained by the tested models. Experiments 1 and 2 refer to the rotational and scale invariance, respectively.*

Train set vs. test set in %	Classification accuracy in % (stdev)					
	Experiment 1			Experiment 2		
	k-NN	*DBN & k-NN*	*HTM & k-NN*	*k-NN*	*DBN & k-NN*	*HTM & k-NN*
20:80	34.54 (1.52)	56.07 (2.41)	63.53 (1.91)	17.75 (2.13)	39.43 (5.51)	57.31 (3.81)
30:70	37.75 (1.30)	60.92 (3.04)	69.90 (1.99)	17.95 (1.19)	50.67 (4.85)	61.34 (3.53)
40:60	38.33 (1.25)	64.10 (2.32)	73.35 (2.90)	19.79 (2.19)	64.18 (2.14)	65.39 (3.87)
50:50	38.82 (1.09)	66.76 (2.91)	75.36 (2.46)	20.10 (1.77)	58.80 (3.48)	66.44 (3.48)

6. Conclusions

In this paper we provide a comparative study on the performance of the Deep Belief Network (DBN) and Hierarchical Temporal Memory (HTM) models in the task of invariant object classification of tree leaves selected from a benchmark image database. For both compared network models, we have considered the k-NN classifier. As a baseline, we applied k-NN in the input (edge feature) space too.

The following conclusions can be drawn from the obtained results:

- both network models yield classification accuracy (CA) values significantly greater than those achieved in the original data space,
- the improvement of CA when increasing the ratio of training images is apparent; in the case of Experiment 1, CA of DBN improved by 10.69% while CA of HTM improved even more by 11.83%,
- finally, for both the rotational and scale invariance experiments, HTM significantly outperforms the results achieved by DBN.

Acknowledgements

This work has been supported by the Slovak Grant Agency for Science (project No. 2/0043/13).

References

[1] Bengio, Y. (2009). Learning Deep Architectures for AI. Foundations and Trends in Machine Learning, 2(1), 1-127.

[2] Arel, I., Rose, D., and Karnowski T. (2010). Deep machine learning - a new frontier in artificial intelligence research. IEEE Computational Intelligence Magazine, 5:13-18.

[3] Hawkins, J. and Blakeslee, S. (2004). On intelligence. Henry Holt and Company, New York.

[4] George, D. and Hawkins, J. (2009). Towards a mathematical theory of cortical micro-circuits. PLoS Computational Biology 5(10). DOI 10.1371/journal.pcbi.1000532.

[5] Hinton, GE. (2009). Deep belief networks. Scholarpedia, 4(4):5947.

[6] Hinton, GE. and Sejnowski, TJ. (1983). Optimal Perceptual Inference. In Proceedings of the IEEE conference on Computer Vision and Pattern Recognition, 448-453, Washington DC.

Comparison of Novel Methods for Correlation Dimension Estimation

[1]H. Budáčová, [2,1]S. Štolc

[1]Institute of Measurement Science, Department of Theoretical Methods,
Slovak Academy of Sciences, Bratislava, Slovakia

[2]Austrian Institute of Technology, GmbH, Seibersdorf, Austria

Email: hana.budacova@savba.sk

Abstract. *We introduced and implemented two numerical methods, which estimate the correlation dimension from a finite set of data. The first is focused on identification of the scaling region in the correlation sum computed from the data. We find candidates for the linear region of various lengths and then combine the obtained results to compute the correlation dimension estimate. The second method uses Gaussian mixture method to predict behavior of the correlation integral and location of the scaling region. The aim of this paper is to compare these methods on various datasets with known correlation dimension.*

Keywords: Chaotic Attractors, Correlation Dimension, Scaling Region, Gaussian Mixture Model

1. Introduction

Correlation dimension is a measure of the dimensionality of a set of points and can be understood as a parameter that characterizes the complexity of strange attractors. It is a frequently used tool for detecting chaotic behavior in dynamical systems. According to [1] the correlation dimension (further denoted as D_2) of the attractor reconstructed from one variable using time delays and embeddings in higher dimensions is equal to the correlation dimension of the original attractor. These results engendered an extensive study of computational estimates of D_2 from measured data. In practice, this property can be used to help us understand the dynamics of many biological, chemical, climatological or financial dynamical systems.

In the past decades, the computational power experienced a rapid development. That leaves space for further improvements of methods that compute D_2 more accurately.

Definition of Correlation Dimension

Let us denote $x_1, x_2, \cdots, x_N$ the set of k-dimensional data points lying on a chaotic attractor of our interest. We follow the Grassberger-Procaccia algorithm [2] and define the correlation sum $C(r)$ as

$$C(r) = \frac{2}{N(N-1)} \sum_{i=1}^{N} \sum_{j=i+1}^{N} \Theta\left(r - \left\|x_i - x_j\right\|\right) \tag{1}$$

where $\|\cdot\|$ computes the Euclidean distance, N is the number of the data points, $\Theta(\cdot)$ is called Heaviside function defined by

$$\Theta(s) = \begin{cases} 1 & \text{for } s > 0, \\ 0 & \text{for } s \leq 0. \end{cases} \tag{2}$$

The right-hand side of the Eq. (1) computes number of pairs of given data points whose distance is less than some given radius $r > 0$, normalized by the total number of pairs. Equivalently, it is the cumulative distribution of probability that two random points from given dataset are closer than r.

Furthermore, it can be interpreted as an estimate of the cumulative distribution of probability of the pair distances of the data on the original attractor.

Taking increasingly larger data sets, the probability is expected to behave as the power law r^{D_2} for small r. Subsequently, the logarithm of the correlation sum $C(r)$ is expected to be a linear function of the logarithm of r for small r. The correlation dimension is defined as the slope of this linear function, i.e.,

$$D_2 = \lim_{r \to 0} \lim_{N \to \infty} \frac{\partial \ln(C(r))}{\partial \ln(r)} \tag{3}$$

Problems with Finite Datasets

In practice, we encounter only finite datasets. Hence, the Eq. (3) cannot be applied exactly in practical computations. Our choice of the size of the dataset is restricted by various factors from measurement requirements and limitations (practical reasons) to time complexity of computations (computational reasons).

Due to the self-similarity of strange attractor, we assume that $\ln(C(r))$ behaves as a linear function of $\ln(r)$ for some range of r. The key problem is to detect this so-called scaling region. The size of the dataset limits the smallest reasonable choice of r. For very small r, due to the lack of data, there are none or only a few pairs within such a small distance. That makes $C(r)$ a poor estimate of the cumulative distribution function of pair distances for such small values. For r that approaches the actual size of the attractor, the edge effects begin to play an important role and $\ln(C(r))$ is no longer linear, but becomes saturated.

In the past years, the most common method to find the scaling region was the so-called visual inspection. The plot of $\ln(C(r))$ was shown to an expert, who decided where the linear region was and the slope in this region was denoted as D_2. Many have tried to improve and automatize this method. Surprisingly, many ideas failed, giving poorer results than this oracular method. In [3], the method where the middle quarter of the vertical axis is used to determine the scaling region (the time series is normalized to [0,1]) is mentioned. In [4] the approximation of $\ln(C(r))$ by a sum of linear and non-linear functions of $\ln(r)$ is used, followed by the limit of r to 0. The nonlinear term is chosen so that its limit is 0. This approach gives very good results especially for some systems with slow convergence. A new method using K-means is introduced in [5]. The latter paper contains also citations of several notable methods examined recently.

Aside from the aforementioned problems we also need to be careful with temporal and geometrical correlations. In a time series some points are close not due to geometrical attributes of the attractor, but due to the closeness in time. This was proven to cause underestimation of the correlation dimension and the cure called the Theiler window was introduced in [6]. Another factor that can affect the accuracy of computed results is the embedding dimension of the data. The higher the dimension, the more data we need to capture the attractor. The estimate of the size of the dataset and the underestimation of correlation dimension in case of deficient data can be found for example in [7]. In this paper we overcame these last two problems by choosing N to be large enough.

2. Subject and Methods

We propose two methods, each with its own way of dealing with the problem of identification of the scaling region. The main aim of our work was to find a method, which is accurate, fast and can be used to evaluate D_2 automatically for large datasets.

Method 1: Linear Region Finding (LRF)
In the first method we begin with computation of the correlation sum for logarithmically equidistant values of r. The data are normalized, so that the size of attractor is less than 1. We concentrate on finding the region on which $\ln(C(r))$ is linear and this region has certain defined length. For this purpose we use linear regression and least square method to compute and compare the error terms. Then we compare the obtained values of slopes and the position of these regions for various lengths and combine these results to obtain the value of D_2.

This method can be considered as an improved visual inspection method, with the slight difference that not the expert, but the computer chooses the linear region and computes D_2.

Method 2: Gaussian Mixture Model (GMM)
In the second method we use a two-pass approach to estimation of the cumulative distribution function of the pair distances and assessment of the scaling region.

In the first pass through the data, we begin with computing mean values and standard deviations of distances to the $1\text{st}, 2\text{nd}, 3\text{rd}, \ldots, (N-1)\text{-th}$ nearest neighbors in the dataset. We assume the distribution of i-th nearest neighbor is log-normal. Then, by using the Gaussian Mixture Model method, we compute a model-based estimate for the cumulative distribution $C(r)$.

In the second pass, we exploit estimate of $C(r)$ to generate a non-uniform binning of the interval between minimum and maximum distance found in the data, so that a reasonable number of pairs is accumulated in each bin. This approach efficiently addresses the problem of insufficient statistics for a good estimation $C(r)$ in small radii.

Finally the scaling region is assumed between the right boundary of the first bin and the radius where $\partial \ln(C(r)) / \partial \ln(r)$ reaches its maximum.

Data Specification
We tested both our algorithms on two different data groups:

1. Cantor set, Sierpinsky triangle, and Fractal pyramid,
2. Logistic map ($r = 4$), Normally distributed one-, two-, and three-dimensional data.

The first group was generated using random generator and iterative algorithm that placed each point deeper and deeper into the fractal structure. We decided for these fractal sets because their correlation dimensions are well known. The data for logistic map were obtained using iterative algorithm $x_{n+1} = r \cdot x_n \cdot (1 - x_n)$ with $r = 4$. The correlation dimension of this dataset is exactly 1 (proof can be found in, e.g., [4]). The last three datasets were generated by means of an independent identically distributed Gaussian pseudo-random generator which, in theory, delivers data with correlation dimension equal to the number of dimensions.

Each data set consisted of 100 000 points. In the experiments with smaller size of data we used a subsample of the original data.

3. Results and Discussion

In Table 1., the results provided by our methods are shown. GMM gives in general better results than LRF. The computations from randomly distributed data are falling behind with increasing dimension, which is in consensus with the ideas in Introduction. This happens because in higher dimensions more data points are needed to capture the behavior of the correlation integral with the same accuracy. It follows that the accuracy must drop if the number of data is kept constant.

The poorest accuracy is obtained in the computation of D_2 of the logistic map. In [4] one can find the proof that the convergence of the correlation sum is very slow. It is only natural that, in such a case, much more data is needed to reach certain accuracy and that is the reason why our results are underestimated. As already mentioned, in [4] authors address this issue by adding a non-linear term, which led very precise results limiting r to 0. However, the results for 1D and 2D random data are more accurate with our methods, with even less data points that they had in their experiment (they obtained 1.072 and 2.133 for N greater than 10^6).

Table 1. Comparison of computed values of correlation dimension by the Linear Region Finding (LRF) method and Gaussian Mixture Model (GMM) method for $N = 10\,000$ and $N = 100\,000$ with the exact values. The grayed cells indicate the winning method given the dataset and its size.

Dataset	$N = 10\,000$		$N = 100\,000$		Theoretical value
	LRF	GMM	LRF	GMM	
Cantor set	0.6201	0.6298	0.6217	0.6297	0.6309
Sierpinsky triangle	1.5818	1.5814	1.5683	1.5811	1.5849
Fractal pyramid	2.3041	2.3179	2.3099	2.3110	2.3219
Logistic map (r=4)	0.9041	0.9284	0.9041	0.9254	1.0000
1D normal data	0.9964	1.0002	0.9999	1.0023	1.0000
2D normal data	1.9798	1.9815	1.9923	1.9931	2.0000
3D normal data	2.9420	2.9489	2.9780	2.9766	3.0000

4. Conclusions

We have shown that the results computed by the GMM and LRF methods are in good consensus with the exact values of the correlation dimension of various tested datasets. Moreover, the GMM method gives consistently better results than the LRF method.

It is quite clear, that these methods work well for computer generated noise-free data. However, most real-world data are usually contaminated with some level of noise. In many practical situations, one may need to reconstruct the system from a small number observed variables. That means our methods have to be tested under such conditions before applied to such tasks. The level of accuracy that we obtained in our existing experiments hints on promising results in this area too.

Acknowledgements

This work has been supported by the Slovak Grant Agency for Science (project No. 2/0043/13) and the Slovak Research and Development Agency (project No. APVV-0096-10).

References

[1] Sauer T.D., Yorke J.A. Are the dimensions of a set and its image equal under typical smooth functions? *Ergodic theory and dynamical systems,* 17(4): 941-956, 1997.

[2] Grassberger P., Procaccia I. Measuring the strangeness of strange attractors. *Physical Review Letters*, 50(5):346 - 349, 1983.

[3] Mekkler A. Calculation of EEG correlation dimension: Large massifs of experimental data. *Computer methods and programs in biomedicine,* 92(1):154-160, 2008.

[4] Sprott J.C., Rowlands G. Improved correlation dimension calculation. *International journal of bifurcation and chaos*, 11(7):1865 - 1880, 2001.

[5] Ji C.C., Zhu H., Jiang W. A novel method to identify the scaling region for chaotic time series correlation dimension calculation. *Chinese Sci Bull*, 56:925 - 932, 2011.

[6] Theiler J. Spurious dimension from correlation algorithms applied to limited time-series data. *Physical Review A*, 34(3):2427 - 2432, 1986.

[7] Krakovská A. Correlation dimension underestimation. *Acta physica slovaca*, 45(5):567 - 574, 1995.

Interdependence Measure Based on Correlation Dimension

A. Krakovská, H. Budáčová
Inst. of Measurement Science, Slovak Academy of Sciences,
Bratislava, Slovak Republic
Email: anna.krakovska@savba.sk

Abstract. *We use correlation dimension to study unidirectional coupling and synchronization of interconnected dynamical systems. The method is illustrated on coupled Hénon systems with variable coupling strengths. Results show that correlation dimension can be used to estimate the active degrees of freedom of the coupled dynamical systems, detect full synchronization, and reveal the direction of coupling.*

Keywords: Correlation Dimension, Hénon, Synchronization, Unidirectional Coupling

1. Introduction

Nowadays, the study of synchronization and drive-response relationships between oscillators or between dynamical systems in general is a topic of increasing interest. Applications are found, among others, in domains as economy, chemistry, climatology, causal relations in electrical activity of brain, or cardio-respiratory relations.

In this paper the following definition of *generalized synchronization* will be used:

Denote by X and Y two dynamical systems. Assume they are unidirectionally coupled:

$$\dot{x}(t) = F(x(t)),$$

$$\dot{y}(t) = G(y(t), x(t)),$$

where the x and y are the state vectors of driving system X and the driven response Y.

If the following relation

$$y(t) = \Psi(x(t))$$

exists for some smooth and invertible function Ψ, then there is said to be a *generalized synchronization* between X and Y. If Ψ is an identity, the synchronization is called identical. After some definitions, Ψ does not need to be smooth. E.g., Pyragas defines as *strong* and *weak synchronizations* the cases of smooth and non-smooth transformations [1].

Detection of Synchronization
Identical synchronization of systems of known dynamics can easily be checked visually. Run the response system from two different initial conditions. If the trajectories get synchronized after some transient, they are obviously independent of the initial conditions, but dependent on the driver.

In case of generalized synchronization of X and Y any recurrence of X implies a recurrence of Y. In real data, exact recurrences cannot be expected. However, we can assume that closeness of points in the state space X implies a closeness of the contemporary states of Y (based on the assumption of the existence of a smooth map between the two trajectories). It can be tested by making nonlinear forecasts of x_i using local neighborhood and comparing the quality of the forecasts with that of forecasts based on the equal time partners of the nearest neighbors of y_i.

Detection of Coupling without Synchronization

The direction of coupling can only be uncovered when the coupling is weaker than the threshold for emergence of synchronization. Once the systems are synchronized, there is a one-to-one relation between the states of the systems. Then the future states of the driver X can be predicted from the response Y equally well as vice versa.

First mathematical approaches to the coupling detection include the notion of Granger causality which evaluates the causal relations of time series by study of predictability in autoregressive models [2]. However, the linear concept requires generalizations to enable investigation of complex nonlinear processes. Therefore, new approaches were proposed, including nonlinear Granger causality, transfer entropy, cross predictabilities, measure based on conditional mutual information, measures evaluating distances of conditioned neighbors in reconstructed state spaces, etc. (see [3, 6] and references therein).

In this study, new approach for detecting driver – response relationships is introduced. The method utilizes the fact that the unsynchronized coupling of the systems is more complex than the driving system alone.

As a testing example, we use unidirectionally coupled identical Hénon maps at different coupling strengths.

2. Subject and Methods

To detect causal relationships we propose to use the well-known complexity measure called correlation dimension (D_2), computed after Grassberger-Proccacia algorithm [4].

Suppose we have a driving system X and response Y with a unidirectional coupling. Let us create $X+Y$ combining state vectors of X and Y.

Then our approach to study the coupling effects is based on the next expectations:

- for uncoupled X and Y the active degrees of freedom (estimated through the correlation dimension) of the combined system are equal to the sum of the active degrees of freedom of X and Y
- for coupled but not synchronized case, the number of active degrees of freedom of $X+Y$ is equal to that of the response Y and higher than the number of degrees of freedom of the driver
- the dimension of the attractor of response system saturates to the dimension of the driving system's attractor as the coupling reaches the synchronization level ($D_X=D_Y=D_{X+Y}$)

Similar approach was proposed in [5], leading to the index $(D_X+D_Y)/D_{X+Y}$ named dynamic complexity coherence measure. However, the index revealed the presence of the coupling but not the direction of the coupling. Regarding the later task, the authors only suggest to utilize the variability in the correlation dimension, which is supposed to be greater in the case of the response system Y (influenced by dynamics of X) in comparison to the dimension of the driving system X alone.

Unlike in [5], we are going to define the following *dimension-based interdependence measures*:

$$D(X|Y) = D_Y/D_{X+Y}\,, \quad D(Y|X) = D_X/D_{X+Y}\,, \quad \text{and their difference} \quad \Delta D = D(X|Y) - D(Y|X),$$

where D_X is the correlation dimension of the driving dynamics X (estimated in state space of dimension m_X), D_Y is the correlation dimension of response Y (in state space of dimension m_Y)

and D_{X+Y} is the correlation dimension of the combined system estimated in state space of dimension m_X+m_Y.

Our measure ΔD should be zero when the systems are independent or synchronized, positive when X is driving Y, and negative when Y is the driver and X is the response system.

3. Results and Discussion

To demonstrate the effectiveness of the proposed technique we will concentrate on an example of unidirectionally coupled identical Hénon maps with the driving system

$$x_1[n+1] = 1.4 - x_1^2[n] + 0.3x_2[n]$$
$$x_2[n+1] = x_1[n]$$

and the response system

$$y_1[n+1] = 1.4 - (Cx_1[n]y_1[n] + (1-C)y_1^2[n]) + 0.3y_2[n]$$
$$y_2[n+1] = y_1[n] .$$

The same case of unidirectionally coupled system was also studied in [3, 5, 6]. Starting from any initial point, after a transient regime the dynamics of Hénon map is trapped to a chaotic attractor of correlation dimension of about 1.22 (see Fig. 1 on the left).

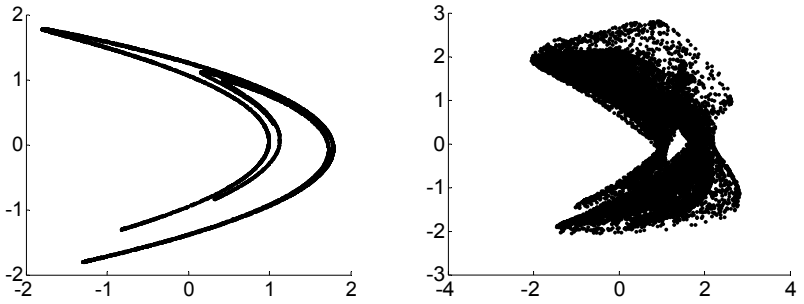

Fig. 1. Driving Hénon attractor (left) and the response system for coupling $C = 0.6$ (right).

In our toy example the coupling strength C varies from 0 to 0.8. The attractor of the response looks the same as the driver for $C = 0$ (independent systems) and $C > 0.72$ (identical synchronization). An example of unsynchronized coupling ($C = 0.6$) can be seen in Fig.1.

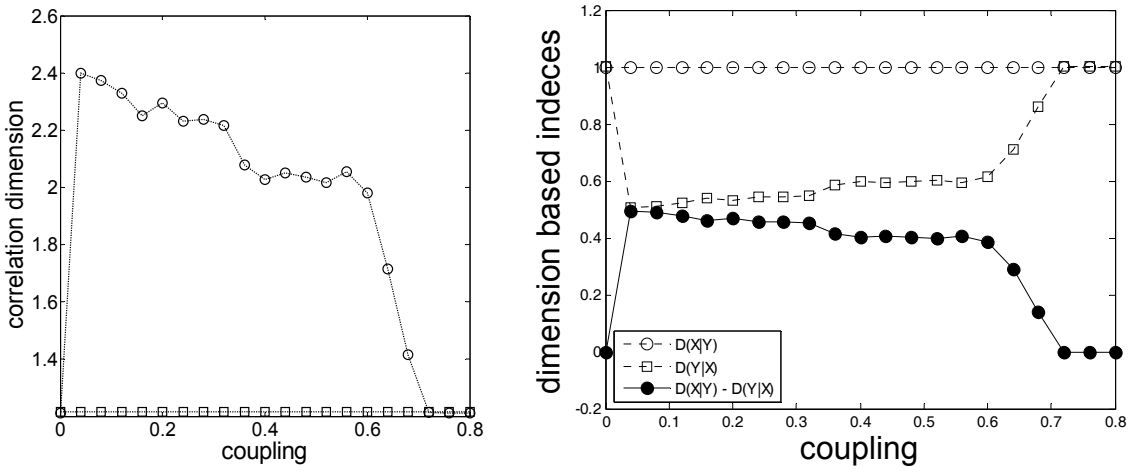

Fig. 2. Left: Estimates of D_2 for driving Hénon system (squares), and the coupled system (circles). Right: The dimension-based interdependence measures for coupled Hénon system.

Our results show that, in case of noise-free and long data, detection of the driver and response in the coupled systems by correlation dimension is possible.

Estimates of correlation dimension of the Hénon map, computed for 200000 numerically generated data (Fig. 2, on the left) lead to values about $D_X = 1.22$ for the driving system and values D_Y below 2.44 for the coupled system. Then the dimension-based index ΔD (on the right on Fig. 2), indicates by positive values that X is the driver and Y the response system and also clearly reveals the onset of synchronization by drop to zero for the synchronization threshold.

4. Conclusions

The reliable detection of the coupling from experimental signals is an important task. The dimension-based approach introduced in this paper enables very reliable detection of the direction of coupling and the threshold of synchronization for artificial benchmark data. It was demonstrated on an example of coupled Hénon maps, which allows the use of a large amount of data to estimate the probability distributions in state spaces of considerable dimensions. However, the world of real-life experiments is much more complicated: the time series are noisy and of finite length and the representative state portrait in multidimensional space is usually reconstructed from single measured observable. In such cases, the effectiveness of our dimension-based measures will depend on the achievable quality of the dynamics reconstruction.

At this point, the most important contribution of the proposed measure is that it can be used as a standard for preliminary testing of other interdependence measures that are continuously invented to evaluate synchronization phenomena in real coupled systems.

Acknowledgements

This work was supported by Slovak Grant Agency for Science (Grant VEGA No. 2/0043/13) and the Slovak Research and Development Agency (project No. APVV-0096-10).

References

[1] Pyragas K. Weak and strong synchronization of chaos. *Physical Review E*, 54 (5): R4508-11, 1996.

[2] Granger CWJ. Investigating Causal Relations by Econometric Models and Cross-spectral Methods. *Econometrica*, 37 (3): 424-438, 1969.

[3] Paluš M, Vejmelka M. Directionality of coupling from bivariate time series: How to avoid false causalities and missed connections. *Physical Review E*, 75: 056211, 2007.

[4] Grassberger P, Procaccia I. Measuring the strangeness of strange attractors. *Physical Review Letters*, 50 (5): 346 - 349, 1983.

[5] Janjarasjitt S, Loparo KA. An approach for characterizing coupling in dynamical systems. *Physica D* 237: 2482–2486, 2008.

[6] Quiroga RQ, Arnhold J, Grassberger P. Learning driver-response relationships from synchronization patterns. *Physical Review E*, 61(5): 5142-5148, 2000.

On Exact Multiple-Use Linear Calibration Confidence Intervals

[1]V. Witkovský

[1]Institute of Measurement Science, Slovak Academy of Sciences, Bratislava, Slovakia
Email: witkovsky@savba.sk

Abstract. *The multiple-use calibration problem is a problem of constructing appropriate simultaneous interval estimators (calibration confidence intervals) for values of the variable of primary interest, say x, based on possibly unlimited sequence of future observations of the response variable, say y, and on the results of the given calibration experiment, which was modeled/fitted by a linear regression model. Such calibration intervals can be obtained by inverting the simultaneous tolerance intervals constructed for the regression (calibration) function.*

Keywords: Multiple-Use Calibration, Linear Regression Model, Simultaneous Tolerance Intervals, Calibration Confidence Intervals

1. Introduction

In many experimental sciences, acquisition of the measurement results frequently requires measurement procedures involving instrument calibration which can be modeled as linear (polynomial) regression problem. Then, the required measurement result, say x, is obtained through measuring the observable response variable, say y, and by inverting the fitted regression (calibration) function. Here we consider a problem of constructing and computing the appropriate (exact according to the definition given bellow) confidence intervals for the unobservable values of the explanatory variable x, based on given fitted calibration function (a result of the calibration experiment), for possibly unlimited sequence of future observations of the response variable y (which are assumed to be independent of the calibration experiment and based on the assumption that the considered regression model was correctly specified).

As proposed by Scheffé (1973), such calibration intervals for x values can be obtained from simultaneous tolerance intervals for the considered regression (calibration) function, with warranted minimum $(1-\gamma)$-content for all such intervals simultaneously, and with confidence at least $(1-\alpha)$, for selected small probabilities γ and α. The interpretation of this requirement is that such simultaneous tolerance intervals will cover at minimum $(1-\gamma)\times 100\%$ content of all values y from the same (unknown) population and this will be true in more than $(1-\alpha)\times 100\%$ of hypothetical calibration experiments.

However, the known simultaneous tolerance intervals in regression are typically conservative in that the actual confidence level exceeds the required nominal level $(1-\alpha)$, and as such are generally broader than they necessarily should be. For a brief overview of the methods for simultaneous tolerance intervals in linear regression and suggested improvements see e.g. Chvosteková (2013). For more details on tolerance intervals see Mathew and Krishnamoorthy (2009).

The exceptions leading to narrower intervals are the simultaneous tolerance intervals as proposed by Mee et al. (1991) and Mathew and Zha (1997), however, they are based on slightly changed requirements. That is, the warranted properties of such simultaneous tolerance intervals are either valid on restricted range only, i.e. on a given and fixed interval $x \in (x_{min}, x_{max})$, and/or the requirement of warranted minimum content $(1-\gamma)$ for all

intervals is changed by the requirement that the average content is warranted to be $(1-\gamma)$, for more detailed discussion see e.g. Mee and Eberhardt (1996). Moreover, the suggested methods and algorithms for computing such tolerance intervals seem to be too complicated for practical purposes.

2. Subject and Methods

We shall assume that the calibration experiment, say $\mathcal{E}$, is modeled by the linear regression model $y = X\beta + \varepsilon$, where y is n-dimensional vector of responses measured for n values x_i, $i = 1, \ldots, n$, of the explanatory variable $x \in \mathcal{X} \subseteq \mathbb{R}^q$. However, here we shall assume that the explanatory variable is one-dimensional, i.e. that $x \in (x_{min}, x_{max}) \subseteq \mathbb{R}$. Further, the matrix X represents the $n \times (p+1)$-dimensional calibration experiment design matrix with rows $f(x_i)'$ for $i = 1, \ldots, n$, i.e. $(p+1)$-dimensional functions of x_i. β is the $(p+1)$-dimensional vector of regression coefficients and ε is n-dimensional vector of (homoscedastic) measurement errors with its assumed distribution $\varepsilon \sim N(0, \sigma^2 I_n)$.

For example, in simple p-order polynomial linear regression model we get $f(x_i) = (1, x_i, x_i^2, \ldots, x_i^p)'$ for $x_i \in \mathcal{X} = (x_{min}, x_{max})$. Based on the calibration experiment $\mathcal{E}$ we get the best linear unbiased estimator (the least squares estimator) of the calibration function $X\hat{\beta} = X(X'X)^{-}X'y$ and the estimator of the measurement error variance $S^2 = \frac{1}{\nu}(y - X\hat{\beta})'(y - X\hat{\beta})$, with mutually independent distributions of the variables $\frac{\hat{\beta}-\beta}{\sigma^2} \sim N\left(0, (X'X)^{-}\right)$ and $\frac{S^2}{\sigma^2} \sim \frac{1}{\nu}\chi^2_\nu$, where $\nu = n - (p+1)$.

In the first step, given the results of the calibration experiment $\mathcal{E}$, we shall construct the simultaneous tolerance intervals for all possible future realizations of the response variable $Y(x) = f(x)'\beta + \sigma Z$ (where $x \in \mathcal{X}$ and $Z \sim N(0,1)$ is independent of the calibration experiment $\mathcal{E}$), say $(L_{x,\mathcal{E}}, U_{x,\mathcal{E}})$, and such that

$$\Pr_{\{\mathcal{E}\}}\left(\Pr_{\{Y(x)\}}\left(L_{x,\mathcal{E}} \le Y(x) \le U_{x,\mathcal{E}} \,|\, \mathcal{E}\right) \ge 1-\gamma, \text{ for all } x \in \mathcal{X}\right) = 1-\alpha. \qquad (1)$$

The two-sided simultaneous tolerance intervals, $(L_{x,\mathcal{E}}, U_{x,\mathcal{E}})$, are typically given in the form

$$L_{x,\mathcal{E}} = f(x)'\hat{\beta} - k(x)\sqrt{S^2}, \qquad U_{x,\mathcal{E}} = f(x)'\hat{\beta} + k(x)\sqrt{S^2}, \qquad (2)$$

where by $k(x)$ we denote the required tolerance factors evaluated at $x \in \mathcal{X}$.

In the second step, for given observation $Y_* = Y(x_*)$, we shall construct the calibration confidence interval for the unobservable value of the explanatory variable, say $x^* \in \mathcal{X}$, by inverting the simultaneous tolerance intervals. So, the calibration confidence interval is given by the random set

$$\mathcal{S}(Y_*, \mathcal{E}) = \{x \in \mathcal{X} : Y_* \in (L_{x,\mathcal{E}}, U_{x,\mathcal{E}})\}. \qquad (3)$$

Notice, that the set (3) is not necessarily an interval. However, for most practical situations where the calibration function is (significantly) strictly monotonic, the confidence set (3) typically results in an interval. Based on (1) and (3) we directly get basic probability property of the calibration confidence intervals:

$$\Pr_{\{\mathcal{E}\}}\left(\Pr_{\{Y(x_*)\}}\left(x_* \in \mathcal{S}(Y(x_*), \mathcal{E}) \,|\, \mathcal{E}\right) \ge 1-\gamma\right) = 1-\alpha. \qquad (4)$$

3. Results

Here, we propose to consider a new method for computing the tolerance factors of the simultaneous tolerance intervals in linear regression by a straightforward generalization of the method for computing the tolerance factors for simultaneous tolerance intervals for m independent normal populations.

For given parameters d_x, ν and m, let $k_x = k(d_x, \nu, m)$ be a solution to the following integral equation

$$2m \int_0^\infty \Pr_{\{Q_\nu\}} \left(Q_\nu \geq \frac{\nu \chi^2_{1;1-\gamma}\left(d_x z^2\right)}{k_x^2} \right) \left(2\Phi(z) - 1\right)^{m-1} \phi(z)\, dz = 1 - \alpha, \qquad (5)$$

where $d_x = f(x)'(X'X)^- f(x)$ is the scale parameter at location $x \in \mathcal{X}$, ν represents the degrees of freedom used in estimation of the measurement error variance, and $m \geq 1$ represents the parameter of simultaneosity, i.e. the number of independent normal populations for which the simultaneous tolerance intervals are to be constructed. Notice that for $m = 1$ the tolerance factors given by (5) define the non-simultaneous tolerance intervals.

Further, $\Phi(\cdot)$ denotes the CDF and $\phi(\cdot)$ the PDF of the standard normal distribution, and $Q_\nu \sim \frac{1}{\nu}\chi^2_\nu$ is a chi-square distributed random variable with $\nu = n - q$ degrees of freedom (n denotes the sample size of the calibration experiment and q denotes the rank of the linear regression model design matrix X used for calibration). The probability $1-\alpha$ is the required nominal confidence level and $\chi^2_{1;1-\gamma}(\delta^2)$ denotes the $(1-\gamma)$-quantile of the non-central chi-squared distribution with 1 degree of freedom and the non-centrality parameter δ ($1-\gamma$ is the required coverage/content of the tolerance interval).

For more details on derivation of the equation (5) see Mathew and Krishnamoorthy (2009), and their equations (1.2.3), (1.2.4), (2.5.7) and (2.5.8).

The suggested form of the proposed tolerance factors is $\tilde{k}_x = k(d_x, \nu, \tilde{m})$, where $\tilde{m}$ denotes the appropriate value of the simultaneousity parameter, i.e. such value of $\tilde{m} \geq 1$ (minimal possible) that the following criterion is fulfilled

$$\Pr_{\{B,Q_\nu\}} \left(\min_{x \in \mathcal{X}} \left\{ \Phi\left(f(x)'B + \tilde{k}_x \sqrt{Q_\nu} \right) - \Phi\left(f(x)'B - \tilde{k}_x \sqrt{Q_\nu} \right) \right\} \geq 1 - \gamma \right) = 1 - \alpha. \qquad (6)$$

Here $B \sim N(0, (X'X)^-)$ and $Q_\nu \sim \frac{1}{\nu}\chi^2_\nu$ are independent random variables (which represent/model the variability of estimated parameters resulted from all hypothetical calibration experiments), and $\mathcal{X}$ denotes the set of all potential values of the explanatory variable x in a possibly infinite sequence of future independent observations $Y(x) = f(x)'\beta + \sigma Z$, $Z \sim N(0,1)$, with $d_x = f(x)'(X'X)^- f(x)$.

In linear regression model with $p = 1$ we get $f(x)'\beta = (1, x)(\beta_1, \beta_2)' = \beta_1 + \beta_2 x$, with order $p = 3$ we get $f(x)'\beta = (1, x, x^2, x^3)(\beta_1, \beta_2, \beta_3, \beta_4)' = \beta_1 + \beta_2 x + \beta_3 x^2 + \beta_4 x^3$.

Notice that here $\tilde{m}$ can be any real number such that $\tilde{m} \geq 1$. The parameter $\tilde{m}$ represents the complexity of the regression function $f(x)'\beta$ over the considered range $x \in \mathcal{X}$. $\tilde{m}$ depends on the on the design of the calibration experiment $\mathcal{E}$: the polynomial order p, the considered set $\mathcal{X}$, the design matrix X, and the degrees of freedom ν. For example, in simple linear regression (polynomial of the order $p = 1$) the value $\tilde{m} = 2$ is a good starting point for

numerical (iterative) search procedure (i.e. the complexity of the simple linear regression function for all $x \in \mathcal{X}$ is similar to the complexity of two independent normal populations). We have developed the MATLAB algorithm for efficient computation of the tolerance factors as defined by the integral equation (5).

An earlier version of the algorithm is available at the web page http://www.mathworks.com/matlabcentral/fileexchange/24135-tolerancefactor. The implementation of the algorithm suitable also for computing the tolerance factors as defined by the equations (5) and (6) and the related calibration confidence intervals (3) is currently under development and will be available on request from the author.

4. Discussion

The new method for simultaneous tolerance intervals in linear regression was compared for several special situations with the methods for constructing simultaneous tolerance intervals as proposed by Mee et al (1991) and by Chvosteková (2013). Based on such preliminary studies, the new intervals lead to narrower simultaneous tolerance intervals with guaranteed minimum coverage $(1 - \gamma)$ and the exact confidence level $(1 - \alpha)$.

Acknowledgements

The work was supported by the Slovak Research and Development Agency, projects APVV-0096-10, SK-AT-0025-12, and by the Scientific Grant Agency of the Ministry of Education of the Slovak Republic and the Slovak Academy of Sciences, projects VEGA 2/0038/12 and VEGA 2/0043/13.

References

[1] Scheffé H. A Statistical Theory of Calibration. *Annals of Statistics*, 1(1): 1-37, 1973.

[2] Krishnamoorthy K, Mathew T. Statistical Tolerance Regions: Theory, Applications, and Computation. John Wiley & Sons, Inc., Hoboken, New Jersey, 2009.

[3] Chvosteková M. Simultaneous Two-Sided Tolerance Intervals for a Univariate Linear Regression Model. *Communications in Statistics - Theory and Methods*, 42(7): 1145-1152, 2013.

[4] Mee RW, Eberhardt KR, Reeve CP. Calibration and Simultaneous Tolerance Intervals for Regression. *Technometrics*, 33(2): 211-219, 1991.

[5] Mee RW, Eberhardt KR. A Comparison of Uncertainty Criteria for Calibration. *Technometrics*, 38(3): 221-229, 1996.

[6] Mathew T, Zha W. Multiple Use Confidence Regions in Multivariate Calibration. *Journal of the American Statistical Association*, 92(439) 1141-1150, 1997.

Random Effects ANOVA in Uncertainty Evaluation

B. Arendacká, A. Täubner, S. Eichstädt, T. Bruns, C. Elster

Physikalisch-Technische Bundesanstalt, Braunschweig and Berlin, Germany,
Email: barbora.arendacka@ptb.de

Abstract. *Random effects ANOVA models are well established and implemented in statistical software, they provide enough freedom to model dependencies between repeated measurements (e.g. a stronger dependency between measurements obtained within one day as compared to measurements obtained on different days) and they offer a closer look at the structure of the uncertainty (by splitting the variability due to different sources). The paper illustrates these concepts and advocates the use of random effects ANOVA models for analysis of long-term repeated experiments conducted to assess repeatability of a measurement. Variability revealed by such an experiment is important when creating an uncertainty budget. The concepts are illustrated with the help of data coming from calibration of accelerometers.*

Keywords: Random Effects, ANOVA, Type A Uncertainty

1. Introduction

To assess repeatability of a measurement, a long-term repeated experiment can be carried out. For example, in the context of calibration of accelerometers, an accelerometer may be repeatedly mounted into the measurement setup and then the frequency response function (FRF) may be measured repeatedly in a usual manner. Such a long-term experiment reveals variability that may not be observed when an accelerometer is mounted into the setup only once or twice, which is what would be done in a routine calibration. Thus the variability observed in the long-term experiment is important when creating an uncertainty budget. In order to determine this uncertainty, the simplest way one may think of, is to look at the mean values (and their variability) for each of the different mountings of the accelerometer. However, this would give us a valid result only if the numbers of repeated measurements per mounting, as well as the variability of measurements within each mounting, are always the same. Moreover, this approach does not exploit the data to the fullest and leaves much of potentially useful information untouched. A finer view can be achieved by employing random effects ANOVA(= Analysis Of VAriance) models. We describe them in detail in the next section. We then illustrate the method using data obtained within the EMRP project IND09 'Traceable dynamic measurement of mechanical quantities'. There, torque, force and pressure are of main interest. However, since acceleration is a fundamental quantity for dynamic measurements and a traceable primary calibration of accelerometers has been realised in PTB, see e.g. [1], calibration of accelerometers provides a good basis for gaining experience with implementation of the approach that can be later directly transferred to the other mechanical quantities the project focuses on.

2. Subject and Methods

Data

To illustrate the capabilities of random effects ANOVA models, we will use a part of a large dataset obtained in an experiment conducted to assess repeatability of FRF measurements for calibration of an accelerometer. The measurement campaign involved two different accelerometers that were repeatedly mounted into the measurement setup used for calibration

of accelerometers in PTB (for details see [1, 2]). However, to make the presentation concise, we will consider only data resulting from a repeated mounting of a back-to-back accelerometer, type 8305 (Brüel & Kjaer) and excitation of the system by a sinusoidal excitation at frequency 4000 Hz. In addition, we will focus only at the amplitude of the FRF and show the values in arbitrary units. The input acceleration was determined from measurements by a laser interferometer pointing its rays at the top of the mounted accelerometer. The accelerometer was mounted repeatedly 20 times within a period of roughly 5 weeks. Each time the frequency response was determined repeatedly from a sinusoidal fit to the measured signals; 10 times with laser interferometer in 'position 0°' (i.e. with laser rays pointing at 2 points on the top of the accelerometer lying on a line having 0° angle with a certain reference surface), 10 times in 'position 90°'. Thus, our dataset consists of sets of 10 and 10 measured amplitudes (position 0° and 90°) obtained for 20 different mountings (see Fig. 1). The main interest is to assess the variability of an average of amplitudes obtained for a single mounting, which would be the value, reported for the amplitude of the FRF in a routine calibration. However, as we will see, employing random effects ANOVA models we can obtain a finer picture of the structure of the uncertainty and answer also such questions as e.g. what improvement in uncertainty the averaging over positions 0° and 90° brings.

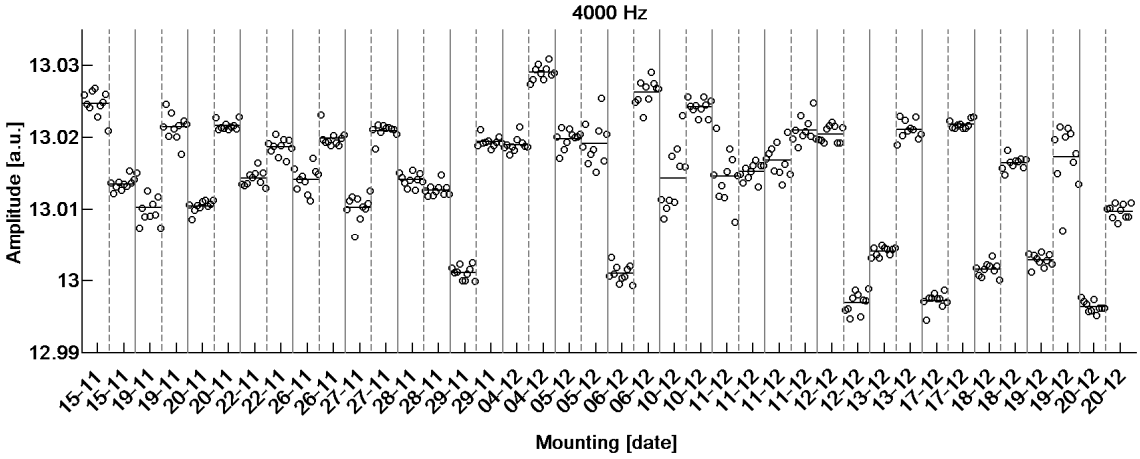

Fig. 1. Amplitude of the frequency response (a.u.) for 20 different mountings of the accelerometer, each time for two different adjustments of the laser interferometer. The horizontal lines show respective averages.

Random Effects ANOVA

The ANOVA model in our case can be of the form:

$$y_{mpr} = a + b_p + A_m + B_{mp} + E_{mpr}\,, \qquad (1)$$

where y_{mpr} denotes the rth (r=1,..,10) amplitude measured for mounting m (m=1,...,20) at position p (p=1,2), a denotes the common mean (our measurand), b_p is the fixed effect of position p, $A_m \sim N(0,\ \sigma_M^2)$, $B_{mp} \sim N(0,\ \sigma_{MP}^2)$ are mutually independent random effects and $E_{mpr} \sim N(0,\ \sigma^2)$ are mutually independent random errors. $N(.,.)$ denotes a normal distribution.

To make it clearer, observe the data in Fig. 1. It seems that for each combination of mounting and position, the measured values fluctuate around a certain level. These fluctuations are modelled by the random errors. The levels around which the measured values fluctuate are moreover shifted up and down around some common value (not shown) in a random manner. These shifts are modelled by the random effects. The effect due to mounting, A_m, brings a

shift common for measurements obtained within 1 mounting, the effect due to the combination of mounting-position, B_{mp}, refines further the shift due to mounting by adjusting it with a random value for each mounting-position combination. Since these effects are random, we are interested in their possible size captured by the variances σ_M^2, σ_{MP}^2. In contrast, the fixed effects b_p account for a possible systematic effect of the two different positions, i.e. their contribution to the shift is constant for a given position, and thus we are interested in their values directly. To make the model identifiable, we assume that the fixed effects $b_1 + b_2$ sum to 0, so that the shifts from the common level *a* have zero mean. This also ensures that the average of amplitudes obtained within one mounting, $\bar{y}_{m..}$, is an unbiased estimator of our measurand *a*. Before fitting the model in Eq. 1 to our data, we may look once more at Fig. 1 and observe closely the fluctuations of the measured values around the depicted levels. It seems that the variability of these fluctuations varies, being rather large for some combinations of mounting-position. Thus instead of our original assumption $E_{mpr} \sim N(0, \sigma^2)$, we may rather assume a different variance for the random error within each mounting–position combination; $E_{mpr} \sim N(0, \sigma_{mp}^2)$.

Implied (Co)variance Structure

The model in Eq. 1 implies a certain covariance structure of the measurements. For a given mounting, the single measured value, y_{mpr}, the average of values at position *p*, $\bar{y}_{mp.}$ and the average of all values within the mounting, $\bar{y}_{m..}$, have the following distributions:

$$y_{mpr} \sim N(a + b_p, \sigma_M^2 + \sigma_{MP}^2 + \sigma_{mp}^2) \tag{2}$$

$$\bar{y}_{mp.} \sim N(a + b_p, \sigma_M^2 + \sigma_{MP}^2 + \sigma_{mp}^2/10) \tag{3}$$

$$\bar{y}_{m..} \sim N(a, \sigma_M^2 + \sigma_{MP}^2/2 + \frac{1}{4}[\sigma_{m1}^2/10 + \sigma_{m2}^2/10]) \tag{4}$$

Moreover, measurements within one mounting-position have covariance $\sigma_M^2 + \sigma_{MP}^2 \geq 0$, while measurements obtained within one mounting but at different positions have covariance $\sigma_M^2 \geq 0$. It is easy to see that if all random errors have the same variance, i.e. $\sigma_{mp}^2 = \sigma^2$, the variance in Eq. 4 turns into the expected $\sigma_M^2 + \sigma_{MP}^2/2 + \sigma^2/20$. The type A relative standard uncertainty of $\bar{y}_{m..}$ can be expressed via relative standard uncertainties due to mounting, mounting-position interaction and random errors as $\sqrt{u_{rM}^2 + u_{rMP}^2 + u_{rE}^2}$, where $u_{rM} = \sigma_M / a$, $u_{rMP} = \sigma_{MP}/(\sqrt{2}a)$, see Eq. 4. When the accelerometer is mounted anew, u_{rE}^2 can be determined from the sampling variances of the repeated measurements at the two positions. The other two contributions $u_{rM}^2 + u_{rMP}^2$ must be taken from a (past) long-term experiment.

3. Results

For fitting the model in Eq. 1 to our data (Fig. 1), we used function *lme* in the library *nlme* of R [3] and estimated the parameters with the restricted maximum likelihood method. σ_M was estimated as $1.6*10^{-6}$, σ_{MP} as 0.0075687. Moreover the 95% confidence interval for σ_M (obtained with function *intervals()*) contained 0. This suggests that the effect of mounting

is negligible and supports the current practice of mounting an accelerometer applying a torque of 2 N.m, which was established in order to prevent any effects on the measured values. Thus, refitting the data to a model in Eq. 1 with A_m (the mounting effect) omitted (i.e. σ_M^2 fixed at 0), yields the final estimates: a=13.014408, σ_{MP}=0.00757 and all the different σ_{mp} between 0.00062 and 0.00452. Taking the minimum (maximum) of these in place of both the σ_{m1}, σ_{m2} in Eq. 4 and dividing the square root of the resulting variance by a, we obtain that the type A relative standard uncertainty of $\bar{y}_{m..}$ ranges roughly from 0.0411% to 0.0418%. Similarly, using Eq. 3 we can see that the relative standard uncertainty for average over only one position ranges from 0.0582% to 0.0592%. Correcting the average for the systematic bias b_p and including its uncertainty changes these numbers only slightly. Thus the improvement factor due to taking an average of 2 positions is approximately $1/\sqrt{2}$: clearly, in the variances in Eq. 3 and Eq. 4 with σ_M^2=0, σ_{MP}^2 is the dominant part. However, were σ_M^2 non-zero, the improvement factor would be closer to 1 (1 means no improvement). In the extreme case of σ_M^2 being dominant, averaging over two positions would not lead to a real improvement.

4. Discussion

Functions for fitting random effects models can be found in other statistical software as well. If one assumes common variance for random errors, MATLAB and *nlmefit* can be used. In our case, we could then use even textbook formulas from the so called ANOVA table. However, more general approaches allow accommodating further features, e.g. a possible trend observed within the mounting-position repeated measurements, and one can then verify whether the trend is negligible with respect to the overall uncertainty as desired.

Of course, before drawing conclusions from the estimates, one should check the goodness of the fit of the chosen model, see e.g. [3]. In our case, in model with common error variance a plot of standardized residuals versus fitted values would suggest going for the more complex model (fitted above) with different variances for the mounting-position groups.

All in all, with the help of statistical software fitting random effects ANOVA models to similar long-term experiments is not difficult and does justice to the effort invested in the experiment by enabling deeper insights into and verification of different assumptions about the measurement process.

Acknowledgements

The research leading to these results has received funding from the European Union on the basis of Decision No. 912/2009/EC.

References

[1] von Martens HJ et al. Recent advances in vibration and shock measurements and calibrations using laser interferometry. *SPIE* 5503: 1-19, 2004.

[2] International Standard ISO 16063-11, Methods for the calibration of vibration and shock transducers – Part 11: Primary vibration calibration by laser interferometry. International Organization for Standardization, Geneva, 1999.

[3] Pinheiro J, Bates D. Mixed Effects Models in S and S-PLUS. Springer, New York, 2000.

The Method to Evaluation of Calibration for Pressure Transmitter

[1,2]R. Palenčár, [1]M. I. Maniur, [1,2]S. Ďuriš, [2]Ľ. Šooš, [3]M. Dovica

[1]Slovak Institute of Metrology, Bratislava, Slovakia,
[2]Slovak University of Technology, Bratislava, Slovakia,
[3]The Technical University of Košice, Košice, Slovakia
Email: rudolf.palencar@stuba.sk

Abstract. *The evaluation of calibration for pressure transmitter is based on determination of calibration function in the form of polynomial p degree. The paper describes procedure for evaluation of calibration for pressure transmitter based on finding the polynomial coefficients of the calibration curve by least squares method. This method allows to include uncertainty of a measurement standard pressure to the evaluation of uncertainty by linearization of the model development in Taylor series and neglecting the higher terms. The proposed method is based on conditions of calibration in the Slovak Institute of Metrology. It is compared with methods used in practice not considering uncertainty (standard and influence quantities) for estimation of parameters of the calibration curve.*

Keywords: Calibration, Measurement Uncertainty, Measurement Model

1. Introduction

Calibration of gauges is one of the fundamental tasks in metrological practice. The result of calibration is the assignment of data values of calibrated gauge to the values of measurement standard with the appropriate expanded uncertainty. If the transmitter has a continuous scale then the calibration curve must be found and in most cases it is in the polynomial form. The pressure transmitter is an instrument for pressure measurement (vacuum, pressure, absolute pressure, pressure difference) and the output signal can be in numerical form (numeric display) or in the form of output signal (current, voltage). In practice uncertainties from calibration are not considered for estimation of parameters. They are considered in determining of uncertainty of the estimated parameters of the calibration curve. Further in this paper is presented a procedure for evaluation of pressure transmitter calibration by application of the model for calibration of continuous scale. Assuming that the piston gauge is as a measurement standard then the output signal from the pressure transmitter will be measured by multimeter.

2. Subject and Methods

We consider a theoretical model of calibration in linear form

$$\begin{aligned} p_{\mathrm{E}_1} &= -a-(b-1)p_{\mathrm{sk}_1}-cp_{\mathrm{sk}_1}^2 \\ p_{\mathrm{E}_2} &= -a-(b-1)p_{\mathrm{sk}_2}-cp_{\mathrm{sk}_2}^2 \\ &\vdots \quad\quad \vdots \\ p_{\mathrm{E}_n} &= -a-(b-1)p_{\mathrm{sk}_n}-cp_{\mathrm{sk}_n}^2 \end{aligned} \qquad (1) \qquad \text{i.e.} \qquad \begin{aligned} \delta p_{\mathrm{sk}_1} &= a+bp_{\mathrm{sk}_1}+cp_{\mathrm{sk}_1}^2 \\ \delta p_{\mathrm{sk}_2} &= a+bp_{\mathrm{sk}_2}+cp_{\mathrm{sk}_2}^2 \\ &\vdots \quad\quad \vdots \\ \delta p_{\mathrm{sk}_n} &= a+bp_{\mathrm{sk}_n}+cp_{\mathrm{sk}_n}^2 \end{aligned} \qquad (2)$$

where

$\delta p_{ski} = p_{ski} - p_{Ei}$ is an error of calibrated pressure transmitter
p_{Ei} – is a value of measurement standard (piston gauge),
p_{ski} – is a value of calibrated pressure transmitter,
a, b, c – are unknown parameters of the calibration function. They are estimated by calibration.

The output signal value of calibrated pressure transmitter measured by multimeter is converted to the unit of pressure using equation (3). It is assumed linear relationship between the output signal and the measured pressure.

$$p_{ski} = \frac{\Delta p}{\Delta x}(x_i - x_d) \tag{3}$$

where

Δp – is the span of measuring range for pressure transmitter (Pa),
Δx – is the span of the output signal for pressure transmitter (mA or V),
x_i – is the value of the output signal from pressure transmitter in individual calibration points (mA or V),
x_d – is the lowest limit of the output signal from pressure transmitter (mA or V).

Model (2) is non-linear, so it must be linearized at the point (a^0, b^0, c^0, p^0_{ski}) by the development in Taylor series and neglecting the higher terms. Then the calibration model for the *i*-th calibration point is [1, 2, and 3]

$$W_i = a + b\, p_{sk_i} + c\, p_{sk_i}^2 \tag{4}$$

and

$$W_i = \left(p_{sk_i} + \Delta p_{sk_i} + \Delta_{multi}\right) - \left(p_{E_i} + C_{mzi}\Delta m_{zi} + C_{Aef}\Delta A_{ef}\right) - d_i\left(\Delta p_{sk_i} + \Delta_{multi}\right) \tag{5}$$

where
for simplicity p^0_{ski} is taken as p_{ski} and . $d_i = -(b^\circ + 2c^\circ p^\circ_{ski})$,

$a^\circ, b^\circ, c^\circ$ - initial estimates of the unknown parameters of the calibration function,
p°_{ski} - initial estimate of the pressure transmitter pressure (measured value),
Δp_{sk_i} - is an error of the pressure value from pressure transmitter,
Δ_{multi} - is an error of the value of multimeter,
Δm_{zi} - is an error of the weights in *i*-th pressure point,
ΔA_{ef} - is an error of the effective piston area (piston gauge),
$C_{m_{zi}}$ - is the sensitivity coefficient of weights,
C_{Aef} - is the sensitivity coefficient of the effective piston area (piston gauge),

In matrix form

$$\boldsymbol{W} = \boldsymbol{A}\,\boldsymbol{a} \tag{6}$$

Linear stochastic model

$$(\boldsymbol{W}, \boldsymbol{Aa}, \boldsymbol{U_w}) \tag{7}$$

where $\boldsymbol{W}$ is a vector of input random variables with a mean $E(\boldsymbol{W}) = \boldsymbol{Aa}$ and covariance matrix $D(\boldsymbol{W}) = \boldsymbol{U_w}$. $\boldsymbol{A}$ is a known matrix, $\boldsymbol{a}$ is a vector of output variables (the vector of unknown parameters).

Vector of input variables has the following form

$$\boldsymbol{W} = \left(\boldsymbol{P}_{\mathrm{sk}} + \Delta\boldsymbol{P}_{\mathrm{sk}} + \boldsymbol{C}_{\boldsymbol{P}_{\mathrm{sk}}}\boldsymbol{\Delta}_{\mathrm{multi}}\right) - \left(\boldsymbol{P}_{\mathrm{E}} + \boldsymbol{C}_{m\,zi}\Delta\boldsymbol{m}_{\mathrm{z}} + \boldsymbol{C}_{A\,\mathrm{ef}}\,\Delta\boldsymbol{A}_{\mathrm{ef}}\right) - \boldsymbol{D}\left(\Delta\boldsymbol{P}_{\mathrm{sk}} + \boldsymbol{\Delta}_{\mathrm{multi}}\right) \quad (8)$$

Estimation of parameters of calibration function and covariance matrix of a vector of parameters estimation are determined (see e.g. [1, 2]) as $\hat{\boldsymbol{a}} = \left(\boldsymbol{A}^{\mathrm{T}}\boldsymbol{U}_{\boldsymbol{W}}^{-1}\boldsymbol{A}\right)^{-1}\boldsymbol{A}^{\mathrm{T}}\boldsymbol{U}_{\boldsymbol{W}}^{-1}\boldsymbol{w}$ respectively $\boldsymbol{U}_{\hat{\boldsymbol{a}}} = \left(\boldsymbol{A}^{\mathrm{T}}\boldsymbol{U}_{\boldsymbol{W}}^{-1}\boldsymbol{A}\right)^{-1}$. For initial parameters estimates of the calibration curve, the parameters are taken that are evaluated without considering the uncertainties, i. e. it is taken the method used in practice. As a rule, two steps of calculation are sufficient. The evaluation for $\boldsymbol{U_w} = \sigma^2\,\boldsymbol{I}$ was done for the data from the Slovak Institute of Metrology [3] (Tab. 1). $\boldsymbol{I}$ is the identical matrix, i.e., without considering the uncertainties in estimating the model parameters and also for

$$\boldsymbol{U}_{\boldsymbol{w}} = \left(\boldsymbol{U}_{\Delta\boldsymbol{P}_{\mathrm{sk}}} + \boldsymbol{C}_{\boldsymbol{P}_{\mathrm{sk}}}\boldsymbol{C}_{\boldsymbol{P}_{\mathrm{sk}}}^{\mathrm{T}}u_{\boldsymbol{\Delta}_{\mathrm{multi}}}^{2}\right) + \left(\boldsymbol{C}_{m\,zi}\boldsymbol{U}_{\Delta\boldsymbol{m}_{\mathrm{z}}}\boldsymbol{C}_{m_{zi}}^{\mathrm{T}} + \boldsymbol{C}_{A\,\mathrm{ef}}\,\boldsymbol{U}_{\Delta\boldsymbol{A}_{\mathrm{ef}}}\boldsymbol{C}_{A_{ef}}^{\mathrm{T}}\right) - \boldsymbol{D}\left(\boldsymbol{U}_{\Delta\boldsymbol{P}_{\mathrm{sk}}} + \boldsymbol{C}_{\boldsymbol{P}_{\mathrm{sk}}}\boldsymbol{C}_{\boldsymbol{P}_{\mathrm{sk}}}^{\mathrm{T}}u_{\boldsymbol{\Delta}_{\mathrm{multi}}}^{2}\right)\boldsymbol{D}^{\mathrm{T}} \quad (9)$$

Table1. Measured and calculated values.

p_{E} (MPa)	p_{sk} (MPa)	δp_{sk} (MPa)	$\sigma_{p_{\mathrm{skm}}}$ (MPa)
0,000000000	-0,002565	-0,002565000	0,000256032
2,000531531	2,002185	0,001653469	0,000108942
4,000948101	4,003240	0,002291899	0,000468368
6,001410389	6,005990	0,004579611	0,000640641
8,001808350	8,006450	0,004641650	0,000701502
10,002307802	10,007280	0,004972198	0,000564381
12,002776912	12,006665	0,003888088	0,000892233
14,003286455	14,005570	0,002283545	0,000976082
16,003723784	16,003535	-0,000188784	0,001160887
18,004197462	18,000715	-0,003482462	0,001318801
20,004635311	19,997730	-0,006905311	0,001588885

Uncertainty of parameters estimation of calibration function by method used in practise is evaluated by statistical analysis for $\boldsymbol{U_w} = \sigma^2\,\boldsymbol{I}$ and for uncertainties of measurement standard and multimeter. For the proposed evaluation method of calibration for $\boldsymbol{U_w}$ in the form (9) is the uncertainty of the calibration curve determined by applying the law of uncertainty propagation on calibration model (1) respectively (2) for the estimated parameters for $\boldsymbol{U_w}$ in the form (9). Results for model (2) are shown in Fig. 1. where $\Delta_{p_{\mathrm{ski\,prax}}}$ and $\Delta_{p_{\mathrm{ski\,m}}}$ are the estimates of error pressure values of pressure transmitter using the methods in practice. $\Delta_{p_{\mathrm{ski}}}$ is the estimate of error pressure value of pressure transmitter using the proposed method.

$U_{\hat{\Delta}_{p\mathrm{ski}}}$ is the uncertainty estimate of error pressure value of pressure transmitter using the proposed method. $U_{\hat{\Delta}_{p\mathrm{skiprax}}}$ is the uncertainty estimate of error pressure value of pressure transmitter using the methods in practice.

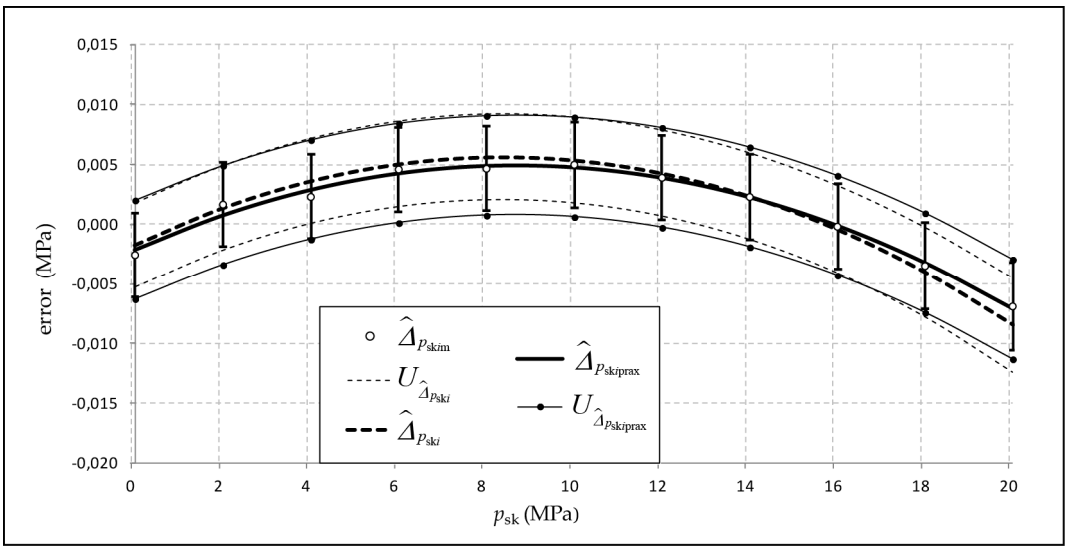

Fig. 1. The graphical presentation of calibration.

3. Discussion and Conclusions

Theory of calibration of continuous scale was applied for the evaluation of the calibration of pressure transmitters. The results of calibration are the estimates of parameters of calibration function and the covariance matrix of the estimated parameters. The results of the evaluation of the calibration using theory for calibration of continuous scale and the results of the evaluation by methods used in practice are slightly different for the conditions considered in this paper. In this case the uncertainties of the estimated values of pressure determined by method B do not affect the estimation of parameters of the calibration function.

Acknowledgements

The authors are grateful for support for this work to the Slovak University of Technology in Bratislava, Faculty of Mechanical engineering, to the Slovak Institute of Metrology and to the Grant Agency APVV - grant No. APVV– 0096-10, VEGA - grant No. 1/0120/12, KEGA – grant No. 005STU - 4/2012.

References

[1] Wimmer G, Palenčár R, Witkovský V. Processing and evaluation of measurements Spracovanie a vyhodnocovanie meraní), Veda, Bratislava, 2002, ISBN 80-224-0734-8.

[2] Palenčár R, Ruiz M J, Janiga I, Horníková A. Statistical methods in metrology and testing laboratories (Štatistické metódy v metrologických a skúšobných laboratóriách), Bratislava STU, 2001. 336 s. ISBN 80-968449-3-8.

[3] Maniur, M. I. Calibration evaluation for pressure transmitters (Vyhodnotenie kalibrácie prevodníkov tlaku). Dissertation. SjF STU, Bratislava, 2012.

Uncertainty of the Dynamic DAC Testing by DC Voltage with Superimposed Dithering Signal

L. Michaeli, J. Šaliga, M. Sekerák, J. Lipták

Department of Electronics and Telecommunications,
Technical University of Košice, Letná 9, 041 20 Košice, Slovak Republic
Email: linus.michaeli@tuke.sk

Abstract. *The DAC testing method studied by authors is based on the comparison of a time-varying sawtooth signal generated by the DAC under test with a reference signal by a fast comparator. The reference signal is the superposition of DC voltage measured by a precise DC voltmeter and slow dithering voltage with known amplitude. The comparator detects the sequence of DAC control codes which determines the DAC nonlinearities. The paper provides analysis of the proposed method uncertainty. As results the requirement on the dithering voltage and DC precision will be estimated.*

Keywords: Digital to Analog Converter, DAC Dynamic Test, Dithering

1. Introduction

The appropriate use of such DACs requires a simple and reliable test procedure realizable in laboratories equipped with general purpose instruments. The common practical implementation of some of these test procedures is limited by requirements on instrumental equipment of laboratories performing standardized DAC testing [1]. Some of them require expensive high performance spectrum analyzers with high dynamic range and/or high quality notch filters. The authors proposed a dynamic DAC testing procedure in [2] based on the conversion of the DAC output level into record of the of input control codes of DAC under test in the fast memory. The registration instants are determined by the fast comparators.

2. Principle of the Proposed Method

A block diagram describing the proposed test method is shown in Fig. 1. The voltage comparator CMP compares the dynamic output voltage of the DAC under test (DAC UT) with the testing voltage $V_{SUM}= V_{DC}+ V_{DITH}$ created as a sum of reference DC voltage V_{DC} and a small superimposed dithering voltage V_{DITH}. Dithering voltage generated by the dithering DAC (D-DAC) with the known amplitude $W_{D\text{-}DAC}$ is attenuated by resistor divider $a=R_2/(R_1+R_2)$. Attenuation of D-DAC output suppresses the distortion of the dithering voltage V_{DITH}: [2]. The reference DC voltage is measured by a precise DC voltmeter with a long integration constant (Agilent 3458A), which ensures the averaging of the testing voltage and suppresses influence of the dithering voltage on DC measurement.

The difference ΔV(k) between the real transition code level T(k) and the known reference voltage VDC is proportional to the average number of the code words k(i) in the acquired record as it is shown in Fig. 1.b. The recorded code words k(i) are replaced by new values $p_k(i)$ equal to +1 or -1 as follows:

$$p_k(i)=\begin{cases} 1 & \text{if } k(i)\le k \\ -1 & \text{if } k(i)>k \end{cases} \qquad (1)$$

Then the voltage difference $\Delta V(k)$ between the tested transient code level $T(k)$ and the analog voltage V_{DC} measured by the precise voltmeter for the known amplitude W of the dithering

signal can be estimated as: .The known V_{DC} voltage measured with high precision allows to determine the transition code level $T(k)$ at the DAC UT for code k can be:

$$T(k) = V_{DC} + \Delta V(k) \cong V_{DC} + W \cdot \frac{1}{M} \sum_{i=1}^{M} p_k(i) \tag{2}$$

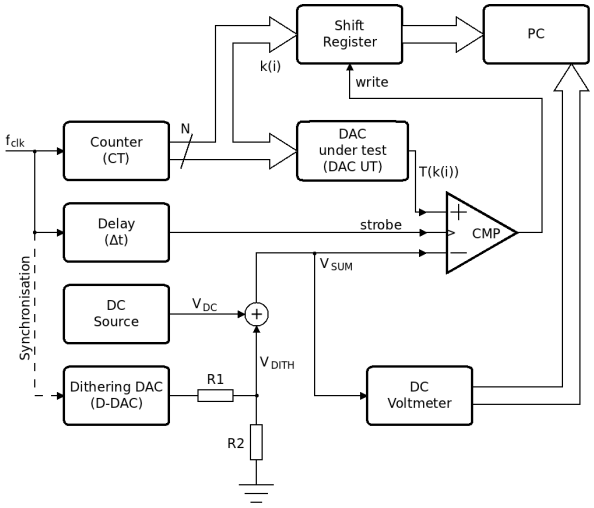

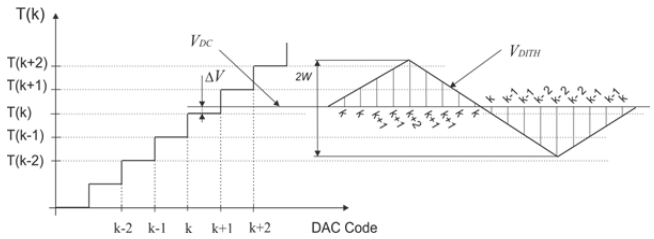

Fig. 1. a.) Block diagram of the proposed test method setup b.) and registration of input codes during one dithering period.

Where M is record length and W is peak-peak value of dithering voltage. The tested transition code levels $T(k)$ allow to estimate differential $DNL(k)$ according formulas [1].

$$DNL_{cor}(k) = \frac{\Delta V(k+1) - \Delta V(k) - Q}{Q} - \delta; \qquad \delta = \frac{1}{2^N} \sum_{k=0}^{2^N-1} \frac{\Delta V(k+1) - \Delta V(k) - Q}{Q} \tag{3}$$

Uncertainty Analysis

The total uncertainty of the proposed method is given by the uncertainty $u(T(k))$ of determination of transition code level $T(k)$ (2). Error sources and uncertainties influencing the accuracy of measurement are:

- Errors and uncertainties of reference voltage VDC that include errors and uncertainties of DC source and DC voltmeter and offset of the comparator
- The nonlinearity of dithering voltage covering its quantisation noise and nonlinearity of D-DAC
- The uncertainty of finite record $p_k(i)$ in (2) given by the statistical uncertainty and uncertainty of dithering amplitude W
- Errors caused by dynamic properties of the voltage comparator CMP. The overdrive dispersion and the dynamic errors of CMP can be suppressed by a convenient time shift Δt of strobe pulse (Fig. 1) synchronization of D-DAC and DAC UT.

Because of their different origin, we can assume that these sources are statistically independent. Most of them contain a bias component: offset of the comparator, accuracy of DC voltmeter. These bias components are removed from test results by applying the terminal definition. Moreover, using the same record for determination of results for a few adjacent transition code levels covered by $2W$, e.g., for DNL estimation suppresses these bias errors also.

The uncertainty of the DC voltmeter consists of the uncertainty given by a voltmeter vendor and intrusion of superimposed dithering signal on the measured DC voltage. The incoherency between the DC voltmeter measuring time and the dithering period causes a voltage shift of

the measured DC value. Let suppose that the integration time of the DC voltmeter covers (J+ε) periods of the dithering signal, where J is an integer number and ε is a decimal remainder in the range -0.5≤ ε <0.5. Then the maximal value of the uncertainty component caused by this effect is 0.5W/(J+0.5). Let suppose, Then the uncertainty $u_q(V_{DITH})$ of dithering voltage V_{DITH} at the output of D-DAC is:

$$u_q(V_{DITH}) = a \cdot \left(\frac{2W_{D-DAC}}{2^b - 1}(c+1) \right) \tag{4}$$

The constant b represents the resolution of D-DAC with the maximal DNL=c [LSB]. The combined uncertainty of measurement results from equation (2) is:

$$u^2(T(k)) = u^2(V_{DC}) + u^2(\Delta V(k)) \tag{5}$$

The first component covers the above analyzed effects. The second component in (6) expresses uncertainty consisting of uncertainty of dithering amplitude u(W)=$a.u$(WD-DAC) and statistical uncertainty given by processing of finite record of pk(i) - u(pk(i)):

$$u^2(\Delta V(k)) = u^2(W)\left(\frac{1}{M}\sum_{i=1}^{M} p_k(i) \right)^2 + \frac{W^2}{M^2}\sum_{i=1}^{M} u^2(p_k(i)) = u^2(W) + u^2(pk) \tag{6}$$

The second component - $u(p_k(i))$ is given by the uncertainty of values in the transformed array $p_k(i)$, where the elements in the recorded array have binomial distribution. The maximum dispersion of the second component (2) σ^2 = 0.25 M, and the total uncertainty in the worst case is:

$$u^2(p(k)) = \frac{W^2}{M} 0.25 \tag{7}$$

Dithering voltage covers only a few LSBs of DAC UT, and therefore uncertainty of its amplitude u(W) is relatively very small in comparison with the total uncertainty of determination of $T(k)$ and could be neglected.

3. Experimental Results

The simulation of the combined dependence of the uncertainty on record length M as well as on amplitude of dithering W is shown on Fig.2.a.). Simulation results confirm the theoretical analysis, that the most important uncertainty factor is the number of samples and influence of dithering amplitude W.

The effect of the incoherency on the final uncertainty of measurement is shown in Fig. 2.b.). The number of samples in record M is constant and equals to 10000, and the number of period of dithering voltage L was chosen to be relatively prime. Error of coherency ε from interval [-0.5,0.5] was added to L. The strict coherency is required only for a small number of dithering signal periods L. The influence of coherence error ε quickly decreases with the increase of the number of periods of dithering.

Experimental validation was performed using the 14 bits DAC UT AD7534T by Analog Devices. Because of the high accuracy of the tested DAC, a chosen number of the most significant bits (8 or 10 bits mode) was used to generate DAC UT basic sawtooth signal. The rest of the least significant bits were used to insert additional known nonlinearity representing the 0,25 LSB of the tested resolution. The DNL_n characteristics of the DAC UT measured by the new proposed method were compared with reference DNL_s obtained from the static testing procedure. The standard deviations σ of deviation of DNL measured by static and proposed method $\sigma(\Delta DNL(k))= \sigma(\Delta(DNL_s(k)) - DNL_n(k)))$ are shown in Table 1 for both DAC UT modes.

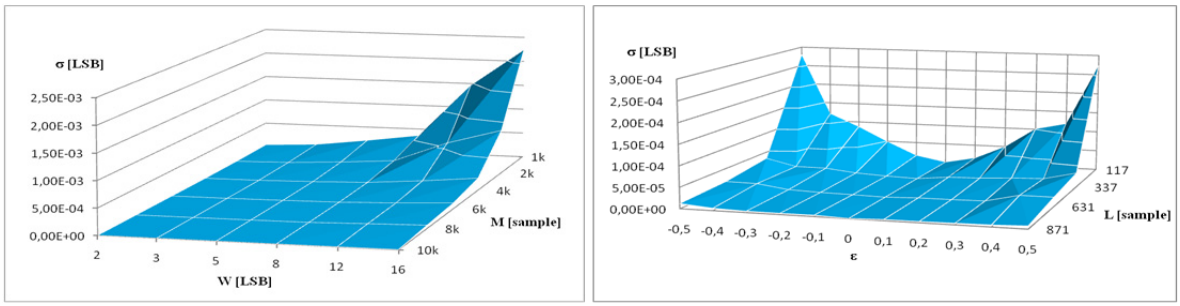

(a) (b)

Fig. 2. Dependence of standard deviation of difference between INL characteristics on amplitude of dithering W and different record length M at constant ratio M/L=11.48.

Record length	σ (Δ*DNL*(*k*)) - 8 bit	σ (Δ*DNL*(*k*)) – 10 bit		Dithering voltage amp.	σ (Δ*DNL*(*k*))
$M=10^4$	0.0215 LSB	0.0415 LSB		W = 2 LSB	0.0290 LSB
$M=10^5$	0.0125 LSB	0.0283 LSB		W = 5 LSB	0.0272 LSB
$M=5.10^5$	0.0102 LSB	0.0251 LSB		W = 8 LSB	0.0327 LSB

Table 1. Measured standard deviations ΔDNL characteristics measured as functionby of record length M for superimposed errors 0,25 LSB and amplitude of the dithering voltage for 8/bit and 10 bit mode of the DAC UT.

4. Conclusion

In the paper, a new method for DAC testing under dynamic conditions was analysed. A detailed description of the test setup followed by mathematical models and uncertainty analysis is presented. The new proposed method was validated both by simulations and experiment on real setup under different working conditions. The results were compared with the results obtained from the standard static test method. The juxtaposition showed that the results achieved by this method are quite similar to the results obtained by the standardized static test method.

Acknowledgments

The work is a part of the project supported by the Science Grant Agency of the Slovak Republic (No. 1/0555/11).

This work was supported by the Slovak Research and Development Agency under the contract No. APVV-0333-11.

References

[1] Draft Standard for Terminology and Test Methods for Digital-to-Analog Converters, IEEE STD P1658, Sep. 2008

[2] Michaeli L., Sekerak M., Šaliga J., Serra A.C.,: "Dynamic DAC Testing by Registering the Input Code when the DAC output matches a Reference Signal", Proc. IMEKO IWADC 2011 International Workshop on ADC Modelling, Testing and Data Converter Analysis and Design and IEEE 2011 ADC Forum: Orvieto, Italy, 2011, ISBN 978-88-906201-0-2

[3] A. Baccigalupi, M. D'Arco, A. Liccardo, M. Vadursi, "Testing high resolution DACs: a contribution to draft standard IEEE P1658", Measurement, Vol. 44, Issue 6, July 2011, pp. 1044-1052.

Model of Errors Caused by Discrepancies in Gain and Phase of Input Channels in TDEMI system

M. Kamenský, K. Kováč, G. Války

Slovak University of Technology in Bratislava, Faculty of Electrical Engineering and Information Technology, Institute of Electrical Engineering, Bratislava, Slovakia
Email: miroslav.kamensky@stuba.sk

Abstract. *Multiresolution analog-to-digital converter (MRADC) is used for very fast signal sampling with sufficient dynamic range in Time domain electromagnetic interference (TDEMI) measuring system for spectrum measurements. Properties of resulting spectrum influenced by imperfections in MRADC are analyzed in the paper. For precise estimation of errors caused by differences of gain and phase shift in parallel channels concept of error signal of cosine shape pulses have been considered in the model. Mathematical model of spectral error using this concept has been created.*

Keywords: Time Domain EMI Measurement, Multiresolution Quantization, Gain and Phase Error

1. Introduction

Measuring of electromagnetic interference (EMI) spectra is obviously long lasting procedure. Super heterodyne principle used in conventional analog EMI receivers or spectrum analyzers provides high dynamic range. However, only one narrow frequency band is transferred to the detector via the intermediate frequency amplifier at the time. Therefore time-consuming sweeping through the whole bandwidth is needed and several tens of minutes are often required to complete the whole EMI spectrum measurement by measuring receiver.

EMI measurements according to standards are required for commercial production of electronic equipment. Development of new faster principles leads to reduction of costs and time to market. Time domain EMI (TDEMI) system [1] was introduced quite recently. It is based on FFT spectrum estimation performed by fast DSP aids in connection with multiresolultion analog-to-digital converter (MRADC) technology, which engages several parallel ADC channels to achieve required high dynamic range of the system [2].

In traditional systems with one input channel or individual channels (like spectrum analyzer or oscilloscope) there is always compromise between bandwidth processed at the time and dynamic range. TDEMI devices process complete spectral content at the time. However new error sources arise in the system where parallel channels with different characteristics are used. Errors caused by those differences seem to be serious sources of spurious spectral components. Model of error spectrum is discussed in the paper, which should help to understand leakage of spurious higher harmonics in spectrum obtained for simple harmonic input signal. The model considers gain and phase error of MRADC.

2. TDEMI and concept of error model

Principal block structure of TDEMI device is depicted in Fig. 1a. Power splitter distributes analog signal to all parallel paths. Recently 3 channels are usual. Limiter protects ADC from out of range voltage. Separate amplifiers/attenuators provide different range and voltage resolution of individual channels. All channels are simultaneously sampled and converted by identical 8 or 10 bit very fast flash ADCs. Final discrete value is created by extracting the

output from that ADC offering the best resolution but with the range still covering the actual input value. Short time Fast Fourier transform (FFT) is finally applied to sampled data [3].

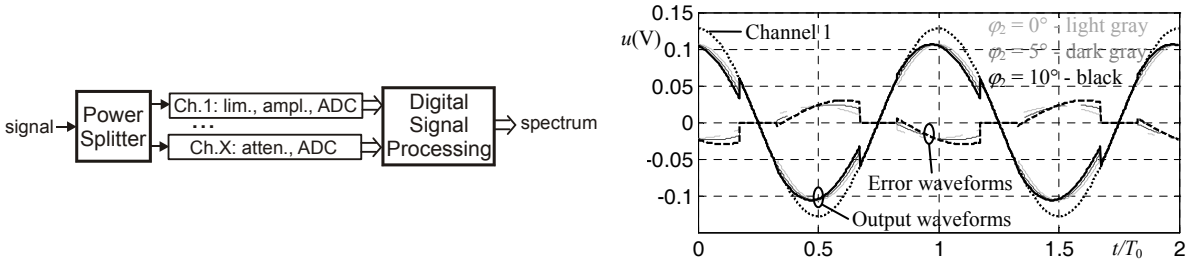

Fig. 1. Principal of TDEMI: a) Block structure of TDEMI system; b) examples of waveforms

Even if perfectly realized a quantization system like MRADC generates disturbance in spectrum of e.g. harmonic signal [4] due to quantization error. However practical experience shows that in real systems there are more serious sources of errors. Amplitude and phase frequency characteristics in each channel are not perfectly matched in the whole frequency range. Moreover it is hardly possible to avoid slope difference between channels. So serious signal discontinuities arise in points where the system switches from one ADC output to another. Spurious spectrum components generated by those discontinuities significantly restrict spurious free dynamic range of real TDEMI device for continues input signal types.

Harmonic input signal may be considered as suitable for modeling the measured interference of devices operating on switched mode power supply principle, where disturbance is like a mixture of sinusoids. For harmonic input signal differences between channels result in disturbances similar to time-domain error pulses like sketched in Fig. 1b (see error waveforms). For theoretical analysis of discontinuities present in the waveform reconstructed from sequence of samples the erroneous waveform could be simply modeled as additive impulsive error signal. In [5] simplified error model was based on rectangular pulses. However for gain and phase error it more suitable to use pulses of cosine shape like proposed in this paper.

3. Derivation of the model

Consider pure harmonic input signal

$$u_{\mathrm{in}}(t) = A_{\mathrm{in}} \cos(\omega_0 t) \tag{1}$$

Spectrum of ideal harmonic signal has only one component. As spectrum of sum of two signals is the sum of both signal spectra the higher harmonics present in MRADC output waveform are just higher harmonics of error signal. If we identify higher harmonics of error pulses, those could be regarded as theoretical spurious components in measured spectrum. The first harmonic of error waveform still means corruption of value of the first harmonic shown by the measuring unit.

Let us consider gain error and phase between channels. For the harmonic input signal two error pulses are typical within the interval of one period (t_0; t_0+T_0) for zero offset and amplitude higher than range R_1 of the channel 1 but still in range of channel 2, like in examples depicted in Fig. 1b. Time representation of error could be expressed as

$$u(t) = \begin{array}{ll} A_{\mathrm{e}} \cos(2\pi f_0 t + \varphi_{\mathrm{e}}) & \text{for} \quad \left(\left[(t - t_0) \bmod T_0\right] + t_0\right) \in \langle t_{\mathrm{r1}}, t_{\mathrm{f1}}\rangle \cup \langle t_{\mathrm{r2}}, t_{\mathrm{f2}}\rangle \\ 0 & \text{for} \quad \left(\left[(t - t_0) \bmod T_0\right] + t_0\right) \notin \langle t_{\mathrm{r1}}, t_{\mathrm{f1}}\rangle \cup \langle t_{\mathrm{r2}}, t_{\mathrm{f2}}\rangle \end{array} \tag{2}$$

Time values of rising and falling edge t_{r1}, t_{f1} apply for the first pulse while t_{r2}, t_{f2} for the second one. We assume that the MRADC system switches from the first channel to the second, or vice-versa, when the value from the first channel is just crossing its range R_1. And we will take the signal from channel 1 for reference so (1) represents channel 1 signal. To start with rising edge we could write following formulas for time parameters of one period ($-T_0/4$; $-T_0/4+T_0$) of error pulse signal

$$t_{r1} = -\frac{T_0}{2\pi}\arccos\left(\frac{R_1}{A_{in}}\right) \; ; \; t_{f1} = -t_{r1} \; ; \; t_{r2} = t_{r1} + \frac{T_0}{2} \; ; \; t_{f2} = t_{f1} + \frac{T_0}{2} \tag{3}$$

If there is phase shift φ_2 between channels we should expect nonzero phase φ_e of harmonic signal forming inner part of error pulses. Phase φ_e and amplitude A_e of error could be found from difference of voltage phasors of both channels

$$A_e\angle\varphi_e = A_{in}\angle 0 - A_{in}(\delta G_2 + 1)\angle\varphi_2 \tag{4}$$

where δG_2 is relative gain error of channel 2 in comparison with channel 1.

As there are two error pulses per period T_0 we will form the model of error spectrum from two members

$$\mathbf{U}_{COS,n} = \mathbf{U}_{CP,n}(f_0, t_{r1}, t_{f1}, A_e, \varphi_e) + \mathbf{U}_{CP,n}(f_0, t_{r2}, t_{f2}, A_e, \varphi_e) \tag{5}$$

We have already recognized all parameters entering into analytical expression (5) of error model. However formulas for spectral components $\mathbf{U}_{CP,n}=f(f_0,A,t_r,t_f,\varphi)$ of a pulse of cosine shape have to be identified. Considering exponential form of Fourier series we have derived following expressions for real and imaginary part of complex spectral components

$$\mathrm{Re}\{\mathbf{U}_{CP,0}\} = \frac{A}{2\pi}[\sin(2\pi f_0 t_f + \varphi) - \sin(2\pi f_0 t_r + \varphi)] \tag{6}$$

$$\mathrm{Re}\{\mathbf{U}_{CP,1}\} = \frac{Af_0}{2}(t_f - t_r)\cos(\varphi) + \frac{A}{8\pi}(\sin(4\pi f_0 t_f + \varphi) - \sin(4\pi f_0 t_r + \varphi)) \tag{7}$$

$$\mathrm{Im}\{\mathbf{U}_{CP,1}\} = \frac{Af_0}{2}(t_f - t_r)\sin(\varphi) + \frac{A}{8\pi}(\cos(4\pi f_0 t_f + \varphi) - \cos(4\pi f_0 t_r + \varphi)) \tag{8}$$

and (for n>1)

$$\begin{aligned}\mathrm{Re}\{\mathbf{U}_{CP,n}\} = \frac{A}{2\pi(n^2-1)}\{&n\cos(2\pi f_0 t_f + \varphi)\sin(n2\pi f_0 t_f) - \sin(2\pi f_0 t_f + \varphi)\cos(n2\pi f_0 t_f) \\ &- n\cos(2\pi f_0 t_r + \varphi)\sin(n2\pi f_0 t_r) + \sin(2\pi f_0 t_r + \varphi)\cos(n2\pi f_0 t_r)\}\end{aligned} \tag{9}$$

$$\begin{aligned}\mathrm{Im}\{\mathbf{U}_{CP,n}\} = \frac{A}{2\pi(n^2-1)}\{&n\cos(2\pi f_0 t_f + \varphi)\cos(n2\pi f_0 t_f) + \sin(2\pi f_0 t_f + \varphi)\sin(n2\pi f_0 t_f) \\ &- n\cos(2\pi f_0 t_r + \varphi)\cos(n2\pi f_0 t_r) - \sin(2\pi f_0 t_r + \varphi)\sin(n2\pi f_0 t_r)\}\end{aligned} \tag{10}$$

4. Results

Properties of proposed theoretical model were compared with simulation results. Parameters of simulated TDEMI system are roughly apparent from curves shown in Fig. 1b. Switching level R_1=60 mV was used while input signal amplitude was A_{in}=128 mV. For generalization channel 1 is considered ideal with zero phase and unity gain. Simulated error parameters associated with differences between channels are comparable with a real TDEMI device [5]. Gain error of the second channel is δG_2=-17%. As visible from waveforms depicted in Fig. 1b three values of phase shift between channels were simulated: φ_2=0°; 5°; 10°. For all of them the spectrum of error is depicted in Fig. 2a. The model quite precisely estimates spectra as

values obtained from model lie close to dots representing simulation results not only for zero phase but also for significant phase shift between channels.
The results also demonstrate how spurious free dynamic range (SFDR) of TDEMI system could be restricted by discrepancies between channels. It should be expected that with increasing phase φ_2 amplitude of dominant spurious component rises and therefore SFDR drops. To investigate also influence of signal amplitude or ration A_{in}/R_1 on quality of spectrum measurement SFDR dependency from A_{in} was depicted in Fig. 2b for constant R_1=60 mV. Shown results were collected from designed error model which made analysis easier and faster. Finally we can see that drop in SFDR is significant for amplitude A_{in} rising just above threshold R_1. Then there is a point of minimum representing the worst case from where SFDR increases with rising A_{in}. This fact encourages thinking about possibility of system adjusting to amplitude of input signal using e.g. cascade of switchable attenuators at the input of system. It is interesting that positions of SFDR minima are not affected by phase difference between channels - φ_2.

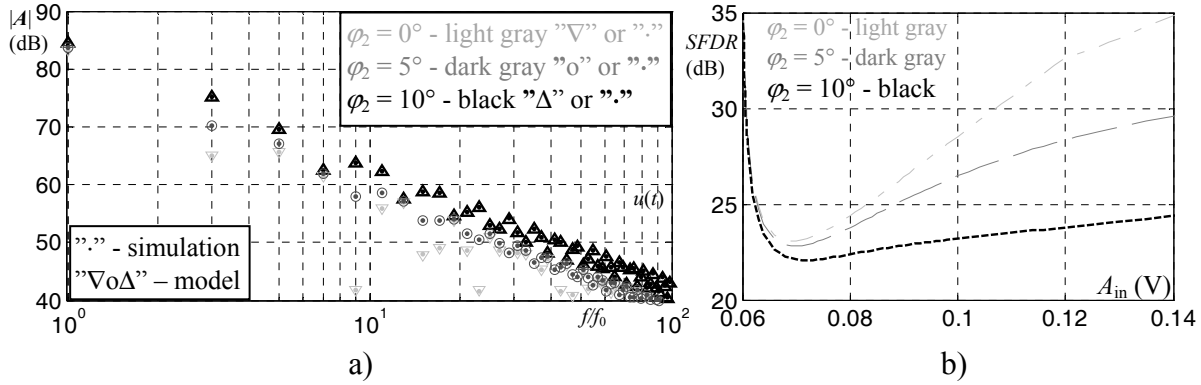

Fig. 2. Analysis of error spectrum for δG_2=-17% and three different φ_2 using proposed error model: a) error spectra – model compared with simulation; b) SFDR dependencies on input signal amplitude.

Acknowledgements

This work was supported by Slovak Ministry of Education under grant No. 2003SP200280802 and the Slovak Grant Agency VEGA under grant No. 1/0963/12.

References

[1] Braun S, Russer P. A low-noise multiresolution high-dynamic ultra-broad-band time-domain EMI measurement system. *IEEE Transactions on Microwave Theory and Techniques*, 53 (11): 3354- 3363, 2005.

[2] Braun S, Russer P. The dynamic range of a Time-Domain EMI Measurement System using several parallel Analog to Digital Converters. In proc. of the 16th International Zurich Symposium on EMC, Zurich, Switzerland, 2005, 203-208.

[3] Krug F, Mueller D, Russer P. Signal Processing Strategies With the TDEMI Measurement System. *IEEE Transactions on Instrumentation and Measurement*, 53 (5): 1402-1408, 2004.

[4] Kamenský M, Kováč K, Války G. Improvement in Spectral Properties of Quantization Noise of Harmonic Signal Using Multiresolution Quantization. *IEEE Transactions on Instrumentation and Measurement*, 61 (11), 2888-2895, 2012.

[5] Války G, Kamenský M, Kováč K. Analysis of Errors Caused by Input Channels Amplitude Discrepancies in Time Domain EMI Measuring System. In proc. of 22nd Intern. Conference EMD'2012, Vilnius, Lithuania, 2012, 126-129.

New Procedure for Calculating the Uncertainty of One Output Quantity in Calibration Certificates

[1]G. Wimmer, [2]V. Witkovský

[1]Mathematical Institute Slovak Academy of Sciences, Bratislava, Slovakia, Faculty of Natural Sciences, Matej Bel University, Banská Bystrica, Slovakia, and Department of Mathematics and Statistics, Faculty of Science, Masaryk University, Brno, Czech Republic,
[2]Institute of Measurement Science, Slovak Academy of Sciences, Bratislava, Slovakia
Email: wimmer@mat.savba.sk

Abstract. *Using the software "Tail probability calculator" (see [1],[2]), the (1-α)-confidence region for unknown output quantity in calibration certificates is stipulated. Specified is also the real coverage probability corresponding to the expanded uncertainty of the measurand. This expanded uncertainty is determined according to regulation [3].*

Keywords: One Output Quantity Calibration Certificate, Confidence Interval, Tail Probability Calculator

1. Introduction

This contribution is based on EA (European co-operation for Accreditation) document EA 4/02. For calibration laboratories is there described "an unambiguous and harmonised way of evaluating and stating the uncertainty of measurement" (see [3], p.4). In accordance with EAL decision (see [3]) calibration laboratories shall state an expanded uncertainty U of measurement, obtained by multiplying the standard uncertainty of the output estimate by coverage factor k. For k=2 the assigned expanded uncertainty (in the case where a normal (Gaussian) distribution can be attributed to the measurand) corresponds to a coverage probability of approximately 95%. On p. 12 in [3] is claimed, that this condition is fulfilled in the majority of cases encountered in calibration work. But in effect in (almost) all real cases it is not possible to attribute a normal distribution to the measurand (see all examples in [3]). This contribution answers the questions:
(i) How to obtain the *(1-α)*-confidence region for unknown output quantity in calibration certificates ?
(ii) What is the real coverage probability corresponding to expanded uncertainty determined according to regulation [3] ?

2. Subject and Methods

As stated in [3], p. 5, the set of input quantities $X_1,X_2,...,X_n,Z_1,...,Z_m$ can be grouped into two categories according to the way in which the value of the quantity have been determined.

(a) quantities $X_1,...,X_n$, whose estimate are directly determined in the current measurement;

(b) quantities $Z_1,...,Z_m$, whose estimate are brought into the measurement from external sources.

Considered case of calibration deals with only one measurand or output quantity Y.

The **theoretical** (mathematical, physical) model of calibration is understood as the equation

$$Y = f(X_1,..., X_n, Z_1,..., Z_m), \quad (1)$$

where the model function *f* represents the procedure of the measurement and the method of evaluation. Measuring the real (true) value X we mathematically denote by the random variable ξ_X and the estimate of the quantity X (the measured value) is denoted as x.

The **stochastic** model of calibration is understood as the equation

$$\xi_Y = f(\xi_{X_1},...,\xi_{X_n},\xi_{Z_1},...,\xi_{Z_m}) . \qquad (2)$$

In accordance with [EA4/02] we suppose that

-- measurements $\xi_{X_1},...,\xi_{X_n}$, $\xi_{Z_1},...,\xi_{Z_m}$ are independent,

-- probability distributions of measurements $\xi_{X_1},...,\xi_{X_n}$, $\xi_{Z_1},...,\xi_{Z_m}$ are known, measurements obey one of the following distributions: normal, rectangular, triangular, Student's t,

-- estimates of all quantities $X_1,X_2,...,X_n,Z_1,...,Z_m$ i.e. the realizations $x_1,...,x_n,z_1,...z_m$ of random variables $\xi_{X_1},...,\xi_{X_n}$, $\xi_{Z_1},...,\xi_{Z_m}$ are known.

Saying more precise, if the mean value of the random variable ξ_j is $E(\xi_j)$ (unknown), then the distribution of ξ_j - $E(\xi_j)$ is normal with zero mean and known variance or rectangular with zero mean and known support or triangular with zero mean and known support or Student's t with known degrees of freedom.

The stochastic model of calibration (2) we shall linearize in realizations $x_1,...,x_n,z_1,...z_m$ (using Taylor series expansion) and neglect the terms of second and higher order. So we obtain

$$\xi_Y \cong f(x_1,\dots,x_n,z_1,\dots,z_m) + \left.\frac{\partial f(\xi_{X_1},\dots,\xi_{X_n},\xi_{Z_1},\dots,\xi_{Z_m})}{\partial \xi_{X_1}}\right|_{\xi_{X_1}=x_1,\dots,\xi_{Z_m}=z_m} (\xi_{X_1}-x_1)+\dots$$

$$+\left.\frac{\partial f(\xi_{X_1},\dots,\xi_{X_n},\xi_{Z_1},\dots,\xi_{Z_m})}{\partial \xi_{X_n}}\right|_{\xi_{X_1}=x_1,\dots,\xi_{Z_m}=z_m} (\xi_{X_n}-x_n)+$$

$$+\left.\frac{\partial f(\xi_{X_1},\dots,\xi_{X_n},\xi_{Z_1},\dots,\xi_{Z_m})}{\partial \xi_{Z_1}}\right|_{\xi_{X_1}=x_1,\dots,\xi_{Z_m}=z_m} (\xi_{Z_1}-z_1)+\dots$$

$$+\left.\frac{\partial f(\xi_{X_1},\dots,\xi_{X_n},\xi_{Z_1},\dots,\xi_{Z_m})}{\partial \xi_{Z_m}}\right|_{\xi_{X_1}=x_1,\dots,\xi_{Z_m}=z_m} (\xi_{Z_m}-z_m)=$$

$$=(a_0-a_1x_1-\dots-a_nx_n-b_1z_1-\dots-b_mz_m)+a_1\xi_{X_1}+\dots+a_n\xi_{X_n}+b_1\xi_{Z_1}+\dots+b_m\xi_{Z_m}=$$

$$=A+a_1(\xi_{X_1}-\mathrm{E}(\xi_{X_1}))+\dots+a_n(\xi_{X_n}-\mathrm{E}(\xi_{X_n}))+b_1(\xi_{Z_1}-\mathrm{E}(\xi_{Z_1}))+\dots+b_m(\xi_{Z_m}-\mathrm{E}(\xi_{Z_m}))=$$

$$=A+\xi ,$$

where A is unknown, $a_1,...,a_n,b_1,...,b_m$ are known values. Understandably A is considered as the true value of the output quantity Y. That is $\xi_Y = Y + \xi$. The distribution of ξ is a linear combination (with known coefficients) of known distributions, each of them has zero mean. In addition the distribution of ξ is according to our assumptions symmetrical around zero. Using the software [1] or [2] we can easy calculate the *(1-α/2) quantile* $\gamma_{(1-\alpha/2)}$ of ξ and obtain the interval $(-\gamma_{(1-\alpha/2)},\gamma_{(1-\alpha/2)})$ for which is

$$P\{-\gamma_{(1-\alpha/2)} \le \xi \le \gamma_{(1-\alpha/2)}\} = 1-\alpha .$$

It holds

$$P\{Y- \gamma_{(1-\alpha/2)} \leq Y+ \xi = \xi_Y \leq Y+ \gamma_{(1-\alpha/2)}\}=1-\alpha$$

i.e.

$$P\{ \xi_Y - \gamma_{(1-\alpha/2)} \leq Y \leq \xi_Y + \gamma_{(1-\alpha/2)}\}=1-\alpha$$

and so

$$(\xi_Y - \gamma_{(1-\alpha/2)}, \xi_Y + \gamma_{(1-\alpha/2)}) \qquad (3)$$

is the $(1-\alpha)$-confidence interval for measured output quantity Y. If the realization of ξ_Y is $y=f(x_1,...,x_n,z_1,...,z_m)$, the realization of the $(1-\alpha)$-confidence interval is $(y - \gamma_{(1-\alpha/2)}, y + \gamma_{(1-\alpha/2)})$.

3. Example

We shall demonstrate the above mentioned procedure for calculating the uncertainty of one output quantity in calibration certificates on the example given in Supplement 1 of [3], p. 29 "Calibration of a weight of nominal value 10 kg" (exactly on the little corrected version of this example given in [4], p.5).

The unknown output quantity Y is the unknown conventional mass m_X obtained from (1), where

$X_1 = \delta m$ is the (measured) difference in mass between the unknown mass and the standard; there were realized three measurements $\xi_{\delta m}^{(1)}$, $\xi_{\delta m}^{(2)}$, $\xi_{\delta m}^{(3)}$ using the substitution method and substitution scheme ABBA ABBA ABBA, all measurements are supposed to have normal distribution, the realization of $\xi_{\delta m} = 1/3\ (\xi_{\delta m}^{(1)} + \xi_{\delta m}^{(2)} + \xi_{\delta m}^{(3)})$ is 0,020 g and the estimate of its standard deviation (obtained from prior evaluation) is 14,4 mg;

$Z_1 = m_S$ is the conventional mass standard, the calibration certificate gives the value of 10 000,005 g (the realization of ξ_{mS}) with an associated normal distribution of ξ_{mS} and standard uncertainty of 22,5 mg;

$Z_2 = \delta m_D$ is the drift of value of the standard since its last calibration, the distribution of $\xi_{\delta mD}$ is (assumed to be) rectangular in the interval 0 - 15 mg and its realization (estimate) is set to 0;

$Z_3 = \delta m_C$ is variation due to eccentricity, the distribution of $\xi_{\delta mC}$ is (assumed to be) rectangular in interval ± 10 mg and its realization is (set to) 0;

$Z_4 = \delta B$ is air buoyancy, the distribution of $\xi_{\delta B}$ is (assumed to be) rectangular in interval ± 1 x 10^{-6} of the nominal value and its realization is (set to) 0.

The proposed v theoretical model of calibration (1) is

$$m_X = \delta_m + m_S + \delta m_D + \delta m_C + \delta B$$

The expanded uncertainty calculated according to [3] is U=57 mg (coverage factor k=2).

Using the software "Tail probability calculator" (see [1], [2]), the measured mass of the nominal 10 kg weight is 10,000 025 kg and the 0,95-confidence region for this weight is ± 55,4 mg. The 0,9-confidence region for this weight is ± 46,5 mg and we can stipulate using the software [1], [2] any confidence region for the calibrated quantity.

On the other hand, we can determine the unknown coverage probability for the expanded uncertainty calculated according to [3]. In previous example is this coverage probability 0,978.

4. Discussion

The example analysed in this contribution was developed (according to [3], p. 28) by a special expert group. Laboratories should determine the probability distribution of measurements acting in the proposed stochastic model (2) of calibration which is based on suggested theoretical model (1) of calibration. It is recommended in many cases to assess the realizations of the measurements ξ_{Zi} using simulations. Another way for determining the proper confidence interval (3) for calibrated value is via Monte Carlo simulations in accordance with [5].

Acknowledgements

The work was supported by the Slovak Research and Development Agency, grant APVV-0096-10 and by the research grant VEGA 2/0038/12.

References

[1] Duby T, Wimmer G, Witkovský V, Tail probability by characteristic function inversion, Measurement 2013, Proceedings, 2013.

[2] Witkovský V, Matlab algorithm TDIST: The distribution of a linear combination of Student's t random variables. In: J. Antoch, editor COMPSTAT 2004 Symposium. 2004, 1995-2002. Physica-Verlag/Springer 2004, Heidelberg, Germany.

[3] Expression of the Uncertainty of Measurement in Calibration, European co-operation for Accreditation - EA 4/02, 1999.

[4] Expression of the Uncertainty of Measurement in Calibration (Slovak translation of EA 4/02), Slovenská národná akreditačná služba, MSA-L/12, Bratislava, 2010.

[5] Evaluation of Measurement Data – Supplement 1 to the "Guide to the expression of uncertainty in measurement" – Propagation of distributions using a Monte Carlo method, JCGM 101:2008.

Uncertainty Analysis of Piston Gauge

[1]M. I. Maniur, [1,2]R. Palenčár, [1,2]S. Ďuriš, [2]P. Pavlásek

[1]Slovak Institute of Metrology, Bratislava, Slovakia,
[2]Slovak University of Technology, Bratislava, Slovakia,
Email: maniur@smu.gov.sk

Abstract. *Piston gauge is typically used for the calibration of pressure gauges and pressure transmitters. The principle of pressure definition is based on the physical pressure definition (known value of force that perpendicularly acts on known size of area). In practice, the uncertainty of the reproduced pressure by piston gauge is mostly determined by the calibration for specific conditions. Uncertainty of reproduced pressure is rarely evaluated on the basis of uncertainty for determination of the piston and balances weights as well as the uncertainty of the effective area of pressure gauge. In the latter case, it is important to analyze the uncertainties caused by the piston gauge conditions of use. The paper presents the analysis of the uncertainties of individual components of piston gauge for pressure measurement, where liquid oil is used as crusher liquid.*

Keywords: Piston Gauge, Uncertainty of Measurements, Uncertainty Analysis

1. Introduction

Now the precision of piston gauges expressed by permissible error is about 0.005% of reading and in some cases even better than 0.002%. Uncertainties of measurement are affected by the measurement conditions. Therefore the accuracy data from manufacturer are uncontrollable without any assumptions of conditions.

This paper presents the uncertainty analysis for pressure determination reproduced by piston gauge in case when we have the data from calibration certificate for piston weight, balances weights, effective piston area and their uncertainties. Analysis is based on the basic relationship for determining of pressure caused by piston gauge on which the law of uncertainty propagation is applied. It is necessary to determine the values of all contributions of influencing factors to the uncertainty of reproduced pressure.

2. Subject and Methods

For the piston oil gauge measuring overpressure the pressure defined by the relation [1, 2]

$$p_{\mathrm{et}} = \frac{m_j \cdot g_{\mathrm{m}} \cdot \left(1 - \frac{\rho_{\mathrm{vz}}}{\rho_{\mathrm{z}}}\right) + \pi \cdot D \cdot T}{A_{\mathrm{ef}} \cdot \left[1 + \left(\alpha_{\mathrm{p}} + \alpha_{\mathrm{c}}\right)\left(\theta - 20\right)\right] \cdot \left(1 + \lambda p\right)} + \rho_{\mathrm{oil}} \cdot g_{\mathrm{m}} \cdot h \qquad (1)$$

where

- p_{et} is pressure on the output of piston gauge (Pa),
- m_j is the actual total weight of the loaded balances (kg),
- g_{m} is the local gravitational acceleration (m/s^2),
- ρ_{gas} is the density of gaseous medium (kg/ m^3),
- ρ_{vz} is the density of ambient air (kg/m^3),

- ρ_z is the average density of the loaded balances (kg/m^3),
- ρ_{oil} is the density of oil medium (kg/m^3),
- πDT is the affect caused by surface tension (N/m)
- A_{ef} is the effective piston area at 20 °C and null pressure (m^2),
- α_p is the temperature coefficient of linear expansion of piston (°C^{-1}),
- α_c is the temperature coefficient of linear expansion of container (°C^{-1}),
- θ is temperature of pressure gauge (°C),
- λ is the coefficient of pressure deformation of pressure gauge (Pa $^{-1}$),
- h is the height differences of levels of inputs points (m),
- p is pressure value affecting on pressure gauge (nominal pressure value) (Pa).

The next section describes different uncertainties (in the case described by equation (1)) their evaluation and inclusion into the total uncertainty of defined pressure.

Expected limiting values of environment variables in this analysis are [5]:

- ambient temperature: (19 to 23) °C,
- ambient relative humidity: (5 to 95) %,
- ambient pressure: (70 to 110) kPa.

Calculation of the Standard Uncertainty by the Method A
Evaluation of uncertainty by the method A is determined as the standard deviation of the arithmetic mean when we estimate the output variable as the arithmetic mean of the measured data.
If we do not have enough number of pressure data at one measurement point to be able to evaluate the uncertainty by the method A then we determine the repeatability by the method B.

Calculation of Standard Uncertainty by the Method B
On the basis of the law of uncertainty propagation which assumes the dependence of output quantity p on input quantities in the form $p = f(x_1, ..., x_n)$, there will be for uncorrelated input quantities [4]

$$u(p) = \sqrt{\sum_{i=1}^{m} C_i^2 u^2(x_i)} \qquad (2)$$

where

C_i – is the sensitivity coefficient which will be determined as $C_i = \frac{\partial f}{\partial x_i}$,

$u(x_i)$ – is standard uncertainty of estimation x_i.

We will assume the value of the component – πDT of the effect caused by surface tension as negligible for corresponding analysis.

For this purpose it is necessary first to determine estimates and uncertainties of the input quantities. According to equation (1) assuming that the piston gauge is used and the same high of reference levels is assured are:

- m_j is the actual total weight of the loaded balances (kg),
- g_m is the local gravitational acceleration (m/s^2),
- ρ_{gas} is the density of ambient air (kg/ m^3),
- ρ_z is the average density of the loaded balances (kg/m^3),
- A_{ef} is the effective piston area at 20 °C and null pressure (m^2),
- α_p is the temperature coefficient of linear expansion of piston (°C^{-1}),
- α_c is the temperature coefficient of linear expansion of container (°C^{-1}),
- θ is temperature of pressure gauge (°C),
- λ is the coefficient of pressure deformation of pressure gauge (Pa $^{-1}$),

Individual input variables for pressure determination of the pressure piston gauge can be split into two groups. The first group consists of the base component to determine the pressure (m, A_{ef}, g_m) and the second group consists of components that are used for correction of the basic components. If we analyze the relationship from the other point of view then we can include all quantities except (m, A_{ef}, α_c, α_p, ρ_z,λ). According to [3] components with the maximal value in the total uncertainty of a piston manometer are A_{ef}, m, T

3. Results

Data from the Slovak Institute of Metrology specified in [5] were used for the uncertainty analysis. All uncertainty contributions of the input quantities were determined as estimates by application of the law of uncertainty propagation on relationship (1) according to [1], [2]. Results of the analysis are shown in Table 1 for the pressure point p_{20} = 20,00464 MPa.

Table1. Uncertainty budget for i = 20 pressure point of piston pressure gauge.

Input quantity	Estimation	Standard uncertainty	Probability contribution	Sensitivity coefficient *	Contribution to the total uncertainty
m_{z20} (kg)	20,397	$4{,}3.10^{-5}$	rectangular	0,98	$1{,}28.10^{-5}$
g_m (ms^{-2})	9,80873243	$1{,}0.10^{-7}$	rectangular	2,034	$2{,}04.10^{-7}$
ρ_{vz} (kgm^{-3})	1,192	$1{,}4.10^{-5}$	rectangular	0,0025	$3{,}54.10^{-6}$
ρ_z (kgm^{-3})	7904,721	$1{,}9.10^{-2}$	rectangular	$3{,}82.10^{-7}$	$7{,}26.10^{-9}$
A_{ef} (m^2)	$9{,}9995.10^{-6}$	$1{,}6.10^{-10}$	rectangular	2000563	$3{,}2.10^{-4}$
$(\alpha_p + \alpha_c)$ (°C^{-1})	1.10^{-5}	$1{,}0.10^{-6}$	rectangular	9,002	$9{,}0.10^{-9}$
T_{20} (°C)	20,45	$2{,}5.10^{-2}$	rectangular	0,0002	$5{,}0.10^{-6}$
λ (MPa^{-1})	8.10^{-10}	$2{,}4.10^{-10}$	rectangular	400,2	$9{,}61.10^{-8}$
p_{et20} (MPa)	20,00464	$1{,}4.10^{-6}$	Gaussian	1	$1{,}4.10^{-6}$

* sensitivity coefficients have units based of definition.

Graphical presentation of the uncertainty value of input quantities is in Figure 1.

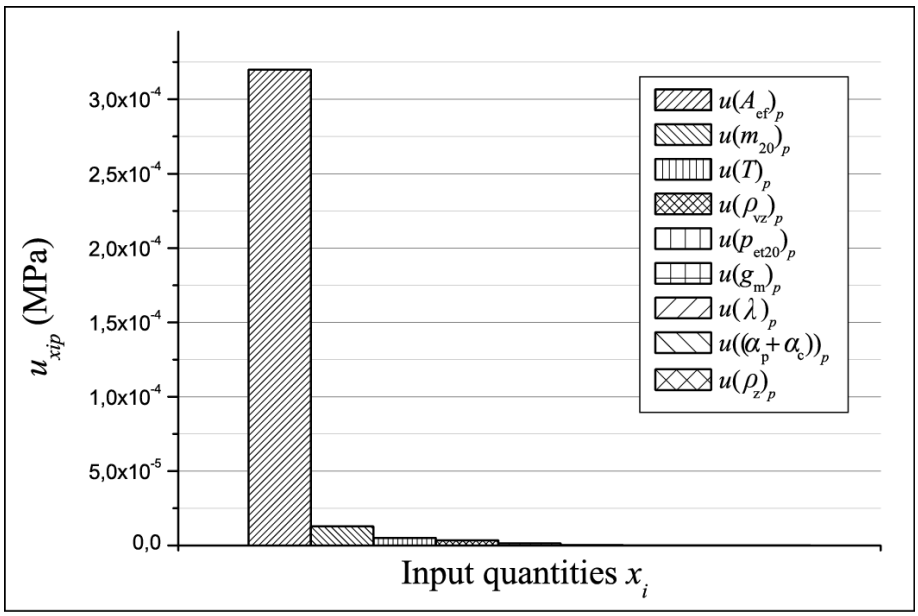

Fig. 1. Uncertainty contributions of individual input quantities.

4. Discussion and conclusions

Detailed uncertainty analysis of piston pressure gauge gives us in particular measurement system a possibility to deteremine correctly the value of individual partial uncertainties, or vice versa after proper consideration some uncertainty neglect. As we can see from Table 1 and from Figure 1 it was cnfirmed that the dominant uncertainty components of piston gauge are A_{ef}, m, T, but component T and m are almost negligible comparing to the impact A_{ef} component.

The impact of tilt piston was nglected in the analysis. In analyzing. For that reason there was necessary to control the vertical deviation piston spirit levels. The effects of sensitivity, stability and linearity was also considered in the analysis.

Acknowledgements

The authors are grateful for support for this work to the Slovak University of Technology in Bratislava, Faculty of Mechanical engineering, to the Slovak Institute of Metrology and to the Grant Agency APVV - grant No. APVV– 0096-10, VEGA - grant No. 1/0120/12, KEGA – grant No. 005STU - 4/2012.

References

[1] EAL – G26 Calibration of Pressure Balances, 1997.

[2] Maniur M. I. Components of uncertainty piston gauges (Zložky neistôt piestových tlakomerov), in: *Metrológia a skúšobníctvo*, vol. 4, p. 11-15, 2011.

[3] Farár P, Chytil M. Pressure measurement and calibration of pressure transmitter (Meranie tlaku a postupy kalibrácie prevodníkov tlaku, seminár tlaku) SMU, 2010.

[4] EA 4/02 Expression of the uncertainty of measurement in calibration, 1999.

[5] Maniur M. I. Calibration evaluation for pressure transmitters (Vyhodnotenie kalibrácie prevodníkov tlaku). Dissertation. SjF STU, Bratislava, 2012.

Image Classification Based on Hierarchical Temporal Memory and Color Features

[1, 2]R. Škoviera, [1]I. Bajla

1 Institute of Measurement Science, Department of Theoretical Methods, Slovak Academy of Sciences, Bratislava, Slovakia
2 Faculty of Mathematics, Physics, and Informatics, Department of Applied Informatics, Comenius University, Bratislava, Slovakia
Email: rado.skoviera@gmail.com

Abstract. *The research in the domain of content-based image retrieval (CBIR) is concentrated on several problems, among which two problems are essential: – development of efficient image classification algorithms, and selection of suitable image features. Recently, a biologically inspired Hierarchical Temporal Memory (HTM) network demonstrated promising results in image classification tasks. The focus of this paper is to explore possibilities of this network to be applied to CBIR. In particular, we study the performance of the HTM network when, instead of conventional grey-level images and features, color features are used. The results of our experiments show that using color texture features, defined for a reduced range of color quantization values, performs comparably well as the grey-scale image features.*

*Keywords**:** Hierarchical Temporal Memory (HTM); Content-Based Image Retrieval, Image Color Features*

1. Introduction

The rise of digital techniques for image acquisition and ubiquity of internet connections in recent decade evoked the creation of a huge number of image databases. Searching/retrieving images from such databases, which are suitable for particular purposes, become a frequent and important task in many application areas, e.g. the so-called content-based image retrieval (CBIR) techniques and systems [1]. However, though a number of methods have been proposed and explored in recent years, no satisfying general solutions still exist. The core problems are: i) definition of suitable image features for image content representation, and ii) efficient clusterization of images represented by specific features. Independently, a progress in development of novel models for computational neuroscience has been achieved in the recent decade. One of such models is a biologically inspired Hierarchical Temporal Memory (HTM) network, proposed by George and Hawkins [2], which manifested encouraging results in the field of grey-level image classification problems [3, 4]. In this paper we present a novel application of the HTM network to the problem of CBIR task, in which the HTM has been extended to be able to process color features instead of only grey-level ones.

2. Subject and Methods

Image Features

In CBIR tasks a textual description is usually absent, instead, various image features (descriptors) are used to find images similar to the given query image. Different features may account for particular properties of images from a database. They are grouped into four basic types: (a) local features, (b) shape features, (c) color features, and (d) texture features. Recently, the attention of researchers has been focused on color features and a combination of color and texture features [5]. Color of pixels can be represented in different color spaces,

however, for the given image database, no apriori best-suited color space for image discrimination is known.

Selection of Color Features (Color Spaces)

Before comparing the performance of color features we first tested the HTM network with grey-scale features. More specifically, we used simple grey-scale images, and two texture features based on grey-level pixels – Grey-Level Co-occurrence (GLC) and Grey-Level Difference (GLD) [6]. For color features, we selected simple images converted to one of the selected color spaces and then fed to HTM a vector composing of individual color components for each pixel. As an alternative to the two grey-scale texture features, we used Color Co-occurrence Matrix (CCM), in particular, the Reduced Space variant of the CCM defined in [5]. The standard CCM is defined for a couple of color components C_i and C_j (i, j <1, 3> for three-component spaces). It is computed as $Q \times Q$ matrix, where Q is the number of levels used to quantify the value of color. After specification of the displacement vector $\boldsymbol{d} = [dx, dy]$, the value of C_i is determined as the i-th component of the color of a pixel at the given position $[x, y]$. The value of C_j is then determined as the j-th component of the color of a pixel at the position $[x + dx, y + dy]$. The cell of the resulting matrix with the coordinates $[C_i, C_j]$ is incremented by a constant value. For the RSCCM reduced number of quantization levels Q is used. Similarly to [5], in our experiments we used 3×3 isotropic pixel neighborhood instead of a single displacement vector, and the number of quantization levels Q=8. This means that the co-occurrence for every pixel is calculated with all neighboring. We selected six possible color component combinations $C_1\&C_2$, $C_1\&C_3$, $C_2\&C_3$, $C_1\&C_1$, $C_2\&C_2$, $C_3\&C_3$. Then, for each image patch to be fed as an input to the HTM network, we calculated six RSCCMs for the above color combinations. Based on the results of preliminary testing, we concentrated ourselves on four color spaces: *RGB, I1I2I3*, *UVW*, and *Lab* color spaces [6].

Hierarchical Temporal Memory

An HTM network can consist of several levels of elementary nodes which implement the same learning and inference algorithms. HTM has a hierarchical tree-like structure; its zero (sensory) level receives input vectors (vectorized image features) to the first level of nodes. The top level comprises one node serving as a classifier. The HTM nodes operate in two distinct stages – learning and inference. In the first step of the learning process, the node memorizes the representative spatial patterns from its receptive field, generating thereby a codebook of image patterns. The nodes in the level that is learning can be trained separately or use shared representations. After reaching the requested number of quantization points, the memorization process is finished. The ultimate goal of the HTM learning is to detect correct invariant representations of the input world based on the temporal relations contained in the learning sequence. To achieve this, one needs a frequency of transition events, i.e., co-occurrences of the memorized coincidences in adjacent time instances. A sequence of the input patterns generates a sequence of the n coincidences within the node. The last step of the learning process within each HTM node is the generation of a set of temporal groups. A node that has completed its learning phase can be switched into the inference mode. In this mode, the node produces an output vector for every input pattern provided. This vector indicates the degree of membership of the input pattern into each of the temporal groups. There are two phases of the inference process inference in the "spatial pooler" followed by inference in the "temporal pooler". Finally, we obtain an overall belief vector $\boldsymbol{y} = [y_1, y_{2, \ldots,} y_n]$ that represents closeness of the input pattern to all memorized coincidences [2]. Such a vector is inferred in the spatial pooler for every input pattern. In the second phase of the inference, the temporal pooler makes use of the learned temporal groups and calculates the output vector for the

nodes that are above in the HTM hierarchy. Each individual component of the output vector represents a belief that the vector ***y*** comes from a particular temporal group.

HTM for CBIR

The HTM network can be used for transformation of input image feature vectors to a vector space better representing original data, thereby better suited to image classification. This is achieved by increased invariance to affine transformations of the transformed feature vectors. As a result, improved classification accuracy is obtained.

3. Experiments

The proposed features have been tested on images selected from the Caltech-256 database. Ten image categories have been selected, each with 100 images for training and 100 for testing. A random classifier with normal distribution would therefore score a classification accuracy of 10% on this database. All the images have been resized to 128 x 128 pixels due to the network's requirement to have standardized input image sizes. In Fig. 1 examples of color images from the database are shown.

Fig. 1. Examples of images used in the experiment. Each image represents a different image category.

We used our implementation of the HTM network, setup as 1-layer network with node-sharing and node size of 8 x 8 pixels. Thus, the network comprised of 16 x 16 nodes. The codebook was created from the training images using online *k*-means clustering. The process started with just one cluster center (image pattern). A new cluster center was added each time, when none of the existing cluster centers was similar enough to the currently processed pattern. Similarity was calculated using Gaussian and Euclidean distance. The minimum required similarity was 0.95. This procedure has run repeatedly until the required amount of cluster centers was achieved (512 in our case). The temporal learning was implemented as a random walk within the training images, and the temporal groups were created from the time adjacency matrix ([2]) using the agglomerative hierarchical clustering. The classification in the top node was carried out using the *k*NN classifier with $k = 1$. The single layer HTM network can be expected not to perform as well as multi-layer network but the relative difference in performance using different features should be the same. However, the computational complexity of single layer network is much smaller and is therefore more feasible to use it for testing of several image features.

The RSCCM was calculated as described in [5]. The two grey-level texture features, GLC and GLD, require a displacement vector to be defined. This was set to [1, 0]. We tested several variations of the displacement vector, but the results showed no significant variation in the classification accuracy. In the GLC, as well as in RSCCM, we used eight quantization levels.

4. Results

In *Table 1*, the results of our experiment are listed. The lowest row of the table shows classification accuracy values achieved by the 1-NN classifier, incorporated as a top node of the HTM network applied to the different image features specified in the first two rows. The image features are divided into three groups: color patches (the specific color space is mentioned in the second row), the reduced scale color co-occurrence matrix (the specific color space is in the second row), and image features based on grey scale images (image patches, GLC, and GLD). For comparison, we applied the 1-NN classifier to the original image space (i.e., without HTM). The classification accuracy obtained for the same dataset was 39,2% for RGB images and 41,2% for grey scale images. The results show that the best performance was achieved with the GLD feature.

Table 1. Classification accuracy (%) for individual image features.

feature	Color Patches				RSCCM				Grey Scale		
	RGB	I1I2I3	UVW	Lab	RGB	I1IJ2I3	UVW	Lab	Patches	GLC	GLD
CA (%)	42,9	43,1	43,5	45,4	39,2	41,6	43,4	44,4	39,8	40,6	45,7

5. Discussion

We can conclude that the use of the HTM network yields higher values of CA than in the case of classification applied to the original data space (both for grey-level and color images). We have showed that using color features as an input for the HTM is encouraging and it performs comparably well as the features based on grey-scale images. Not all possible values of the parameters of co-occurrence matrices, defined for color features, have been tested. Therefore, our future research will be focused on further examination of possibilities how to improve their performance, e.g., using the RSCCM with higher values of Q and development of a color feature similar to the best performing grey-scale GLD.

Acknowledgement

This work has been supported by the Slovak Grant Agency for Science (VEGA project No. 2/0043/13).

References

[1] Deselaers T, Keysers D, Ney H. Features for Image Retrieval: An Experimental Comparison. *Journal of Information Retrieval* 11, 77–107, 2008. DOI 10.1007/s10791-007-9039-3

[2] George D, Hawkins J. Towards a mathematical theory of cortical micro-circuits. *PLoS Computational Biology* 5(10), 2009. DOI 10.1371/journal.pcbi.1000532.

[3] Štolc S, Bajla I. On the optimum architecture of the biologically inspired Hierarchical Temporal Memory model applied to the hand–written digit recognition. *Measurement Science Revue* 10(2), 28–49, 2010. DOI 10.2478/v10048-010-0008-4.

[4] Štolc S, et al. Pair-wise temporal pooling method for rapid training of the HTM networks used in computer vision applications. *Computing and Informatics,* 31, 901–919, 2012.

[5] Porebski A, Vandenbroucke N, Macaire L. Supervised texture classifi-cation: color space or texture feature selection? *Pattern Analysis and Applications* 16, 1–18. DOI 10.1007/s10044-012-0291-9, 2013.

[6] Lew M S. Principles of visual information retrieval. Springer, 2001.

The Training Stand Controlled Remotely for ADC Study

L. Michaeli, M. Godla, J. Šaliga, J. Liptak

Deptartment of Electronics and Multimedia Communications,
FEI TU of Košice, Slovak Republic,
Email: linus.michaeli@tuke.sk

Abstract. *The training stand (measuring workplace) controlled remotely allows students performing laboratory exercises in the course "Microelectronics" by the analog to digital converters (ADCs) with adjustable error characteristics using standardized testing procedures. Each training workplace is accessible independently across the Internet. The control program for all training workplaces was developed in the LabVIEW. Remote user can change stimulating signals, character of ADC error function represented by integral nonlinearity and noise through html protocol using any web browser with installed plug-in Run-time engine by NI. Front panel of the workplace simulates real laboratory instruments. The training stand for simulation of ADC properties and the testing by standardized methods is a part of the virtual laboratory where other measuring stands controlled remotely are being built.*

Keywords: Remote Teaching Laboratory, ADC Test and Simulation, LabVIEW

1. Introduction

Explanation of ADC testing methods requires prevalence of the practical exercises for better understanding of the testing procedures. Laboratory stands for ADC testing have to be equipped by the expensive precise instruments and laboratory task is rather time consuming. This limits the applicability of laboratory exercises focused on single testing procedure. The virtual laboratory stands simulating ADC converters with the error parameters involved by the user and possibility to measure them by the chosen testing procedure are the tools reducing these drawbacks of real testing laboratory for education. Remote control of those stands allows students to perform practical exercises through internet. Proposed stand represents new components in the continuously built virtual laboratory at the department of authors (html://meas-lab.fei.tuke.sk) [3].

The paper presents four testing workplaces with simulated AD converter where the integral nonlinearity is designed by the user. The nonlinearity could be proposed in various forms. First one is represented by the continuous polynomial function which is typical for ADCs with inherent integration principle. Here the order of polynomial function is two and user can select maxmal value of INL. The second possibility is integral nonlinearity in the form the sum of N characteristic *DNL*j values joint with each code bit position according the rules described in [1]. Periodicity and initial code shift depends on the implemented architecture. The properties corresponding to the Rademacher functions are typical for SAR ADCs while the harmonic periodicity for highest two code bits is typical for cyclic ADCs. The user can select characteristic *DNL*j values. Third possibility is random occurrence of $DNL(k)$, typical for flash ADCs, with the maximal value selected by user. The last possibility is linear selectable nonlinear function with selectable offset and gain coefficients.

2. Design of Workplaces for the Training of ADC Tests

The proposed system consists of following testing stands:

1. The stand for assessment of the standardized static test.
2. The stand for dynamic testing methods by i) FFT test, ii)histogram test and iii) best fitting method
3. The laboratory stand controlled remotely for FFT test provided on the real ADC.

The acquired data for each testing stand for simulated error function as input block for an ideal ADC converting block allow to calculate functional ADC characteristics *INL*, *DNL* and integral error features like THD, SINAD, ENOB. These parameters are computed according to the IEEE standard test method for Analog to Digital converter [2].

The measurement of transient code levels $T[k]$ for one selected code k allows students to understand the testing principle in the reduced time. The student has to chose two voltages $V_H(k)$, $V_L(k)$ around expected transient code level $T[k]$. The code level $T[k]$ is estimated by them using information about code bin width Q from the panel and chosen code value k. For the selected record length program determines the probabilities $P(k \leq k_{test}/V_L)=P_L$, $P(k \leq k_{test}/V_H)=P_H$ and for voltages V_H, V_L respectively. The user has to select both voltages until the probabilities are slightly around 50% , one lover and other higher. The measured transition code level $T[k]$ is calculated of-line by the equation (1)

$$T[k_{test}] = \frac{0{,}5}{(P_H V_L - P_L V_H)} \frac{(V_H - V_L)}{(P_H - P_L)} \tag{1}$$

On the base of the measured $T[k]$ levels the user can of-line calculate ADC nonlinearities.

$$INL[k] = \frac{T[k] - T_{id}[k]}{Q} \quad \Rightarrow \quad DNL[k] = \frac{T[k] - T[k-1] - Q}{Q} \tag{2}$$

The ideal code levels $T_{id}[k]$ in (2) is taken from the front panel.

Testing panels for the dynamic tests use the same ADC error characteristic for all methods. It allows user to compare sensitivity of each method on chosen error parameters. The stimulus signal is harmonic function with the amplitude covering full scale range (FSR).

The dynamic method suitable for assessment of the functional parameters is the histogram test. According to standard [2] the values of the minimal and maximal occurrences are M_{min}, M_{max}. Using the total amount of samples M the estimate of the amplitude ${}^eA$ and offset ${}^eC$ are calculated. Form the cumulative histogram $H_c[k]$ the measured code levels ${}^eT[k]$ are obtained using formulae

$${}^eT[k] = {}^eC - {}^eA \cos\left(\pi \frac{H_c[k-1]}{M}\right) \tag{3}$$

where estimated signal parameters ${}^eA$ and ${}^eC$ are calculated according to

$${}^eC = \frac{{}^eT\left[2^N - 1\right] \cos\pi \frac{M_{min}}{M} - {}^eT[1] \cos\pi \frac{M_{max}}{M}}{\cos\pi \frac{M_{min}}{M} + \cos\pi \frac{M_{max}}{M}} \quad , {}^eA = \frac{{}^eT\left[2^N - 1\right] - {}^eT[1]}{\cos\pi \frac{M_{min}}{M} + \cos\pi \frac{M_{max}}{M}} \tag{4}$$

Nonlinearities of simulated ADC are calculated by the equation (2). Taken into account terminal definition DNL must be corrected by the mean value $DNL_{Cor}[k] = DNL[k] - (\sum_{i=1}^{N-1} DNL[i])$

ADC parameters THD, SNR and SINAD will be computed in the case of the FFT dynamic test. User has possibility to asses also impact of the incoherency between testing signal and

recording period. Another utility is the selection of the window functions. Final value of total harmonic distortion is calculated from the FFT spectra by

$$THD = \sqrt{\sum_{h=2}^{m} X_{rms}^2(f_h)} \Big/ X_{rms}(f_1) \tag{5}$$

where $X_{\mathrm{rms}}(f)$ is effective value of harmonic frequency f. Next parameter which user can obtain from the program is $SINAD_{\mathrm{dB}}$.

$$SINAD_{dB} = 20 \log \frac{A_{1rms}}{eff.value\_of\_noise} \tag{6}$$

Here, $A_{1\mathrm{rms}}$ is amplitude of stimulated sine signal in the spectrum. The calculated value of $SINAD_{\mathrm{dB}}$ from equation (6) allows estimate even the effective number of bits ENOB.

$$ENOB = N - \log_2 \frac{\eta_{rms}}{Q}\sqrt{12} = \frac{SINAD - 1.76}{6.02} \tag{7}$$

The best fitting method utilise three and four parametric estimation of the stimulus input signal. The effective value of noise RMS for ENOB η_{rms} represents difference between best fitted function and recorder file $y(m)$. It allows to calculate ENOB as reduction of the resolution N caused by the deterioration of the ideal quantization noise $Q/\sqrt{12}$ by of the real noise (7)

$$\eta_{rms} = \sqrt{\frac{1}{M}\sum_{m=1}^{M-1}\left[y(m) - A\cos(2m\pi f_{in}) - B\sin(2m\pi f_{in}) - C\right]^2} \tag{8}$$

All dynamic testing panels allow users to study impact of the record length, amplitude and frequency of the stimulus signal and sampling on the measurement precision.

Workplace for the remote laboratory tests utilize the 12-bit SAR ADC (AD574A) which is controlled by the NI USB 6008 card. The stimulus signal is generated by the DAQ card NI PCI 6251 with the resolution 16 bits and sampling frequency 2,86 MS/s. Combination of both components allow to test ADC UT for various frequencies by FFT test. Identical error characteristics of simulated ADC with measured ADC allow to compare simulated and measured testing results.

3. Design of Workplaces for the Training of ADC Tests

Application software was developed in the LabVIEW. LabVIEW built in web server is used for publishing on the Internet. The server publishes front panels of applications in the form of web pages and performs interactions among remote users and applications control. Any web browser with installed plug-in Run-time engine by National Instruments is available for remote control by user. Distant clients are managed by the LabVIEW web server that ensures also transferring of the access among clients according the administrator's rules. Dynamic sharing hardware in laboratory stand is internally controlled by semaphores.

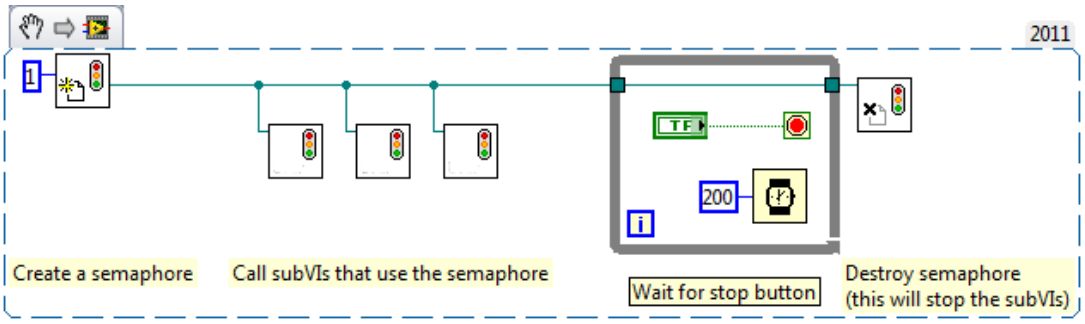

Fig. 1. Program for control of whole work stand.

The semaphore (Fig.1.) is the way how to create a group of tasks virtually running in parallel on the same hardware. The virtual parallel running is based on the fact that human sensing is much slower that a measured process similarly as it is in movie or TV. Every application is running only necessary time for test DUT and the data processing. This solution gives more effective exploitation of the measuring hardware in the laboratory stands.

Access to the described Laboratory Workplace is permanently open. The system allows monitoring activities of students enrolled in the course. Results of monitoring and answer on short questioner give possibility teacher to evaluate students attending virtual laboratory and gives new suggestions to improve testing stand. Whole idea about learning through the internet offers students first touch with electronics and instruments. Afterwards students will be able to deal with real laboratory equipment and circuits especially.

4. Conclusions

Presented testing stands give students possibility to become familiar with AD converters and standardized testing methods. An ADC is available for performing basic ADC tests on real ADC component and role of all control signals. Measurements are executed in subject Basic of Electronics in a testing mode. Testing stand with simulated ADC is still in process of improving.

Acknowledgements

The work is a part of project supported by the Educational Grant Agency of Slovak republic (No. 029TUKE-4/2012).

References

[1] Arpaia P, Daponte P, Michaeli L. The influence of the architecture on ADC modelling, *IEEE Trans. on Instrumentation and Measurement*, Vol. 48, No. 5, October 1999, 956-967.

[2] IEEE Std. 1241 - 2010, "IEEE Standard for Terminology and Test Methods for Analog-to-Digital Converters", Institute of Electrical and Electronics Engineers, Inc. New York, USA Rev. 2010.

[3] Godla M, Michaeli L, Šaliga J, Sekerák M. The Measuring Workplace for Studying Basic Characteristic of Operational Amplifiers with Remote Access Across the Internet : Measurement 2011 : 8th International Conference on Measurement, Smolenice, Slovakia. - Bratislava : Veda, 2011. - ISBN 978-80-969-672-4-7, 274-277.

[4] Vargha B, Shoukens J, Rolain Y. Non-linear Model Based Calibration of A/D Converters, Proc. of the 6th EWADC, Lisbon, Portugal , Sept.2001, 79-83.

[5] Arpaia P, Daponte P, Rapuano S. A state of the art on ADC modelling. *Comp. Stand. & Interf.*, vol.26, No.1. January 2004, 31-42.

Bloch Simulations on a Desktop Computer Exploiting a Parallel Framework

[1]P. Latta, [2]M. L.H. Gruwel, [2]J. Hovdebo, [2]B. Tomanek

[1]CEITEC – Central European Institute of Technology, Masaryk University, Brno, Czech Republic
[2] NRC-CNRC, 435 Ellice Avenue, Winnipeg, Manitoba, Canada R3B 1Y6
Email: lattape@gmail.com

Abstract. *A common approach in magnetic resonance imaging is to use Bloch simulations to explore different aspects of the spin behaviour. Typical for these calculations is the high computational demand, which put restrictions on the number of spins involved in such simulations. In this paper we present a performance comparison for two parallelization techniques; multi-core versus graphics processing unit. Both techniques result in an increase in computational performance. The results from 2D and 3D experiments are presented with comparison of the computational accelerations. The performance tests indicate that the graphics processing unit introduces an effective and affordable increase in computational efficiency.*

Keywords: *MRI Simulation, Bloch Equation, Graphics Processing Unit* (*GPU*)

1. Introduction

The easy and convenient way to investigate various aspects of spin behavior in magnetic resonance imaging (MRI) is to use Bloch simulations. A common problem for such simulations is the finite, however large volumes of isochromats. This makes simulation very demanding on the computational power. In many occasions this is solved by the usage of computer clusters [1]. Despite of its computational effectiveness, such clusters might be expensive, maintenance demanding and are not always accessible. However, recent progress and development in multi-core (MC) CPU and a graphics processing unit *(*GPU) use provides an opportunity to use massive parallelism on desktop or even on laptop computers [2]. Here we present and compare the effectiveness of two different parallelization approaches.

2. Subject and Methods

The home made Bloch simulator [3] has been extended with two parallel mechanisms:

1. Intel® Threading Building Blocks – allows to take advantage of multi-core computation.
2. CUDA – allows harnessing the computational power of the graphics processing unit GPU.

In order to evaluate the MC and GPU computational performance, three different simulations tasks have been performed:

a) reconstruction from projections using the two dimensional (128x128 voxels) Shepp-Logan phantom shown in Fig 1(A -B),
b) inhomogeneity simulation with a cylindrical phantom (128x128 voxels) containing an axially placed air-filled tube using 3 isochromat per voxel, (see [3]) shown in Fig 1(C-D),
c) gradient echo sequence with slice selection using 3D (128x128x64) phantom shown in Fig 1(E-F).

All simulations were performed on a DELL Precision T7500 desktop computer , with 2 CPUs Intel Xeon® X5570, 2.93 GHz, 4 cores each, and capable to run 16 hyper threads in total, with 6GB memory. The Dell T7500 was equipped with a GeForce GTX285 (240 Processor Cores) graphics card which was used for GPU computing. All simulations were running on the Linux/Kubuntu 11.10 (Oneiric Ocelot) operating system and the sequence preparation and data reconstruction were performed using Octave mathematical package.

Table 1 Comparison of effectiveness of MC and GPU performance against the single core simulation experiment.

		Total simulation time / simulation speedup relative to single core	
Phantom size	single core	multi core with 16 hyper threads	GPU
128x128 reconstruction from projections (1 isochromat per voxel)	23.1 sec	4.6 sec / 5.0x	2.63 sec / 8.7x
128x128 inhomogeneity simulation (3 isochromats per voxel)	68 sec	9.5 sec / 7.1x	5.8 sec / 11.7x
128x128x64 grad. echo with slice selection (1 isochromat per voxel)	5937 sec	807 sec / 7.3x	293 sec / 20.2x

3. Results

The simulation experiments were tested and the net execution time recorded i.e. time for data reconstruction was excluded from time measurement. The results are summarized in Table 1. The parallelization of simulation brought a significant increase of performance for all types of scenarios and even for relatively small 2D input data matrices. For 2D simulations the relative acceleration was in the range of 5 – 11.7 times, however, there was no significant difference between MC and GPU parallelism. This changed dramatically when huge volumes of data were involved as in the case of 3D simulations, where a 20.2 times GPU acceleration was measured against a single core computing and a 2.77 acceleration of GPU versus MC. This can be explained by fact that for such computational and time demanding simulations the data transfer from CPU to GPU memory does not represent substantial time consumption and the full power of many GPU processor cores brings a full advantage [2].

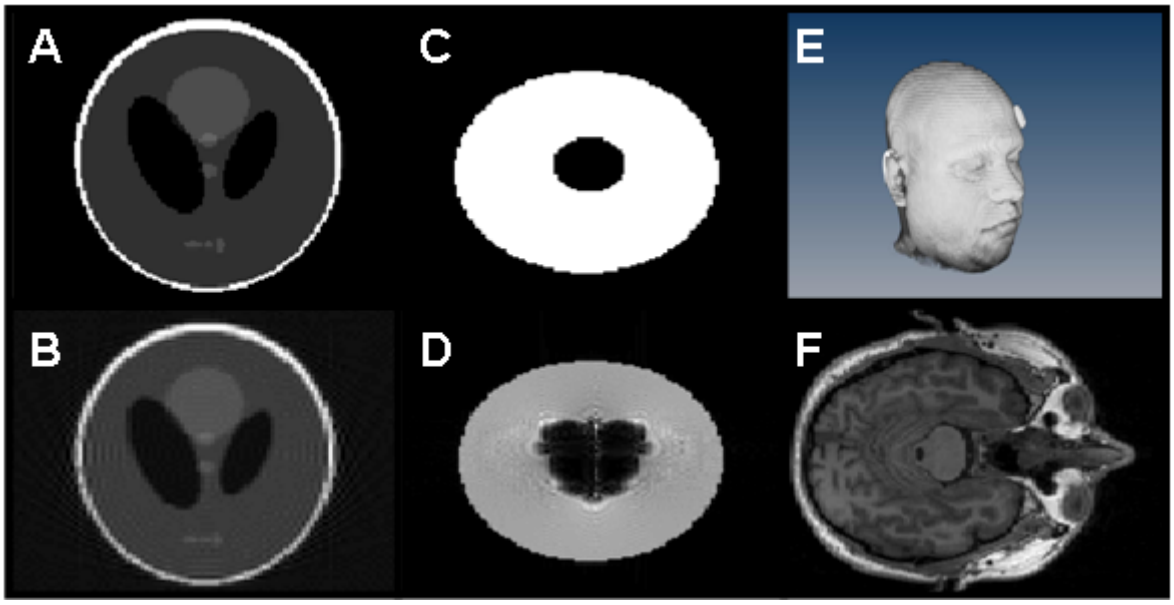

Fig. 1. Input phantoms and output images from GPU simulation experiment: A–B reconstruction from projections, C-D inhomogeneity simulation, E-F gradient echo with slice selection.

5. Conclusions

Using a MC or GPU implementation of the Bloch simulation could significantly speed up the simulation process compared to single core calculation. This is even more obvious for simulations involving 3D data, where the GPU simulation version exhibits an acceleration of more than 20 times. In all simulation experiments the GPU over-performed the MC, most significantly in 3D simulations. A significant advantage of the GPU computational platform is its scalability, which allows the construction of a powerful multiple board configuration and which may help further improvement of the speed performance in relatively reasonable price.

Acknowledgment: We would like to thank Dr. V. Jellúš for his helpful suggestions and help with preparation of this manuscript.

References

[1] Stöcker T, Vahedipour K, Pflugfelder D, Shah NJ. High-performance computing MRI simulations. *Magnetic Resonance in Medicine,* (64): 186–193, 2010.

[2] Lechner SM, Butnaru D, Bungartz HJ, Chen D, Vogel MW. Bloch solver simulation realization on a graphics-processing unit (GPU), p. 2695, *ISMRM 17th Scientific Meeting & Exhibition*, Honolulu, 2009.

[3] Latta P, Gruwel MLH, Vladimír Jellús V,Tomanek B. Bloch simulations with intra-voxel spin dephasing. *Journal of Magnetic Resonance,* (203): 44–51, 2010.

Distortion Power Measurements in Education

E. Králiková, O. Čičáková

Slovak University of Technology in Bratislava, Faculty of Electrical Engineering and Information Technology, Institute of Electrical Engineering
Ilkovičova 3, 812 19 Bratislava, Slovak Republic
Email: eva.kralikova@stuba.sk

Abstract. *This paper deals with digital measurement of single-phase power using DAQ card NI USB-6009 and other similar equipment. Main attention is paid to distortion power measurement. In LabVIEW environment a program for counting and describing all power components based on harmonic analysis of time behaviour of measured voltage and current was created. The program (virtual instrumentation) describes basic characteristics of input signals and similar information about harmonics. This virtual instrumentation is used for the laboratory experiments in electrical measurement undergraduate course at the faculty.*

Keywords: Distortion Power, Automated Measurement, Virtual Instrumentation (VI), Data Acquisition (DAQ), LabVIEW

1. Introduction

With increasing progress in electrical technology and electronics as well as in production and distribution of electric power the need of effective and accurate measurement of electric power is increasing, too. Power measurement still presents complicated task, mainly if taking in account an expansive economical thyristor and other heavy-current and also light-current semiconductor elements. When used then in low-voltage networks the harmonics distortion of both voltage and current time behaviour occurs with higher harmonic components. Created virtual instrument enables students to see and to measure the influence of distorted currents on each power component for linear and non-linear loads.

2. Electric Power

The instantaneous power delivered to a load can be expressed as

$$p(t) = u(t) \cdot i(t) \tag{1}$$

where $u(t)$ and $i(t)$ are the time varying voltage and current waveforms [1]. The instantaneous power may be positive or negative depending on the sign of $u(t)$ and $i(t)$, which is related to the sign of the signal at a given time. A positive value means that the power flows from the supply to the load, and a negative value indicates that the power flows from the load to the supply.

Active power consumed on a load is defined as the mean value of the instantaneous power

$$P = \frac{1}{T}\int_0^T u(t)\,i(t)\,dt \tag{2}$$

We use the following terms to describe energy flow in a system: real or active power P [W], reactive power Q [VAr], complex power $\boldsymbol{S}$ [VA] and apparent power $S=|\boldsymbol{S}|$ [VA] that is the magnitude of complex power. We assign each of them a different unit to differentiate between them.

In the case of a perfectly sinusoidal waveform, P, Q and S can be expressed as vectors that form a vector triangle: $S^2 = P^2 + Q^2$. The mathematical relationship among them can be represented by vectors or expressed using complex numbers, $\boldsymbol{S} = P + jQ$.

Apparent power S is the product of rms values of voltage U and rms values of current I [2]. It is important because it represents the total capacity that must be available to supply power to the load - even though only a part of this is useful power.

$$S = U\,I \tag{3}$$

In case of harmonic supply

$$\boldsymbol{S} = P + jQ = U\,I\,(\cos\varphi + j\sin\varphi) \tag{4}$$

where the active power $P = U\,I\cos\varphi$ and the reactive power $Q = U\,I\sin\varphi$.
The cosine of the phase angle φ between the voltage and the current is called the power factor

$$\lambda = \cos\varphi = \frac{P}{S} \tag{5}$$

When the current is non-sinusoidal the influence of harmonics has to be considered, because it caused that the powers P and Q are done by harmonics of the same order of both voltage and current

$$P = \sum_{k=0}^{\infty} U_k I_k \cos\varphi_k \quad [\mathrm{W}] \qquad\qquad Q = \sum_{k=1}^{\infty} U_k I_k \sin\varphi_k \quad [\mathrm{VAr}] \tag{6}$$

Apparent power is

$$S = U \cdot I = \sqrt{\sum_{k=0}^{\infty} U_k^2}\sqrt{\sum_{k=0}^{\infty} I_k^2} \quad [\mathrm{VA}] \tag{7}$$

In case of non-sinusoidal signals the inequality $S^2 \geq P^2 + Q^2$ is valid. The influence of so called distortion power D occurs. It consists of unequal harmonics of voltage and current

$$D = \sqrt{\sum_{j\neq k}^{\infty}\left[U_k^2 I_j^2 + U_j^2 I_k^2 - 2U_k I_k U_j I_j \cos(\varphi_k - \varphi_j)\right]} \quad [\mathrm{VA}] \tag{8}$$

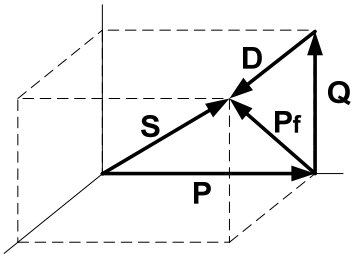

Fig. 1. 3D graph representation of power components

The powers active, reactive and distortion are connected by a relation $S = \sqrt{P^2 + Q^2 + D^2}$. Geometric sum of reactive and distortion powers is equal to non-active power $P_f = \sqrt{Q^2 + D^2}$. The function representation of mentioned powers is in Fig. 1.
Power factor in this case is

$$\lambda = \frac{P}{S} = \frac{\sum_{k=0}^{\infty} U_k I_k \cos\varphi_k}{\sqrt{\sum_{k=0}^{\infty} U_k^2}\sqrt{\sum_{k=0}^{\infty} I_k^2}} \tag{9}$$

Harmonic content is expressed by total harmonic distortion THD

$$THD = \frac{\sqrt{\sum_{k=2}^{\infty} I_k^2}}{I_1}\cdot 100 \quad [\%] \tag{10}$$

This parameter mainly determinates signal distortion. It is calculated by use of harmonic analysis.

3. Application

The measurement of electric power is necessary in various experiments. Computer-aided laboratory exercises based on the LabVIEW system are efficiently used on the topic of Power measurement. In the next example of LabVIEW application the virtual instrument system in

the education of measurement distortion power in single-phase system is presented [3]. Automated procedures have been developed for quantifying various components of power.
In many common measurement applications a DAQ card, with a personal computer and software, can be used to create an instrument - virtual instrument (VI) - for all user interaction and control. In our measurements voltage and current signals through a load are transferred to the computer by means of DAQ card.

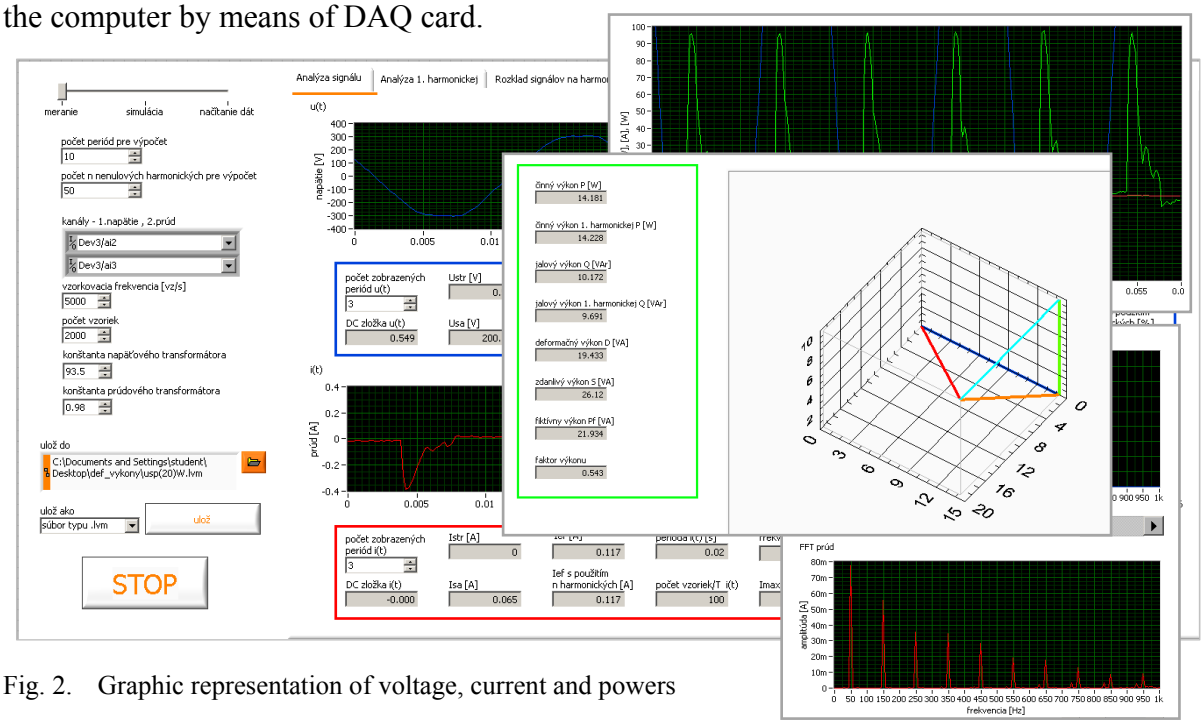

Fig. 2. Graphic representation of voltage, current and powers

Program realises or simulates both voltage and current measurements. The sampled time behaviour is represented in graph. From the samples the parameters of voltage and current (e.g. mean value, rms value, offset, form factor, THD, …) are calculated. There is a possibility to choose the calculation and representation of either the instantaneous power or the powers in 3D graph. Review of relations between the powers, voltage and current and FFT of voltage and current is possible, too – as seen in Fig. 2.
The 3D phasor diagram of powers is displayed to understand the geometric connection. The application allows the presentation of voltage and current phasor diagrams.

4. Measurement and Results

This program was used in the experiment for characterizing the most frequently used electrical light sources - a classic filament lamp 60 W (linear load), LED lamp 20 W and compact fluorescent lamp 15 W (both non-linear loads, equivalent to 60 W filament). To measure the power of concrete lamps the DAQ card NI USB-6009 was selected. It is compatible with LabVIEW program. To adapt a signal in consideration of DAQ input voltage parameters a simple voltage divider was used. Currents were obtained by measuring the voltages across the resistor.

In all cases the voltage time behaviours were almost sinusoidal, but the current time behaviours were different, in upper part in Fig. 3. The current time behaviour of classic filament lamp was also almost sinusoidal as it was expected. Similarly, in LED lamp as in fluorescent one the current was distorted. The great part of their power was created just by distortion component. As seen in lower part in Fig. 3 and Tab.1 this component is smaller for LED lamp in comparison with fluorescent lamp, but LED lamp has lower value of power factor. Because of reactive impedance its reactive power is higher. Similar results are also in [4].

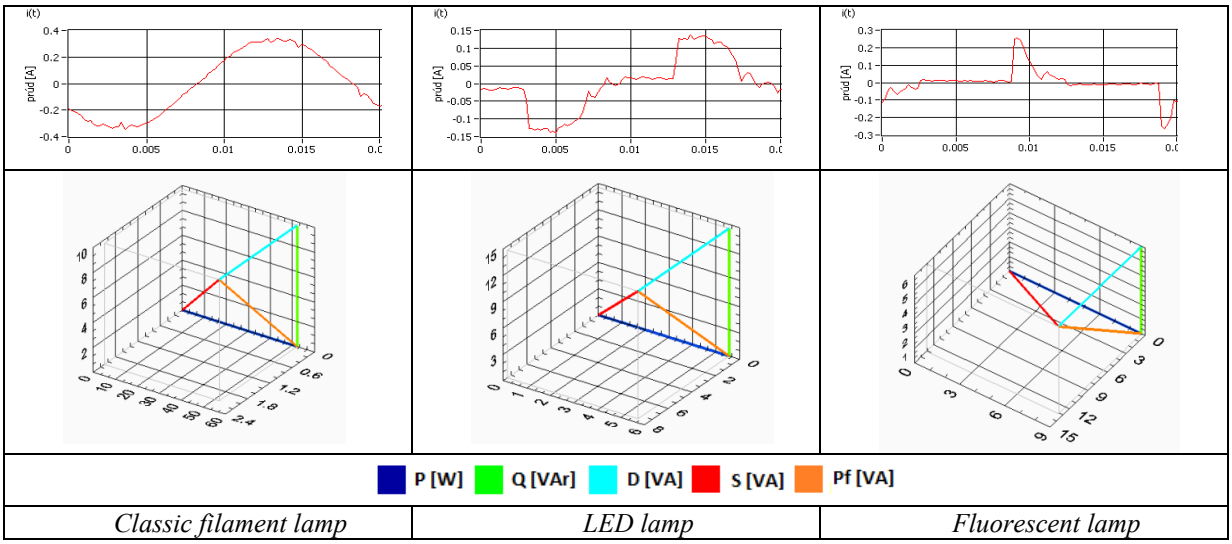

Fig.3 Current time behaviours (upper) and power components (lower) of measured lamps

Table 1. The power components for Incandescent light bulb, LED bulb and Fluorescent light bulb

		Classic	LED	Fluorescent
Active power	P (W)	52.15	5.16	8.77
Reactive power	Q (Var)	9.64	14.68	5.79
Distortion power	D (VA)	2.09	7.65	13.11
Apparent power	S (VA)	53.07	17.35	16.81
Non-active power	Pf (VA)	9.87	16.56	14.33
Power factor	PF	0.98	0.29	0.52

5. Conclusions

Taking into consideration harmonic distortion the automated system presented in this paper proved to be effective and valid for measuring single-phase power systems. It may be used for any kind of periodic voltage and current waveforms, as it calculates power from the harmonic components, extracted from a FFT analysis. The instantaneous, active, reactive, distortion, apparent and fictive power as well as power factor are calculated and presented on the screen. Distortion power has raised increasing interest with the expansion of non-linear electric loads connected to the electrical system.

The application is being used as a powerful tool for teaching single-phase electrical systems and it enriches traditional experiments in objects focused on power measurements in bachelor study. It is suitable for distance measurement and in simulation mode for self-study.

Acknowledgements

This work was supported by the Slovak Grant Agency VEGA under grant No. 1/0963/12.

References

[1] Gyárfáš J, Kukuča P. The powers of distorted currents and voltages. Bratislava, Alfa, 1987 (in Slovak).

[2] Kaluš E, Kukuča P. Measurement of the basic electrical quantities – apparent power and other powers. IN EE. Vol. 15, No. 1, 10 – 14, 2009. ISSN 1335-2547 (in Slovak)

[3] Janáček M. Single-phase power measurement using the DAQ card, Master thesis, FEI STU Bratislava, 2012 (in Slovak).

[4] Dimitrijević M. A, Litovski V. B. Power Factor and Distortion Measuring for Small Loads Using USB Acquisition Module. *Journal of Circuits, Systems and Computers,* Vol. 20, No. 5, 867-880, 2011.

Measurement in Biomedicine

Model Interpretation of Pathological Body Surface QRST Integral Maps Related to Action Potential Heterogeneity

[1]G. Tuboly, [1]G. Kozmann, [2]V. Szathmáry, [3]J. Švehlíková, [3]M. Tyšler

[1]Department of Electrical Engineering and Information Systems, Faculty of Information Technology, University of Pannonia, Veszprém, Hungary,
[2]Institute of Normal and Pathological Physiology, Slovak Academy of Sciences, Bratislava, Slovakia
[3]Institute of Measurement Science, Slovak Academy of Sciences, Bratislava, Slovakia
Email: tuboly.gergely@virt.uni-pannon.hu

Abstract. *According to theoretical and clinical considerations the risk of re-entry type malignant arrhythmia can be predicted by body surface QRST integral maps. Our aim was to understand better the intracardiac processes causing noninvasively measurable action potential (AP) heterogeneity. For this task we used a computer model of human cardiac ventricles with modifiable AP patterns to investigate the process on source level. To estimate the relevant potential maps on the body surface, we used a realistically shaped piecewise homogeneous torso model. The level of AP heterogeneity was quantified by the non-dipolarity index (NDI) of the QRST integral maps, calculated beat-to-beat. We found that the source level origin of extreme NDIs was in the apical region of the heart, due to significantly diminished or reversed transmural action potential gradients or myocardial necrosis.*

Keywords: Malignant Arrhythmia, QRST Integral Maps, Heart Model, Torso Model, Non-dipolarity Index

1. Introduction

While atrial fibrillation is considered to be a major risk factor of stroke, ventricular fibrillation can end in sudden cardiac death. According to experimental and theoretical studies, the enhanced ventricular fibrillation is related to the heart muscle cells' pathological action potential (AP) heterogeneity. Based on recent scientific statements, effective ventricular arrhythmia risk assessment methods are not available, therefore the currently used techniques have to be improved [1].

In our long term pursuit for such an improved non-invasive sudden cardiac death risk assessment method, we used body surface QRST integral maps instead of signals resulted by conventional ECG systems, in order to consider the whole AP heterogeneity related information accessible on the thoracic surface [2].

Due to the spatial smoothing effect of the body as a volume conductor, the physiological level of AP heterogeneity on the epicardial surface generally results in a dipolar QRST integral map on the thoracic surface. However, if this level of heterogeneity is pathological, QRST integral maps usually appear as non-dipolar. To quantify whether the non-dipolarity is significant, we used non-dipolarity indices (NDIs), computed from the coefficients of Karhunen-Loeve (KL) series expansion of the QRST integral maps. This way it can be characterized the spatio-temporal variability of the subsequent QRST integral maps [2]. In our small-sample study, beat-to-beat NDI plots sensitively illustrated the increased lability of AP heterogeneity in the group of implanted cardioverter defibrillator (ICD) patients with documented malignant arrhythmia vulnerability, compared to the normal subjects.

In this study we attempted to give a source level explanation of the observed normal and pathological NDI behaviour, with a special regard to the extremely large NDI spikes. This investigation was performed by the help of a numerical heart and torso model.

2. Subject and Methods

Heart Model

For AP property settings, we used a computer model of human cardiac ventricles. This model consists of small volume segments with modifiable AP patterns (MoAPs). Each segment includes 5 different layers from the endocardium to the epicardium and each layer is represented by a modifiable AP both in duration and amplitude. The starting points and initial time instants of the activation can also be programmed, just like the propagation velocity [3]. The default configuration of this model represents a normal heart (Fig 1), consequently cardiac cycle with low NDI value.

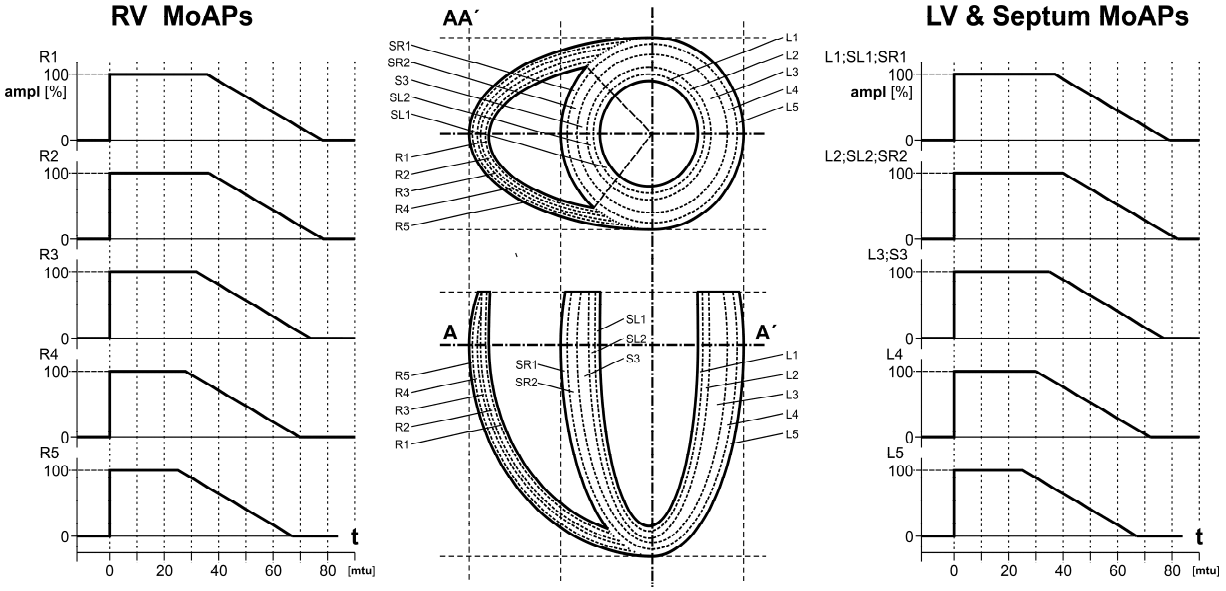

Fig. 1. The default configuration of the heart model. The left part shows the MoAP of the right ventricle and the right part represents the MoAP of the left ventricle and the septum.

Torso Model

To obtain the QRST integral maps on the body surface, we inserted the heart model into a realistically shaped piecewise homogeneous torso model. In this model lungs are taken into consideration with 4 times lower conductivity than general conductivity of the torso, ventricular cavities with 3 times higher conductivity. The electric potentials on the body surface are computed in the surface points of the torso model using boundary element method [4].

According to Geselowitz, the amplitude of QRST integrals at an arbitrary body surface point P is a function of the AP heterogeneity, in other words, it is the function of the gradient of the μ of MoAP areas (1) of the myocardium [5]. Consequently, beat-to-beat application of (1) provides a non-invasive tool that can be used to study the spatio-temporal variability of AP properties i.e. the AP heterogeneity.

$$\int_{QRST} \phi(P,t)dt = -k \iiint_{V_s} \mathbf{z}(P,\mathbf{r}) \nabla \mu(\mathbf{r}) dV_s \qquad (1)$$

$$\mu(\mathbf{r}) = \int_{QRST} [\phi_m(\mathbf{r},t) - \phi_{mr}(\mathbf{r})]\, dt \tag{2}$$

where

$\phi_m(\mathbf{r},t)$ membrane potential at time t

$\phi_{mr}(\mathbf{r})$ membrane resting potential at point $\mathbf{r}$

V_s volume of sources (myocardium)

k constant

z vector of transfer coefficients between point P and $\mathbf{r}$.

In a concise way QRST integral maps are characterized by the beat-to-beat sequence of NDI (3), based on the c_i components of the KL series expansion.

$$NDI = \frac{\sum_{i=4}^{12} c_i^2}{\sum_{i=1}^{12} c_i^2} = \frac{P_{ND}}{P_D + P_{ND}} \tag{3}$$

where

P_D BSPM signal power represented by the "dipolar" KL components (i: 1-3)

P_{ND} BSPM signal power represented by the "non-dipolar" KL components (i: 4-12) [6].

3. Results

NDI values obtained by the reference (normal) AP properties and by the 3 types of AP modulations (cases 2-84) are shown in Fig. 2.

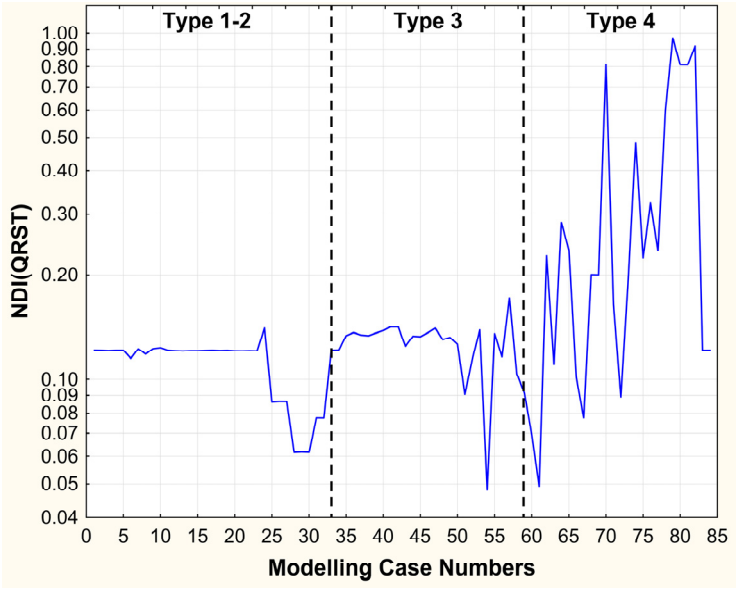

Fig. 2. NDI values of the simulated QRST integrals. Case 1 represents the normal configuration of the model (Type 1) and cases 2-84 show the NDI values of AP modulated simulations (Type 2-4).

Type 1 represents case 1, i.e. the baseline configuration of the heart model when no modifications were made. In Type 2 (cases 2-33) simulations the modulation of wavefront

starting points on endocardium and starting time instants were modulated in anterior, posterior, lateral and septal regions. According to Fig. 2 these changes did not result in high NDI values.

Type 3 (cases 34-57) modifications show cases related to mid-wall and basal AP modulations. Even the large extent changes caused minimal perturbation of the NDI values.

Type 4 (cases 58-84) simulations represent AP property changes in the apical region. Fig 2 shows that the extreme high NDI values belong to this group. Largest values were obtained by reversing the direction of the transmural gradient of AP durations and by simulating transmural, subendocardial and subepicardial myocardial infarction in the apical region.

4. Discussion

The results show that extreme NDI cardiac cycles could be produced by local changing the AP properties in the apical region. Similar changes in the mid-anterior, mid-lateral and mid-posterior locations could evoke measurable, but significantly smaller changes in the NDIs.

Acknowledgements

We acknowledge the financial support of the Hungarian State and the European Union under the programmes TÁMOP-4.2.2-08/1/2008-0018, TÁMOP-4.2.2/B-10/1-2010-0025, TÁMOP-4.2.2.A-2011/1/KONV-2012-0073, the financial support of the Slovak Research and Development Agency under the programme APVV-0513-10 and of the financial support of VEGA Grant Agency, Slovakia under the programme 2/0131/13.

References

[1] Goldberger JJ, Cain ME, Hohnloser SH, Kadish AH, Knight BP, Lauer MS, Maron BJ, Page RL, Passman RS, Siscovick D, Stevenson WG, Zipes DP. American Heart Association/American College of Cardiology Foundation/Heart Rhythm Society Scientific Statement on Noninvasive Risk Stratification Techniques for Identifying Patients at Risk for Sudden Cardiac Death: A scientific statement from the American Heart Association Council on Cardiology Committee on Electrocardiography and Arrhythmias and Council on Epidemiology and Prevention. *Circulation,* 118: 1497-1518, 2008.

[2] Kozmann G, Haraszti K, Préda I. Beat-to-beat interplay of heart rate, ventricular depolarization, and repolarization. *J. Electrocardiol.*, 43: 15-24, 2010.

[3] Szathmáry V, Osvald R. An interactive computer model of propagated activation with analytically defined geometry of ventricles. *Comput. Biomed. Res.*, 27: 27-38, 1994.

[4] Stenroos M. The transfer matrix for epicardial potential in a piece-wise homogeneous thorax model: the boundary element formulation. *Physics in Medicine and Biology*, 54: 5443-5455, 2009.

[5] Geselowitz DB. The ventricular gradient revisited: relation to the area under the action potential. *IEEE Trans. Biomed. Eng.*, 30: 76-77, 1983.

[6] Lux RL, Evans AK, Burgess MJ, Wyatt RF, Abildskov JA. Redundancy reduction for improved display and analysis of body surface potential maps. I. Spatial compression. *Circulation*, 49: 186-196, 1981.

Application of Independent Component Analysis for Rejection of Motion Artefact in BSPM Recorded During Exercise

H. Zavala-Fernandez, M. Kania, D. Janusek, R. Maniewski

Nalecz Institute of Biocybernetics and Biomedical Engineering, Warsaw, Poland
Email: hzavala@ibib.waw.pl

Abstract. *Acquisitions of body surface potentials require in some studies that, patients perform exercise on cycle ergometer to increase their heart rate. Under this condition recordings are highly affected by the muscular activity derived from the pedalling (motion artefact). To reject this interference we propose the use of independent component analysis (ICA) by applying two different algorithms (FastICA and temporal decorrelation). Datasets from 13 subjects were used. For quantification of the results, the signal-to-noise ratios were compared after suppressing the motion artefact. ECG signals showed an average improvement of about 4 to10 dB.*

Keywords: ECG Denoising, Exercise Recording, Motion Artefact, ICA.

1. Introduction

Body surface potential mapping (BSPM) is a technique for recording of electrical activity of the heart by measuring the ECG signal from large number of unipolar electrodes covering the whole surface of the thorax. Thus, the BSPM offers spatial resolution and higher selective sensitivity to individual cardiac regions than standard ECG [1-2]. This advantage is of great importance in interpretation and assessment of electrocardiographic exercise tests, however, the clinical application of BSPM is in this case limited not only by the time consumed electrode placement but also by increased level of noise caused by patients motion. The increase of physical load and heart rate is usually obtained by exercise on ergometers or treadmill where the power of muscular activity increases mainly by the movement of the legs. It causes the artefacts and noise in measured signals related to movement of whole body. An increase of noise related to cable movement is also observed at stress in comparison to ECG signals measured at rest [3-4]. Independent component analysis (ICA) [4] is a method used already in other applications for improvement of the quality of signals, e.g., in conventional 12-lead ECG [4-7]. The common goal by using ICA for the analysis of ECG data is the separation of components that are assumed to belong to heart activity and those related to disturbances (artefacts and noise). In spite of that there are a few papers addressing the application of ICA to body surface ECG recordings. Zhu et al. showed the potential of ICA to decompose BSPM in independent components related to P-, QRS-, and T-waves suggesting that ICA might be an useful tool for the analysis of high-density ECG recording [5]. In this paper, ICA is tested to its ability to decompose the motion artefact resulting from pedalling and its subsequent suppression from BSPM recordings acquired during exercise. Motion artefact is termed as the component originated by the movement of the legs.

2. Methods

The ICA belongs to the class of blind source separation (BSS) methods [3]. It is considered as blind because it tries to recover the sources **s** by looking only at the statistical information contained in the observations **x** assuming that the mixed sources are mutually statistically independent. ICA is based on the superposition model which states that signals **x** are the product of an unknown mixing matrix **A** and an unknown source vector **s**, given by

$$\mathbf{x} = \mathbf{As}. \quad (1)$$

In ICA signals are supposed to be stationary, which implies that the mixing matrix **A** does not change over time and there are as many independent components as provided signals **x**. This supposition clearly holds for the motion artefact. Then sources can be separated theoretically by estimating a demixing matrix $\mathbf{W} = \mathbf{A}^{-1}$. Estimates **y** of the original sources **s** are found by applying the demixing matrix to the measured variables: $\mathbf{s} = \mathbf{Wx}$. The linear relationship in Eq. 1 corresponds to the forward formulation of the measured potentials at the electrodes as, $\mathbf{v} = \mathbf{Eu}$, where **v** is the electric potential recorded at the electrodes on the skin, **u** represents the dipole sources and rows of **E** specify the lead fields at the electrodes, i.e., how the potential varies with the strength of each dipole source [8].

Two ICA algorithms were tested: the fast independent component analysis (FastICA) based on higher order statistics [9] and the temporal decorrelation source separation (TDSEP) based on second order statistics [10]. The FastICA [9] algorithm is based on an iteration scheme for finding a projection that maximize the non-Gaussianity. The basis of the TDSEP algorithm is a set of time-lagged covariance $R_x(\tau) = \langle x(t+\tau) \cdot x^T(t) \rangle$ with $\tau \neq 0$**.** Independent components are carried out by simultaneous diagonalization of R_x. In this study, the $\tanh(y)$ was used as the non-linear function for FastICA and as time delays τ the set of prime numbers lower than 200 was chosen in the calculations. In total, a set of 46 time-lagged covariance matrices had to be simultaneously diagonalized. The calculation was performed for each of the subjects separately.

Thirteen healthy volunteers were recorded during exercise on supine ergometer using a high resolution BSPM system (Biosemi Active Two) with 64 leads covering the whole thorax, as shown in Fig. 1 [11]. The sampling frequency of 4096 Hz was applied. All subjects were asked to keep pedalling frequency of around 60 cycles per minute (shown in a display) during examination at fixed load of 25 watts. Each recording session lasted 5 minutes. These data were used as input for the ICA algorithms.

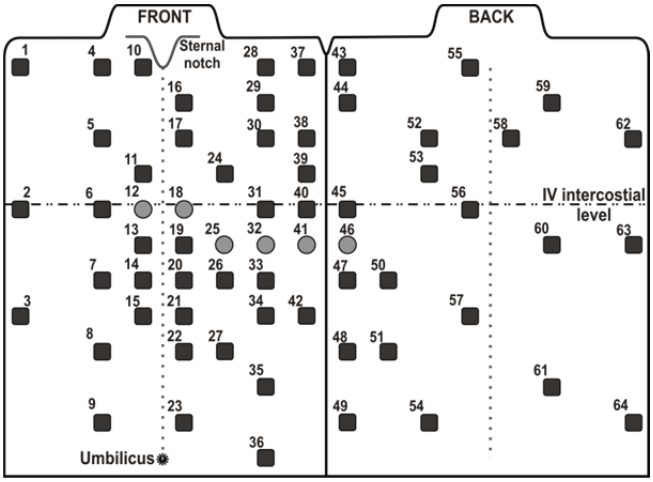

Fig. 1. ECG electrode layout on the thorax of 64 measurement channels. Standard leads V1-V6 are indicated by gray circles.

Independent components to be removed were performed manually by looking at the time-series, the power spectra and the field distribution of the components. Then a back-projection was performed for every dataset with the suppressed component(s).

To assess quality of denoising, the root-mean-square (rms) at every channel was computed before and after suppression of component related to motion and then the signal-to-noise ratio (SNR) in the corresponding sensor was calculated.

3. Results

The ICA methods (FastICA and TDSEP) were applied to 5 min recordings in each dataset. Individual data are separately arranged in data matrix $\mathbf{x}$ ([channels × samples]). After the calculations 64 independent components were obtained. Components due to the heart activity presented the typical ECG morphology visible in the time series, as well as, frequencies related to the heart beating (Fig. 2a). An spatial representation of the estimated component is generated by interpolation of a column of the estimated mixing matrix $\mathbf{A} = \mathbf{W}^{-1}$.

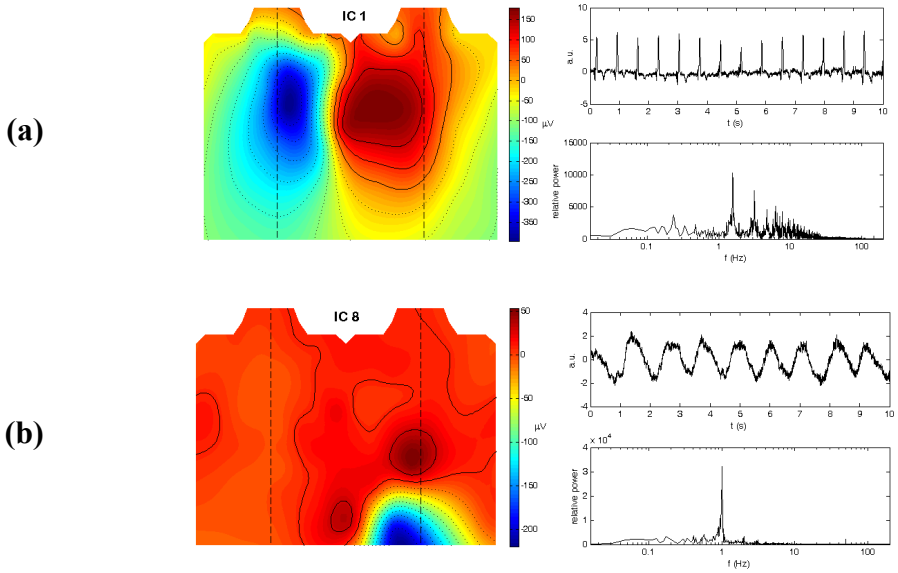

Fig. 2. Example of 2 of 64 computed independent components for one studied subject. (a) Related to heart activity. (b) Related to pedalling. It can be observed that the field distribution is concentrated in the lower part of the map which is the position of the left leg.

The motion artifact shows a dominant peak in the spectrum at 1 Hz, which is clearly related to pedaling (60 cycles/min) (see Fig. 2b). Moreover, it reflects a clear sinus wave as result of moving the leg synchronous. From the map, it can be observed that the field power is concentrated in the lower part of the map in the position of the left leg. The mean values of SNR calculated in the study group for each measured ECG channel showed a considerable benefit of using ICA based ECG denoising methods specially for channels placed close to the extremities (Fig. 3).

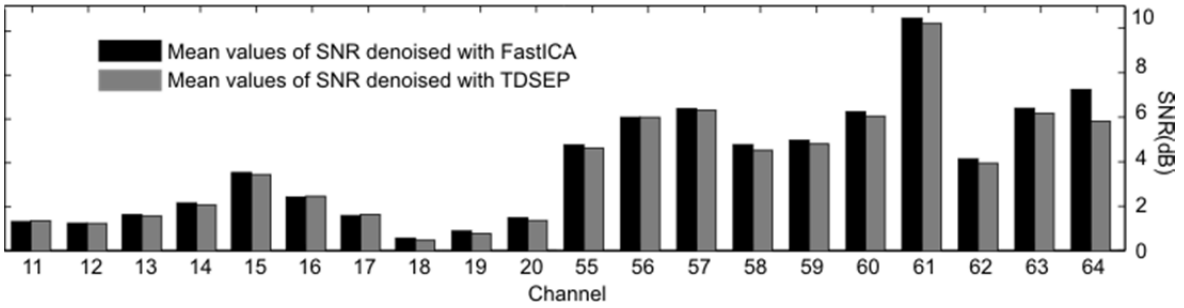

Fig. 3. Improvement of the group average SNR of selected channels after removing the motion artefact separated by ICA algorithms.

4. Discussion

During exercise test an increase of muscular activity is observed in BSPM recordings. This is reflected in considerable disturbances of the signals which most of the case make impossible

the subsequent analysis. We have shown that the ICA method with proposed algorithms could be a powerful tool for removing of at least the motion artefact without much loss of information related to the heart activity. Since the motion artefact is considered stationary generated, it fulfil the restrictions for applying ICA to the data under analysis. After rejection of the motion artefacts, the SNRs show an average improvement of about 4 to 10 dB in leads located on the back and close to the extremities. ECG signals measured in electrode locations close to position of a heart were not as substantially affected (about 0.5 dB). Both ICA algorithms presented comparable results. Artefact suppression by removal of selected components might be a valuable pre-processing step to enhance the SNR in multi-channel ECG recordings, e.g. BSPM. Since, stationary of BSPM signals do not always hold [4], it is still under discussion whether the independent components appeared to be related to heart activity and can be treated as independently generated.

Acknowledgements

This work was supported in part by National Science Centre of Poland grants no. 2011/01/N/ST7/06690, NN 518 504 339 and grants DEC-2011/-01/B/ST7/06801.

References

[1] Fereniec M, Stix G, Kania M, Mroczka T, Janusek D, Maniewski R. Risk assessment of ventricular arrhythmia using new parameters based on high resolution body surface potential mapping. Medical Science Monitor 2011; 17(3):MT26–33.

[2] Kania M, Fereniec M, Janusek D, Zbiec A, Kepski R, Karpinski G, Maniewski R. Optimal ECG lead system for arrhythmia assessment with use of TCRT parameter. Biocybernetics and Biomedical Engineering 2009; 29:75-82.

[3] Hyvarinen A, Karhunen J, Oja E. Independent Component Analysis. Wiley Series on Adaptive and Learning Systems for Signal processing, Communications, and Control. Wiley-Interscience, 2001.

[4] He T, Clifford G, Tarassenko L. Application of independent component analysis in removing artefacts from the electrocardiogram. Neural Computing and Applications 2006; 15(2):105–116.

[5] Zhu Y, Shayan A, Zhang W, Chen T, Jung TP, Duann J, Makeig S, Cheng C. Analyzing high-density ECG signals using ICA. IEEE Transactions on Biomedical Engineering 2008;55(11):2528–2537.

[6] Hubka P, Rosik V, Zdinak J, Tysler M, Hulin I. Independent component analysis of electrogastrographic signals. Measurement science review 2005;5, Section 2.

[7] Chawla M, Verma H, Kumar V. Artifacts and noise removal in electrocardiograms using independent component analysis. Int Journal of Cardiology 2008;129:278–281.

[8] Malmivuo J, Plonsey R. Bioelectromagnetism: Principles and Application of Bioelectric and Biomagnetic Fields. Oxford University Press, New York, 1995.

[9] Hyvarinen A, Oja E. A fast fixed-point algorithm for independent component analysis. Neural Computation 1997; 9:1483–1492.

[10] Ziehe A, Müller, K R. Tdsep – an efficient algorithm for blind separation using time structure. In Proceedings of the 8th ICANN, pages 675–680. Springer Verlag, 1998.

[11] Fereniec M, Kania M, Stix G, Mroczka T, Maniewski R. Relation between Depolarization and Repolarization Phases in Body Surface QRST Integral Map. Proceedings of the Computers in Cardiology. Durham, North Carolina, USA 2007. p. 439-42.

Repolarization Stratification for Dipole Electrocardiotopography

E. A. I. Aidu, V. G. Trunov

Institute for Information Transmission Problems,
Russian Academy of Sciences, Moscow, Russia
Email: aidu@iitp.ru

Abstract. *The dipole component of the heart electric field has been analyzed in the context of distribution of the action potential onset timing and its duration. It has been demonstrated that the process of repolarization can be visualized as a sequence of layers with equal action potential (AP) completion time. Dipole moments of these layers can be calculated from the repolarization part of VCG and visualized as by dipole electrocardiography method (DECARTO) with the use of simple biophysical models. Such presentation will be useful for the analysis of heterogeneity of action potential characteristics in the ventricular myocardium and evaluation of its vulnerability to life-threatening arrhythmias.*

Keywords: Dipolar Electrocardiotopography, Repolarization.

1. Introduction

Association between the heterogeneity of the myocardium repolarization process and its vulnerability to life-threatening arrhythmias has been demonstrated in multiple studies [1, 2]. Moreover, pronounced morphological changes in the repolarization part of the ECG (T-wave) in response to biochemical alterations in the myocardium have been found [3, 4]. A number of T-wave characteristics have been proposed and tested for their diagnostic validity. Basing on these characteristics, new diagnostic criteria have been developed [5-7].

The possibilities of the dipole electrocardiotopography (DECARTO) [8] can be extended by a more detailed analysis of the ventricular repolarization and graphical representation of this process on the spherical quasiepicardium (or image sphere) with the use of simple biophysical models based on three-component vectorcardiograms (measured directly by the vectorcardiographic leads or synthesized from the 12 standard leads).

2. Subject and Methods

Heterogeneity of the repolarization process is primarily determined by the diversity of action potential (AP) duration in the myocardium. The typical shape of AP in the ventricular cardiomyocytes and analytical approximations commonly used in model studies are shown in Fig. 1.

Distribution of AP duration may be calculated from local AP onset and completion timings. Rapid upstroke (duration 1-2 ms) facilitates calculations of the spreading depolarization wave. In DECARTO, it is visualized as a sequence of equivalent spherical double electric layers whose dipole moments are calculated from orthogonal electrocardiograms, whereas the calculation of distribution of AP completion time is much more problematic. During repolarization, VCG is a sum of dipole moments of layers with different values of AP completion time.

The aim of this study was to calculate dipole moments of consecutively turned-off myocardial layers and visualize them similarly to the process of activation. For this purpose, let us consider the process of stratification of the depolarization part of VCG by the moments of AP onset and then turn to analyzing the possibility of stratification of the repolarization part.

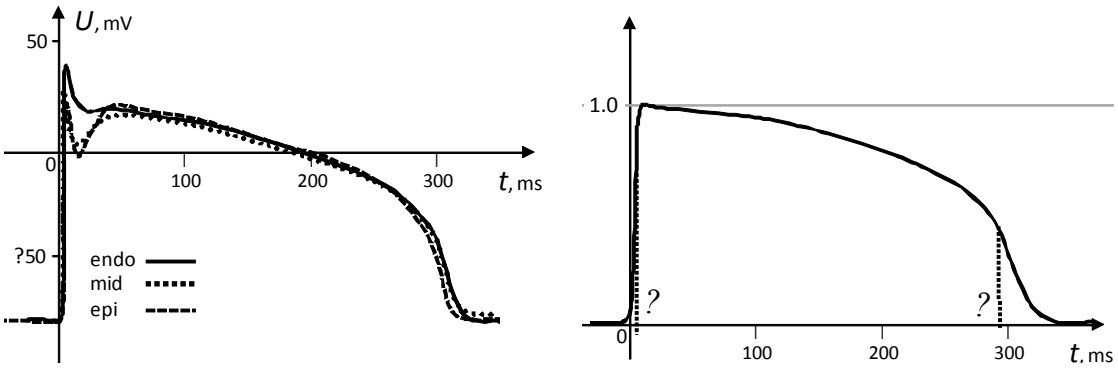

Fig. 1. The action potential of cardiomyocyte (transmembrane potential change when cell is stimulated at time t = 0). On the left, the measured transmembrane action potentials in the endocardium (endo), midmyocardium (mid) and epicardium (epi). The curves are adopted from [9] and aligned by the depolarization onset. On the right, an example of analytical AP approximation used in theoretical and model studies [10].

Depolarization Stratification

The heart vector or dipole moment vector $\mathbf{d}(t)$ at an instant t is expressed as integral of current density $\mathbf{J}(t, \boldsymbol{r})$ over the excitable media region $\mathcal{M}$ ($\boldsymbol{r} \in \mathcal{M}$). For bidomain model of the excitable media, the current density is determined by gradient of the transmembrane potential [11]. Then the result is an expression for the dipole moment:

$$\mathbf{d}(t) = \int_{\mathcal{M}} \mathbf{J}(t, \boldsymbol{r})\, \mathrm{d}v_{\boldsymbol{r}} = -\sigma_{\mathrm{i}} \int_{\mathcal{M}} \nabla \mathrm{U}(t - \tau(\boldsymbol{r}), \kappa)\, \mathrm{d}v_{\boldsymbol{r}}\,;\ \boldsymbol{r} \in \mathcal{M} \qquad (1)$$

where σ_{i} – intracellular conductivity,

$\mathrm{U}(t - \tau(\boldsymbol{r}), \kappa)$, action potential (AP), i.e. the time course of transmembrane potential at point r of myocardium;

τ, the AP onset time, and $\tau(\boldsymbol{r})$ is its distribution over myocardium;

κ, some characteristics of the AP increase rate.

The whole volume of the myocardium may be divided into layers by the time τ of the AP onset. Suppose that κ is always the same for all points in a single layer, i.e. AP upstroke is quite the same for points of the layer, and therefore the potential gradient is zero along the layer. With a suitable choice of curvilinear coordinates in Eq. 1, so that AP upstroke varied along one of them, and remained unchanged along the other, and after simple manipulations, the expression for dipole moment is obtained:

$$\mathbf{d}(t) = -\sigma_{\mathrm{i}} \int_{\mathrm{I}_{\mathrm{QRS}}} \frac{\partial \mathrm{U}(t - \tau, \kappa)}{\partial \tau}\, \mathbf{g}(\tau)\, \mathrm{d}\tau\ ; \quad t, \tau \in \mathrm{I}_{\mathrm{QRS}}\,; \qquad (2)$$

where $\mathrm{I}_{\mathrm{QRS}}$, QRS complex (depolarization) time interval;

τ, as well as above, is the AP onset time;

$\mathbf{g}(\tau)$, dipole moment of the layer τ if potential gradient across the layer equals 1.

AP ascending part is relatively small period of time from the viewpoint of electrocardiography, about 1-2 ms. It can be replaced by Heaviside step function multiplied by AP amplitude, and its gradient across the layer τ is proportional to delta function:

$$\mathbf{d}(t) = a\,\sigma_{\mathrm{i}} \int_{\mathrm{I}_{\mathrm{QRS}}} \delta(t-\tau)\mathbf{g}(\tau)\ \mathrm{d}\tau = a\sigma_{\mathrm{i}}\ \mathbf{g}(t)\,. \tag{3}$$

Functions **d** and **g** coincide up to a constant multiplier. In DECARTO, the ventricular depolarization is presented as a sequence of successively activating double layers of the current sources that are spherical segments with the dipole moments proportional to the equivalent generator **g**(t).

Repolarization Stratification

Equations 1 and 2 can also be applied for the analysis of repolarization with the AP downstroke time θ instead of AP upstroke time τ, repolarization time interval I_{T} instead of time interval $\mathrm{I}_{\mathrm{QRS}}$, and κ to be some characteristics of the AP decrease rate:

$$\mathbf{d}(t) = -\,\sigma_{\mathrm{i}} \int_{\mathrm{I}_{\mathrm{T}}} \frac{\partial\,\mathrm{U}(t-\theta,\,\kappa)}{\partial\theta}\,\mathbf{g}(\theta)\ \mathrm{d}\theta;\ \ t,\theta \in \mathrm{I}_{\mathrm{T}} \tag{4}$$

AP descending part takes a considerable period of time relatively to the AP duration and all the layers contribute to the heart vector during the repolarization. The summary dipole moment is a convolution of two functions – the t layer dipole moment $\mathbf{g}(t)$ and AP derivative $\mathrm{u}(t,\,\kappa)$:

$$\mathbf{d}(t) = \sigma_{\mathrm{i}} \int_{\mathrm{I}_{\mathrm{T}}} \mathrm{u}(t-\theta,\,\kappa)\,\mathbf{g}(\theta)\ \mathrm{d}\theta = \mathrm{u}^{*}\mathbf{g};\quad \mathrm{u}(t,\,\kappa) = \frac{\partial\,\mathrm{U}(t,\,\kappa)}{\partial t};\ \ t,\theta \in \mathrm{I}_{\mathrm{T}} \tag{5}$$

The deconvolution is needed to present the ventricular repolarization as a sequence of successively deactivating double layers of the current sources that are spherical segments with the dipole moments proportional to the equivalent generator **g**(t).

3. Results

The deconvolution algorithm was developed for the repolarization part of orthogonal ECG to present it as a sequence of successively deactivating double layers in a form similar to the visual graphical representation of depolarization process in DECARTO method [8].

The algorithm solves a nonlinear least squares minimization problem [12] to find both: the approximation for the spline representation of the layer dipole **g**(t) (as function of AP downstroke time), and the AP decrease rate characteristics of an analytical AP time course representation. As deconvolution method is ill-posed, regularization methods are applied.

4. Discussion

The proposed deconvolution algorithm of repolarization stratification needs to be investigated on real clinical data as a diagnostic tool for evaluating the heterogeneities of action potential characteristics in the ventricular myocardium and its vulnerability to life-threatening arrhythmias; diagnostic criteria should be developed and validated.

Acknowledgements

This work was partially supported by RFBR grant 11-01-00806.

References

[1] Kuo CS, Munakata K, Reddy CP, Surawicz B. Characteristics and possible mechanism of ventricular arrhythmia dependent on the dispersion of action potential durations. Circulation, 67:1356-1367, 1983.

[2] De Ambroggi L. Heterogeneities of ventricular repolarization and vulnerability to arrhythmia. How to detect them with noninvasive methods? Cardiologia, 44 (4): 355–360, 1999.

[3] Gima K, Rudy Y. Ionic Current Basis of Electrocardiographic Waveforms. A Model Study. Circulation Research, 90: 889-896, 2002.

[4] Rosen MR, Plotnikov AN. The pharmacology of cardiac memory. Pharmacology & Therapeutics, 94 (1-2): 63–75, 2002.

[5] Graff C, Andersen MP, Xue JQ, Hardahl TB, Kanters JK, Toft E, Christiansen M, Jensen HK, Struijk JJ. Identifying drug-induced repolarization abnormalities from distinct ECG patterns in congenital long QT syndrome: a study of sotalol effects on T-wave morphology. Drug Saf., 32 (7): 599-611, 2009.

[6] Ono T, Saitoh H, Yi G, Hnatkova K, Kobayashi Y, Atarashi H, Katoh T, Takano T, Malik M. Clinical implication of T-wave morphology analysis as a new repolarization descriptor. Circ J., 69 (6): 666-70, 2005.

[7] Badilini F, Vaglio M, Dubois R, Roussel P, Sarapa N, Denjoy I, Extramiana F, Maison-Blanche P. Automatic analysis of cardiac repolarization morphology using Gaussian mesa function modeling. J Electrocardiol., 41 (6): 588-94, 2008.

[8] Titomir LI, Trunov VG, Aidu EA, Sakhnova TA, Blinova EV, Kneppo P. Electrocardiographic diagnosis of left ventricular hypertrophy on the basis of dipole electrocardiotopography method. J Electrocardiol., 41 (6): 697.e1-6, 2008.

[9] Janse MJ, Coronel R, Opthof T, Sosunov EA., Anyukhovsky EP, Rosen MR. Repolarization gradients in the intact heart: Transmural or apico-basal? Progress in Biophysics and Molecular Biology, 109 (1–2): 6–15, 2012.

[10] van Dam PM, Oostendorp TF, Linnenbank AC, van Oosterom A. Non-Invasive Imaging of Cardiac Activation and Recovery. Ann Biomed Eng., 37 (9): 1739–1756, 2009.

[11] Miller WT, Geselovitz DB. Simulation studies of the electrocardiogram. 1. The normal heart. CirculationResearch, 43: 301-315, 1978.

[12] Coleman TF, Li Y. An Interior, Trust Region Approach for Nonlinear Minimization Subject to Bounds. SIAM Journal on Optimization, 6: 418–445, 1996.

Identification of Two Lesions with Local Repolarization Changes Using Two Dipoles in the Inverse Solution

J. Svehlikova, M. Teplan, M. Tysler

Institute of Measurement Science, SAS, Bratislava, Slovakia
Email: jana.svehlikova@savba.sk

Abstract. *In the simulation study the method for inverse identification of two distinct simultaneous lesions with changed repolarization in the ventricular myocardium is described. The inverse localization of two lesions was obtained from the difference STT integral body surface potential maps (DIMs). The DIMs corresponding to 48 single lesions and 96 double lesions were simulated on the surface of an inhomogeneous torso using a numerical model of the ventricles. It was supposed that the double lesions can be represented by two dipoles. Twenty three characteristics of the obtained inverse solution were specified and used as the features in a discriminant analysis that should distinguish the inverse solutions that correctly identify two lesions from those yielding incorrect results or corresponding to single lesion.*
The mean lesion localization error in cases with two lesions was 1.2 cm. For optimally selected subset of 7 features the quadratic discriminant analysis with cross-validation and feature selection yielded an overall double lesion classification error smaller than 12% for input ECG data with added noise if the signal to noise ratio was above 20 dB.

Keywords: Difference Integral Maps, Lesions with Changed Repolarization, Clusters of Results, Added Noise, Discriminant Analysis

1. Introduction

In patients with ischemic heart disease and atherosclerosis one, two or more simultaneously occluded coronary arteries can be present. For inverse localization of single small lesions with changed repolarization the inverse solution to one dipole was suggested in [1]. Analogically for two lesions, the inverse solution to two dipoles was proposed and described in [2]. In such a computation the additional problem arises whether we need the a priori information about the number of lesions or we are able to determine the number of lesions (one or two) from the properties of the obtained two resulting dipoles.

In this study various characteristics of the inverse solution to two dipoles were proposed and tested as discriminating features enabling to recognize the correct inverse solutions representing two lesions with changed repolarization and to distinguish from the other results obtained either for one lesion or incorrectly identifying two simultaneous lesions.

2. Subject and Methods

Simulation of Surface ECG and Inverse Localization of Local Ischemic Lesions
In the geometrical model with analytically defined heart ventricles small lesions with changed repolarization were modeled as part of a sphere or part of an ellipsoid located in the subendocardial or subepicardial myocardium as it is described in [1]. The changed repolarization within each lesion was modeled by shortening the myocytes' action potential duration by 20%. Six positions of the lesions typical for stenosis of one of the three main coronary vessels were defined. The lesions varied in size (from 0.1 to 6.1% of the modeled ventricular volume) and in shape (eight variations for each position). Together 48 variations of single lesions were created. To simulate two simultaneous lesions representing the two-

vessel disease, twelve combinations of pairs of ischemic lesions were modeled considering eight different shapes, resulting together in 96 pairs of modeled lesions. The mean mutual distance between the centers of the lesions was 5.6 cm.

To compute body surface potential maps (BSPMs) corresponding to normal ventricular activation and to activations with modeled lesions, the cardiac generator was inserted into an inhomogeneous torso model with lungs and ventricular cavities. BSPMs in 64 points representing the positions of measuring electrodes on the body surface were computed by the boundary element method [3].

As it was shown in [4], the local repolarization changes are reflected in difference integral maps (DIMs) computed by subtraction of STT integral maps obtained during normal activation from STT integral maps obtained during activation of the ventricular model with local ischemia. To mimic the real measurements, three levels of random noise with zero mean and normal distribution were added to the input DIM. The noise levels were characterized by the signal-to-noise ratio (SNR), expressed in dB and defined as:

$$SNR = 20log_{10}\frac{rms(DIM)}{rms(noise)} \quad [\text{dB}] \qquad (1)$$

For each input DIM, three levels of noise were added corresponding to SNR of 20, 30 and 40 dB. For each noise level thirty noise realizations were generated.

Because two simultaneous lesions were searched in this study, the equivalent integral generator (EIG) computed by the inverse solution was a pair of dipoles as described in [2]. Possible locations of the inversely estimated dipoles representing the modeled lesions were in 168 predefined points evenly distributed throughout the modeled ventricular volume. The mean distance between the neighboring predefined positions was approximately 1 cm. The inverse solution with two dipoles was computed from DIMs simulated for two modeled lesions as well as for one modeled lesion.

The best pair of dipoles was selected according to the criterion of minimal relative residual error RMSDIF (in the range 0 to 1) between the input DIM and the map generated by particular EIG. The value of RMSDIF was computed for all possible pairs of inversely estimated dipoles and characterized the quality of the obtained inverse solution. To observe the stability and reliability of the results, all pairs of dipoles with RMSDIF fulfilling the condition (2) were taken into account for further analysis:

$$RMSDIF \leq \min RMSDIF + 0.01 \qquad (2)$$

The modified K-means clustering method based on Euclidean distance between the dipoles was applied on all analyzed dipoles in the group to divide them into two clusters by an iterative algorithm [5]. The gravity center of each cluster represented the position of one modeled ischemic lesion.

The modeled left ventricle was divided into three parts, each representing the volume supplied by one of the three main coronary vessels. The cluster of dipoles was considered a correct representative of the modeled lesion if more than 2/3 of the cluster's members belonged to the corresponding part of the ventricular model. The results obtained from the DIMs computed for two simultaneous lesions were considered correct if both clusters correctly denoted the positions of the modeled lesions. All other results as well as results obtained from DIMs computed for single lesions were considered incorrect. The groups of correct and incorrect results served as classes in the following discriminant analysis.

Classification of the Inverse Results

The presented inverse method always gives the result with two dipoles or two clusters of dipoles regardless of the original situation (one lesion or two lesions) from which the input

DIM was computed. Therefore 23 different characteristics of the clusters of dipoles were specified and tested as possible input features for a two class discriminant analysis.

Quadratic variant of the Fisher discriminant analysis was applied on the data [6]. Then a cross-validation technique in a form of repeated random sub-sampling validation was applied. In 1000 trials, 80 % of available data was randomly chosen for training and remaining 20 % for validation. Classification rule was obtained during the training. Resulting classification rates were obtained as a mean rate of false positives, false negatives and their average. Greedy forward selection algorithm was used by adding the best feature in each round [7]. Starting from one feature with the least classification error, subset of features was built by consecutive steps. The most appropriate feature from the remaining set of features was added during each step in order to form the next dimension of the feature space. The optimal number of features for separation of correct results for two lesions from the results for single lesions or incorrect results for two lesions was searched.

3. Results

The localization error was evaluated from the DIMs computed for two lesions in the modeled heart as the distance between the gravity center of the modeled lesion and the gravity center of the closer cluster of inversely estimated dipoles (Table 1).

Table 1. Summary for the inverse solutions using two dipoles from DIMs computed for two simultaneous lesions in the modeled ventricular myocardium.

Signal to noise ratio [dB]	40	30	20
Percentage of correct results [%]	85.8	86.4	80.2
Localization error of correct results [cm]	1.2±0.8	1.2±0.8	1.2±0.7

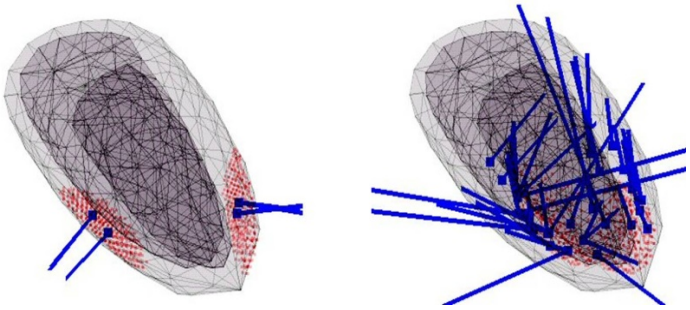

Fig. 1. Examples of groups of analyzed inversely estimated pairs of dipoles from input DIMs computed for two simultaneous lesions. Left – correct result, right – incorrect result. Dotted areas indicate the positions of modelled lesions.

From the graph in Fig. 2 it implies that the mean classification error decreased rapidly when the first two discriminating features were used. Adding more features to the classification decreased the mean error only slightly. The best two features were the same for all levels of noise. The best feature was the ratio between the mutual distance of clusters and the standard deviation of positions of dipoles in the clusters. The second best feature was the minimal value of the standard deviation of angles of the dipoles in the cluster. The optimal number of features (seven) was chosen as the number of features when the rate of false positives and false negatives were similar in each level of noise.

For SNR from 40 to 20 dB, if only two features were used, the sensitivity of the double lesion identification was from 94 to 85 % and the specificity was from 86 to 89%. If seven most informative features were used, the sensitivity was from 94 to 89% and the specificity from 92 to 86%.

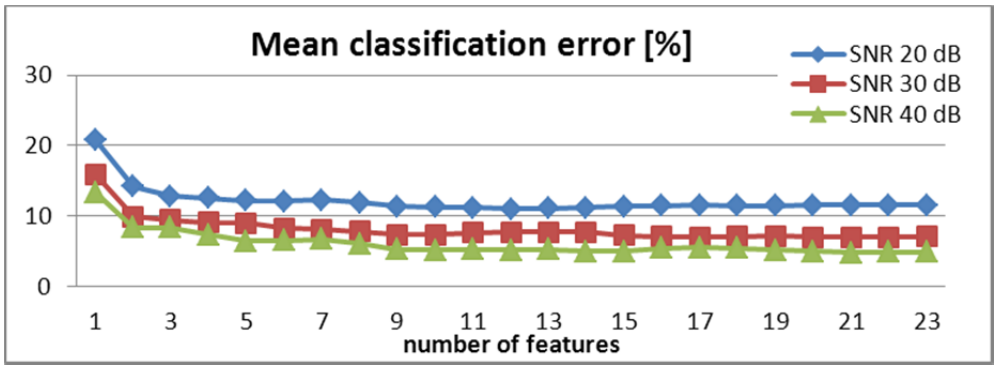

Fig. 2. The average classification error depending on the number of used features.

4. Discussion and Conclusions

As it can be seen from the obtained results, using the proposed inverse solution it was possible to correctly identify two simultaneous lesions with changed repolarization in more than 80% of simulated input data with the SNR not lower than 20dB. The localization error of correctly identified lesions was not influenced by the added noise.

The presented analysis of the obtained inverse solutions and their subsequent classification allowed distinguishing of the reliable results from the incorrect results and from results for input data corresponding to single lesions.

The inverse solution with two dipoles together with the proposed analysis and classification of obtained results yields the identification of two simultaneous lesions with the sensitivity and specificity higher than 85% for input data with added noise with SNR not lower than 20dB without the need of some a-priori information about the number of lesions.

Acknowledgements

The study was supported by the research grant 2/0131/13 from the VEGA Grant Agency and by the grant APVV-0513-10 from the Slovak Research and Development Agency.

References

[1] M. Tysler, P. Kneppo, M. Turzova, J. Svehlikova, S. Karas, E. Heblakova, K. Hana, and S. Filipova, "Noninvasive assessment of local myocardium repolarization changes using high resolution surface ECG mapping," *Physiological Research*, vol. 56, pp. S133–S141, 2007.

[2] Svehlikova, J. Lenkova, M. Turzova, M. Tysler, M. Kania, and R. Maniewski, "Influence of individual torso geometry on inverse solution to 2 dipoles.," *Journal of Electrocardiology*, vol. 45, no. 1, pp. 7–12, 2012.

[3] M. Stenroos and J. Haueisen, "Boundary element computations in the forward and inverse problems of electrocardiography: Comparison of collocation and Galerkin weightings," *IEEE Transactions on Biomedical Engineering*, vol. 55, no. 9, pp. 2124–2133, 2008.

[4] M. C. Trudel, B. Dube, M. Potse, R. M. Gulrajani, and L. J. Leon, "Simulation of QRST integral maps with a membrane-based computer heart model employing parallel processing," *IEEE Transactions on Biomedical Engineering*, vol. 51, no. 8, pp. 1319–1329, 2004.

[5] C. M. Bishop and J. K. M.Jordan B.Scholkopf, "K-means Clustering," in *Pattern Recognition and Machine Learning*, 1st ed., New York: Springer Science+Business Media,LLC, 2006, pp. 424–430.

[6] C. Therrien, *Decision, Estimation and Classification: an Introduction to Pattern Recognition and Related Topics*. New York: John Wiley and Sons, 1989.

[7] S. Theodoridis and K. Koutroumbas, *Pattern recognition*, 4th ed. San Diego: Academic Press, 2006.

Simplified Flexible Model of Human Heart Atria

[1]S. Fialová, [1]J. Švehlíková, [1]E. Cocherová, [2]V. Szathmáry, [1]M. Tyšler

[1]Institute of Measurement Science, Slovak Academy of Sciences, Bratislava, Slovakia
[2]Institute of Normal and Pathological Physiology, Slovak Academy of Sciences, Bratislava, Slovakia
Email: umersari@savba.sk

Abstract. *It is known that origin of atrial activation has impact on ECG signals. We developed a simple computer model of heart atria that allows changing the geometry of atria and location of the sino-atrial (SA) node and conduction pathways. We used it to study the impact of the location of the SA node within the atria on the ECG signals. Although the developed model was quite simple, we were able to reproduce the natural variability in body surface potential maps observed in healthy young adults.*

Keywords: Atrial Activation, Body Surface Potential Mapping, Mathematical Model, Simulations

1. Introduction

Electrocardiography is one of the most frequently used non-invasive diagnostic techniques in cardiology. Although, it is widely and often used in the clinics, many phenomena are not fully understood or explained yet. Because of that, it is very useful to apply mathematical modelling in this field. In silico approach has many advantages, which are useful especially in research that involves humans. With this tool one can perform experiments and evaluate hypotheses that cannot be done on living subjects.

It is known that origin of the atrial activation has impact on surface ECG signals [1]. In [2] it was showed that ectopic pacing of atria produced different patterns in the body surface potential maps (BSPM). Also in [3] it was shown that young adults and children have different BSPM, although they all had no history of cardiovascular disease and normal electrocardiographic and echocardiographic findings. Atrial function can be impaired by atrial enlargement, inter-atrial conduction delay or block, fibrosis and changes in electrical properties of atrial cells. That can result in serious medical problem – atrial fibrillation. In clinics, it is often difficult to recognize, if the P-wave abnormalities are due to inter-atrial conduction delay or atrial enlargement [1], which has different treatment strategies.

Because of that, we developed a transformable model of the heart atria that allow us to change the geometry of atria and the location of the SA node and conduction pathways. We used this model to study the impact of the SA node location on ECG signals and BSPM.

2. Subject and Methods

In our in silico experiments we have used a new mathematical model of the human heart atria developed in Matlab. It was inspired by the model of the heart ventricles developed earlier by Szathmáry and Osvald [4]. Basic geometry of the atria was created from two groups of ellipsoids. The first group represent outer surface and the second group, with slightly smaller dimensions than the first one, represents inner surface of the atria. Space between these two groups of ellipsoids was filled with cubic elements; each has size 1x1x1 mm and represents a piece of the atrial tissue. In each group of ellipsoids there were four ellipsoids, two bigger represent the body of the atria and two smaller represent the appendices of the atria, see

Fig. 1. In the body of the atria there are fenestrae corresponding to intrusions of large blood vessels. This configuration allows us to change the size and the shape of the model.

In recent anatomical studies [6] it was shown that SA node has bigger size than what is usually used on schematics and simplified illustrations. Therefore in the model the SA node was defined as an intersection of the atrial wall and another ellipsoid with the size of approximate 15x10x5 mm. Since the position of SA node is not very strict [5], at first, we placed it in correspondence with literature at the most anterior position in the right atrium and then gradually moved it more posteriorly. Thus we created five positions of the SA node as it can be seen in Fig. 2.

Preferential conduction pathways were simulated like areas with 3 time faster velocity of propagation of activation front like in normal tissue. These areas were located in the appendices, in the septum, and between the bodies of the atria. They were created as intersections of the atrial mass and several ellipsoids with desired shapes and positions.

To simulate the shape of the action potential we used the Courtemanche-Ramirez-Nattel model of human atrial cell [7]. The action potential propagation was simulated using the Huygens principles implemented by a cellular automaton [4]. The surface potentials were computed by solving the forward problem of electrocardiology. The equivalent multiple dipole model described in details elsewhere [8] was used to represent the cardiac electric generator and potential were computed on the surface on an realistic inhomogeneous torso model.

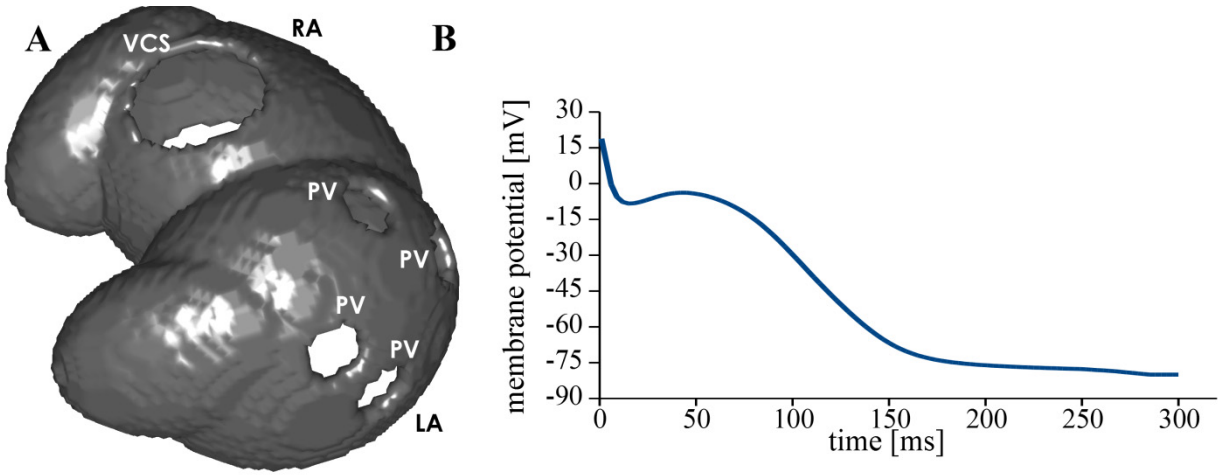

Fig. 1. A: 3D model of the atria. The auriculi (smaller ellipsoids) and the body of atria (larger ellipsoids) with visible openings assigned to large vessels can be recognized. RA – right atrium, LA – left atrium, VCS – vena cava superior, PV – pulmonary vein.
B: Simulated shape of the action potential of an atrial cell that was used in the model.

3. Results

Results of the simulations are shown in Fig. 2. There are visible differences in the patterns of BSPM corresponding to different SA node positions. These results are similar to the data measured in [3]. Also in individual leads there are some visible differences, e.g. in lead V1 the signal shapes in cases D and E are different from those in cases A, B and C.

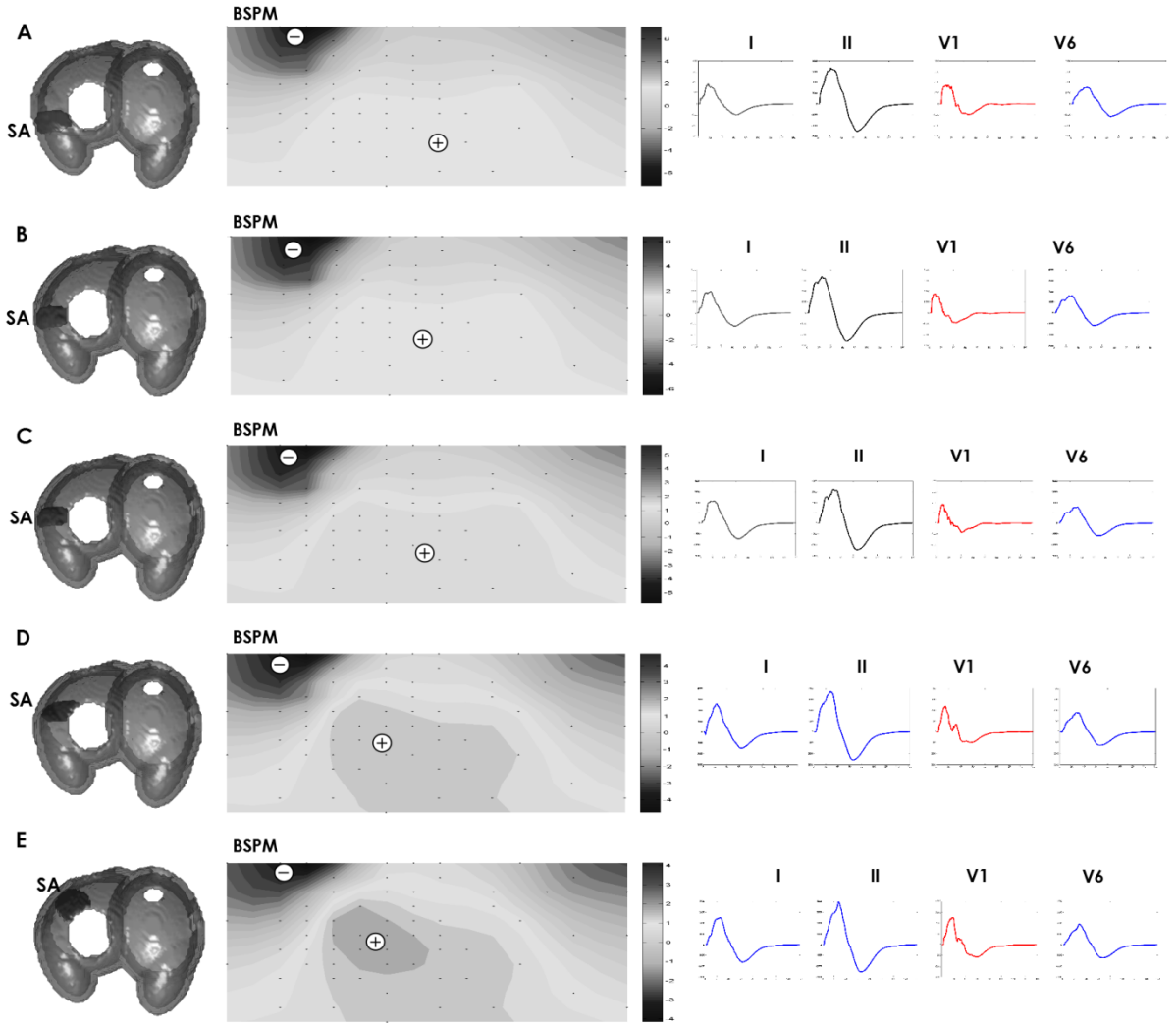

Fig. 2. Results of simulations – A to E represent different positions of the SA node. In each picture from left to right: model of the atria with the location of the SA node (black), simulated BSPM and simulated signals of ECG leads I, II, V1, V6.
Differences between integral BSPM corresponding to atrial models with different SA position are visible, although the differences in ECG signals are not so evident. All ECG signals are with the same scale and integral BSPM were calculated from the whole atrial activation sequence (contain the P-wave and the Ta-wave corresponding to the atrial depolarization and repolarization).

4. Discussion

Despite the presented model of the atria is quite simple, we have found it sufficient to simulate distributions of the body surface potentials that are in agreement with the data measured in [3]. The variations in body surface potential maps could be explained by different locations of the SA node. As it is stated in [9], for detailed study of the atrial activity based on surface ECG signals modified position of ECG leads should be used. In our study we simulated only signals in positions of standard 12-lead ECG. When simulating the preferential conduction pathways, we assigned the same velocity of activation propagation to all these regions regardless of the position of the SA node.

5. Conclusions

Using the developed simple model of the atria, we were able to reproduce the observed natural variability in body surface potential maps recorded in healthy young adults. We demonstrated the impact of the location of the SA node on the BSPM. Variations in body

surface potential maps in healthy subjects can be explained by this. This can be one of the many possible reasons, why patient specific approach in interpreting the surface ECG is important. These first results suggest that our simple model can be used to study the variability of ECG signals caused by changed configuration of the atria.

Acknowledgements

This study was supported by the research grant 2/0131/13 from the VEGA Grant Agency and by the grant APVV-0513-10 from the Slovak Research and Development Agency.

References

[1] Platonov PG. P-wave morphology: underlying mechanisms and clinical implications. *Annals of noninvasive electrocardiology : the official journal of the International Society for Holter and Noninvasive Electrocardiology, Inc*, 17 (3): 161–9, 2012.

[2] SippensGroenewegen A, Peeters H a P, Jessurun ER, Linnenbank C, Robles de Medina EO, Lesh MD, van Hemel NM. Body Surface Mapping During Pacing at Multiple Sites in the Human Atrium: P-Wave Morphology of Ectopic Right Atrial Activation. *Circulation*, 97 (4): 369–380, 1998.

[3] Kozlíková K. P-wave body surface isointegral maps in children and in young adults. *Physiological research / Academia Scientiarum Bohemoslovaca*, (56, Suppl 1): S123–S128, 2007.

[4] Szathmáry V, Osvald R. An interactive computer model of propagated activation with analytically defined geometry of ventricles. *Computers and biomedical research*, 27: 27–38, 1994.

[5] Boineau JP, Canavan TE, Schuessler RB, Cain ME, Corr PB, Cox JL. Demonstration of a widely distributed atrial pacemaker complex in the human heart. *Circulation*, 77 (6): 1221–1237, 1988.

[6] Sánchez-Quintana D, a Cabrera J, Farré J, Climent V, Anderson RH, Ho SY. Sinus node revisited in the era of electroanatomical mapping and catheter ablation. *Heart (British Cardiac Society)*, 91 (2): 189–194, 2005.

[7] Courtemanche M, Ramirez RJ, Nattel S. Ionic mechanisms underlying human atrial action potential properties: insights from a mathematical model. *American Journal of Physiology,* 275: 1522–1539, 1998.

[8] Tysler M, Kneppo P, Turzová M, Svehlíková J, Karas S, Hebláková E, Hána K, Filipová S. Noninvasive assessment of local myocardium repolarization changes using high resolution surface ECG mapping. *Physiological research/Academia Scientiarum Bohemoslovaca*, (56 Suppl 1): S133–S141, 2007.

[9] Ihara Z, Design and performance of lead systems for the analysis of atrial signal components in the ECG. Thesis, Lausanne, EPFL, 2006.

Clustering Probabilistic Sleep Microstate Curves: a Functional Data Analysis Approach

R. Rosipal

Department of Theoretical Methods, Institute of Measurement Science
Slovak Academy of Sciences, Bratislava, Slovak Republic
Email: roman.rosipal@savba.sk

Abstract. *We introduced and validated an EEG data-based model of the sleep process with an arbitrary number of different sleep states and a high time resolution allowing modelling of sleep microstructure. The proposed probabilistic sleep model describes sleep via posterior probabilities of a finite number of microstates. Using the model, we extracted objective sleep parameters describing quantitative and qualitative characteristics of the probabilistic sleep microstate curves and proved their usefulness when assessing selected aspects of sleep quality. In the current work we are investigating functional data clustering methods applied to sleep microstate posterior curves. The hierarchical structure of the data given by the repeated visits of subjects in the sleep lab motivates our focus on recently proposed multilevel functional clustering analysis approaches. We are applying the multilevel functional principal component analysis to the sleep posterior curves. Preliminary results show promising potential of the approach to separate age-related sleep profiles and extracting subjects' specific night deviations from the mean sleep profiles.*

Keywords: Probabilistic Sleep Model, Functional Data Clustering, Multi-level Functional Principal Component Analysis

1. Introduction

In spite of the fact that sleep accounts for about one-third of human live, the purposes and mechanisms of sleep are only partially clear and are the subject of substantial research. One of the long-term open questions in sleep research is how to define and objectively measure 'normal' sleep and its quality. A different but not less important question is how sleep structure relates to selected daytime quality of life measures, including cognitive, emotional, psychometric or physiological tests and measures. The conventional description of sleep architecture from polysomnographic (PSG) recordings is carried out through applying the standardized Rechtschaffen and Kales (R&K) scoring manual [1] or the recently published update of the rules [2]. However, some aspects of the R&K sleep staging rules were criticized in the past and new ways of analysing sleep have been discussed [3]. With the aim of avoiding known drawbacks of R&K, an alternative computerized sleep model was introduced [4]. The model based on solid probabilistic principles allows describing sleep on an arbitrarily fine time scale and allows considering sleep as a continuous process of transitions between a larger number of sleep sub-states (microstates). Microstates can be combined into subsets. This feature allows defining new sleep states whose physiological interpretation and specific task-related performances can be studied. In the current study we considered posterior values of combined microstates as continuous time curves and we used advanced functional data analysis tools [5,6] to cluster curves into a meaningful structure. The validity of the approach is demonstrated on tasks of clustering age-dependent sleep profiles and clustering specific night deviations observed on subjects spending two consecutive nights in the sleep lab.

2. Subject and Methods

Data of 175 subjects (94 males and 81 females), age between 20 and 95 (mean 51 years and

standard deviation 20 years), from the sleep database created during the EU Siesta project were used [7]. One aim of the Siesta project was to create a normative database of healthy sleepers and sleep-disturbed patients. According to the Siesta recording protocol all subjects had to document their sleep habits over 14 nights. Subjects spent two consecutive nights (7th and 8th night) in the sleep laboratory during which PSG recordings were obtained. Subjects used in this study were classified as healthy sleepers without sleep related disorders [7].
The PSG recording protocol specified 16 channels of biosignals: 6 EEG channels with mastoid as reference (Fp1-M2, C3-M2, O1-M2, Fp2-M1, C4-M1, O2-M1), an additional EEG channel (M1-M2) for re-referencing, 2 EOG channels, submental EMG and EMG recorded from electrodes placed at the musculus anterior tibialis of the left and right leg (electrodes were linked), electrocardiogram and respiratory signals (airflow; movements of the chest wall and abdomen and O2 saturation of arterial blood).
First, using the PSG recording the sleep structure was analysed in 30 sec epochs according to the standard R&K scoring rules for sleep staging [1]. To this aim, the computerized system Somnolyzer 24x7 was used [8]. Next, a new probabilistic sleep model (PSM) was used to represent sleep as a continuum [4].

Probabilistic Sleep Model (PSM)
We use the C3-M2 (or C4-M2 as a substitute) EEG channel. For each 3 sec segment a AR(10) parameter vector $a = (a_1, \ldots, a_{10})$ is fitted: $X_t = a_1 X_{\{t-1\}} + a_2 X_{\{t-2\}} + \cdots + a_{10} X_{\{t-10\}} + e_t$
To each 3 sec interval a value $s \in \{0,1,2,3\}$ is assigned (0: no spindle, 1,2,3: spindle with increasing certainty). The R&K labels c are assigned by the automatic sleep scoring system to each 30 sec long data segment. The PSM assumes the existence of a latent variable Z with K possible states (Fig. 1, left)

$$p(a,c,s) = \sum_{z=1}^{K} p(z)p(a|z)p_R(c|z)p_S(s|z)$$

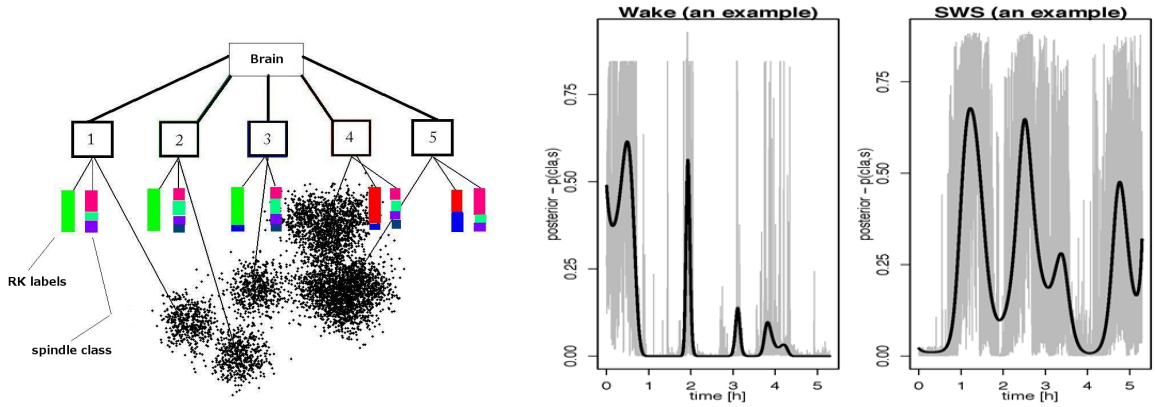

Fig. 1. *Left:* The schematic structure of the probabilistic sleep model (PSM). *Right:* An example of the PSM posterior values (light grey) and the B-spline smoothed curve (black). SWS – slow wave sleep.

The PSM with $K = 20$ sleep microstates was fitted using the EM algorithm [4]. Applying a model means to present an

$$p(z|a,s) = \frac{p(z)p(a|z)p_S(s|z)}{\sum_k p(k)p(a|k)p_S(s|k)}$$

or the R&K posteriors

$$p(c|a,s) = \sum_{z=1}^{K} p(z|a,s)p_R(c|z) \qquad (1)$$

Two-way Functional ANOVA & Multilevel Functional Clustering

We consider the two-way functional ANOVA model for our sleep profiles of subjects $i = 1, \dots, 175$ and nights $j \in \{1,2\}$

$$X_{ij}(t) = \alpha(t) + \beta_j(t) + Y_i(t) + W_{ij}(t) + \epsilon_{ij}(t)$$

where $\alpha(t)$ and $\beta_j(t)$ are fixed functional means specifying the global and night specific functional trends; $Y_i(t)$ is the subject-specific deviation from the night-specific mean and $W_{ij}(t)$ is the subject- and night-specific deviation from the subject-specific mean. Posteriors curves were positive smoothed by using B-splines with 20 basis functions and down-sampled to 30 sec intervals (Fig. 1, right). Nights were aligned to 5.3 hours starting by sleep latency. We use multilevel functional PCA [5] for extracting intra- and inter- subject specific component scores ξ, ζ and eigenfunctions $\phi(t)$

$$Y_i(t) = \sum_k \xi_{ik}\phi_k^{(1)}(t), \quad W_{ij}(t) = \sum_l \zeta_{ijl}\phi_l^{(2)}(t)$$

where $\phi_k^{(1)}(t) \sim K_B(s,t)$, $\phi_l^{(2)}(t) \sim K_W(s,t)$

and $K_T(s,t), K_B(s,t)$ and $K_W(s,t) := K_T(s,t) - K\_B(s,t)$ are the *total, between*, and *within* subjects covariance functions. The number of used eigenfunctions $\phi_k^{(1)}(t)$ and $\phi_l^{(2)}(t)$ was determined by the explained variance of 90%. Finally, we adapted clustering scheme proposed in [6]:

Level-1 Clustering:

Clustering of subject-specific means: subjects i_1 and i_2 will be in the same cluster if their subject-specific deviations $Y_{i1}(t)$ and $Y_{i2}(t)$ are similar in shape.

Level-2 Clustering:

Clustering of night-specific deviations: subjects i_1 and i_2 will be in the same cluster if their deviations from the subject-specific means $W_{i1,j}(t)$ and $W_{i2,j}(t), j \in \{1,2\}$ are similar.

3. Results

First, 20 sleep microstates of the PSM were combined into the R&K representation (wake, S1, S2, SWS – slow wave sleep, and REM – rapid-eye movement) using eq. (1). In addition, microstates representing SWS ($p(\text{SWS}|z) > 0.5$) were combined into a sleep state, which we denote mixMicro-SWS. Using the Level-1 clustering and considering the existence of three clusters we observed for all sleep states a structure with two dominant clusters. The percentage of samples falling into these two clusters was for wake – 99%, S1 – 94%, S2 – 95%, SWS - 94%, REM – 92% and mixMicro-SWS – 94%.

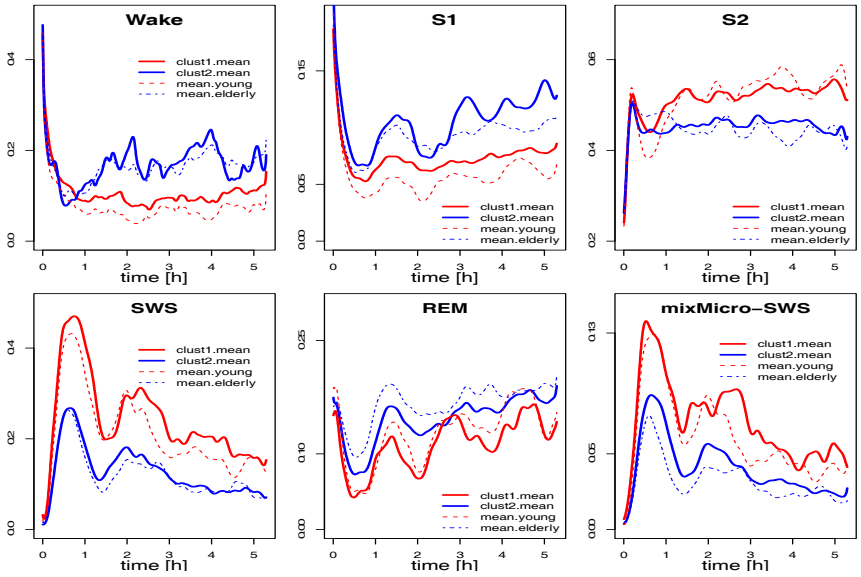

Fig. 2. The averaged sleep profiles of the two dominant clusters (thicker-solid lines) and the averaged sleep profiles of the young and elderly subjects. Curves represent 5.3 hours of sleep aligned by sleep latency. SWS - slow wave sleep, REM - rapid-eye movement.

Following our previous studies [9], we considered three age-related groups of subjects: young (< 40 years old), middle-age (40 to 60) and elderly (≥ 60). We compared averaged posterior curves computed for each age group with averages obtained by averaging posteriors curves falling into each of the two dominant clusters (Fig. 2). Close match between a mean curve of each cluster and averaged sleep profile either for the young or elderly subjects can be observed for every sleep state. For clarity, the averaged sleep profile of the middle-age subjects is not plotted, however, for all six sleep states this profile lies between the averaged sleep profiles of the young and elderly subjects. Finally, by considering the Level-2 clustering we observed strong night effects for wake state reflecting known phenomenon of the first-night effect associated with a higher level of wakefulness and longer sleep latency. Nigh effects were also observed for other sleep states and these are subject of further studies and validation.

4. Discussion

Multilevel functional data clustering was applied to smoothed posterior sleep profiles of the PSM. Preliminary results show promising potential of the approach to separate age-related sleep profiles and extracting subjects' specific night deviations from the mean sleep profiles. Further studies will focus on correlating extracted cluster information and subjects' daytime performance.

Acknowledgements

This work was supported by the Slovak Research and Development Agency under the contract No. APVV-0096-10 and by the Scientific Grant Agency of the Ministry of Education of the Slovakia Republic and the Slovak Academy of Sciences VEGA 1/0503/13 and VEGA 2/0043/13 grants.

References

[1] Rechtschaffen A, Kales A. A Manual of Standardized Terminology, Techniques and Scoring System for Sleep Stages of Human Subject. U.S. Dept. of Health, Education, and Welfare, Bethesda, MD, 1968.

[2] Iber C, Ancoli-Israel S, Chesson A, Quan S. The AASM Manual for the Scoring of Sleep and Associated Events: Rules, Terminology and Technical Specifications, 2007 .

[3] Himanen S, Hasan J. Limitations of Rechtschaffen and Kales. *Sleep Medicine Reviews*, 4, 149-167, 2000.

[4] Lewandowski A, Rosipal R, Dorffner G. Extracting more information from EEG recordings for a better description of sleep. *Computer Methods and Programs in Biomedicine*, 108, 961-972, 2012.

[5] Di Ch-Z, Crainiceanu CM, Caffo BS, Punjabi NM. Multilevel Functional Principal Component Analysis, *Annals of Applied Statistics*, 3, 458-488, 2009.

[6] Serban N, Jiang H. Multilevel functional clustering analysis. *Biometrics*, 68: 805-814, 2012.

[7] Klösch et al. The SIESTA project polygraphic and clinical database. *IEEE Engineering in Medicine and Biology Magazine*, 20, 51-57, 2001.

[8] Anderer et al. An E-Health Solution for Automatic Sleep Classification according to Rechtschaffen and Kales: Validation Study of the Somnolyzer 24×7 Utilizing the Siesta Database. *Neuropsychobiology*, 5, 115-133, 2005.

[9] Rosipal R, Lewandowski A, Dorffner G. In search of objective components for sleep quality indexing in normal sleep. *Biological Psychology*, under review.

SOLO: An EEG Processing Software Framework for Localising Epileptogenic Zones

[1]Z. Juhasz, [1]I. Vassanyi, [1]A. G. Nagy, [1]A. Papp, [2]D. Fabo, [1]Gy. Kozmann

[1]University of Pannonia, Veszprem, Hungary,
[2]National Institute of Neurosciences, Budapest, Hungary
Email: juhasz@virt.uni-pannon.hu

Abstract. *The paper describes an EEG signal processing software framework designed for performing validation tests in the ENIAC-CSI FP7 project for wireless EEG measurement sensors. The project aims at improving imaging devices and processing methods used in the localisation of epileptogenic zones in epileptic patients. The developed software allows specialist to view multi-channel EEG signals, identify epileptic features and perform source localisation operations based on realistic head models, and generate equivalent dipole data that can be used in localisation accuracy and reproducibility error analysis.*

Keywords: EEG processing, Epilepsy, Interictal Spikes, Source Localisation

1. Introduction

Epilepsy is a devastating disease affecting about 1% of the population. About 60% of all epilepsy patients have symptomatic focal epilepsies [1]. In these cases, one particular portion of the brain is affected by the disease. This region, referred to as focus, is responsible for the epileptic seizures. The focal concept of the epilepsies can be formed by overlapping epileptic zones representing different aspects of the epileptic transformation in the patient's brain [2]. These zones may be measured or estimated by various diagnostic tools, the most important of which is the EEG, which is selectively capable of detecting interictal and ictal electrical changes, thus identifying the irritative, ictal onset and spread zones. The final purpose of the identification of these zones is to plan surgical intervention, in order to remove the epileptogenic zone (EZ) and render the patient seizure free. Epilepsy surgery is superior to drug therapy in drug resistant epilepsy groups [3], with powers of average 60% (range 45-90%) seizure freedom with surgery versus 2-3% with additional drugs. The failure of the surgery, occurring 40% on average, is most often due to the false localisation of the EZ. Even intracranial placement of the electrodes cannot localise EZ in all cases requiring additional electrode placement [4].

The goal of improving source localisation techniques is inherently linked to epilepsy surgery and to the need of better localisation of the EZ. The work reported in this paper is part of the ENIAC Central Nervous System Imaging project[1] which is aiming at developing new brain imaging sensors, devices and data processing methods. Our focus in this cooperation is the evaluation of the accuracy, reliability and reproducibility of wireless EEG sensor-based measurements with respect to epileptogenic zone localisation. Since no software system was found suitable for this task, a new EEG processing and visualisation software framework was developed helping to conduct the source localisation experiments.

In Section 2 the validation goals and experiment protocol is described followed by an overview of the features and architecture of the developed SOLO program in Section 3. Section 4 presents the results of our development to date following with a discussion on future tasks.

[1] http://www.eniac-csi.org/CSI/

2. Proposed Validation Methods

This section describes the context of the validation tasks required in the project. The clinical partner performs long-term EEG monitoring of a selected set of epileptic patients. The EEG data is recorded simultaneously by a wired reference and a wireless development electrode set. The recorded EEG data are stored and later examined and annotated by a specialist. Interictal spikes whose presence indicates epilepsy are identified and marked in the data set. Short segments of the large data set containing the interictal spikes are stored in separate files for effective further processing.

The data segment files are next processed in the SOLO program, which includes the display of the 64-channel EEG data, setting a marker at the interictal spike time epoch and executing an equivalent dipole search based on solving the electromagnetic inverse problem on a patient-specific realistic head model using anatomy based anisotropic conductivity values.

The location, magnitude and orientation of the located best matching dipoles representing the centres of epileptogenic zones are recorded. The validation focuses on the error between localisation results of the reference and the new wireless electrode measurements. Subsequently, the accuracy and reproducibility are also examined verifying that spikes of a given patient localise to regions that math those also found with the reference electrodes and confirmed by clinical examinations.

3. Features and Architecture of the SOLO Software

A rich feature set is required for the processing software to perform the above validation experiments. A complete EEG signal browser, shown in Fig. 1, is developed to display and browse the multi-channel data set. The time scale and amplitude range adjustments help specialists to locate the interictal spikes quickly. A moveable marker is provided to mark the time instance, i.e. the measurement epoch, for which the dipole source localisation is performed.

Source localisation is performed using a realistic, patient-based head model. Patient MR images are segmented into scalp, inner and outer skull and brain surface meshes using the third party programs FSL[2] and Freesurfer[3]. The SOLO program can input these mesh objects and display a 3D view of the patient head geometry. The Electrode Manager module of the program computes the location of the measurement electrodes on the patient head geometry based on the cap layout system. The 3D head model, the placement of the electrodes and the visualisation of the measured potential values using spherical spline interpolation is shown in Fig. 2. Once the measured potential data set is selected with the marker, the program generates a configurable number of candidate dipole positions on the cerebral cortex by travelling the cortical surface following its curvature. The orientation of the dipole thus can always be set perpendicular to the cortical surface.

A boundary element solver [5] is used to compute the simulated potentials on the scalp at the electrode locations based on the parameters of each candidate dipole. The dipole producing the minimum squared mean error for the potential values is selected as the source. Once the localisation stops, the data describing the selected dipole is stored and the location is marked on the 3D model of the cortex.

[2] http://fsl.fmrib.ox.ac.uk/fsl/fslwiki/
[3] http://surfer.nmr.mgh.harvard.edu/

Fig. 1. The EEG signal browser panel (partial snapshot). The specialist can change the time resolution and amplitude range of the signals, browse the data setto locate and mark interictal events.

4. Results

The work presented in this paper is still in progress. At the time of writing, the SOLO software system is fully functional in displaying the EEG data, selecting measurement epochs, visualizing patient head, the electrode cap and the measured potential values. It also performs the dipole search based source localisation.

Collaboration with the National Institute of Neurosciences (Budapest, Hungary) within the project has led to further additional developments in the program. In order to better support epilepsy surgery planning, special visualisation functionality has been added to display intracranial electrodes within the patient head geometry model. This allows the specialist to better understand the anatomical location of the electrode grids or strips, as well as to display the measured intracranial potential values on the head model. One such example with a rather complex set of intracranial electrodes is shown in Fig. 3.

5. Discussion

The first functional version of the SOLO software is functional. The wireless electrodes are in the final testing stage as of March 2013. Live measurements on selected patients are expected to start in April allowing the validation work to start by May. Since the evaluation must finish by the summer, the execution time of the source localisation stage is of prime importance. The current solver finds one dipole in 4 minutes, resulting in approx. 8.5 days execution time per epoch assuming 2500 candidate dipoles (approx. 1 dipole per cm^2 resolution). Execution time becomes prohibiting should we need to analyze several epochs per interictal spike. We are actively working on optimizations of the solver as well as on the development of a massively parallel, GPU-based solver implementation in order to reduce localisation execution time to an acceptable level.

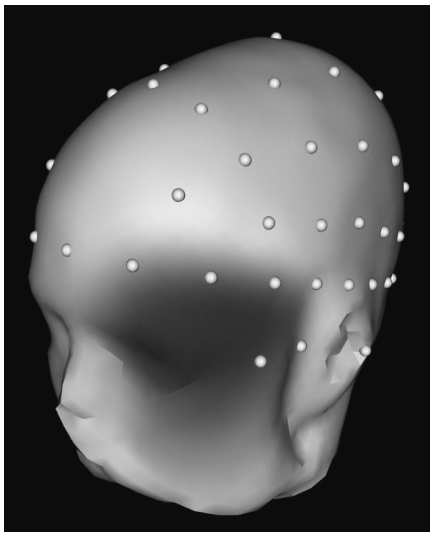

Fig. 2. 3D visualisation of the potential map, electrodes and the realistic head model.

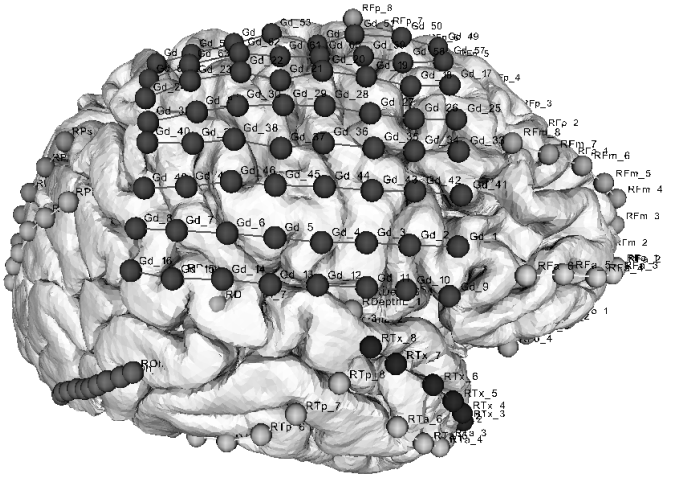

Fig. 3. 3D visualisation of the intracranial electrodes. The colour of the electrodes may represent either electrode group membership or the potential value measured at the given position of cortical surface.

6. Conclusions

This paper described the validation tasks to be performed within the ENIAC CSI project related to the development of new EEG measurement sensors, devices and data processing methods. A new EEG processing and visualisation software framework has been developed within the project to execute the required dipole-based source localisation based validation and error analysis tests. The first version of the software is functional and further improvements are in development to ensure the evaluation can be finished by the required deadline. It is hoped that the software in its full form will support epilepsy and EEG imaging research outside our current project as well.

Acknowledgements

This project was financed by the Hungarian Government and the European Union under the programme CSI: Central Nervous System Imaging (ENIAC_08-1-2011-0002).

References

[1] Engel, J., & International League Against Epilepsy ILAE. (2001). A proposed diagnostic scheme for people with epileptic seizures and with epilepsy: report of the ILAE Task Force on Classification and Terminology. *Epilepsia*, *42*(6), 796–803.

[2] Rosenow, F., & Lüders, H. (2001). Presurgical evaluation of epilepsy. *Brain*, *124*(Pt 9), 1683–1700. doi:10.1093/brain/124.9.1683

[3] Tellez-Zenteno, J. F. (2005). Long-term seizure outcomes following epilepsy surgery: a systematic review and meta-analysis. *Brain*, *128*(5), 1188–1198. doi:10.1093/brain/awh449

[4] Vadera, S., Mullin, J., Bulacio, J., Najm, I., Bingaman, W., & Gonzalez-Martinez, J. (2013). SEEG Following Subdural Grid Placement for Difficult to Localize Epilepsy. *Neurosurgery*. doi:10.1227/NEU.0b013e318285b4ae

[5] Cook MJ, Koles ZJ. "The effect of tissue anisotropy on the EEG inverse problem.", *Conf Proc IEEE Eng Med Biol Soc*. 2008;2008:4563-6. doi: 10.1109/IEMBS.2008.4650228.

Neural Networks in Keystroke Dynamics for Multi-Factor Authentication in Biomedicine

[1,2]A. Schlenker, [3]M. Sarek

[1]Institute of Computer Science, Academy of Sciences of the Czech Republic, Prague, Czech Republic,
[2]Institute of Hygiene and Epidemiology, First Faculty of Medicine, Charles University, Prague, Czech Republic
[3]CESNET, z.s.p.o., Prague, Czech Republic
Email: schlenker.anna@gmail.com

Abstract. *This paper presents an improved authentication method for biomedicine based on behavioural biometrics. A brief definition of keystroke dynamics and neural networks is provided. The main part of the work focuses on evaluation of typing dynamics which is then proposed as an interesting behavioural biometric characteristic for use in computer security not being widely used so far. The result of the work will be a new application, which allows optimal multi-factor authentication method regarding its comfort, cost and reliability.*

Keywords: Neural Network, Keystroke Dynamics, User Authentication

1. Introduction

With still growing extension of computer systems the need for their appropriate security increases [1]. After the user has successfully logged into the system, he/she has the opportunity to not only see, but also modify and copy sensitive data.

A wide range of authentication methods have accompanied us through during the whole existence of human society. One group of these methods is directly associated with human physiognomy. These are so called biometrics. Firstly, there are anatomical-physiological characteristics such as fingerprints, palm prints, hand geometry, blood vessel in the hand, patterns in the face, and patterns in the iris or retina. Secondly, there are behavioural characteristics such as signature, voice, and keystroke or mouse dynamics [2].

On the other hand, we can use some external attributes, whether it is a knowledge factor like password, or a possession factor like a magnetic strip card [2].

Based on the shortcomings of single-factor authentication methods, only multi-factor authentication seems adequately reliable to eliminate unauthorized access securely. It can be for example combination of anatomical or behavioural features with an external attribute or a password [2].

2. Subject and Methods

Keystroke dynamics is a type of behavioural biometrics that authenticates users based on habitual typing rhythm patterns [2]. It has been shown already [3, 4, 5] that the keystroke rhythm, during typing user's account name or password, is a good sign of identity.

Unlike other biometric systems, programs using keystroke dynamics do not require any hardware modifications and can be easily integrated with most computer systems [5, 6, 7].

During typing the username or password we can measure so called timing vector [8] which consists of the keystroke duration times and keystroke latencies [2]. The keystroke duration is

a period time during which a key is held for (see Fig. 1) and keystroke latency is the time between individual keystrokes (see Fig. 1). During fast typing when the next key is pressed before a previous key is released [8], the negative time can be measured (see Fig. 2). Figure 2 shows the timing vector when a password of eight characters is typed. This timing vector consists of eight keystroke duration times and seven keystroke interval times (two of them are negative).

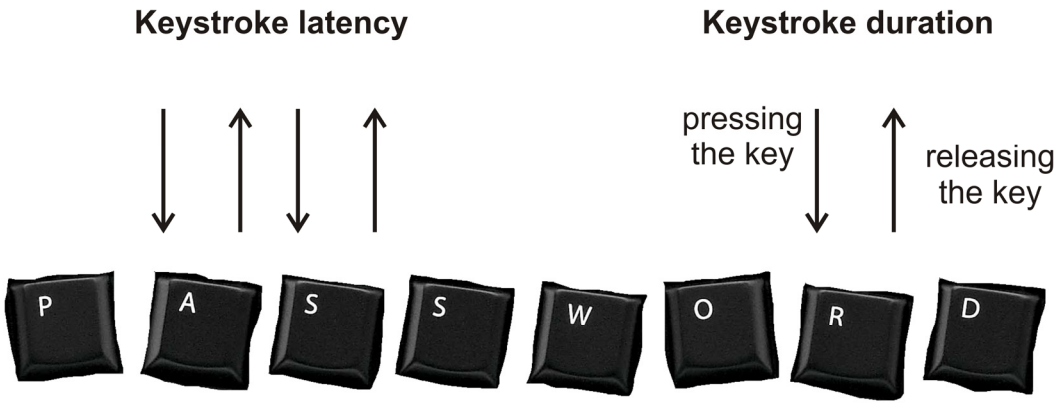

Fig. 1. Keystroke duration and keystroke latency (adapted from [2]).

Basis for Comparison

Samples for evaluation are obtained from users who type their name or username. These samples are then compared with samples obtained from other users (imposters), who try to imitate real users by typing the same name or username [3].

A basis for comparison is provided by two simple metrics: rejection of an authorized user and acceptance of an unauthorized user.

For the rate of rejection authorized users several metrics are used. The False Alarm Rate (FAR) represents a number of authentic user samples rejected by the authentication method and is used by Brown and Rogers [3] or Lin [5]. The False Rejection Rate (FRR) is the measure of the likelihood that the biometric security system will incorrectly reject an access attempt by an authorized user and it is used by Loy et al. [4] or Cho et al. [8].

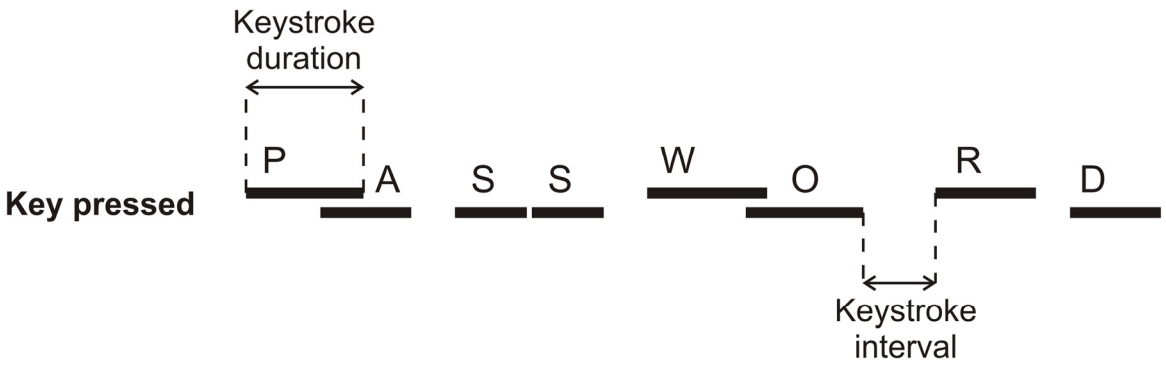

Fig. 2. Timing vector corresponding to “PASSWORD” (adapted from [8]).

For the rate of acceptance of unauthorized users several metrics are used, too. The Imposter Pass Rate (IPR) represents a number of imposter samples incorrectly authenticated and it is used by Brown and Rogers [3] or Lin [5]. Another metric is called the False Acceptance Rate (FAR) and it is used by Loy et al. [4] or Cho et al. [8]. The False Acceptance Rate is the measure of the likelihood that the biometric security system will incorrectly accept an access attempt by an unauthorized user.

Different biometric security systems determine different values for threshold for the False Acceptance Rate and False Rejection Rate. Therefore another metric called the Equal Error Rate (EER) is introduced [4]. The Equal Error Rate determines the point at which the proportion of false acceptances is equal to the proportion of false rejections. The lower is value of this variable, the higher is accuracy of the biometric system.

3. Experimental Approach

In previous studies, different types of neural networks are used for solving the problem of identifying users through the typing characteristics.

The Backpropagation Neural Network (BPNN) used by Akila and Suresh Kumar [1] is a typical multilayer neural network. This neural network uses the back propagation learning rule. The network consists of one input layer, one output layer and at least one hidden layer [1, 3, 9].

The Kohonen Neural Network used by Brown and Rogers [3] is a relatively simple self-organizing map. This neural network consists of two layers, an input layer and a Kohonen layer.

The Counterpropagation Neural Network (CPNN) is a hybrid network developed by Robert Hecht-Nielsen and used by Obaidat [9]. The simplest version of this network consists of two layers. The first layer is the Kohonen layer trained in the unsupervised mode. The second layer is an outstar array, called the Grossberg layer.

The Dynamic Backpropagation Neural Network used by Lin [5] has a changeable number of input nodes.

4. Discussion and Future Work

Based on previous research, there is a fairly surprising result that for the identification of a user only a short text is needed. In most cases it is a string of 6-8 characters which corresponds to user's name. We believe that the selection of a suitable neural network technique will help us to reach high accuracy of our application and to create a highly reliable biometric system for multi-factor authentication in biomedicine.

The proposal to further increase safety involves also the use of keystroke dynamics while typing a password.

Our work is now in the stage of selecting an appropriate method. The future work will focus on creating a pilot application and its testing on a group of volunteers. This method will be suitable also for on-line applications, due to the fact that it does not require any hardware modification on the side of a user.

5. Conclusion

For centuries the handwritten signature is maintained as an important identification sign. Nowadays, we have to accept replacing handwriting by typing on a keyboard. This paper summarizes the available information about this phenomenon. Combination of keystroke dynamics with neural network techniques offers better possibilities to use it for computer security. Using keystroke dynamics and neural networks during typing a username and a password can improve a multifactorial authentication system in biomedicine rapidly.

References

[1] Akila M, Suresh Kumar S. Improving feature extraction in keystroke dynamics using optimization techniques and neural network. In proceedings of International Conference on Sustainable Energy and Intelligent Systems, 2011, 891-898.

[2] Schlenker A, Sarek M. Behavioural biometrics for multi-factor authentication in biomedicine. *European Journal for Biomedical Informatics,* 8 (5): 19-24, 2012.

[3] Brown M, Rogers SJ. User identification via keystroke characteristics of typed names using neural networks. *International Journal of Man-Machine Studies*, 39:999-1014, 1993.

[4] Loy CC, Lai WK, Lim CP. Keystroke patterns classification using the ARTMAP-FD Neural Network. In proceedings of International Conference on Intelligent Information Hiding and Multimedia Signal Processing, 2007, 61-64.

[5] Lin DT. Computer-access authentication with neural network based keystroke identity verification. In proceedings of International Conference on Neural Networks, 1997, 174-178.

[6] Ilonen J. Keystroke Dynamics. In Advanced Topics in Information Processing – Lecture, 2003.

[7] Monrose F, Rubin D. Keystroke dynamics as a biometric for authentication. *Future Generation Computer Systems*, 16(4):351-359, 2002.

[8] Cho S, Han CH, Han DH, Kim H. Web based keystroke dynamics identity verification using neural network. *Journal of Organizational Computing and Electronic Commerce*, 10(4):295-307, 2000.

[9] Obaidat MS, Sadoun B. Verification of computer users using keystroke dynamics. *IEEE Transactions on Systems, Man, and Cybernetics – Part B: Cybernetics*, 27(2):261-269, 1997.

Experimental Setup for Estimation of the Parameters for Magnetic Permeabilization of Biological Objects

[1,2]V. Novickij, [1,2]A. Grainys, [1,2]J. Novickij, [1,2]S. Tolvaišienė

[1]High Magnetic Field Laboratory, Vilnius Gediminas Technical University, Lithuania,
[2]Department of Electrical Engineering, Faculty of Electronics, Vilnius Gediminas Technical University, Lithuania
Email: vitalij.novickij@vgtu.lt

Abstract. *The computerized experimental setup for investigation of the cuvette parameters for further application in the field of contactless permeabilization of the biological objects such as cells, fungi or bacteria by subjection to the high pulsed magnetic fields has been developed. The experimental facility was automated using LabVIEW software package. The setup allows investigation of the high current pulse form, estimation of the resultant magnetic and induced electric fields and evaluation of the heat generated due to Joule heating based on the cuvette size, inductive coil structure and current pulse parameters. Application of the proposed facility creates opportunity to define critical parameters of the cuvettes for magnetic permeabilization in order to prevent other factors such as temperature influencing the outcome of the experiment. Also the setup provides possibilities for the calibration of the magnetic field generators for use in the field of magnetoporation.*

Keywords: Magnetoporation, Pulsed Magnetic Field, Joule Heating, Cuvette, Biological Cells

1. Introduction

Magnetic permeabilization or magnetoporation of the biological objects by application of pulsed high magnetic fields in the range of 4 – 15 T is gaining value in the field of biotechnology, environmental sciences and biomedicine as a contactless technique causing effects similar to electroporation such as reversible or irreversible permeabilization of the thin bilayer lipid membrane of the biological samples [1]. However, even though the technique has some superior features compared to electroporation, the generation of high pulsed magnetic fields requires peak currents in the range of 0.5 – 2 kA, the structure of the cuvette for magnetoporation is more complex, and the estimation of the generated magnetic and induced electric field the biological objects are subjected to is not as straightforward as in the electroporation case [2]. Other factors influencing the treatment such as the heat generated due to Joule heating should be also eliminated, therefore, certain limitations of the allowed treatment intensities or the number of pulses for each cuvette is specific. All these problems created a requirement to develop a computerized measurement system, which could allow efficient estimation of the cuvette output parameters, limitation of the maximum allowed pulse parameter values and also accurate calibration of the magnetic field facilities for application in the field of magnetoporation.

2. Subject and Methods

The structure of the cuvette that is applied for magnetoporation consists of an inductive coil having a form of a solenoid and a plastic container inside the coil where the cells are put. When the high current is flowing through the coil high magnetic field and induced electric field are generated inside the plastic container, which results in the contactless permeabilization of the biological samples. According to the Biot-Savart's law the magnetic field is proportional to the peak current flowing through the coil [3]. The most significant

factor limiting the current is the heat that is generated due to the Joule heating [4]. It should be noted that during the treatment the temperature inside the cuvette should not exceed 32 – 37 ^{o} C because it could severely distort the experimental results and overall evaluation of the efficiency of the technique. Therefore, the maximum allowed values of the pulse parameters for each cuvette should be defined. The measurement and calibration setup should be able to measure two main parameters such as the current waveform and the temperature inside the cuvette. The resultant magnetic field and the induced electric field inside the coil could be evaluated analytically or either measured using magnetic field sensors [5]. The block diagram of the proposed measurement facility is shown in Fig. 1.

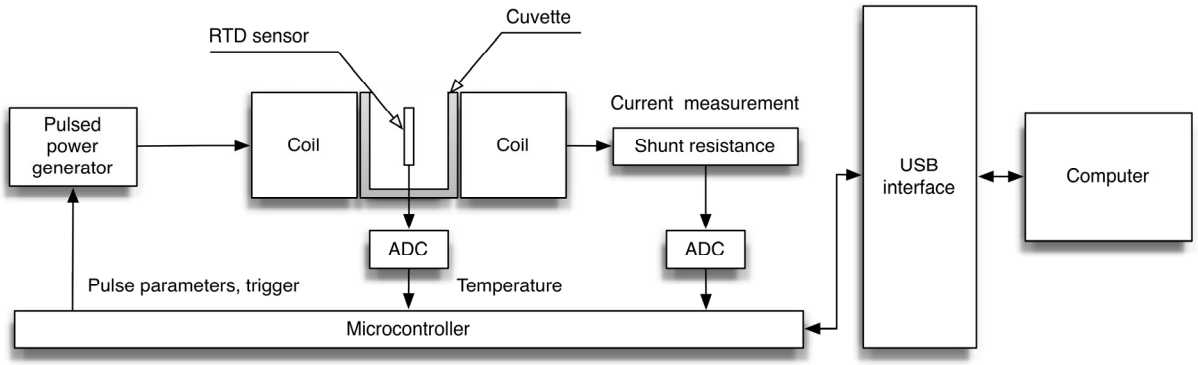

Fig. 1. The block diagram of the proposed measurement and calibration setup

The processing units of the facility are the computer and the microcontroller. The microcontroller based on the instructions received from the computer user configures the output parameters of the pulsed power generator and simultaneously triggers both pulse generation and measurement of the output parameters. The measurement modules are the temperature sensor and a shunt resistance with analog to digital converter for current pulse acquisition. The synchronization is achieved by application of high-speed dual channel optocouplers, which are not shown on the block diagram. The data from the temperature sensor and the microcontroller is further post processed using LabVIEW software package. Based on the coil parameters that are submitted by the user in the beginning of the experiment and the measured current waveform, the program analytically estimates the generated pulsed magnetic and induced electric fields inside the cuvette. The temperature response is also monitored and recorded throughout the whole experiment. It is possible to select an automatic calibration mode when the facility repeats the pulse generation and measurement until the temperature does not exceed the desired value. If the measured temperature value is higher than the desired one, the current is reduced and after a time pause required for the coil to cool down the experiment is repeated. As a result it is possible to classify any coil that is used for the magnetoporation and define the maximum allowed parameters. Also it is possible to determine the parameters required for different coils to generate same magnetic field. If the coil structure is complex, it is possible to connect an external magnetic field sensor. Application of the proposed measurement and calibration facility simplifies the methodology and the analysis of the cuvettes for magnetoporation, which could result in further popularisation of the magnetic permeabilization technique.

3. Results and Conclusions

A computerized measurement and calibration facility for estimation of the parameters of the magnetoporation cuvettes has been developed. The resultant facility is compact and fully automated, which simplifies the analysis of the cuvettes of any shape and size. Application of the proposed setup ensures that during magnetoporation there will be no thermal influence on

the samples and the parameters of the generated pulsed magnetic and induced electric fields could be accurately determined. The photograph of the facility in the Vilnius High Magnetic Field Centre is shown in Fig. 2.

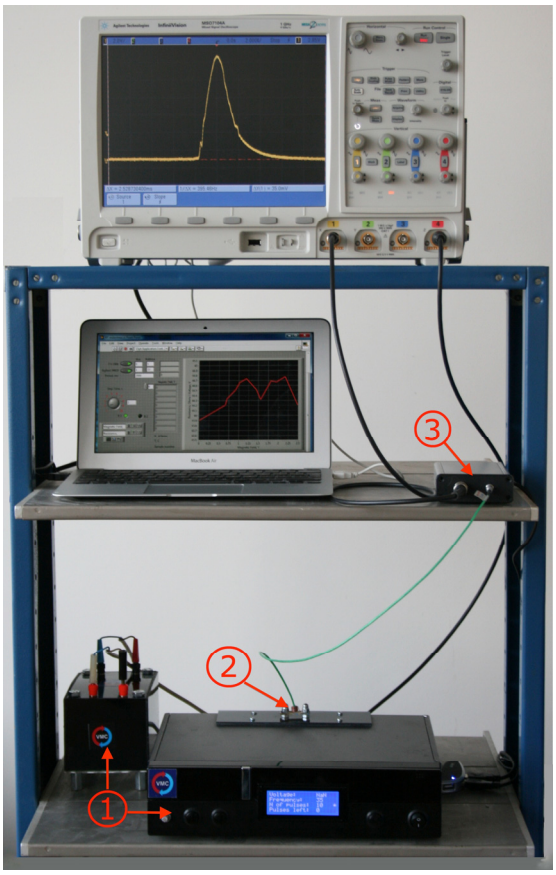

Fig. 2. Photograph of the measurement and calibration facility; 1: pulsed power generator; 2: magnetoporation cuvette; 3: ADC and data processing unit.

The magnetoporation cuvettes could be easily switched. Also other laboratory equipment such as an external oscilloscope could be additionally implemented in the setup as shown in the photograph, which offers flexibility in the acquisition of the experimental data.

References

[1] Grainys A, Novickij V, Novickij J, Stirke A, Kaseta V. High power facilities for electroporation of biological cells in pulsed magnetic fields. 19th Internation Conference on Microwaves, Radar and Wireless Communications, MIKON, 508-511, 2012.

[2] Kotnik T, Kramar P, Pucihar G, Miklavcic D, Tarek M. Cell membrane electroporation-part 1: The phenomenon. *IEEE Electrical Insulation Magazine*, 5 (28), 14-23, 2012.

[3] Garcia A, Carrasco J, Soto J, Maganto F, Moron C. A method for calculation the magnetic field produced by a coil of any shape. *Sensors and Actuators A*. 91, 230-232, 2001.

[4] Davalos R, Rubinsky B. Temperature considerations during irreversible electroporation. *International Journal of Heat and Mass Transfer*. 51, 5617-5622, 2008.

[5] Zurauskiene N, Balevicius S, Stankevic V, Kersulis S, Schneider M, Liebfried O, Plausinaitiene V, Abrutis A. B-scalar sensor using CMR effect in think polycrystalline manganite films. *IEEE Transaction on Plasma Science*, 1(39), 411-416, 2011.

Application of Nakagami Distributions in Ultrasound Contrast Imaging

[1]V. Slávik, [1,2]R. Kolář, [1,3]R. Jiřík, [1,2]V. Harabiš

[1]Department of Biomedical Engineering, Faculty of Electrical Engineering and Communication, Brno University of Technology, Brno, Czech Republic,
[2]International Clinical Research Center, Center of Biomedical Engineering, St. Anne's University Hospital, Brno, Czech Republic
[3]Institute of Scientific Instruments of the ASCR, v.v.i., Brno, Czech Republic
Email: xslavi16@stud.feec.vutbr.cz

Abstract. *Recent developments saw Nakagami and extended Nakagami distributions being used for extracting useful information about ultrasound scenes by matching local histograms from envelope of radiofrequency signals. This information is conveyed by distribution parameters' values. On the other hand, in research literature, new distributions or their extensions are proposed mostly on basis of quality of local histogram match in LMS sense. This measure is not linked in any way to significance of information contained in parameters of these distributions, though. As is shown here, in the context of contrast imaging, the Extended Nakagami distribution significantly improves neither quality of fit, nor information about local area, despite the additional parameter.*

Keywords: Nakagami Distribution, Histogram Fitting, Ultrasound Imaging, Contrast Agents

1. Introduction

Perfusion analysis in ultrasound applications is a modern, dynamical field with many open problems. Ultrasound contrast agents (UCA) in form of various types of microbubbles are used in these applications. The spectrum of echoes returning from UCA contains relatively higher amount of harmonics due to nonlinear behaviour of UCAs. Estimation of perfusion then typically depends on analysis of second harmonic signal, or manipulation of signals such as phase inversion or amplitude modulation, which extract signal content arising from UCA nonlinearities.

An alternative approach to analyse the envelope of the backscattered signal is to model the local statistical properties of the first and second harmonics. One of the general statistical models is Nakagami distribution, which can describe different scattering conditions.

This paper describes an experiment, where ultrasound data are processed with the goal of estimating UCA concentration, particularly the differences caused by generalizing the basic Nakagami distribution to an extended form.

2. Subject and Methods

Nakagami Models

The Nakagami distribution has been originally proposed for modelling multipath-spreading radio signals. As the similarity with ultrasound signal suggests, it is applicable to modelling ultrasound data as well [1]. Its properties, namely ability to exhibit heavy tails, allow the Nakagami distribution to match real data better than e.g. Rayleigh or Gamma distribution. In its basic form, Nakagami distribution is expressed as

$$f(x) = \frac{2m^m x^{2m-1} e^{-\left(\frac{m}{\Omega}x^2\right)}}{\Gamma(m)\Omega^m}, \quad (1)$$

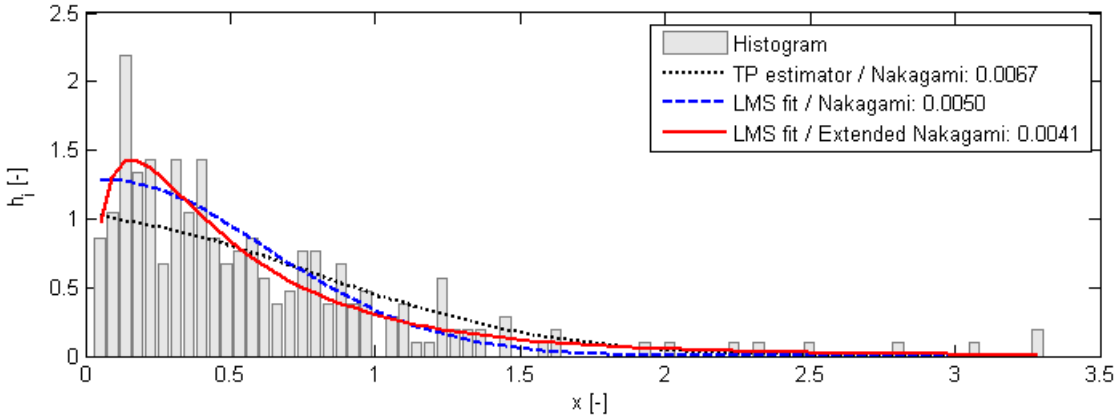

Fig. 1. Typical results of fitting Extended Nakagami and Nakagami distributions to a histogram, along with parameter estimation. Numbers in legend correspond to LMS quality of match.

where x is the independent variable, Γ is the gamma function, m is the shape parameter and Ω the scaling factor. There exist various estimators for the Nakagami distribution [2], among them the Tolparev-Polyakov (TP) estimators:

$$\widetilde{\Omega} = \frac{1}{N}\sum_{i\in ROI} x_i^2 \,; B = \left(\prod_{i\in ROI} x_i\right)^{1/N};\ \widetilde{m} = \frac{1+\sqrt{1+\frac{4}{3}ln\left(\frac{\mu_2}{B}\right)}}{4\,ln\left(\frac{\mu_2}{B}\right)}. \tag{2}$$

To adapt the probability density function (PDF) for heavy tails, common for PDF of ultrasound envelope signals, the variable X describing returning signal can be transformed as $Y = X^{2/s}$. Thus, the extended Nakagami distribution is obtained, with PDF in the form of

$$f(x) = \frac{|s| m^m x^{sm-1} e^{-\left(\frac{m}{\Omega}x^s\right)}}{\Gamma(m)\Omega^m}. \tag{3}$$

The parameter s does not have any direct physical meaning; with its value of 2 the PDF reverts to the basic Nakagami distribution. It can be shown that this generalization of Nakagami distribution is identical to a generalization of Gamma distribution.

Previous research shows that for the (basic) Nakagami distribution, the parameter m (shape parameter) depends linearly on UCA concentration in certain range [3].

Experiment Setup

To evaluate a range of ultrasound contrast agent (UCA) concentrations, an experimental measurement setup was designed. A SonoVue (Bracco International, BR 14) UCA solution contained in a plastic bottle was immersed in a tank filled with water. The initial concentration was 100 mg/ml. During the experiment it was lowered seven times, always halving it, to final concentration of 0.78125 mg/ml. Thus, the range that can be expected in clinical applications was covered.

A conventional ultrasound scanner (GE Vingmed System Five) was used to collect the data. The system was set to base frequency (first harmonic) of 2.4 MHz, mechanical index 0.1 and focus to 7 cm, which corresponded to plastic container position.

Data Processing

Using the previous setup, radiofrequency (RF) data were collected and bandpass-filtered for 1st and 2nd harmonic components. From these datasets, the respective images were

reconstructed. Values of these grayscale images were then normalized by scaling in such way that the maximal value was always converted to 100.

Nine regions of interest were selected within the area of plastic container for further processing. Histograms from image data in these regions (75 bins) were scaled to allow fitting with PDFs, according to Eq. 4.

$$\Delta = \frac{\max(h) - \min(h)}{bins}, \; h' = h \cdot \Delta \tag{4}$$

The histograms were then fitted with Nakagami and Extended Nakagami PDFs, along with estimating (basic) Nakagami parameters by TP estimator. For fitting, least mean square (LMS) minimization has been employed using functions from Matlab Optimization toolbox. A single example of results of this step is shown in Fig. 1. For each of the parameters gathered from all nine regions, median was calculated at each concentration as the final value.

Apart from distribution parameters, we obtained the quality of fit in LMS sense. This allows a direct comparison of the three methods used, after normalization according to Eq. 5.

$$err_{norm} = err_{fit} \cdot \Delta^2 \tag{5}$$

3. Results

As can be seen, the Nakagami PDFs fit the local histograms of obtained data with comparable success. The resulting parameters and LMS error of distribution can be seen in Fig. 2 for 1st harmonic images. Both models give similar results for both harmonics, therefore the following discussion will consider only 1st harmonic images.

Of particular interest is Fig. 3, showing in detail the range described in previous work (1.5625-12.5 mg/l), where the parameter *m* exhibits linear dependence on UCA concentration (R^2=0.97 for estimator and 0.98 for LMS fitting).

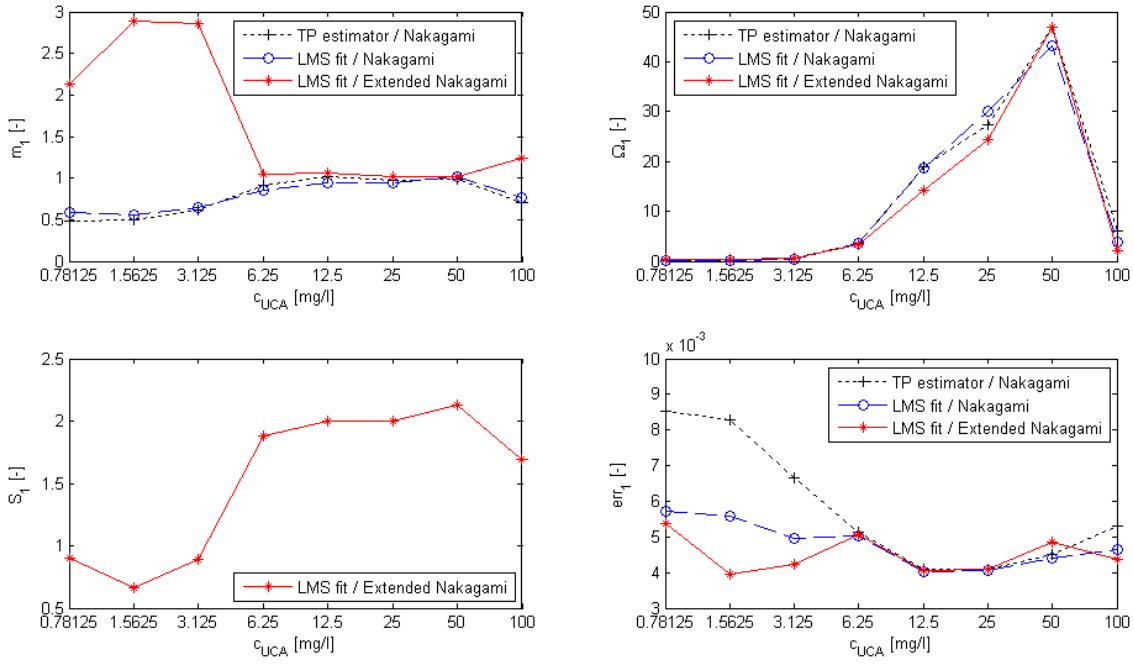

Fig. 2. Parameter values and LMS error of various methods for the first harmonic component. Second harmonic behaves similarly and is omitted for clarity. The values shown are medians calculated from values computed for all nine ROIs. All charts have on x axis the concentration in log scale.

4. Discussion

As can be seen from Fig. 2 and 3, the linear relation between UCA concentration and value of shape parameter *m* is valid for both estimation methods using basic Nakagami distribution. Of note is also that in range 6.25-50 mg/l, the parameter *s* stays very close to its default value of 2, meaning that the Extended Nakagami distribution reverts back to its non-generalized version.

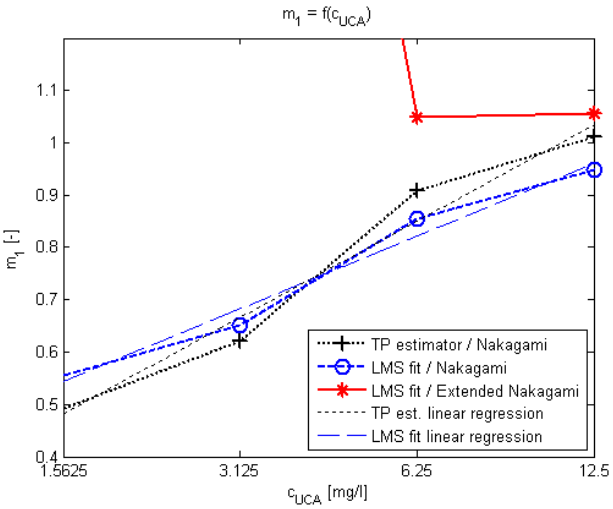

Fig. 3. Detail of parameter m_1 in range where it depends linearly on concentration.

All three methods result in different quality of fit in LMS sense, with LMS fit of Extended Nakagami distribution performing best of the three methods. The improvement is strongest in lower concentrations, with roughly 33% improvement of the LMS-error from fitting basic Nakagami dist. and 53% improvement from TP estimator in best case.

Fig. 3 shows also that the Extended Nakagami distribution does not exhibit the linear dependency of parameter *m* on UCA concentration at all, unlike basic Nakagami distribution.

5. Conclusions

We have shown that the Extended Nakagami PDF leads to lower LMS errors for lower concentration. However, the improvement of fitting quality is not significant (Fig. 2). It should be also mentioned that more parameters (additional parameter *s*) increase the computation complexity, which can lead to instability during fitting procedure. Given the lack of additional parameter's physical interpretation, a phenomenon already criticized [4], the Extended Nakagami distribution does not appear to be useful in contrast imaging.

Acknowledgements

This work has been supported by the project of Czech Science Foundation no. P102/12/2380 and by European Regional Development Fund – Project FNUSA-ICRC (No. CZ.1.05/1.1.00/02.0123).

References

[1] SHANKAR, P.M. Ultrasonic tissue characterization using a generalized Nakagami model. In *IEEE transactions on ultrasonics, ferroelectrics, and frequency control* [online]. 2001. Vol. 48, No. 6, 1716–20.

[2] KOLAR, R., JIRIK, R., JAN, J. Estimator comparison of the Nakagami-m parameter and its application in echocardiography. In *Radioengineering* [online]. 2004, No. 7, 8–12.

[3] KOLAR, R., JIRIK, R., HARABIS, V. Nakagami model of scattering in ultrasound contrast media. In Proceedings of the IEEE International Ultrasonics Symposium 2012, in press (2012).

[4] DESTREMPES, F., CLOUTIER, G. A critical review and uniformized representation of statistical distributions modeling the ultrasound echo envelope. In Ultrasound in Med. & Biol. 2010. Vol. 36, No. 7, 1037–1051.

Fast and Localized ^{31}P Saturation Transfer Measurement at 7 T Reveals Slower Hepatic Metabolic Rates in Patients with Steatohepatitis

[1,2]L. Valkovič, [1]M. Gajdošík, [3]S. Traussnigg, [1]M. Chmelík, [2]I. Frollo, [3]M. Trauner, [1]S. Trattnig, [1,3]M. Krššák

[1]Department of Radiology, Medical University of Vienna, Vienna, Austria
[2]Institute of Measurement Science, Slovak Academy of Sciences, Bratislava, Slovakia
[3]Department of Internal Medicine III, Medical University of Vienna, Vienna, Austria
Email: ladislav.valkovic@meduniwien.ac.at

Abstract. *Invasive liver biopsy is currently the only method used for distinction between non-alcoholic fatty liver (NAFL) and steatohepatitis (NASH). Phosphorus magnetic resonance spectroscopy (^{31}P-MRS) with saturation transfer (ST) technique enables a non-invasive in vivo measurement of hepatic energy metabolism alterations that can indicate liver diseases. Ten suspected NAFL/NASH patients and four healthy volunteers were measured by ^{31}P-MRS 1D-ISIS ST on a 7 T MR system. All patients underwent a liver biopsy for diagnostic purposes. Significantly lower exchange rate constants ($p<0.01$) were found in NASH patients when compared to healthy volunteers and also to NAFL patients. Strong correlation was also found between the chemical exchange rate and steatosis degree. Thus, we believe that the ^{31}P-MRS ST might provide a clinical tool for future distinction between NAFL and NASH.*

Keywords: ^{31}P-MRS, Saturation Transfer, 7 T, Liver Metabolism, NASH

1. Introduction

Non-alcoholic fatty liver disease (NAFLD) refers to a clinical condition characterized by steatosis and increased lipid content with varying degrees of inflammation in individuals consuming <20g of alcohol per day [1]. The histologic spectrum of NAFLD includes benign non-alcoholic fatty liver (NAFL) and potentially progressive steatohepatitis (NASH) [1, 2]. Although originally considered to occur exclusively in obese diabetic women [3], NASH is now known to occur in both genders and even in those who are not obese [4]. Currently, the only established method for distinction between NAFL and NASH is invasive liver biopsy.

It has been recently shown, in type II diabetes patients, that alterations in hepatic energy metabolism are indicative for inflammatory and neoplastic liver diseases [1, 5]. A non-invasive tool dedicated for *in vivo* energy metabolism measurements through concentration assessments of high energy metabolites, e.g., adenosine-tri-phosphate (ATP) or inorganic phosphate (Pi), is called phosphorous magnetic resonance spectroscopy (^{31}P-MRS). This method can be furthermore combined with a saturation transfer (ST) technique and measure the metabolic rate of Pi-to-ATP chemical exchange [6].

Quantitative measurement of resting ATP synthesis in human liver by 1D-ISIS localized ^{31}P-MRS ST has been successfully demonstrated at 3 T [7], but because of low signal-to-noise ratio (SNR), the examination took almost 2 h, what is unpractical for clinical praxis. Recently, it has been shown that going to ultra-high field strengths (7 T) can significantly reduce the measurement time needed for non-localized ST experiments in human skeletal muscle [8] and even for 1D-ISIS localized ST examinations of the liver [9], enabling measurements of chemical exchange rates in clinically feasible scan time.

Therefore, the aim of this study was to test the feasibility of the ^{31}P-MRS ST technique at 7 T for fast non-invasive distinction between NAFL and NASH.

2. Subject and Methods

Ten suspected NAFLD patients (six males, four females; 49.5 ± 13.2 years) and four young healthy male volunteers (25.3 ± 2.9 years) participated in this study. Written, informed consent was obtained from all volunteers and the local ethics committee approved the protocol. All patients underwent an invasive liver biopsy, for diagnostic differentiation of the NAFL and NASH, one day after the MR examinations.

The MR examinations were performed on a 7 T MR system (Siemens Healthcare, Erlangen, Germany) using a double-tuned (^{31}P/^{1}H) surface coil (Rapid Biomedical, Wimpar, Germany), with a 10 cm diameter. Participants were examined in early morning hours after overnight fasting in a lateral position with the right lobe of the liver positioned over the coil, what was further adjusted according to localizer images.

The 30 mm wide ISIS localization slab was placed parallel to the coil through the liver minimizing muscle contamination (see Fig. 1). ST experiment consisted of 1D-ISIS localized liver spectra acquisition with selective saturation, of the γ-ATP frequency (saturation state) and of the frequency mirrored downfield around the Pi (equilibrium state). The apparent longitudinal relaxation time (T_1^{app}) of Pi was measured with an inversion-recovery (IR) sequence with eight inversion times (TI=0.08-3 s) with continuous saturation of the γ-ATP resonance. Unsaturated 1D-ISIS spectra were obtained to estimate the Pi concentration, using the γ-ATP as an internal concentration reference (2.5 mM [1]). The measurement parameters were set as follows: rectangular 400 ms excitation, TE*=0.4 ms, TR=5 s and total acquisition time ~23 min.

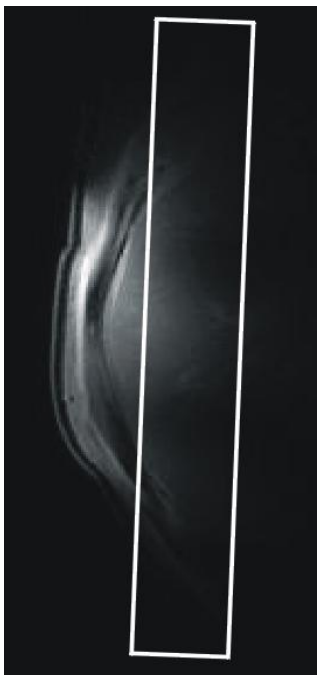

Fig. 1. 1D-ISIS localization volume depicted on the localizer image

The chemical exchange rate constant, *k*, of the basal Pi-to-ATP reaction was calculated from saturation and equilibrium liver spectra according to Eq. 1.

$$k = \left(1 - M_z / M_0\right) / T_1^{app} \qquad (1)$$

where

M_z saturation state magnetization of Pi measured during γ-ATP saturation
M_0 equilibrium magnetization of Pi measured during saturation mirrored around Pi

The resting unidirectional forward exchange flux (F_{ATP}) was then calculated by multiplying the forward rate constant, *k*, with the estimated resting concentration of Pi.

The MR measured metabolic parameters (k, F_{ATP}) were compared between the subgroups with an unpaired Student's t-test with a significance level cut off at $p<0.01$. In addition, linear correlation with the histology, regarding the disease status and steatosis degree was investigated by the Pearson correlation coefficient.

3. Results

Summarized data from the ST measurements are given in Table 1, where the patient group is already resolved by the histological diagnosis into NAFL (n=4) and NASH (n=6) subgroups. The NASH patients had significantly lower *k* values in comparison to NAFL patients (*, $p<0.01$) and also to healthy volunteers ($^{\#}$, $p<0.01$). There was no overlap in *k* values between the NASH patients and the other two subgroups. Similar results were found in the

comparison of the uni-directional metabolic fluxes (F_{ATP}) of the NASH patients and the other two groups investigated in this study.

Table 1. Hepatic metabolism parameters measured by the ^{31}P-MRS ST technique. (* - NASH vs. NAFL, $p<0.01$; $^{\#}$ - NASH vs.Healthy controls, $p<0.01$)

	NAFL (n=4)	NASH (n=6)	Healthy controls
[Pi]' (mM)	1.23 ± 0.16	1.09 ± 0.23	1.25 ± 0.04
T_1^{app} (s)	0.80 ± 0.09	0.72 ± 0.19	0.79 ± 0.18
k (s^{-1})	0.34 ± 0.04	0.18 ± 0.05$^{*\#}$	0.31 ± 0.03
F_{ATP} ($mM.s^{-1}$)	0.41 ± 0.04	0.20 ± 0.08$^{*\#}$	0.38 ± 0.05

Strong correlation according to Pearson correlation coefficient was found between the forward rate constant of the Pi-to-ATP reaction, *k*, determined by the ^{31}P-MRS ST technique, and the degree of liver steatosis, histologically assessed form the liver biopsy sample. This linear correlation is depicted in Fig. 2.

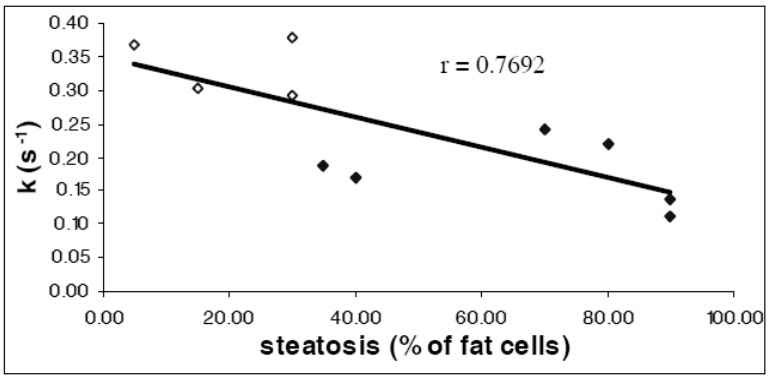

Fig. 2. Correlation between the exchange rate constant (ST) and steatosis degree (biopsy). Empty diamonds depict NAFL and full NASH patients. Note no overlap between the groups.

4. Discussion

In this study, we investigated the possibility of fast non-invasive differentiation between two states of NAFLD – benign fatty liver and progressive steatohepatitis, by a 1D-ISIS localized ^{31}P-MRS ST technique at 7 T. We were able to show that NASH patients have significantly slower Pi-to-ATP exchange rate and metabolic flux compared to NAFL patients and healthy volunteers. In addition, a strong correlation between the exchange rate constant and steatosis degree, determined by invasive liver biopsy, was found. To the best of our knowledge, no investigation of NAFL and NASH differentiation by ST has been previously reported.

Hepatic ATP synthesis rate constants have been previously measured in healthy volunteers and type II diabetes, with no significant differences between the groups [5, 7]. The values of healthy volunteers (k=0.31 ± 0.03) measured in this study are in good agreement with previous reports (k=0.33 ± 0.12 in [5] and 0.30 ± 0.02 in [7]). As no absolute quantification was performed, no valid comparison regarding the assumed Pi concentrations or calculated uni-directional fluxes can be given.

We report significant differences in basal metabolic rate constants of the Pi-to-ATP reaction between the NASH patients and the NAFL patients as well as between NASH patients and healthy volunteers. No overlap in *k* values between NASH group and the other two groups suggests that *k* values can be used in future for differentiation between NAFL and NASH. These findings might be associated with the mitochondrial abnormalities previously found in NASH patients [2], NASH can be also associated with progressive hepatic fibrosis compromising liver metabolism and resulting into cirrhosis [10].

Furthermore, we report strong linear correlation between the forward rate constant determined by the ST measurement and the histologically determined degree of liver steatosis.

5. Conclusions

Liver Pi-to-ATP chemical reaction, measured *in vivo* by the 1D-ISIS localized ^{31}P-MRS ST technique at 7 T, is decreased in NASH patients in comparison to NAFL patients and healthy controls. This difference is connected to the lower exchange rate constant and might provide a valuable clinical tool for future non-invasive distinction between NASH and NAFL.

Acknowledgements

The financial support by the Vienna Spots of Excellence des Wiener Wissenschafts-und Technologie-Fonds (WWTF) - Vienna Advanced Imaging Center (VIACLIC) and the OeNB Jubilaeumsfond (grant #13629, #13834), the Slovak Grant Agency VEGA (grant #2/0090/11) and APVV (grant #APVV-0513-10) is gratefully acknowledged.

References

[1] Szendroedi J, Chmelik M, Schmid A I, Nowotny P, Brehm A, Krssak M, Moser E, Roden M. Abnormal hepatic energy homeostasis in type 2 diabetes. *Hepatology*. 50(4): 1079-1086, 2009.

[2] Sanyal A J, Campbell-Sargent C, Mirshahi F, Rizzo W B, Contos M J, Sterling R K, Luketic V A, Shiffman M L, Clore J N. Nonalcoholic steatohepatitis: association of insulin resistance and mitochondrial abnormalities. *Gastroenterology*. 120(5): 1183-1192, 2001.

[3] Baker A L. Nonalcoholic steatonecrosis: a unique histopathologic lesion of the liver with multiple causes. *Survey of Digestive Diseases*. 3(3): 154-164, 1985.

[4] Bacon B R, Farahvash M J, Janney C G, Neuschwandertetri B A. Nonalcoholic steatohepatitis - an expanded clinical entity. *Gastroenterology*. 107(4): 1103-1109, 1994.

[5] Schmid A I, Szendroedi J, Chmelik M, Krssak M, Moser E, Roden M. Liver ATP synthesis is lower and relates to insulin sensitivity in patients with type 2 diabetes. *Diabetes Care*. 34(2): 448-453, 2011.

[6] Brown T R, Ugurbil K, Shulman R G. 31P nuclear magnetic resonance measurements of ATPase kinetics in aerobic Escherichia coli cells. *Proceedings of the National Academy of Sciences of the United States of America*. 74(12): 5551-5553, 1977.

[7] Schmid A I, Chmelik M, Szendroedi J, Krssak M, Brehm A, Moser E, Roden M. Quantitative ATP synthesis in human liver measured by localized 31P spectroscopy using the magnetization transfer experiment. *NMR in Biomedicine*. 21(5): 437-443, 2008.

[8] Valkovič L, Chmelík M, Just Kukurová I, Kršňák M, Gruber S, Frollo I, Trattnig S, Bogner W. Time-resolved phosphorous magnetization transfer of the human calf muscle at 3T and 7T: a feasibility study. *European Journal of Radiology*. 82(5): 745-751, 2013.

[9] Valkovič L, Bogner W, Gajdošík M, Just Kukurová I, Kršňák M, Frollo I, Trattnig S, Chmelik M. 1D-ISIS localized 31P magnetization transfer in liver at 7T. In proceedings of the *ESMRMB 2012*. 2012. 91

[10] Dezortova M, Taimr P, Skoch A, Spicak J, Hajek M. Etiology and functional status of liver cirrhosis by 31P MR spectroscopy. *World Journal of Gastroenterology*. 11(44): 6926-6931, 2005.

Multi-parametric Segmentation of MR images of the Brain

[1, 2]P. Dvořák, [2]K. Bartušek

[1]Dept. of Telecommunications, Faculty of Electrical Engineering and Communication, Brno University of Technology, Brno, Czech Republic,
[2]Institute of Scientific Instruments of the ASCR, v.v.i., Brno, Czech Republic
Email: pavel.dvorak@phd.feec.vutbr.cz

Abstract. *This work deals with segmentation of magnetic resonance images. For better distinguishing between particular tissues, particular properties of tissues and their manifestation in different types of imaging are used. Specifically, T1 and T2 images are used. The segmentation is based on the approximation of more dimensional histograms. Since the noise distribution in MR images is close to Gaussian distribution for large signal-to-noise ratio, the approximation is done by Gaussian Mixture Model, where the number of components is determined using Bayesian Information Criterion and Elbow method.*

Keywords: GMM, Image Segmentation, MRI, Multi-parametric Image Segmentation, Tissue Classification.

1. Introduction

This paper focuses on automatic segmentation of magnetic resonance images, which belongs to the general problem of image segmentation. General image segmentation is still an unsolved problem, therefore specific methods have to be applied for particular types of images. General method that could be applied for all kinds of images has not been developed so far and in the near future the situation will remain the same.

For MR image segmentation, the classic techniques such as thresholding, region growing, active contour, etc. can be used [1]. These methods work only with one type of image. If more types of images such as T1-weighted, T2-weighted or Diffusion weighted are present, it is useful to take advantage of all of them. The advantage can be seen in Fig. 1. It is obvious in this figure that tissues, which have similar intensities in one type of image, can be distinguished on another type and vice versa.

The proposed method is related to MR images with large signal-to-noise ratio, because they can meet the condition of approximately Gaussian distribution of noise. Here, images acquired by Spin Echo and Turbo Spin Echo sequence are used. All processed images were acquired in the Faculty Hospital in Brno Bohunice by the Philips Achieva MRI system ($B_0 = 1.5$ T).

2. Noise in MR Images

The noise in real and imaginary MR images can be described by Gaussian distribution [2]. Since the magnitude images are created by non-linear operation, the distribution of noise in this type of image is no longer Gaussian. Here, the noise distribution is Rician. The Rician distribution is described by Eq. 1 [3].

$$p_M(M) = \frac{M}{\sigma^2}\exp\left(\frac{-\left(M^2 + A^2\right)}{2\sigma^2}\right) I_0\left(\frac{AM}{\sigma^2}\right) \qquad (1)$$

where σ is the standard deviation of the Gaussian noise in the original real and imaginary images. They are assumed to be the equal. I_0 denotes the modified zeroth order Bessel

function of the first kind. A and M mean the pixel intensity in the absence of noise and the measured pixel intensity, respectively.

The Rician distribution for large signal-to-noise ratio is comparable to Gaussian distribution. Since the input images of brain, which are used in this work, meet the condition of large signal-to-noise ratio, the noise is approximated by the Gaussian distribution. The Gaussian distribution is described by Eq. 2 [2].

$$p_M(M) = \frac{1}{\sigma\sqrt{2\pi}} \exp\left(\frac{-(M-A)^2}{2\sigma^2}\right) \tag{2}$$

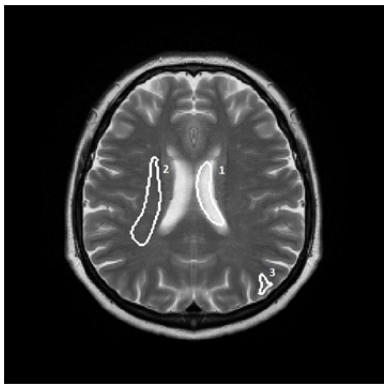

(a)

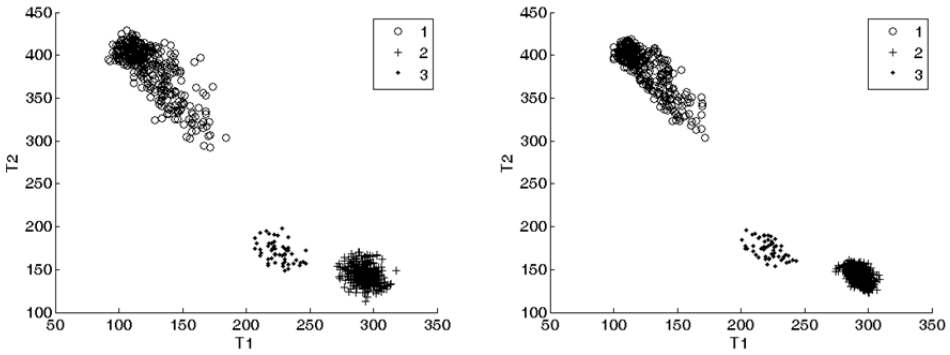

(b) (c)

Fig. 1. Distribution of pixel intensities of lateral ventricle (1), white matter (2) , and grey matter (3) in T1-T2 space. (a) selected regions, (b) distribution of pixels in original image, (c) distribution of pixels in filtered image.

3. Segmentation

The proposed method is based on unsupervised classification of particular pixels into several groups. At first, the N-dimensional histogram is approximated by a mixture of Gaussians, where the N denotes the number of modalities. Here, we use 2 different modalities – T1- and T2-weighted images. Then, all pixels of the brain are classified as a pixel of particular Gaussian, which depends on the probability density function of every Gaussian in particular point in the N-dimensional space. Only the pixel intensity in every image type is considered for the classification. No relations between neighbour pixels are considered. The post processing step consists of the operations with the resulting image. Before the segmentation itself, only the brain is extracted from the image according to method described in [4]. Then

the image is filtered by Gaussian filter to make particular parts of the brain more consistent. The comparison is shown in Fig. 1.

Histogram Approximation

The approximation of *N*-dimensional histogram is based on the assumption that the distribution of the noise in magnitude MR image is approximately Gaussian [2]. The histogram of the brain area is approximated by a mixture of Gaussians. The method is based on Gaussian Mixture Model (GMM) [5], which is one of the unsupervised learning and its typical use is for the clustering. It is a statistical probability model. The computation is based on the probability density of all pixels in the data space. The algorithm tries to find a statistical model of the density function that minimizes the square error of probability function of the model and the true data.

The GMM algorithm uses an algorithm called Expectation Maximization (EM) [5], which is an iterative algorithm searching for the maximum likelihood estimation of the statistical model. This iterative process leads to the local optima.

For the component number estimation of the mixture model, the Akaike Information Criterion (AIC) [6] or Bayesian Information Criterion (BIC) [7] are commonly used. Their comparison can be found in [8]. On the other hand, the algorithm can work under the assumption of knowledge of the image and the number of tissues. Here, we use the BIC with the so-called Elbow method. The idea behind this method is to choose a number of components so that adding another one does not improve the results significantly. The dependence of BIC on the number of components is shown in Fig. 3.

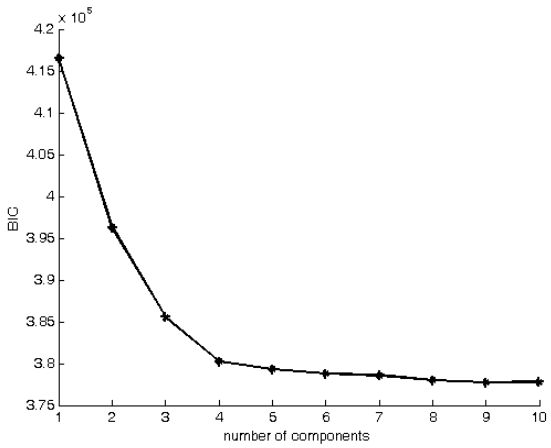

Fig. 2. Dependence of the Bayesian Information Criterion on the number of components.

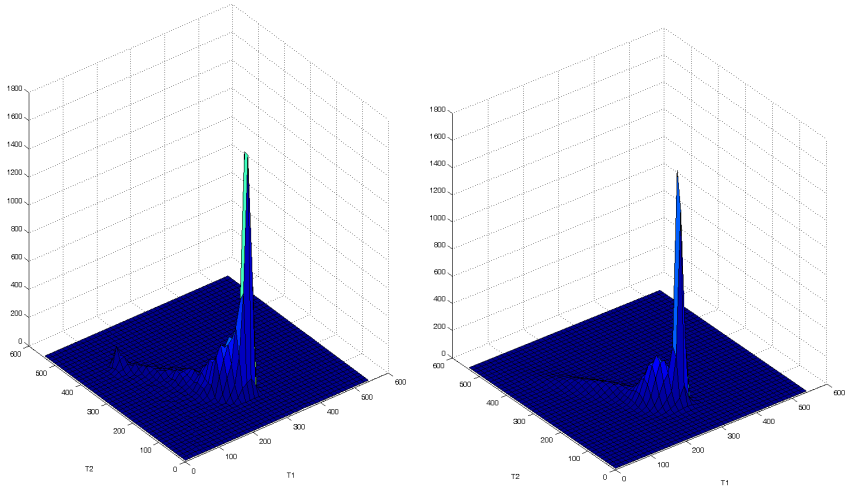

Fig. 3. Approximation of a 2-dimensional histogram by different numbers of mixture components. (a) original histogram, (b) approximation by 4 Gaussians, (c) approximation by 10 Gaussians.

The output of the described process is a probability density function. This denotes the probability of the pixel value of every tissue in the *N*-dimensional data space. In Fig. 2, one can see the approximation of a 2-dimensional histogram by 4 Gaussians.

4. Results

The results of the proposed method can be seen in Fig. 4, where the comparison of different number of components is shown. Despite the fact that the BIC penalize the larger number of components, the coefficient is still lower than for smaller number of components. But this could lead to oversegmentation, as can be seen in Fig. 4b. For this reason, the Elbow method is used and the result of segmentation with Elbow method is in Fig. 4a.

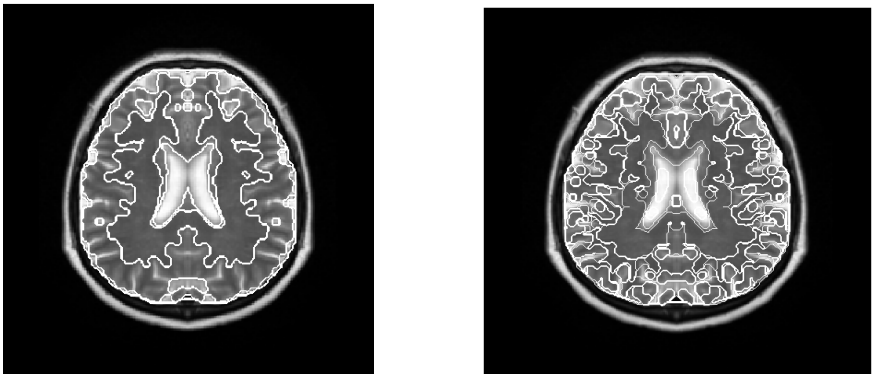

(a) (b)

Fig. 4. Segmentation of brain by GMM with (a) 4 components and (b) 10 components.

Acknowledgements

This research work was funded by project SIX CZ.1.05/2.1.00/03.0072, EU ECOP EE.2.3.20.0094, CZ.1.07/2.2.00/28.0062, project GACR 102/12/1104, and project CZ.1.05/2.1.00/01.0017 (ED0017/01/01), Czech Republic.

References

[1] Zhang, H., Fritts, J. E., Goldman, S. A., Image segmentation evaluation: A survey of unsupervised methods, *Computer Vision and Image Understanding*, v.110 n.2, May, 2008, pp. 260-280

[2] Gudbjartsson, H, Patz, S. The Rician distribution of noisy MRI data. *Magn Reson Med*. 1995, pp. 910–914.

[3] Rice, S. O., Mathematical Analysis of Random Noise. Bell *System Technical Journal 24*, 1945, pp. 46–156.

[4] Dvorak, P., Kropatsch, W., Detection of Brain Tumors Based on Automatic Symmetry Analysis, *Proceedings of the 18th Computer Vision Winter Workshop*, Hernstein, Austria, February 4-6, 2013, pp. 24-31.

[5] McLachlan, G., and D. Peel. *Finite Mixture Models*. Hoboken, NJ: John Wiley & Sons, Inc., 2000.

[6] Akaike, H., A new look at the statistical model identification, *IEEE Transactions on Automatic Control* 19 (6), 1974, pp. 716–723,

[7] Schwarz, G. E., Estimating the dimension of a model. *Annals of Statistics* 6 (2), 1978, pp. 461–464.

[8] Burnham, K. P.; Anderson, D. R., *Model Selection and Multimodel Inference: A Practical Information-Theoretic Approach* (2nd ed.), Springer-Verlag, 2002.

Bi-exponential T2* Analysis of Meniscus

[1,2]V.Juras, [1]S. Apprich, [1,2]P. Szomolanyi, [3]S. Domayer, [2]I. Frollo, [1]S. Trattnig

[1]MR Centre of Excellence, Department of Radiology, Medical University of Vienna, Vienna, Austria,
[2]Department of Imaging Methods, Institute of Measurement Science, Bratislava, Slovakia,
[3]Department of Trauma Surgery, Medical University of Vienna, Vienna, Austria,
Email: vladimir.juras@meduniwien.ac.at

Abstract. *A quantitative MRI of meniscus is challenging due to high level of collagen fibers organization resulting in short T_2 and hence low MR signal. The development of the new MRI techniques allows for decreasing echo time dramatically. This opens many possibilities of quantitative assessment of collagen matrix and water content in meniscus. In this study, we utilized a novel MRI technique, variable echo time sequence (vTE) which is capable of delivering the echo time below 1 ms. MR images from this sequence were fitted with bi-exponential curve to separate short and long T_2* component known to be related to the bound and free water, respectively.*

Keywords: Meniscus, MRI, T_2, Collagen Matrix, Tear, Degeneration*

1. Introduction

The degeneration of the meniscus is usually accompanied by weakness of the meniscal tissue, which can no longer distribute load sufficiently, and may eventually result in a meniscal tear (1). Grades of meniscal degeneration correlate with grades of articular cartilage degeneration. According to statistics, 85% of osteoarthritis (OA) patients who underwent joint replacement surgery suffer from degenerative menisci (2). Conventional morphological MR imaging is currently the preferred imaging modality for evaluating the menisci (3). On images with longer echo times (TE), menisci usually appear dark. The recently introduced, three-dimensional, spoiled gradient echo sequence with a variable echo time scheme (3D vTE Cartesian SPGR, hereafter referred to as vTE) minimizes the above-mentioned issues and was shown to be useful for visualizing MSK structures with a short T_2, within short and clinically adequate scan times (4). Since the relaxation constants, such as T_2, T_2*, or T1ρ, reflect the collagen structure organization in the meniscus, they are regionally dependent.

When calculating T_2 or T_2* using a simple mono-exponential fitting, the results may be remarkably underestimated, particularly in the areas with clear bi-component decay. To the best of our knowledge, there is no study that has comprehensively discussed the multiple compartment T_2* mapping of the human menisci in vivo.

Therefore, the aim of this study was to compare the ability of mono- and bi-exponentially calculated T_2* to differentiate between normal, degenerative meniscus, and meniscal tears.

2. Subject and Methods

Seventeen subjects enrolled in this study (eight males, 34±10 years; and nine females, 36 ±14 years). All MRI examinations were performed on a 3T MR system (Tim Trio, Siemens Healthcare, Erlangen, Germany) with an eight-channel knee coil (In vivo, Gainesville, FL, USA). A custom 3D Cartesian spoiled gradient echo (SPGR) technique was adapted to enable the use of a variable echo time (vTE) approach in combination with an asymmetric readout (5). The vTE sequence was applied with 10 echoes: TE = [0.75, 3.51, 5.87, 8.23, 10.6, 12.96,

15.33, 17.69, 20.06, and 22.42] ms, and the rest of the parameters were as follows: flip angle 13 degrees; repetition time (TR) 29 ms; and one signal average. The bandwidth was 320 Hz/ pixel; 144 sections; with a total acquisition time of 12 minutes and 16 seconds. The field of view (FOV) was 120 x 180 mm, with a consecutive in-plane resolution of 0.47 x 1.02 mm; a slice thickness of 0.7 mm; and matrix size was 256 x 176 pixels. All menisci segments were graded morphologically into three groups: normal (grade 0); degenerated (grade 1-2); and meniscal tear (grade 3). Images from the vTE sequence were analyzed using a custom-written script in IDL 6.3 (Interactive Data Language, Research Systems, Inc, Boulder, CO, USA). A mono- as well as a bi-exponential fitting procedure was employed on all MR data sets on a pixel-by-pixel basis. For mono-exponential fitting, a three-parametric function was used to fit the signal intensity

$$S_m = A_0 e^{-TE/A_1} + A_2 \quad (1)$$

where A_0 is the signal intensity at a TE of ~ 0ms, A1 corresponds to the actual T_2*_m (mono-exponentially calculated T_2*), and A_2 is the baseline (mostly the noise). The same dataset was also processed bi-exponentially, using the function

$$S_b = B_0 e^{-TE/B_1} + B_2 e^{-TE/B_3} + B_4 \quad (2)$$

where B_1 corresponds to the short component of T_2* (T_2*_s), B3 corresponds to the long component of T_2* (T_2*_l), and B_0 and B_2 are the component ratios expressed further as a percentage value of $B_0 + B_2$: $F_s = 100*B_0/(B_0 + B_2)$ and $F_l = 100*B_2/(B_0 + B_2)$. B_4 is the offset given primarily by noise. During the calculation of T_2*, only those pixels that satisfied the following condition were considered bi-exponential: $4 \times T_2*_s < T_2*l$.

Descriptive statistics were performed in order to calculate the mean and standard deviation (SD) of age, T_2*_m, T_2*_s, T_2*_l, component ratios, and M/B values separately for normal, degenerative, and torn menisci. In order to compare average T_2*_m, T_2*_s, T_2*_l, and M/B of different meniscal parts (anterior/posterior, medial/lateral, healthy/degenerated/tear) a hierarchical linear model (HLM) was used in order to consider multiple measures per patient. In addition, ROC analyses were performed to compare healthy with combined degenerated and torn meniscal parts.. A p value equal to or below 0.05 was considered to indicate significant results.

3. Results

From a total of 68 evaluated menisci segments, 48 were graded as normal, 12 as degenerated, and eight as torn. Six patients underwent a surgical procedure after the MR examination. One normal meniscus, one degenerated meniscus, and four meniscal tears were confirmed by a surgeon through visual examination to be in agreement with the results of the MRI evaluation. Examples of T_2* maps for a degenerative meniscus are depicted in Figures 1. The results from descriptive statistics for all relaxation parameters are summarized in Table 1. When considering the red and white zones of the menisci separately, from 48 cases of normal menisci, the mean and SD of T_2*_m was 7.89±1.25 ms in the white zone, and 10.49±3.26 ms in the red zone. This difference was statistically significant ($p = 0.026$, 95% CI -4.25 to -0.27). As for the results of bi-exponential analysis, the difference between the red and white zones was statistically significant only for the M/B ratio ($p = 0.017$, 95% CI 0.55 to 3.49).

Table 1. Summary of mean values for mono-exponential T_2*_m, the short and long components of T_2* calculated bi-exponentially, T_2*_s, and T_2*_l , respectively, and the ratio between mono- and bi-exponential pixel count (M/B ratio) calculated from both horns of the lateral and medial menisci.

	Units	Status	Number of Cases	Mean Value	Standard Deviation	R^2
T_2*_m	ms	normal	48	7.61	2.49	0.985
		degenerated	12	9.54	2.25	0.981
		tear	8	14.59	5.24	0.974
T_2*_s	ms	normal	48	0.82	0.38	0.991
		degenerated	12	1.29	0.53	0.986
		tear	8	2.05	0.73	0.979
T_2*_l	ms	normal	48	15.0	5.4	0.991
		degenerated	12	19.97	5.59	0.986
		tear	8	26.83	7.72	0.979
M/B	a.u.	normal	48	3.88	1.73	-
		degenerated	12	2.7	0.88	-
		tear	8	2.13	0.49	-

Table 2. The difference in mono- and bi-exponentially calculated T2* between normal and degenerated menisci and meniscal tears. The asterisk represents statistical significance.

interactions	T_2*_s	T_2*l	M/B	$T*_m$
MED/LAT	0.704	0.547	0.274	0.626
ANT/POS	0.661	0.563	0.461	0.256
STATUS	0.000*	0.000*	0.000*	0.000*
MED/LAT × ANT/POS	0.057	0.857	0.493	0.556
MED/LAT × STATUS	0.001*	0.509	0.272	0.225
ANT/POS × STATUS	0.898	0.404	0.014*	0.097
MED/LAT × ANT/POS × STATUS	0.150	0.433	0.744	0.749

The acronyms have the following meaning: MED - medial meniscus; LAT - lateral meniscus; ANT - anterior horn of meniscus; POS - posterior horn of meniscus; STATUS - normal, degenerative, or tear.

4. Discussion

In this paper, we proposed a technique for in vivo, quantitative, bi-component T_2* analysis of the human meniscus based on a 3D vTE Cartesian SPGR sequence with sequentially shifted echo times. The results of this study showed that bi-exponential analysis of the human meniscus in vivo may better distinguish between normal and degenerative menisci, as well as meniscal tears, compared to uncorrected, mono-exponential decay. These differences most likely reflect the compositional alteration of the collagen matrix, which is most pronounced in meniscal tears, but is also present in degenerative menisci. To the best of our knowledge, meniscal degeneration was previously studied using quantitative MR imaging by only a few groups. Williams and colleagues studied mono-exponential T_2*, measured by UTE, as a potential marker for degenerative menisci (6). They observed significantly lower T_2* values in asymptomatic volunteers (9.8ms) than in patients with meniscal degeneration (18.3ms). T_2* also correlated strongly with the degree of joint pathology. Rauscher and colleagues successfully used T_2 as a marker for detecting early OA stages through meniscal matrix analysis, and also showed that T_2 relaxation times in menisci correlate with the morphological

score of cartilage in OA (7). Our study has some limitations. no histological assessment was performed in order to confirm the MRI findings. Some bias may have also been introduced by choosing the bi-exponential condition to $4 \times T_2*_s < T_2*_l$, which was based on empirical findings.

5. Conclusions

In conclusion, the results of this study suggest that a bi-exponential analysis of meniscal tissue is more robust than a mono-exponential approach. The short component of T_2* better reflects the anisotropy of collagen fibers and the change in degeneration processes that may result in meniscal tear.

Acknowledgements

Funding support provided by the Austrian Science Fund P 25246 B24, the Vienna Advanced Imaging Center (VIACLIC), and the Slovak Scientific Grant Agency VEGA; Grant number: 2/0090/11.

References

[1] Fahmy NR, Williams EA, Noble J. Meniscal pathology and osteoarthritis of the knee. *J Bone Joint Surg Br* 1983; 65(1): 24-28.

[2] Sun Y, Mauerhan DR, Honeycutt PR, Kneisl JS, Norton JH, Hanley EN, Jr., Gruber HE. Analysis of meniscal degeneration and meniscal gene expression. *BMC Musculoskelet Disord* 2010; 11:19.

[3] Fox MG. MR imaging of the meniscus: review, current trends, and clinical implications. *Radiol Clin North Am* 2007; 45(6): 1033-1053.

[4] Deligianni X, Bär P, Scheffler K, Trattnig S, Bieri O. High-resolution Fourier-encoded sub-millisecond echo time musculoskeletal imaging at 3 Tesla and 7 Tesla. *Magnetic Resonance in Medicine* 2012; DOI: 10.1002/mrm.24578.

[5] Deligianni X, Bär P, Scheffler K, Trattnig S, Bieri O. Water selective high resolution imaging of short T2 components of the knee at high and ultra high field strenghts. Proc Intl Soc Mag Reson Med 2012; 20: 3315.

[6] Williams A, Qian Y, Golla S, Chu CR. UTE-T2 * mapping detects sub-clinical meniscus injury after anterior cruciate ligament tear. Osteoarthritis and cartilage / OARS, *Osteoarthritis and Cartilage* 2012; 20(6): 486-494.

[7] Rauscher I, Stahl R, Cheng J, Li XJ, Huber MB, Luke A, Majumdar S, Link TM. Meniscal Measurements of T1(rho) and T2 at MR Imaging in Healthy Subjects and Patients with Osteoarthritis. *Radiology* 2008; 249(2): 591-600.

MR T2 Study of Human Knee Cartilage Using In-vivo Compression Device

[1,2]P. Szomolányi, [1]E. Schönbauer, [1,2]V. Juráš, [1]Š. Zbýň, [2]I. Frollo, [1]S.Trattnig

[1]MR Center of Excellence - High field MR, Department of Radiology,
Medical University of Vienna/Vienna General Hospital, Vienna, Austria,
[2]Department of Imaging Methods, Institute of Measurement Science,
Slovak Academy of Sciences, Bratislava, Slovakia
Email: pavol.szomolanyi@meduniwien.ac.at, pavol.szomolanyi@savba.sk

Abstract. *Degeneration of cartilage in the knee joint associated with osteoarthritis is a very common disease. Magnetic resonance imaging (MRI) has become the method of choice for the evaluation of cartilage. Series of T2 mapping images under unloading and loading conditions were obtained using multi-slice multi-echo (MSME) technique. In a volunteer study, the mean cartilage T2 relaxation times exhibited a statistically significant decrease in the first loading phase and also statistically significant increase of T2 relaxation times in recovery period. Dynamic of T2 change in cartilage compression phase as well as in cartilage recovery phase were similar. In a patient study, during unloading or loading conditions* statistically *significant changes were observed in T2 relaxation times in transplant deep zone ($P < 0.0001$), in posterior deep zone ($P = 0{,}003$), in central deep zone ($P < 0.0001$), in central superficial zone ($P = 0.007$), and in tibia superficial zone ($P < 0.0001$). Results of this study show that the T2 mapping under loading conditions can provide useful information on cartilage transplant in post-surgery period and help to evaluate the efficacy of cartilage-repair surgery.*

Keywords: MRI at 3 Tesla; Loading of Human Knee Cartilage Transplant In-vivo; T2 Mapping of Cartilage

1. Introduction

Degeneration of cartilage in the knee joint associated with osteoarthritis is a very common disease. Therefore it is important to discover cartilage damage as early as possible, so that preventive treatment could stop the progression of degeneration. In case the cartilage transplant surgery was the last solution to treat cartilage defects, it is necessary to assess the quality of repair tissue during maturation process, preferably by non-invasive technique.

Magnetic resonance imaging (MRI) has become the method of choice for the evaluation of cartilage, as it allows morphological assessment of the cartilage surface, thickness, volume and status of a subchondral bone, as well as additional properties of repair tissue, such as filling of the defect, integration into adjacent cartilage and bone, surface, structure and signal intensity of transplants [1-3]. Therefore MRI is becoming important tool for non-invasive follow-up of patients after cartilage repair surgery [4].

2. Subject and Methods

Volunteers

Nine healthy volunteers were measured between July 2011 and November 2011, (mean age 31 years ± 7; six men and three women). These volunteers had no history of knee pain or stiffness, and had never undergone any knee surgery. The study protocol was approved by local Institutional Review Board. All volunteers provided written informed consent after procedures of the study were explained to them.

Patients

Between January 2012 and September 2012 fourteen patients were enrolled to the study. Out of these, four patients were excluded from this study due to too thin transplant tissue, which could not be evaluated. Ten patients (mean age 40 years ± 8; six males and four females) after matrix-associated autologous chondrocyte transplantation (MACT) were included into this study. Six transplants were located on the medial femoral condyles (MFC) and four on the lateral femoral condyles (LFC). Exclusion criteria were previous cruciate ligament reconstruction, previous meniscectomy, losen or not detectable transplant. The knee surgery at every patient was performed at least two years up to eight years before MRI measurements for this study. Study was performed in compliance with the regulations of the local ethics committee and subjects provided written and informed consent to this study.

MR Imaging

All measurements were performed on a 3 Tesla MR imaging system (Magnetom Trio; Siemens, Erlangen, Germany) using a Tx/Rx 8-channel knee coil (In Vivo Corp, Gainesville, FL, USA) with a multi-slice multi-echo (MSME) Carr-Purcell-Meiboom-Gill (CPMG) technique for T2 mapping. During MR imaging, the volunteers and patients were measured in a supine position, the examined knee was fully extended, and the leg was tightly fixed to a MR-compatible compression device, as well as the pelvis was fixed on MRI bed using a dedicated belt. The foot of the examined leg was secured in a neutral rotational position by fixation on a foot rest of the sliding foot plate. (Fig. 1) The use of dedicated MR-compatible, custom-made, pneumatically controlled compression device allows simulating physiological load of 120 N.

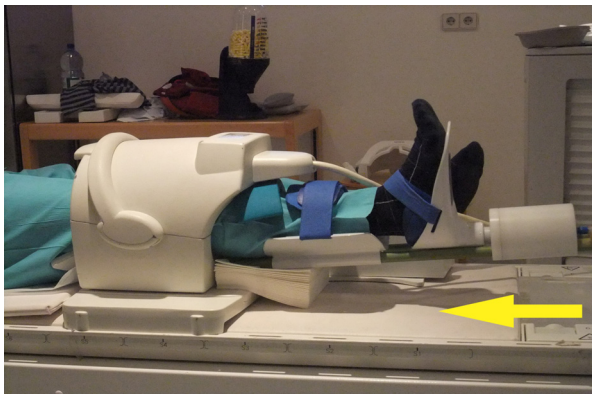

Fig. 1: MR compatible compression device is installed on the MR bed. Patient laying supine was fixed to the bed (fixation not shown on the figure). Knee coil was used for the signal acquisition. Yellow arrow shows the direction of pressure. Piston is located right on the figure. The compression device was controlled by the compressed air through the plastic tube, and the piston provided load to the foot plate.

A series of T2 measurements started with load-free measurement. After this initial load-free measurement, a load of 120 N was applied. Series of loaded T2 measurements were performed. At the end of series, load was released and one more load-free measurement was performed.

Under each unloading and loading conditions, sagittal T2 maps were obtained using MSME-CPMG, with the following parameters: repetition time (TR): 1110ms; 6 evenly spaced echoes from 11.8 to 70.8 ms; field of view: 160x160mm; matrix: 320 × 320 interpolated to 640 × 640; slice thickness: 3mm; signal averaging: 2; total acquisition time: 7min 35s. A frequency-selective fat-suppression technique was used to minimize the chemical shift artefact at the cartilage-bone interface. At each volunteer, one to two sagittal images passing through the center of the lateral and medial femoral condyle were obtained. In this imaging plane the femoral and tibial articular cartilage in the weight-bearing area consisted on cartilage covered by the anterior meniscus, cartilage in contact with the opposing articular cartilage, and cartilage covered by the posterior meniscus. On each slice, up to six regions of interest (ROIs) were drawn manually by a radiology resident E.S. under supervision of an experienced

radiologist S.T. (18 years of experience). In total, three ROIs were drawn. First ROI was drawn in the central tissue in the weight bearing zone of the femoral cartilage (CF). Second ROI was drawn in the posterior area of the femoral cartilage (PF) in the low weight bearing zone. Last, third ROI was drawn in the weight bearing zone of the tibial cartilage (CT). Each ROI was separated into deep and superficial zone. In case of patients, one additional ROI was drawn at the cartilage transplant (Fig. 2, 3 and 4).

3. Results

Volunteers

In the volunteer study a characteristic "U" shape course of T2 values was demonstrated (fig. 5). Mean cartilage T2 relaxation times exhibited a significant decrease in the first loading phase of ten minutes (60.8ms±7.5 → 54.6ms±6.2, $p< 0.05$ in the superficial layer; 47.2ms±8.6 → 44.2ms±8.6, $p< 0.05$ in the deep layer), however during another four loading periods of ten minutes stable T2 values were seen. At the last ten minutes without load application a significant increase of T2 values was detected (54.6ms±7.4 → 61.5ms±7.5, $p< 0.05$ in the superficial layer; 43.7ms±8.3 → 46.4ms±8.1, $p< 0.05$ in the deep layer).

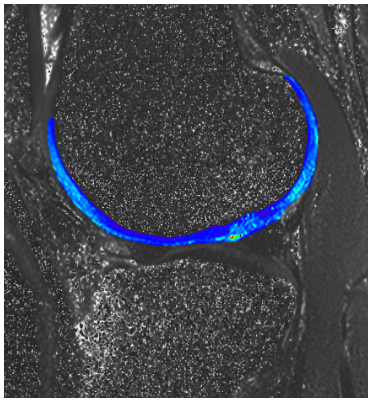

Fig. 2. Sagittal color-coded T2 map of a human knee after MACT.

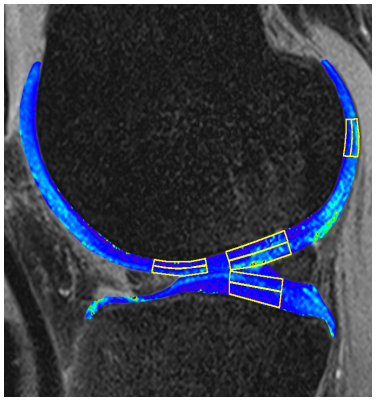

Fig. 3. T2 image of a human knee after MACT in the load-bearing zone.

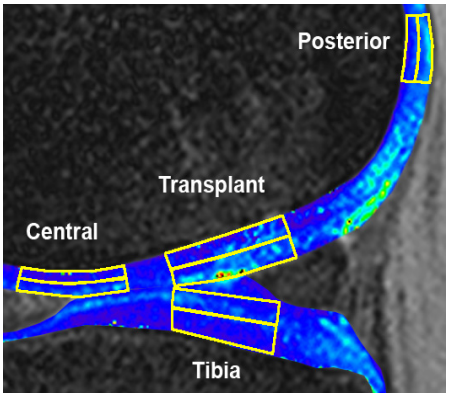

Fig. 4. Definition of regions of interest (ROI) in the femoral and tibial cartilage.

Patients

In the weight bearing zone, repair tissue showed statistically significant increase of T2 relaxation times in comparison to the reference native cartilage in the central region ($P<0.0001$). Characteristic "U" shape of T2 values was not as obvious as in volunteers (Fig. 6). During unloading or loading conditions statistically significant changes were observed in T2 relaxation times in transplant deep zone ($P < 0.0001$), in posterior deep zone ($P = 0.003$), in central deep zone ($P < 0.0001$), in central superficial zone ($P = 0.007$), and in tibia superficial zone ($P < 0.0001$) (Table 1) .

Table 1: T2 Values of each ROI (Mean ± SD) in each zone under Unloading and Loading conditions.

Zone	1. No Load (ms)	1. Load (ms)	2. Load (ms)	2. No Load (ms)	P-value
1. Transplant superficial	55.09 ± 10.30	53.96 ± 9.69	53.98 ± 10.06	56.38 ± 9.91	= 0.133
2. Transplant deep	47.65 ± 7.99	44.84 ± 8.01	44.50 ± 7.29	47.10 ± 7.70	**< 0.0001**
3. Posterior superficial	57.82 ± 14.84	57.48 ± 13.55	54.91 ± 11.95	58.42 ± 13.37	= 0.075
4. Posterior deep	48.43 ± 8.92	46.23 ± 9.89	46.10 ± 8.84	48.58 ± 8.53	**= 0.003**
5. Central superficial	51.39 ± 8.00	50.84 ± 9.95	49.95 ± 9.00	53.28 ± 10.19	**= 0.007**
6. Central deep	39.44 ± 8.29	36.89 ± 9.26	36.65 ± 9.34	40.34 ± 10.18	**< 0.0001**
7. Tibia superficial	44.55 ± 12.09	42.21 ± 11.25	42.81 ± 12.03	45.76 ± 12.04	**< 0.0001**
8. Tibia deep	33.13 ± 6.77	32.76 ± 7.76	32.87 ± 7.33	34.74 ± 8.76	= 0.237

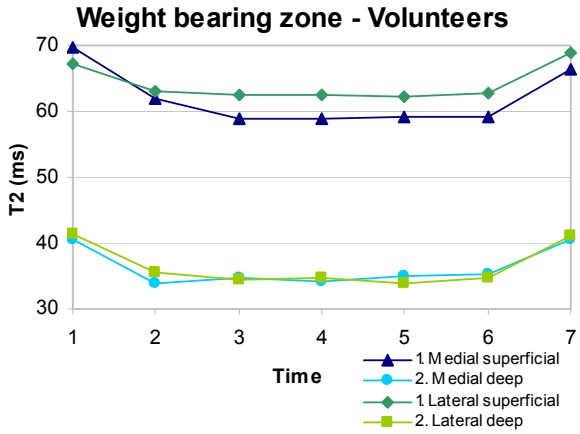

Fig. 5. T2 load dependence of the medial and lateral femoral condyle in the weight bearing zone cartilage of volunteers.

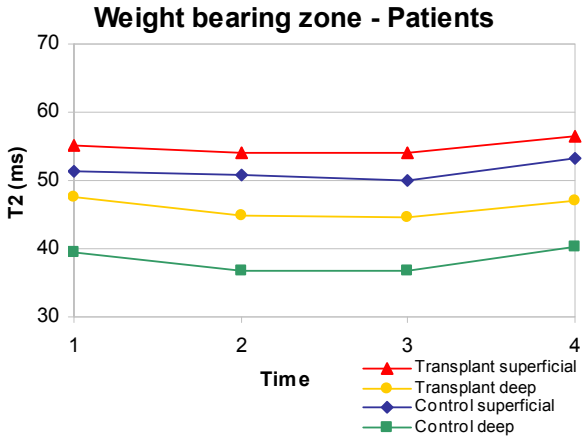

Fig. 6. T2 load dependence of superficial and deep cartilage in the weight bearing zone of patients.

4. Discussion

Unlike in healthy volunteers, where both superficial and deep zone showed significant drop of T2 values, in cartilage transplant of patients, the significant decrease in T2 was observed only in deep zone. This may imply that the collagen fiber organization within the repair tissue had not yet developed after MACT cell-based cartilage transplantation technique, and therefore, the matrix within the repair tissue had reacted differently to the static load applied during these experiments. This suggest that the proposed method could be used for the further evaluation of cartilage transplant maturation over time, in the post-surgery period, and may give insight into the biomechanical properties of repair tissue after surgery.

5. Conclusions

T2 mapping may provide new parameter useful in early cartilage degeneration diagnosis, and help to evaluate the efficacy of cartilage-repair surgery.

Acknowledgements

This study was supported by the Vienna Spots of Excellence des Wiener Wissenschafts-und Technologie-Fonds (WWTF), Vienna Advanced Imaging Center-VIACLIC (FA102A0017), the Slovak Scientific Grant Agency VEGA 2/0090/11. Authors would like thank to Mrs. Heidi Moosbauer for her strong support during MR measurements.

References

[1] Trattnig, S., et al., Matrix-based autologous chondrocyte implantation for cartilage repair: noninvasive monitoring by high-resolution magnetic resonance imaging. *Magn Reson Imaging*, 2005. 23(7): 779-87.

[2] Trattnig, S., et al., MR imaging of osteochondral grafts and autologous chondrocyte implantation. *Eur Radiol*, 2007. 17(1): 103-18.

[3] Regatte, R.R., et al., T1rho relaxation mapping in human osteoarthritis (OA) cartilage: comparison of T1rho with T2. *J Magn Reson Imaging*, 2006. 23(4): 547-53.

[4] Marlovits, S., et al., Cartilage repair: generations of autologous chondrocyte transplantation. *Eur J Radiol*, 2006. 57(1): 24-31.

Measurement of the Iron Oxide and Gadolinium Based Contrast Agent Relaxation Properties in the Presence of the Saline and Glucose Molecules during Low-Field MRI

[1]O. Štrbák, [2]M. Masárová, [1]D. Gogola, [1]I. Frollo

[1]Institute of Measurement Science SAS, Bratislava, Slovakia
[2]Faculty of Electrical Engineering University of Žilina, Žilina, Slovakia
Email: oliver.strbak@savba.sk

Abstract. *The contrast agents are usually used in clinical practice for the enhanced contrast imaging of the human tissue. They are iron oxides or gadolinium based nanoparticles in a carrier fluid. In a previous study we have found, that the elevated levels of the human metabolites can change the relaxation properties of the magnetite nanoparticles during 4.7 T MRI. Therefore the aim of this paper is to find out if the different concentration levels of the saline and glucose molecules, which are typical for the several pathological processes, can change the relaxation properties of these contrast agents during low-field MRI (0.178). We have found that physiological concentration of the saline and glucose molecules have little, but not negligible influence to the signal intensity for different concentration of the contrast agent (maximum ≈ 30% in comparison with water). The different concentration of the saline and glucose molecules alters the signal intensity for the selected pulse sequence and contrast agent concentration in a similar way, with maximum intensity change up to 17%. Such changes are hardly visible to the naked eye in low-field MRI, however they can have influence to the post-processed data analysis, e.g. in relaxation time comparison. Definitely, these findings should be verified in standard high-field MRI tomographs 1.5 and 3 T, before final conclusions.*

Keywords: MRI, Contrast Agents, Contrast Changes, NaCl and Glucose Molecules

1. Introduction

Currently, the Magnetic Resonance Imaging (MRI) is a technique routinely used in clinical practice. MRI provides an anatomical picture of tissue based on different intrinsic contrast. Contrast in MRI arises from the difference in signal intensity, which can be modified by intrinsic parameters (spin density ρ, relaxation times T_1 and T_2) and by the pulse sequence parameters (repetition time TR, echo time TE). Modification of TR and TE results in T_1, T_2 or proton density weighted imaging. For contrast enhancement in clinical practice the paramagnetic contrast agents (CA) are often used. The signal enhancement is caused by coupling of proton magnetic moments with larger magnetic moments of paramagnetic nanoparticles [1]. The contrast agents can be either iron oxides or gadolinium based nanoparticles. In this study we focused on MRI contrast properties of both types of contrast agents in the presence of the saline and glucose molecules. NaCl and glucose are the essential molecules of the human body. The modified concentration levels of these molecules are usually accompanied with different pathological processes. The aim of the study, due to our previous results [2], is to find out, if the altered concentration of the saline and glucose molecules can have influence to the MRI contrast in the presence of clinical contrast agents (iron oxides and gadolinium based).

2. Subject and Methods

The MRI experiments were performed at the Institute of Measurement Science SAS Bratislava, using the ESAOTE E-Scan XQ 0.178 T system. For image data processing and anlysis we used the following software tools: Marevisi, developed by NRC - Institute for Biodiagnostic, Winniped, Canada and Matlab - Mathworks Inc., Natic, USA. Firstly, we have investigated eight different concentrations of contrast agent in various pools - distilled water, NaCl, glucose and NaCl + glucose together. Molecules were in physiological concentration: NaCl - 9 g/l and glucose - 1 g/l. Secondly, the one concentration of contrast agent was choosen (similar to in-vivo application, Resovist - iron oxide nanoparticles concentration was 103.3 µg/ml and MultiHance - gadolinium concentration was 1.3 mg/ml) and investigated with different concentrations of saline and glucose molecules: NaCl - 0, 4.5, 9 and 13.5 g/l, glucose - 0, 0.5, 1 amd 1.5 g/l. As an iron oxide contrast agent model was choosen the Resovist (Bayer Schering Pharma AG), which consists of carboxydextran coated iron oxide nanoparticles and as a gadolinium one the MultiHance (ALTANA Pharma AG), which consists of gadobenate dimeglumine molecules. Images were acquired using both spin echo (SE) and gradient echo (GE) sequences in T_1 and T_2 weighted modes. For each contrast agent the most appropriate pule sequence and parameters for contrast imaging were selected.

3. Results

We have tried to identify the signal changes induced by the contrast agent relaxation time modification in system with saline and glucose molecules. Several types of the pulse sequences have been investigated to find out the most appropriate parameters. Both for the iron oxide and gadolinium based contrast agents, the least suitable pulse sequence for the enhanced contrast imaging were GE sequences. Finally, we selected T_2 weighted Turbo Spin Echo sequence (TR = 3000 ms and TE = 120 ms) for the Resovist contrast imaging and T_1 weighted Spin Echo sequence (TR = 600 ms and TE = 26 ms) for the MultiHance contrast imaging. In Fig. 1a and Fig. 2a are shown the contrast changes for different Resovist and MultiHance concentrations in distilled water with physiological concentration of saline and glucose. As is shown in Fig. 1b and 2b, the saline and glucose molecules in physiological concentration have little, but not negligible effect to the decay (for the Resovist) or the increase (for the MultiHance) of the signal intensity. The maximum change for the iron oxide sample is ≈ 30%, while for the gadolinium sample it is only ≈ 15% in comparison with water.

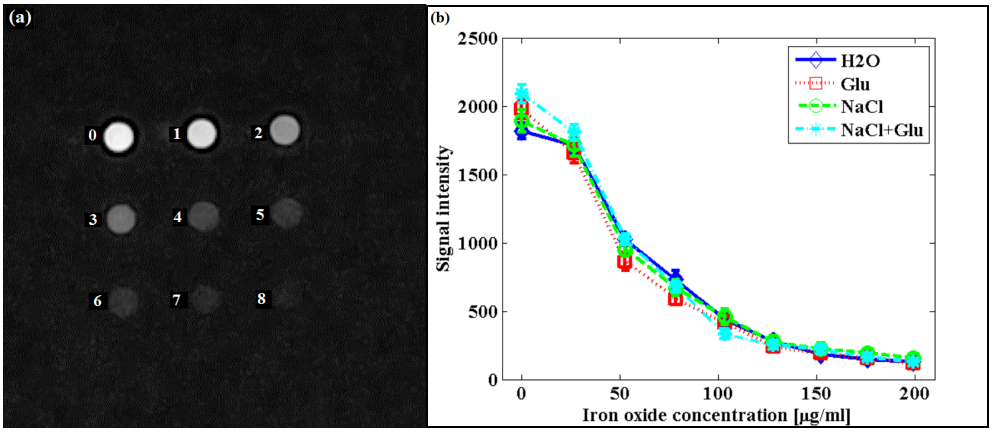

Fig. 1. (a) Different concentration of the Resovist in distilled water and physiological concentration of saline and glucose molecules ([0] - 0 µg/ml, [1] - 26.6 µg/ml, [2] - 52.7 µg/ml, [3] - 78.2 µg/ml, [4] - 103.3 µg/ml, [5] - 127.9 µg/ml, [6] - 152.1 µg/ml, [7] - 175.8 µg/ml, [8] - 199 µg/ml).
(b) Plot of the signal intensity in dependence on the iron oxide concentration in various pools. Used pulse sequence: Turbo Spin Echo T_2, TR = 3000 ms, TE = 120 ms.

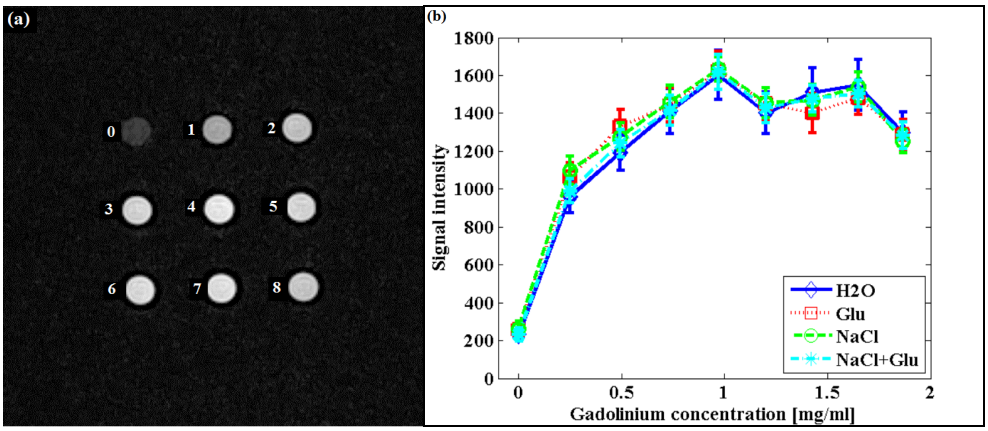

Fig. 2. (a) Different concentration of the MultiHance in distilled water and physiological concentration of saline and glucose molecules ([0] - 0 μg/ml, [1] - 0.249 mg/ml, [2] - 0.494 mg/ml, [3] - 0.734 mg/ml, [4] - 0.969 mg/ml, [5] - 1.2 mg/ml, [6] - 1.426 mg/ml, [7] - 1.648 mg/ml, [8] - 1.866 mg/ml).
(b) Plot of the signal intensity in dependence on the gadolinium concentration in various pools. Used pulse sequence: Spin Echo T_1, TR = 600, TE = 26.

Similar signal intensity changes we have found for the samples with different concentration of the saline and glucose molecules. For the selected pulse sequence and contrast agent concentration it is change up to 17% for the Resovist and 16% for the MultiHance. The data for the iron oxide concentration 103.3 μg/ml and the gadolinium concentration 1.3 mg/ml for the selected pulse sequence are shown in Fig. 3. In the Table 1 is shown increase or decrease of the signal intensity for the saline and glucose samples in comparison with contrast agent in distilled water. The increase of the signal intensity we observed only in Resovist samples with the highest concentration of the NaCl molecules and the lowest concentration of the glucose molecules. In all other samples we observed the decrease of the signal intensity in comparison with distilled water. The range of the changes for both CA is hardly visible to the naked eye, during the low-field MRI, in comparison to the intensity changes influenced by the different CA concentration (≈ 110% for the Resovist and ≈ 280% for the MultiHance, Fig. 1a, 2a).

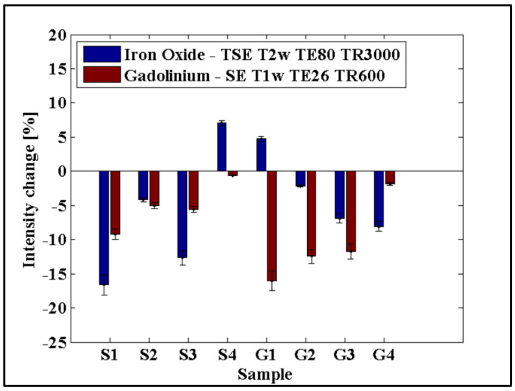

Fig. 3. Contrast agents relative signal intensity (compared to distilled water) for the selected pulse sequences in dependence on the different concentration of the NaCl and glucose molecules. Samples: S1 - 4.5 g/l NaCl, S2 - 9 g/l NaCl, S3 - 13.5 g/l NaCl, S4 - 18 g/l NaCl, G1 - 0.5 g/l glucose, G2 - 1 g/l glucose, G3 - 1.5 g/l glucose, G4 - 2 g/l glucose.

Table 1. Signal intensity increase (↑) or decrease (↓) in % for the saline and glucose samples in comparison with contrast agent (Resovist and MultiHance) in distilled water. Samples: S1 - 4.5 g/l NaCl, S2 - 9 g/l NaCl, S3 - 13.5 g/l NaCl, S4 - 18 g/l NaCl, G1 - 0.5 g/l glucose, G2 - 1 g/l glucose, G3 - 1.5 g/l glucose, G4 - 2 g/l glucose.

CA / SAMPLE	S1	S2	S3	S4	G1	G2	G3	G4
Resovist	↓(16.6)	↓(4.1)	↓(12.7)	↑(7.0)	↑(4.7)	↓(2.1)	↓(6.9)	↓(8.1)
MultiHance	↓(9.2)	↓(5.0)	↓(5.6)	↓(0.6)	↓(16.1)	↓(12.4)	↓(11.8)	↓(1.8)

4. Discussion

Several types of the pulse sequences have been investigate to find out the most appropriate parameters for the Resovist and MultiHance enhanced contrast imaging. The least suitable pulse sequences both for iron oxide and gadolinium particles imaging were GE sequences. Probably it is caused by tiny magnetic field inhomogeneities from the paramagnetic nanoparticles in Resovist and MultiHance, to which the GE sequences are very sensitive. As the most appropriate sequence for the Resovist imaging we found out the T_2 weighted Turbo Spin Echo sequence with TR = 3000 ms and TE = 120 ms. For the MultiHance imaging it is the Spin Echo sequence with TR = 600 ms and TE =120 ms. Physiological concentration of the saline and glucose molecules had little but not negligible influence to the signal intensity in dependence on the contrast agent concentration (Fig. 1b, 2b). Similar situation we have found for the samples with different concentration of the saline and glucose molecules. For the selected pulse sequence and contrast agent concentration the change is up to 17% for the Resovist and 16% for the MultiHance. Although, the changes are not very dramatic and are hardly visible to the naked eye during the low-field MRI, they can have influence to the specific data analysis (e.g. relaxation time calculation) and alter the conclusions for the processes associated with the altered levels of the saline and glucose molecules. These findings are in agreement with our previous results with magnetite nanoparticles and human body metabolites during 4.7 T MRI, although in that case the changes were significantly higher [2]. Therefore, before the final conclusions, it is necessary to verify these results in standard high-field MRI tomographs 1.5 and 3 T.

5. Conclusions

We have found out that various concentrations of the saline and glucose molecules have the influence (in the specific pulse sequences) to the signal intensity during low-field MRI with iron oxide and gadolinium contrast agents. The changes are up to 17% and although they are hardly visible to the naked eye, they can have influence to the post-processed data analysis of the processes associated with the altered levels of the NaCl and glucose molecules. Also we have not found out very significant influence (30%) of the saline and glucose molecules in physiological concentration to the signal intensity of the samples with the different concentration of the both investigated contrast agents. However, these findings should be verified in standard clinical MRI tomographs (1.5 and 3 T) before final clinical conclusions.

Acknowledgements

This work was supported by the Slovak Scientific Grant Agency VEGA 2/0090/11.

References

[1] Gillis P, Moiny F, Brooks RA. On T_2 shortening by strongly magnetizes spheres: a partial refocusing model. *Magnetic Resonance in Medicine,* 47: 257-263, 2002.

[2] Strbak O, Starcuk Z, Dzarova A, Zavisova V, Koneracka M, Timko M, Starcukova J, Graveron-Demilly D, Kopcansky P. Metabolites solutions signal changes induced by magnetosomes in NMR experiment. In the 8th International Conference of the Scientific and Clinical Applications of Magnetic Carriers, Rostock Germany, May 25-29 2010.

Fractal Behaviour of Mitochondrial Chloride Channels

[1]M.Tomasek, [2]Z.Tomaskova

[1]Faculty of Chemical and Food Technology SUT, Bratislava, Slovakia,
[2]Institute of Molecular Physiology and Genetics SAS, Bratislava, Slovakia
Email: zuzana.tomaskova@savba.sk

Abstract. *Mitochondrial chloride channels are integral membrane proteins located in the inner membrane of mitochondria. These ion channels contribute to the mitochondrial membrane potential which is necessary to drive the production of "energy-containing" molecules – ATP. The method of ion channel reconstitution into artificial lipid membrane allows the measurement of ionic current flowing through a single ion channel. Analysis of single-channel current provides means for the insight into the conformational changes of the protein structure. We analysed the gating kinetics at different time scales. The transition from open (conductive) state into closed (non-conductive) state is characterized by a defined number of kinetic rate constants. In the contrary, the transition from closed to open state is better described with continuum set of kinetic rate constants, which is typical for fractal behaviour.*

Keywords: Membrane Protein, Single-channel Current, Gating Kinetics, Fractal Behaviour

1. Introduction

Ion channels are membrane proteins that provide hydrophilic pathway for ions transport across the hydrophobic lipid membrane. Due to thermal fluctuations the ion channels undergo frequent conformational changes leading to transitions between two functionally different states – open (conductive) state and closed (non-conductive) state. Transitions between open and closed states are called *channel gating* [1]. Method of ion channel reconstitution into artificial lipid membrane (BLM method) is commonly used to obtain ionic current from a single protein. This current is in order of picoamperes. The analysis of the duration of the sequential transitions (dwell time) gives us the information about the kinetic of conformational changes. Each type of ion channels is characterized by a specific number of open and closed conformational states and each of these states has a typical kinetic rate constant. The gating kinetics of ion channels has been commonly described as Markov process, which means that the kinetic rate constants are independent of the time spent in the current state and of the previous transitions [2]. However, these assumptions are not always valid when one studies the conformation changes of a protein. A novel approach was developed by Liebovitch and co-workers that sees the ion channel as a protein having a continuum of conformational states leading to complex behaviour over several orders of time scale what is a typical fractal property [3]. The method is based on analysis of dwell times in a chosen (open or closed) state; these are visualized in histogram with bins having exponentially growing width (logarithmic histogram).

2. Subject and Methods

Our aim was to characterize the gating kinetics of the mitochondrial chloride channel. Hearts were excised from anesthetized and decapitated rats and homogenized. The crude mitochondrial fraction was obtained in several steps of differential centrifugation and finally purified on Percoll density gradient. Purified mitochondria were sonicated at 30 kHz for 2 minutes to obtain submitochondrial vesicles. The vesicles containing chloride channels were incorporated into artificial lipid membrane that was formed by application of solution of

synthetic phospholipids in n-decane onto an orifice in a septum separating two compartments of the measurement chamber. Single-channel current was measured (Fig.1). The signal was amplified with ratio 100 mV/pA, filtered by analogue low-pass 8-pole Bessel filter (cut-off frequency 1 kHz) and digitized with sampling frequency 5 kHz. We measured the single-channel currents in non-physiological gradient of potassium chloride (1 mol.l^{-1}/ 50 mmol.l^{-1}) to have good signal-to-noise ratio so that the noise fluctuations would not affect the measured gating of the channels. The solutions were buffered with 10 mmol.l^{-1} HEPES and Tris to 7.4 pH. The dwell times of open and closed states, respectively, were detected in pClamp 10.0 software (Axon Instruments, Inc.). This information was further processed in program developed in Matlab 2012b.

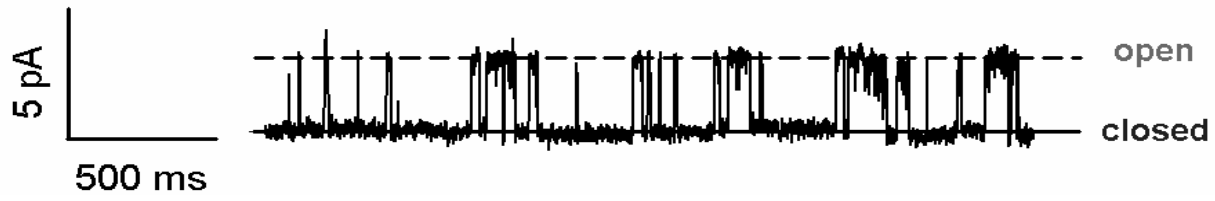

Fig. 1. Representative single-channel current. A typical current trace is in general characterized by step transitions between two levels corresponding to open (conducting) state and to closed (non-conducting) state.

3. Results

We analyzed separately the time that the channel spent in open state and in closed state (dwell time). By plotting number of dwell times $N(t)$ lying in interval $(t;\ t + \Delta t)$ we created histograms for open dwell times and closed dwell times, respectively. Width of the interval Δt increases exponentially (Δt = 1, 2, 4, 8 ... ms) for this reason the number of events $N(t)$ is normalized by Δt (Fig.2). Histogram of open dwell times has approximately linear trend in semi-log plot what is characteristic of exp(-kt) distribution. Obtained kinetic rate constant for shorter dwell times (1 ÷ 20 ms) was k = 220 Hz while for longer dwell times it was k = 109 Hz. On the contrary, histogram of closed dwell times has linear trend in log-log plot which is typical for continuum set of kinetic rate constants. In this case the rate constants were uniformly distributed within the range 0,1 ÷ 1 kHz.

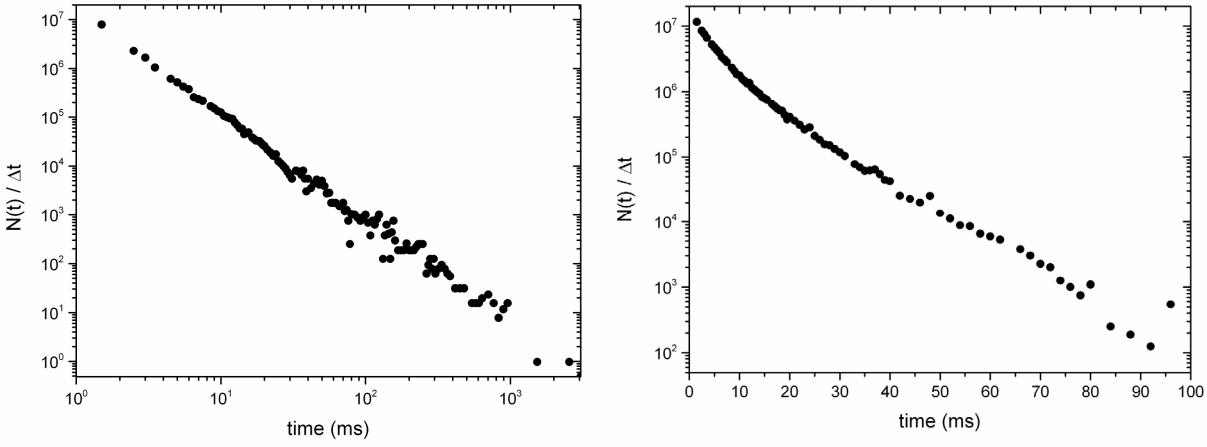

Fig. 2. Histograms for closed (left) and open (right) dwell times. Data on the left have linear behaviour in log-log plot while data on the right are approximately linear in semi-log plot. The (left) histogram has linear trend in log-log plot, which is a characteristic for fractal behaviour and the (right) histogram has linear trend in semi-log plot, which is considered as characteristic of Markov behaviour.

4. Discussion and Conclusions

We described the gating kinetics of mitochondrial chloride channels. Despite the role that these channels have in mitochondrial physiology and pathophysiology, their molecular identity remains unknown. So far, the only way to approach to their identity is to characterize these channels from electrophysiological measurements. The method used here provides a glimpse into the physical properties and function of the ion channel. It gives us information about the energy barriers separating different conformations of the channel and their possible time-dependence. Not the least, structurally similar ion channels, originating from one ion channel family, may display similar behaviour of gating kinetics, as this is connected to the structural features of the protein. Unfortunately, this analysis was applied only on a very limited number of ion channel types. From these, one was chloride channel located in the plasma membrane of skeletal muscle cells [4]. The behaviour of this channel was different from what we described, indicating that these channels are not identical. Nevertheless, similar description of the gating kinetics was presented in [2], where the authors studied voltage-dependent potassium channels. The non-Markov behaviour of other type of ion channels was confirmed also in case of calcium-activated potassium channel [5]. However, the fractal behaviour is not a general feature of ion channels; in some cases the Markov model is more suitable for the description of gating kinetics [6].

The open dwell times of mitochondrial chloride channels can be described by either two kinetic rate constants (109 and 220 Hz) or by one constant, the value of which is in this limited range. On the other side, the closed dwell times clearly displayed a broad range of kinetic rate constants spreading through several orders of magnitude. The Markov or fractal character of the ion channel kinetics can be determined from the dwell time histograms with varying bin width. According to the theory described in [3], the histogram that has linear trend in log-log plot is characteristic for fractal behaviour and when the histogram has linear trend in semi-log plot, it is considered as characteristic of Markov behaviour. This behaviour can be explained by a static approach or by a dynamic approach. From the static point of view, the channel possesses a set of closed states, each having a kinetic rate constant slightly different (smaller) from the previous one [7]. The dynamic explanation is that the ion channel has only one closed state whose kinetic rate constant is changing in time. From the molecular view, this can be considered as if the protein was settling down in the membrane to an ultimate conformation from which it will switch to open state with very low probability unless it is overcome by some other stimulus (e.g. application of voltage) [8].

Acknowledgements

This work was supported by VEGA-2-0094-12 and APVV-0074-11.

References

[1] Wonderlin WF, French RJ, Arispe NJ. Recording and Analysis of Currents from Single Ion Channels. In: Neuromethods: Neurphysiological Techniques. Basic methods and Concepts. Boulton AA, Baker GB, Vanderwolf Ch, The Humana Press Inc., Clifton, NJ, USA, 1990, 41-45

[2] Liebovitch LS, Sullivan JM. Fractal analysis of a voltage-dependent potassium channel from cultured mouse hippocampal neurons. *Biophysical Journal*, 52(6):979-988, 1987.

[3] Liebovitch LS, Scheurle D, Rusek M, Zochowski M. Fractal Methods to Analyze Ion Channel Kinetics. *Methods*, 24(4): 359-375, 2001.

[4] Blatz AL, Magleby KL. Quantitative description of three modes of activity of fast chloride channels from rat skeletal muscle. *J Physiol.* 378:141-174, 1986.

[5] Bandeira HT, Barbosa CT, De Oliveira RA, Aguiar JF, Nogueira RA. Chaotic model and memory in single calcium-activated potassium channel kinetics. *Chaos.* 18(3): 033136. doi: 10.1063/1.2944980, 2008.

[6] McManus OB, Weiss DS, Spivak CE, Blatz AL, Magleby KL. Fractal models are inadequate for the kinetics of four different ion channels. *Biophys J.* 54(5):859-870, 1988.

[7] Läuger P. Internal motions in proteins and gating kinetics of ionic channels. *Biophys. J.* 53: 877-884, 1988.

[8] Liebovitch LS. Testing fractal and Markov models of ion channel kinetics. *Biophys. J.* 55: 373-377, 1989.

Recurrence Analysis in Patients with Vasovagal Syncopes

[1]J. Schlenker, [2]T. Nedělka

[1]Czech Technical University, Faculty of Biomedical Engineering , Prague, Czech Republic,
[2]Department of Neurology 2nd Medical school Charles University, Prague, Czech Republic
Email: jakub.schlenker@fbmi.cvut.cz

Abstract. *This paper presents the possibility of using recurrence analysis for the vasovagal syncopes detection. The recurrent analysis is very promising nonlinear technique which is able to analyse system's dynamics. The main part of the work focuses on evaluation of heart rate variability using recurrence analysis in group of patients with vasovagal syncope and control group. The result of the work is the set of measures derived from recurrence analysis suitable for vasovagal syncope detection.*

Keywords: Recurrence Analysis, Recurrence Plot, Heart Rate Variability, Vasovagal Syncope

1. Introduction

Vasovagal syncopes are one of the causes for symptomatic orthostatic hypotension, associated with increased tone of parasympathetic part of autonomic nervous system, leading to sudden drop of blood pressure and heart rate, resulting in occasional fainting and black-outs, usually after standing-up. Blood pressure and heart rate drop can be diagnosed by head up tilt testing and heart rate as well as blood pressure variability analysis. Human heart rate is strongly influenced by autonomic nervous system, which is a typical example of non-linear system [1, 2]. Recent studies shows that recurrence analysis is very promising nonlinear technique used in cardiology and neurology, which is capable to describe discrete abnormalities in heart rate regulation [2, 3, 4, 5].

Recurrence plot (RP) is basic tool of recurrence analysis and it is used for graphical representation of recurrences in dynamical system [5, 6]. The great advantage of RP is visualization of multidimensional phase space in two-dimensional graph (see Fig. 1). The starting point of recurrence analysis is phase space reconstruction. Phase space represents all possible states of system. One of the most commonly used methods for phase space reconstruction is Taken's theorem [7]. In Taken's method there are two input parameters, embedding dimension and time delay. The optimal set of these parameters is important for the space reconstruction that fully describes system dynamics [6]. After phase space reconstruction the pair test of all states is done. For distance between two states in phase space trajectory smaller than given threshold, recurrent point in RP arises [7]. There are several methods for threshold distance setup. However, authors are not uniform about it so far [8, 9]. RP are quantified by recurrence quantification analysis (RQA). This RQA is a set of measures based on diagonal and vertical structures [5, 6].

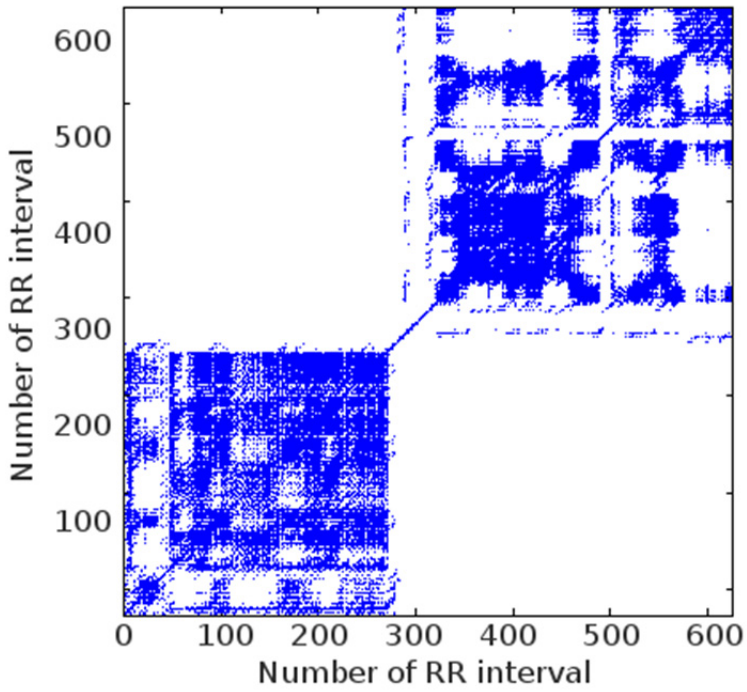

Fig. 1. An example of recurrence plot (input signal: R-R intervals measured during orthostatic test).

2. Subject and Methods

In this study 26 subjects divided into two groups participated. The first group (Syncope) consisted of 13 patients with vasovagal syncope. The control group consisted of 11 women and 2 men aged 15 to 28 years (mean age 21 and median 21 years). The second group (Control) consisted of 13 healthy subjects. There were 6 women and 7 men in control group aged 20 to 33 years (mean age 24 and median 24 years). All subjects gave their informed consent to examination. All subjects were examined from 8 to 12 am in a quiet room. We use R-R intervals from orthostatic test as an input signal. Orthostatic test has two phases (resting in supine position and standing position). Subjects were resting in supine position for 5 minutes then they were asked to stand up slowly and recording was continued in standing position for another 5 minutes. Schwarzer FAN Study (FAN®, Schwarzer, Germany) was used for heart rate monitoring and blood pressure measuring.

We use a script created in Matlab for the recurrence analysis. The lengths of R-R intervals are used as an input signal. For each recording we determine the optimal embedding dimension using false nearest neighbor method [10] and optimal time delay as the first minimum of the mutual information function [11]. For threshold distance we use method with fixed percentage of recurrence points %RR = 5% [2, 5].

The calculated measures of RQA were statistically evaluated by two-sample t-test and chosen measures were processed in a form of boxplot graphs. Values with $p < 0.05$ were considered statistically significant.

3. Results

We found significant differences between several RQA measures in patients with vasovagal syncope compared with control group. There are significantly higher percentage of points forming diagonal lines (Determinism – DET) and length of the longest diagonal line (LMAX). Higher DET means that system returns to the previous states more often and this

measure is associated with system predictability. RQA measurement also shows significant differences in the Divergence (DIV) which is related with Kolmogorov-Sinai entropy [6], and Shannon entropy (ENTR). Our results in boxplot graphs are shown in Fig. 2. Boxplot shows maximum, minimum, median, first and third quartile. Cross points are outliers.

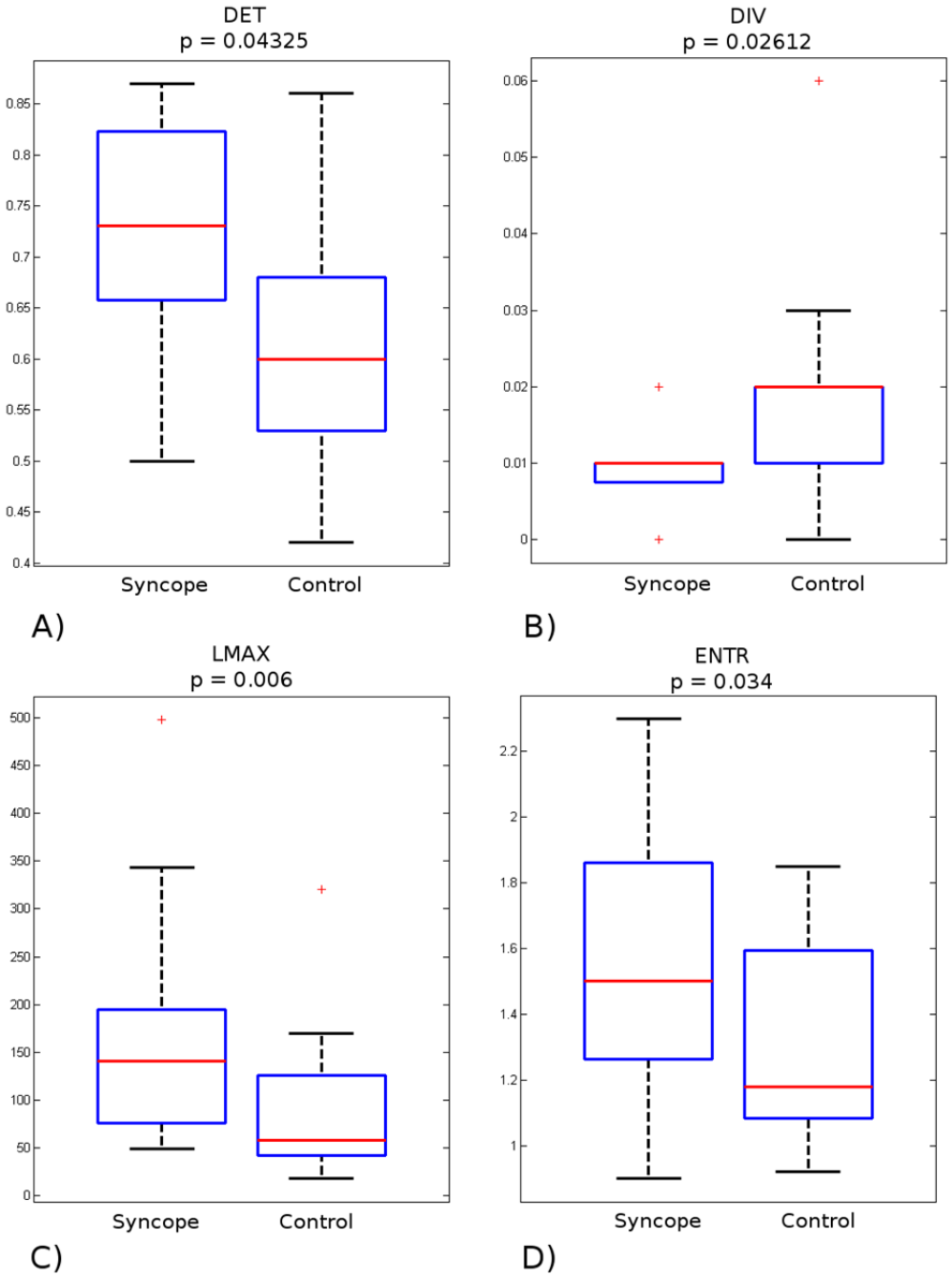

Fig. 2. Boxplots illustrating the comparison between patients with syncope and control group. A) Determinism (p = 0.04225). B) Divergence (p = 0.02612). C) The length of the longest diagonal line (p = 0.006). D) The Shannon entropy (p = 0.034).

4. Discussion

The major findings of our study are significant differences in measures derived from recurrence analysis in patients with vasovagal syncope. The lower heart rate variability is indicated by the higher "percentage of points forming diagonal lines" (DET) and the higher "length of the longest diagonal line" (LMAX) in patients group. These changes in HRV

revealed by recurrence analysis may indicate pathological conditions. The main limitation of our study is small number of subjects in the groups and no gender-matched control group. Therefore, future studies on this field are needed.

5. Conclusions

We discovered the reduced complexity of heart rate control in young patients with vasovagal syncope using the recurrence analysis. The main RQA measures suitable for the evaluation of HRV in patients with vasovagal syncope are determinism (DET), divergence (DIV), length of the longest diagonal line (LMAX) and Shannon entropy (ENTR).

Acknowledgements

This work was supported by the Grant Agency of Czech Technical University in Prague, grant No. SGS11/173/OHK4/3T/17.

References

[1] Sharma V. Deterministic chaos and fractal complexity in the dynamics of cardiovascular behavior: perspectives on a new frontier. *Open Cardiovasc Med J.* 3: 110-123, 2009.

[2] Nedělka T, Schlenker J, Riedlbauchová L, Mazanec R. Recurrence quantification analysis of heart rate variability in early diagnosis of diabetic autonomic neuropathy. *Cesk Slov Neurol N*, 75/108(6): 721-728, 2012.

[3] Mohebbi M, Ghassemian H. Prediction of paroxysmal atrial fibrillation using recurrence plot-based features of the RR-interval signal. *Physiol. Meas.* 32: 1147–1162, 2011.

[4] Acharya UR, Sree SV, Chattopadhyay S, Yu W, Ang PC. Application of recurrence quantification analysis for the automated identification of epileptic EEG signals. *Int J Neural Syst.* 21(3):199-211, 2011.

[5] Javorka M, Trunkvalterova Z, Tonhajzerova I, Lazarova Z, Javorkova J, Javorka K. Recurrences in heart rate dynamics are changed in patients with diabetes mellitus. *Clinical Physiology and Functional Imaging*, 28(5): 326-331, 2008.

[6] Marwan N. Encounters with neighbours: current developments of concepts based on recurrence plots and their applications. University of Potsdam, Potsdam, 331, 2003.

[7] Traut HM. Matlab® Recipes for Earth Sciences. Potsdam: Springer, 2007.

[8] Schinkel S, Dimigen O, Marwan N. Selection of recurrence threshold for signal detection. *The European Physical Journal Special Topics: Special Topics*, 164(1): 45-53, 2008.

[9] Ding H, Crozier S, Wilson S. Optimization of Euclidean distance threshold in the application of recurrence quantification analysis to heart rate variability studies. *Chaos, Solitons & Fractals*, 38(5):1457-1467, 2008.

[10] Cao L.. Practical method for determining the minimum embedding dimension of a scalar time series. *Physica D*, 110(1-2): 43-50, 1997.

[11] Fraser A, Swinney H. Independent coordinates for strange attractors from mutual information. *Physical Review A,* 33(2): 1134-1140, 1986.

Theoretical View on Estimation of Postural and Induced Stressors Intensities in the Human Body by a Mathematical Dynamic Model

E. Hlavacova, J. Chrenova, Z. Rausova, L. Dedik

Institute of Automation, Measurement and Applied Informatics, Faculty of Mechanical Engineering, Slovak University of Technology, SK-81231 Bratislava, Slovakia
Email: editahlavacova@gmail.com

Abstract. *The work presents a theoretical view on applied system approach in orthostatic response by a linear transfer model of a dynamic system. From the viewpoint of parameters estimation theory, it regards to the nonlinear model of measurement. From the viewpoint of system theory, it regards to the identification of the system with incomplete information about the input function to the system and measured output function in discrete points. The results present the new potential markers for clarification of orthostatic dysregulation diagnosis.*

Keywords: Stressor, Nonlinear Model of Measurement, Orthostatic Test, Physiological Circulatory Factor

1. Introduction

The work deals with the identification of indirect measurements of the dynamic object investigation - human body, in the medical field, and mathematical formulation of responses by defining the system model of orthostatic test [1] from a theoretical point of view. The study is aimed to replace of non-computerized processing of the problem of change physiological circulatory factor (PCF), such as systolic pressure, diastolic pressure and hearth rate, based on postural change and represented stressors, with a model in the form of a linear transfer function of a dynamic system. A contribution to clarification of orthostatic dysregulation diagnosis [2-3] through the estimated parameters as potential new markers within the orthostatic criteria [4] is expected.

2. Subject and Methods

The identification of measurement orthostatic test, the pictogram of Fig. 2, is based on the methodological approach used in the Human Endocrinology Laboratory, the Institute of Experimental Endocrinology the Slovak Academy of Sciences in Bratislava [5-8]. The relationship of the cause and the consequence between stressors and the measured profiles of PCF explains the settlement of the orthostatic response to orthostatic test. The starting points to formation of a model system and to understanding the physiological function of the regulatory mechanisms of the real object present the question of quantification stimulus of stressors and distinguishing of dynamic and static properties of linear dynamic models on the tested system *en bloc*, respectively.

From the viewpoint of system approach in Fig. 1, the postural change, such as quick tilting bed with the subject shown in pictogram of Fig. 2, means the step input function $I(t)$ describing the stressors intensities-time profile connected in serial during the course *en bloc* of orthostatic test, where the individual values of intensity I_i of stressors are not known [1]. The output function $V(t)$ presents the step response of measured value PCF, as a result of stressors exposure with unknown values of intensities I_i. In the reaction are known the time intervals $[t_{i-1}, t_i)$, $i = 1,...,n$ of postural changes, where n is the number of postural changes, exactly.

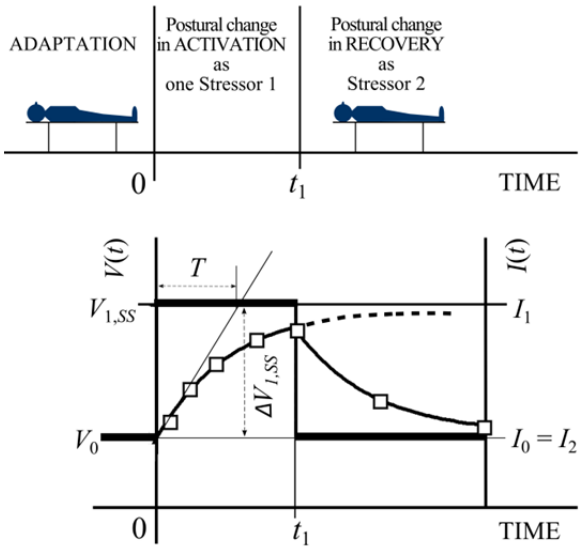

Fig. 1. System approach of General Orthostatic Test. $I(t)$ - input function of system, $V(t)$ - output function of system, t - time, V_0 - basal value of measured PCF in the time of 0 min, $V_{1,SS}$ - value of PCF in hypothetic steady state, $\Delta V_{1,SS}$ - increase of PCF in hypothetic steady state, $\Delta V(t) = V(t) - V_0$, $\Delta V_{SS} = \Delta V(t)$ in time $t \to \infty$, T - time constant, squares - measured PCF values, full line – simulation of model input function $I(t)$, I - intensity of stressor, $I_i = \Delta V_{i,SS}$, kde $i = 1, 2; \Rightarrow I_1 = \Delta V_{1,SS}, I_2 = \Delta V_{2,SS}$.

The system defined by input-output functions is considered as linear, time-invariant, continual, dynamic system with incomplete information about the input function $I(t)$ [9].

Regarding the superposition property of the linear dynamic system, the time profile of output function $V(t)$ of measured values PCF, can be described as

$$V(t) = V_0 + \Delta V(t) \tag{1}$$

where $V(t)$ measured profile-values of PCF as output function of the system
V_0 basal value of measured PCF in the time of $t = 0$ min
$\Delta V(t)$ increase of PCF value induced by the orthostatic test.

The linear system with input $I(t)$ and output $V(t)$ characterizes the transfer function of the system as

$$H(s) = \frac{G}{1+Ts} = \frac{\Delta V(s)}{I(s)} \tag{2}$$

where $H(s)$ transfer function of the system
G gain of the system
$\Delta V(s)$ Laplace transform of the system output
s complex variable
T time constant

The Laplace transform of the system input $I(s)$ is expressed as

$$I(s) = I_0 + \sum_{i=1}^{n+m} (I_{i-1} - I_i)\, e^{t_i - 1 - t} \tag{3}$$

where I_i is the intensity of stressors under the zero initial conditions, t_0=0, I_0=V_0 as constant values.

The identification presents the determination of transfer function (2). For the description of system with the incomplete information, it is necessary to use the probability theory. Then the intensity value I of stressor can be interpreted as the increase ΔV_{SS} of measured value of PCF in steady state; and static properties to estimate as a constant intensity I_i of input function $I(t)$ at appropriate intervals of exposure of the stressor [1].

Instead of the gain parameter G, the static properties indicate parameter I_i and dynamic properties indicate the parameter T.

3. Results

According to Fig. 2, one postural change may represent at least one stressor; and in the process of homeostasis is realized continually through physiological mechanisms in studied human body, though in the evaluation of orthostatic test is still not used.

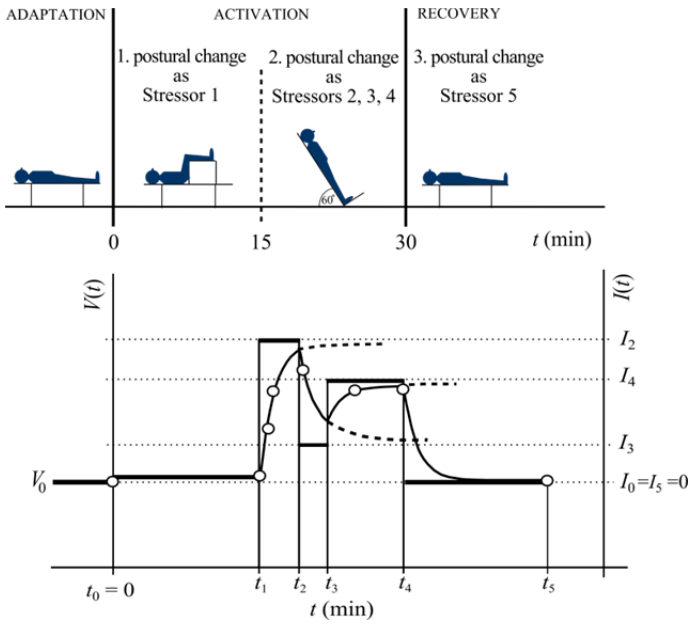

Fig. 2. The model of orthostatic test, where one postural change (2. postural change) represents three stressors, one hypothetical stressor and two induced stressors. $I(t)$ - input function of system, $V(t)$ - output function of system, circles - measured PCF values [1].

Figure 2 describes that second postural change in the activation phase of orthostatic test represents Stressor 2 and two induced Stressors 3 a 4.

The vector of estimated parameters λ of the nonlinear deterministic model has the form as

$$\lambda = (T, I_i; i = 1,2,...,(n+m); t_{x_j}, j = 0,1,...,m) \qquad (4)$$

where
T time constant
I_i intensity of stressors, $I_i = \Delta V_{i,SS}$
x_j induced stressors
m number of induced stressors
n number of postural change
t_{xj} starting-time exposure of induced stressors.

Presented idea was confirmed in processing of measured profiles of PCF by the CTDB software package [9] in the work [1].

4. Discussion

Exposure to stressors, such as the postural changes, body temperature, hormones and chemicals, of the dynamic system - human body, is non-trivial to identify and quantify [6]. This work points to the theoretical severity and extensiveness of this problem together with previous publication [1] can represent the simple initial approach. It is a complex problem with time-consuming solving of the functional/dysfunctional regulatory mechanisms, in order to identify the possible causes. Therefore, the connection of the scientific disciplines is clearly required. The study of orthostatic response indicates a worldwide problem, where its final objectives, conclusions and proposed solutions depend on the complexity evaluable in time sequence. The development of mathematical models of observed system and distinguishing of dynamic and static properties, as the potential of new markers of linear dynamic models on tested system, can present the important contribution for better specification of diagnosis associated with orthostatic dysregulation [2,3].

Acknowledgements

This work was supported by Scientific Grant Agency VEGA (Bratislava), grant No. 1/0120/12 and No. 2/0084/12, and Competence Center for SMART Technologies for Electronics and Informatics Systems and Services, ITMS 26240220072, funded by the Research & Development Operational Program from the ERDF.

References

[1] Hlavacova E, Chrenova J, Rausova Z, Vlcek M, Penesova A, Dedik L. Identification of regulatory mechanism of orthostatic response. *World Academy of Science, Engineering and Technology*, to be published.

[2] Nozawa I, Imamura S, Hisamatsu K, Murakami Y. The relationship between orthostatic dysregulation and the orthostatic test in dizzy patients. *Eur. Arch. Otorhinolaryngol.*, 253 (4-5): 268-272, May 1996.

[3] Winker R, Prager W, Haider A, Salameh B, Rüdiger HW. Schellong test in orthostatic dysregulation: a comparison with tilt-table testing. *Wien. Klin. Wochenschr.*, 117 (1-2): 36-41, Jan. 2005.

[4] Rada M. Zivna R., An evaluation of the effectiveness of hypertension treatment in aviation personnel: Perspectives and the present situation. *Miletary Medical Science Letters*, no. 2, pp. 63-67, 2003.

[5] Vigas M. Neuroendocrine reaction of man in stress [Neuroendokrinna reakcia v strese u cloveka]. Macho L, Editor. Veda, Publishing House of the Slovak Academy of Sciences, Bratislava, 1985, 15-40.

[6] Kvetnansky R, Sabban EL, Palkovits M. Catecholaminergic systems in stress: Structural and molecular genetic approaches. *Physiol. Rev*., 89: 535-606, 2009.

[7] Koska J, Ksinantová L, Kvetnanský R, Marko M, Hamar D, Vigas M, Hatala R. Effect of head-down bed rest on the neuroendocrine response to orthostatic stress in physically fit men. *Physiol. Res*., 52 (3): 333-339, 2003.

[8] Radikova Z, Penesova A, Koska J, Kvetnansky R, Jezova D, Huckova M, Vigas M, Macho L. Does orthostatic stress influence the neuroendocrine response to subsequent hypoglycemia in humans? *Ann. N. Y. Acad. Sci*., 1018: 576-581, Jun. 2004.

[9] Dedík L, Durisova M. System approach in technical, environmental, and bio-medical studies. Publishing House of Slovak University of Technology, Bratislava, 1999. Available: http://www.uef.sav.sk/advanced.htm.

MRI Contrast in the Examination of Early Somatic Embryos

[1]R. Korinek, [3]L. Havel, [2]E. Hutova, [1]K. Bartusek

[1]Institute of Scientific Instruments, ASCR, Brno, Czech Republic
[2]Brno University of Technology, Brno, Czech Republic,
[3]Faculty of Agronomy, Mendel University in Brno, Brno, Czech Republic.
Email: korinek@isibrno.cz

Abstract. *The article deals with the MRI-based in vivo examination of early somatic embryos. The volume of water in the embryos was measured using two different methods. The first technique applied was proton density (PD) measurement of the sample via MRI (realized at the ISI, ASCR Brno). The second approach consisted in the dehydration and subsequent weighing of the sample (realized at MENDELU, Brno). Both the methods were compared. The correlation coefficient of the volume of water measured by these techniques is 0.816. The aspects of major interest for the investigation of the related biological processes are the various image contrasts and the change of the relaxation times T_1 and T_2 on the boundary between the embryo and the substrate.*

Keywords: MRI Contrast, Somatic Embryos, Plants, Water Changes, Relaxation T_1 and T_2.

1. Introduction

Magnetic resonance imaging (MRI) is a non-invasive tool applied by many researchers to study molecules. The MRI approach is frequently used not only in medicine, but also in biological, biochemical, and chemical research. In plant biology, MRI is utilized to support the research of water and mineral compounds transported within a plant [1, 2], the determination of plant metabolites [3, 4], the investigation of cellular processes [5], and the examination of the growth and development of plants [6]. MRI is also instrumental towards monitoring water changes in early somatic embryos of spruce (ESEs) [7]. These embryos constitute a unique plant model system applicable for the study of various types of environmental stresses (including metal ions) under well-controlled experimental conditions [8-10].

2. Method

The general aim of the experiment was to perform in vivo measurement of the ESEs using MRI techniques, and the entire process comprised several stages. Within the first step, a comparison was carried out of the volumes of water in the cultures (proton density measurement using a 4.7 T system) with the volumes of water determined upon the weight changes observed after desiccation of the sample. Subsequently, we compared the acquired MR images weighted by proton density (PD) and relaxation times T_1, T_2, and the last stage of the experiment consisted in determining the changes of the basic magnetic field B_0 caused by the magnetic susceptibility of ESEs. The acquired results will be used for the examination of growth focused on ESEs contaminated with heavy metals. To measure the T_2 relaxation, we applied the spin echo (SE) method; the measurement of the T_1 relaxation was realized using inversion recovery (IR) and rapid acquisition with relaxation enhancement (RARE). All the described experiments were performed on the 4.7 T (Magnex) and 9.4 T (Bruker) MRI systems operated by the Institute of Scientific Instruments, Brno. The MAREVISI (8.2) and MATLAB (7.11.0) programs were used for the processing.

3. Plant Material and Cultivation Conditions

A clone of early somatic embryos of the Norway spruce (Picea abies/L./ Karst.) marked as 2/32 and a clone of the Blue spruce (Picea pungens Engelm.) designated as PE 14 were used in our experiments. The cultures were maintained on a semisolid (Gelrite Gellan Gum, Merck, Germany) half-strength LP medium [11] with modifications [12]. The concentration of 2,4-dichlorofenoxyacetic acid and N^6-benzyladenine was 4.4 and 9 µM, respectively [13]. The pH value was adjusted to 5.7 - 5.8 before autoclaving (121°C, 100 kPa, 20 min). The organic part of the medium, excluding saccharose, was sterilized by filtration through a 0.2 µm polyethylensulfone membrane (Whatman, Puradisc 25 AS). The cultivation was carried out in Petri dishes (diameter 50 mm). The sub-cultivation of stock cultures was carried out in 2-week intervals; the stock and experimental cultures were maintained at the temperature of 23±2°C in a cultivation box kept in a dark place. The experiment started with colonies of early somatic embryos which weight was about 3 mg. Ten colonies per one Petri dish were cultivated. After 2 weeks the colonies of early somatic embryos were harvested and after fresh weight determination they were dried at 105°C to stable weight. Thirty colonies were used for weighing and statistical analysis.

4. Results

A comparison of the volumes of water in the embryos measured via the above-discussed methods can be seen in Figs. 1 and 2. While the measurement using desiccation and subsequent weighting was conducted at MENDELU, the proton density measurement with the SE technique was performed at the ISI Brno.

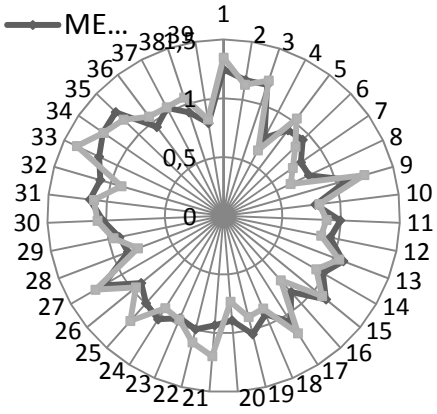

Fig. 1. Comparison of the normalized values of the samples 1-39 measured at the ISI and MENDELU.

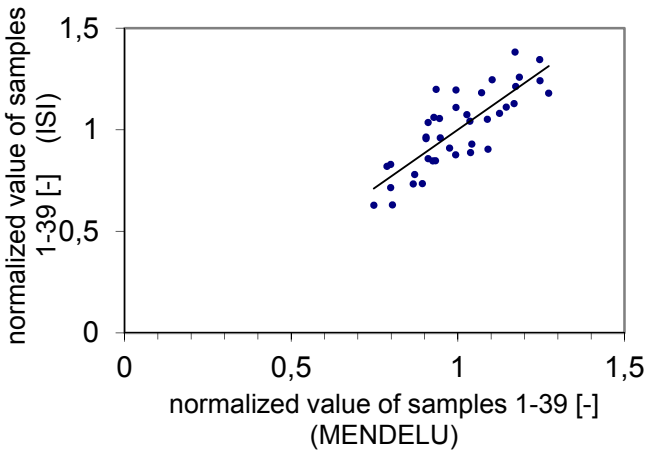

Fig. 2. Normalized value of the samples measured at the ISI and MENDELU.

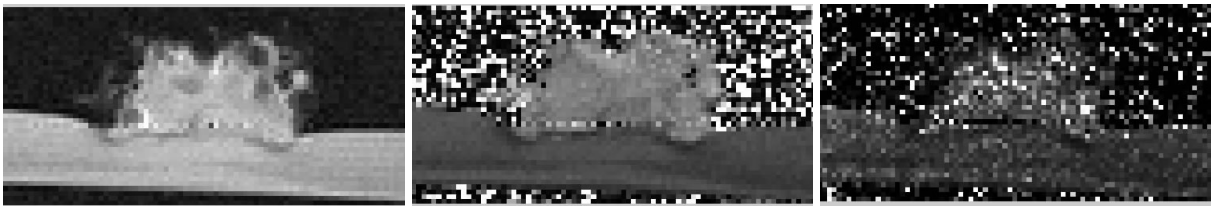

Fig. 3. Images of the ESEs measured with the 4.7 T magnet. Left: image of the PD; centre: the T_1 map; right: the T_2 map.

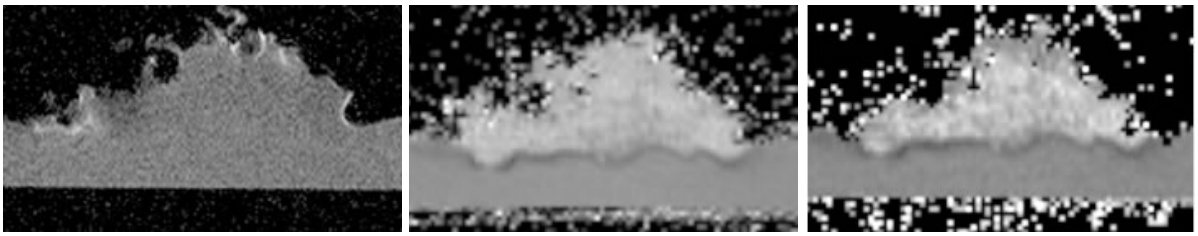

Fig. 4. Images of the ESEs measured with the 9.4 T magnet. Left: image of the PD; centre: the T_1 map; right: the T_2 map.

The data from MENDELU and the ISI were normalized to the mean value for all the samples examined. The correlation coefficient of the volumes of water measured by both methods is 0.816. The proton density, relaxation times T_1 and T_2, and B_0 maps of the embryos measured using the 4.7 T and 9.4 T MRI systems are shown in Figs. 3, 4, and 5.

The difference of the magnetic field between the embryos and the medium ($\Delta B_0 = 16{,}92\mu T$) was established from the map of the magnetic field B_0. To measure the magnetic field B_0 map, we applied the gradient echo method ($\Delta T_E = 5$ ms, 9.4 T MRI system). Susceptibility difference ($\Delta\chi = 1.8 \cdot 10^{-6}$) is calculated from ΔB_0. Susceptibility difference is difference between susceptibility of embryos and substrate. A comparison of the relaxation times T_1 and T_2 in the embryos and the substrate can be seen in Table 1. The measurement was performed with the 4.7 T and 9.4 T MRI systems.

Fig. 5. Map of the magnetic field ΔB_0 in a measured sample; the 9.4T MRI system.

Table 1. Table of the relaxation times T_1 and T_2 in the ESEs and the substrate.

B_0 field	T_1 [ms]	T_2 [ms]	Method
ESEs			
4.7 T	748	64	IR/SE
9.4 T	1540	90	RARE/SE
ESEs			
4.7 T	492	36	IR/SE
9.4 T	988	51	RARE/SE

5. Discussion and Conclusion

The authors utilized two methods to carry out a comparison of the volumes of water in early somatic embryos. The first technique consists in MRI-based proton density (PD) measurement of the sample. The second method requires double weighting of the embryos before and after desiccation. The difference in weight is equal to the volume of water in the embryos. The correlation coefficient between the normalized results measured via both

methods was 0.816; the results after the normalization of the mean value of the determined volumes shown in Figs. 1 and 2 exhibit differences. Generally, MRI may be used as an effective approach to non-invasive measurement of water in organic structures.

The above-mentioned differences between the volumes are caused by several factors: a) the volume of water is also evaluated for the area affecting the substrate (nutrient medium), b) low sensitivity of the RF coil, c) imperfect image segmentation. With the second method, the removal of embryo from the substrate can accompanied by accidental withdrawal of a larger amount of material than is necessary for the subsequent desiccation and weighing. The use of a higher magnetic field in combination with a small RF coil having high sensitivity can improve the signal-to-noise ratio (SNR) and, consequently, provide higher resolution and thinner slices. Table 1 shows the relaxation times T_1 and T_2 of the samples in different magnetic fields. The change of the relaxation times T_1 and T_2 on the boundary between the embryo and the substrate are of interest for the investigation of biological processes.

Acknowledgements

The research described in the paper was financially supported by the EC and MEYS CR (project No. CZ.1.05/2.1.00/01.0017).

References

[1] Scheenen TWJ., Vergeldt FJ., Heemskerk AM., Van As H. Intact plant magnetic resonance imaging to study dynamics in long-distance sap flow and flow-conducting surface area. *Plant Physiol*., 144(2): 1157-1165, 2007.

[2] Ionenko I. F., Anisimov A. V. and Dautova N. R., Early changes of water diffusional transfer in maize roots under the influence of water stress, Biol. Plant., 54 (2010) 488.

[3] Y. Q. Pu, F. Chen, A. Ziebell, B. H. Davison and A. J. Ragauskas, *BioEnergy Res*., 2 (2009) 198.

[4] K. G. Zulak, A. M. Weljie, H. J. Vogel and P. J. Facchini, BMC Plant Biol., 8 (2008)

[5] J. Lambert, P. Lampen, A. von Bohlen and R. Hergenroder, Two- and three-dimensional mapping of the iron distribution in the apoplastic fluid of plant leaf tissue by means of magnetic resonance imaging, *Anal. Bioanal. Chem*., 84 (2006) 231.

[6] S. M. Glidewell, M. Moller, G. Duncan, R. R. Mill, D. Masson and B. Williamson, *New Phytol.*, 154 (2002) 197.

[7] V. Supalkova, J. Petrek, J. Baloun, V. Adam, K.Bartusek, L. Trnkova, M. Beklova, V. Diopan, L. Havel and R. Kizek, Multi-instrumental Investigation of Affecting of Early Somatic Embryos of Spruce by Cadmium(II) and Lead(II) Ions, *Sensors*, 7 (2007) 743.

[8] R. Mikelova, J. Baloun, J. Petrlova, V. Adam, L. Havel, H. Petrek, A. Horna and R. Kizek, *Bioelectrochemistry*, 70 (2007) 508.

[9] J. Petrek, J. Vitecek, H. Vlasinova, R. Kizek, K. J. Kramer, V. Adam, B. Klejdus and L. Havel, *Anal. Bioanal. Chem*., 383 (2005) 576.

[10] Víteček, J., Adam, V., Petřek, J., Vacek, J., Kizek, R., Havel, L.: Esterases as a marker for growth of BY-2 tobacco cells and early somatic embryos of the Norway spruce, *Plant Cell Tissue Organ Cult.* 79, (2004) 195-201.

[11] von Arnold, S.J. Improved efficiency of somatic embryogenesis in mature embryos of Picea abies (L.). *Plant Phys.* 1987, 128, 233-244.

[12] Havel, L.; Durzan, D.J. Apoptosis during diploid parthenogenesis and early somatic embryogenesis of Norway spruce. *Int. J. Plant Sci*. 1996, 157, 8-16.

[13] Vlasinova, H.; Mikulecky, M.; Havel, L. The mitotic activity of Norway spruce polyembryonic culture oscillates during the synodic lunar cycle. *Biol. Plant*. 2003, 47, 475-476.

Support Vector Machines in MR Images Segmentation

[1]J. Mikulka, [2]K. Bartušek, [3]P. Dvořák

[1,3]Brno University of Technology, Brno, Czech Republic,
[2,3]Institute of Scientific Instruments ASCR, Brno, Czech Republic
Email: mikulka@feec.vutbr.cz

Abstract. *The problem most frequently encountered in the practical processing of medical images consists in the lack of instruments enabling machine evaluation of the images. A typical example of this situation is perfusion analysis of brain tumor types. The first and very significant step lies in the segmentation of individual parts of the brain tumor; after segmentation, the rate of penetration by the applied contrast agent is observed in the parts. The common method, in which a high error rate has to be considered, is to mark these tumor portions manually. The quality of brain tissue segmentation exerts significant influence on the quality of evaluation of perfusion parameters; consequently, the tumor type recognition is also influenced. The authors describe classification methods enabling the segmentation of images acquired via magnetic resonance tomography. During the edema segmentation, we obtained the following data: sensitivity 0.78±0.09, specificity 1.00±0.00, error rate 0.45±0.24 %, surface overlap 69.36±12.04 %, accuracy 99.55±0.24 %, and surface difference - 7.80±9.13 %.*

Keywords: Perfusion Analysis, Brain Tumor Segmentation, Data Classification, Support Vector Machines, Multi-parametric Segmentation.

1. Introduction

The problem of brain tissue segmentation has been widely discussed in recent years, mainly owing to the fact that the understanding of information acquired via various tomographic methods is very important for the classification of tumors, monitoring of their development, and assessment of treatment efficiency. This paper presents the development of methods for the processing of images acquired via magnetic resonance tomography (MR), a technique that finds application in various disciplines of research, for example within medicine [1], [2], agriculture, or ecology [3], [4]. The aim of the described image processing is to secure brain tumor segmentation. The area of a brain tumor can be subdivided into the actual tumor, the inner necrotic section, and the edema surrounding the tumor. An exemplary image of a tumor and its part in one slice acquired via the MR technique is provided in Fig. 1. Here, the T2-weighted image and the Turbo Spin Echo (TSE) sequence are applied to show the tumor; the slice thickness is 5 mm.All processed images were acquired in the Faculty Hospital in Brno Bohunice by the Philips Achieva MRI system (B_0 = 1.5 T).

At present, multi-parametric image analysis is frequently discussed within the scientific community [5]. This technique, even though it can be based on traditional segmentation methods (thresholding, active contours), exploits information obtained from more images or modalities at the same time. Another approach is to interpret image segmentation as the classification of multi-dimensional data. The problem of multi-parametric segmentation of MR images is described within several research reports, for example reference [6]. The authors of the report propose the segmentation of brain tissue into 15 classes; in each class, a model approximates the distribution of its parameters using Gaussian Markov random fields. For the actual segmentation, the T1, T2, Gd+T1-weighted images and perfusion images are applied.

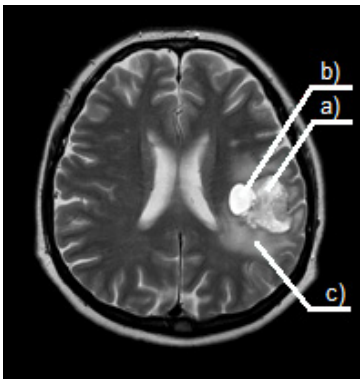

Fig. 1. Brain tumor imaging based on MR tomography; a) the tumor, b) the necrosis, c) the edema.

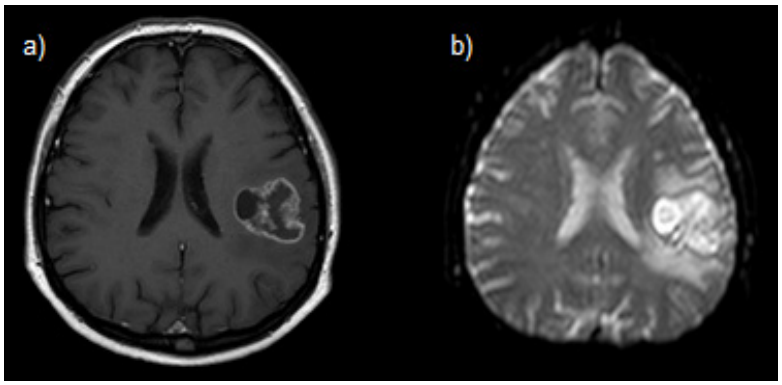

Fig. 2. a) a T1-weighted image of the tumor slice, b) a diffusion weighted image (DWI) of the tumor slice.

2. Methods for the Evaluation of Processing Quality

The proposed methods will be evaluated via calculation of the following parameters: sensitivity S_n, specificity S_p, error rate E_r, surface overlap O_S, accuracy A, and surface difference D_S. These parameters are defined as follows:

$$S_n = \frac{n_{TP}}{n_{TP} + n_{FN}}, \; S_p = \frac{n_{TN}}{n_{TN} + n_{FP}}, \qquad (1, 2)$$

$$E_r = \frac{n_{FP} + n_{FN}}{n_{TP} + n_{TN} + n_{FP} + n_{FN}} \cdot 100, \; O_S = \frac{p_S(A) \cap p_S(R)}{p_S(A) \cup p_S(R)} \cdot 100 \qquad (3, 4)$$

$$A = \frac{n_{TP} + n_{TN}}{n_{TP} + n_{TN} + n_{FP} + n_{FP}} \cdot 100, \; D_S = \frac{p_S(A) - p_S(R)}{p_S(R)} \cdot 100 \qquad (5, 6)$$

where n_{TP} is the number of true positives, n_{TN} is the number of true negatives, n_{FP} is the number of false positives, n_{FN} is the number of false negatives, $p_S(A)$ is the set of pixels inside the segmented area, and $p_S(R)$ is the set of pixels inside the ground truth area.

3. Processing of the Test Images

Description of the Proposed Method

In order to facilitate segmentation of the tumor parts, we implemented a trainable approach in the RapidMiner environment [7], [8]. The image processing chain is shown in Fig. 3.

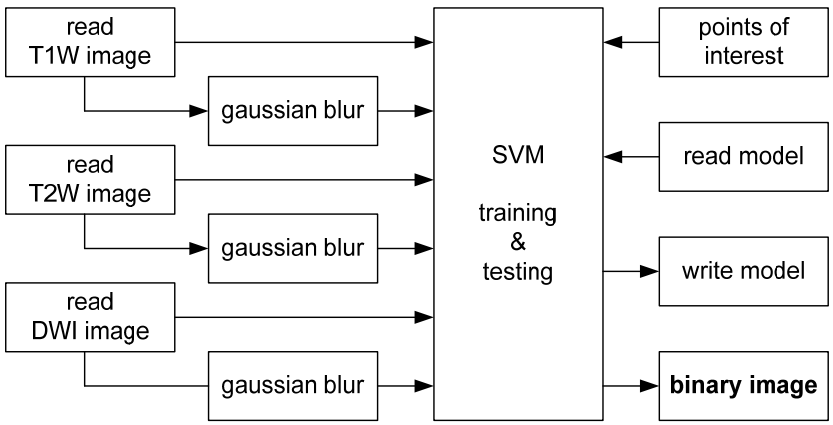

Fig. 3. The designed multi-parametric image processing chain.

The segmentation operator is realized via the Support Vector Machine (SVM) classification model with radial kernel ($\gamma = 1.0$). The aim of the classification is recognition of tumor kernel area, edema area and necrosis area in the healthy tissue. Thus, the segmentation process consists of two stages: training and testing. During the training, the pixels inside and outside the areas of interest (tumor kernel, edema and necrosis) are manually marked. The set of intensities at the marked points in the images (T1, T2, DWI) constitutes the training data of the model; then, the testing of the model is performed over the test images.

Test Image Processing Results

The segmentation results are shown in Fig. 4. The red outline indicates the brain tumor boundaries. The boundary of the surrounding edema is added to the brain tumor boundary. The areas of interest are clearly delimited by the outlines.

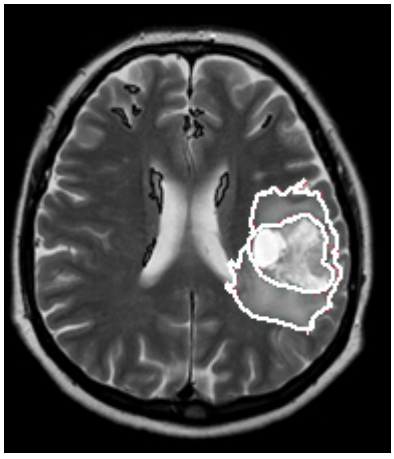

Fig. 4. Segmentation results for the tumor and edema; the ROI is marked by the white curve.

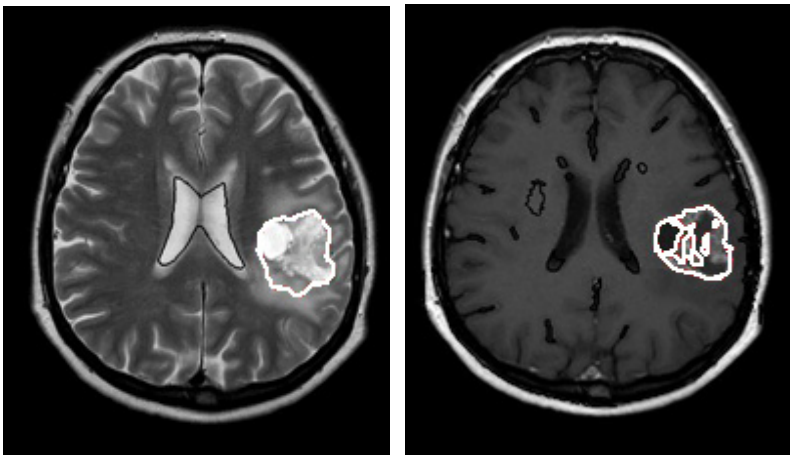

Fig. 5. Results of incorrect brain tumor segmentation realized by means of the same SVM classification method and a single input image (T2W left, T1W right).

Figure 5 shows the results of brain tumor segmentation via the SVM approach in a single image. The left section of the figure presents the results of segmentation in the T2W image, and the right section exhibits the results obtained with the T1W image. Thus, the disadvantages of single-image segmentation are clearly illustrated. In the T2W section, the outline crosses the boundaries of the edema, whose intensity is very similar to that found in the vicinity of the tumor. In the T1W image, the edema is not visible; here, segmentation fails because of inhomogeneities inside the tumor area.

Processing Quality

The processing results obtained via the designed segmentation method were compared with the ground truth segmentation approach. The results acquired in individual slices are shown in Tab. 1. The table indicates the accuracy of segmentation performed on the surrounding edema.

Table 1: Segmentation quality in the edema in several MR slices of the patient brain

Slice	S_n	S_p	E_r [%]	O_S [%]	A [%]	D_S [%]
1	0.66	1.00	0.17	58.97	99.83	-23.36
2	0.71	1.00	0.57	57.26	99.43	-4.28
3	0.87	1.00	0.41	80.92	99.59	-4.90
4	0.80	1.00	0.79	66.68	99.21	0.58
5	0.88	1.00	0.30	82.97	99.70	-7.03
mean value	0.78	1.00	0.45	69.36	99.55	-7.80

4. Conclusions

The paper presents the principles and application of classification methods for MR image segmentation. The discussed segmentation method has been designed to separate individual parts of a brain tumor, namely the actual tumor, the surrounding edema, and the necrotic tissue. The authors of this article describe a technique in which segmentation is interpreted as a set of multidimensional data. These data are then classified into pre-defined classes based on a training set. The training set is defined via manual marking of the images. Suitable metrics have been chosen to enable proper evaluation of both the similarity of the segmented area to the ground truth approach and the area location (degree of overlapping). During the edema segmentation, we obtained the following data: sensitivity $S_n = 0.78 \pm 0.09$, specificity $S_p = 1.00 \pm 0.00$, error rate $E_r = 0.45 \pm 0.24$ %, surface overlap $O_S = 69.36 \pm 12.04$ %, accuracy $A = 99.55 \pm 0.24$ %, and surface difference $D_S = -7.80 \pm 9.13$ %. These values indicate lower sensitivity of the method as well as a lower level of segment overlapping. This fact partly follows from the quality of ground truth segmentation, which always brings a certain degree of inaccuracy; this characteristic of the technique manifests itself especially in cases when the regions are not clearly delimited (the brain edema in Fig. 1c is a typical example). The error can be suppressed via extending the image training database.

Acknowledgements

This work was supported by the Grant 102/12/1104, by the project FEKT-S-11-5/1012 and by the project CZ.1.05/2.1.00/01.0017 (ED0017/01/01).

References

[1] Mikulka J, Gescheidtová E, Bartusek K. Soft-tissues Image Processing: Comparison of Traditional Segmentation Methods with 2D active Contour Methods. *Measurement Science Review*, vol. 12, pp. 153-161, ISSN 1335-8871.

[2] Bartusek K, Gescheidtova E, Mikulka J. Data processing in Studying Biological Tissues, Using MR Imaging Techniques, In 33th International Conference on Telecommunications and Signal Processing. Budapest, 2010, 171-175, ISBN 978-963-88981-0-4.

[3] Mikulka J, Gescheidtová E, Bartusek K. Perimeter Measurement of Spruce Needles Profile Using MRI. In Progress in Electromagnetics Research Symposium (PIERS 2009), Beijing, ISBN 978-1-934142-08-0.

[4] Marcon P, Bartusek K, Burdkova M. Magnetic Susceptibility Measurement Using 2D Magnetic Resonance Imaging. *Measurement Science & Technology*, 22(10), 2011, ISSN 0957-0233.

[5] Benes R, Burget R, KarásekJ, Říha K. Automatically designed machine vision system for the localization of CCA transverse section in ultrasound images. *Computer Methods and Programs in Biomedicine.* 2013, 109(3). 92-103, ISSN 0169-2607.

[6] Zavaljevski A, Dhawan A.P, Gaskil M, et al. Multi-level adaptive segmentation of multi-parameter MR brain images. *Comp. Med. Imaging and Graphics* 2000, *2*, 87-98.

[7] Burget R, Karasek J, Smekal Z, Uher V, Dostal O. Rapidminer image processing extension: A platform for collaborative research. In The 33rd International Conference on Telecommunication and Signal Processing. 2010, 114-118, ISBN 978-963-88981-0-4.

[8] Uher V, Burget R. Automatic 3D Segmentation of Human Brain Images Using Data-mining Techniques. In Proceedings of the 35th International Conference on Telecommunication and Signal Processing. 2012, 578-580, ISBN 978-1-4673-1116-8

Portable High Resolution Multichannel ECG Measuring Device

M. Tyšler, V. Rosík, P. Kaľavský, G. Bukor

Institute of Measurement Science, Slovak Academy of Sciences, Bratislava, Slovakia
Email: tysler@savba.sk

Abstract. *Advanced electrocardiographic diagnostic methods of various cardiovascular diseases need high resolution multichannel measurement of ECG signals that offer much more information than the standard 12-lead ECG. To obtain such ECG signals in required quality a special multichannel electrocardiograph ProCardio 8 was developed. The system is designed as a virtual instrument consisting of an external intelligent measuring unit connected via optical USB interface to a controlling PC running the measuring and data analyzing software. The system can be configured for measurement of up to 144 standard and/or mapping ECG leads using active or passive Ag-AgCl or carbon electrodes. Most of the measuring and newly designed data processing software is written in MATLAB and its compiled version can be deployed as a stand-alone application on any computer running Windows. The modular software architecture consists of real–time modules for the control and checking of the measuring system, data acquisition and signal monitoring as well as modules for off-line data analysis including ECG processing, body surface potential mapping, integral mapping and data preparation for non-invasive model-based electrocardiographic imaging based on inverse solutions and serving as an advanced diagnostic tool.*

Keywords: Intelligent ECG Measuring System, Multichannel Data Acquisition, Body Surface Potential Mapping, Non-invasive Identification of Local Ischemia

1. Introduction

High resolution multichannel measurement of surface ECG signals and computation of body surface potential maps (BSPM) is a non-invasive procedure used in electrocardiographic diagnostics that enables detailed analysis of cardiac disorders based on 24 to 256 ECG leads that offer much more information on the physiological state of the heart than the commonly used standard 12-lead ECG. Measured ECG signals and BSPM can be used for immediate analysis and diagnostics. However, many studies suggest that BSPM together with information on torso geometry and electrical structure obtained from imaging techniques such as MRI or CT can be used for advanced diagnostic methods enabling non-invasive assessment of abnormal configuration of electrical sources in the heart. [1]. In this paper, a powerful high resolution measuring system that can be used for advanced BSPM based cardiac studies is presented and its ability to non-invasively localize small ischemic regions is demonstrated.

2. Material and Methods

Based on the long term experience with multichannel measuring systems [2] a battery-powered high resolution ECG mapping system ProCardio 8 has been developed. The system enables measurement and processing of ECG signals needed for diagnostics based on BSPM and provides input data for solution of the inverse problem of electrocardiology.

Hardware of the ProCardio System

The measuring system (Fig. 1) consists of a set of ECG electrodes, intelligent measuring unit and a personal computer that controls the data measurement, processing and analysis. ECG

signals can be sensed by disposable Ag-AgCl or carbon electrodes that can be connected to active or passive adapters. The use of active adapters helps to reduce the noise in measured ECGs, passive adapters in combination with carbon electrodes and lead wires offer the possibility to use the system during CT examinations. The basic electrode configuration consists of individual electrodes that enable universal configuration of leads. However, for faster electrode application also the use of strips with several electrodes is possible.

The measuring unit is placed in a patient terminal box that is connected to the USB port of the host PC by an optical cable with USB interface. The unit contains an amplifying and measuring subsystem powered by rechargeable Li-ion battery. The system enables recording of up to 128 ECG signals from unipolar chest leads and 4 to 16 standard limb or chest leads. The system is modular and each input module includes 16 analog channels connected to two robust 24-pin Centronix connectors. One input module is used to record signals from R, L, F leads and contains also the circuits for active neutralization of the patient using a DRL (driven right leg) electrode that minimizes the common mode signal. All signals are measured relatively to a special CMS (common mode sense) electrode that can be placed so that the overall noise in ECG signals is minimized. Each measuring channel is equipped by a DC-coupled ECG amplifier with a fixed gain of 40 and a 22-bit σ-Δ A/D converter. Sampling frequency can be set between 125 Hz and 2 kHz per channel. The data acquisition system is controlled by a 16-bit microprocessor. Commands for selection of measured channels, formatting of the digitized data and checking of correct function of the unit are received from the controlling PC. Data sampled from the analog channels are streamed via four serial DMA-controlled UART channels to an USB FIFO chip and optical USB interface that provides bidirectional data transfer between the measuring unit and the controlling PC with the data rates of up to 1 MB/s.

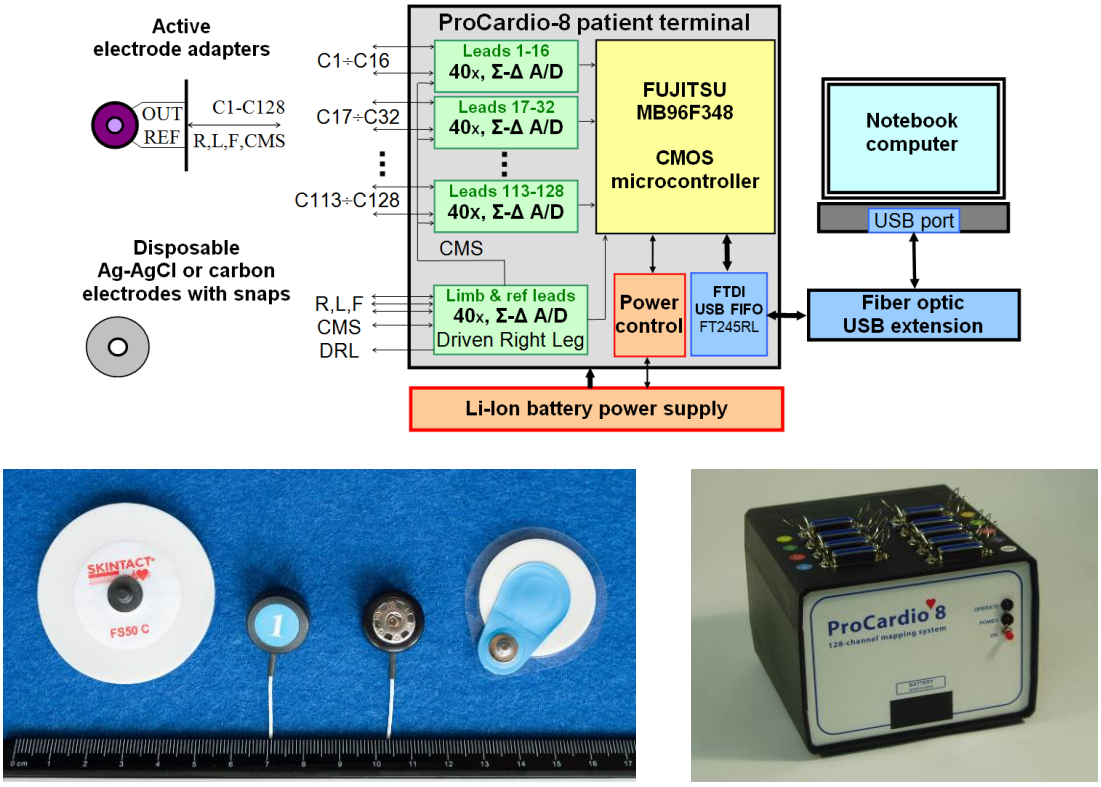

Fig. 1 Block scheme (top) and view (bottom righ) of the high-resolution multichannel measuring device ProCardio 8. The system can use passive or active 2-wire electrode adapters with both, Ag-AgCl and carbon disposable electrodes (bottom left).

ProCardio Software Architecture and Mmodules

The application software of the ProCardio-8 system was designed as a Matlab application consisting of separate tasks controlled by individual sets of parameters stored in global variables. After the application start, they are loaded from system configuration files, can be individually modified by each user and saved on disk for future use.

The **real-time measuring software** has two main modules (Fig. 2): 1) testing of electrode contacts and signal properties and 2) signal recording and monitoring. The first module is executed before each ECG recording. Electrode contacts are checked by measurement of the electrode-skin polarization voltages. Simultaneously, offsets and amplitudes of ECG signals in all channels are analyzed and this information is used for subsequent setting of measuring channels. The module is terminated after successful electrode and signal testing. The second module includes functions for the low-level control of the measuring unit, data transfer between the measuring unit and the PC, for visualization of measured signals in desired format on the PC screen and functions for storing of the recorded data on the hard disk.

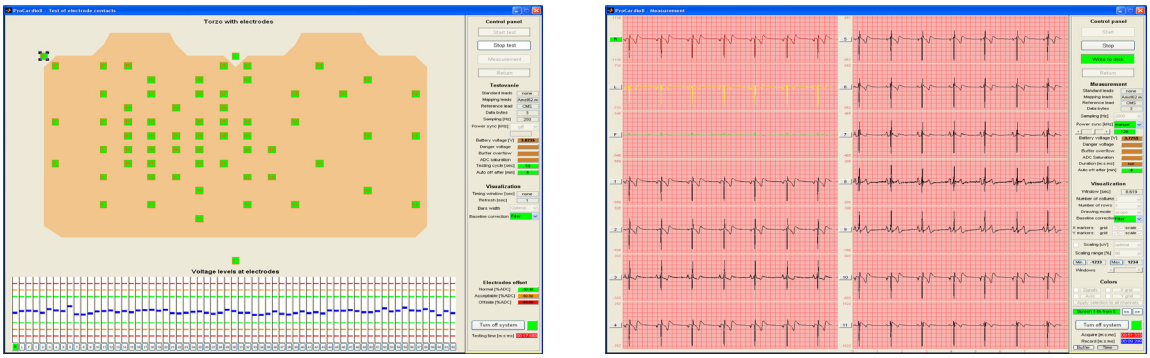

Fig.2. The real-time control and data acquisition software. Left: Checking of all electrode contacts, signals and measuring unit parameters. Right: During the ECG recording the measuring unit parameters and ECG signals can be monitored in desired format.

The **off-line ECG signal processing and analysis** enables the user to process the stored ECG signals and to compute several types of body surface maps. Typical tasks of the signal processing are filtration, baselines wandering corrections, signal averaging and identification of waves and instants in the ECG signals. ECG data from selected time instants or intervals are then used for computation of body surface potential maps and integral maps (Fig. 3, left). Departure integral maps displaying the departures of patient integral map from selected template (expressed in standard deviations) can be used for direct cardiac diagnostics. Difference integral maps revealing the changes in patient maps e.g. due to ischemia can be used for noninvasive model-based localization of the affected cardiac tissue (Fig. 3, right) [3].

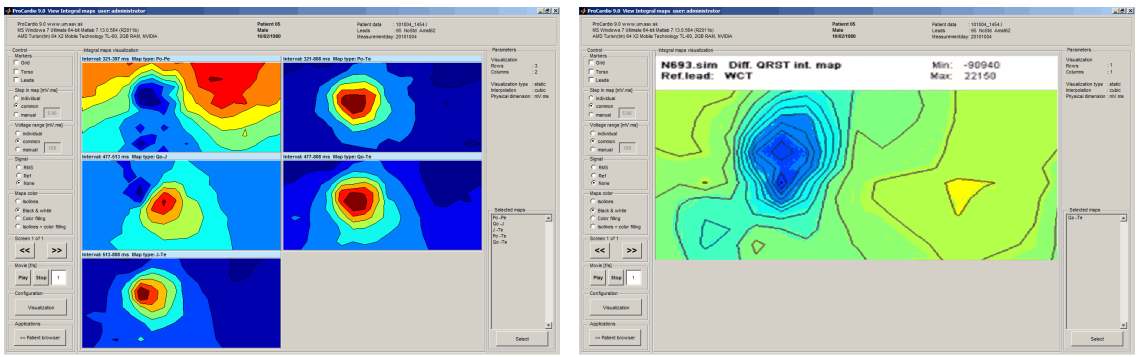

Fig. 3. Left: Example of normal body surface integral maps (for intervals P, PQRST, QRS, QRST and STT). Right: QRST difference integral map with negative area indicating ischemia in anterior wall of the LV.

3. Results

Difference integral maps recorded at rest and after a stress test from 62 leads in patients with one or two ischemic lesions were used to solve the inverse solution and identify one or two ischemic lesions represented by dipoles. In 8 evaluated patients the obtained results were in agreement with SPECT images and identified 2 lesions in 3 patients and 1 lesion in another 3 patients. For remaining 2 patients no local ischemic lesions were identified what was in agreement with SPECT results. Example of the inversely located dipoles in a patient with 2 lesions located at the base on the anterior wall of the left ventricle and in the middle part of the inferior wall is shown in Fig. 4.

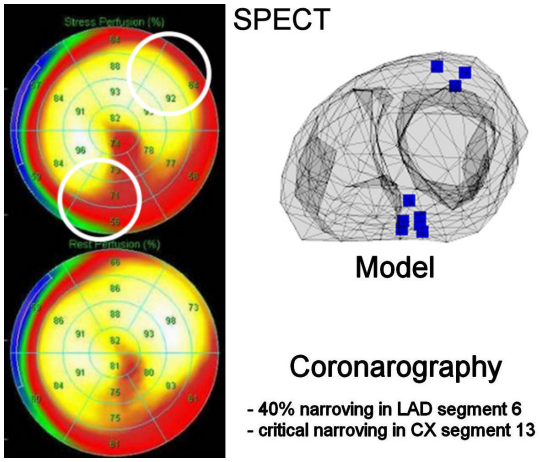

Fig. 4. Comparison of the localization of a double ischemic lesion based on BSPM with SPECT and coronarography results

4. Discussion and Conclusions

The introduced the ProCardio 8 system is intended for BSPM with 64 or more leads. Despite it enables direct cardiac diagnostics based on maps, our previous attempts to detect local ischemic regions by using departure integral maps [4] showed that changes in BSPMs in many cases can hardly be detected. The newer results using model-based approach indicate that this method and the presented device provide promising tools for identification of the presence of local ischemia during exercise. Our current results are based on using BSPM and a general model of the torso geometry. The use of patient individual torso could further improve the accuracy of the ischemia identification [5]. Hence also the possibility to create patient torso model from CT or MR data will be included in the ProCardio software in the future.

Acknowledgements

The work was supported by the research grant 2/0131/13 from the VEGA Grant Agency and by the grant APVV-0513-10 from the Slovak Research and Development Agency.

References

[1] Hanninen H, et al. ST-T integral and T-wave amplitude in detection of exercise-induced myocardial ischemia evaluated with body surface potential mapping. *J. of Electrocardiology*, 2003, 36, 89.

[2] Rosik V, Tysler M, Jurko S, Raso R, Turzova M: Cardio 7 - Portable System for High Resolution ECG Mapping. *Studies in Health Technology and Informatics*, 2002, 90, 41 - 46.

[3] Tyšler M, Turzová M, Švehlíková J, Hebláková E: Noninvasive identification of ischemic lession in the heart. *Advances in Electrical and Electronic Engineering*, 2005, 4, 124-127.

[4] Filipova S, Tysler M, Turzova M, Rosik V.: Reference ECG-mapping etalons improve the diagnostic accuracy of myocardial ischemia according to departure isointegral surface maps. *Int. J. of Bioelectromagnetism*, 2003, 5, 369 - 370.

[5] Lenkova J., Svehlikova J., Tysler M.: Individualized model of torso surface for the inverse problem of electrocardiology. *J. of Electrocardiology*, 2012, 45, 231 - 236.

Mobile Smart Specialization of Optodigital Shape, Color and Spectral Measurements in Industry, Biology and Medicine

D. Hofmann, P-G. Dittrich, E. Düntsch, D. Kraus, D. Görlich

SpectroNet c/o Technology- and innovation Park Jena GmbH, Jena, Germany,
Email: d.hofmann@spectronet.de

Abstract. *Information specific topics in research and development, application and training are changing fairly quickly. The special task for researchers and developers as well as for users and trainers is to stay informed about new methods and technologies in their field of work. In the Internet there are many information sources for researchers and developers as well as for users and trainers. But it is difficult to find and filter the appropriate information anytime anywhere on demand. Smart factories and laboratories, the Internet of things and individualized medicine are on the way. Mobile smart optodigital measurements are essential links in their supply chains. Aim of the paper is to show that smart specialization is one method to increase the labour productivity in measurement theory and practice, education and training in the era of measurement 4.0. Practical examples are given for mobile smart optodigital shape, color and spectral measurements in industry, biology and medicine.*

Keywords: Shape, Color, Spectral, Imaging, Industry, Biology, Medicine

1. Introduction

The computer market is changing. Miniaturization and mass production are in progress. The special advantages of smartphones and/or smartpads are their mobility and their multitouch user interfaces. Market leaders currently are Apple with iOS operation system and Google with Android operation system. Microsoft with Windows 8 operation system is a late follower (Fig. 1a). The innovative computers are equipped with consumerized interfaces for wired and/or wireless communications (Fig. 1b). Smartphones and/or smartpads are also equipped with powerful internal hardware apps for image acquisitions that are light sources, cameras, camcorders and scanners. Smartphones and smartpads are mobile because they are light weight and battery powered. In addition, the number, quality and diversity of external hardware apps for smartphones and/or smartpads are increasing. In the next chapters selected examples will be given for optodigital hardware apps and digital software apps which are applicable for industrial, biological and medical measurements as well as for scientific investigations or mobile education and training in measurements.

Fig. 1a Innovative mobile computers

Fig. 1b Innovative mobile interfaces

2. Mobile Optodigital Hardware Apps for Shape, Color and Spectral Measurements

In industrial, biological and medical measurements as well as in measurement science, measurement education and measurement training shape, color and spectrum are playing significant roles. Typical buzz words are microscopy, colormetry and spectrometry. Up to now it is usual to transfer the objects of interest for special investigations into laboratories. The fundamental reasons are the mass (weight) of the measuring instruments and their power supply. With smartphones and smartpads the situation can be changed enormously. Microscopes, colormeters and spectrometers with smartphones and smartpads can be directly applied in-field or at the point-of-care. Practical solutions for hardware apps are shown in the following figures (Fig. 2a, Fig. 2b, Fig. 2c, Fig. 2d). For easier use, the sources are indicated [1]. For biomedical measurements increasingly microfluidic components are used (Fig. 2e). Several practical examples have been compiled in the platform of the specialized international innovation cluster SpectroNet [2], [3], [4], [5].

Fig.2a Mobile optodigital scanner

Fig.2b Mobile optodigital microscope

Fig. 2c Mobile optodigital colormeter

Fig.2d Mobile optodigital spectrometer

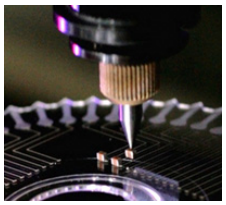

Fig.2e Mobile microfluidic module

3. Mobile Digital Software Apps for Shape, Color and Spectral Measurements

Smartphones and /or smart pads and cloud computing are unbeatable conditions for mobile software apps. These innovative conditions have never been existed before the year 2013 taking into account that most laboratory software packages are running under Microsoft Windows operation systems. It has been proved that multi-touch Windows 8 is in most cases downwards compatible. Practical solutions for software apps are shown in the following figures (Fig. 3a, Fig. 3b, Fig. 3c). For easier use, the sources are indicated [1].

Fig. 3a Software apps for shape measurements

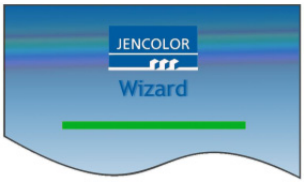

Fig. 3b Software apps for color measurements

Fig. 3c Software apps for spectral measurements

4. Modularized Applications for Shape, Color and Spectral Measurements

In combination of the contents of chapter 1, 2 and 3 now the practical solutions for innovative mobile modularized hybrid measuring instruments can be shown (Fig. 4, Fig. 4b and Fig. 4c). A very special solution is the immunoassay (Fig. 4d) which has been explained in detail in source [1].

Fig. 4a Mobile smart shape measurements

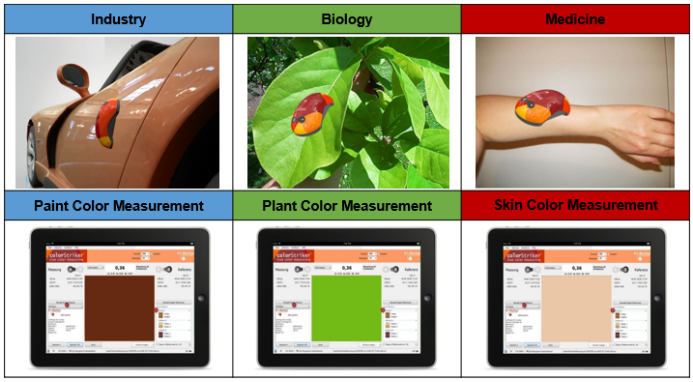

Fig. 4b Mobile smart color measurements

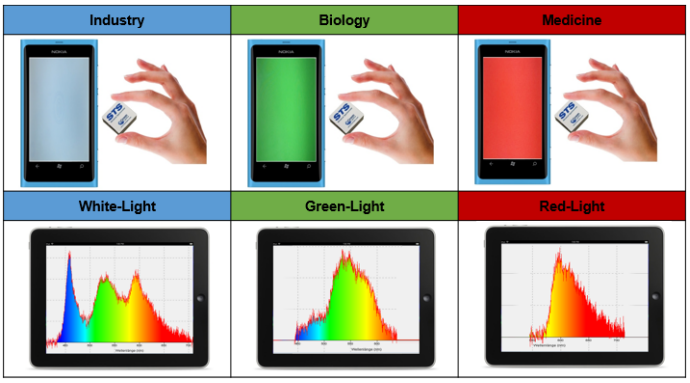

Fig. 4c Mobile smart spectral measurements

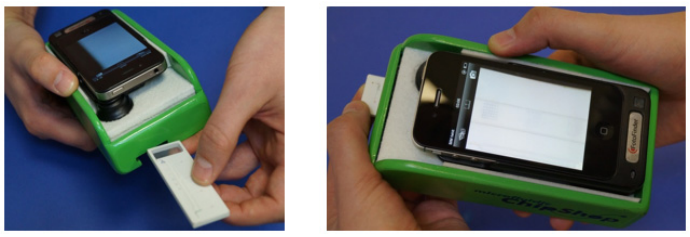

Fig. 4d Colorimetric immunological detection

5. Mobile Smart Education and Training for Shape Color and Spectral Measurements

In modern education and training are the actuality and applicability of the biggest challenges. Networking and web services are recommendable. For these purposes optodigital papers and presentations, trailers and videos in the field of shape, color and spectal measurements have been stored for open use in www.spectronet.de (Fig. 5a). Supplementary optodigital channels with companies, experts and keywords in the fields of optodigital shape, color and spectal measurements have been elaborated (Fig. 5b and Fig. 5c) [6], [7], [8].

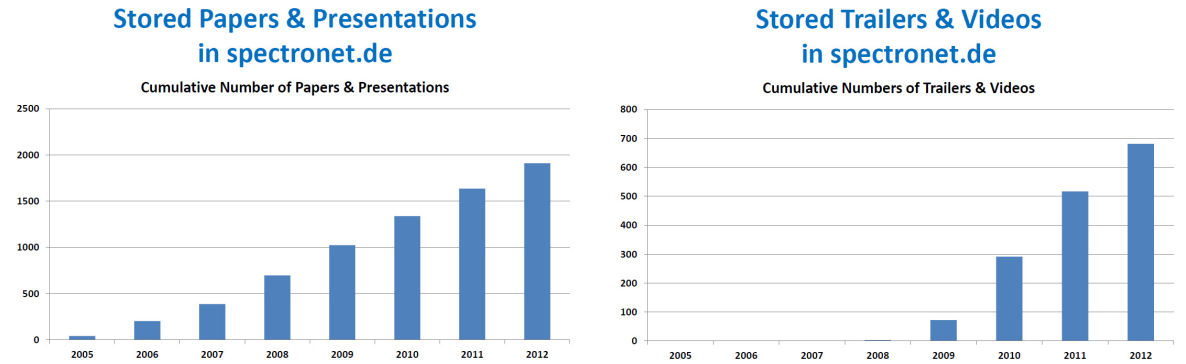

Fig. 5a Cumulative numbers of papers, presentations and videos in spectronet.de

Fig. 5b Opt digital channels with companies and experts

Fig. 5c Optodigital channels with keywords in spectronet.de

6. Conclusions

Smartphones and Smart pads became global mass products with great convenience, high reliability and affordable prices. These market developments enable a paradigm shift in industrial, biological and medical measurements. With modular hardware apps and software apps new classes of hybrid measurement instruments can be created. Modular hardware apps and software apps are reducing development time, cost & risk. Smartphones & smart pads are revolutionary game changers in lifestyle and work style. Miniaturization & consumerization inspire each other with increasing speed. Field instrumentations will be based on re-invented laboratory instrumentations. First steps on innovative routes are already gone successfully. An interesting convergence of measurements in industry, biology and medicine can be expected.

References

[1] http://spectronet.de/portals/visqua/story_docs/vortraege_2013/130202_photonics_west/130202_hofmann_spectronet.pdf

[2] http://spectronet.de/portals/visqua/story_docs/vortraege_2013/130202_photonics_west/130202_01_becker_mfcs.pdf

[3] http://spectronet.de/portals/visqua/story_docs/vortraege_2013/130202_photonics_west/130202_02_becker_mfcs.pdf

[4] http://spectronet.de/portals/visqua/story_docs/vortraege_2013/130202_photonics_west/130202_03_becker_mfcs.pdf

[5] http://spectronet.de/portals/visqua/story_docs/vortraege_2013/130202_photonics_west/130202_ozcan_ucla.pdf

[6] http://spectronet.de/de/unternehmen/

[7] http://spectronet.de/de/experten/

[8] http://spectronet.de/de/keywords/

Mesurement of Physical Quantities

Redetermination of the Abbe Errors' Uncertainty Contributions at the Nanometer Comparator

R. Köning, C. Weichert, P.Köchert, J. Guan, J.Flügge

Physikalisch-Technische Bundesanstalt (PTB), Braunschweig, Germany
Email: rainer.koening@ptb.de

Abstract. *The measurements of the angle deviations of the measurement slide and the determination of the measurement line were repeated in the course of the ongoing upgrade of the Nanometer Comparator, the current line scale interferometer of the PTB. The results show that the use of calibrated angle interferometers in angular control loops reduces the angle deviations significantly, but does not eliminate them completely. The Abbe offsets and the position of the measurement line of the interferometer in the vacuum enclosure are determined with the aid of a high resolution incremental encoder. Finally, we demonstrate that by aligning the measurement object to the measurement line and by closing the angular control loops, the Abbe errors can be reduced to negligible levels even for the most demanding dimensional metrology tasks.*

Keywords: Line Scale Interferometer, Vacuum Interferometry, Abbe Error, Measurement Uncertainty

1. Introduction

The Nanometer Comparator [1] provides traceable measurements of line scales, photo-masks, incremental encoders and interferometers in the range up to 540 mm with expanded measurement uncertainties of a few nanometer only. This level of uncertainty is reached by operating the optical interferometers, which are well integrated in the mechanical setup, completely in vacuum. In the ongoing upgrade [2] the Nanometer Comparator is equipped with a Zerodur sample carrier that contains a mirror at one sidewall parallel to the measurement direction, which will be used by an additional interferometer to allow straightness reference measurements [2]. In order to determine the mirror topography the TMS method [3] will be implemented.

Abbe errors are important uncertainty sources in many dimensional metrology tasks [4]. They occur if the measurement lines of the measurement object and the reference displacement interferometer do not agree and an angular motion between the two measurement systems occurs during the measurement, e.g. by guidance deviations of a slide. The value of the Abbe error Δx in the measurement direction x is given in first order by

$$\Delta x = d_y \times \Delta\varphi_z + d_z \times \Delta\varphi_y, \quad (1)$$

where

d_y, d_z	Distance between the measurement lines in y, z-direction, Abbe offsets
$\Delta\varphi_y$, $\Delta\varphi_z$	Change of rotation angle about the y- and z-axis, Pitch and Yaw

In order to minimize this uncertainty contribution at the Nanometer Comparator, vacuum angle interferometers and piezoelectric actuators are used together in control loops. Furthermore, for a reliable determination of the remaining Abbe errors, the angle deviations in closed loop mode and the Abbe offsets still need to be determined. Once the Abbe offsets are determined, the location of measurement line of the displacement interferometer is known as well. In order to reduce the Abbe errors even further, in all subsequent measurements, the measurement object will be aligned such that the Abbe offsets nominally vanish. These

experimental investigations have already been performed some years ago [5] but had to be repeated recently, because the new sample carrier adds a substantial amount of weight to the measurement slide and its installation required a realignment of all interferometers.

2. Measurements and Results

Measurement Setup

For the calibration of the angular vacuum interferometers and the determination of the position-dependent angle deviation of the angular control loops a high resolution autocollimator (Möller Wedel HR) was employed. It has been calibrated in the central region about zero with an uncertainty of 44 nrad internally at the PTB [6]. The measurement setup is shown in the left schematic of Fig. 1. Due to its large weight and size, the autocollimator was

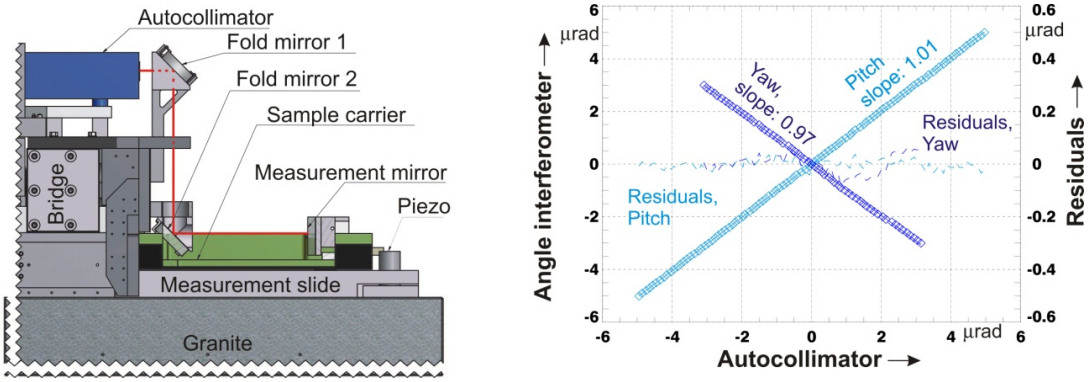

Fig.1. Setup of Autocollimator measurements (left) and the calibration results of the angle interferometers

located on top of the bridge. Its beam was directed by two fold mirrors parallel to the motion axis of the measurement slide and orthogonal to a measurement mirror fixed at the sample carrier. To assure this alignment, a laser beam of 3 mm diameter was aligned parallel to that motion axis by means of a quadrant detector. Then the measurement mirror was aligned using the inference pattern of the incoming and reflected beam. The measurement mirror was aligned until less than one interference fringe remained visible, which is equivalent to a remaining misalignment smaller than 200 µrad.

Calibration of the vacuum angle interferometers

First the angle interferometers need to be calibrated because the distance of their beams, which is required to determine the angle change to be measured cannot be measured with sufficient accuracy directly. Furthermore due to deviations of the beam profile from a Gaussian shape additional deviations are likely to occur. The diagram on the right side of

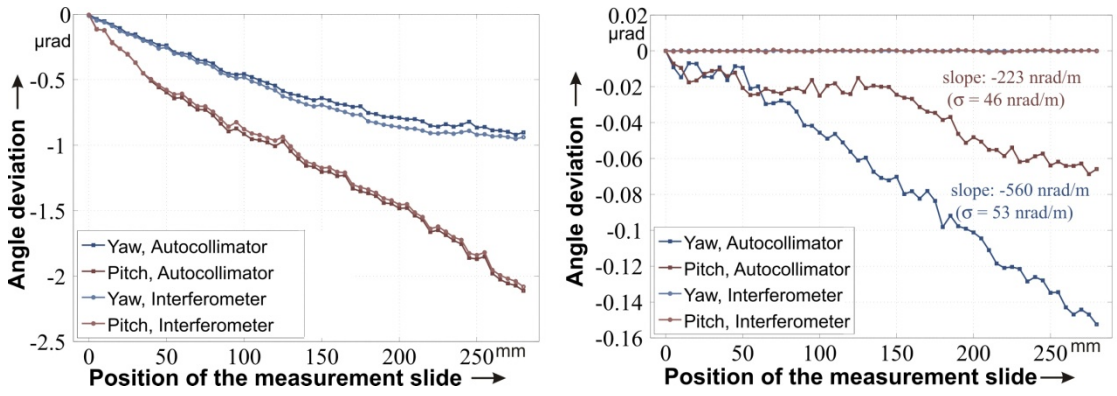

Fig. 2. Dependence of angle deviation on the position of the measurement slide without (left diagram) and with (right diagram) angular control loop.

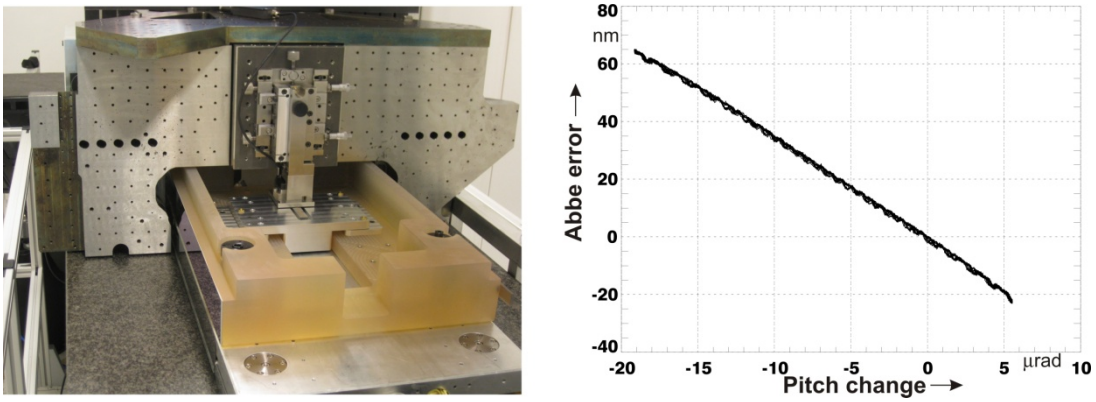

Fig. 3. Image of the measurement setup for incremental encoders (left) and Abbe error introduced by a pitch change with an intentionally enlarged Abbe offset (right)

Fig. 1 shows the results of a calibration of both angle axes at a fixed position within the measurement range. For this purpose the angular orientation of the measurement slide was changed by the piezoelectric elements and the resulting angular motion was measured by the autocollimator and the interferometer. The calibration constant varied a few percent if the calibration was repeated at different positions of the slide. The obtained variation of the calibration constant was within the scattering range observed if the experiment is repeated at the same location.

Determination of the Position-dependent Angle Deviation in Closed Loop Mode
During the length measurements the angular control loops are closed to maintain the angular orientation of the measurement slide. In this case the angle deviations measured by the autocollimator, which occur while moving the slide over the measurement range, has to be taken into account for the determination of uncertainty contribution of the Abbe error. Fig.2 shows the dependence of angle deviations in open and closed mode on the position of the measurement slide. The measurement range was limited by the position of the measurement mirror in the sample carrier to 280 mm. But this still comprises the measurement range used for the most accurate measurements. However, the right diagram reveals that the use of the control loops reduces the angle deviations by more than a factor of 10, but does not eliminate them completely. This leads to an uncertainty contribution of 73 nrad for the yaw interferometer and 51 nrad for the pitch interferometer.

Determination and Reduction of the Abbe Offsets, Measurements using an Incremental Encoder
Abbe errors can be observed instantly if another displacement sensor is compared to the displacement interferometer of the Nanometer Comparator. If an angle change is introduced by the piezoelectric elements intentionally and reported in addition to the related Abbe error then the Abbe offset can be determined as well. Here, a high resolution incremental encoder (Heidenhain LIP 382), which already has proven to be a valuable tool in the characterization of the displacement interferometer [7], was used again. An image of the setup is shown in the left part of Fig. 3. An example of the Abbe error caused by a pitch change is illustrated in the right diagram of Fig.3. In this case the incremental system was mounted intentionally about 3 mm above the measurement line of the interferometer. Fig. 4 shows the result of a change of Yaw and Pitch for an optimized alignment of the measurement lines of the incremental encoder and displacement interferometer of the Nanometer Comparator. The remaining Abbe offsets d_z and d_y are estimated to -0.03 mm and 0.16 mm, respectively.

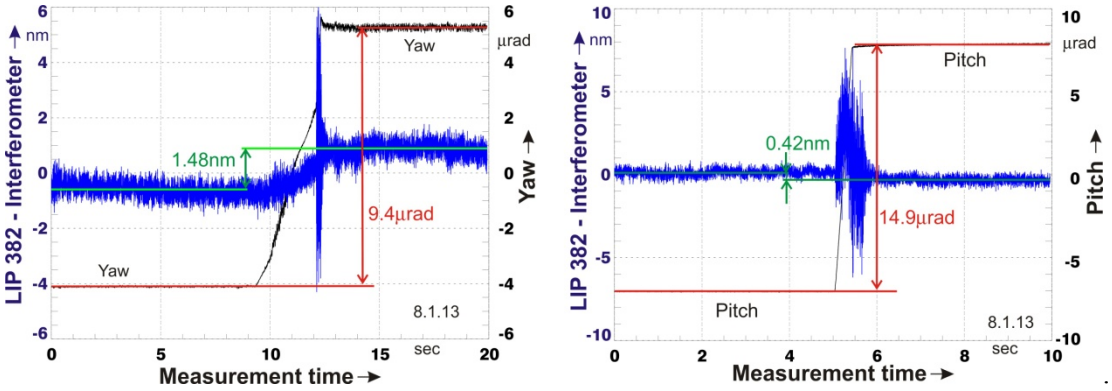

Fig. 4. Remaining Abbe errors after an optimized alignment

3. Conclusions

The results of Fig. 2 show that position-dependent angle deviations occur although calibrated angular interferometers are used in control loops to correct them. A further discussion of the origin of these deviations and the limitations of the whole approach is beyond the scope of this paper. However, these deviations lead to residual Abbe errors, which need to be included in the measurement uncertainty estimation. In order to reduce this uncertainty contribution even further, we demonstrated that the piezoelectric actuators and the angle interferometers can be used to optimize the alignment of the measurement object, so that the Abbe offsets almost vanish. In this case the remaining uncertainty contribution, even if calculated under worst case assumptions (all length dependent angle deviations are caused by the angle interferometer, both contributions added and uncertainty of the calibration included as well), remains negligible.

This approach can be applied as well to other dimensional metrology systems equipped with angular control loops. It allows not only the reduction of the Abbe errors but also to determine the Abbe offsets and the remaining Abbe uncertainty contributions in a reliable way.

References

[1] Flügge J, Köning R, Status of the nanometer comparator at PTB. In proceedings of the conference "Recent Developments in Traceable Dimensional Measurements" edited by Decker J E and Brown N; 2001, SPIE Vol. 4401, 275-283, and references there in.

[2] Flügge J, Köning R, Weichert C, Häßler-Grohne W, Geckeler R D, Wiegmann A, Schulz M, Elster C, Bosse H.: Development of a 1.5D reference comparator for position and straightness metrology on photomasks. In proceedings of Photomask Technology, 2008, Proc. SPIE 7122, 71222Y

[3] Elster C, Weingrätner I and Schulz M. Coupled distance sensor systems for high-accuracy topography measurement: Accounting for scanning stage and systematic sensor errors, Precision Engineering 30 (2006) 32–38

[4] Köning R Flügge J and Bosse H. A method for the in situ determination of Abbe errors and their correction, 2007, Meas. Sci.Technol. **18** 476 – 481

[5] Flügge J, Köning R, Bosse H. Angle metrology and measurement of high resolution linear encoders on the PTB Nanometer Comparator. In proceedings of 4th Euspen, 2004,p.272-273

[6] Just A, Krause M, Probst R, Wittekopf R. Calibration of high resolution electronic autocollimators against an angle comparator, 2003, Metrologia 40, 288 - 294

[7] Köning R, Flügge, J Bosse H. Characterizing the performance of the PTB line scale interferometer by measuring photoelectric incremental encoders. In proceedings of Recent developments in traceable dimensional measurements, San Diego, Proc. SPIE; 5879; ISBN 08194-5884-8,2005, p. 5879 – 08

Imaging and Mapping of Thin Layer Organic Materials Using Magnetic Resonance Imaging Methods

I. Frollo, T. Dermek, P. Andris

Institute of Measurement Science, SAS, Bratislava, Slovakia
frollo@savba.sk

Abstract. *Thin organic samples were placed into the homogenous magnetic field of an imager based on nuclear magnetic resonance. Several samples like oil slicks and soft magnetic material (cut from a data disc) were tested. Theoretical computations based on a magnetic double layer were performed. For experimental verification an MRI 0.2 Tesla ESAOTE Opera imager was used. For experiments a homogeneous rectangular parallel piped block (reference medium) - a container filled with doped water - was used. The resultant image corresponds to the magnetic field variations in the vicinity of the samples. For data detection classical gradient-echo imaging methods, susceptible to magnetic field inhomogeneities, were used. Experiments proved that the proposed method is perspective for thin organic and soft magnetic material testing using magnetic resonance imaging methods (MRI).*

Keywords: Thin Organic Samples, Weak Magnetic Material, Magnetic Resonance Imaging, Gradient Echo

1. Introduction

Imaging methods used for biological and physical structure, based on Nuclear Magnetic Resonance (NMR), have become a regular diagnostic procedure. Specific occurrence is observed when a thin layer organic or inorganic object is inserted into a static homogeneous magnetic field. This results in small variations of the static homogeneous magnetic field near the sample. It is possible to image the magnetic contours caused by the sample using a special rectangular phantom filled with a water-containing substance near the sample. The acquired image represents a variations of the basic homogeneous magnetic field of the imager superimposed with NMR signals directly detected from the sample.

Description of the first attempt of a direct measurement of the magnetic field variations utilizing the divergence in gradient strength that occurs in the vicinity of a thin current-carrying copper wire was introduced in [1]. A simple experiment with thin, pulsed electrical current-carrying wire and imaging of a magnetic field, using a plastic sphere filled with agarose gel as phantom, was published in [2]. Single biogenic soft magnetite nanoparticle physical characteristics in biological objects were introduced in [3]. It was shown that for susceptibility imaging one need to measure local magnetic field variations of the basic magnetic field of the imager representing sample properties [4].

In this paper an imaging method used for thin organic and soft magnetic material detection was proposed. Computation of the magnetic field variations based on double layer magnetic theory and a comparison of theoretical results with experimental images were performed.

2. Subject and Methods

We suppose that the thin layer sample is positioned in the x-y plane of the rectangular coordinate system (x, y, z) and the thickness of the layer is neglected. According to Fig.1a the layer is limited by lengths of $2a$ and $2b$, with the left - right symmetry. The basic magnetic field B_0 of the NMR imager is parallel with the +z axis. The task is to calculate the $B_z(x,y,z)$ component of the magnetic field in the point $A[x_0, y_0, z_0]$.

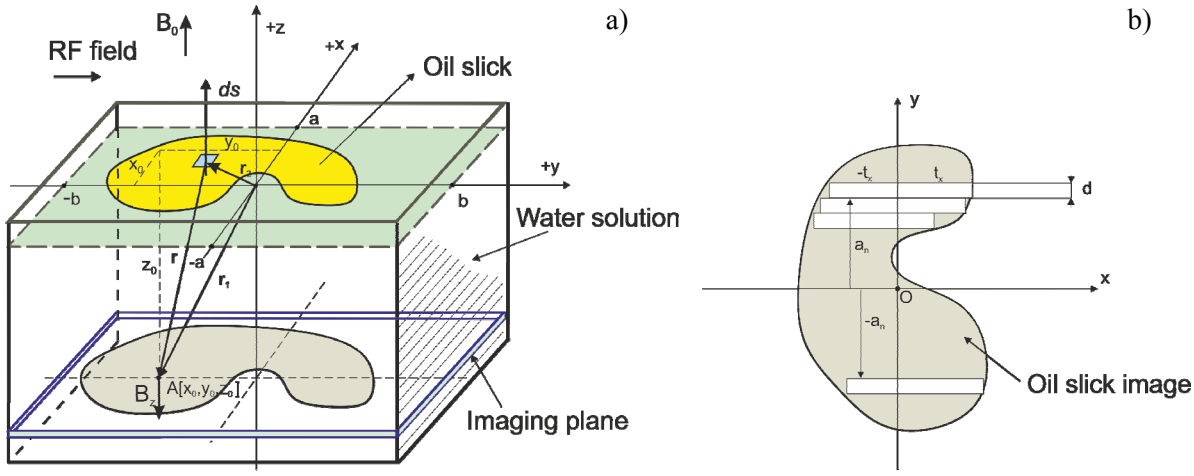

Fig. 1. a) Theoretical configuration of the thin layer sample positioned in x-y plane of the rectangular coordinate system. In calculations the thickness of the layer and imaging planes are neglected. b) Oil slick thin layer sample positioned in x-y plane of the rectangular coordinate system. Principles of incremental elements integration.

For theoretical calculation of a thin layer sample the magnetic double layer model can be considered to have magnetic dipoles continuously distributed on surface ds. Magnetic double layer is considered having a homogeneous density of the dipole moment that is oriented in every point in the direction of surface normal vector perpendicular to the layer surface. Bearing in mind the superposition principle, it is possible to express the vector potential of the double layer in the shape of surface integral:

$$\mathbf{A}(\boldsymbol{r}) = \frac{\mu_0}{4\pi} M_S \int_S \frac{\mathrm{d}\boldsymbol{S} \times \boldsymbol{r}}{r^3} = -\frac{\mu_0}{4\pi} M_S \int_S \operatorname{grad} \frac{1}{r} \times \mathrm{d}\boldsymbol{S} \ . \tag{1}$$

Using general formula for vector potential and magnetic induction $\mathbf{B} = \operatorname{curl} \mathbf{A}$, we get the final formula for magnetic induction of the magnetic double layer, which is also applicable for the closed current loop calculation as follows:

$$\mathbf{B} = -\frac{\mu_0 I}{4\pi} \oint \frac{\mathbf{r} \times d\mathbf{s}}{r^3} = \frac{\mu_0 I}{4\pi} \int_S \left(\frac{3\mathbf{r}.\mathbf{r}}{r^5} - \frac{\mathbf{I}}{r^3} \right) d\mathbf{S} , \tag{2}$$

where **r** - is a position vector, I - is a current equivalent to planar density of a dipole moment of the magnetic double layer. Assuming the position vectors according to Fig.1 we can write:

$$\mathbf{r} = \mathbf{r}_1 - \mathbf{r}_2 \qquad \text{and} \qquad \mathrm{r} = \sqrt{(\mathrm{x}_0 - \mathrm{x})^2 + (\mathrm{y}_0 - \mathrm{y})^2 + (\mathrm{z}_0 - \mathrm{z})^2} \ . \tag{3}$$

The final formula in a double integral form is in the following shape:

$$\mathrm{B}_z(\mathrm{x},\mathrm{y},\mathrm{z}) = \frac{\mu_0 I}{4\pi} \int_{-a}^{a} \left[\int_{-b}^{b} \frac{3 - I}{\left[(x_0 - x)^2 + (y_0 - y)^2 + (z_0 - z)^2 \right]^{\frac{3}{2}}} dy \right] dx \ , \tag{4}$$

where limits for integration are: [-a, a] and [-b, b].

Numerical evaluation of Eq. 4 in analytical form is relatively complicated. After integration one obtaines relatively huge and problematical expressions. To calculate the general resultant expressions in analytical and numerical form and to obtain the final graphical interpretation of the $B_z(x,y,z)$ component we used a simplified incremental calculation model using rectangular elements, see Fig.1b.

For the final numerical calculation the following simplifying conditions were assumed: thickness of the layer is negligible and for the graphical interpretation of a rectangular magnetic double layer sample we assume the following relative values: $\mu_0 I / 4\pi = 1$, position of the imaging plane $z_0 = 3.2$, dimmensions of the magnetic double layer t_x and $-t_x$ were asigned proportional to real slick thin layer dimensions.

The final simplified formula for incremental calculation using rectangular elements is in the form:

$$B_z(x,y,z) = \sum_{-n}^{+n} \int_{-t_x}^{+t_x} \left[\int_{\pm a_n}^{\pm a_n \pm d} \frac{1}{\left[(x_0 - x_t)^2 + (y_0 - y_n)^2 + (z_0)^2 \right]^{\frac{3}{2}}} dy \right] dx \qquad (5)$$

The resultant 3D and 2D plots of relative values of magnetic field for {x0, -40, 40} and {y0, -4, 36} are depicted in Fig.2. The experimental results confirmed that the density plot representation corresponds best with the obtained MR image, see Fig.2 right.

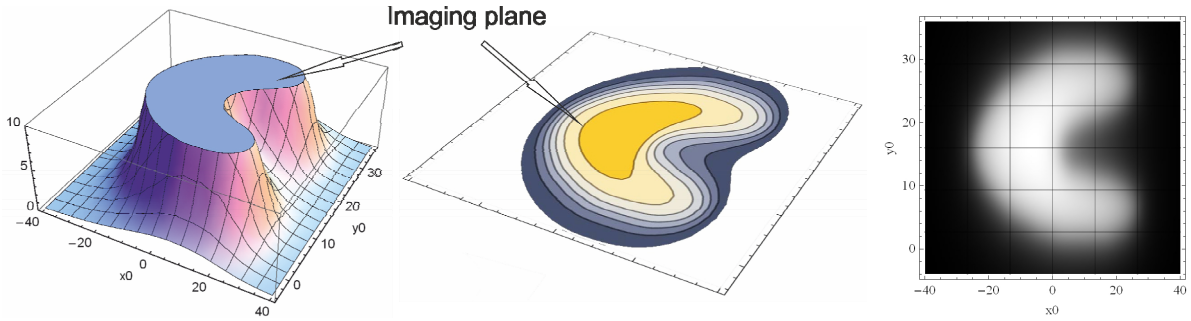

Fig. 2. Calculated magnetic field variations near the organic slick sample positioned in the x-y plane of the rectangular coordinate system, relative values. Left: 3D-plot. Centre: Contour plot. Right: Density plot.

3. Experimental Results

As a physical object, oil slick (dimensions 75 x 60 mm) was used. For comparison, a soft magnetic sample from a data disc, thickness 82 μm and a thin copper wire formed in the shape of an oil slick were used, Fig.3. The samples were placed at the centre of a rectangular plastic holder – homogeneous phantom filled with liquid containing 5 mM $NiCl_2$ + 55 mM NaCl in distilled water.

Fig. 3. Left: Image of the oil slick, GRE imaging sequence, TR = 800 ms, TE = 10 ms, slice thickness 2 mm. Center: Image of the soft magnetic sample, GRE, TR = 400 ms, TE = 10 ms, slice thickness 2 mm. Right: Image of the thin coil wire up into the oil slick shape, DC current 20 mA, GRE, TR = 500 ms, TE = 10 ms.

4. Discussion and Conclusion

A modified method for mapping and imaging of the planar organic samples and weak magnetic inorganic samples placed into the homogenous magnetic field of an NMR imager was proposed. First experiments showed the suitability of the method even in the low-field MRI. The goal of this study was to propose an MRI method used for soft magnetic material detection. Computation of the magnetic field variations based on double layer magnetic theory showed acceptable correspondence of theoretical results with experimental images.

Mathematical analysis of an oil slick shape object, representing a shaped magnetic double layer, showed theoretical possibilities to calculate magnetic field around any type of sample. Calculated 3D images showed expected shapes of the magnetic field in the vicinity of the double layer samples. Density plot images showed magnetic field variations caused by samples placed into the homogeneous magnetic field of the NMR tomograph, very similar to the images gained by magnetic resonance imaging using a GRE measuring sequence.

The experiments proved that it is possible to map the magnetic field variations and to image the specific structures of thin samples using a special rectangular holder. The shapes of experimental images, Fig.3, correspond to the real shapes of the samples. Some of the resultant images are encircled by narrow stripes that optically extend the width of the sample. This phenomenon is typical for susceptibility imaging, when one needs to measure local magnetic field variations representing sample properties [4].

The experimental results are in good correlation with the mathematical simulations. This validates the possible suitability of the proposed method for detection of selected thin layer organic materials using the MRI methods. Presented images of thin objects indicate perspective possibilities of this methodology even in the low-field MRI.

The proposed method could be used in a variety of imaging experiments, e.g., on very silky samples, textile material treated by magnetic nanoparticles, biological samples, documents equipped with hidden magnetic domain, magnetic tapes, credit cards and travel tickets with magnetic strips, banknotes, polymer fibres treated by a solution of nanoparticles in the water used in surgery, and more.

Acknowledgements

The financial support by the Grant Agency of the SAS, project no. VEGA 2/0090/11, ITMS project No. 26240220073 and APVV–0513–10 is gratefully acknowledged.

References

[1] P. T. Callaghan, J. Stepisnik, Spatially-distributed pulsed gradient spin echo NMR using single-wire proximity. *Physical Review Letters,* 75, 4532-4535, 1995.

[2] M. Sekino, T. Matsumoto, K. Yamaguchi, N. Iriguchi, S. Ueno, A method for NMR imaging of a magnetic field generated by electric current. *IEEE Transactions on Magnetics*, 40, 2188-2190, 2004.

[3] O. Strbak, P. Kopcansky, M. Timko, I. Frollo, Single biogenic magnetite nanoparticle physical characteristics. A biological impact study, *IEEE Transactions on Magnetics,* 49, 457-462, 2013.

[4] E. M. Haacke, R. W. Brown, M. R. Thompson, R. Venkatesan, Magnetic Resonance Imaging: Physical Principles and Sequence Design, first ed. Wiley-Liss, John Wiley and Sons Ltd, United States, 1999.

Investigation of the Influence of the Dynamic Mechanical Loads on the Crystalline Structure of Photovoltaic Cells

[1,2]V. Novickij, [3] V. Višniakov, [4]A. Kilikevičius, [1,2] J. Novickij, [1,2]A. Grainys, [2]P. Zapolskis

[1]High Magnetic Field Laboratory, VGTU, Vilnius, Lithuania,
[2]Department of Electrical Engineering, VGTU, Vilnius, Lithuania,
[3]Institute of Welding and Material Science, Vilnius, Lithuania,
[4]Department of Machine Engineering, VGTU, Vilnius, Lithuania,
Email: vitalij.novickij@vgtu.lt

Abstract. *The efficiency of modern photovoltaic systems is strongly reduced when the crystalline structure of the solar cells is being damaged due to extensive mechanical stress caused by climatic factors such as heavy wind or snow. In this work the measurement and experimental setup has been applied to produce dynamic mechanical loads in order to simulate various weather conditions and investigate the reliability of the solar panels when they are subjected to stress. During experiments the solar panels have been treated up to 20 Hz vibrations with the maximum magnitude of the shift of the solar panel in the range of 0 - 0.3 mm. The acquired experimental data using electroluminescence setup showed appearance of micro fractures in the crystalline structure of the photovoltaic modules.*

Keywords: Solar Cells, Degradation, Measurement of Mechanical Stress, Reliability, Climatic Stress Simulation

1. Introduction

Reliability is a crucial parameter of photovoltaic systems and there are a number of standards covering the maximum allowed performance reductions influenced by heavy mechanical stress [1, 2]. During heavy mechanical loads the crystalline structure of the photovoltaic modules is damaged and the micro fractures appear, which negatively affect the conversion effectiveness of the energy of light into electricity and stimulates further degradation of the module [3]. In order to meet the standards and estimate the degradation ratio the measurement setup must be developed, which could allow accurate prediction and accumulation of statistical data of the solar cell performance in harsh weather conditions and under heavy dynamic mechanical loads. The area of research is new and still lacks accurate statistical and experimental data of mechanical stress influence on the appearance of micro cracks in the photovoltaic modules. In this work a computer controlled vibrational stand and an array of 3-axis mechanical stress evaluating sensors has been applied in order to investigate the influence of dynamic mechanical loads on the crystalline structure of a typical solar cell.

2. Subject and Methods

As it was mentioned above in order to simulate the mechanical stress the photovoltaic module might be experiencing in the real weather conditions a vibrational stand has been used. The alteration of the magnitude and the frequency of the vibrations allows to simulate dynamic mechanical stress due to burst of heavy wind the photovoltaic modules may be experiencing. In the experimental setup the solar panel has been attached to the shaker and the arrays of 3-axis mechanical stress sensors have been applied to the solar panel corners, the back plate, the middle point and the shaker itself. The block diagram of the resultant dynamic mechanical load generating facility is shown in Fig. 1. The position and the quantity of sensors that are shown in the block diagram do not scale with the prototype facility and are shown for

schematic purposes. The simultaneous data acquisition, the control of the frequency and the magnitude of the vibrations have been performed and monitored using a computerized setup.

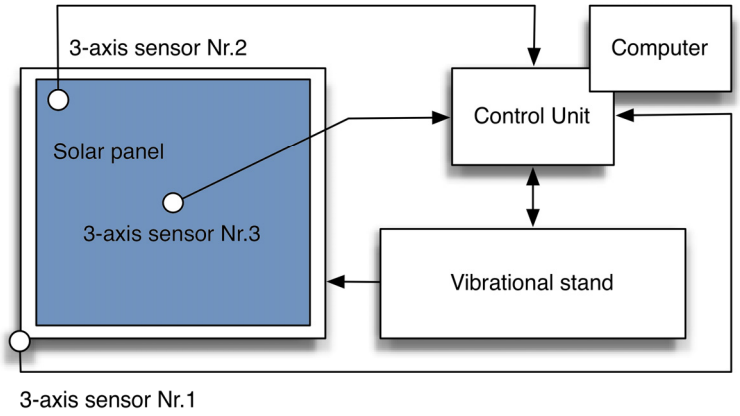

Fig. 1. The block diagram of the dynamic mechanical load generating facility

During experiments the magnitude and the frequency of the vibrations have been altered in the range of 0 – 0.3 mm and 0 – 20 Hz, respectively. The ranges have been selected in accordance to meet the goal of accurate simulation of real weather conditions when short bursts of heavy wind are possible. The maximal values of the parameters were limited by the maximum output characteristics of the shaker. The resultant displacement spectrum in the middle point of the solar panel is shown in the Fig. 2.

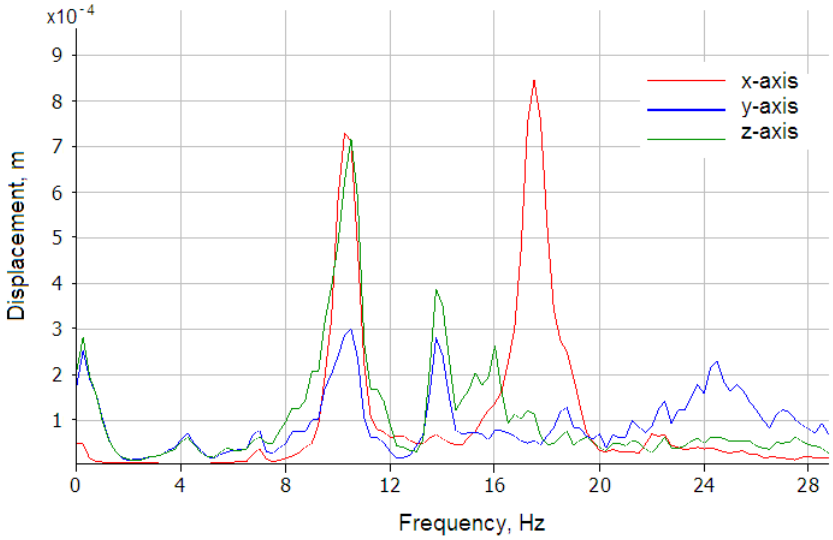

Fig. 2. The displacement spectrum in the middle point of the solar panel

During investigation it was determined that there were two resonance frequencies of 9.8 Hz (displacement amplitude 0.72 mm) and 17.5 Hz (displacement amplitude 0.85 mm). Based on the acquired data the experiment has been narrowed to the two frequencies mentioned above because it was presumed that there was the highest probability of micro fractures in the crystalline structure of photovoltaic cells to occur when the modules are subjected to dynamic mechanical load. The exposure time to the mechanical stress under these conditions has been varied in the range of 0.1 – 3 hours. Each time after exposure the photovoltaic modules have been checked using electroluminescence technique [4]. The modules have been connected to

the 35 V DC power supply and a constant current have been maintained. The resultant luminescence of silicon has been observed using computerized CCD camera in dark room to remove any influence of light on the experiment. During each experiment the number of resultant micro cracks has been calculated and further exposure to mechanical stress has been carried out.

3. Results and Conclusions

A computerized vibrational stand simulating the real weather conditions causing dynamic mechanical stress on the photovoltaic cells has been applied to determine the influence of the mechanical stress on the appearance of micro fractures in solar panels. It was determined that there were two resonance frequencies of vibrations 9.8 Hz and 17.5 Hz, which resulted in the appearance of micro cracks. The appearance of micro cracks inside the crystalline structure of photovoltaic module due exposure to dynamic mechanical loads was analysed using electroluminescence technique. Electroluminescence image after exposure to 0.1 mm 20 Hz vibrations for 45 minutes is shown in Fig. 3.

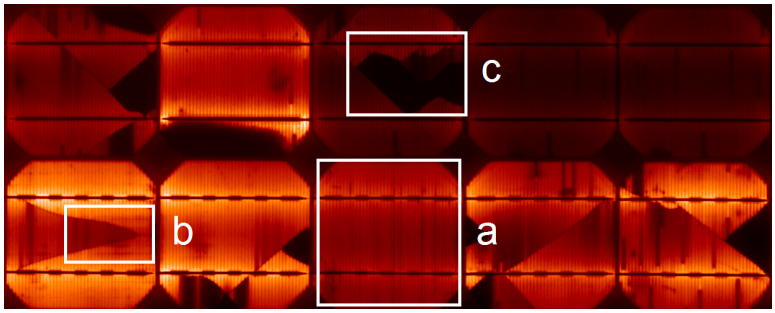

Fig. 3. Appearance of micro cracks inside the crystalline structure of solar cells after exposure to dynamic mechanical stress (a) damage of the reflective layer, (b) appearance of micro cracks, (c) microcracks resulting in appearance of inactive dark spots.

It was shown that low frequency mechanical loads simulating windy weather could cause considerable damage to the photovoltaic cell and therefore reduce the effectiveness of the module. Since the stated working cycle of a photovoltaic cell is assumed to be 15 – 20 years it is crucial to perform express mechanical load tests to ensure decent performance of the system. It assumed that the proposed measurement setup and the acquired data could help supply recommendations for the producers of the modern solar panels and improve the reliability.

References

[1] IEC 61215 2nd. Crystalline silicon terrestrial photovoltaic modules, 2005.

[2] IEC 61646 2nd. Thin-film terrestrial photovoltaic modules, 2008.

[3] Wolden C, Kurtin J, Baxter J, Repins I, Shaheen S, Torvik J, Rockett A, Fthenakis V, Aydil V. Photovoltaic manufacturing: Present status, future prospects, and research needs. *Journal of Vacuum Science & Technology A*, 3 (29), 2011.

[4] Koch S, Kupke J, Tornow D, Schoppa M, Krauter S, Grunow P. Dynamic mechanical load tests on crystalline silicon modules. *25th Photovoltaic Solar Energy Conference and Exhibition*, 2010.

Study of Uncertainty Sources in Incident Angle Dependence of Regular Reflectance and Transmittance using a STAR GEM Accessory

[1,3]E.Kawate, [1,2]M.Hain

[1]AIST, 1-1-1, Tsukuba Central 2, Umezono, Tsukuba, Ibaragi 305-8568, Japan
[2]Institute of Measurement Science, Slovak Academy of Sciences, Bratislava, Slovakia
[3]TRAS, Inc., 725-28 Shimohirooka, Tsukuba, Ibaragi 305-0042, Japan
Email: e.kawate@aist.go.jp

Abstract. *The study of uncertainty sources is carried out to evaluate the performance of a new developed instrument. The sources of the uncertainties are listed according to the uncertainties induced not only by optical scatterings, non-linearity of a detector and imperfections and surface roughness of used ellipsoidal mirrors but also by misalignments concerning many degrees of freedom of translation and rotation of the instrument. Many uncertainties will be estimated by Type A method.*

Keywords: Uncertainty Estimation, STAR GEM, Absolute Reflection, Symmetry X System

1. Introduction

Though a huge number of optical accessories to measure reflectance (*R*) and/or transmittance (*T*) have been proposed and several have been realized [1], an accessory, which is devised to measure both *R* and *T* with the same accuracy, was close to nil [2],[3]. Such an accessory is an important but really difficult product, because the absorptance of non-absorbing samples, which can be obtained from the measured *R* and *T* of specular samples according to energy conservation, should be zero. Furthermore, an accessory, which can measure the incident angle dependence of the absolute *R,* was only a gonio-reflectometer. A new developed STAR GEM accessory can absolutely measure both regular *R* and regular *T* with the same accuracy at an incident angle from 0 to 90 degrees. This paper is a scheme drawing of the uncertainty estimation of *R* measured by the STAR GEM.

2. Description of the STAR GEM

The STAR GEM, which consists of two equivalent belt-shape ellipsoid mirrors of revolution (E1 and E2) in Fig.1, 2 and 3, can continuously change both an angle of incidence and that of collection independently. The STAR GEM, which is constructed on the basis of the Symmetry X idea [3], can absolutely measure both regular *R* and *T* with the same accuracy. These measured *R* and *T* are independent each other, because a rotation angle (ψ) of the RM2 mirror in Fig.2 is automatically fine-turned in order to always search the rotation angel (ψ_0), which gives us the maximum intensity of each signal in every six modes [4].

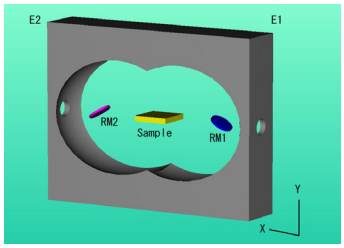

Fig.1. 3D figure of the GEM

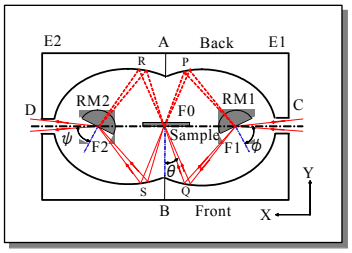

Fig.2. Cross section along meridian plane

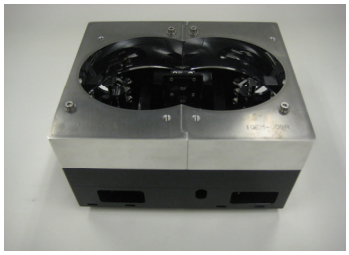

Fig.3. STAR GEM Type1

3. Measurement system

An optical setup to estimate the uncertainty is shown in Fig.4. An illuminator consists of a halogen lamp (HL), a band pass filter (F1), a neutral density filters (F2), a light chopper (LC), a beam-splitter (WW1), a monitor receiver, a space filter (SF), a parabolic mirror (PM1), a beam-splitter (WW2) and a polarizer (PO). The radiant flux through the polarizer enters the STAR GEM Type1 and is focused

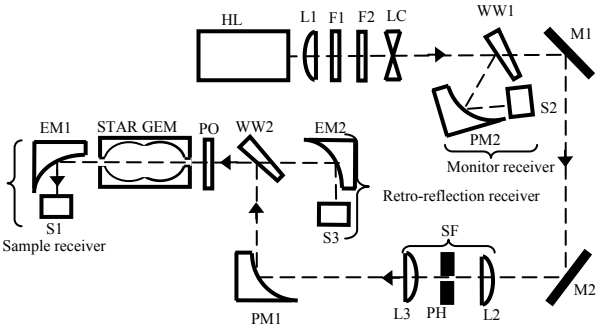

Fig.4. Schematic to measure uncertainty of STAR GEM

on the F1 focus in Fig.2 by the PM1 mirror. After an interaction with the sample or a non-interaction for a background measurement, the exiting flux is measured by a sample receiver. The receiver consists of an ellipsoidal mirror (EM1), a silicon photodiode detector (S1) and a lock-in amplifier. For this study, the RM1 and RM2 mirrors and the STAR GEM itself are held on multi-axes linear and rotational stages. A line connecting between the halogen lamp and the detector is called an external axis. The direction of light propagation is an X-axis and that of sample translation is a Z- axis. A sample was a non-absorbing and parallel-plate fused quartz and its shape was a disk of a 40-mm diameter and 1-mm thickness with specular surfaces.

4. Measurement Equation and Uncertainty Analysis

Although the STAR GEM can measure both R and T, at first we estimate the uncertainty of the reflectance measured by the STAR GEM. This paper treats the case where all variables, Q_1, Q_2, …., Q_N, are independent. A measured R is determined from these variables through a functional relationship f:

$$R = f(Q_1, Q_2, ..., Q_N) \tag{1}$$

The standard uncertainty of r, where r is the estimate of the measured R and thus the result of the measurement, is obtained by combining the standard uncertainties of the variable estimates q_1, q_2,.., q_N. The combined standard uncertainty $u_c(r)$ is the positive square root of the combined variance $u_c^2(r)$,

$$u_c^2(r) = \sum_{i=1}^{N} \left(\partial f \big/ \partial q_i \right)^2 u^2(q_i) \tag{2}$$

where each $u(q_i)$ is a standard uncertainty evaluated in Type A evaluation or in Type B evaluation. The partial derivatives $\partial f / \partial q_i$ are called sensitivity coefficients and are sometimes determined experimentally: one measures the change in R produced by a change in a particular Q_i while holding the remaining variable quantities constant.

5. Sources of uncertainty

One ellipsoidal mirror possesses two foci. This natural feature was considered as a merit for a reflectometer, where a sample and a detector were put on each focus. Until the middle of 1980's, many scientists studied about the reflectometer using a hemi-ellipsoidal mirror. However, all investigations failed and there is no reflectometer using the ellipsoidal mirror today. Dr. K.A. Snail and Dr. L.M. Hansen [1] enumerated eight problems. They are the misalignment of the sample and detector, the inter-reflection between two foci and ellipsoidal mirror imperfections and so on. The sources of the uncertainty exist in the STAR GEM, in the illuminator, in the sample, in the receiver and so on. In the following, each source of uncertainty is chosen to be independent each other and is considered separately.

(A) STAR GEM Type1

(1) Misalignment between the GEM axis and the external axis

Three degrees (X, Y, and Z) of freedom of translation and two degrees (Y-axis and Z-axis) of freedom of rotation induce the uncertainty concerning a misalignment between two axes. The translation along X-axis makes the beam spot on the RM1 mirror blur, because the distance between PM1 and RM1 changes. The translations along Y-axis and Z-axis increase the distance between two axes. The rotations around Y-axis and Z-axis at the center of the F1 focus degenerate the degree of parallelization between two axes. In order independently to estimate the uncertainties of 5 categories, the change in R produced by a change in a particular freedom is measured, while holding the remaining degrees of freedom constant. A remaining degree (X-axis) doesn't induce the uncertainty, because the beam entering into the STAR GEM has the symmetry of rotation around the external axis.

(2) Misalignment between the F1 focus and the RM1 mirror
Two degrees (X and Y) of freedom of translation induce the uncertainty concerning a misalignment between the F1 focus and the RM1 mirror. A degree (Z-axis) of freedom of rotation induces the uncertainty of the incident angle. A remaining degree (Z) of freedom of translation doesn't induce the misalignment because of translation on the RM1 mirror. Another degree (X-axis) of freedom of rotation makes the RM1 mirror tilt to the meridian plane in Fig.2. But this doesn't induce the uncertainty because of the revolving ellipsoidal mirrors. This is an advantage of the STAR GEM but the gonio-reflectometer doesn't possess this. The other (Y-axis) makes the RM1 mirror rotate around its normal, so that this doesn't induce the uncertainty.

(3) Misalignment between the F2 focus and the RM2 mirror
Two degrees (X and Y) of freedom of translation induce the uncertainty concerning a misalignment between the F2 focus and the RM2 mirror. The degree (Z-axis) of freedom of rotation is the rotation of the RM2 mirror and its uncertainty is considered to be zero, because the RM2 is automatically fine-turned in order to always search the rotation angel, which gives the maximum intensity. The remaining three degrees are the same reasons in Sec.(2).

(4) Misalignment between the F0 focus and the sample
Two degrees (X and Y) of freedom of translation induce the uncertainty concerning a misalignment between the F0 focus and the sample. Two degrees (X-axis and Z-axis) of freedom of rotation tilt to the meridian plane and rotate the sample, respectively. The tilt induces the uncertainty concerning a misalignment because of the fall of the Symmetry X system. The rotation induces the uncertainty of not only incident angle but also the position of beam on the E2 mirror especially for the reflection measurement. Two remaining degrees of freedom of Z-translation and Y-axis-rotation don't induce the misalignment but move the beam on the sample surface. These are estimated in Sec. (8).

(5) Inter-scattering in the STAR GEM induced by a transparent sample
When either reflection or transmission measurement of a transparent sample is made, either transmission light or reflection light remains inside the STAR GEM and emerges stray-light due to scattering from the rear of the RM2 mirror, respectively. The intensity is measured by the retro-reflection receiver.

(B) Illuminator
(6) Stray-light of light source
The stray-light is radiant flux that reaches the detector at wavelengths outside the nominal spectral bandwidth of the band pass filter. The intensity of the stray-light is different whether the reflection, the transmission or the background measurements is made, because reflectance and transmittance of the sample aren't equal to unity. The uncertainty is estimated by Type B evaluation.

(7) Uncertainties in wavelength setting and in polarizer setting
The uncertainties are induced due to error of the center wavelength of the band pass filter and due to error of the rotation angle of the polarizer.

(C) Sample
(8) Non-uniformity of the sample
When the non-absorbing and parallel-plate sample is illuminated by incoherent light, there is no parameter concerning the sample thickness, which directly affects the sample signals. The uncertainty, which is induced by the non-uniformity of the sample, is counted by increase of signal noise mentioned in Sec. (13).

(9) Scattering and diffraction from the sample
The scattering and diffraction from the sample induce the uncertainty of sample signals. The intensity is measured by the measurement of the maximum profile.

(D) Receiver
(10) Nonlinearity of the detector
The nonlinearity of the Si-photodiode detector is a possible source of uncertainty. The nonlinearity results in the ratio of the signals not being equal to the ratio of the reaching fluxes. Nonlinearity also may arise within the ranges of the lock-in amplifier.

(11) Non-uniformity of the detector

While the RM2 mirror of the STAR GEM in Fig.2 is rotated little by little angle to find the maximum intensity of each signal in every six modes, the flux exiting from the STAR GEM is focused on the detector by the EM1 mirror in Fig.4 and is moving on the sensitive area of the detector. The non-uniformity of the detector induces the uncertainty.

(12) Retro-reflection from the detector

There is no inter-reflection between two foci of the STAR GEM different from a previous reflectometer using a hemi-ellipsoidal mirror. The reflection from a window of the detector in Fig.4 may cause the retro-reflection through the STAR GEM. The intensity is measured by the retro-reflection receiver.

(E) Others

(13) Signal noise

A signal noise is the result of random processes in both the sample and monitor receivers, in the optical source, in the sample and in the STAR GEM such as imperfections and surface roughness of the GEM.

Table 1 Uncertainty estimations

	Class	Variables	Measurements
A	STAR GEM	14+1	14 degrees of translation and rotation and scattering from the rear of RM2
B	Illuminator	2+1	Two errors and stray-light from the band-pass filter
C	Sample	1	Scattering from the sample
D	Detector	2+1	Two error and scattering from the window of the detector
E	Others	1	Signal noise
Total		$N = 23$	

6. Discussion

There are few papers about uncertainty estimations of optical accessories, except a gonio-reflectometer [5]. Because of the simple structure of the gonio-reflectometer, its estimation of the standard uncertainty of measurement isn't complex. However, it was difficult to construct the STAR GEM, which can measure *R* and *T* spectra with high accuracy. The main sources of the uncertainty are considered to be the optical alignment from our experience. 23 categories for the uncertainty estimations in Table 1 are too many, but 60 % is concerning to the alignments. It is considered that the detailed analysis of uncertainties may make the suggestion of a new construction way and a new alignment method. Next we evaluate the uncertainty of *T* measured by the STAR GEM at the same time and also evaluate the covariance between *R* and *T*. This makes the degree of independence between *R* and *T* clear from the view of the Statistics.

Acknowledgements

The authors thank Hideyuki Tanaka and Katsuhiro Shirono for several useful discussions.

References

[1] Workman J. and Springsteen A.W., APPLIED SPECTROSCOPY, ACCADEMIC PRESS, San Diego, 1997.

[2] Hansen L. Integrating-sphere system and method for absolute measurement of transmittance, reflectance, and absorptance of specular samples. *Applied Optics*, 40, 3196-3204, 2001.

[3] Kawate E. Symmetry X system and method for absolute measurements of reflectance and transmittance of specular samples. *Applied Optics*, 42, 5064-5072, 2003.

[4] Kawate E. and Hain M. (2009). Regular reflectance and transmittance measurements of transmissive materials using a STAR GEM® optical accessory, 20-23 May 2009 (pp. 431-435).

[5] Foo S. C. A Gonio-reflectometer for Measuring the Bidirectional Reflectance of Material for using in Illumination Computation, A thesis of Cornell University, 1997.

An Experimental Method for Predicting the Magnetic Properties of Ferromagnetic Materials Subjected to Harmonic Excitation

M. Kosek, M. Novak, P. Svoboda,

Technical University of Liberec, Liberec, Czech Republic
Email: miroslav.novak@tul.cz

Abstract. *Probably a new method for the full description of ferromagnetic material was tested and verified. It is based on the approximation of waveforms in the time domain by the use of the Fast Fourier Transform (FFT). Usually 10 waveforms give a perfect approximation. In order to predict the waveform or a hysteresis loop, experiments were performed using systematically increasing harmonic excitation. The most important harmonics were selected and their dependence on the applied input voltage was approximated. Thus the waveform can be created from values of harmonics for any voltage. If the voltage step in the experiment is 10 V or lower, a good prediction can be obtained even in the case of strong excitation.*

Keywords: Ferromagnetic Material, Hysteresis Loop Approximation, Harmonic Analysis, FFT

1. Introduction

Non-linearity and hysteresis are typical phenomena of ferromagnetic materials, which make their complete description extremely difficult. Therefore, more or less exact models must be used. The simplest models use several well-known material parameters, but more precise models need a lot of parameters in order to match experimental results.

Two types of model are used: theoretical and experimental. Theoretical models are based on the magnetic domain structure. The well-known Preisach model [1] uses ideal small volume magnets and exhibits all the basic properties of the material. In principle, experimental models approximate the measured characteristics, especially the hysteresis loop. Very often the hysteresis loop is approximated using a high degree polynomial [2], but a combination of other analytical functions is possible [3]. To our knowledge, the approximation of waveforms in a time domain is less well-known. Our approach is based on the approximation in the time and frequency domain. Since the waveforms are periodic (or harmonic), the use of the Fourier series is well suited for this type of approximation.

2. Subject and Methods

The goal of the measurements and the special processing of the measured results is to get a system that makes it possible to predict the time domain waveforms or the hysteresis loops for harmonic excitation. The solution consists of two parts: experimental and theoretical or computational.

The ferromagnetic parameters of UI core transformers were measured and recorded. The laboratory setup for a no-load transformer test is shown in Fig. 1a. The transformer under test (T) was fed from a programmable power supply (PS) Kikusui PCR-2000 LA. The output offset of the power supply was in the range of tens of mV and the produced DC current influenced hysteresis loop symmetry. Therefore, the testing circuit contained a serial capacitor (C) of 3.4 mF in order to stop the DC current flow. Voltages and the primary current were measured by a Norma 5000 power analyzer. The sampling frequency of the analyzer was 1 MSPS. All the instruments were computer controlled. The scanned voltage and current waveforms were downloaded directly to the computer; typical waveforms are in Fig. 1b.

The theoretical part applies time and frequency domain theory. The transition between the domains is achieved using the Fast Fourier Transform (FFT). It must be applied to an integer number of periods. Where the ascending section of the waveforms crossed the *x* axis was used as the criterion of the period start and finish, as shown in Fig. 1b. All the mathematical operations were performed on these well-defined waveforms. The correct numeric integration of the secondary voltage is necessary in order to get the magnetic flux used for the construction of the hysteresis loop.

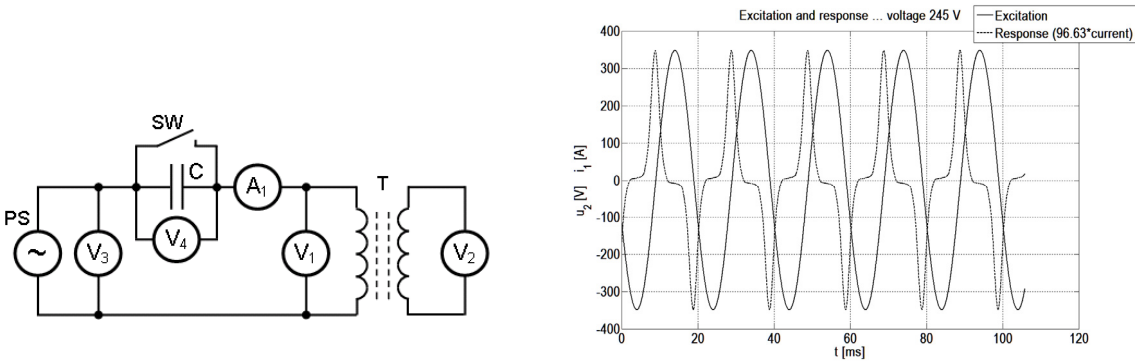

Fig. 1. Experimental part. a) Fully automated laboratory setup, b) Scanned primary current and secondary voltage waveforms.

The waveform spectrum was obtained using FFT. The most important spectral lines were used for the waveform and hysteresis loop approximation. The criterion was a fraction of the most important harmonics; practically, it varies from 1 to 0.1 %. In order to predict the waveform or hysteresis loop the experiment was repeated many times using a slightly higher input voltage on each iteration. From this, the dependence of the most important harmonics on the input voltage was determined. If the dependence is well approximated for every harmonic used, then the waveform or the hysteresis loop for the selected voltage can be produced with a high degree of accuracy. The simplest form of harmonic approximation is achieved using interpolation or polynomial regression.

3. Results

A lot of curves were produced, both from the experimental and theoretical data processing. Therefore, only representative and typical results are shown here in the thematic order: experiment, approximation and prediction. The systematic measurements were made on a soft ferromagnetic material with losses of 1.65 W/kg used as the UI core transformer of windings 360:360 and open circuited secondary winding, see Fig. 1a. The frequencies were 6, 12, 25, 50, 100 and 300 Hz. The amplitude of the input voltage was increased in steps of 2.5 V at 50 Hz or bigger steps at other frequencies. Magnetic field strength and hysteresis loop in Fig. 2 are for every eighth applied voltage in order to be seen clearly. The average curves for one period are shown (see explanation in previous part).

By applying the FFT to waveforms like those in Fig. 2a we get a spectrum. The spectrum lines dependence on the applied voltage is shown in Fig. 3. In Fig 3a several starting odd harmonics are shown. Higher harmonic values are multiplied by a suitable constant to have approximately the same maximum. Fig. 3b shows the 13th harmonic in detail. A harmonic change of order six corresponds to a voltage change from 2.5 to 250 V (order two).

The effect of frequency is presented in Fig. 4. Circuit parameters are used, primary current i and integral u_{int} of secondary voltage, which corresponds to the total Magnetic flux in the core. The width of the loop increases, since the losses increase with frequency.

An approximation was made by the selection of the most significant harmonics. The level of significance is a fraction of the first harmonic; the used fractions were 10, 3, 1, 0.3 and 0.1 %. The results are given in Fig. 5. The criterion of 1% gives an almost perfect approximation.
The goal of this work is the prediction of waveforms and hysteresis loops. The necessary methodology involves the description of the dependence of each harmonic on the input voltage. As shown in Fig. 3, the dependence is very complicated as well as the selection of harmonics to be used in the calculation. Cubic interpolation and fixed harmonics after their sorting were used. The details for the experiment which used a step of 20 V have been omitted as it gave the worst results as shown in Fig. 6. The deviation between the calculation and neighboring experimental curves is visible only in the details.

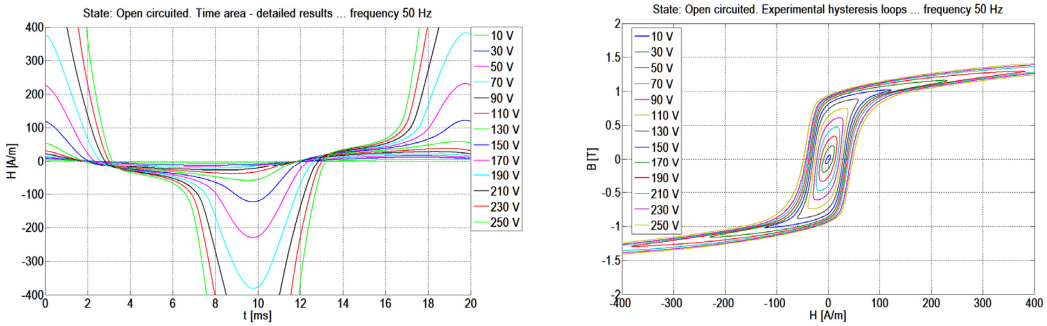

Fig. 2. Experimental results at frequency of 50 Hz. a) Details of field strength waveform. b) Centre part of hysteresis loop.

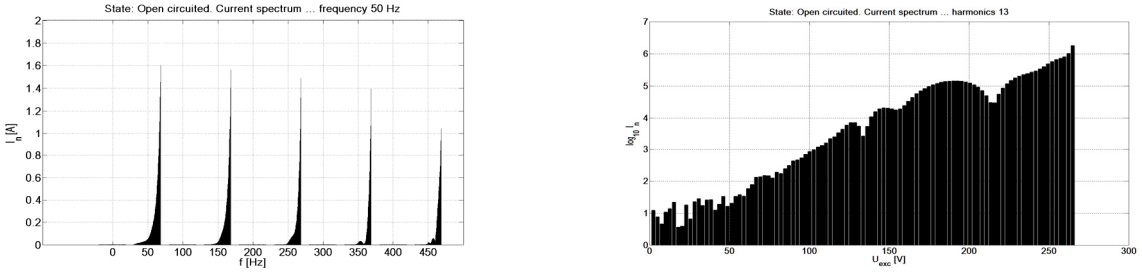

Fig. 3. Waveform spectrum at frequency of 50 Hz. a) First nine harmonics in linear scale. b) Details for 13th harmonics in logarithmic scale.

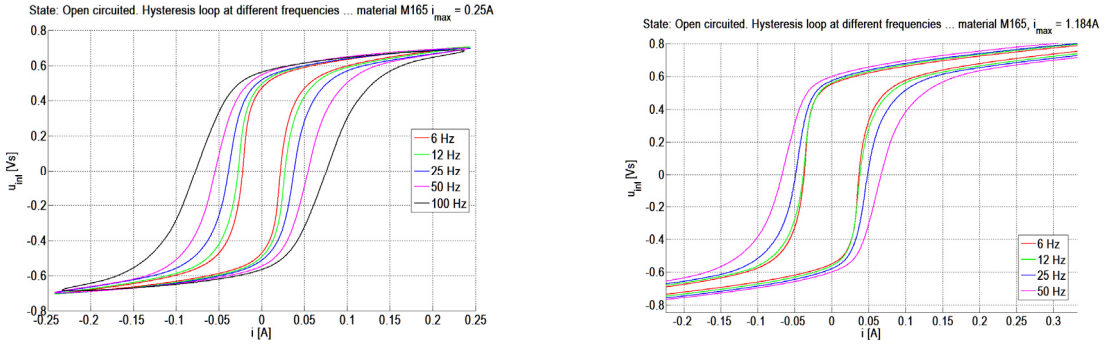

Fig. 4. Effect of frequency. a) Low excitation. b) High excitation, only the central part of hysteresis loop is shown.

4. Discussion and conclusions

In practice, the exciting quantity is the voltage, although the hysteresis loop experiment assumes a harmonic current. The reason is that good current sources are expensive. Among many other models for experimental data processing, the use of harmonic analysis is a natural approach, since each component has its physical significance and the method is a basic one in circuit theory. We have shown that the hysteresis loop is well defined by about 15 parameters,

depending on the applied voltage. Therefore, the three main material parameters defined in a hysteresis loop are not sufficient, which is confirmed by literature [3].

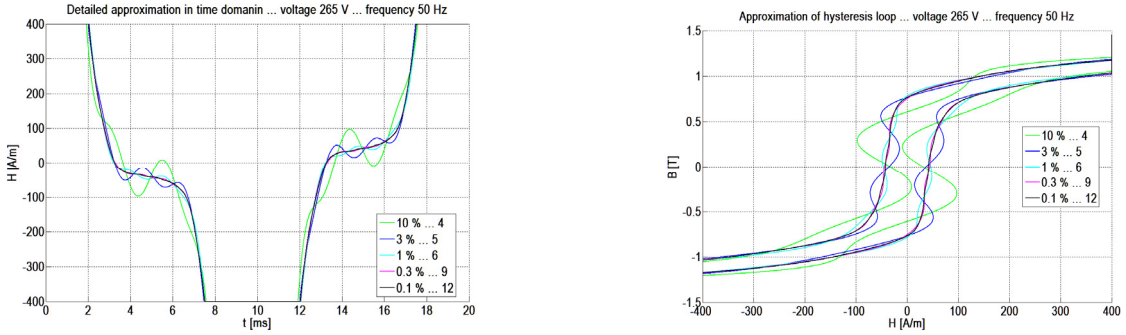

Fig. 5. Approximation. a) Time area. b) Hysteresis loop. The legend shows the importance criterion and number of used harmonics.

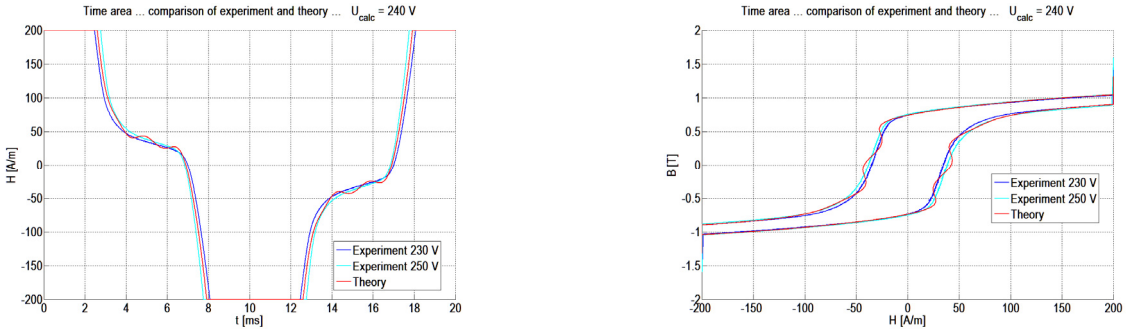

Fig. 6. Comparison of prediction and experiment. a) Detail in time area. b) Central part of hysteresis loop.

Good prediction of waveform and hysteresis loop assumes the knowledge of dependence of harmonics on the applied voltage, which is very complicated. The popular regression method cannot be used because of the complexity of the task and the change of 6 orders among other things. The interpolation method was found to be acceptable. A general rule is valid: The smaller the step in experimental voltage, the better the interpolation. Good results can be obtained for steps of 10 V. The full description of the material needs about 4 thousand parameters.

The next task requires the automated processing of all the experimental data in order to get a file of parameters and then the application of a simple algorithm that includes the file into circuit theory.

Acknowledgement

This work was supported by Student grant TUL SGS 2013/78000 “Progressive mechatronics, control and measurement systems with application of advanced simulation methods”.

References

[1] Mayergoyz I. Mathematical Models of Hysteresis and their Applications. Academic Press Elsevier, Waltham, 2004.

[2] Drapela J, Toman P, Orsagova J, Kratky, M. Simulation of Ferroresonance Phenomena in Power Systems. *In proc. of the 5th WSEAS/IASME Int. Conf. on Electric Power Systems, High Voltages, Electric Machines*, Tenerife, Spain, December 16-18, 2005, pp. 373-377.

[3] Nova I, Havlicek V, Zemanek I. Dynamic Hysteresis Loops Modeling by Means of Extended Hyperbolic Model. *IEEE Trans. on Magnetics*, vol.49, no.1, 2013, pp. 148-151.

Precise Measurement of T_2 Using the Turbo FLASH Method

R. Korinek, K. Bartusek

Institute of Scientific Instruments, Academy of Sciences of the Czech Republic,
Kralovopolska 147, Brno, Czech Republic,
Email: radim.korinek@gmail.com

Abstract. *The authors discuss the problem of using the Turbo FLASH sequence for the measurement of T_2 in samples with short relaxation T_1. In the case of the Turbo FLASH sequence, the relaxation T_1 plays an essential role during the measurement of the T_2 relaxation. The verification of the correct value of the T_2 relaxation was performed using the spin echo (SE) approach with precise adjustment (RF flip angles). In order to clarify the errors occurring in the course of the T_2 measurement, the authors used the ROMAG software (by Zenon Starcuk jr.) to carry out the simulations for the preparatory part of Turbo FLASH.*

Keywords: Turbo FLASH, Relaxation T_1 and T_2, Measurement, Relaxometry

1. Introduction

The article presents a method for precise measurement of the T_2 relaxation based on the Turbo FLASH sequence. High accuracy results are indispensable for precise relaxometry. The Turbo FLASH sequence is suitable for dynamic MRI [1] and real-time [2, 3] measurements. In this sequence, the magnetization for the T_2 measurement in a defined volume is provided during the preparatory part before the FLASH module. The prepared magnetization is subsequently captured by using FLASH (single shot or segmented). The main disadvantage of this measurement method consists in its sensitivity to the inhomogeneity of the magnetic field B_0 (geometric distortion, artifacts).

2. Subject and Methods

Two samples with known relaxation T_1 and T_2 were measured. The first sample was a phantom (deionized water) with pre-defined relaxations ($T_1 \sim T_2$), and the second one was a plant (euphorbia). To measure the samples, we applied the spin-echo (SE) [5] and the Turbo FLASH (ultra-short sequence) techniques as indicated in Fig. 1. The residual magnetization $M_{Z(\mathrm{err})}$ is caused by the T_1 relaxation of the samples during the τ interval (between the end of the preparatory part and the beginning of FLASH); importantly, the magnetization causes errors in the T_2 measurement with Turbo FLASH. The progress of the Turbo FLASH measurement sequence is shown in Fig.1 and can be described by the following formula: **Preparatory part** $\{\pi/2_x - T_E/2 - \pi_{x(y)} - T_E/2 - \pi/2_{x(-x)}\} + \tau +$ **FLASH** $\{(\beta - T_R - \beta)n\}$, where β is the flip angle and n expresses the number of repetitions.

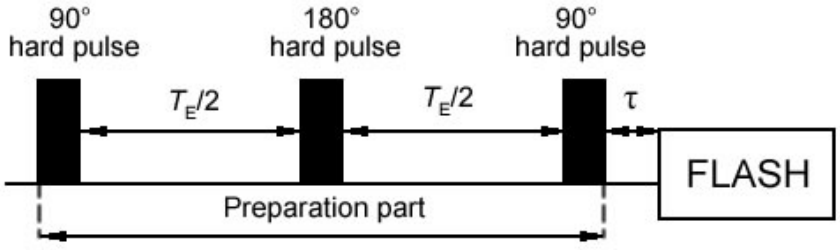

Fig. 1. Pulse diagram of the Turbo FLASH sequence for the T_2 measurement.

The simulations performed using the ROMAG software (by Z. Starcuk jr.) exhibit the relaxation T_1 of the samples during the τ interval. This effect is caused by the residual magnetization $M_{Z(err)}$ in all echo times within the MR images. The magnetization is significant for the samples characterized by short T_1. The time interval τ = 3.5 ms (instrumentation pause) is the time between the end of the preparatory and the beginning of the FLASH parts.

All the experiments were performed using the 4.7T (Magnex) MRI system operated by the ISI Brno, AVCR. The simulations were conducted in the ROMAG software, and the processing of the measured data was carried out in the MAREVISI (8.2) and MATLAB (7.11.0) programs.

3. Results

The results of the simulations presented in Fig. 2 indicate significant impact of the T_1 relaxation and the time interval τ on the magnetization M_Z.

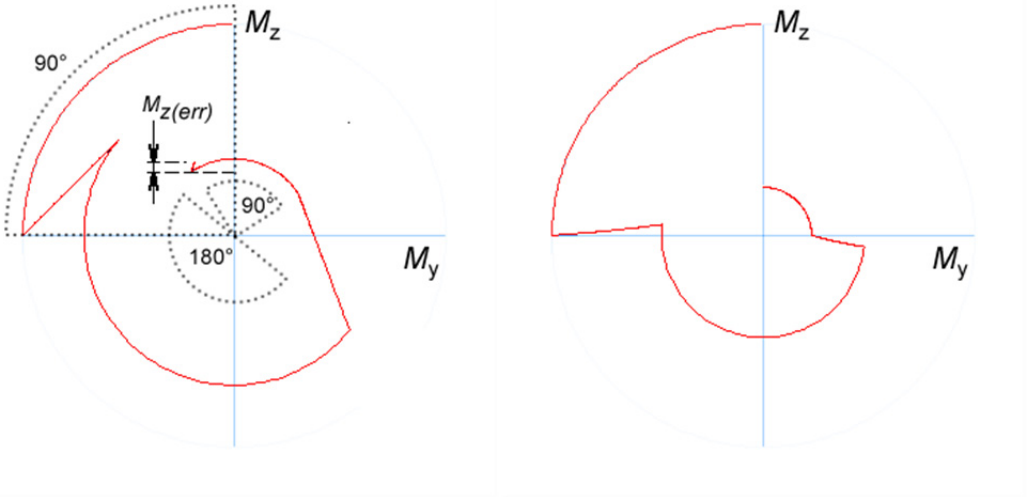

Fig. 2. Simulation of the Turbo FLASH sequence in the ROMAG software. Visualization of the magnetization behaviour during the preparatory part until the end of the interval τ. Left (simulation of the phantom): T_1= 42 ms, T_2 = 42.9 ms. Right (simulation of the euphorbia): T_1 = 470 ms, T_2 = 34 ms.

The measured phantom of deionized water exhibits short relaxations $T_1 \sim T_2$; moreover, the Turbo FLASH-based measurement of T_2 in this phantom, where T_1 (42 ms) >> T_2 (42.9 ms), has clearly shown the effect of the T_1 relaxation upon residual magnetization in the measured data (Figs. 3 and 5). In the euphorbia (Figs. 4 and 6), the residual magnetization during the T_2 measurement is negligible.

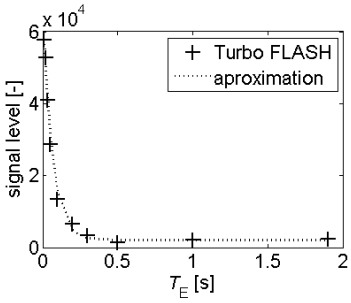

Fig. 3. Measurement of the T_2 relaxation (phantom: T_1 = 42 ms, T_2 = 42.9 ms) using Turbo FLASH.

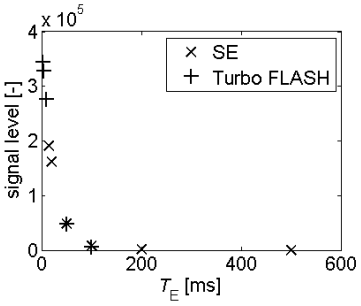

Fig. 4. Measurement of the T_2 relaxation (euphorbia: T_1 = 470 ms, T_2 = 34 ms) using the SE and Turbo FLASH.

A comparison of the spin echo approach and the Turbo FLASH sequence for the euphorbia, where T_1 (470 ms) >> T_2 (34 ms), can be seen in Figs. 4 and 6.

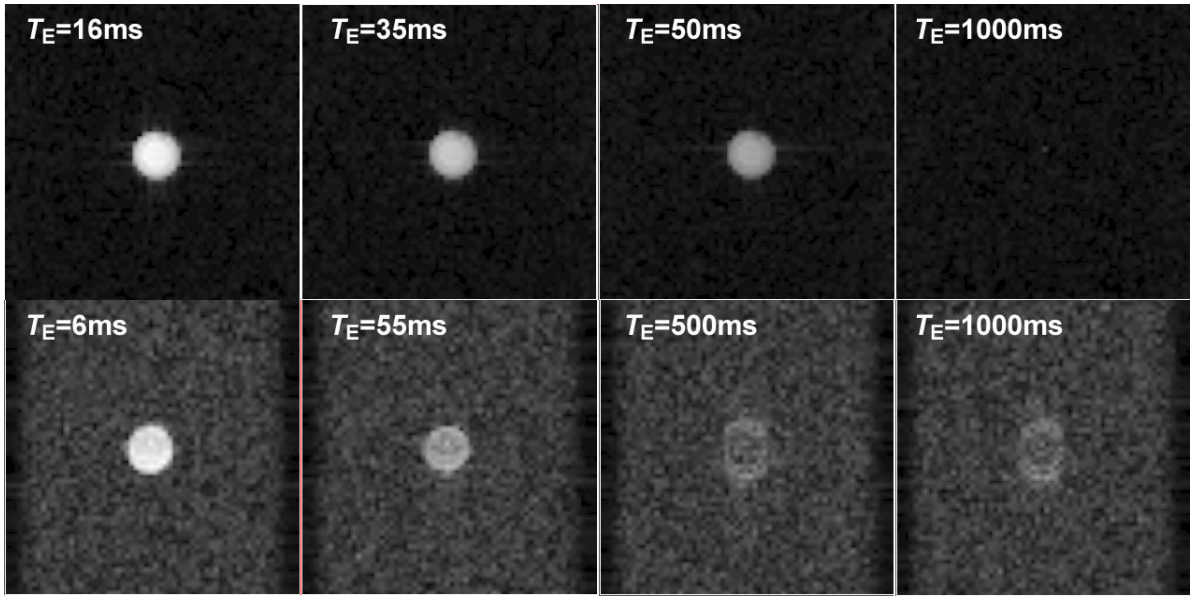

Fig. 5. MR images for the different echo times T_E of the phantom (T_1 = 42 ms, T_2 = 42.9 ms). While the upper row exhibits the SE-based measurements, the bottom row contains measurement images acquired via the Turbo FLASH sequence.

In Fig. 5, the effects of residual magnetization in MR images are shown; the magnetization occurs during the time interval τ in the samples having short T_1.

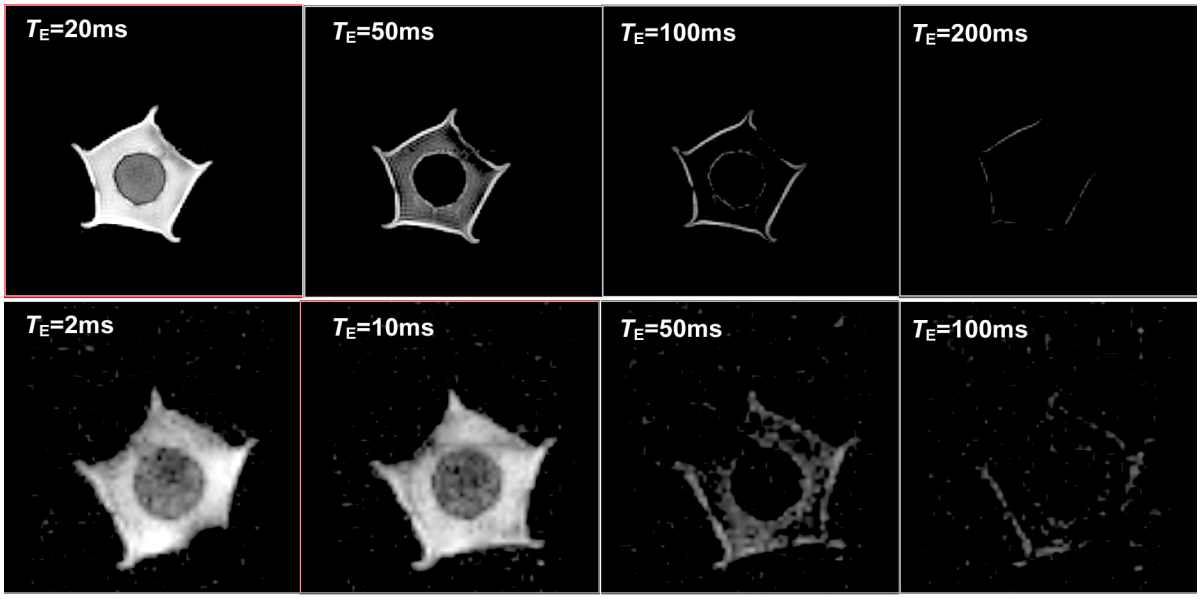

Fig. 6. MRI images of the euphorbia measured via the spin echo approach (upper row) and the Turbo FLASH sequence; T_1 (470 ms) >> T_2 (32 ms).

The reason for the actual measurement of the euphorbia (Fig.6) consists in the fact that, in this plant, the T_1 relaxation is significantly greater than the T_2 relaxation. Thus, we can easily launch an experiment to demonstrate how the Turbo FLASH sequence behaves at T_1>>T_2.

A comparison of the values of T_1 and T_2 measured in the phantom via the spin echo and Turbo FLASH techniques is presented in Tab. 1 below.

Table 1. A comparison of the values of T_1 and T_2 measured in the phantom via the spin echo and Turbo FLASH techniques.

Relaxation	SE	Turbo FLASH	Turbo FLASH (without residual magnetization)
		Phantom	
T_1 [ms]	42	56.6	41.4
T_2 [ms]	42.9	42.8	42.8

4. Discussion and Conclusions

By simulating the preparatory stage for the encoding of relaxation T_2, we determined the magnitude of the error magnetization M_z(err) before the FLASH acquisition. The measurements realized with the phantoms and the euphorbia have clearly demonstrated the effects of residual magnetization for various magnitudes of T_1 at the interval of $\tau = 3.5$ ms. The greatest residual magnetization is shown by the phantom No. 1, which exhibits the relaxation value of $T_1 \sim T_2 \sim 43$ ms. Conversely, the measurement of the euphorbia, whose relaxation is expressed as $T_1 = 470$ ms, indicated very low residual magnetization which does not significantly influence the measured data. This status is caused by the fact that $T_1 >> \tau$. In the measurement of samples exhibiting long T_1 relaxation, the above-described problem does not occur, and residual magnetization is negligible. However, residual magnetization (added to the wanted signal) exerts significant influence on the data acquired in the measurement of samples with short relaxation T_1. Another aspect of importance for the measurement - in addition to T_1 - is the interval τ between the end of the preparatory part and the beginning of the FLASH acquisition. Thus, it is vital to obtain the largest possible ratio between the T_1 of the sample and the time interval τ. If the relaxation T_2 in a sample with short relaxation T_1 ($T_1 = T_2$) is to be measured, we need either to minimize the time interval τ (parameters of the hardware permitting) or to perform approximation considering the T_1 relaxation.

Acknowledgements

The research described in the paper was financially supported by the grand agency of the Czech Republic (projects No. P13-09086S and No. P102-11-0318) and EC and MEYS CR (project No. CZ.1.05/2.1.00/01.0017).

References

[1] Frahm, J., Haase, A. and Matthaei, D. Rapid NMR imaging of dynamic processes using the FLASH technique. *Magn. Reson. Med.*, 3: 321–327, 1986.

[2] Zhang S., Uecker M., Voit D., Merboldt KD., Frahm J. Real-time cardiovascular magnetic resonance at high temporal resolution: radial FLASH with nonlinear inverse reconstruction. *Journal of Cardiovascular Magnetic Resonance*, 12(1): 39, 2010.

[3] Uecker M., Zhang S., Voit D., Karaus A., Merboldt KD., Frahm J. Real-time MRI at a resolution of 20 ms. *NMR in Biomedicine*, 23(8): 986–994, 2010.

[4] Haase A., Frahm J., Matthaei D., Hanicke W., Merboldt KD. FLASH imaging. Rapid NMR imaging using low flip-angle pulses. *Journal of Magnetic Resonance (1969)*, 67(2): 258-266, 1986.

[5] Haacke EM., Brown RW., Thompson MR., Venkatesan R. Magnetic Resonance Imaging: Physical Principles and Sequence Design. Wiley-Liss, 1999.

Estimation of B_0 and B_1 MR Inhomogeneity via Relaxations

R. Kubasek, K. Bartusek

Brno University of Technology, Brno, Czech Republic
Email: kubasek@feec.vutbr.cz

Abstract. *The authors describe a method for the basic and RF field inhomogeneity estimation in NMR based on the measurement of T2 and T2*. The method combines the gradient and spin echo acquisition techniques to differentiate the T2 and T2* relaxation times. Exponential approximation of the relaxation process has to be performed. Experimental results for the plastic and copper specimens are shown.*

Keywords: NMR, Inhomogeneity, B0, B1, Relaxations

1. Introduction

The physical phenomenon in which the magnetic field of the nuclei of some atoms contained in the examined substance reacts with a rotating magnetic field is referred to as NMR (Nuclear Magnetic Resonance). NMR spectroscopy and tomography require the basic magnetic field B_0 to be generated with a high homogeneity [1]. Homogeneity of the basic magnetic field can be distorted by the measured object, and this object does not necessarily have to be magnetic: image distortion may occur already as a result of different susceptibility.

High homogeneity of the RF (Radio Frequency) field in the working space of an MR tomograph depends on the structure and setting of the applied probe. Mapping of the RF magnetic field is commonly based on MR image measurement of the homogeneous test specimen; in the measurement, the flip angle is optimally determined to ensure the maximum contrast of the measured RF magnetic field map, [2] and [3]. The local B_1 field strength in each slice can be obtained using repeated acquisitions with different RF-impulse amplitudes ('transmit gain', 'flip angle') [4]. The inhomogeneity can be corrected by the use of a map of the spatial distribution of the B_1 field acquired either through computer simulation or through the measurement of the field. The actual measurement of the B_1 distribution provides two major advantages: it makes the registration of the map against the MR images easier, and the measured B_1 field compensates for imperfections in the coil design. The paper describes the first instance of relaxation measurement using the SE (Spin Echo) and GE (Gradient Echo) methods applied for the B_0 inhomogeneity estimation. The method of B_1 estimation from the relaxation times via the magnetization transfer ratio is described in the following chapter of this article.

2. Inhomogeneity estimation from relaxation times

The GE and SE methods are well known within NMR measurement techniques, [4]. We can measure the relaxation process after excitation by changing the echo time, Fig. 1a. The number of realized measurements depends on the requirements and the time available. The measurement proper can be performed by a hard excitation pulse on the whole specimen, on a selectively chosen layer or area of the specimen, or on a pixel/voxel in an imaging sequence.

The measured data is must be approximated by an exponential function. Both constants of the exponential course, namely the magnetization after excitation M_{xy} and the time constant T_2 or T_2*, are needed. At least three measured magnitudes of the FID (Free Induction Decay) signal at different TE echo times are necessary for the approximation. The TE echo times should be

chosen with care. The first echo time should be set to the lowest possible value with respect to technical parameters of the tomograph. The last echo time can be chosen either on the basis of the known inhomogeneity or experimentally. Other echo times can be distributed linearly between these two points. If a whole image is measured, we need to perform approximation in every pixel/voxel of the image. For high-resolution images, it is important to consider the computational complexity of the approximation algorithm. For example, the genetic algorithm is not a suitable option.

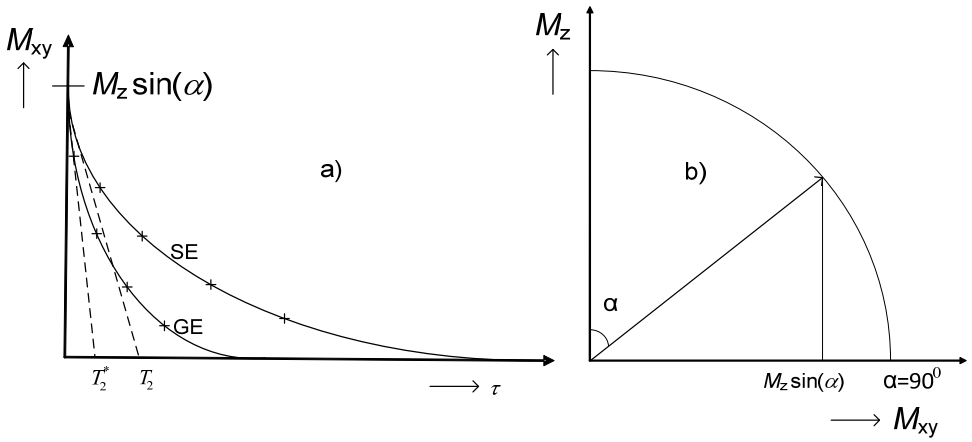

Fig. 1. a) Relaxation process after excitation b) flip angle representation.

The basic field inhomogeneity B_0 exerts influence on the relaxation process; thus, any deformation of B_0 causes the dephasing of magnetization. Dephasing leads to a faster drop of the FID signal and shortens the relaxation time T_2*. Figure 2 shows five magnitude images obtained by the GE and SE technique. Magnitude drop in the bottom left corner is marginal; it is caused by the B_0 inhomogeneity not successfully corrected by the shim coils. This is a limiting factor for any successful approximation of relaxation.

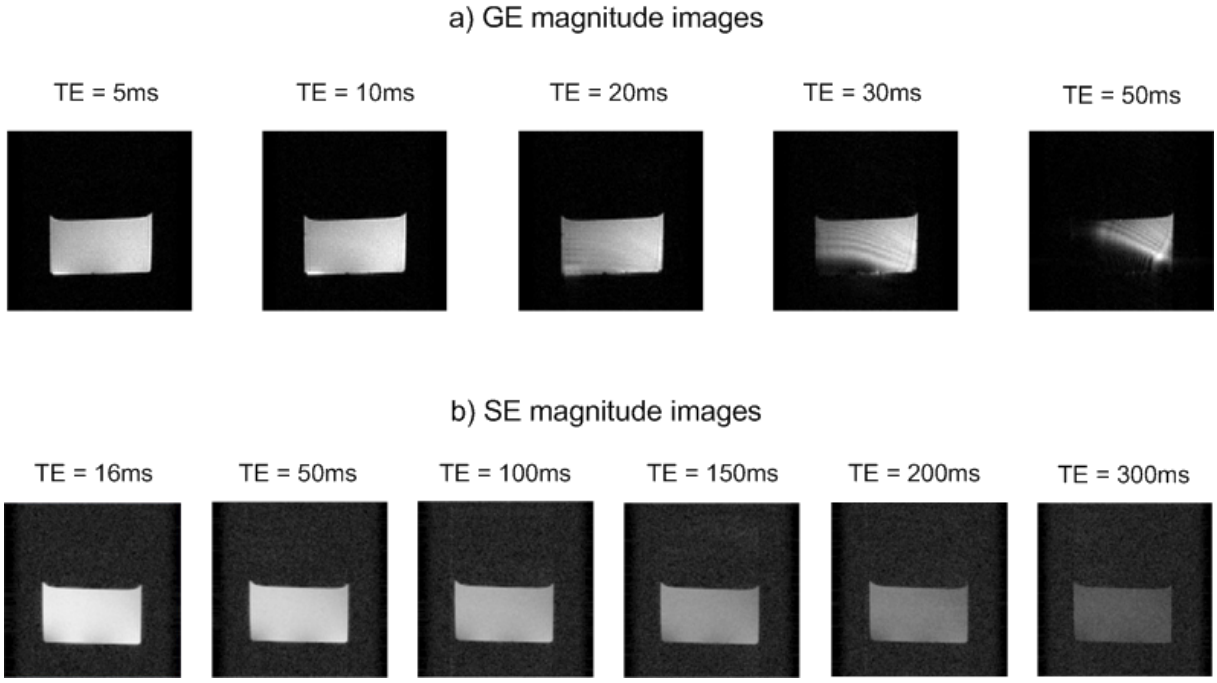

Fig. 2. Magnitude images a) for the GE sequence, b) SE sequence.

B_0 inhomogeneity estimation

The SE method compensates inhomogeneity B_0; therefore, we measure true relaxation T_2. It is, however, necessary to select a suitable specimen to exclude the influence of diffusion and movements. The basic field inhomogeneity B_0 is given by

$$\frac{1}{T^*_2} = \frac{1}{T_2} + \frac{1}{T'_2} = \frac{1}{T_2} + \gamma \Delta B_0,$$
$$\Delta B_0 = \frac{\frac{1}{T^*_2} - \frac{1}{T_2}}{\gamma}, \qquad (1)$$

where γ is the gyromagnetic ratio of ^{1}H. The value ΔB_0 is the overall and, in a way, average value of the B_0 inhomogeneity in any pixel/voxel.

Figure 3 shows the B_0 inhomogeneity maps measured using a 4.7 T tomograph. A cube filled by long- relaxing water was used. The specimen, namely a plastic or copper plate placed on a glass vessel, was inserted in the cube. The B_0 inhomogeneity with no sample is presented as background and can be subtracted from the measurement. The plastic sample is non-conducting and exhibits a significant (not exactly determined) value of susceptibility. In the plastic sample, B_0 changes significantly in the whole space of the water-filled cube. The maximal value of B_0 inhomogeneity is $4 \cdot 10^{-7}$ T. The B_0 inhomogeneity map for cooper sample will be presented on poster. Copper sample is a good conductor with a low susceptibility value; this sample exerts minimal influence on the B_0 inhomogeneity in compare to plastic sample.

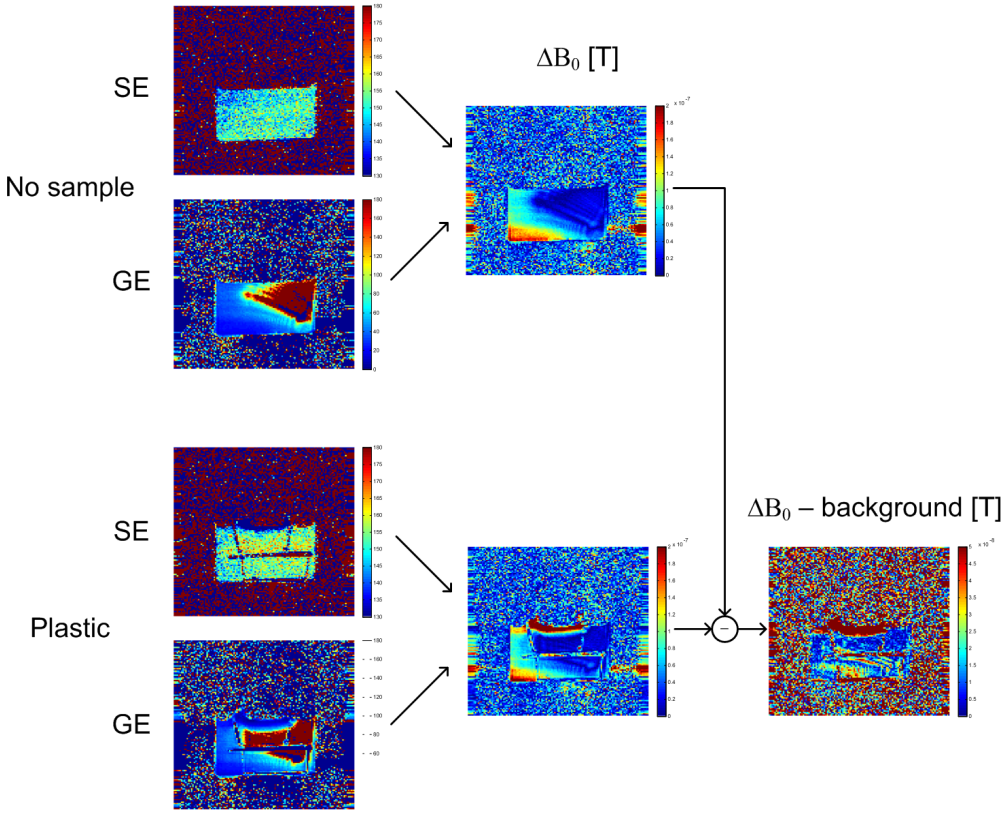

Fig. 3. Maps of the B_0 inhomogeneity estimation, and the final results.

B_1 inhomogeneity estimation

Immediately after excitation, the NMR signal magnitude is proportional to the basic field strength represented by M_{xy} and flip angle α. The magnetization is expressed by:

$$M_{xy}=M_z \cdot \sin(\alpha). \quad (2)$$

The flip angle is a linear function of the B_1 field strength and length of the excitation pulse t_e:

$$\alpha = \gamma B_1 t_e. \quad (3)$$

The B_1 inhomogeneity map can be represented by the map of flip angle α. The task is to find M_{xy} in time $t = 0$. The M_{xy} ratio is theoretically the same for both the GE and SE methods. We can use the average M_{xy} of the GE and SE weighted by the exponential approximation accuracy. The B_1 inhomogeneity map for cooper and plastic sample will be presented on poster. Result show that the plastic sample exhibits minimal influence of excitation in the whole space. Conversely, the copper sample has a substantial effect on the RF field; there are regions where the nuclei are over-stimulated or inadequately excited.

The major disadvantage of the proposed method is that we cannot recognize if the flip angle is over or below 90°. For example, the magnitude of the signal after excitation is the same for flip angles of 80°and 100°. That disadvantage can be suppressed by choosing small flip angle to avoid over-excitation.

3. Conclusions

Estimation of the B_0 and B_1 inhomogeneity from relaxation times T_2 and T_2* and initial magnetization after excitation M_{xy} is a useful method. The benefit consists in the fact that there does not have to exist any mutual influence between the inhomogenities. The described approach is limited by two aspects, namely loss of the FID signal magnitude below the noise level in the case of a high inhomogeneity and the fact that we know only the absolute flip angle error. The quality of the B_0 inhomogeneity strongly depends on successful approximation of T_2.

Acknowledgements

This work was supported within the project funded by the Education for Competitiveness Operative Programme CZ.1.07.2.3.00.20.0175.

References

[1] M. Vlaardingerbroek, Magnetic Resonance Imaging, *Springer-Verlag*, (2000).

[2] H.Ch. Cunningham, J. M. Pauly, K. S. Nayak, Saturated Double-Angle Method for Rapid B1 Mapping, *Magnetic Resonance in Medicine*, 55:1326–1333.

[3] D. W. S. Zuehlsdorff, A. C. Larson, Rapid 3D radiofrequency field mapping using catalyzed double-angle method, *NMR Biomedicine,* 22: 882–890 2009.

[4] K. Bartusek, E. Gescheidtova, R. Kubasek, Mapping of Radiofrequency Magnetic Field in MR Tomography, *i*nternational conference on fundamentals of electrotechnics and circuit theory, gliwice 2006 p. 135 - 138.

[5] E. M. Haacke, R. W. Brown, M. R. Thompson, R. Vankatesan, Magnetic Resonance Imaging Physical Principles and Sequence Design, Wiley & Sons 1999.

Integrated Microfluidic System for Magnetic Cell Separation, Electroporation, and Transfection: Conceptual Design

[1]A. Krafčík, [2]P. Babinec

[1]Institute of Measurement Science, Slovak Academy of Sciences, Bratislava, Slovakia,
[2]Faculty of Mathematics, Physics and Informatics, Comenius University, Bratislava, Slovakia
Email: andrej.krafcik@savba.sk

Abstract. *For the purposes of a successful ex vivo gene therapy we have proposed and analyzed a new concept of an integrated microfluidic system for combined magnetic cell separation, electroporation, and magnetofection. For the analysis of magnetic and electric field distribution (given by Maxwell equations) as well as dynamics of magnetically labelled cell and transfection complex, we have used finite element method (FEM) directly interfaced to the MATLAB routine solving Newton dynamical equations of motion. Microfluidic chamber has been modelled as a channel with height and length 1 mm and 1 cm, respectively. Bottom electrode consisted of 100 parallel ferromagnetic straps and the upper electrode was plate of diamagnetic copper. From the dynamics of magnetic particle motion we have found that the characteristic time-scales for the motion of cells (mean capture time ~ 4 s) and gene complexes (mean capture time ~ 3 min), when permanent magnets are used, are in the range suitable for efficient cell separation and gene delivery. The largest electric field intensity (~ 10 kV/m) was observed at the edges of the microelectrodes, in the close proximity of magnetically separated cells, which is optimal for subsequent cell electroporation. [1]*

Keywords: Magnetic Nanoparticles, Cell Separation, Cell Transfection, Simulation

1. Introduction

Electroporation, is a significant increase in the electrical conductivity and permeability of the cell plasma membrane caused by an externally applied electrical field. As has been shown the use of a two-pulse technique allows separating two effects provided by a pulsed electric field: membrane electroporation and DNA electrophoresis. The first pulse (e.g. 6 kV/cm, 10 ms) creates pores efficiently, whereas transfection efficiency is low. The second pulse of much lower amplitude, but substantially longer (e.g. 0.2 kV/cm, 10 ms), does not cause poration and transfection by itself, but enhances transfection efficiency by about one order of magnitude [2]. In two-pulse experiments, transfection efficiency rises monotonously with the increase of the second pulse duration. In another study, was monitored transport of propidium iodide into electropermeabilized Chinese hamster ovary cells, and became detectable as early as 60 ms after the start of the pulse, continued for tens of seconds after the pulse [3].

The principle of our approach is used as a driving force instead of a second pulse inducing DNA electrophoresis into the cells, the magnetophoresis of DNA attached to magnetic particle. The electrophoresis last just for 10 ms, and magnetic movement of the DNA can be effective about 1000 times longer. The diameter of the pore in electro-permeabilized cell membrane is of the order 100 nm, which is sufficient for the translocation of the DNA-nanoparticle complex. As has been already shown, electroporation can be used also for internalization of magnetic nanoparticles [4].

Another modification of this approach is to combine it also with magnetic separation. Cells with attached magnetic microparticles would be easily attracted to magnetic electrode, which is analogous to situation when cells form confluent monolayer at the bottom of Petri dish. At

the standard magnetofection protocol, the magnet is placed under these cells and nanoparticles with attached gene added to solution are attracted to the cell layer and translocated through the membrane into the cell interior. Now we have analogous situation, the nanoparticles with DNA are also attracted to electrode, and therefore to bounded cells, although with smaller force compared to microparticles, and magnetofection take place. At this moment electric pulses can be applied. Because the separation between the electrodes in microfluidic systems is ~ 0.1 – 1 mm, and typical value of electric intensity in electroporation is ~ 100 - 1000 V/cm only low voltage of 10 - 100 V would be needed.

2. Subject and Methods

Integrated microfluidic system – Basic description

Own separator consists of the channel (see Fig. 1), with flowing water carrying magnetically labelled objects (MLO) - cells or genes - by superparamagnetic particles (Table 1). Presence of electrodes above and below the channel, allows apply short high intensity electric pulse to generate electric field (FEM model (FEMM v4.2, D. Meeker, 2008) see in Fig. 2c) able to create membrane pores on cells localized in the chamber. Channel with electrodes are located in an external magnetic field with gradient (FEM model see in Fig. 2a, b), that allows us to use this field for separation of MLO and their targeting to the bottom surface of the chamber.

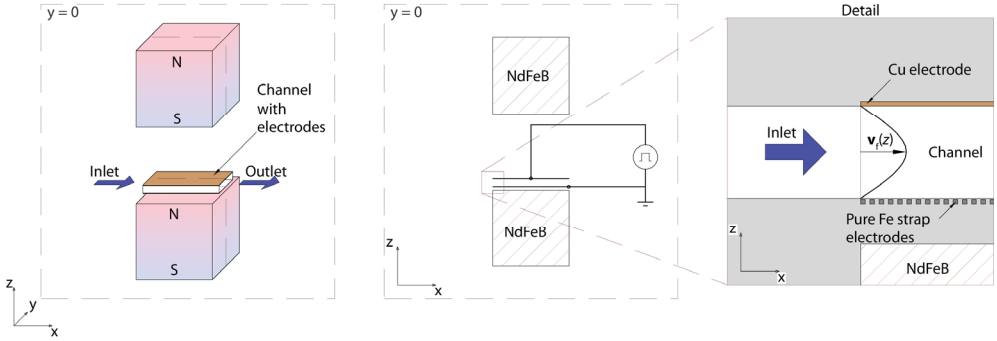

Fig. 1. A schematic illustration of a microfluidic system for combined separation, electroporation and magnetofection. The channel (treatment zone) with electrodes and two NdFeB magnets as source of magnetic field. (right) Detail of inlet of the channel with electrodes.

Table 1. Specifications of used magnetically labelled objects (MLO) [1].

Object	Diameter	Weight [kg]	Magn. moment [A m^2]
Magn. labelled CELL	10 μm	1.0×10^{-12}	1.0×10^{-11}
Magn. labelled GENE	300 nm	1.0×10^{-17}	2.0×10^{-15}

Simulation of motion

MLO motion simulation has involved a magnetic force and a Stokes viscous-drag force occurring in the Newton dynamical equation of motion for single particle problem:

$$m_p \frac{d\mathbf{v}_p}{dt} = |\boldsymbol{\mu}_p| \left(\frac{\mathbf{B}}{B} \cdot \nabla \right) \mathbf{B} - 3\pi\eta_f D_p (\mathbf{v}_p - \mathbf{v}_f) \qquad (1)$$

in which object is represented as sphere with diameter D_p, mass m_p, velocity $\mathbf{v}_p$ and has magnetic moment with magnitude $|\boldsymbol{\mu}_p|$. External magnetic field with flux density $\mathbf{B}$ has gradient $(\mathbf{B}/B \cdot \nabla)\mathbf{B} \equiv \mathbf{G}$. Water as carrying fluid media has dynamical viscosity η_f and

velocity $\mathbf{v}_f$. Its flow in the channel (with height h) is described as Poiseuille flow problem of Newtonian fluid with no-slip boundary condition on static infinite parallel plates, i.e. with parabolic profile $\mathbf{v}_f(z) = [v_{f,mean}\, 6(h-z)z/h^2, 0, 0]$ where $\mathbf{v}_{f,mean}$ is its mean velocity. As simplification we suppose planar magnetostatic problem and assume fully magnetically saturated MLO. Objects motion simulations in viscous fluid and external magnetic field described by Eq. 1 were done by using MATLAB (The MathWorks, Inc.) ordinary differential equations solver *ode45*, or *ode15s* and *ode23s* in the case if the problem was too stiff.

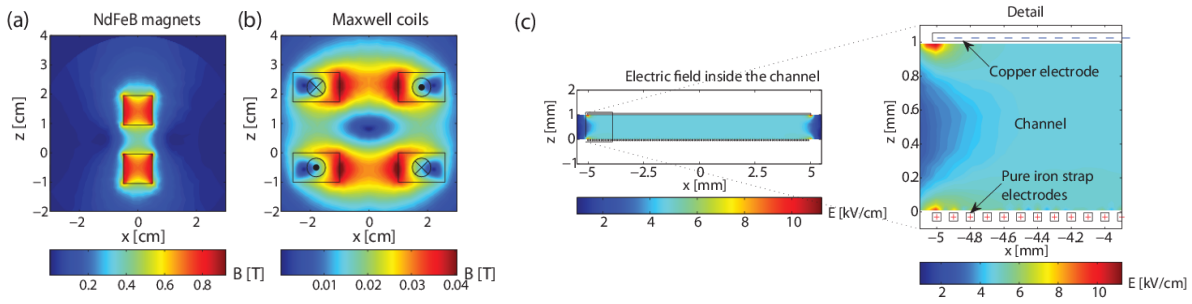

Fig. 2. (a, b) External sources of magnetic field (FEM): (a) two NdFeB N40 magnets, and (b) Maxwell coils [1]. (c) Electric field intensity distribution in the 1 mm height chamber with applied voltage difference 15 V between bottom and upper electrodes (FEM), which is sufficient for cell electropermeabilization.

3. Results and discusion

Electrodes designed so that to modulate external magnetic field by localized increasing of magnetic field gradient on bottom part of the channel (see Fig. 3), allow catch MLO to the bottom of the chamber along its whole length in suitable mean flow velocity ($v_{f,mean}$ in Fig. 4 or $v_{f,t}$ in Table 2), and prevent its next dragged movement by fluid ambient. The MLO capturing efficiency in the channel was described by time needed to move of the object from its random initial position in the channel to its bottom surface (by capturing) or out of the chamber (due to drift). As we can see from simulations results (Fig 4 and Table 2), motion of smaller MLO - genes (Fig. 4a) - in comparison with cells (Fig. 4b) is slower in about two orders of magnitude, and also for both types of objects in the case of NdFeB magnets as the source of external magnetic field is still in the range of periods for existence of membrane pores of electropermeabilized cells [3]. That shows possibility to combine magnetic separation of cells to the bottom of the chamber with their subsequent electroporation and magnetic targeting of genes to their surface, all-in-one integrated microfluidic system.

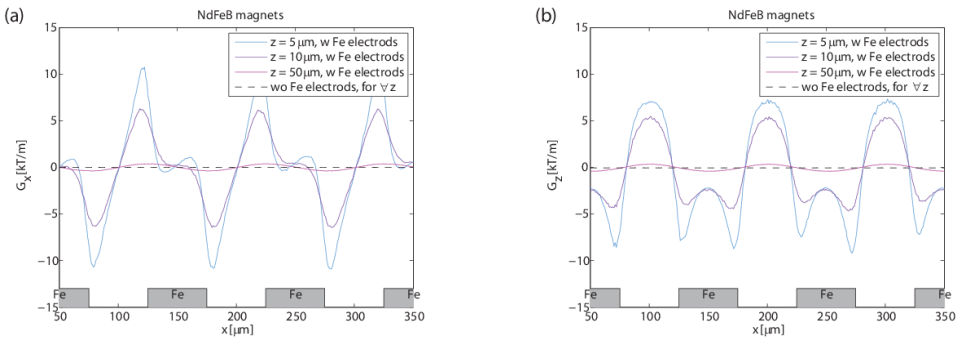

Fig. 3. Components: (a) G_x and (b) G_z of magnetic field gradient over the bottom strap Fe electrodes (z = 5, 10, 50 µm) in the middle part of the chamber in the field of NdFeB magnets (planar problem: $G_y = 0$).

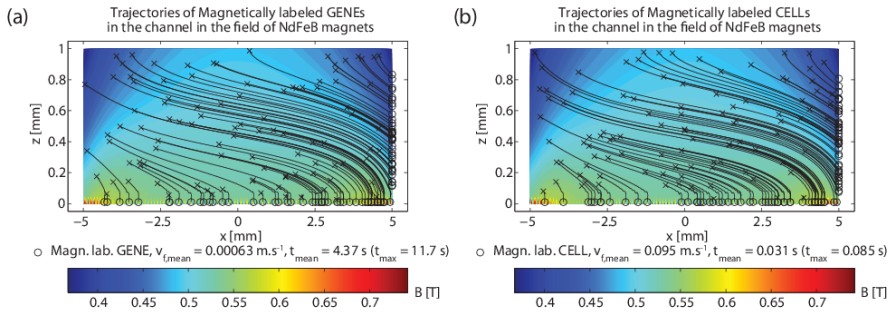

Fig. 4. Trajectories of magnetically labelled (a) genes and (b) cells in the channel with flowing water in the *x*-axis direction with mean flow velocity ($v_{f,mean}$) in the field of two NdFeB magnets. There are also shown the mean capture time of 100 objects (t_{mean}) and the movement time of the slowest one (t_{max}).

Table 2. Capturing of magnetic objects (magnetically labelled gene/cell) in the channel.

Object	External magnetic field sources					
	NdFeB N40 magnets			Maxwell coils		
	$v_{f,t}$ [a] [m/s]	t_{mean} [s]	t_{max} [s]	$v_{f,t}$ [a] [m/s]	t_{mean} [s]	t_{max} [s]
Magn. label. CELL	9.5×10^{-2}	0.031	0.085	2.6×10^{-4}	0.90	3.22
Magn. label. GENE	6.3×10^{-4}	4.37	11.7	1.7×10^{-5}	165	416

[a] Threshold velocity of fluid media flow for effective capturing of magn. label. objects along the bottom of the channel.

4. Conclusions

According to recent studies of magnetofection mechanism magnetic fields influence only the extracellular phase of lipoplex delivery but does not induce a direct entry of the lipoplex into the cytoplasm via the plasma membrane. Combination of the magnetofection with electroporation, which is able to open plasma membrane for magnetic nanoparticles bearing plasmid, as proposed in this study, is therefore very natural and able to overcome cellular barrier for gene transfer. Also, low voltages due to the close electrode spacing employed, leading to reduced heat generation and higher cell viability.

Acknowledgements

The financial support by the Grant Agency of the SAS, project no. VEGA 2/0090/11 and 1/0642/11 is gratefully acknowledged.

References

[1] Durdík Š, Krafčík A, Babincová M, Babinec P. Conceptual design of integrated microfluidic system for magnetic cell separation, electroporation, and transfection. *Physica Medica*, 2012. In press. http://dx.doi.org/10.1016/j.ejmp.2012.11.003

[2] Chang DC, Chassy BM, Saunders JA. Guide to electroporation and electrofusion. San Diego, US: Academic Press, 1992.

[3] Pucihar G, Kotnik T, Miklavcic D, Teissie J. Kinetics of trans-membrane transport of small molecules into electro-permeabilized cells. *Biophys. Journal*, 95:2837-2848, 2008.

[4] Walczak P, Kedziorek DA, Gilad AA, Lin S, Bulte JW. Instant MR labeling of stem cells using magnetoelectroporation. *Magnetic Resonance in Medicine* 54 (4): 769-774, 2005.

Barium Overdoped $Gd_{1-x}Ba_{2+x}Cu_3O_{7-\delta}$ Superconductors – Transport and Low Field Magnetic Properties

M. Majerová, A. Cigáň, A. Dvurečenskij, R. Bystrický, J. Maňka, M. Škrátek

Institute of Measurement Science, Slovak Academy of Sciences
Dúbravská cesta 9, 841 04 Bratislava, Slovakia
Email: melinda.majerova@savba.sk

Abstract. *We studied effects of slight Ba overdoped in $Gd_{1-x}Ba_{2+x}Cu_3O_{7-\delta}$ superconducting compounds on their transition, structural, and magnetic properties. A series of samples of $Gd_{1-x}Ba_{2+x}Cu_3O_{7-\delta}$ with Gd/Ba composition deviation x from stoichiometric value from 0 to 0.1 were synthesized by the solid-state reaction method. All the samples in the studied composition range show the critical temperature T_c and the transition width ΔT_c around 93 K and 1 K, respectively. AC magnetization measurements confirm a slight deterioration magnetization and magnetization hysteresis at low magnetic field and 77 K from x= 0.01 to 0.1. Magnetization measurements at 20 K and higher field show a stabilization effect of Ba excess to magnetic flux pinning properties for $x \geq 0.04$, however, there is an evidently worse magnetization hysteresis compared to the stoichiometric sample.*

Keywords: High-T_c superconductor, $Gd_{1-x}Ba_{2+x}Cu_3O_{7-\delta}$, Cation Nonstoichiometry, Critical Temperature, Magnetization, Paramagnetic Contribution

1. Introduction

In LRE-123 family superconductors with a light element (LRE) like La, Nd, Eu or Gd, with the ionic radius close to Ba, the solid solutions with the LRE-Ba substitution can be formed. This usually leads to a reduction of the superconducting properties, e.g., critical transition temperature T_c mainly at high LRE-Ba substitution levels [1-3]. To avoid this, the synthesis method in the atmosphere with a decreased or controlled oxygen content is usually used, and/or an addition of Ba-excess (in the form of precursors such as BaO, BaO_2, $BaCuO_x$, or Ba-rich phase as $GdBa_6Cu_3O_y$, etc.) to effectively suppress the substitution and therefore the formation of solid solutions of the $LRE_{1+x}Ba_{2-x}Cu_3O_y$ type [4]. In the last case of the Gd, it was observed that superconducting properties of the single grain bulk Gd-123 were not degraded even when they were fabricated in air, however, Ba excess compositions were used [5]. However, for nonstoichiometry Gd-123 thin film, opposite results were also observed. T. Kakeshitaet et al. [6] reported the worst superconducting properties (T_c, j_c) for Ba-rich thin films. Moreover, it is seen that Ba excess results in a different effect on critical temperature T_c and critical current density j_c. In addition, no systematic study of the systems has been performed yet and it must be noted that the compound properties are strongly dependent on technological processing parameters. In our former works [7, 8], we studied light non-stoichiometric bulk sintered samples of the Eu-123 and Sm-123 composition. In this work, we prepared a series of light non-stoichiometric bulk samples of $Gd_{1-x}Ba_{2+x}Cu_3O_{7-\delta}$ and investigated composition deviation x effects on their superconducting, structural, and mainly magnetic properties.

2. Subject and Methods

Samples of $Gd_{1-x}Ba_{2+x}Cu_3O_{7-\delta}$ with the nominal composition deflection x = 0, 0.01, 0.02, 0.04, 0.05, 0.07 and 0.1 were prepared by a standard solid-state reaction method using commercial 99.99 % purity oxide powders of Gd_2O_3, CuO, and $BaCO_3$. Prior to weighing and mixing, the Gd_2O_3, CuO, $BaCO_3$ powder was pre-annealed at 950 °C for 8 h in air to release

contaminations, e.g., moisture. Thereafter, the powders were carefully weighed in appropriate weight amounts, homogenized in acetone in an agate mortar for five minutes, put into alumina crucibles and calcined at 950 °C for 40 hours in air. The obtained precursors were again homogenized, pressed into pellets (with the diameter of 12 mm) and sintered in a horizontal tube furnace in flowing oxygen of 20 ml/min) at about 1000 °C for 72 h, then cooled to 450 °C and held at this temperature for 24 h and thereafter cooled in the furnace to room temperature. The series of samples were prepared in the same thermal cycle. $T_c(R=0)$ was determined by a standard resistance four-point method and the transition width, ΔT_c, was characterized by the 10-90 % criterion. The inaccuracy of temperature measurements was less than 0.2 K. The phase composition was studied by X-ray diffraction measurements (CuKα radiation). AC low field magnetization at 77 K was measured by a compensation method using the second-order SQUID gradiometer [9] and DC magnetization at higher field and lower temperature by the Quantum Design SQUID magnetometer MPMS XL-7.

3. Results and Discussion

From X-ray diffraction data, it can be concluded that the samples are single-phase, however, for higher contents of Ba some new peaks for 2θ in the range of 28°-29° could be ascribed to the excess Ba-Cu-O phase. The XRD patterns of some samples of $Gd_{1-x}Ba_{2+x}Cu_3O_y$ series are shown in Fig. 1.

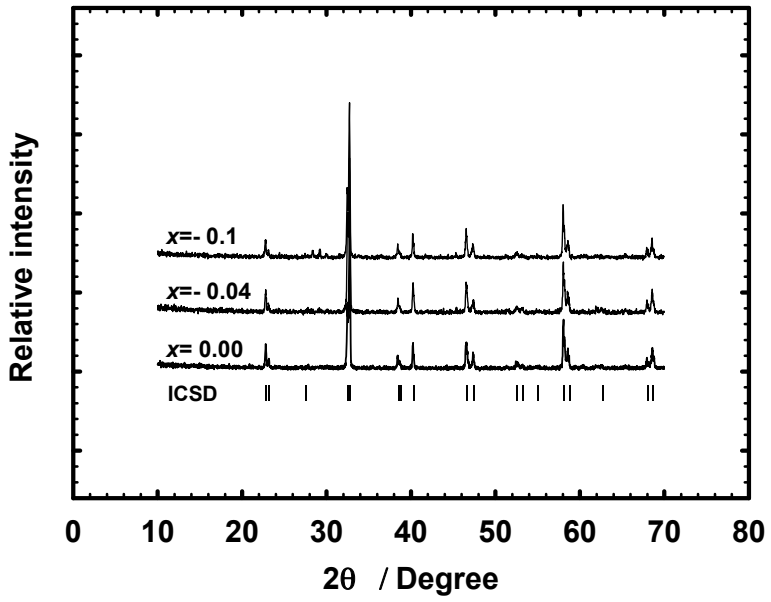

Fig. 1. XRD patterns of $Gd_{1-x}Ba_{2+x}Cu_3O_{7-\delta}$ samples with shown x values.

Dependences of T_c and ΔT_c vs. x are shown in Fig. 3 and Fig. 4, respectively. As awaited, they confirm a positive effect of the barium excess on T_c and ΔT_c as a consequence of depressing of Gd entering into the Ba position. T_c and ΔT_c change slightly only. However, there is a weak trend of worsening both T_c and ΔT_c with an increasing x, whereas the values of T_c are still mostly about 93 K and ΔT_c about 1 K.

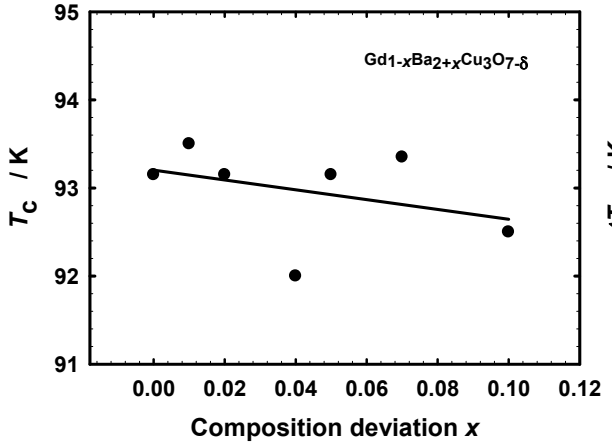

Fig. 2. T_c vs. x for $Gd_{1-x}Ba_{2+x}Cu_3O_{7-\delta}$.

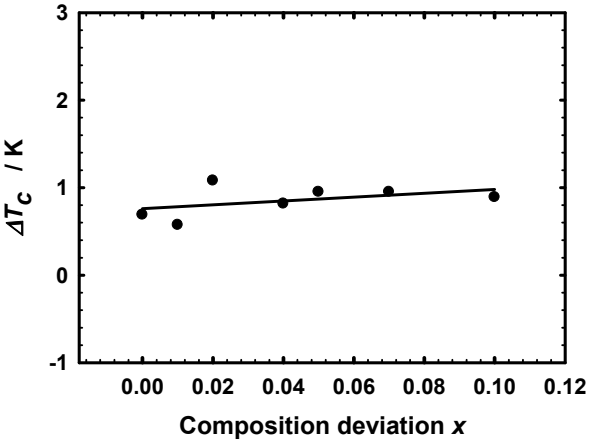

Fig. 3. ΔT_c vs. x for $Gd_{1-x}Ba_{2+x}Cu_3O_{7-\delta}$.

Hysteresis curves of mass magnetization M vs. applied field H for a series of $Gd_{1-x}Ba_{2+x}Cu_3O_{7-\delta}$ samples at 77 K and low applied field are shown in Fig. 4, for samples with x = 0, 0.04, 0.05 and 0.1 at 20 K and at higher field in Fig. 5.

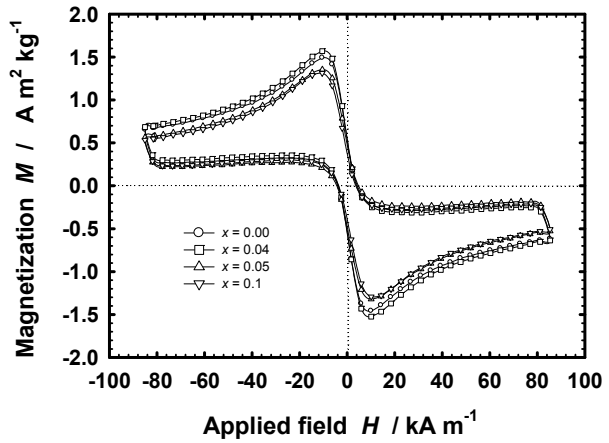

Fig. 4. M vs. H dependences of $Gd_{1-x}Ba_{2+x}Cu_3O_{7-\delta}$ at 77 K.

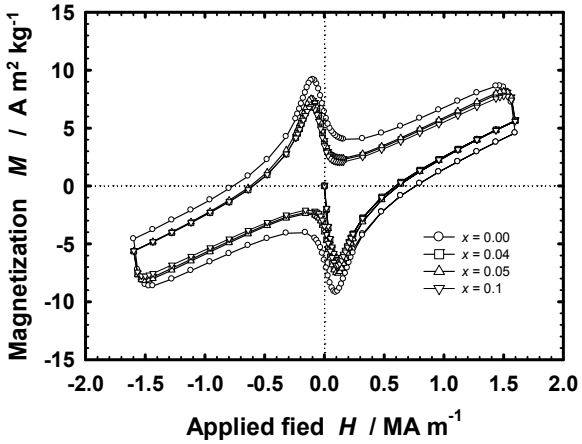

Fig. 5. The same as in Fig. 4 at 20 K.

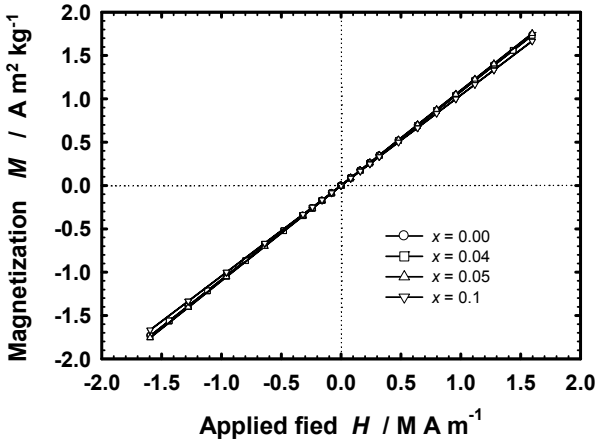

Fig. 6. M vs. H dependences of $Gd_{1-x}Ba_{2+x}Cu_3O_{7-\delta}$ at 100 K.

All the samples at 77 K show Z-shaped magnetization curves typical for polycrystalline samples at a weak applied field. We can see that magnetization curves are approximately the same. The best hysteresis properties and thus critical current density belong to the samples with the 0.01 Ba excess. The next hysteresis slowly continues to decrease with x. When

compared with this at 20 K, the form of magnetization curves is diametrically different. The curves involved a superconducting component (diamagnetic slope at low field and hysteresis) and paramagnetic contribution - slope of the curves point to the first and third quadrants. The presence of the paramagnetic component is clearly displayed at a temperature higher than critical temperature. Fig. 6 shows dependences of mass magnetization on the applied field at 100 K, where the superconducting component is absent. It is accepted that magnetic properties in the Gd-123 superconductors are mainly determined by magnetic moment of Gd cations. A weak decrease in magnetization for the sample with the lowest value of Gd content (x = 0.1) is in line with this. However, it is presently still questionable, whether or how the magnetic ordering RE cations affect superconductivity in the RE-123 type superconductors [10].

4. Conclusions

We studied transport and magnetization properties in a series of $Gd_{1-x}Ba_{2+x}Cu_3O_{7-\delta}$ samples with a composition deviation x from 0 to 0.1. The samples were synthesized by the solid-state reaction method at ~ 1000 °C for 72 h in flowing oxygen. The obtained results supported a positive effect of slight Ba excess doping on stabilization of T_c and ΔT_c and magnetization hysteresis at low field and 77 K. T_c and ΔT_c of the samples is about 93 K and 1 K, respectively. We can see that magnetization hysteresis at 77 K and low field is approximately the same. The best hysteresis properties and thus critical current density belong to the samples with the 0.01 Ba excess. In addition, magnetization hysteresis measurements at a higher field and lower temperature indicate that the slight excess Ba doping x can be used for tailoring critical current density with respect to the temperature and magnetic field application range, namely, e.g. the second peak effect.

Acknowledgements

This work was supported by the Agency of the Ministry of Education of the Slovak Republic for the Structural Funds of the EU, Operational Programme Research and Development, Project Code 26240220073 and by the grant APVV-0528-11.

References

[1] Shi Y, Babu NH, Iida K, Cardwell DA. *Physica C* **468**: 1408, 2008.
[2] Wu H, Dennis KW, Kramer MJ, McCallum RW. *Appl. Superconductivity* **6**: 87, 1998.
[3] Xu C, Hu A, Sakai N, Izumi M, Hirabayashi I. *Physica C* **417**: 77, 2005.
[4] Dai JQ, Zhao ZX, Xiong JW. *Supercond. Sci. Technol.* **16**: 815, 2003.
[5] Hinai H, Nariki S, Seo S-J, Sakai N, Murakami M, Otsuka M. *Supercond. Sci. Technolog*. **13**: 676, 2000.
[6] Kakeshita T, Hirose K, Lee S. *Physica C* **463-465**: 986, 2007.
[7] Cigáň A, Maňka J, Kopčok M, Jurdák P, Koňakovský A. *Acta Phys. Polonica A* **113**: 219, 2008.
[8] Maňka J, Cigáň A, Polovková J, Koňakovský A, Prnová A. *Meas. Sci. Rev*. **11**: 9, 2011.
[9] Zrubec V, Cigáň A, Maňka J. *Physica C* **223**: 90, 1994.
[10] Rogacki K. *Phys. Rev. B* **68**: 100507(R), 2003.

Determination of Parameters in the Jiles - Atherton Model for Measured Hysteresis Loops

Z. Roubal, V. Smejkal

Dept. of Theoretical and Experimental Electrical Engineering, Brno University of Technology, Technická 12, 612 00 Brno, Czech Republic.
Email: roubalz@feec.vutbr.cz

Abstract. *The Jiles-Atherton model of a hysteresis loop enables us to capture the behaviour of a magnetic material at the level of domains. At present, the model finds a large number of applications, for example in Spice simulators, where it facilitates the description of the behaviour of a core made from a magnetic material. The paper contains a discussion of constraints related to the original algorithm for the calculation of the model parameters and presents the results obtained via the least-squares method. Based on the measured typical behaviour of hysteresis loops (rounded and flat), we calculated the error between the measured and the calculated loops. To facilitate better approximation of the measured loop, the original computation model was modified, and the acquired results are presented within this article.*

Keywords: Hysteresis Loop, Jiles - Atherton Model, Magnetic Measurements.

1. Introduction

The laboratory of magnetic measurements at the DTEEE (Fig. 1, left) supports fully automated measurement of hysteresis loops. Real parameters of the examined materials can be measured on both open and closed samples, which enables us to record the behaviour of the materials at a point very close to operating use and conditions. Thanks to the applied high-quality fluxmeter, it is possible to select for the measurement of a quasi-static hysteresis loop a suitably long measuring period to ensure the suppression of the effect of eddy currents. Fig. 1 (right) shows that, in the measured toroidal sample of the Behanit material, it is necessary to select the measuring period of up to 80 s; given this precondition, the measured coercivity satisfactorily approached (in the limiting manner) its static value. The measured data are processed in the Matlab program (via a PC), and the calculated hysteresis value is corrected with respect to the systematic errors that occur during the measurement. A detailed description of certain elements of the process, for example correction of the fluxmeter zero, is provided by reference [1].

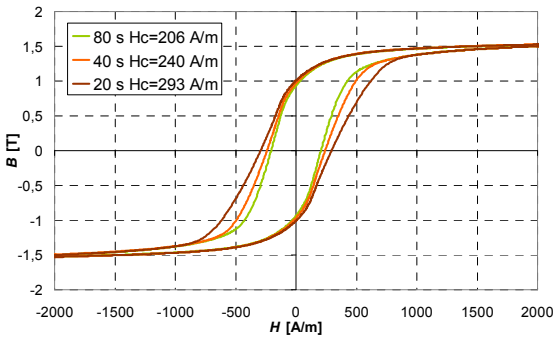

Fig. 1. The laboratory of magnetic measurements at the DTEEE, left; effect of the measured period length upon the measured hysteresis loop of the Behanit material and the resulting requirements placed on the fluxmeter, right.

To optimize the magnetic circuits, is necessary to create, based on the measured data, a suitable mathematical model of the hysteresis loop. With respect to the less intensive computation requirements and the possibility of application in Spice programs, we selected the Jiles - Atherton hysteresis loop model.

2. The Jiles – Atherton Hysteresis Loop Model

The basic equation for this model consists in the formula describing the behaviour of a magnetic material at the level of domains [2]. This formula provides a differential description that changes the output according to variation in the direction of the input value , namely the magnetic field intensity. The total magnetization M is then given by the formula:

$$M = M_{irr} + M_{rev} \tag{1}$$

where M_{irr} is the irreversible magnetization and M_{rev} denotes the reversible magnetization. With any magnetization change, there occur irreversible shifts defined according to

$$\frac{\mathrm{d}M_{\mathrm{irr}}}{\mathrm{d}H} = \frac{M_{\mathrm{an}} - M_{\mathrm{irr}}}{k \cdot \delta - \alpha\left(M_{\mathrm{an}} - M_{\mathrm{irr}}\right)} \tag{2}$$

In the above-shown relation (2), M_{an} and M_{irr} denote the anhysteretic and irreversible magnetization, respectively, $_{\mathrm{k}}$ is the parameter determining the widening of the curve, δ is the sign parameter, and α is the molecular field parameter. The sign function follows the variation of the magnetic field intensity direction and is therefore given by the formula:

$$\delta = \begin{cases} +1 \; pro \; dH/dt > 0 \\ -1 \; pro \; dH/dt < 0 \end{cases} \tag{3}$$

Anhysteretic magnetization is an idealized process in which no errors occur in the crystal lattice during magnetization. Thus, the course of the process is given by the shift of the domain walls and the displacement of the spontaneous magnetization of these domains in the direction of the external field. This relation is most often expressed by the Langevin function in the form:

$$= M_{\mathrm{sat}} \cdot \left[\coth\left(\frac{H + \alpha \cdot M}{a} \right) - \frac{a}{H + \alpha \cdot M} \right] \tag{4}$$

where M_{sat} is the saturation magnetization and a denotes the shaped, temperature-dependent parameter. The parameter assumes values in the order of approximately 10^{-3} to 10^{-7}. However, the relation of anhysteretic magnetization may generally be indicated by any monotonously growing function, and it is also possible to use the measured curve. The last part of the formula (1) consists in reversible magnetization; in the model, this magnetization is expressed as the difference of the anhysteretic and the irreversible magnetization. This difference is reduced to

$$M_{\mathrm{rev}} = c \cdot \left(M_{\mathrm{an}} - M_{\mathrm{irr}}\right) \tag{5}$$

where the parameter c is from the interval $0 < \mathrm{c} < 1$.

3. Identification of the Jiles - Atherton model in selected materials

For the calculation, we need to use an iteration method and apply suitably chosen initial coefficient values. The iteration procedure presented by basic reference [2] does not converge for certain hysteresis loops, as noted by the authors of source [3]; this claim was verified during the calculation of the flat hysteresis loop of a nanocrystalline material. For this reason, we used the least-squares method utilizing only the initial estimation indicated by [2].

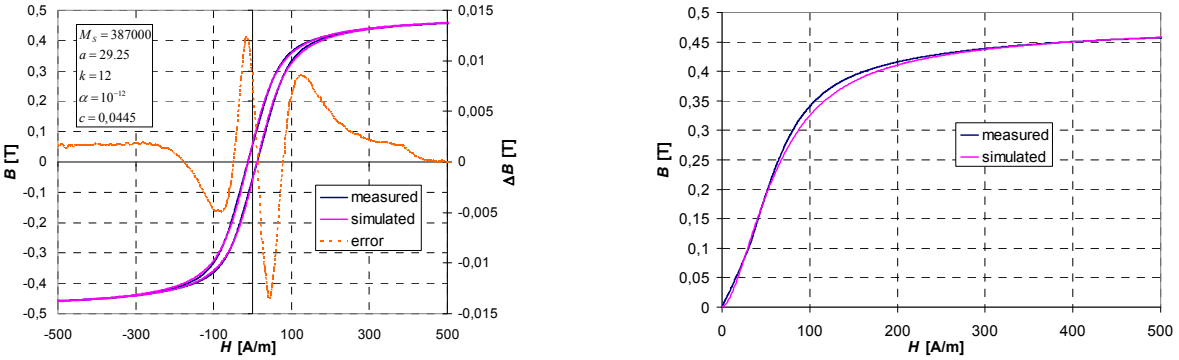

Fig. 2. The measured and simulated hysteresis loop of the 3C90 ferrite, left; the initial magnetization curve, right

The results for the 3C90 ferrite and the correct definition of the initial magnetization curve are both shown in Fig. 2.

If the Langevin function is applied to a material with a flat hysteresis loop having a sharp elbow such as required in, for example, switching forward converters, the approximation does not give satisfactory results. We measured the promising VITROPERM 500F nanocrystalline material. Its approximation for the least sum of the deviation squares is shown in the left section of Fig. 3; the right section of the figure then indicates the condition that, in $H_{\max}$, the simulated hysteresis loop does not exceed the value of $B_{\max}$. Here, it is obvious that the model does not capture correctly the shape of the hysteresis loop in the elbow and generally exhibits higher initial permeability. The limitation to $B_{\max}$ has proved beneficial for lower excitation levels.

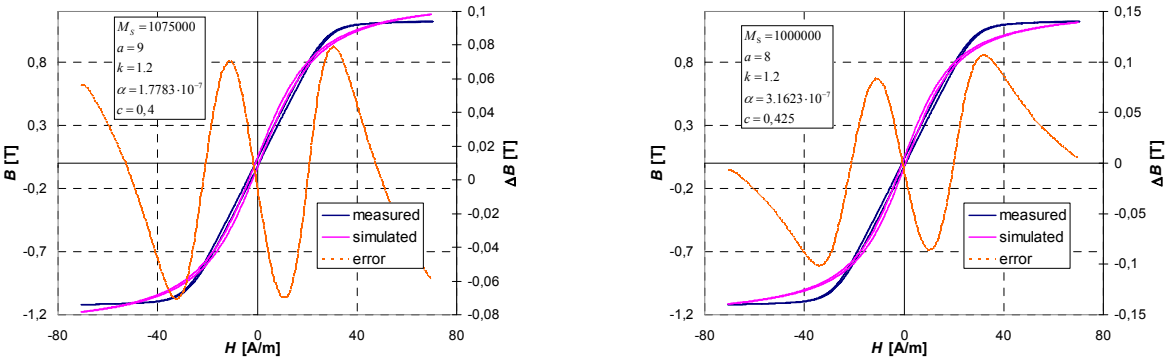

Fig. 3. The VITROPERM 500F hysteresis loop, left; with the $B_{\max}$ constraint, right.

Better consistency between the simulations and the measured hysteresis loop can be achieved if the parameter in the formula (2) is separated from the parameter in the Langevin function as present in the equation (4). With the model thus widened, better inclination of the hysteresis loop can be ensured.

The simulation of a hysteresis loop can be most faithfully captured using the measured curve of anhysteretic magnetization. As the measurement of the curve requires special behaviour of the magnetizing current [3], its course was estimated from the mean value of the measured hysteresis loop graphically. Despite this deficit, the achieved results are very good; the relative error between the measured and the simulated boundary hysteresis loops did not exceed 1%. A comparison between the measured and the simulated loops for unipolar excitation is shown in Fig. 5.

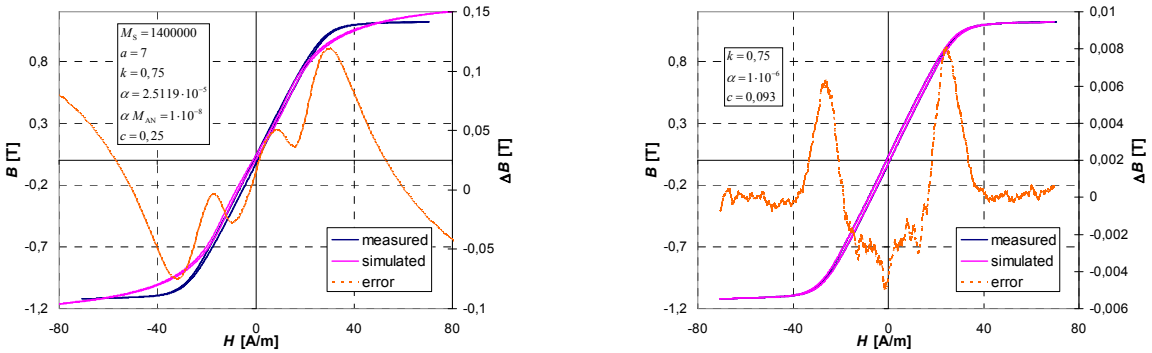

Fig. 4. The hysteresis loop for the separation of α parameters (left) and for the given behaviour of M_{man} (right)

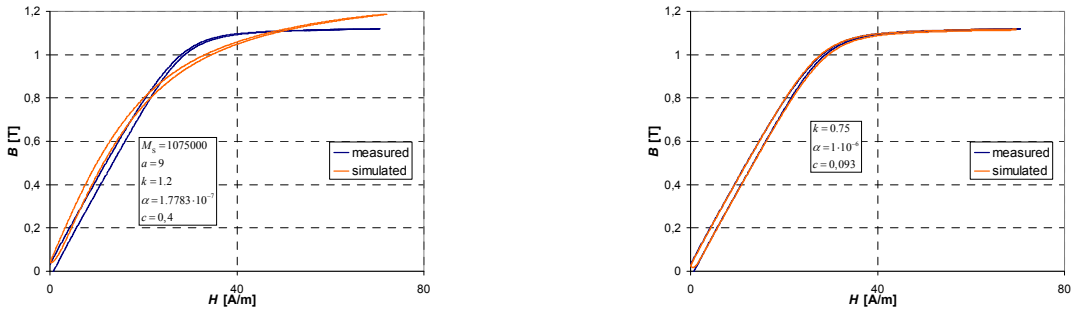

Fig. 5. Fig. 3. Unipolar excitation of VITROPERM 500F for the Langevin function (left) and for the preset antihysteretic curve (right).

4. Conclusions

The authors present a discussion of constraints characterizing the Jiles-Atherton hysteresis loop model under the Langevin function-based approximation of the anhysteretic magnetization curve. Further research will be directed towards setting up a system for the measurement of the anhysteretic magnetization curve. The accuracy of the given approximation is well defined by the determination of the difference between the measured and the simulated curves.

Acknowledgements

The research described in the paper was financially supported by project of the BUT Grant Agency, FEKT-S-11-5/2012 project from Education for Competitiveness Operative Programme CZ.1.07.2.3.00.20.0175, (Electro-researcher).

References

[1] Roubal Z, Marcon P, Čáp M. Analysis of magnetic properties measurement in closed samples. In proceedings 9th International Conference 2012 ELEKTRO, 2012, 460-464.

[2] Jiles D, Thoelke J, Devine M. Numerical Determination of Hysteresis Parameters for the Modeling of Magnetic Properties Using the Theory of Ferromagnetic Hysteresis. *IEEE Transaction on Magnetics,* 1 (28): 27-35, 1992.

[3] Novák M. Přechodový děj při zapnutí transformátoru: Způsoby omezování zapínacího proudu. Disertační práce, Liberec, 2003.

On-Site Power Quality Measurements in a Photovoltaic System Connected with the Distribution Network

D. I. Alexandrescu, P. Vrabcek

Slovak Institute of Metrology, Karloveska 63, 842 55, Bratislava, Slovakia,
Email: alexandrescu@smu.gov.sk

Abstract. *This paper analyse the power quality in a Photovoltaic System connected with the Distribution Network Grid. The work was performed in the framework of the European Metrology Research Programme Project "Metrology for Smart Electrical Grids", Work Package 3 – Tools for portable and remote measurement of Power Quality [1].*

Keyword: Power Quality, Photovoltaic System, Distribution Network Grid, Harmonics, Voltage Unbalance

1. Introduction

The power quality (PQ) measurement and the data acquisition is based on the existing standards EN 50160 [2] which provides recommended levels for different power quality parameters, including a time-based percentage during which the levels should be kept and IEC 61000-4-30 [3] which provides measurement methods, describes measurement formulas, sets accuracy levels and defines aggregation periods.

2. Description of the network and measurement apparatus

The PQ measurements were performed in an electrical cabinet with the nominal voltage 230V, current transformers ratio 150A/5A, 3phase with neutral, fed by low voltage (LV) from a MV/LV substation. The Photovoltaic (PV) System is connected with the electrical cabinet via a 3phase underground cable.

We used for the measurement a Fluke Power Quality Analyzer and transducers (voltage sensors 600V and current clamps 50A/5A). The voltage measurement connections were made direct on 3phase bus bars using crocodile clips. Current clamps were connected on the secondary windings (5A) of the current transformers. The Power Quality Analyzer was calibrated prior starting on-site measurements. Current transformers were calibrated before installation within the electrical cabinet.

The exact phasing of the PV connections is unknown however from the results it can be inferred that the distribution between the three phases in uneven and is approximately distributed 35% - 40% - 25% across phases L1-L2-L3.

3. Measurement results and analysis

The power quality measurements were performed within the period June (before the PV panels were installed) and July 2012 (after the PV panels were installed), 2 months measurement campaigns.

A huge amount of data was collected during these surveys. The graphs presented in this section are for a period of 2 weeks, one week before the PV panels were installed and one week after the PV panels were installed.

It is interesting to consider the power flow at the monitoring point over a period of time when the PV systems are receiving variable exposure from the sun.

Voltage Level

We are expecting that the voltage will rise during periods of PV system generation due to the real (active) power flow from the PV to the distribution network grid. By measuring voltages before and after the PV panels were installed changes in the voltage level with generation were investigated.

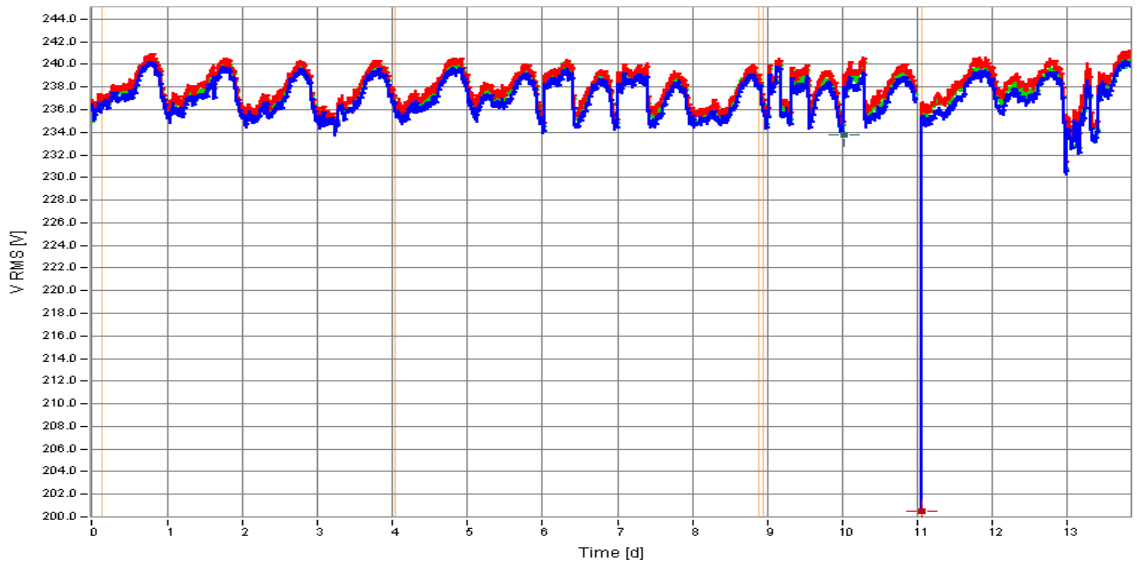

Fig. 1 Vrms (L1 blue, L2 red, L3 green) – June & July 2012

Fig. 1 shows the 3phase voltage levels within the 2 weeks period. We can visualize the variation in voltage due to PV generation compared to no generation.

Active Power and Reactive Power

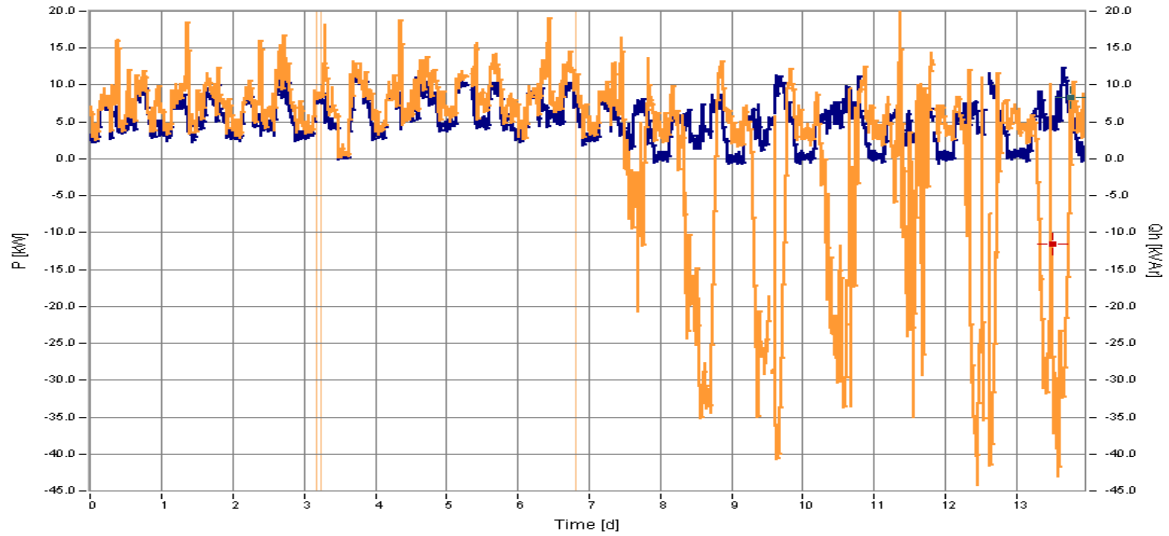

Fig. 2 Real Power P (orange) vs Reactive Power Qh (dark blue) – June & July 2012

Fig. 2 shows the sum of the Real Power vs the sum of the Reactive Power within the studied period. The Reactive Power is not strongly correlated to solar generation as PV panels/ inverter systems are only providing the active power during periods of generation.

As the reactive power for loads still needs to be supplied, it is left to the network to generate this wattless power for no revenue return. Aggregation of PV and other inverter generation on the network will leave an ever-increasing burden on network operators to generate the reactive power to satisfy the load.

Distortion and Harmonics

It is instructive as well to examine the recorded data for any effect of PV generation.

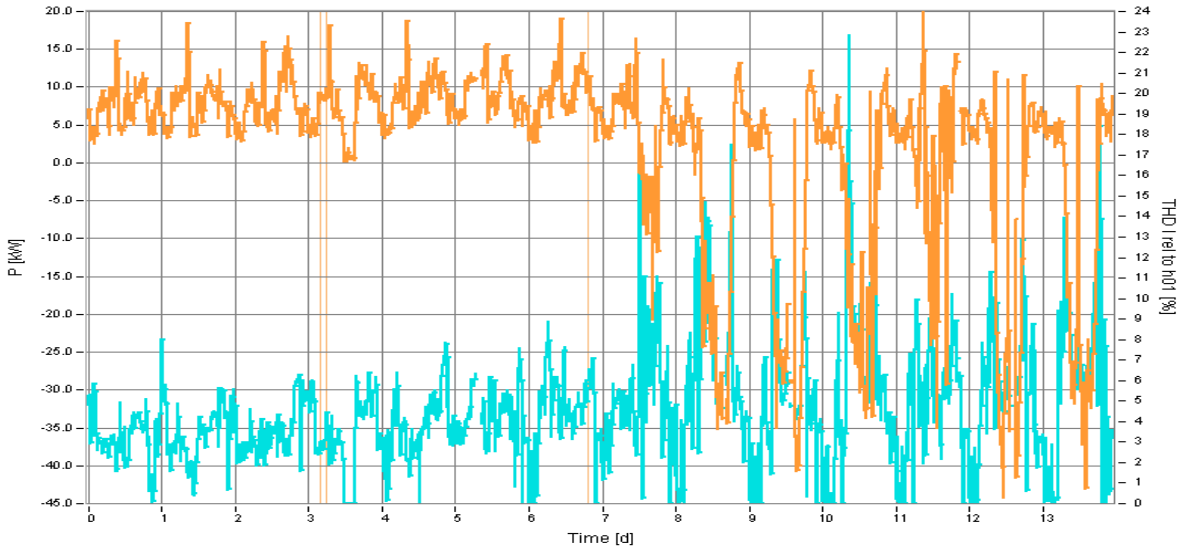

Fig. 3 Real Power P (orange) vs THD Irel to h01 (L2 light blue) - June & July 2012

Fig. 3 shows a chart of current total harmonic distortion (THD) on L2 without and with the generation of the real power into the distribution network grid. We can see that current THD increases as PV export increases. This effect occurs on all three phases, the L1&L3 effect being less visible due to a little bit lower generation on these phases.

The rise in current THD with generation is most likely to do with the increasing dominance of the sinewave (inverter output) generation current increasingly overwhelming generally low-level load current.

This raises the issue (as with the case of reactive power) that whilst the fundamental current is supplied by the PV systems during periods of generation, the harmonic currents required by the agitate load, must be supplied by the network. This could lead to planning issues as the proportion of inverter-based generators continues to grow.

Voltage & Current Unbalance

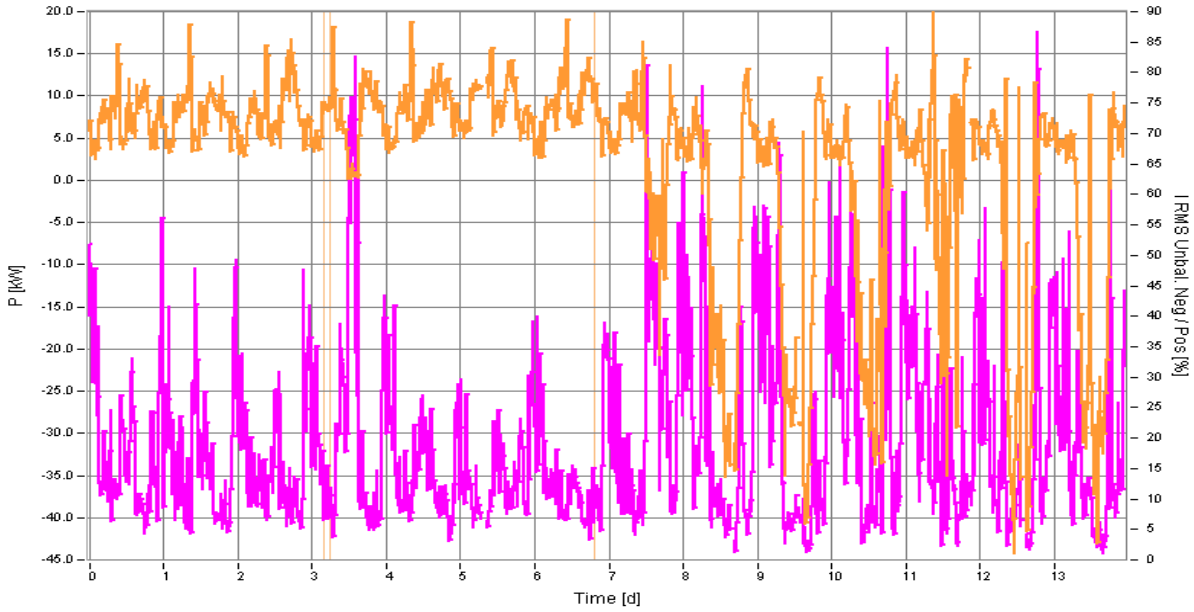

Fig. 4 Real Power P (orange) vs Irms Unbalance (pink) - June & July 2012

Voltage unbalance factor is defined in EN 50160 as the ratio of the negative sequence voltage to the positive sequence voltage. In all cases no unbalance factors above the 2 % limit in EN50160 were observed.

We can see in Fig. 4 that the current unbalance negative /positive was higher when the PV exports increases.

4. Conclusions

The monitoring of power quality on a low voltage feeder connecting a significant amount of PV generation reveals power quality degradation during periods of PV generation.

A significant effect seen during the study was a rise in voltage associated with PV generation. The analysis of the results presented shows that the voltage at the electrical cabinet increased by about 3 V during periods of generation. It was also observed a Voltage Dip and a Short Interruption (approx. 1.5 min.) during the PV generation.

It is noteworthy that on average the PV units are generating at approximately full capacity on the sunniest days during the survey.

The other point of interest is more general and concerns the supply of reactive power and harmonics during periods of PV generation. As the inverters in the system generate fundamental active power, the grid is required to supply the harmonics and the reactive power as it would without the presence of the PV, but with reduced billable watts.

Acknowledgements

The research leading to the results described in this paper is part of the European Metrology Research Program (EMRP), which is jointly funded by the EMRP participating countries within EURAMET and the European Union.

References

[1] Gert Rietveld – VSL, the Nederlands, Project Protocol “Metrology for Smart Grids”, October 2010.

[2] EN 50160:2010, “Voltage characteristics of electricity supplied by public distribution systems”.

[3] IEC 61000-4-30:2009, “Testing and measurement techniques – Power quality measurement methods”.

[4] T. Degner, J. Schmidt, P. Strauss, Dispower, Distributed Generation with High Penetration of Renewable Energy Sources, Final Public Report, iSET, Kassel, 2005.

[5] P.S. Wright and P. Clarkson, “Development of an Ethernet Enabled Digitizer for On-Site AC Measurements”, IEEE Transactions and Meas. & Instrum., 6-7 July 2011, Page(s): 2229-2235.

[6] S. Cobben, B. Gaiddon, H. Laukamp, “Impact of Photovoltaic Generation on Power Quality in Urban Areas with High PV Population”, Intelligent Energy Europe Project “PV Upscale”, 2008.

The Reliability Evaluation of Measuring System Designed to Calibrate Direct Current Watt-Hour Meter

[1]P. Otomański, [2]P. Zazula

[1]Poznan University of Technology, Institute of Electrical Engineering and Electronics, Piotrowo street 3a, 60-965 Poznań, Poland
[2]Regional Verification Office in Poznań, Krakowska street 19, 61-893 Poznań, Poland
Email: otoman@et.put.poznan.pl

Abstract. *The paper presents a method for evaluating the accuracy of indications of the direct current Watt-hour meters in a designed and constructed measuring system. Such measuring system is composed of two multi-function calibrators, and a specialised high-voltage attachment dedicated for this system, which makes it possible to generate direct voltages in a required range up to 4 kV with a suitably high precision. The authors described in detail particular elements of the measuring system together with the results of its calibration. The measurement results were completed with a presentation of uncertainty budgets, developed for all quantities measured.*

Keywords: Measuring System, Direct Current Watt-Hour Meter, Measurement Uncertainty

1. Introduction

The evaluation of metrological parameters of direct current Watt-hour meters is a complex measurement problem. In practice, calibration is frequently assumed as the proper form of such evaluation. The values obtained as result of calibration, associated with the uncertainty of determining them, should be defined in specified measuring points, according to respective standards and other supplementary documents. The paper presents a method for evaluating the parameters of DC Watt-hour meter LE3000plus. Meters of that type find application in measuring the power and energy of direct current in the railway traction network. These meters are modern, microprocessors measurement devices, equipped with an additional measurement interface that allows the remote transmission of registered measurement results. The evaluated Watt-hour meter of type LE3000plus consists of: high-voltage, measuring part LE3000plus_HVM, low-voltage, communication part - LE3000plus_KOM, measuring shunt, fiber optic cable connecting the high-voltage and low-voltage parts, GSM/GPS antenna, together with antenna wires. A detailed description of all the functions and potential of this meter is included in [1].

2. Measuring system

The measuring system consists of two multi-function calibrators, and a specialised high-voltage attachment dedicated for this system, which allows the generation of direct voltages in a demanded range of up to 4 kV with suitably high precision. Fig. 1 presents a diagram of the prepared measuring system for the testing of direct current Watt-hour meters together with the tested Watt-hour meter LE3000plus. The signal between terminals A and B corresponds, in working conditions, to the voltage drop on the external measurement shunt, and the signal between terminals A and C is the voltage corresponding actually to a high voltage in electrical traction. In the developed measuring system voltage U_{AB} attained small values, and therefore the costs of insulation between internal blocks of the measuring system were minimized. Terminal C of the developed measuring system is located on a high minus potential, of the order of 4 kV. The developed measuring system provides appropriate metrological parameters, minimum energy consumption from the supply network, as well as adequate

separation of components. The determined relative value of expanded uncertainty of this part of the measuring system equals 0.06 % and it is stated in the current calibration certificate. In the original version of the system, during the determining of electrical energy values, time was measured with mechanical stopwatch. At the time measurement of the order of 30 min. with such stopwatch, the value of expanded uncertainty at a level of 0.12 s was achieved. A detailed description of these problems can be found in work [2].

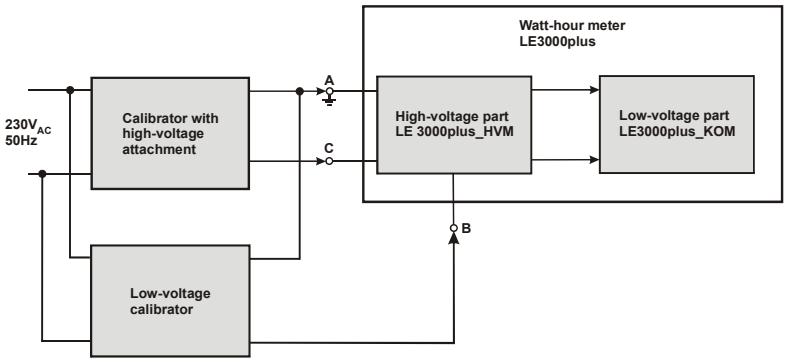

Fig. 1. Diagram of measuring system for testing the direct current Watt-hour meter

Essential modifications were introduced in the present version of measuring system, which enabled the energy measurement inaccuracies to be significantly limited. The modifications allowed the error related to the reaction time of the person conducting the measurements to be eliminated. High voltage obtained from the voltage calibrator with attachment is connected to the investigated meter for the whole duration of measurements. During normal work of a meter in railway traction network the load current is measured by the meter indirectly, through a voltage drop on the external shunt. In the measuring system the load current measured by the meter is simulated by the low-voltage calibrator, the output signal of which simulates the voltage drop from the shunt. The calibrator is equipped with a precise time distributor with a range of settings 1 ÷ 85 min. It generates a signal during a strictly specified time interval; in standard version it is a 15-minute interval. This calibrator, together with the time distributor that is its integral part, was calibrated in order to evaluate the inaccuracies of time and voltage measurement. The measurement uncertainty was determined according to the recommendations in document [3]. A detailed description of these problems can be found in work [4].

3. Experimental research

In the measuring system presented in Fig. 1, the Watt-hour meters of direct current LE 3000plus were calibrated. During this process, the indications of the same meter were compared with the settings on control devices. The readings were made from the display of the very meter, with resolution equal to 0.1 kWh. The results presented in the paper were based on high experience of the authors, who tested over 90 meters of class 0.5 and 1. For each meter, the test consisted in multiple measurements, necessary to evaluate the dispersion of results achieved, or, alternatively, to eliminate excessive errors, which made it possible to determine the standard uncertainty of type A. For each meter, the following quantities were measured: voltage, current, and energy imported from and exported to the network. Due to the limited publication space, only the results related to research on exported/imported energy have been discussed in the paper. It is authors' intention to present full results during the conference presentation. The import energy E_p of tested direct current energy meter LE3000plus was measured in test points, for specified values of current and voltage, in time $t = 0.25$ h. In order to increase the reliability, the measurements were carried out many times. Examples of results achieved are shown in Table 1.

Table 1. Results of calibrating LE3000plus meter at the measurements of import energy E_p.

Import energy measurement U = 3300 V, I = 1000 A, t = 0.25 h, E = 825 kWh								
U			I			E_p		
W_{wsk}	W_{zad}	Δ	W_{wsk}	W_{zad}	Δ	W_{wsk}	W_{zad}	Δ
V	V	V	A	A	A	kWh	kWh	kWh
3300.0	-3300.6	-0.6	-999.4	-1000.0	-0.6	824.5	825.33	-0.83
3300.0	-3300.6	-0.6	-999.4	-1000.0	-0.6	824.5	825.33	-0.83
3300.0	-3300.6	-0.6	-999.5	-1000.0	-0.5	825.0	825.33	-0.33

The export energy E_o, of the tested direct current energy meter LE3000plus was measured in a way similar to the measurements of import energy, and the measurements were repeated many times. Examples of measurement results are shown in Table 2.

Table 2. Results of calibrating LE3000plus meter at the measurements of export energy E_o.

Export energy measurement U = 3600 V, I = 1000 A, t = 0.25 h E = 900 kWh								
U			I			E_o		
W_{wsk}	W_{zad}	Δ	W_{wsk}	W_{zad}	Δ	W_{wsk}	W_{zad}	Δ
V	V	V	A	A	A	kWh	kWh	kWh
3600.0	-3601.0	-1.0	-999.0	-1000.0	1.0	-899.0	900.49	1.49
3600.0	-3600.8	-0.8	-999.1	-1000.0	0.9	-898.9	900.49	1.59
3600.0	-3600.8	-0.8	-999.0	-1000.0	1.0	-899.0	900.49	1.49

Correct values W_{zad} were given according to the setting adopted on the control equipment. Because according to the diagram shown in Fig. 1, the system works with the so-called "inverted mass", in this case the indication error Δ takes a form according to equation (1):

$$\Delta = W_{wsk} - (-W_{zad}) \tag{1}$$

where W_{wsk} is the value indicated by the evaluated meter.

4. Uncertainty budget

Statement of all identified component standard uncertainties estimated with A and B Type methods is called uncertainty budget. The aim of creating the uncertainty budget is to prove that the combined uncertainty of measurement result u_c, was estimated in a matter-of-fact, penetrating and verifiable way. On that account, all the component uncertainties taken into consideration, also those with the value estimated as zero, should be listed in the budget. It is essential to assign a suitable type of probability distribution to particular component uncertainties in the uncertainty budget. From formula for energy it results, that in order to determine the value of combined standard uncertainty u_c, it is necessary to determine the values of partial derivatives in relation to voltage, current and time, which determine the values of sensitivity coefficients c_i.

Table 3 shows an example of uncertainty budget for the measurement of import energy, for test point E = 825 kWh. Quantities influencing the value of combined uncertainty put in the below table, denote respectively:

- E_{wsk} - value of indicated energy,
- $\delta\Delta_{rE}$ - correction resulting from the resolution of calibrated meter,
- $u(U)$, $u(I)$, $u(t)$ – uncertainties attributed to the measurements of voltage, current and time.

Table 4 presents the determined values of expanded uncertainty U, for the results of import energy measurement contained in Table 1.

Table 3. Uncertainty budget for selected measurement value of import energy

Quantity symbol	Quantity estimate	Standard uncertainty $u(x_i)$		Probability distribution	Sensitivity coefficient c_i		Part of combined uncertainty	
E_{wsk}	824.7	1.67E-01	kWh	Normal	1	kWh	1.67E-01	kWh
$\delta\Delta_{rE}$	0	2.89E-02	kWh	Rectangular	1	kWh	2.89E-02	kWh
$u(U)$	0	2.92E-01	V	Normal	0.250	kAh	7.30E-02	kWh
$u(I)$	0	6.64E-02	A	Normal	0.825	kVh	5.48E-02	kWh
$u(t)$	0	3.19E-07	h	Normal	3298.13	kVA	1.05E-03	kWh
$E_{wsk\ avg}$	824.7	-		-	-		1.92E-01	kWh

Table 4. Results of calibrating import energy for time t = 0.25 h.

Import energy measurement with U_n = 3300 V, I_n = 1000 A, t = 0.25 h			
Indicated value	Correct value	Indication error	Measurement uncertainty U
kWh	kWh	kWh	kWh
824.7	825.33	-0.67	0.54

For export energy measurements, contained in Table 2, the uncertainty budget was prepared similarly as for the import energy measurements. The results are shown in Table 5.

Table 5. Results of calibrating export energy for time t = 0.25 h.

Export energy measurement with U_n = 3600 V, I_n = - 1000 A, t = 0.25 h			
Indicated value	Correct value	Indication error	Measurement uncertainty U
kWh	kWh	kWh	kWh
-899.0	-900.49	1.53	0.22

5. Conclusions

The authors of the paper attempted to discuss complex problems of experimental research on direct current Watt-hour meters for voltage of the order of 4 kV. A designed and constructed measuring system was presented, consisting of two multi-function calibrators, a specialised high-voltage attachment dedicated for this system, in order to generate direct voltages in a demanded range of up to 4 kV with suitably high precision. The publication contains the results of experiments carried out on a numerous and representative set of direct current Watt-hour meters LE3000plus items, in the conditions of accredited laboratory. The testing of so large population of devices permitted the authors to draw reliable and objective conclusions. When selecting the measurement points of a meter tested in the measuring system, the authors took into account the conclusions drawn from the testing of meters in working conditions, installed in electrical locomotives during their normal work.

References

[1] Operational and Maintenance Manual Direct current Watt-hour meter 3 kV LE3000plus.

[2] Otomański P., Zazula P. Metrological characteristics of measuring position for direct current Watt-hour meter research in range to 4 kV. *Electrical Review*, 12: 315-317, 2008.

[3] EA-4/02 Expression of the Uncertainty of Measurement in Calibration European co-operation for Accreditation, 1999.

[4] Otomański P., Zazula P. The measuring system for the evaluation of the metrological properties of direct current Watt-hour meters. *Measurement Automation and Monitoring*, 58: 764-766, 2012.

Measurement Error of Voltage Responsivity of Pyroelectric Detector Induced by Use of Non-Sinusoidal Modulation of Radiation

A. Odon

Poznan University of Technology, Institute of Electrical Engineering and Electronics,
Piotrowo 3A, 60-965 Poznan, Poland,
Email: andrzej.odon@put.poznan.pl

Abstract. *For the experimental measurements of pyroelectric detectors voltage responsivity, sinusoidal modulated optical radiation should be used. In practice, optical choppers are commonly used in experimental set-ups to modulate optical source and as a result optical radiation may have a square or trapezoidal waveform. In the paper, the frequency dependence of voltage responsivity of pyroelectric detector for different shapes of waveform of absorbed radiation was studied by use either simulation and experimental method. Simulation studies were carried with the program MATLAB-Simulink and verified experimentally. The results of the studies indicated that the frequency responses of pyroelectric detector show considerable differences for different wave profiles of radiation excited detector.*

Keywords: Pyroelectric Sensor, Responsivity, Optical Modulation

1. Introduction

Theoretical and experimental studies of the frequency dependence of voltage responsivity of a pyroelectric detector should be performed applying sinusoidal modulated optical radiation, which follows from well known formal requirements for determination of the Bode frequency plot. However, in the majority of papers the results concerning the detector voltage responsivity as a function of frequency were obtained for the optical radiation signal of trapezoidal or rectangular shape [1-2] because of the use of an electromechanical modulator of optical radiation. Such results must be charged with error.

The aim of this study was to establish the metrological consequences following from the use of optical signals of trapezoidal or square shape concerning the voltage responsivity R_V of a pyroelectric detector as a function of the frequency of the modulated optical radiation signal. The study was performed by the simulation method with the program MATLAB-Simulink whose results were confronted with experimental data. It should be noted that literature on the subject is scarce, although the problem seems important from the point of view of correct realization of optoelectronic experiments. In fact, only one significant paper devoted to this subject has been found [3]. The results it presents and in particular the final conclusions, are consistent with those obtained in this study. The authors of [3] have applied a completely different method than that used in this work. They have determined the voltage responsivity of the detector as a function of frequency on the basis of a mathematical model of the detector for which they determined a superposition of the voltage responsivities to particular harmonics of the non-sinusoidal optical radiation signal.

2. Subject and Methods

Voltage responsivity of a pyroelectric detector R_v is defined as the ratio of the amplitude of a response signal V_m of a detector to the amplitude Φ_m of a sinusoidal input signal as a function of angular frequency ω or frequency f of this signal. Analytical considerations leading to a

mathematical expression for the detector voltage responsivity as a function of angular frequency $R_v = f(\omega)$, are well known [4] and are inferred from the equivalent scheme of a pyroelectric detector [4] shown in Fig. 1.

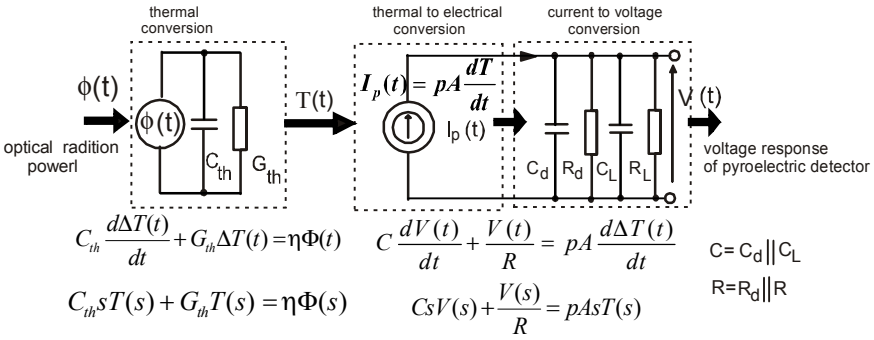

$$C_{th}\frac{d\Delta T(t)}{dt} + G_{th}\Delta T(t) = \eta\Phi(t) \qquad C\frac{dV(t)}{dt} + \frac{V(t)}{R} = pA\frac{d\Delta T(t)}{dt}$$

$$C_{th}sT(s) + G_{th}T(s) = \eta\Phi(s) \qquad CsV(s) + \frac{V(s)}{R} = pAsT(s)$$

Fig. 1 Equivalent scheme of a pyroelectric detector cooperating with voltage amplifier [4, 5]. Symbols in the figure: C_{th} – thermal capacity of pyroelectric detector, G_{th} - thermal conductance of pyroelectric detector, $\Delta T(t)$ - temperature changes of pyroelectric material, η – absorption coefficient of radiation, p – pyroelectric coefficient, A – surface of pyroelectric detector, C – equivalent capacitance for parallel connected pyroelectric capacitance, C_d and input amplifier capacitance, R - equivalent resistance for parallel connected leakage resistance R_d of pyroelectric detector and input amplifier resistance.

In this study the simulation method was applied using the MATLAB-Simulink environment. Because of the specific way of data implementation in this program package, the voltage responsivity $R_V(s)$ of a pyroelectric detector must be presented in the Laplace domain. After some mathematical transformations of the equations in Laplace domain describing subsequent stages of conversion (described detailed in [5]) the relation for voltage responsivity $R_V(s)$ of a pyroelectric detector is obtained, eq. (1):

$$R_v(s) = \frac{V(s)}{\Phi(s)} = \frac{p\eta\tau_{th}\tau_e s}{c'dC(s\tau_{th}+1)(s\tau_e+1)} \tag{1}$$

where c' is the volume specific heat of the detector, τ_{th} is the thermal time constant defined as $\tau_{th} = C_{th} / G_{th}$, τ_e is the time constant found from the relation $\tau_e = C_d R$, d is the thickness of the pyroelectric plate of detector, .

Equation (1) is in fact transfer function of pyroelectric detector model, which may be used also for simulation study of different type, especially for studies of voltage response signal to excitation with a radiation signal of given wave-form [5].

3. Simulation and experimental results

Simulation investigation of voltage responsivity was performed for the model pyroelectric detector made by the author based on the specific pyroelectric detector type PVDF, of known parameters, using excitations by optical radiation signals of sinusoidal, rectangular and trapezoidal shape of the same amplitudes of radiation power. The results of simulations realised within the MATLAB-Simulink package permitted drawing the voltage responsivity of the pyroelectric detector as a function of frequency $R_V = f(f)$ for the sinusoidal, trapezoidal (of the rise and fall time of 20% of period T) or rectangular modulation of the optical radiation signal (Fig. 2). Fig. 3 presents the relative error δ, in percent, of the voltage

responsivity determined for the non-sinusoidal optical radiation signals, i.e. for rectangular one and trapezoid one with the rise and fall times of 20% of period T, with respect to the voltage responsivity obtained for the sinusoidal radiation signal treated as the correct value.

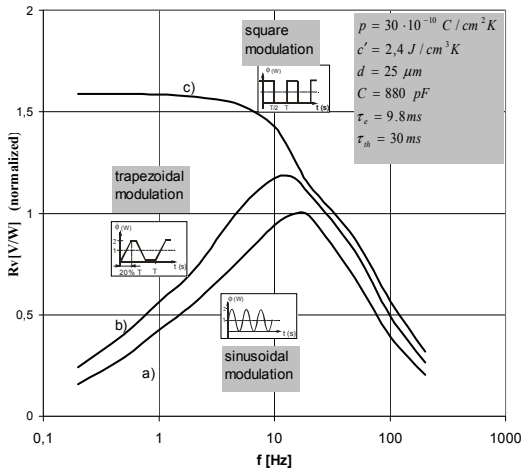

Fig. 2. Frequency dependence of pyroelectric detector responsivity $R_V = f(f)$ with a) sinusoidal modulated radiation, b) trapezoidal modulated radiation with rise and fall times of 20% of period, c) square-wave modulated radiation The studies were performed using computer simulation.

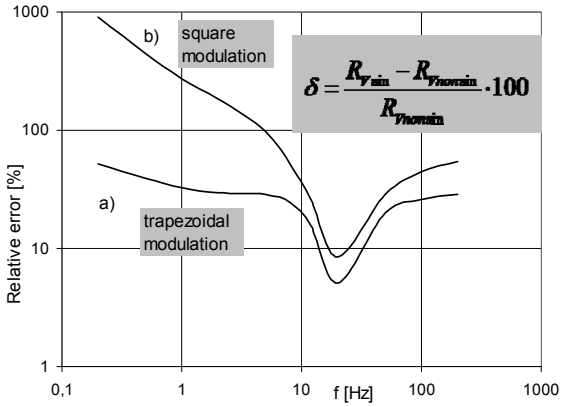

Fig. 3 Relative error δ of frequency dependence of voltage responsivity R_V of pyroelectric detector for non-sinusoidal modulation: a) trapezoidal modulated radiation b) square-wave modulated radiation. The studies were performed using computer simulation.

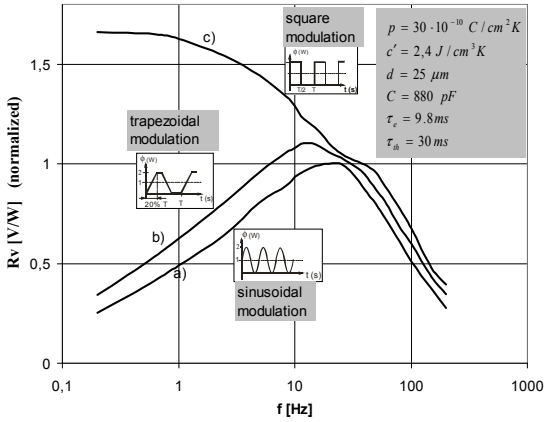

Fig. 4. Experimentally determined frequency dependence of pyroelectric detector responsivity $R_V = f(f)$ with a) sinusoidal modulated radiation, b) trapezoidal modulated radiation with rise and fall times of 20% of period, c) square-wave modulated radiation.

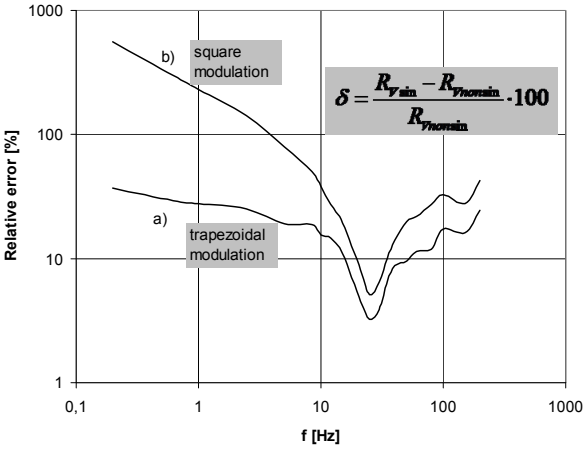

Fig. 5 Relative error δ of experimentally determined dependence of voltage responsivity R_V of pyroelectric detector for non-sinusoidal modulation: a) trapezoidal modulated radiation b) square-wave modulated radiation.

The results of simulation studies of the frequency dependence of voltage responsivity of the pyroelectric detector $R_V = f(f)$, for the sinusoidal, trapezoidal and rectangular modulation of the optical radiation signal are presented in Fig. 2. As shown in these figures, the $R_V = f(f)$ plots obtained for the optical radiation signal of the trapezoidal or rectangular shape can significantly differ from the plot determined for the optical signal of sinusoidal shape, treated as the reference. It should be noted that in particular for low frequencies of optical radiation modulation the voltage responsivity obtained for non-sinusoidal optical radiation signals are

charged with considerable error reaching even up to a few hundred percent (Fig. 3). The error is defined as:

$$\delta = \frac{R_{Vnon\sin} - R_{V\sin}}{R_{\sin}} 100 \tag{2}$$

where: R_{Vnonsin} is voltage responsivity for nonsinusoidal waveform of radiation, R_{Vsin} is voltage responsivity for sinusoidal waveform of radiation.

In the experiment performed to verify the above results, an electronically controlled source of optical radiation, based on a high power light emitting diode, was applied. The voltage responsivity of the PVDF type detector constructed by the author was measured versus the frequency of the optical radiation signal of rectangular and sinusoidal shapes and the same amplitudes. The results are presented in the form of plots of voltage responsivity versus frequency R_V (Fig. 4) and relative error δ versus frequency (Fig. 5). They are in good agreement with the results obtained by simulation study and presented in Figs. 2 and 3.

4. Conclusions

As follows from the results of simulation and experimental studies, the shapes of the plots of voltage responsivity of a pyroelectric detector versus frequency $R_V = f(f)$ obtained for different waveforms of radiation are significantly different and their maximum values occur at different values of frequency. The $R_V = f(f)$ dependence obtained for the optical radiation signal of rectangular shape shows the most pronounced differences from the shape of an analogous dependence for the optical signal of sinusoidal shape. The error related to this difference can reach high values, especially for low frequency of optical radiation modulation.

A general conclusion following from the study is that the use of optical radiation signal of non-sinusoidal shape for experimental investigation of Bode plot of pyroelectric detector is rather unprofessional because brings unreliable results of measurements.

References

[1] Cicco G. D., Morten B., Dalmonego D., Prudenziati M., Pyroelectricity of PZT-based thick-films, *Sensors and Actuators* 76, 409-415, 1999.

[2] Mendes R. G., Eiras J. A., Influence of neodymium and lanthanum doping in the pyroelectric properties of strontium barium niobate (SBN) thin films, *Journal of the European Ceramic Society* 24, 1637-1640, 2004.

[3] Benjamin K. D., Armitage A. F., South R. B., Harmonic errors associated with the use of choppers in optical experiments, *Measurement* 39, 764-770, 2006.

[4] Wheless W. P., Wurtz L. T., Wells J. A., An equivalent-circuit radiation sensor model, Southeastcon 94 – Creative Technology Transfer: A Global Affair. In procedings of IEEE, 1994, 7-11.

[5] Odon A., Modelling and Simulation of the Pyroelectric Detector Using MATLAB/Simulink , *Measurement Science Review*, vol. 10, No 6, 195-199, 2010.

Application of Nanometrology for Assessing the Machining Tool Geometry and Analysis of the Micro/Nano-Structure of the End Milling Tool Surfaces

[1]G. Bas, [1]N.M. Durakbasa, [2]I. Mankova, [2]J. Beno

[1]Vienna University of Technology, Dept. of Interchangeable Manufacturing and Industrial Metrology, Karlsplatz 13/3113, A-1040 Vienna, Austria
[2]Technical University of Kosice, Mäsiarska 74, Kosice, Slovakia
Email: numan.durakbasa@tuwien.ac.at

Abstract. *Nanotechnology is an interdisciplinary field developing for the global markets in all sectors depending strongly on the nanometrology science for quality, health and environment, safety, efficiency and verification of legalized standards and certificates. Therefore, the machining industry in requirement of higher customer and market demands in the global market, needs to integrate the nanometrological process into their structure. Taking this requirement into consideration, in this study the coating nanotechnology applied on cutting tools are observed and compared with the noncoated tools in terms of micro- and macrocharacteristics. The nanometrological process was modeled and carried out using both optical digital microscope and contact mode profilograph as a step to establish a database for a market analysis in the future.*

Keywords: Measurement, Nanometrology, Quality, Cutting Tool

1. Introduction

The development of nanotechnology applications in the machining industry have been indispensible in order to operate competitively in the market[1]. The nanotechnology applications by effective nanomultilayer coating, surface profile and roughness values, micro- and macrocharacteristics are the major influences that affect the cutting tool high precision operation lifetime, the process quality and the industrial requirements compatible with the standards [2]. Together with the nanometrological process integrated in assessment of the nanotechnological improved cutting tools, this study proposes an integrated approach to enhance the operations of the tool and machining industry.

There has been much prior research conducted to improve fatigue strength, corrosion resistance, tool lifetime and that will eventuate in a major influence for the economical and environmental performance of the cutting tools. The major influence of the surface roughness and cutting edge coating has been investigated so far by means of diverse numerical modeling [3-4]. However, the characterization of the micro- and nanocharacteristics of the cutting edge of the end cutting tools is often challenging due to the experimental precision measurements. In this study, the surface roughness characterization process was carried out by nanometrology devices in order to overcome the challenges by predefined limits in compliant with the international standards.

2. A Strategic Approach to Assess the Cutting Tools in the Machining Industry

The experimental tool life determination for real applications of the machine industry is more complex than its suggested mathematical models. The ISO Standard 8688 guides us on the deterioration of tools due to the tool wear [5]. However the end milling tool deterioration must be investigated as a total effect of wear, edge fracture and deformation. Therefore the end milling cutting tool lifetimes are assessed based on the cutting time and process variables

using the response surfaces. The mathematical model of a tool lifetime under constant depth of cut (mm) and feed rate (mm/tooth) using the Taylor's model is as follow [6]:

$$V.\,Tn = C$$

where V : cutting speed (m/min)
T : predicted tool lifetime (min)
C, n : constants (process and material)

For determination of constants in the mathematical model, a logarithmic transformation must be performed. The quality of machining with the end milling tools is affected with the process constants and surface parameters. Due to the importance of the process parameters and the surface characterization, a strategic approach is introduced as a process management model as presented in the Fig. 1 [7].

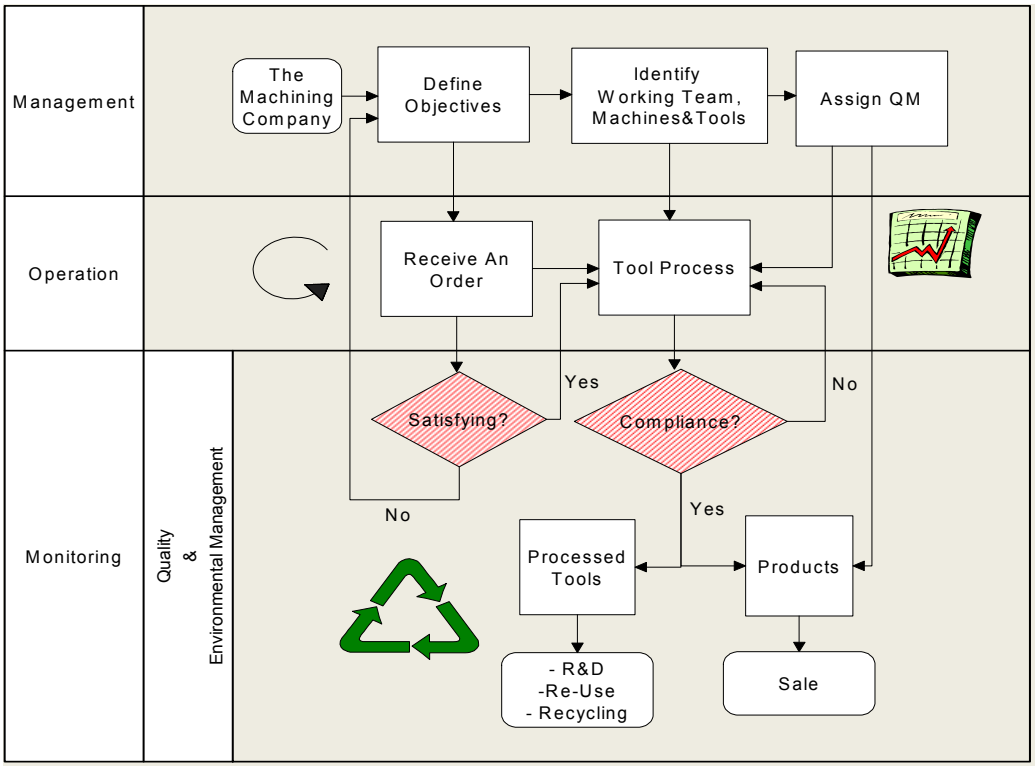

Fig. 1. A Proposal to the Strategical Process Management in Machining Industry

3. Assessment of the Cutting Tools

In this study, surface quality of cutting edges of the selected high precise cylindrical cutting tools was investigated in micro and nano scale. The analyses of the surfaces of the cutting tools were performed for PVD AlTiN coated end mills. The surface investigations consist of the non-contact mode optical capturing of the magnified images by CCD camera of the 3D digital microscope (DM) and a tactile stylus-type surface profilometer for high precise and accurate measurement results compliant with the standards [8, 9, 10].

The capturing results of the magnified surface images measuring the 2D and 3D micro and nanogeometry of the cutting edge (Fig. 2) by the optical digital microscope [11].

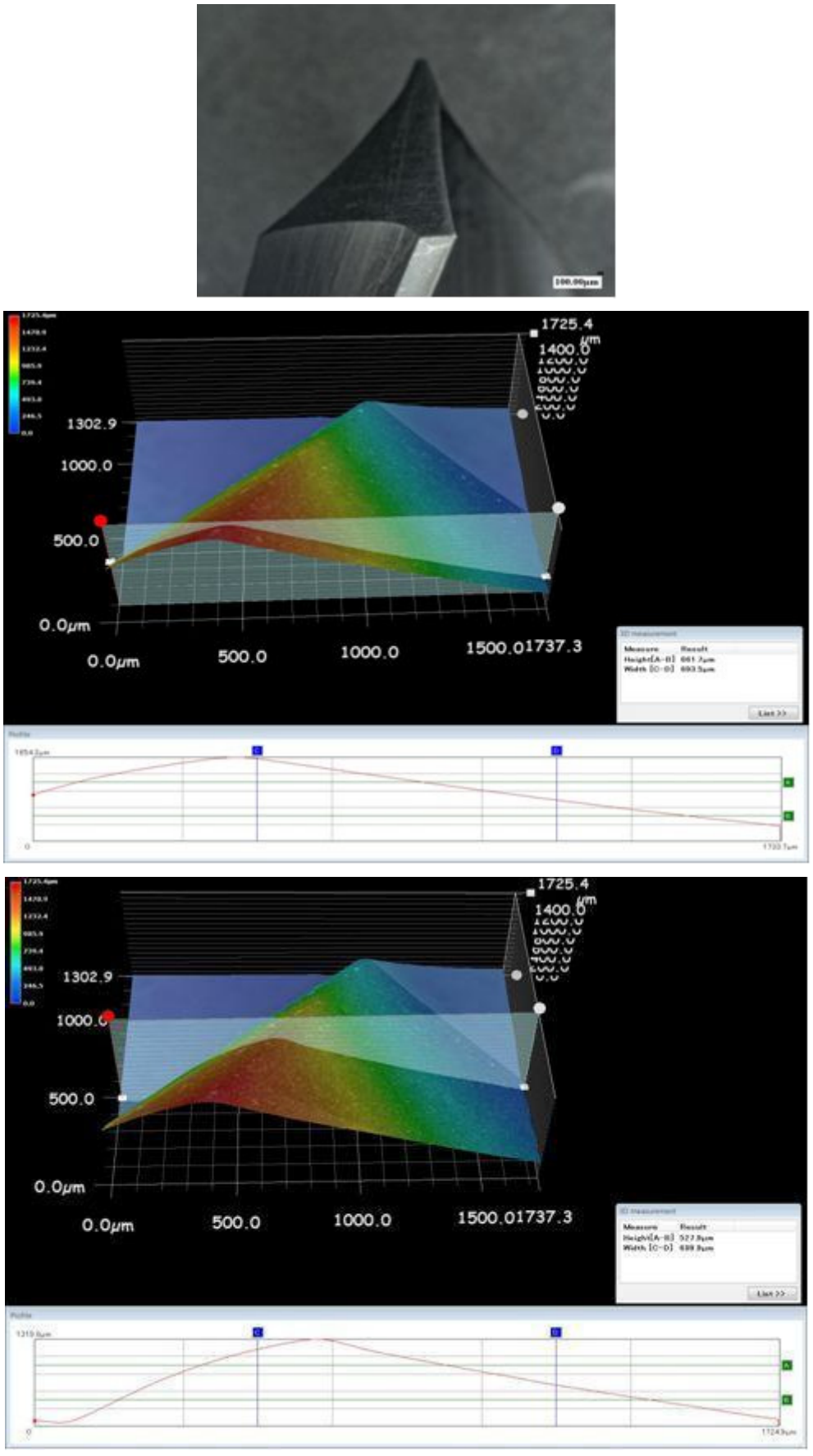

Fig. 2. The micro- and nanogemoetry measurement of the end milling cutting edge using the digital microscope

4. Conclusions

The nanotechnological developments to be applicable on the coatings, surface profile, micro and macrocharacteristics of the cutting tools in order to increase tool lifetime, precision and quality are vital to maintain a competitive operation in today's machining industry. In this study, a startegical nanometrological process is proposed to integrate into the machining industry for assessing the high precision cutting tools compliant with the international standards and measurements are carried out to examine the cutting tools in both 2D and 3D metrological investigations. The micro and nano scale measurements have been stored in order to creative both qualitative and quantitavie data on edge cross-sections that is known to be the most fluential region for quality and life-time of the machining tools.

Acknowledgement

This work was supported by the bilateral project " Wissenschaftlich-Technisches Abkommen mit der Slowakei 2013-14" with the Project Number SK 04/2013 and the title "Implementierung von Nanometrologie Prozessmanagementmodell für die Beurteilung der Werkzeugschneidkanten in der Präzisionsbearbeitung - Implementation of nanometrological process management model into cutting tool edge assessment in precision machining".

References

[1] European Union, Coordination of Nanometrology in Europe (Co-Nanomet) Seventh Framework Programme: *European Nanometrology 2020*. 2009.

[2] Durakbasa M.N., Bas G., Demircioglu P.: A Nanometrological Process Management Model to Assess the End Milling Tools in the Machining Industry. 13th International Conference on Tools, March 2012, Miskolc, Hungary.

[3] Miani F., Guseo R., Mortarino C.: A new Proposal for Tool Life Analysis Response Surface Modelling of the Flank Wear Progression, II International Seminar on Improving Machine Tool Performance Proceedings, 3-5.July, 2000.

[4] Kundrak J.,Raczkövi L.: Definition of Tool Life in hard Boring, Proc. of the International Scientific Conference XXV.microCAD, Section L: Production Engineering and Manufacturing Systems, 2011, pp. 99-104.

[5] ISO International Organization for Standardization: ISO 8688-2 Tool Life Testing in Milling - Part2: End Milling, 1989.

[6] Hung N.P., Boey F.Y.C., Khor K.A., Phua Y.S., Lee H.F.: Machinability of Aluminum Alloys Reinforced with Silicon Carbide Particulates, Journal of Materials Processing Technology 56 (1996), pp. 966-977.

[7] ISO 9001:2008 Quality Management Systems – Requirements.

[8] ISO 4287:1997/prA2:2013 Geometrical Product Specification (GPS)- Surface texture: Profile method - Terms, definitions and surface texture parameters.

[9] DIN EN ISO 25178-6:2010 Geometrical product specifications (GPS)- Surface texture: Areal - Part 6: Classification of methods for measuring surface texture.

[10] ISO 25178-601:2010 Geometrical product specifications (GPS)- Surface texture: Areal – Part 601: Nominal characteristics of contact (stylus) instruments.

[11] EN ISO 4288:1998-04, Geometrical Product Specifications (GPS)- Surface texture: Profile method - Rules and procedures for the assessment of surface texture.

Uncertainty Analysis of Pulse Transient Method for Cylindrical Samples

[1]V. Boháč, [2]P. Dieška, [1]V.Vretenár

[1]Institute of Physics, Slovak Academy of Sciences, Bratislava, Slovakia,
[2]Department of Physics, FEI - STU, Ilkovičova 3, Bratislava, Slovakia
Email: bohac@savba.sk

Abstract. *We have derived several models for the pulse transient methods which accounted for effect of heat losses from the sample surface as well as the geometrical arrangement of a real experiment. The models were derived for cylindrical as well as cuboid shape of specimens [1], [2]. In the past there was published an uncertainty analysis of the models for cuboid samples. In this paper the same analysis was extended for infinitively long cylindrical specimen. The analysis was developed using the theory of sensitivity coefficients. A theoretical calculation of the model parameters uncertainties and derived analytical formulas are presented. Analysis of the measurement error on the base of sensitivity coefficients show propagation of input uncertainty into calculated parameters. Analysed results shows limitations relating to a range of model validity for of non-stochastic dynamic process. The analysis improves the accuracy of the measurements.*

Keywords: Thermophysical Measurements, Dynamic Methods, Uncertainty Analysis

1. Introduction

The experimental problems connected with geometry of specimens are sometimes the results of having limited size of the tested material. This could cause some problems in data evaluation, because the ideal model most often assumes infinitively large media. Typically, the shapes of the specimens used for the measurement are of cylindrical or cuboid forms. The limited amount of the specimen causes an additional effect that decreases the accuracy of the measurement. The contributions to uncertainty come from additional effects caused by the differences between the ideal and the real size of the sample. The main effect is caused by the heat losses from the sample surface and it is included in model.

2. The principle of the Pulse transient method and the model for cylindrical samples of infinite length

The Pulse Transient method [3] is a dynamic method for the measurement of thermophysical parameters. The principle is based on the measurement of the temperature response to a heat pulse generated by a planar heat source generated. Temperature response is recorded by the thermocouple placed apart from the heat source (Fig. 1). Heat losses effect included in this model is represented by heat transfer coefficient α from the sample surface to the surrounding. Thus, the planar isotherms on Fig. 1 of the heat front are deformed during the measurement. The data that are measured within the marked white area in Fig. 1. are still able to be evaluated by the ideal model. In the case when the thermal isotherms are deformed by this effect we need to introduce new models. The solution of the heat transfer equation for the initial and boundary conditions shown in Fig. 2 is

$$T(t,x,r=0)=T_0\frac{R}{x}\sum_{\xi}\frac{\beta}{\xi(\xi^2+\beta^2)}\frac{1}{J_0(\xi)}\left[e^{-2uv}\Phi^*(u-\upsilon)-e^{2uv}\Phi^*(u+\upsilon)\right] \quad (1)$$

where $T_0=\frac{qx}{\lambda}$, $\beta=\frac{R\alpha}{\lambda}$, $u=\frac{x}{2\sqrt{\kappa t}}$, $\upsilon=\xi\frac{\sqrt{\kappa t}}{R}$, and T temperature response described by model, x axial space coordinate, r radial space coordinate. In this case the thermocouple is placed on the axis so the value of $r=0$. R is the radius of the sample, q heat flow density, λ thermal conductivity, κ thermal diffusivity, α heat transfer coefficient for sample–ambient interface, $\Phi^*(u)$ is the complementary error function, ξ is the root of equation $\beta J_0(\xi)-\xi J_1(\xi)=0$ and J_0 and J_1 are the Bessel functions.

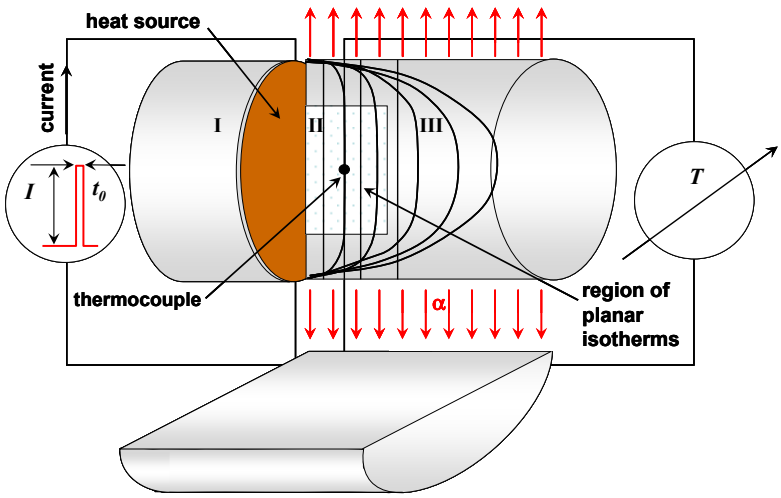

Fig. 1. Wiring diagram and the sample set in a cut. In between first and second part of a sample set a planar heat source is inserted. The thermocouple for the measurement of temperature response to the heat pulse is inserted in between the second and the third part.

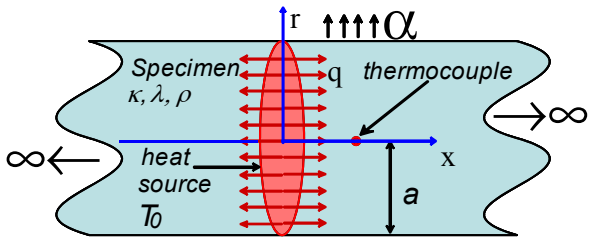

Fig. 2. Initial and boundary conditions for the model assuming two semi-infinite cylindrical specimens and circle shaped heat source in between them.

3. Accuracy estimation results

Generally, uncertainty has different sources and includes errors in the data measurements, parameter estimation procedure and model structures. The uncertainty analysis evaluates how these errors are propagated through the model and calculates their relative importance which is quantified via sensitivity analysis. This type of uncertainty should be supposed as a systematic error of the model. The analysis uses the sensitivity coefficients data derived from the model, along with the underlying data covariance to assess the degree of similarity (linear dependence) between sensitivity coefficients [4] calculated for free parameters. If the sensitivity coefficients are linearly dependent on each other, the parameters could not be

estimated unambiguously and thus their uncertainty is high [4]. The general mathematical background for different shape of samples was already published [1], [2]. The final formula for relative uncertainty of a model parameter a_k has the form

$$u_r(a_k)^2 = C_{kT}^2 \frac{u(T)^2}{a_k^2} \tag{3}$$

where u_r is the relative uncertainty, a_k the tested parameter, C_{kt} is the coefficient that represents the projection of the temperature uncertainty to the uncertainty of the tested parameter [4]. The normalized sensitivity coefficients $\beta_{a_i} = a_i \partial f / \partial a_i$ for the discussed models were calculated for the values of thermophysical parameters close to those measured in experiment performed on sandstone [2].

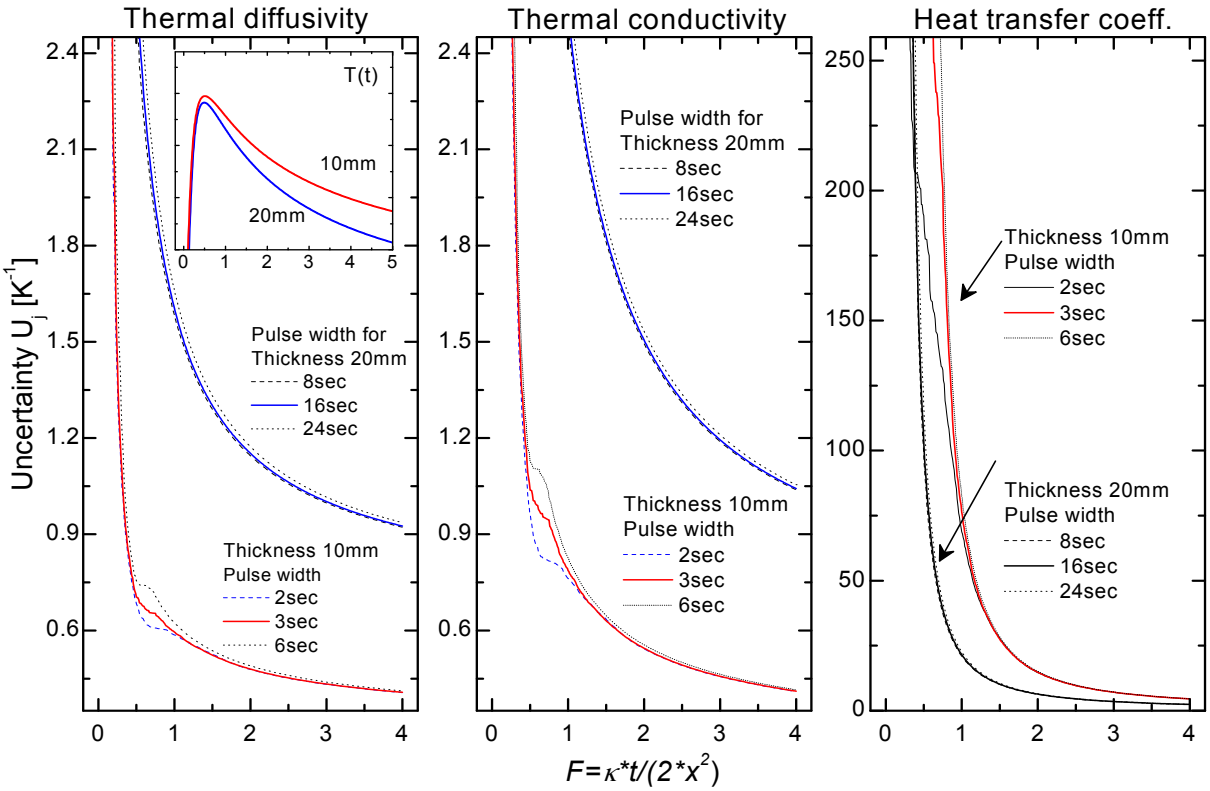

Fig. 3. Uncertainty analysis for sample thickness of 10mm at 2, 4 and 6 seconds of pulse width and thickness 20mm for 8, 16 and 24 seconds of pulse duration. For the illustration of time relation the maximum of temperature response T(t) drawn in blue and red solid lines at 0.5 of the dimensionless time F (Fourier number), that correspond to 42 seconds in real time. Uncertainties in measurement of temperature are propagated through the model and their relative importance is evaluated as uncertainty in K^{-1} for. Relative uncertainty U_j is defined by $U_j = u_j(a_j)/(a_j u(T))$ given in K^{-1} where *u(T)* is uncertainty of measurement of temperature response.

4. Discussion

The sensitivity coefficients for thermal diffusivity and thermal conductivity are of very similar behaviour like in the case of cuboid samples [2] and have a maximum at the lower times of the temperature response record. The values of the sensitivity coefficient of heat transfer coefficient are increasing in time, so higher sensitivities are expected at longer measurement times. This concludes that for the evaluation of the feasible data from this

model we need to perform measurements long enough exceeding times more than 3F. This is confirmed by the uncertainty analysis where the lowest uncertainties are for the dimensionless times evaluated as Fourier number higher than 1.5. For F=3 the uncertainty is 3.55 and for F=4 the uncertainty is 2.4 K^{-1}. The sensitivity analysis in Fig. 3 shows the acceptable error of parameters evaluation for thermal diffusivity and thermal conductivity also for times lower than 1 F. The heat transfer coefficient uncertainty decrease with increasing time of measurement. The uncertainties in Fig. 3 are calculated as uncertainties in respect to input uncertainty of measured temperature. The typical value of temperature uncertainty *u(T)* measured by a thermocouple is about 0.01K. For the evaluation of percentage relative uncertainty we can recalculate uncertainty in the following way $U_{\%} = U_j u(T) * 100\%$.

5. Conclusions

The uncertainty analysis of the pulse transient model for cylindrical samples of infinite length in respect to the heat transfer coefficient was performed and illustrated in the Fig. 3. The accuracy of the results depends on the uncertainty of measured temperature response and in the presence of the effect of the heat losses from the sample free surface depend on the time of the measurement as well as geometry of the specimen. This parameter is affecting the measurement with increasing time of the measurement at larger thicknesses of the sample. The ideal model overestimates values of thermophysical parameters more than ten percent. The heat transfer coefficient is not possible to estimate unambiguously for short times of the measurement because of low sensitivity. The heat transfer coefficient from the sample surface to the surrounding is temperature dependent [4]. The described method of uncertainty analysis is applicable to any kind of the physical model.

Acknowledgements

This work was supported by the Slovak Research and Development Agency under the contract No. APVV-0641-10, Study of rocks properties and investigation of structural and textural characteristic in correlation with thermophysical and physico-mechanical properties and by Scientific Grant Agency of the Ministry of Education, science, research and sport of the Slovak Republic and the Slovak Academy of Sciences under the contract No. 2/0182/12 Development and testing of physical models for the pulse transient method.

References

[1] Boháč V, Dieška P, Vretenár V, Greif V, Model for Cuboid Shape Samples and its Analysis Used for Measurements of Thermophysical Properties of Sandstone, MEASUREMENT SCIENCE REVIEW, Volume 11, No. 6, 192-197, 2011.

[2] Boháč V, Dieška P, Vretenár V, The measurement of thermophysical properties of sandstone by pulse transient method using model for cuboid form samples and influence of heat loss effect, Conference Proceedings 17th International Meeting of Thermophysical Society -Thermophysics 2012. 31st October to 2th November 2012, Podkylava, Slovak Republic, ISBN: 978-80-214-4599-4.

[3] Kubičár Ľ, 1990, Pulse Method of Measuring Basic Thermophysical Parameters. in Comprehensive Analytical Chemistry Vol. XII Thermal Analysis Part E Ed Svehla G, Amsterdam, Oxford, New York, Tokyo: Elsevier, pp 350.

[4] Beck, J.V., Arnold, Kenneth J., Parameter Estimation in Engineering and Science, ISBN: 9780471061182, Better World Books (Mishawaka, IN, USA) John Wiley & Sons, 1977.

High-Speed Optoelectronic System for Surface Inspection of Fuel Pellets

[1, 2]E.V. Vlasov, [1]A.V. Beloborodov, [1]P.S. Zav'yalov, [1]L.V. Finogenov

[1] Technological Design Institute of Scientific Instrument Engineering, Siberian Branch of the Russian Academy of Sciences, 41, Russkaya str., Novosibirsk, 630058, Russia
[2] Novosibirsk State Technical University, 20, Karl Marks prosp., Novosibirsk, 630073, Russia
Email: vlasov@tdisie.nsc.ru

Abstract: *Two high-speed optoelectronic methods and computer vision system for surface inspection of nuclear reactor fuel pellets are considered. In the proposed methods the reflected images of pellet surfaces are taken by digital cameras, which provide high contrast of defective areas against the frame background. Image processing algorithms for identification of defective products are given. A system with productivity of up to 10 pellets per second was designed. Results of real time processing of the obtained images show that the probability of defective pellets detection is not less than 95%.*

Key words: Computer Vision System (Technical Vision), Fuel Pellet, Surface Defects, Image Processing

1. Introduction

Fuel pellets of UO_2 are one of the main components of nuclear reactor fuel elements. In this connection high demands are required as for the quality of pellets, especially their surface. In the production process, many defects may appear on the cylindrical pellet surface. They usually occur in the most strained parts of pellets such as edge chips and cracks on the side surface [1].

In case of visual inspection by operators the probability of false solution by operator may be unacceptable, namely defective fuel pellets are considered as fit production. The above-mentioned drawbacks determine the urgency of the problem of automating the detection of defective pellets. Moreover, it is important that the productivity of visual inspection system must be very high: from 4 to 10 pellets/sec. To solve this problem, we have proposed to use optoelectronic methods and computer vision system combined with a mathematical apparatus for image processing.

In this report two high-speed methods and automatic system for side and edge surfaces inspection are presented. The experimental results of the system testing are given.

2. High-Speed Method for Inspection of the Pellets Side Surface

To solve the problem of fast inspection of fuel pellets' side surfaces the authors have developed an original method based on four parallel channel registration of optical information by the specialized lens. The principle underlying the inspection of the side surface is explained in Fig. 1.

The fuel pellet (1) is being transported along a hole prism (not depicted) along the pellet's axis. The fragment of the image is being formed by the specialized lens (2) and the standard camera lens (5). Then the fragment is being recorded by the linear camera (6). As a light source we used a laser diode (3) which illuminates the side surface of the pellet through a translucent plate (4).

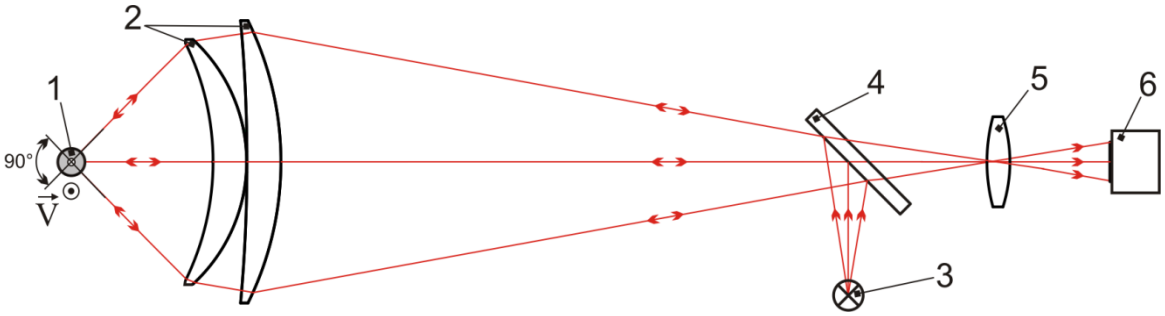

Fig. 1. Principle of image acquisition of the pellet side surface.

The observation and illumination of each point of the product is performed along the normal to the surface, providing high contrast of defects. A full image of the side surface of the pellet moving in the technological flow can be acquired by localization four such optical channels in the same plane.

The image processing algorithm for the side surface [2] determines the boundaries of the side surface, rejects images according to the width and sliding, selects dark and bright defects, determines defect size, and eliminates small, false, and embedded defects. A decision on rejection of cracked pellets of products with other defects is made in accordance with the logical rule

$$\textit{If } (s_i > s_0), \textit{ or } (S > S_0), \textit{ or } (l_j > l_0), \textit{ or } (L > L_0), \textit{ then (Reject)}, \qquad (1)$$

where s_i is the area of an individual defect, s_0 is the permissible area of an individual defect, S is the sum of the areas of the defects, and S_0 is the permissible total area of all defects, l_j is the length of the *j*th crack, l_0 is the permissible length of an individual crack, L is the total length of all cracks, and L_0 is the total permissible length of all cracks.

The industrial version of system was developed and produced (Fig. 2). The inspection speed is up to 100 mm/s (10 pellets/s). The tests showed stable operation of the system with a probability of detection of defective pellets not less than 95%. The processed images of the side surface of real pellets are shown in Fig. 3.

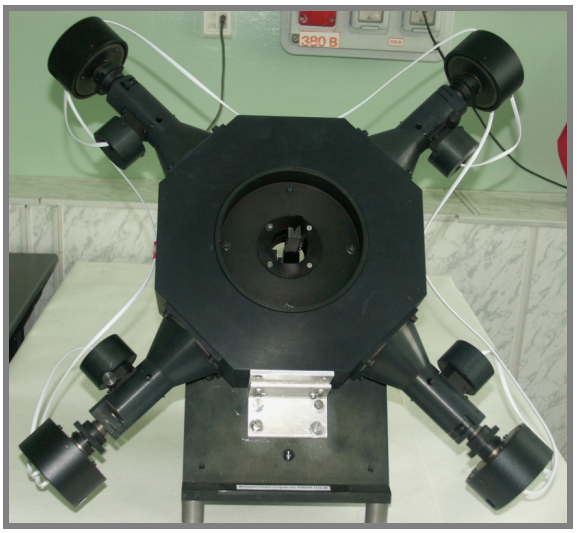

Fig. 2. Four-channel high-speed system for side surface inspection.

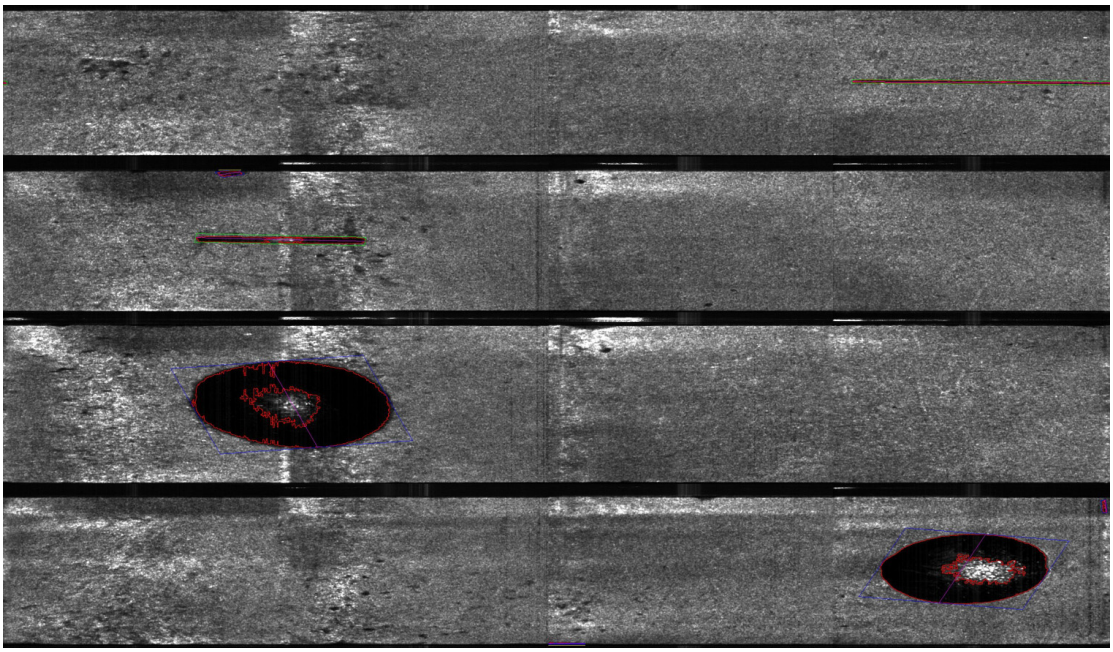

Fig. 3. Examples of processed images of real pellets with characteristic defects like as crakes and cavities. The resolution is 25 μm/pixel in both directions.

3. High-Speed Method for Inspection of the Pellets Edge Surface

The existing engineering solutions [3, 4], which involve detection of the radiation scattered along the pellet surface, failed in under obtaining high-contrast images. Positive results were reached with the scheme where the surface was illuminated and the image was recorded at the same angle with respect to the normal to the surface inspected (reflective require).

In case one is taking an image of the end face of a pellet (Fig. 4), the light source (1) illuminates the face end of the pellet (2) at the angle φ to the normal. The light reflected from the flat part of the end face is recorded by the camera (3). High-performance inspection of the edge surfaces of pellets during their movement was achieved through a new technical implementation of the previously described method, particularly using a focused pulsed light and modern computer technology based on multi-core processors.

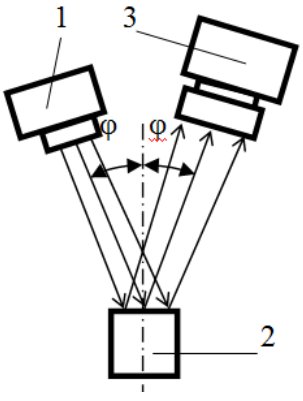

Fig. 4.Diagram of the pellet edge imaging.

Fig. 5. Image recording unit for the edge surfaces inspection.

The edge image processing algorithm comprises the following steps: search for the external contours of white areas, construction of the boundary of white areas, correction of the

boundary of the flat part of the edge, search for opening boundaries, search for defects, and rejection. A decision to reject a product is made using pattern recognition methods based on the logical decision rule

$$If\ (s_i > s_0),\ or\ (S > S_0),\ then\ (Reject), \qquad (2)$$

where s_i is the area of an individual defect, s_0 is the permissible area of an individual defect, S is the sum of the areas of the defects, and S_0 is the permissible total area of all defects.

Example of images of the edge surfaces of tablets obtained by the new recording system (Fig. 5) are shown in Fig. 6.

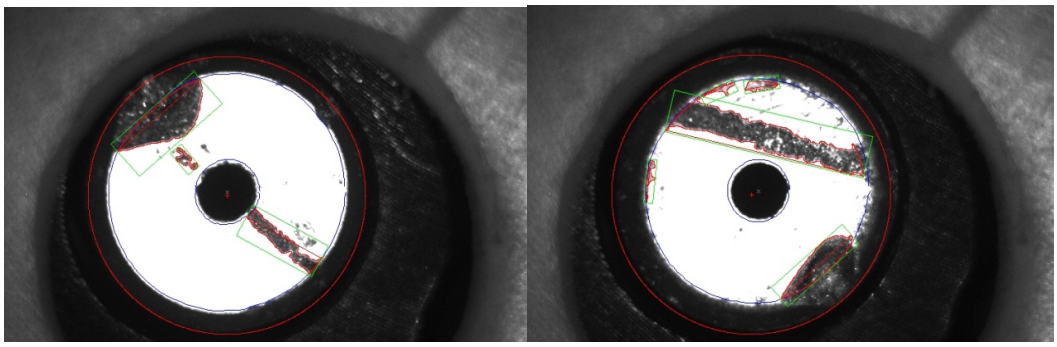

Fig. 6. Processed images of real edge surfaces of tablets with defects like as cavities (productivity is 10 pellets/s, resolution is 18 μm/pixel).

The images of the pellet edge surface have an average contrast of 0.62. This contrast allows using the previously described algorithms to detect the defects on the edge surface with a good relativity.

4. Conclusions

In this paper two high-speed optoelectronic methods and inspection system for side and edge surfaces of nuclear reactor fuel pellets are considered. Image processing algorithms for identifying the defective products were described. The system with productivity of 10 pellets/s was designed. Technical solutions implementing fast image registration of pellet surfaces with a productivity of up to 10 pellets/s were tested on both simulators and real products. The results of real time image processing showed a probability of defective pellets detection not less than 95%.

At the present time the high-speed system for surface pallets inspection is under preliminary exploitation at the technological line in atomic industry (JSC «Novosibirsk Chemical Concentrates Plant»).

References

[1] Reshetnikov F, Bibilashvili Yu., Golovin I. et al. Development, Production, and Operation of Nuclear Reactor Fuel Elements. Energoatom-izdat, Moscow, 1995, Book 1 (in Russian).

[2] Finogenov L., Beloborodov A., Ladygin V. et al. An Optoelectronic System for Automatic Inspection of the External View of Fuel Pellets. *Russian Journal of Nondestructive Testing,* 43(10): 692-699, 2007.

[3] Nakagawa Yasuo, Makihira Hiroshi, and Hamada Toshimitsu. US Patent 4, 226, 539.

[4] Vandergheyns A., and Shihab S. BE Patent WO 00/28549. 1998.

Balancing Devices with Voltage and Current Excitation for the Strain Measurement

V. Kvedaras, R. Kvedaras, R. Masiulionis

Electronics faculty of Vilnius Gediminas Technical University, Vilnius, Lithuania,
Email: Vygaudas.kvedaras@vgtu.lt

Abstract. *The research analyzes the proposed circuits of balancing devices for the strain measurement with voltage or currents excitation. The dependence of measurement codes on strain sensor resistance variation and parameters of the circuits are presented, also, the requirements for the readjusting of power supply range are introduced. The experimental results are presented.*

Keywords: Strain Measurements, Small Resistance Change Measurement, Voltage Excitation, Current Excitation,

1. Introduction

The strain researches are often required for constructions of various materials during their design, construction and operation. This applies to the newly designed structures for carrying out tests to determine durability and resistance to applied forces identify weaknesses, and to provide means for improving or strengthening. Also it is often important to monitor different statuses of existing buildings. In these cases it can be seen that in some time deformation reaches a critical value asked; predict the onset of construction accident, and to take appropriate actions to prevent it [1, 2]. Strain gauges with balanced [1] and not balanced Wheatstone bridges [3] are often used. It is suggested to use the circuits of bridges with current excitation [4] and the current-balanced devices for automated measuring of strains [5], with a lower sensitivity to interference.

The research analyzes the new proposed balanced circuits of small resistance changes with voltage and currents excitation.

2. Analysis of Balancing Methods of Strain Measurement with Voltage and Current Excitation

At present there are many different DACs are manufactured. Multi-bit DACs with several DACs in one integrated circuit with current output are quite common. Such DACs can be successfully used in balancing devices of the strain measurement. Balancing devices embody full range of advantages as greater accuracy; avoids nonlinearities of devices and so on. The summarized circuits of balancing devices with voltage (current) excitation is composed which is shown schematically in Figure 1. It consists of two power sources S1 and S2, and four resistors $R_1 - R_4$. Two resistors of the circuit (R_1 and R_3 or R_2 and R_4) are the sensors of a strain gauge and the active one of them determine the size of deformation, and the second one is compensatory, which compensate resistance change of the active sensor due to environmental conditions. Electrical connections between point's *ab* and sources S1 and S2 can be used when the circuit is powered from the current sources. The output voltages (currents) of one or the other or both of the sources are digitally regulated by the control device CU, so that the circuit would be balanced ($U_{ab} = 0$, applying voltage excitation and $U_{12} = 0$, applying current excitation).
The voltage difference between the points *ab* of circuit, powered from the voltage sources, is equal

$$U_{ab} = \frac{U_1 R_2}{R_1 + R_2} - \frac{U_2 R_4}{R_3 + R_4} \tag{1}$$

where

U_1, U_2 excitation voltages,

$R_1 - R_4$ circuit resistances, two of witch ($R1$ and $R3$ or $R2$ and $R4$) are strain gauges.

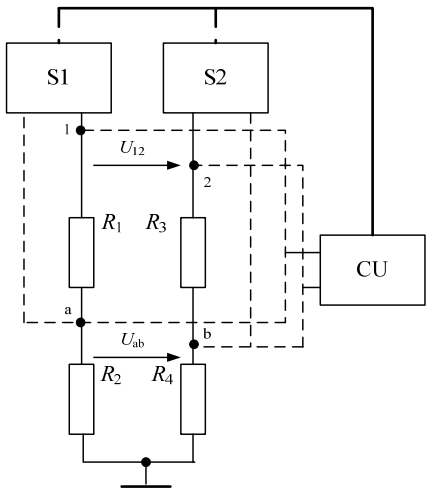

Fig 1. General circuit of balanced devices. S1, S2 – excitation sources; CU – control unit

Sizes of strain gauges, constant resistors, connecting cables resistances are different in the real device and power supply voltage sizes may also be different; installed measuring amplifiers and comparators in control unit (CU) have disbalance of the input voltage. These factors influence eliminated by two measurements – unloaded and loaded measurements. Strain is determined by the values of these two measurements.

There are several ways of realization of devices with voltage excitation:

1. R_2 – active and R_4 compensating strain gauges, $R_1 = R_3$ – constant resistors; device is balanced by changing the value of U_1 and U_2 is kept constant. When a voltage source S1 output voltage is altered digitally, the strain code is equal to

$$m_{1m} = \frac{2^n R_1}{R_1 + R_4}\left(\frac{\Delta R_{2n}}{R_4 + \Delta R_{2n}} - \frac{\Delta R_{2a}}{R_4 + \Delta R_{2a}}\right) \tag{2}$$

where

n number of DAC bytes,

$\Delta R_{ia}, \Delta R_{in}$ changes of loaded and unloaded strain gauge resistance value.

2. R_2 and R_4 – strain gauges, $R_1 = R_3$ – constant resistors; device is balanced by changing the size of U_2, and U_1 is kept constant, then strain measurement code is equal to

$$m_{2m} = \frac{2^n R_1}{R_4}\left(\frac{\Delta R_{2n}}{(R_1 + R_4 + \Delta R_{2n})} - \frac{\Delta R_{2a}}{(R_1 + R_4 + \Delta R_{2a})}\right) \tag{3}$$

3. R_1 and R_2 – strain gauges, $R_2 = R_4$ – constant resistors; device is balanced by changing the size of U_1, and U_2 is kept constant; then strain measurement code is equal to

$$m_{3m} = 2^n\left(\frac{\Delta R_{1n}}{R_3 + \Delta R_{1n} + R_2} - \frac{\Delta R_{1a}}{R_3 + \Delta R_{1a} + R_2}\right) \tag{4}$$

4. R_1 and R_2 – strain gauges, $R_2 = R_4$ – constant resistors; device is balanced by changing the size of U_2, and U_1 is kept constant; then strain measurement code is equal to

$$m_{4m} = 2^n\left(\frac{\Delta R_{1n}}{R_3 + \Delta R_{1n} + R_2} - \frac{\Delta R_{1a}}{R_3 + \Delta R_{1a} + R_2}\right) \tag{5}$$

5. During the measurement the values of U_1 and U_2 can be changed. In this case, the most convenient way to balance the strain monitoring device is to use U_2 source for the unloaded and U_1 source for loaded construction. Then the measurement result is

$$m_{5m} = \frac{-2^n R_1}{R_1 + R_4} \frac{\Delta R_{2a}}{R_4 + \Delta R_{2a}}. \tag{6}$$

Analytic review and research has shown that one of the ways to increase the range of strain measurement is to use circuits with current excitation. The code of strain gauge resistance (strain) change when adjusting the S_2 current excitation source and strain gauges are R_1 (active) and R_3 (compensative) will be equal to:

$$m_{\mathrm{Im}} = m_{\mathrm{a}} - m_{\mathrm{n}} = 2^n \frac{I_1}{I_{2\max}} \cdot \frac{\Delta R_{1a}}{R_2 + R_3}, \tag{7}$$

where

I_1, $I_{2\max}$ the current of the first current source and maximum value of the second source.

As can be seen from (7), the difference of the two codes is directly proportional to the size of the gauge resistance changes during the measurement. Analogically, the code alteration by the adjusting current I_1 is obtained, but in this case the dependence comes more complex, and therefore accepted to regulate the current I_2.

There are current sources which does not require external feedback, and $R_2 = R_4 = 0$, then (7) becomes simpler

$$m_{\mathrm{Im}} = \frac{2^n I_1}{I_{\max}} \frac{\Delta R_{1\mathrm{a}}}{R_3} = \frac{2^n I_1}{I_{\max}} \delta R_{1\mathrm{a}}. \tag{8}$$

The adjustment range of voltage or current sources depends on the maximum possible measured resistance change. This change can be up to ± 30% for steel strains, up to ± 6% for concrete products and so on. Assuming for steel strain measurement $I_1 = 5$ mA, $R_2 = R_1 = 100\ \Omega$, $\Delta R_{1\max} = 30\ \Omega$, then the monitoring devices need $n = 7$ bits, and laboratory devices – $n = 10$ bits for regulation of currents.

Voltage or current DAC may be used as excitation source. They have been formed in one microchip, using the same reference voltage, which reduces the environmental conditions on the monitoring results, as temperature changes almost equally affects both DAC output currents and drift. The DAC current ranges are determined before monitoring by the control code and it can be flexibly chosen for observable construction. The expression of dependence of code on the gauge resistance change is determined.

3. Experimental Results

An experimental model of the circuit with two current sources and one of these sources is adjustable has been made. Dependence of the device adjustable current I_2 on R_1 gauge resistance was measured, which shows that this dependence is linear, the instability of currents and their difference satisfies the requirements for laboratory equipment. During experimental study it has been also found that the proposed circuit allows covering all the required range of adjusting of the current.

The long-term performance stability and the work of the model with the gauges connected by long (10 m) twisted-pair cables and influence of industrial frequency interference has been investigated. The test results (Fig. 2) shows that the stability of current difference in time meets the requirements of laboratory and monitoring equipment in all scenarios; when simply

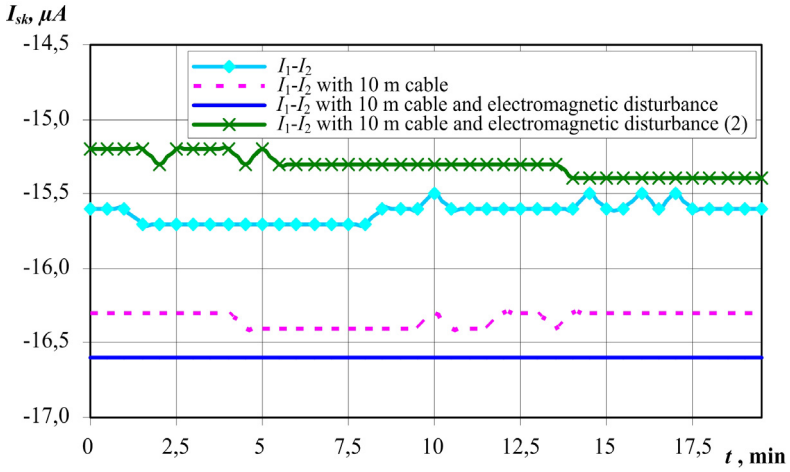

Fig. 2. Dependence of currents difference on time

connecting sensors, when connecting them with long twisted pair cables and when exposing them with an electro-magnetic interfe-rence. Measured disbalance voltage value over time has shown that the experimental circuit is suitable for deformation monito-ring and laboratory test equipment.

4. Conclusions

1. Three new circuits of balancing devices for construction strain monitoring using voltage or current excitation has been proposed designed and analyzed. The obtained results enable to define the required number of control bits for voltage or current in order to receive required resolution.
2. It was confirmed that the easiest option would be to control current of the Wheatstone bridge arm where compensated gauge is switched on which makes the dependence more simple and linear.
3. Voltage or current DACs may be used as an excitation sources. They have been formed in one microchip, using the same reference voltage, which reduces the environmental conditions on the monitoring results, as temperature changes almost equally affects both DACs' output currents and drift.
4. The test results shows that the current change is directly proportional to a change of strain gauge resistance. The stability of current difference in time meets the requirements of laboratory and monitoring equipment in all scenarios including situation with strain gauges connected using long twisted pair cables and exposing them with an electro-magnetic interference.

References

[1] Kvedaras V, Kvedaras R, Masiulionis R. Methods of strain measurements in construction monitoring systems. In proceedings of the 25th International Symposium on Automation and Robotics in Construction (ISARC 2008). Vilnius, Technika, 343-349, 2008.

[2] Harms T, Sedfigh S, Bastianini F. Structural Health Monitoring of Bridges Using Wireless Sensor Networks. *IEEE Instrumentation and Measurements Magazine,* 6 (13), 14-18, 2010.

[3] Kester W. Bridge Circuits. OP AMP Applications. *Analog Devices Inc.,* 4.7-4.37, 2002.

[4] Idźkowski A, Makal J, Warsza Z. Application of Double Current Bridge-Circuit for Simultaneous Measurements of Strain and Temperature. *IEEE Instrumentation, Measurement and Technology Conference, (IMTC 2007)*. – Warsaw, Poland, 1-4, 2007.

[5] Masiulionis R, Kvedaras V, Kvedaras R. Analysis of balancing methods of measurement of small resistance changes. *Elektronika ir elektrotechnika*. 8 (114), 3-6, 2011.

Linearization of Silicon-CCD-Sensors for Multispectral Imaging

M. Rosenberger, M. Schellhorn, M. Preißler, R. Fütterer, B. Reinhardt, G. Linß

University of Technology, Ilmenau, Germany,
Email: mathias.schellhorn@tu-ilmenau.de

Abstract. *Multispectral imaging technologies have a steady increase on importance in the last decades, because of the computing power which can be used for the processing of the data. There are three different types of multi spectral imaging systems: push broom systems, whisk broom systems an filtered systems. All these principles are equipped with different kind of detectors depending on the spectral working range. The detectors have a specific spectral response which depends on the detector material. Mostly it is has a peak on a special spectral range and decreasingly fading out at the end of the spectral working range. This leads to a loss of dynamic range on these edges. The approach, given here delivers possibilities to avoid this dynamic loss by different methods of linearization for a silicon CCD sensor.*

Keywords: Multispectral Imaging, Linearization of Silicon Sensors, Spectral Measurements,

1. Introduction

The analysis of colour space is only possible to a certain limit with an ordinary colour camera [1]. The technical function principle of ordinary RGB cameras with a maximum of three colour channels can dissolve only a limited range in the colour space and loose spectral image information. Narrow wavelength bands in consideration of a broad overall spectrum are particularly difficult or impossible to mapping with a sensor of nonadjustable colour channels. The comparatively large sensitivity of the three individual colour channels results to lose some spectral information. It is acceptable for most colour imaging applications and a cost effective solution. A multispectral camera operates with several colour channels and reconstructs a complete spectrum with specific numerical methods [2]. One important precondition is broadband illumination and precise knowledge of the spectral properties of the whole multispectral camera and illumination system. Filter wheel cameras present an effective and affordable alternative in multispectral image acquisition. Their modular and versatile structure, as well as the consistent enhancements in filter and sensor technology offer many pros for use of these systems. Depending on the procedure of filter setting, it is possible to set a characteristic calibration set for every filter for the specific wavelength. This leads to the possibility to correct the characteristic of the sensor.
For multispectral imaging as well as for high dynamic colour imaging, silicon sensors are used for the most industrial applications. The motivation for the presented work is the use of these sensors for multispectral imaging, enhancing the quality of information on the supported spectral range of the integrated image sensor.

2. Spectral Sensitivity of Silicon CCD Sensors

As mentioned in the introduction many of industrial imaging applications using silicon based image sensors for capturing the visible and the near infrared range of light. A typical spectral characteristic of a silicon based imager is depicted in Fig. 1 beside the characteristic of the penetration depth of different wavelength in silicon. The graph shows an intensity maximum at 500 nm with a cut at 400nm and a slightly decrease in the infrared region down to a relative sensitivity of 5% at 1000nm.

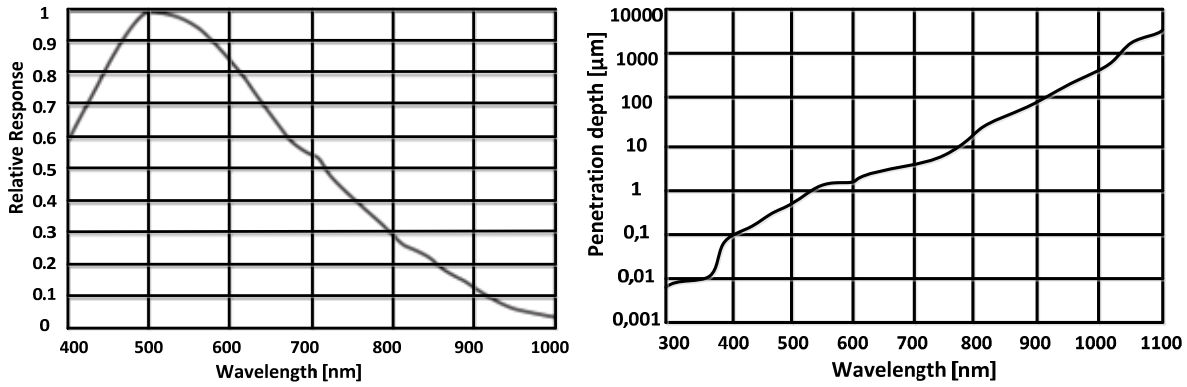

Fig. 1. Spectral response CCD Sensor ICX 424 AL (left), wavelength dependent penetration depth in silicon (right)[3].

Reason therefore is the wavelength dependent penetration depth of light following equation (1) where $\Phi_{e\lambda}(z,\lambda)$ is the spectral radiant flux into the silicon, z the penetration depth and $\alpha(\lambda)$ the absorption coefficient.

$$\Phi_{e\lambda}(z,\lambda) = \Phi_{e\lambda}(0,\lambda)\ e^{-\alpha(\lambda)z} \qquad (1)$$

The Graph on the right side in Fig. 4 illustrates the characteristic penetration depth of silicon. According to the equation (1) short wave light cannot penetrate very deep into the silicon. This leads to a recombination of photons on the surface of the silicon. The electric charges could not reach the potential well of the CCD pixel. That leads to a bad sensitivity into the ultraviolet range, as depicted on the left. The long wave light leads to an opposite effect. The photons can penetrate into the silicon very deep, the longer the wavelength the deeper the penetration depth. Depending on the depth, generation of electric charges may be under the potential well and the electric charges can flow into another pixel region. This effect can lead to a blurred image [4] especially on sensors with small pixels. Otherwise back illuminated sensors using this characteristic of silicon improve the infrared response of the sensor. These effects leading to typical spectral response of silicon (Fig.1. left).

3. Measurment Setup – The Multi Spectral Imager

For the measurement of the spectral behaviour of the CCD silicon sensor as well as for the test system for the linearization methods and the cause to spectral imaging, the multi spectral imager depicted in figure 2 was used. The multispectral imager system [5] is characterized by up to 12 exchangeable band-pass-filters in a wheel and samples a colour spectrum from 375 nm to 975 nm. The spectral resolution is limited by the band-pass-filters and the associated bandwidth of 50 nm or 10 nm. For this purpose several adjustment options are integrated in filter-wheel. Furthermore the spectral channels can be controlled individually for various imaging tasks. An integrated Field Programmable Gate Array (FPGA) offers efficient pre-processing capabilities.

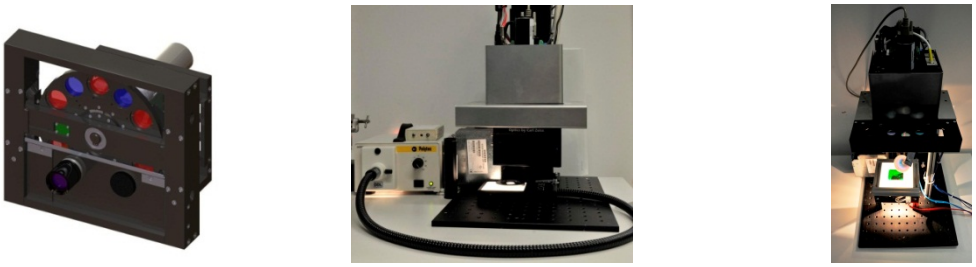

Fig. 2. 3D- model of the Multi-Spectral-Imager (left), measurement setup with the Multi-Spectral-Imager and mirror lens (middle), measurement setup with the Multi-Spectral-Imager and normal lens (right).

4. Linarization – Different Approaches

According to chapter 2 it is a big advantage to correct these characteristic of silicon for spectral measurements, getting a better signal to noise ratio in the infrared and ultraviolet spectral range. Therefore in the following three different possibilities were investigated. For the linearization concerning exposure time based and gain based linearization, a stabilized halogen bulb was used, with the assumption of a well-balanced distribution of light. For these two approaches a system integrated Field Programmable Gate Array detects the position of the filter-wheel and load the correction set for the actual filter. Fig. 3 contain

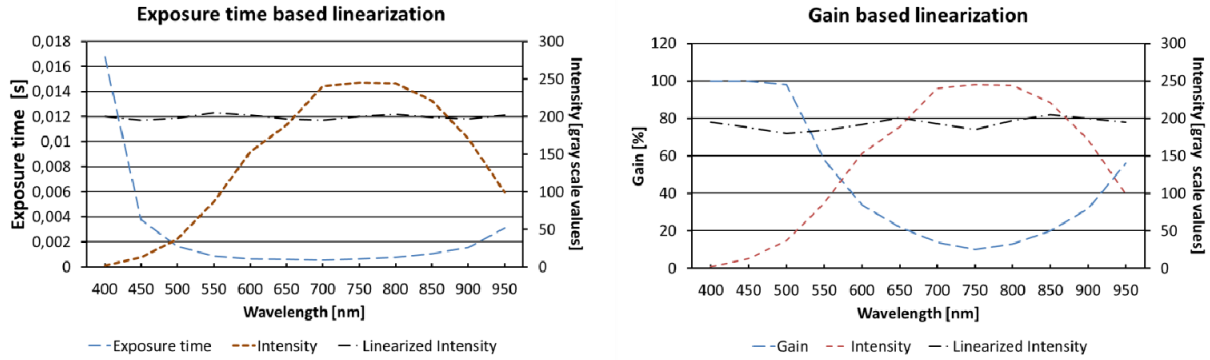

Fig. 3. Exposure time based linearization for the silicon sensor in the multispectral imager (left), Gain based linearization for the silicon sensor in the multispectral imager (right). The blue long dashed lines depicting the correction function (gain/exposure time) for the silicon sensor, the brown shorter dashed lines depicting the sensor modulation amplitude without correction and the black dotted-dashed line the corrected sensor modulation amplitude.

the results of these linearization methods. The target intensity was adjusted to 80% of the sensor modulation amplitude. The intensity values are averaged over the whole image. As depicted in Fig. 3 the exposure variation offers a more stable intensity and more modulation power reserves for low light application beginning with the 450 nm band in comparison to the gain variation method. To get even more modulation power reserves for the sensor, a light mixing method was analyzed. Therefore two halogen bulbs, one filtered with a BG3 filter and one unfiltered, were combined together to control the infrared light independent to the visible light range. Additional a halogen bulb and infrared LED (850nm, 950nm) were controlled independent in the backlight. Fig. 4 illustrating the results of this investigation.

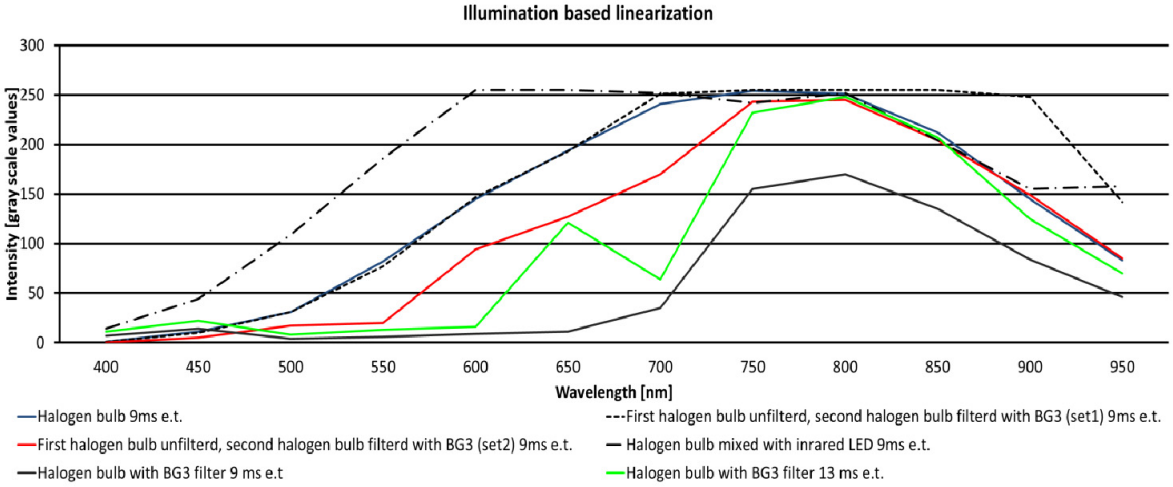

Fig. 4. Light mixing results, analysed in special backlight with different sources and filters (e.t. - equals exposure time)

Best results for an independent light control linearizing the sensor delivers the LED halogen bulb configuration. The halogen bulb mix does not work well because the infrared light of the unfiltered bulb and filtered bulb amplifying together. To get an increase in the ultraviolet and the visible light range, three or better four colour filters for the illumination are necessary. In case of an LED solution even more bands are needed to get a well-balanced light source.

5. Results and Discussion

After the investigation presented in chapter 4 the final method for the MSI is the linearization varying the exposure time at that state of investigation. In case of a better filter characteristic for the illumination, this approach is also well suited for applications in spectral imaging. To gain the visibility and the impact of the linearized MSI two targets were captured in all spectral bands and shown in the visible bands and in the infrared bands. Without the linearization an image processing in the IR bands is impossible.

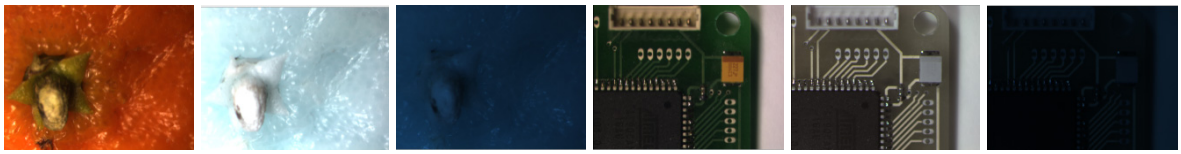

Fig. 5. Result pictures as an RGB mapping for spectral bands (450nm, 550nm, 600nm) and IR RGB mapping (850nm,900nm,950nm) with and without exposure time based linearization in the IR bands, beginning from the left **a.)** Mandarin RGB linearized **b.)** Mandarin IR RGB linearized **c.)** Mandarin IR RGB non-linearized, **d.)** Printed circuit board linearized **e.)** Printed circuit board IR RGB linearized **f.)** Printed circuit board IR RGB non-linearized.

Especially the characterization of biological objects, here a mandarin with the information in the IR band (Fig. 5/b.), is useless without the corrected spectral response (Fig. 5/c.). The second application shows a printed circuit board where the wires could be clearly uncovered in the IR bands with the linearization method (Fig. 5/e.) and colour features can be measured in the RGB bands (Fig. 5/d). Image processing in the uncorrected date (Fig. 5/f.) is hardly possible with the image dynamics.

Acknowledgements

This work was supported by the German research association (DFG) special research department (SFB 622) and the federal ministry of education and research (BMBF).

References

[1] F. Konig and P. Herzog, “On the limitations of metameric Imaging”, Proceedings of IS&T PICS, 1999, pp. 163-168.

[2] M. Yamaguchi, H. Haneishi, and N. Ohyama, “Beyond Red-Green-Blue (RGB): Spectrum-based color imaging technology,” J. Imag. Sci. Technol., vol. 52, no. 1, pp. 010 201-1–010 201-15, Jan. 2008.

[3] E. D. Palik, “ Handbook of Optical Constants of Solids”, Academic Press, Sant Diego 1998.

[4] U. Krüger, “Ausgewählte Aspekte der ortsaufgelösten Erfassung stationärer Licht- und Farbverteilungen”, Fachgebiet Lichttechnik Publikationsreighe 6, Ilmenau 2004.

[5] M. Preißler, M. Rosenberger, M. Correns, M. Schellhorn and G. Linss, „Investigation on a modular high speed multispectral camera“,Proceedings of the 20th IMEKO TC2 Symposium on Photonics in Measurement : May 16 - 18, 2011, [Linz Austria], pp.59-62, Aachen : Shaker, 2011.

Weight Measurements Using Microbending Optical Fibre Sensor and OTDR

J. Červeňová, M. Iglarčík

Slovak University of Technology in Bratislava, Faculty of Electrical Engineering and Information Technology , Institute of Electrical Engineering, Bratislava, Slovakia
Email: jozefa.cervenova@stuba.sk

Abstract. *The paper gives a report of the design and creation of microbending optical fiber weight sensor created for teaching purposes, designed and constructed in the Laboratory of the Department of High-frequency Techniques and Optoelectronics for student's laboratory experiments. In our laboratory we deal with optical time domain reflectometry and with optical fibers as a part of sensor systems. This sensor was built to be used in a chain of laboratory experiments in teaching of optical waveguides properties and principles of sensor technology. The experiment serves not only as an actual example of sensor, but also for an explanation of sensing as a principle. From the point of view of measurement theory we can highlight sensitivity, accuracy, dynamical range, linearity and nonlinearity of various types of sensors.*

Keywords: OTDR, Optical Fiber, Sensor, Microbending

1. Introduction

In our institute in the Department of High-frequency Techniques and Optoelectronics we deal with optical fibers as transmission media and also as sensors. In teaching practice we teach several subjects dealing with optical fibers from mentioned points of view. Usage of optical fiber sensors allows to perform measurements over long distances. [1] We created several measuring experiments for laboratory work, one of them includes optical microbending sensor for weight measurement. The apparatus uses as a detection system optical reflectometer working in time domain. In this case the optical fiber serves as a sensor element itself. We would like to mention the properties of the built sensor and the possibilities of its usage in teaching.

2. OTDR

In the first step of this experiment we explain students Optical Time Domain Reflectometry (OTDR) as a non-destructive measurement method for determining the properties of optical fibers. We show that it is based on the principle of detecting back-scattered Rayleigh scattering and reflected optical radiation. OTDR as a non-destructive method for testing needs the access only to one end of an optical fiber. OTDR allows measurements at several points on the optical path [2]. Short optical pulse is coupled into the input fiber end and is propagating with the group velocity v_g like a lit area along the fiber. The impulse power which was bound into the fiber input end decreases exponentially with the distance. When the failure of fiber properties appears, it appears a sharp change on a reflectogram [3].

3. Microbending Sensor

An optical microbending sensor is built to create periodical microbendings of optical fiber at a short part of it [4]. The sensor structure can be simple; can be created by a pair of deformation plates which cause bends of fiber in a regular pattern (see Fig. 1). These sensors

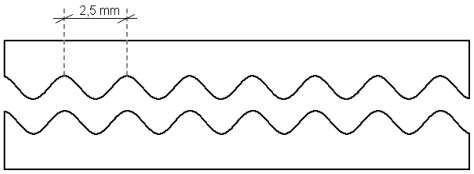

Fig. 1. Geometry of microbending sensor.

are mainly used for temperature and pressure measurements [5]. The explanation to students is given, that when the measurand acts on the fiber, inhomogenities in the fiber index profile are created. By microbendings the fiber is bent to critical angle and some modes escape from the core to the cladding. It leads to changes in the intensity of back-scattered radiation from the place of effect. The plates in response to a change of physical quantity ΔE act by force ΔF on the fiber, creating microbendings of the fiber. The change of transfer coefficient dT according to the applied force can be described by relationship

$$\Delta T = \left(\frac{\Delta T}{\Delta X}\right)\Delta F\left(K_f + \frac{A_S Y_S}{l_S}\right)^{-1} \qquad (1)$$

where $\Delta T/\Delta X$ is a coefficient expressing the rate of change in transmission distortions to change of amplitude deformation ΔX, K_f is force constant of bent fiber, l_S is the distance of deformation plates and $A_S Y_S/l_S$ is a force constant with included change of plates distance [5].

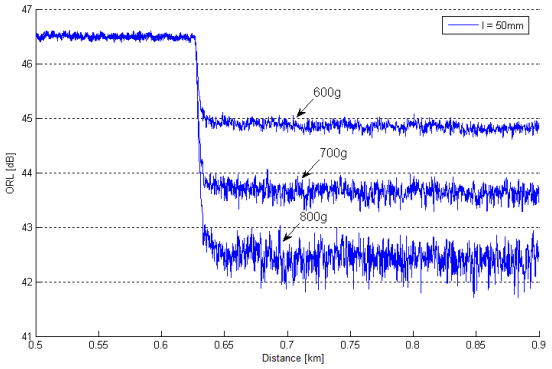

Fig. 2. Attenuation of backscattered signal as a weight dependence.

The change in transmission rate will be reflected as a change in optical power detected by the photodetector (placed in OTDR reflectometer). This change of the output is therefore used to detect changes in physical quantity ΔE. The attenuation in the place of measurement depends by the force acting to the sensor and by the length of the modulator. The local decreasing of backscattered power for 3 measured weights is shown in Fig. 2. The scheme of measuring workplace is given in Fig. 3.

The properties of the microbending sensor (see Fig. 4) are in Table 1. The force which acts to the optical fiber depends on the weight of the load and also on the mutual position of the load and the fiber. We explain the role of the force or load placement at the upper plate of the sensor by measurements, as it is schematically given in Fig. 5. The length of the microbending modulator has an influence to the measurement range and sensitivity. Deformation plates are made with a groove. It allows to use the sensor in two lengths 60 mm and 115 mm. Input and output part of the optical fiber is fixed in foam peaces preventing the damage. Mutual position of plates is fixed. Minimum used load weight was chosen with respect to the accuracy, maximum load weight was chosen to prevent damage of the fiber and to have the measured backscattered signal not in the noise.

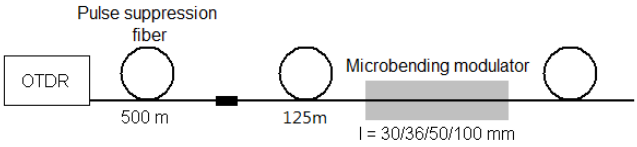

Fig. 3 Measuring workplace with microbending modulator and OTDR reflectometer.

By measurements we use the reflectometer MTS/T-BERD 6000L. Reflectometer settings are in Table 2. Optical fibers PS-9-500-FC/PC/200-FC/PC/200 are used, pulse suppression fiber 500 m long, and second, SMF 28E corning 9/125 2650 m long, with placed modulator. The fibers are connected by a connector SAA-4 JAPAN SII.

The approximation of measured attenuation as a function of weight is nonlinear with the best fit function: $f(x) = b_1 + b_2 e^{b_3 x}$ where b_1, b_2, b_3 are parameters.

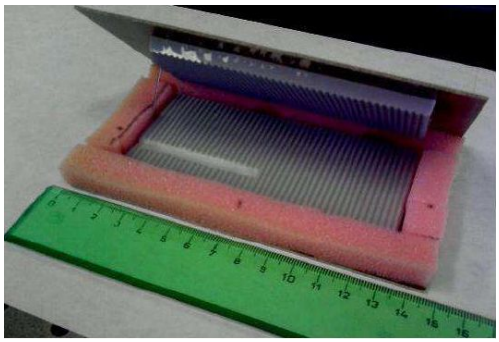

Fig. 4 Realized microbending sensor.

The sensor sensitivity is seen in Fig. 6. The dependence of the sensor accuracy for range of weights is in Fig. 7. The upper and lower weight limit is not the same for different loads. In sensor accuracy in (m±Δm)g, will be Δm maximum limit. We can teach students to construct two functions: recalculation function: the input is measured attenuation function and the output is load weight and accuracy function: the input is measured attenuation function and the output is the accuracy of weight determination [6]. We measure with two fiber places in the sensor and with the load acting in two places as it is shown in Fig. 5. Nonlinearity of the measured functions for the sensor is in Fig. 8.

Table 1. Sensor parameters

	Shorter sensor	Longer sensor
modulator length	60mm	115mm
deformation plate	115mm x 50mm	
novodur cover	145mm x 80mm	
number of tines	24	46

Table 2. Reflectometer settings.

wavelength	1550 nm
impulse duration	10 ns
range	2 km
resolution	4 cm
time of one measurement	120 s

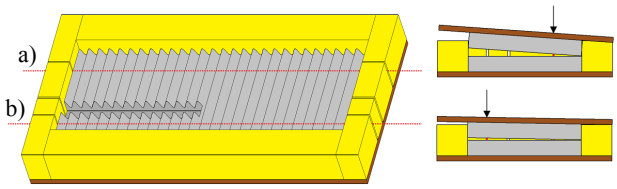

Fig. 5 The position of the fiber in the sensor and the place of the acting force.

The attenuation of these sensors is small and it allows measurements at big distances [2]. The OTDR principle offers the possibility of quasi-distributed measurement. When the sensors are placed in several places of the route (see Fig. 8) the measured signal achieved from reflectometer shows more attenuation steps (see Fig. 9). The condition for dynamic range of every sensor must be fulfilled. By maximum load of all sensors should be the measured backscattered power measurable also in the place of the most distant sensor.

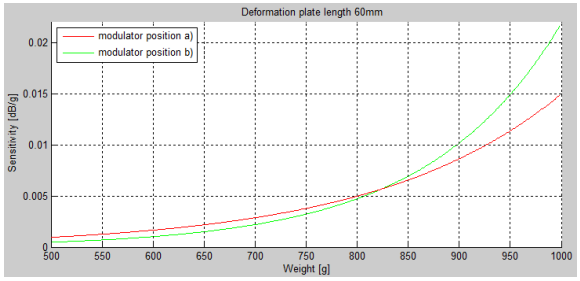

Fig. 6 Sensitivity of the sensor.

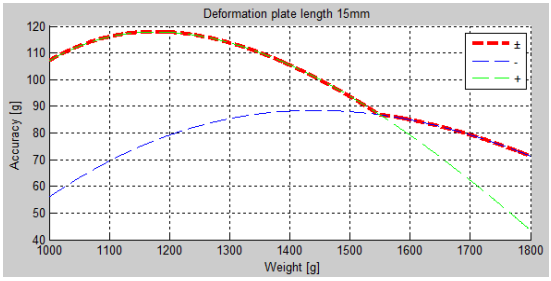

Fig. 7 The sensor accuracy as function of weight.

Conclusions

We created microbending sensor for weight measurements, dynamic range of the sensor for the length of plates 60 mm is from 500 to 1000 g, for the length of plates 115 mm is from 1000 to 1800 g. The sensor was included to students' laboratory experiments.

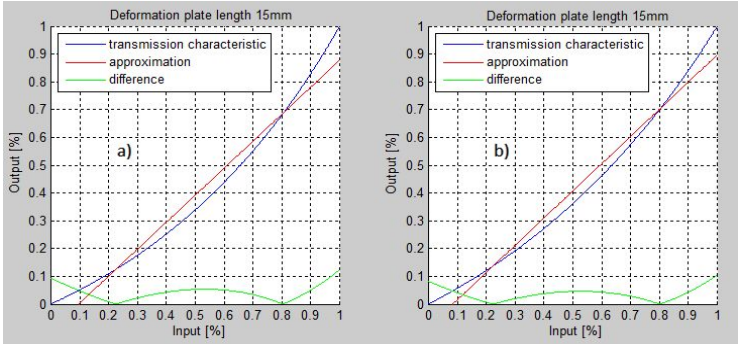

Fig. 8 Nonlinearity of the sensor

We explain theoretical principles and practical measurements with OTDR apparatus we explain principles of sensoric systems based on optical fibers.
We can show by using this experiment the methodology of nonelectrical variables measurements. One more added feature of the experiment is in the teaching possibility in the field of measurement theory: in evaluation of measured curves. We can highlight accuracy, sensitivity, dynamical range, linearity and nonlinearity of various types of sensors.

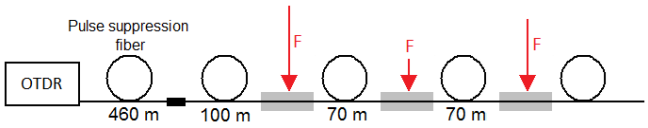

Fig. 9 Optical route for quasi-distributed measurements.

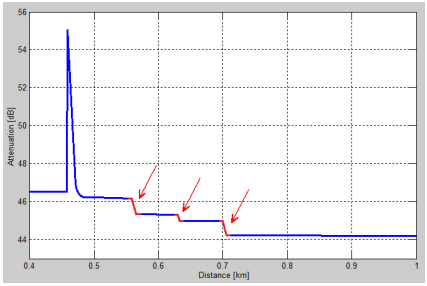

Fig. 10 Quasi-distributed measurement.

Acknowledgements

This work was supported by the Slovak Research and Development Agency under the contract
No. APVV-0062-11.

References

[1] Turán J, Petrík S. Optické vláknové senzory. Alfa, Bratislava, 1990. ISBN 80-05-00655-1 ISBN 80-05-00655-1.

[2] Jasenek J. Optická vláknová reflektometria. STU, Bratislava, 2001. ISBN 80-227-2002-X.

[3] Korenko B. Optické vláknové senzory s rozloženými parametrami a ich aplikácie. FEI STU, Bratislava, 2012, FEI-10850-12090.

[4] Ill, B, John, W. Historical Review of Microbend Fiber-Optic Sensors. Journal of Lightwave Technology, Vol. 13, No. 7, July 1995, pp. 1193-1199.

[5] Lagakos, N, Cole, J. H., Bucaro, J. A. Microbend Sensor. Applied Optics, Vol. 26, 1987, pp. 2171-2180.

[6] Tvarožek, V.: Senzory [online][cit: 2012-05-11]. available on internet <http://www.kme.elf.stuba.sk/kme/buxus/docs/predmety/SE/EL-skripta/02_-_senzory.pdf

Performance Measurements of Laboratory IEEE 802.11 b, g Open Point-to-Multipoint Links

[1,2]J. Pacheco de Carvalho, [2,3]H. Veiga, [2]C. Pacheco, [1,2,4]A. Reis

[1]Departamento de Física, [2]U. de Detecção Remota, [3]Centro de Informática, Universidade da Beira Interior, Covilhã, Portugal
[4]Departamento de Electrónica e Telecomunicações, Instituto de Telecomunicações, Universidade de Aveiro, Aveiro, Portugal
Email: pacheco@ubi.pt

Abstract. *Performance of wireless communications is a most relevant issue, resulting in more reliable and efficient communications. Security is also important. Laboratory measurements were made on several performance aspects of Wi-Fi (IEEE 802.11 b, g) Open point-to-multipoint links. Our study contributes to the performance evaluation of this technology, using available equipments (DAP-1522 access points from D-Link and WPC600N adapters from Linksys). New detailed results are presented and discussed, namely at OSI levels 4 and 7, from TCP, UDP and FTP experiments: TCP throughput, jitter, percentage datagram loss and FTP transfer rate data. Comparisons are made to corresponding results obtained for point-to-point links. Conclusions are drawn about the comparative performance of the links.*

Keywords: WLAN, Wi-Fi, Open Point-to-multipoint and Point-to-Point Links, Wireless Network Laboratory Performance

1. Introduction

Electromagnetic waves in several frequency ranges, propagating in the air, have been decisively important for the development of wireless communications e.g. Wi-Fi and FSO (free space optics), microwave and laser based technologies, respectively.

The importance and utilization of Wi-Fi have been growing for complementing traditional wired networks. It has been used both in ad hoc mode and infrastructure mode. In this case an access point, AP, permits communications of Wi-Fi devices with a wired based LAN, through a switch/router. By this means a WLAN (wireless local area network), based on the AP, is formed. At the personal home level a WPAN (wireless personal area network) allows personal devices to communicate. Point-to-point (PTP) and point-to-multipoint (PTMP) 2.4 and 5 GHz microwave links are used, with IEEE 802.11a, 802.11b, 802.11g and 802.11n standards [1]. Nominal transfer rates up to 11 (802.11b), 54 (802.11 a, g) and 600 Mbps (802.11n) are specified. CSMA/CA is the medium access control. There are studies on wireless communications, wave propagation [2,3] practical implementations of WLANs [4], performance analysis of the effective transfer rate for 802.11b point-to-point links [5], 802.11b performance in crowded indoor environments [6].

Performance has been seen as a fundamentally important issue, giving more reliable and efficient communications. New telematic applications are specially sensitive to performances when compared to traditional applications. Requirements have been given [7].

Wi-Fi security is very important, as microwave radio signals travel through the air and can be easily captured. Besides WEP, more advanced security methods have been developed to provide authentication such as, by increasing order of security, WPA and WPA2.

Several measurements have been made for 2.4 and 5 GHz Wi-Fi open links [8,9], as well as very high speed FSO [10]. In the present work new Wi-Fi (IEEE 802.11 b,g) results arise,

through OSI (Open Systems Interconnection model) levels 4 and 7. Performances are evaluated and compared for laboratory measurements of Open PTMP and PTP links, using available equipments.

The rest of the paper is structured as follows: Chapter 2 is about the experimental details i.e. the measurement setup and procedure. Results and discussion are given in Chapter 3. Conclusions are drawn in Chapter 4.

2. Subject and Method

The measurements used D-Link DAP-1522 bridge/access points [11], Linksys WPC600N wireless adapters [12] and other equipments [8]. The wireless mode was set to access point mode. Interference free communication channels were used for the links. Data were collected under far-field conditions. No power levels above 30 mW (15 dBm) were required as the wireless equipments were close.

The PTP laboratory setup is shown in Fig. 1. The PTMP setup was a generalization of this, involving two wireless links to the AP. TCP and UDP experiments at OSI level 4, were as in [9], permitting network performance results to be recorded. For a TCP connection, TCP throughput was obtained. For a UDP connection with a given bandwidth parameter, UDP throughput, jitter and percentage loss of datagrams were obtained. One PC, with IP 192.168.0.2 was the Iperf server and the other, with IP 192.168.0.6, was the Iperf client. Jitter was continuously computed by the server, as specified by RTP in RFC 1889 [13]. This scheme was also used for FTP measurements, using FTP server and client applications [8]. Batch command files were written to enable the TCP, UDP and FTP tests. The results were obtained through remote control via switch and written as data files to the client PC disk.

3. Results and Discussion

The AP and the PC wireless adapters were configured, for each standard IEEE 802.11 b, g, with typical fixed transfer rates. For every fixed transfer rate, data were obtained for comparison of the laboratory performance of the links, at OSI levels 4 and 7. At OSI level 1, SNR values and noise levels N were recorded, as shown in Fig. 1. For each standard and every nominal fixed transfer rate, an average TCP throughput was determined. This value was used as the bandwidth parameter for every corresponding UDP test, giving average jitter and average percentage datagram loss. The main results, which were reasonably steady versus time, are shown in Figs. 2-3. The statistical analysis, including calculations of confidence intervals, was performed as in [14]. In Fig. 2, polynomial fits were made to the TCP throughput data. The best average TCP throughput performance was found for 802.11g and PTP links (14.5 +- 0.4 and 6.0 +- 0.2 Mbps for PTP and PTMP, respectively). In Fig. 3, the data points for jitter and percentage datagram loss were joined by smoothed lines. The best average jitter performance was found for 802.11 g and PTP links (2.3 +- 0.1 and 3.5 +- 0.4 ms for PTP and PTMP, respectively). Concerning average percentage datagram loss data, the best performances were found, for both standards, for PTP links.

At OSI level 7 we measured FTP transfer rates versus nominal transfer rates for both standards and link types, as in [8]. The results have shown the same trends found for TCP throughput.

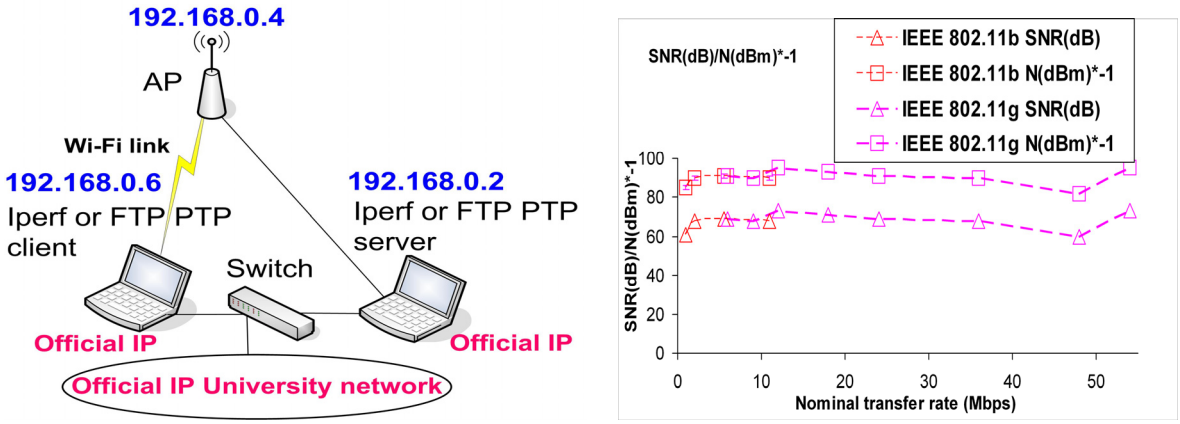

Fig. 1. Wi-Fi laboratory PTP setup scheme and typical SNR (dB) and N (dBm).

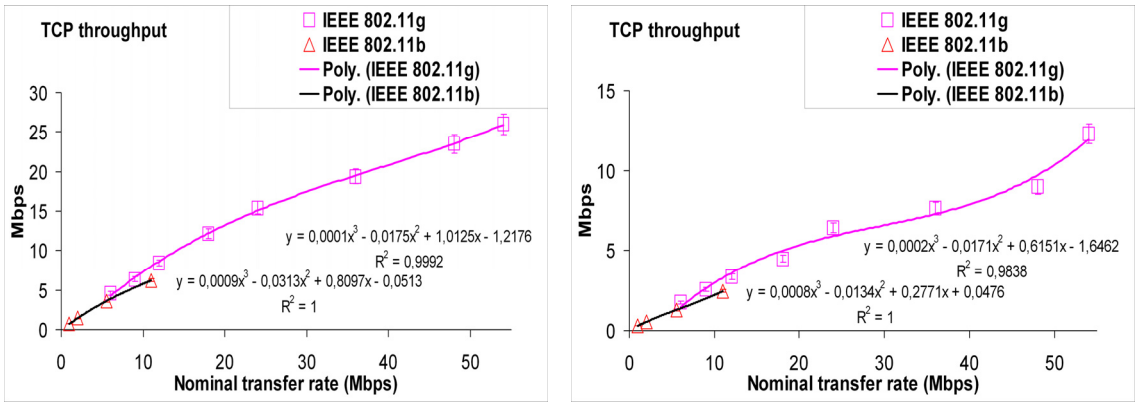

Fig. 2. PTP and PTMP TCP throughput results, versus technology (IEEE 802.11 b,g).

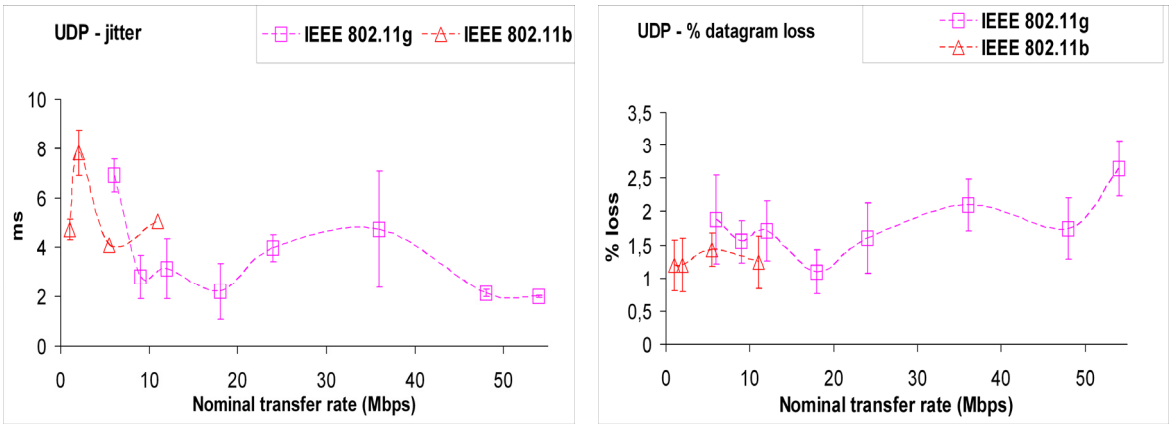

Fig. 3. PTMP UDP jitter and percentage datagram loss results, versus technology (IEEE 802.11 b,g).

4. Conclusions

A laboratory setup arrangement has been planned and implemented, that permitted systematic performance measurements of available wireless equipments (D-Link DAP-1522 access points and Linksys WPC600N adapters) for Wi-Fi (IEEE 802.11 b, g) in Open PTMP links. TCP, UDP and FTP results were obtained and compared, for each standard, to corresponding PTP data. The best average TCP throughput and jitter performances were found for 802.11g and PTP links. Concerning average percentage datagram loss data, the best performances

were found, for both standards, for PTP links. In comparison to PTP links, performance degradations were found for PTMP links. This arises because here the access point has to maintain links between PCs. Future performance studies are planned using several equipments, topologies and security settings, not only in laboratory but also in outdoor environments involving, mainly, medium range links.

Acknowledgements

Supports from University of Beira Interior and FCT (Fundação para a Ciência e a Tecnologia)/PEst-OE-FIS/UI0524/2011 (Projecto Estratégico-UI524-2011-2012) are acknowledged.

References

[1] Web site http://standards.ieee.org; accessed 10 Jan 2013.

[2] Mark JW, Zhuang W. Wireless Communications and Networking. Prentice-Hall, Inc., Upper Saddle River, NJ, 2003.

[3] Rappaport TS. Wireless Communications Principles and Practice, 2nd ed., Prentice-Hall, Inc., Upper Saddle River, NJ, 2002.

[4] Bruce III WR, Gilster R. Wireless LANs End to End, Hungry Minds, Inc., NY, 2002.

[5] Schwartz M. Mobile Wireless Communications, Cambridge University Press, 2005.

[6] Sarkar N, Sowerby K. High Performance Measurements in the Crowded Office Environment: a Case Study. In Proc. ICCT'06-International Conference on Communication Technology, Guilin, China, 27-30 November 2006, 1-4.

[7] Monteiro E, Boavida F. Engineering of Informatics Networks, 4th ed., FCA-Editor of Informatics Ld., Lisbon, 2002.

[8] Pacheco de Carvalho J, Gomes P, Veiga H, Pacheco C, Marques N, Reis A. Measurements of Performance in Laboratory IEEE 802.11 b, g Point-to-Point Links. In Proc. Measurement 2009 – 7th International Conference on Measurement, Smolenice Castle, Slovakia, May 20-23, 2009, 182-185.

[9] Pacheco de Carvalho JAR, Veiga H, Gomes PAJ, Ribeiro Pacheco CF, Marques N, Reis AD. Wi-Fi Point-to-Point Links- Performance Aspects of IEEE 802.11 a,b,g Laboratory Links. In Electronic Engineering and Computing Technology, Series: Lecture Notes in Electrical Engineering, Sio-Iong Ao, Gelman L, Editors. Springer, Netherlands, 2010, Vol. 60, 507-514.

[10] Pacheco de Carvalho JAR, Marques N, Veiga H, Ribeiro Pacheco CF, Reis AD. Experimental Performance Evaluation of a Gbps FSO Link: a Case Study. In Proc. WINSYS 2010- International Conference on Wireless Information Networks and Systems, Athens, Greece, July 26-28, 2010, 123-128.

[11] Web site http://www.dlink.com; DAP-1522 wireless bridge/access point technical manual; 2010; accessed 15 Jan 2012.

[12] Web site http://www.linksys.com; WPC600N notebook adapter user guide; 2008; accessed 10 Jan 2012.

[13] Network Working Group, "RFC 1889-RTP: A Transport Protocol for Real Time Applications", http://www.rfc-archive.org; 1996; accessed 10 Fev 2008.

[14] P. R. Bevington, Data Reduction and Error Analysis for the Physical Sciences, Mc Graw-Hill Book Company, 1969.

A Mobile Instrument GRIBA for Negative Ion Studies

J. Blahins, A. Apsitis

University of Latvia – Institute of Atomic Physics and Spectroscopy, Riga, Latvia
Email: janis_59@inbox.lv

Abstract. *Negative ion research is of particular interest for studies of the mechanism of forming small carbon molecules under conditions in interstellar space. A new mobile instrument is designed and will become available for measurements to explore electronic structure of negative ions in interaction of ion beam with rare or high-energy light sources located in various labs.*
Keywords: *Negative Ions, Photochemical Reactions, Mobile Instrument, Measurements of Detachment Energies, Molecules of Astrophysical Interest*

1. Introduction

Words such as exobiology, extraterrestrial or astrobiology traditionally sound more like science fiction. Yet late high-precision analyses of objects inside and in the vicinity of the Solar System (including cosmic dust samples) captured by NASA [**1, 2**] made at a number of laboratories show, in most of cases, positive contamination with scraps similar, as well as not similar, to Earth-life DNA sequences. Even if confirming cosmic seed-in hypothesis of life, it does not answer the question of how such DNA-like sequences were and/or are forming in interstellar space, where spectrometry shows the presence of carbon-containing molecules [**3**].

Therefore a need exists for more experimental research and advances in measurement instrumentation for studies of high-energy photochemical reactions of small hydrocarbon containing molecules in the interstellar environment. To evaluate the possible chemical reactions and to understand the mechanisms thereof, a good knowledge of the orbital energies and detachment energies is necessary. Most of the positive molecular ions of interest are more or less examined while very little is known about negative ions. Research of negative ion photochemistry may give a crucial answer to the riddle of the source of exobiological scraps.

Negative ion research traditions are well elaborated at Freiburg and Gothenburg (incl. Chalmers) and some other universities (Stockholm etc) [**4**] where equipment includes ion source, mass-spectrometric separation magnet, a quadrupole, and something like an electron energy spectrometer behind a high-vacuum photochemical reaction chamber. Usually such an experimental set-up, including a scanning laser, takes the space more than one room, and can therefore, only be used for the photochemical reactions with the existing at that place lasers or other high power radiation sources .

When the interest shifts to interstellar space shortwave light energies, the need arises for high-energy UV, VUV light source, like some unique lasers, and even synchrotron radiation sources. In this case, it is crucial to have the ability to move the installation producing ion beams to such a stationary light source, which means to have a portable instrument. Such unique apparatus is presented in this paper.

2. Subject and Methods

A cellar full of decommissioned instruments at the Gothenburg University provided the opportunity of re-using old parts to compose a new extra-low budget instrument comprised of two separate parts on wheels which are transportable in a middle-size minibus. The instrument is assembled on “Siemens” aluminum rails allowing for extremely versatile

mounting of parts. The total weight including three roughing pumps, two diffusion pumps, two turbo-molecular pumps, and one ion pump is less than one metric ton. Presently, in 2013. it is based at Gothenburg. Later it will be moved to Riga. The acronym GRIBA stands for Gothenburg-Riga Ion Beam Apparatus.

The instrument has a filament ion source [**6**] that may be used to generate a positive ion beam of sub-microampere scale current or negative ion beam of sub-nanoampere scale of substances of sample (inserted into it) evaporating under 2000 ºC. The efforts are in progress to design laboratory made RF ICP (radiofrequency inductively coupled plasma) chamber to produce more stable ion beam with larger variability of originating ions and in particular eliminating some restrictions of the temperature while not interfering with the plans to explore molecular beams. In the extreme case, the ion head allows the implementation of a sputter source or a spray source, which is not being planned for the nearest future. Long-term expertise in ICP plasma technologies in Riga will be applied to make such innovation to perform measurements in positive and negative ion physics domain. [**7**].

After extracting ions from the plasma, they are focused, accelerated, and then filtered by a Wien filter (Colutron TM) - a double-focusing magnet and three-stage electrostatic field (velocity filter/mass selector) providing an uniform beam with all polluting co-substances being cleaned off. Initial MS (mass spectrometry) testing of the filter showed the sharpness of the cleaning curve ca. 100 for lightweight mass numbers. However there is enough place to mount the RF QMS (quadrupole) mass selector before photochemical reaction chamber, if pollutants occasionally will emerge at very nearby m/z ratio.

The beam then goes through a cesium vapour charge exchange chamber. If cesium is inserted and the vapour temperature stabilised, then majority of positive ions are converted to negative or even double negative ions. However the cell may not be employed, if charge reversing is not required. Cell is essential to get a better beam current.

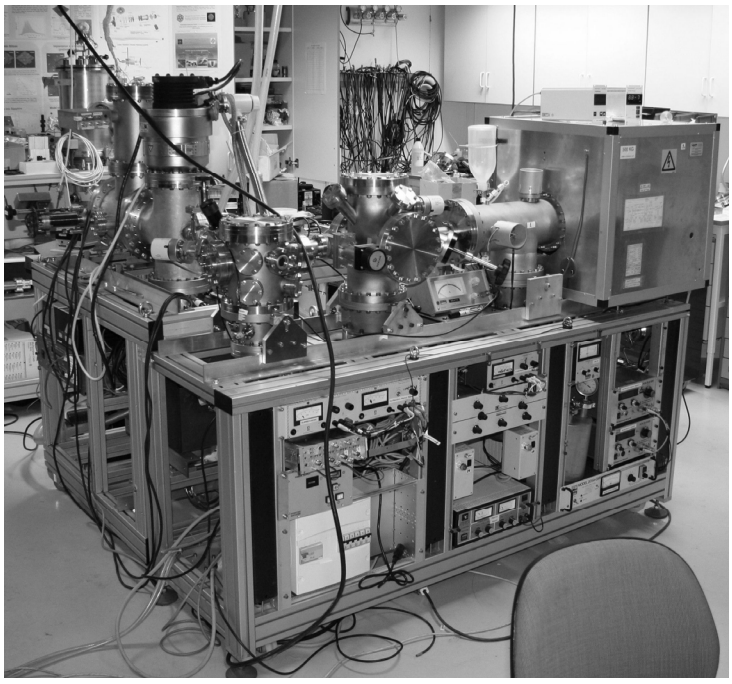

Fig. 1. View of the instrument: quadrupole in the corner, the high-vacuum station ending with TFS – at left, Colutron ending with the ion source – at right.

The first stand ends with an electrostatic deflector – a rectangle bending quadrupole. The bending angle of it is known to be mass indifferent. Thus, the ion beam may be turned to the left or right, or it may remain intact; thus particles with the wrong charge are filtered off the beam that after leaving the chamber, contain exclusively the chosen ions.

The second stand is connected here by a sylphon and vacuum valves, permitting disconnection of the stands for transportation while keeping a good vacuum. The second stand has 600 l/s turbopump in tandem with a 500 l/s ion pump to obtain ultrahigh vacuum in the photochemical reaction zone. The laser beam can be applied through windows from both ends longitudinally or transversally from both sides. A TFL (time-of-flight) electron spectrometer is mounted over the reaction zone, passed to use a transversal light source. However, a novel PEARLS [**5**] angle resolved spectrometer is going be made to be examined at autumn on. A low-grade MCP (micro-channel plate) made by newly developed ALD (atomic layer deposition) technology is placed at the end of the ion beam to enable optical adjustment of the ion beam position.

A high-grade MCP is placed above the TFL for registration. The MCP signal is pre-amplified and fixed on a high sample rate digital oscilloscope. At four positions stays Faraday cups (with easy-to-open ends for light input) for additional adjusting. Most of the ion beam adjustment, filtering and mass-spectroscopy functions are linked-in with DAQ cards and automated in a *LabView* software environment.

3. Results

The build up instrument is significant contribution to the upgrade of measurement infrastructure in the research on ion beams in EU and worldwide. The mobile instrument for negative ion energy studies at present is used in test mode and will be ready for experimental exercises early in summer 2013. The planning of experiments and selection of first target substances are in progress. SIM-ION modeling of the instrument is about ready, making the selection of experimental substances easier. By autumn the instrument will be used for cross-comparison of the TFS and PEARLS detection systems. Size of instrument at work position ca. 2*2*1,5m and of transport position 2,5*1,3*1,5m. Time scale for composing/ /discomposing for transport – hours. Expected life-span of sample substance loaded - with filament source 15 hr, with ICP source ca. 1000 hr. Vacuum at photochemical reaction zone expected 10E-11 Torr, already attained 10E-10 Torr. Ion beam energy already tried 50eV to 3,5 keV, yet at need is not difficult to mount a surplus accelerator for ca. 100 keV. Laser ray may be laid in from each of four direction, thus instrument is adjustable to near any kind of massive light source or accelerator geometry. Initially instrument uses Nd-YAG laser with crystal doubler.

4. Discussion

The installation described above presents a modular multiple purpose instrument with very high flexibility and transform or upgrade capacity, thus making a novel input into EU research infrastructure. It has the advantage of being relatively easily moved to permit the use of unique sources of light unavailable for ordinary negative ion research instruments. GRIBAM is designed to be conveniently rearranged to comply with different energy detectors, diverse sources of ions and charging methods. The proposed use of RF ICP plasma chamber, apart from widening the spectrum of substances for studies, also allows for higher ion currents and less polluted beam before mass selector. The team of designers in Riga and Gothenburg is open to proposals to plan and to perform joint experiments.

Acknowledgements

The construction was supported by the project FOTONIKA-LV, FP7-REGPOT-CT-2011-285912.
The attendance of the conference was supported by the ERAF Nr.2010/0202/2DP/2.1.1.2.0/10/APIA/VIAA/013.
Prof. Dag Hanstorp from the Ion Physics Laboratory at the University of Gothenburg, for ideology of the project, a great deal of much know-how and kind help for access to instrumentation.
Dr. Hab.Phys Uldis Berzins for initiation of the project.
Thanks to technical and engineering personnel in Gothenburg and Riga for support.

References

[1] Guillermo M.Muñoz Caro (Centro de Astrobiologia, SCIC-INTA, Spain): presentation ‹‹*Space missions to comets*›› at Jaca summer school `SPECAT-2009`, July 2009.

[2] Space Missions – *Deep Impact* [http://science.nasa.gov/science-news/science-at-nasa/2005/28jun_deepimpact/], *Stardust* [http://stardust.jpl.nasa.gov/news/lpsc2004.html], *Rosetta* [http://rosetta.jpl. nasa.gov].

[3] Precursors of biological cofactors from ultraviolet irradiation of circumstellar/interstellar ice analogues: Uwe, Meierhenrich, Guillermo, Muñoz Caro, Brack: Chemistry 11 (17): 4895-900 (2005), PMID 15900538

[4] Mark H.Stockett, John D. Alexander, Uldis Bērziņš, Tao Chen, Khadijah Farid, Michael Gatchell, Anders Johansson, Kostiantyn Kulyk, Henning T.Smidt, Henning Zettergren, Henrik Cederquist: Polycyclic Aromatic Hydrocarbons in collisions with atoms (publication in process, May 2013).

[5] PEARLS (Photoelectron Energy and Angle Resolved Longitudinal Spectrometer) is emerging project for ALS (www-als.lbl.gov/index.php/contact/124-1001.html) made on basis of ideas of *D. Hanstorp, C. Bengtsson, and D. J. Larson,* Angular distributions in photodetachment from O- . Phys. Rev. A *»* V 40 *»* Issue 2*, 1989, pp. 670-675.*

[6] Technical description at www.colutron.com/products/kit/source.html.

[7] www.asi.lv, www.fotonika.lv.

Moisture Probe Calibration for Open Air Measurements in Rock Dwellings Locality in Brhlovce

[1]V Boháč, [1]D. Fidríková, [1]V. Vretenár, [2]T. Durmeková, [2]I. Šimková, [2]L. Petrýdesová, [2]J. Vlčko

[1]Institute of Physics, Slovak Academy of Sciences, Bratislava, Slovakia
[2]Department of Engineering Geology, Faculty of Natural Sciences, Comenius University, Bratislava, Slovakia
Email: bohac@savba.sk

Abstract. *The aim of this paper is to show the calibration method of humidity sensors based on hot ball probes. The sensors are used for the monitoring of weathering and the damage of rock dwellings in Brhlovce village (Slovakia). The standard arrangement of hot ball probe is used for measuring thermal conductivity. The thermal conductivity of porous structure is dependent on moisture content in pores, so when pores are filled by air/vapor, water or ice the value of thermal conductivity is increasing. Moisture regime of moisture probes was studied in laboratory condition in order to find the range of thermal conductivity in dry and water saturated states in dependence on temperature. In situ monitoring of the temperature-moisture regime of volcanoclastic rocks has been running for one year.*

Keywords: Thermal Conductivity, Moisture Probe, Humidity Measurement in Porous Stones

1. Introduction

Porous materials – rocks situated in natural conditions are exposed to the sun radiation, precipitation, evaporation, freezing and thawing phenomena. Moisture in the rock walls under different climate conditions, e.g. the freeze and thaw processes at the abrupt temperature changes have destructive impact on stone durability. It is caused by cycles of drying – wetting and freezing – thawing processes. The resulting thermal conductivity of a porous material is a function of temperature and the water content of pores. In order to understand the weathering processes of rock dwellings the moisture regime is monitored by a moisture sensor in connection with RTM electronic unit (fy. TransientMS) constructed for long time monitoring of moisture under the open air conditions. The monitored parameters, e.g. moisture and temperature correlate with amount of rainfall and air temperature.

2. Physical background and principle of Hot-ball method

The investigation of the heat transport properties of materials in stationary and transient (dynamic) regime has been published in several papers [1], [2], [3], [4]. The stationary methods usually operate with gradient temperature over the thickness of specimen and thus it takes reasonable time to get stable or stationary state. This causes moisture redistribution in material bulk and changes of original moisture condition. In the case of transient methods it is used small temperature disturbance, which will take shorter time and causes no or minimal redistribution of moisture and thus the original thermodynamic state is preserved.
In-situ monitoring of moisture content in tuff massive is performed by small apparatus based on the transient hot-ball method on Fig. 1. The measuring procedure consists of the measurement of initially stabilized temperature (base line), switching on the step-wise heating pulse that generates heat flow and simultaneously scanning the temperature response. Model of the hot ball method [5] assumes a constant heat flux q from the empty sphere of radius r_b into the infinitive medium that starts to be generated for times $t > 0$ (Fig. 1 bottom). The long-time approximation of temperature function of the model is derived as the working relation of the measuring method [2]:

$$\lambda = \frac{q}{4\pi r_b T_m (t \to \infty)} \tag{1}$$

where λ is thermal conductivity of the surrounding medium and T_m is stabilized value of the temperature response reached in the long time limit. The measured temperature response is shown in Fig. 1 bottom. The maximum of temperature response is used to calculate the value of q/T_m that is adequate to the thermal conductivity and thus moisture content according a type of calibration.

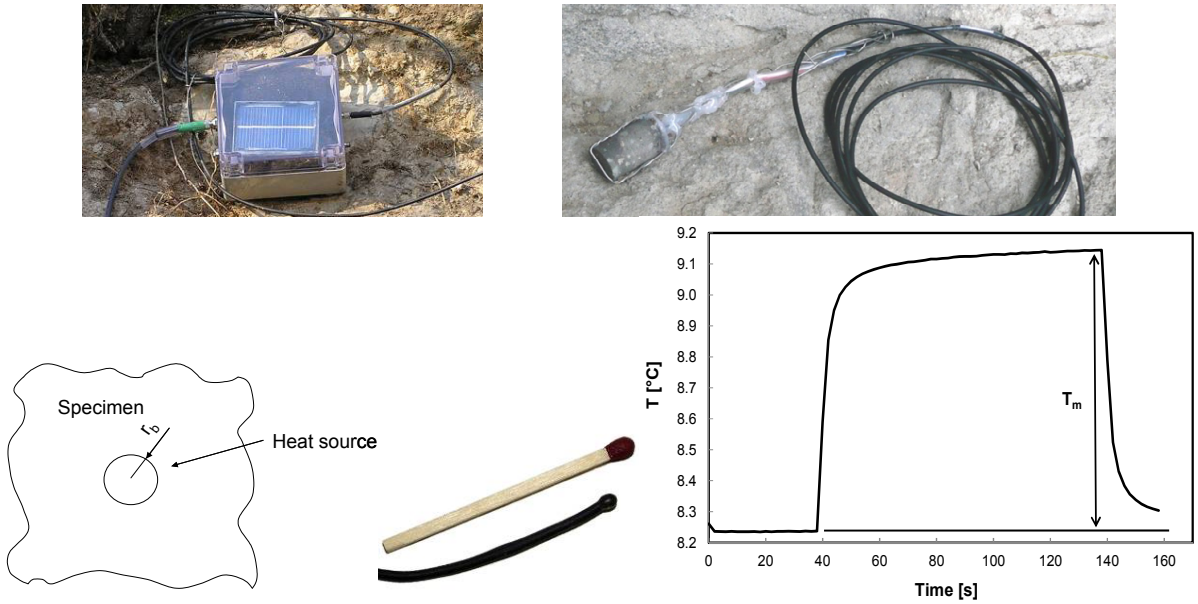

Fig. 1. RTM-electronic unit with solar panel for recharging (up left) and moisture sensor with wire connections (up right), model of the hot ball (down left) and probe real size picture (down middle). The example temperature response measured for tuff. Measurement takes 160s (100s heating) in the bottom right.

3. Experiment and calibration procedures

For the study there were selected the cores from drilling of holes for placing them back as the moisture sensors. The tuff cylinders from Brhlovce rock dwellings having diameter 32 mm were drilled in the middle. Hot ball probe having 2.5 mm in diameter was inserted into a center of such a hole in rock cylinder and cables were supported by cage made of nickel wires (Fig. 1 up right). Physical properties of tuff from Brhlovce locations varies and are the following: specific gravity 1.6÷2.6 g.cm^{-3}, volume density 0.909÷1.466 g.cm^{-3}, total porosity 31.2÷52.3 %, water absorption 16.4 % and uniaxial compression strength 17 MPa.

The moisture probes based on hot ball probe were calibrated in liquid media having different but known value of thermal conductivity. The water and glycerol were used as calibration points, so one can calculate thermal conductivity from measured values of q/T_m. Water and glycerol have the values of thermal conductivities in a range of thermal conductivity values of measured materials. Such a probe is inserted in a cylindrical core from drilling of holes and ready moisture sensor is at Fig. 1 (up right).

The measured value of heat flux and temperature maximum q/T_m inside the moisture sensor represents thermal conductivity that is dependent on moisture content (Fig. 2) in between dry and moisture saturated state. The difference of q/Tm represents 100% moisture scale in between dry and fully saturated content of pores by water. After saturation by water it was inserted in the tuff massif at Brhlovce and in-situ monitoring started in October 31st 2011. The values of thermal conductivity λ in the case of water saturated probes are much higher than

the dried one (see Fig. 2). The calibrated moisture probe in Fig. 2 was inserted into a hole drilled in massive rock at locality of museum of rock dwellings in Brhlovce. The insertion depth of a moisture sensor is 10 cm. At the 23 °C it was monitored the moisturing process that is shown in Fig. 2. The high difference in the value of the q/Tm between dry and reached water-saturated state of tuff also proves its high water absorption.

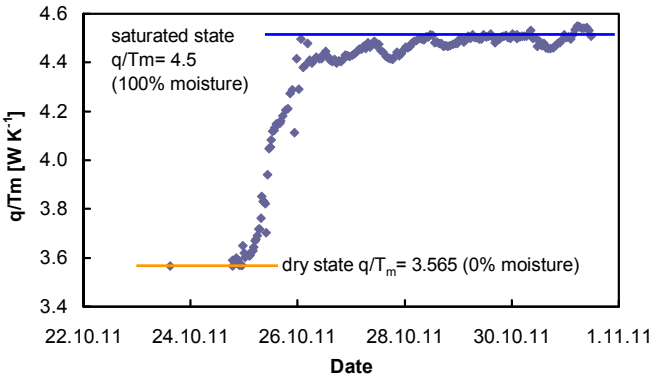

Fig. 2. Calibration of probe made of tuff stone in dry and moisture saturated state. Figure represents moisturing process at 23°C.

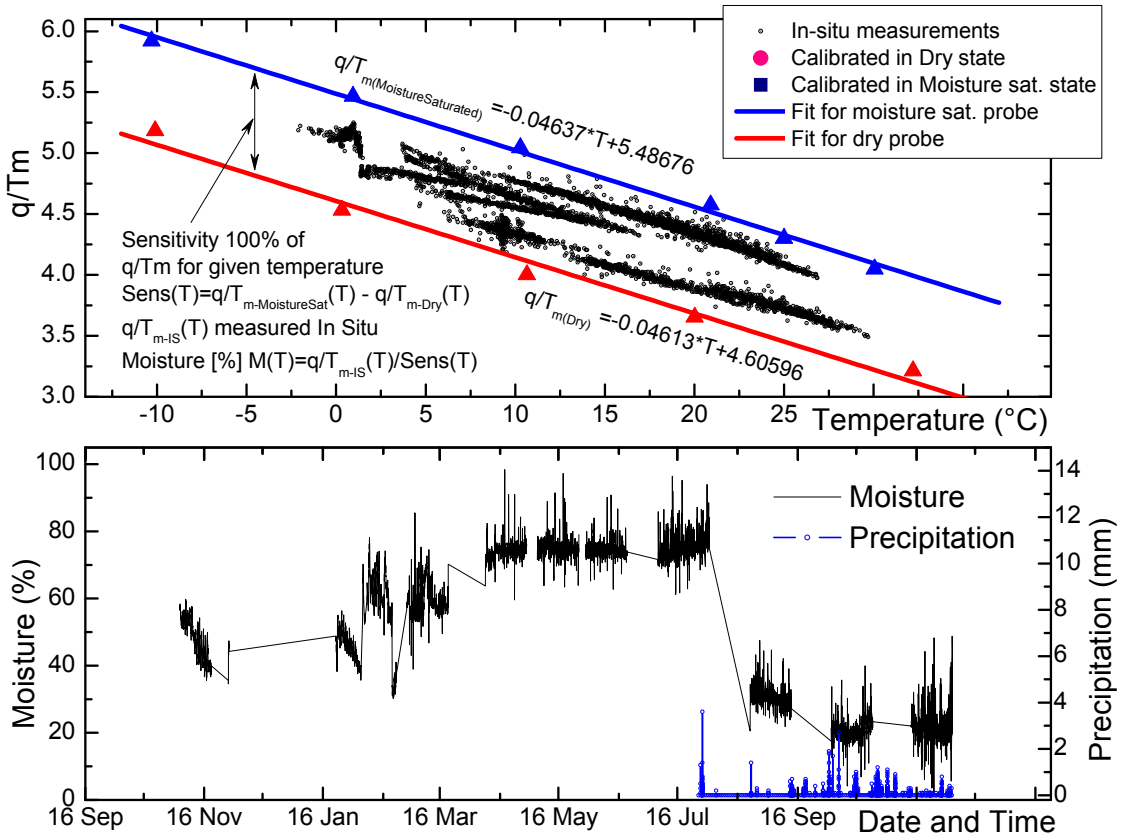

Fig. 3. Calibration lines of the temperature dependency of q/Tm values measured for tuff in dry and water saturated condition. The plot in blue and red are giving the sensitivity for difference in the moisture saturated and dry state and are compared with in-situ measured data in 10 cm of massif depth (Up). Calibration data were statistically averaged for a given temperature [6]. The same data from locality are plotted in time scale with precipitation data (down). The rain gauge station was installed in July 27th 2012.

The data from in-situ measurements were collected along one year and the values of q/T_m in dependency of temperature were plotted with calibration lines in Fig. 3. up. The moisture scale defined by calibration lines in q/T_m values were recalculated to the moisture content and plotted in a time scale in Fig.3. in the bottom. Changes represent a seasonal variation of moisture content. The water was evaporated in several steps so one can see several regions of data measured under similar moisture content. In a time the moisture was changed by very slow drying process. The lower values were measured in summer in August that was very dry with practically no rains and surface temperatures well above 30 °C.
For the next monitoring in depths at 30 and 50cm in tuff massive the new series of 10 probes were tested for the sensitivity. Moisture sensors in dry and moisture saturated state were calibrated in dependence of temperature. Linear dependency was found for different moisture content, so values of q/T_m can be recalculated to thermal conductivity or to moisture content directly from this calibration. The dry-moisture calibration was performed in laboratory conditions for the range of temperatures from -20 up to 22 °C like in Fig. 3.

4. Conclusions

Paper presents data on moisture change in dependency of temperature. Calibration methodology was elaborated and performed in climatic chamber and checked by TROTEC 600 during in situ monitoring of massif at locality in Brhlovce. For all of specimens, e.g. moisture sensors the dependency on humidity content variation with q/T_m parameter was found in dependency on temperature variations. Based on observed physical properties such as porosity, water absorption and thermal conductivity of studied materials; it was shown relationship between water absorption and increases of thermal conductivity.

Acknowledgements

This work was supported by the Slovak Research and Development Agency under the contract No. APVV-0641-10, Study of rocks properties and investigation of structural and textural characteristic in correlation with thermophysical and physico-mechanical properties.

References

[1] Maglić, K.D., Cezairliyan, A. & Peletsky, V.E. (eds.) 1992. Compendium of thermophysical property measurement methods. Volume 2: Recommended measurement techniques and practices, Plenum Press, New York, p. 643.

[2] Kubičár, Ľ., Vretenár, V., Štofanik & V. Boháč, V. 2010. Hot-Ball Method for Measuring Thermal Conductivity, International Journal of Thermophysics, 31, 10, p. 1904-1918.

[3] Kubičár, Ľ. & Boháč, V. 1999. Review of several dynamic methods of measuring thermophysical parameters. In: Gaal, P.S. - Apostolescu, D.E. (eds.): Proc. 24th Int. Thermal Cond./12 Int. Thermal Expansion Symp., Technomic Pub. Co., Pittsburgh, Pennsylvania, p. 135-149.

[4] Krempaský J. 1969. The measurements of the thermophysical Properties, SAV, Bratislava.

[5] Carslaw, H.S. & Jaeger, J.C. 1986. Conduction of heat in solids, Oxford, Clarendon Press, Second edition, p. 348.

[6] Ekkertová, P., Šimková, I., Brček, M., Durmeková, T. & Boháč, V. 2012. Influences of temperature change and moisture content on the thermal conductivity of rocks. Proc. Thermophysics 2012, Podkylava, Slovak Republic, printed by: Brno University of Technology, Faculty of Chemistry, ISBN: 978-80-214-4599-4, p.33-40.

Wireless Sensing Network Management for Landslide Disaster Monitoring

S. Takayama, J. Akiyama, T. Fujiki, N. A. B. Mokhtar

Ritsumeikan Univ.BKC, Shiga, JAPAN
Email: s-tkym@se.ritsumei.ac.jp

Abstract. *This paper shows the network management and operation to monitor landslide disaster at slop of mountain and hill. Natural disasters damage a measuring system easily. It is necessary for the measuring system to be flexible and robust. The measuring network proposed in this paper is the telemetry system consisted of host system (HS) and local sensing nodes network system (LSNNS). LSNNS operates autonomously and sometimes is controlled by commands from HS. HS collects data/information of landslide disaster from LSNNS, and controls LSNNS remotely. HS and LSNNS are communicated by using "cloud" system. The dual communication is very effective and convenient to manage a network system operation.*

Keywords: Network Management, Wireless Sensing, Landslide Disaster

1. Introduction

Natural disasters are terrible and so important concerns for us. They destroy social infrastructures, loss human lives, and damage economic condition of people, companies, organizations and governments. It is very hard for measuring system to monitor landslide disasters. Measuring instruments are broken easily by the disaster. By reason of dangerousness, measuring person cannot be with the system. Measuring system must monitor at a wide area not only a point. As landslide disaster is occurred suddenly, the system waits and senses it at a moment after long time monitoring.

Wireless sensing node network system (WSNNS) is one of effective solution to monitor the landslide disaster. The network formation is mesh. The distributed sensing nodes operate cooperatively. Then the WSNNS becomes possible to measure acceleration, soil moisture and land position at a wide area for long time. As sensing nodes are supporting each other, the WSNNS can continue the measurement even if some nodes have been destroyed by landslide disaster. The sensing node analyses measuring parameters to find a sign of landslide disaster and to estimate the condition of system and sensor devices. The WSNNS operates autonomously as a local system (LSNNS). Then the measurement data and estimated information are transmitted to Host system (HS) at other place where measuring person monitors and collects them safely. There are several kinds of communication method between WSNNS and HS. "Cloud" system presents so useful services to realize a dual way communication method between them. As HS does not demand measuring data transmission from LSNNS in real time, the communication is enough asynchronously. The storage and mail system of "Cloud" realize an effective and convenient communication to transmit the data/information from LSNNS and the command from HS.

In monitoring landslide disasters, the total measurement network system constructed by LSNNS, HS and the communication method using "cloud" system realizes so useful and convenient measurement system. In following, the network management is shown.

2. Measurement Network System for Monitoring Landslide Disaster

Fig.1 shows the system construction of total measurement network to monitor landslide disaster. The system is consisted with Host System (HS), "Cloud" system, Local Sensing Node Network System (LSNNS).

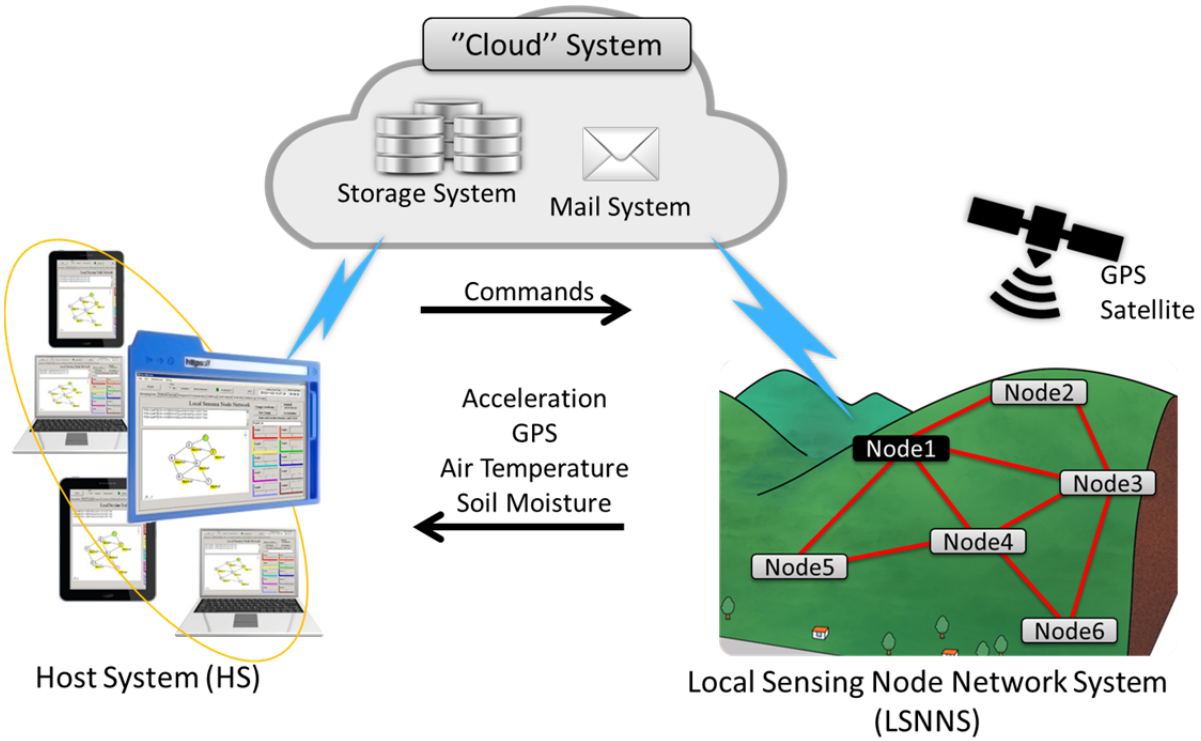

Fig.1 System Construction of Total Measurement Network to Monitor Landslide Disaster

2.1 Local Sensing Node Network System

LSNNS is the local measuring network which is consisted of plural distributed sensing nodes connected with near field wireless communication at around slope of mountain and hill. One of them is a top node which is the gateway of LSNNS for data and command. The top node mounts a smart phone to communicate data and command with "Cloud" system. Each sensing node mounts some sensors, control board and wireless communication device (Fig.2). The sensors are 3D acceleration, GPS, temperature and soil moisture. The 3D acceleration sensor is used to monitor ground acceleration by landslide disaster. The occurrence and types (slide down, rolling down) of landslide are recognized by continuous analyse of 3D acceleration angles and power spectrum of acceleration signal for 1 sec.. GPS is used to know the ground position and movement of sensing node. The position precision is within

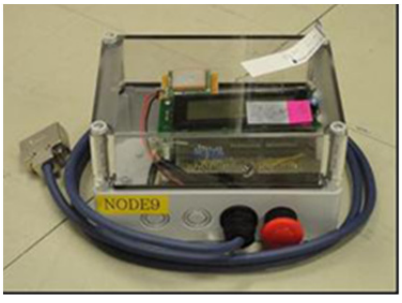

Fig.2 Sensing Node

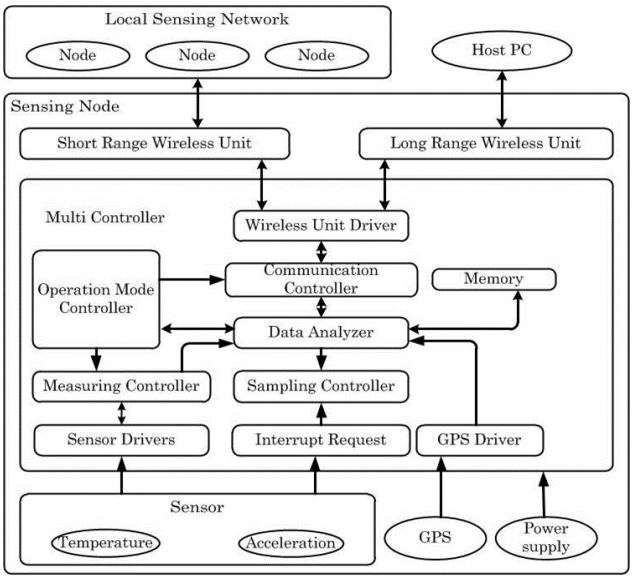

5 m. By information of ground positions of sensing nodes, HS can monitor the topology of LSNNS which becomes the basic information to construct the routing table of LSNNS. The ground movement of sensing node is referred to find a sign of very slow landslide. The wireless communication device connects sensing nodes in near field. The operation frequency is 1.2GHz. The transmission baud late is 9600 bps. The communication distance in wood is about 50-60 m. The control board takes some kinds of role to manage the communication control, to decode and operate commands from HS, to acquire measuring data from sensors and to estimate information of landslide disaster and system condition by analysing the data.

LSNNS has three kinds of operation mode which are initialization, normal and urgency mode. In the initialization mode, sensing nodes recognize the condition of mutual connections each other by beacon test signal transmissions. By these connection data, HS estimates the topology of LSNNS and constructs the routing table. In the normal mode, the sensing node operates on demand by HS. According to the command from HS, the sensing node replaces system parameters like sampling time. And that returns measuring data, estimated information and system conditions to HS. In the urgent mode, the sensing node recognized the occurrence of landslide disaster send urgent information to neighbour nodes. The nodes known the urgent information also send it new neighbour nodes. Repeating this transmission between sensing nodes, the urgent information is influence node to node. Finally, that information reaches to the top node of LSNNS. The top node sends the information to HS via "Cloud" system urgently.

2.2 "Cloud" System

"Cloud" is a collection system of several kinds of service (Storage system, Mail system and so on) which is accessed from everywhere. By using the mail system, the top node of LSNNS accesses "Cloud" system by 13 messages per minute. The command from HS and data/information are packaged in a mail message. As the communication is asynchronously, HS and top node of LSNNS check mail messages regularly. Fig.3 shows series of measuring data transmitted by mail messages. Fig.4 shows the growth of local sensing node network which is informed by measuring data. Data transmission rate is increased by direct access to storage system. It is possible to use 25GB free in commercial "Cloud" system.

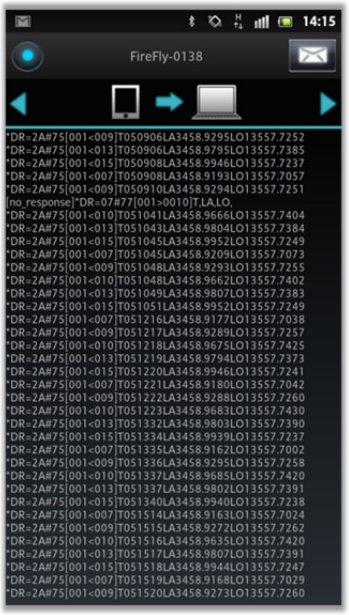

Fig.3 Series of Measuring Data by Mail Messages

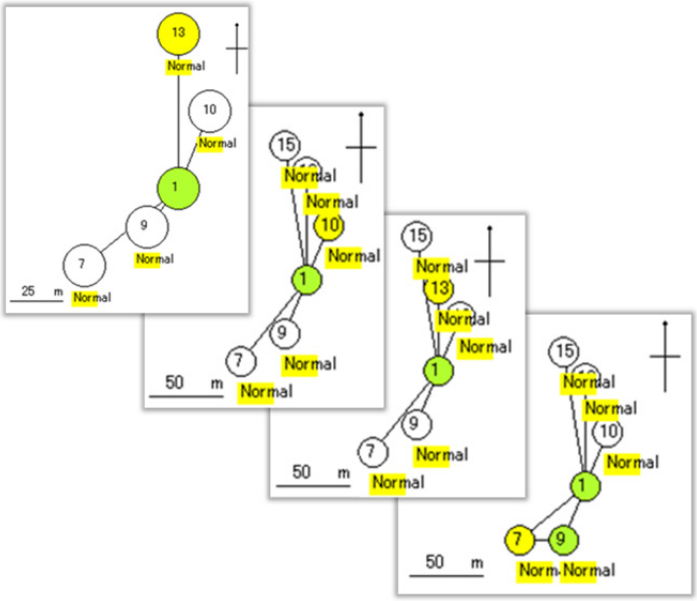

Fig.4 Growth of Local Sensing Node Network by Measuring Data

2.3 Host System

Host system take roles to collect measuring data, show measurement parameter conditions, alarm the occurrence of landslide disaster to measuring person, construct a routing table of LSNNS and make/send the operation command to manage LSNNS. These functions of HS are realized with software. Measuring person can monitor a list of measuring data (acceleration, GPS, temperature soil moisture), status of network topology, time transition of measuring data, status of communication. Fig.5 shows command operation window. By making it as a web program, measuring person can operate measurement network system by any PC and Tablet from everywhere.

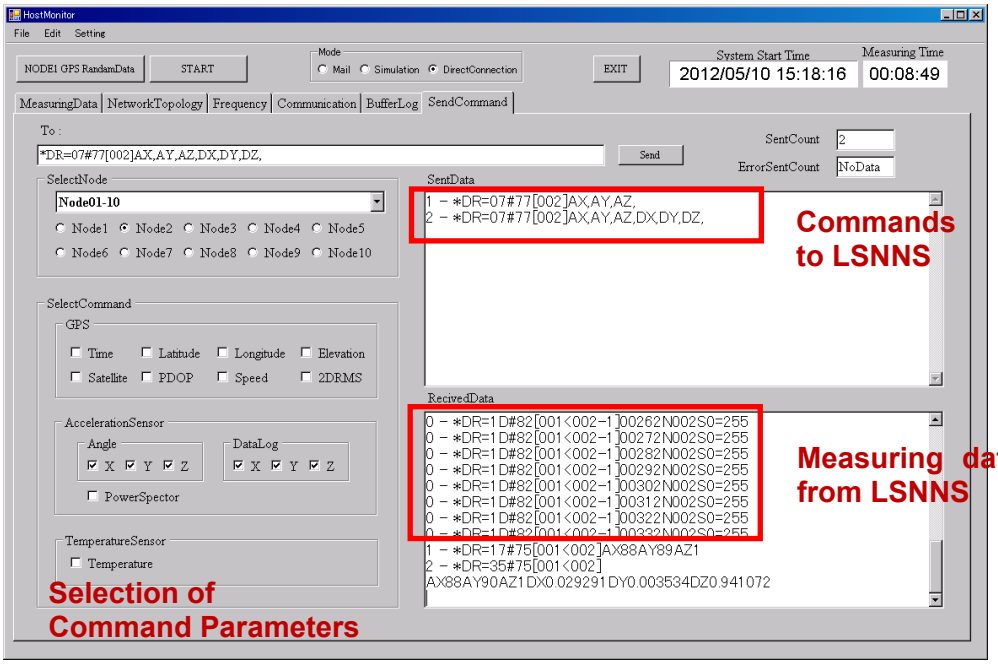

Fig.5 Command Operation Window in Host System

3. Conclusion

In this paper, the system construction of total measurement network to monitor landslide disaster, which is consisted with Host System (HS), “Cloud” system, Local Sensing Node Network System (LSNNS). On the measurement system to monitor natural disasters, robust, flexible, useful and reliable network management is demanded. LSNNS is designed as a robust and flexible system for landslide disaster. “Cloud” system presents usefulness to access the system from everywhere and the flexibleness to communicate data/information and command between HS and LSNNS.

References

[1] S.Taenaka, Y.Watanabe and S.Takayama, “Construction of Wireless Sensing Network System for Landslide Disaster Monitoring”, ACTA IMEKO 2012, pp.TC19-P-5, 2012.

[2] Rahman, F.; Kumar, A.; Nagendra, G.; Gupta, G.S., “Network approach for physiological parameters measurement”, IEEE Trans. Instr. and Meas., Vol.54, pp. 337 - 346, 2005.

[3] S.Taenaka, J.Akiyama, T.Fujiki and S.Takayama, “Design of Flexible Wireless Sensing Network System for Landslide Disaster Monitoring”, Proc. of SICE International Conference 2012, pp.1443-1459, 2012.

Flow Measurement for Dynamic Behaviour of Heavy River Surface

S. Takayama, T. Tomoo

Ritsumeikan Univ.BKC, Shiga, JAPAN
Email: s-tkym@se.ritsumei.ac.jp

Abstract. *This paper shows the monitoring system of dynamic state (flow speed and direction) of river surface by using video image processing. This system is designed for estimation of dynamical behaviour of heavy river at natural disasters. The state of speed and direction estimated continuously from differential image flames. By monitoring the dynamic state, it is possible to find dangerous area and the dangerousness, predict the second water disaster and inform them to people and local/prefectural governments.*

Keywords: Disaster Monitoring, River Surface, Image Processing

1. Introduction

In Japan, rivers are short length and the vertical level of start and end points is high. Then after heavy rain and typhoon, the rivers change the state. The volume and speed of water flow are increasing. The surface becomes muddy and heavy. The water overs bank, sometimes breaks it at winding corners. The heavy river loses many lives and damages life infrastructures like road, houses, facilities, rice/vegetable fields, power lines and natures. The river disaster is dangerous and serious for people who live around it. By the reason, the monitoring system for heavy river flow is so importance for them. Some kinds of the system measure the water speed, force, direction and level of height directly by handy tools/instruments. But it is dangerous for measuring person to face the heavy river. And, standalone measuring system/instrument in river is broken easily at the heavy state of river. On the other hand, remote video monitoring system is safe and effective to measure the surface of heavy river. In this system, video camera takes the situation of river surface near the river. The image is transmitted to host system far from the river and analysed the speed and direction of river surface. By the image processing, dangerous area and level are always estimated, and it is possible to predict the second water disaster around the field.

2. Measurement System for Monitoring Dynamic State of River Surface

The river surface is recorded by video camera. The video is extracted by 7 image frames per second. Firstly, from neighbour two image frames, a differential image is calculated. And the differential image is divided evenly into 80*60 segments (Fig.1). By searching the most resemble segment around a ROI (Region of Interest) and make a vector between them, a couple of speed and direction of river flow is calculated. Repeating this processing to all segments, speed and direction distribution of river flow on a differential image is got (Fig.2).

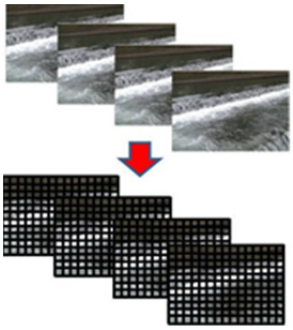

Fig.1 Segmentation of differential image

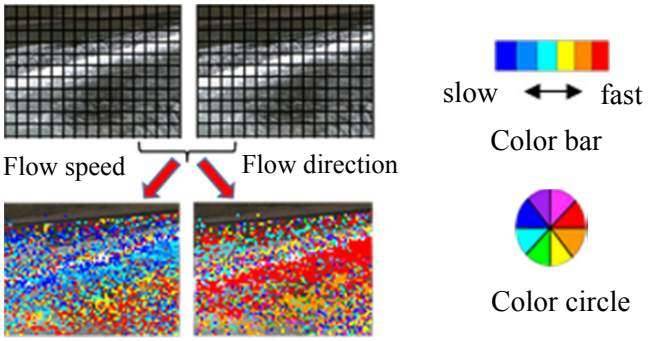

Fig.2 Flow speed and direction on a differential image

Fig.3 shows the definition of a vector to calculate flow speed and direction. On neighbour two differential frame images(DFI), by searching the most resemble segment on later frame image around a ROI on previous frame image and make a vector between their centers. The length expresses flow speed and the inclination angle shows flow direction. Each angle is denoted by a color(Table.1).

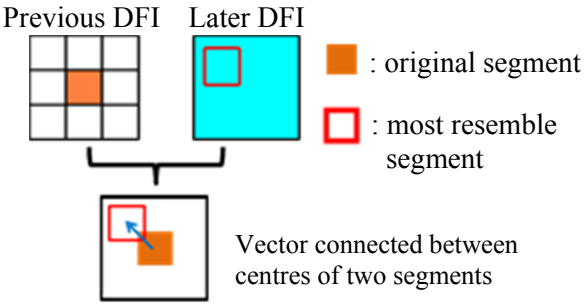

Fig.3 Vector to determine flow speed and direction

Table.1 Relation between directions and colors

direction: 0 to +45 [degree]
direction: +45 to +90 [degree]
direction: +90 to +135 [degree]
direction: +135 to +180 [degree]
direction: 0 to -45 [degree]
direction : -45 to -90 [degree]
direction : -90 to -135 [degree]
direction : -135 to -180 [degree]

By the distribution of flow direction, the turbulent flow of river surface is estimated. Fig.4 shows direction numbers attached to each color. In Fig.5, all segments are numbered according with flow direction. 0 means no direction. Comparing a flow direction distribution with other one measured 1sec. (7 DFIs) ago, disturbance of river flow has been estimated. Firstly, a segment on flow direction distribution at 1 sec. (7 DFIs) ago is defined as ROI. Secondly, comparing numbers of surrounding 9 segments with the number of ROI, the difference of directions becomes obviously. If the difference is within 1, the segment is colored blue. If that is over 2, the segment is colored red (Fig.5). Counting these colors, if red segments are 5 more, it has been decided that the state of this area (colony of 9 segments) is disturbance. And if 4 less, the state is orderly.

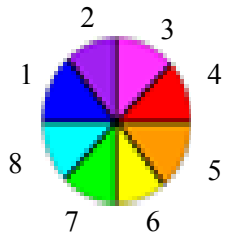

Fig.4 Direction number

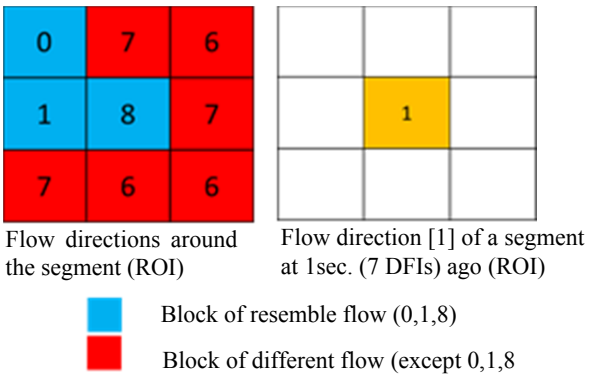

Fig.5 Example of distinction of flow directions

Using the flow speed and disturbance of river flow, the characteristics of dangerousness of river flow is decided (Fig.6). Kinds of the dangerousness are distinguished by relations between the flow speed and disturbance of river flow (Table 2). When the flow speed is high and turbulent flow, the level of dangerousness of segment is “High”. In Fig.6, the segments are colored red. When the flow speed is low and turbulent flow, the level of dangerousness of segment is “Middel”. The segments are colored orange. When the flow speed is high and orderly flow, the level of dangerousness of segment is “Low”. The segments are colored green. When the flow speed is low and orderly flow, the level of dangerousness of segment is “None”. The segments are no color. Fig.7 shows three kinds of dangerous segments distinguished by “High”, “Middle” and “Low” level. In the 1st stage, the distribution of

segments is shown. In the 2nd stage, the distribution of colonies is shown. In the 3rd stage, the distribution of areas is shown. Fig.8 shows the formation of colonies by plural segments. The colonies are surrounded by red lines. Green boxes show local set of colonies. When the box is large enough, it is shown by blue circle instead of green box that the area is dangerous intuitively.

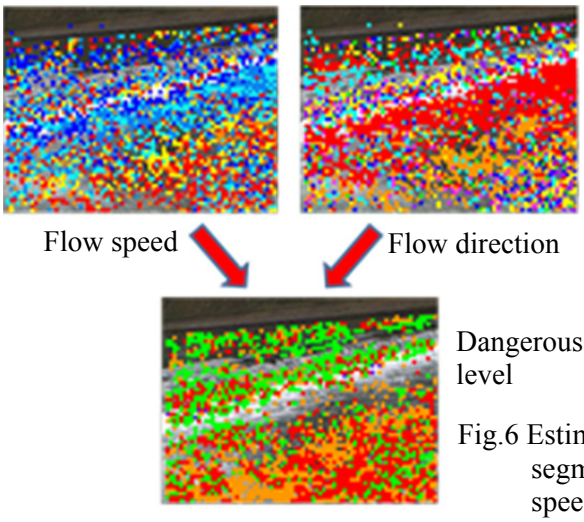

Fig.6 Estimation of dangerous segments and level by flow speed and turbulent flow

Table 2 Distinction of dangerous level by flow speed and turbulent flow

	High speed	Low speed
turbulent flow	High	middle
orderly flow	low	nothing

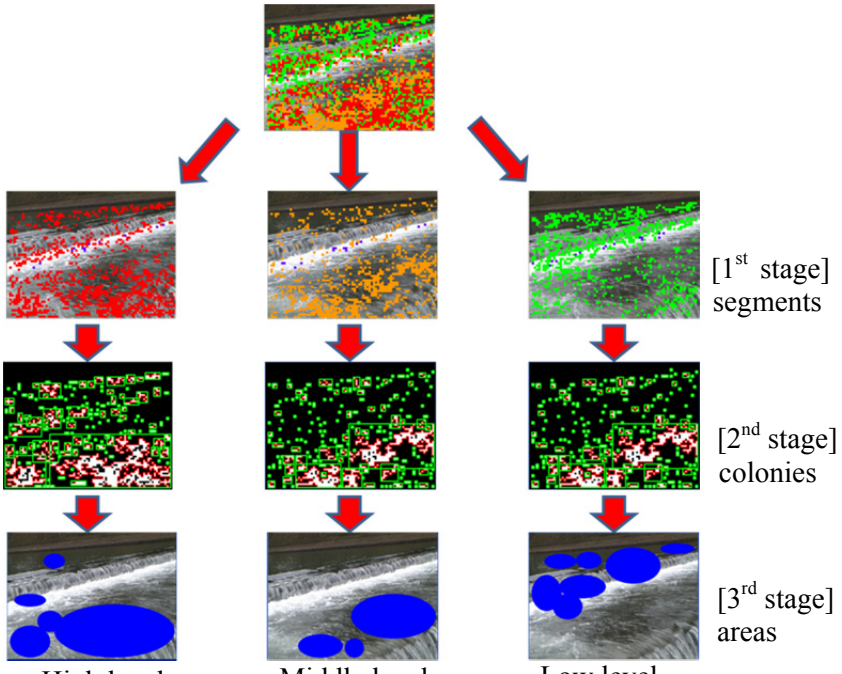

Fig.7 Dangerous segments, colonies and areas distinguished by three kinds of level

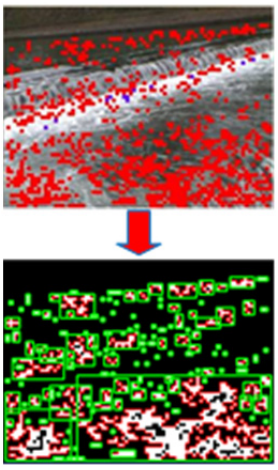

Fig.8 Formation of dangerous colonies

3. Measurement of Flow speed, Direction and Dangerous Level of River Surface

Fig.9 shows an example of measurement result of flow speed, direction and dangerous level of river surface. The flow speed in Fig.9 (b) is shown by the color defined in Fig.9 (c). The flow direction in Fig.9 (d) is shown by the color in Fig.9 (e). The dangerous level Fig.9 (f) is shown by the color in Fig.9 (g). Fig.10 shows dangerous area divided by three kinds of levels. Fig.10 (a) and (b) show the segments and areas in high dangerous level. Fig.10 (c) and (d) show the segments and areas in middle dangerous level. Fig.10 (e) and (f) show the segments and areas in low dangerous level. In Fig.9(b) and (f), no area is confirmed as dangerous area.

(a) Original image

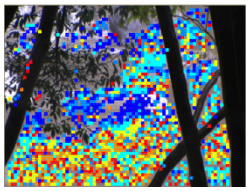

(b) Distribution of flow speed

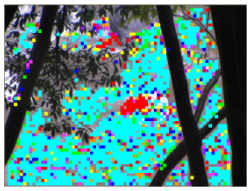

(d) Distribution of flow speed

(c) Flow speed level

(e) Color circle for direction

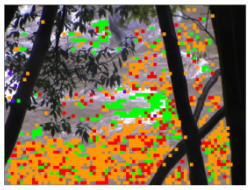

(f) Distribution of dangerous level

(g) Dangerous level

Fig.9 An example of measurement result of flow speed, direction and dangerous level of river flow

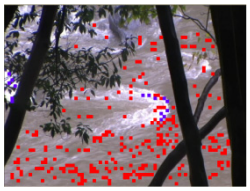

(a) Segments of high dangerous level

(b) No area of high dangerous level

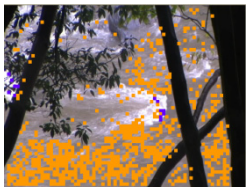

(c) Segments of middle dangerous level

(d) Areas of middle dangerous level

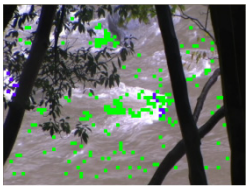

(e) Segments of low dangerous level

(f) No area of low dangerous level

Fig.10 Dangerous segments and area divided by three kinds of level

4. Conclusions

To estimate dynamic state of river, the flow speed and direction of river surface are measured by image processing of video. By these parameters, it has been possible to estimate turbulence and dangerous area on the river surface. These parameters will be so useful to inform the dangerousness to people and to predict future disasters around the river.

References

[1] Shuzo Tanaka, Toshifumi Yamazaki and Takamiti Tanaka “The Propose of the Velocity Measuring Method on River Surface Using Remote Sensing Technique” The Remote Sensing Society of Japan ,Vol.15, No3, pp.66-76,1995.

[2] Motoyosi Okujima, “Flowmetry for rivers and seas”, The Acoustical Society of Japan, Vol. 38, No. 8, pp. 43-30, 1982.

[3] Takashi Yamaguchi and Kunio Nizato “Flood discharge observation using radio current meter”, The Civil Engineers Society of Japan, No. 497, II-28 pp. 41-50, 1994.

[4] Harshad B. Prajapati and Dr. Sanjay K. Vij “Analytical Study of Parallel and Distributed Image Processing” International Conference on Image Information Processing pp1-6, 2011.

Sonic Testing of Long Pipes by Using Longitudinal Waves

N.K. Andreev, A.S. Malatsion, Chernyshova M.G.

Kazan State Power Engineering University, Krasnosel'skaya Str., 51,
420066, Kazan, Russia
Email: ngeikandreev@gmail.com

Abstract. *Application of the sonic testing technique is considered in the context of the detection of defects of long pipes and bond of various materials to the surfaces of pipes. The characteristic property of the proposed technique is that the longitudinal waves at 1 – 20 kHz are used for inspection and only single-sided access is needed for transducers located at a head of a pipe. Some characteristic features of the technique and details of the construction of the sonic testing apparatus are considered.*

Keywords: Sound, Sonic Testing Technique and Apparatus, Long Pipes, Defects, Cementation

1. Introduction

The sonic testing (ST), an especially ultrasonic testing (UT), is the well known technique for material testing [1, 2, 3]. The maximum detection range of a sonic sensor is typically longer for lower frequencies, while the resolution and accuracy are typically better at higher frequencies. Therefore low frequencies of sound should be used for long subjects of testing such that large dimensional pipes. The aim of this paper is to study of possibilities of the sonic testing using longitudinal waves for detecting defects of the structure and bond of various materials to surfaces of long pipes. Mainly discussion is devoted to cement bond logging.

2. Subject and Methods

Usually the transverse waves are used to determine the quality of the cement bond to the production casing, and to evaluate cement fill-up between the casing and the reservoir rock. This technique has been called Acoustic Carottage of Cementation (ACC) (Synonyms: Acoustic Well Logging, Cement Integrity Logs). The technique is invasive. The inspection is carried out by equipments that are located in the inner space of oil wells filled by a liquid. This often used ACC technique has a very good sensitivity, but is very expensive in practice.

In 1992, it was suggested by Kozlov A.V. et al [4] that the inspection the quality of the cement bond to the production casing can be performed by the nondestructive technique, by using longitudinal sonic waves. The technique was designed for "express technology out-of-well cement logging''. The characteristic property of the proposed technique was that the longitudinal waves are used for inspection, and only single-sided access is needed for transducers located at a head of a pipe. The equipment has been elaborated for sonic inspection of oil wells at relatively low frequencies (20kHz). This low-cost technique was named Vibroacoustic Cementometry (VAC) and used for preliminary inspection of oil wells during for more than ten years. This former home-made system has been made using IBM AT personal computer and C++ program. At the last time, the testing system was reconstructed anew by the authors using the modern electronics, notebook and National Instruments LabVIEW program. This system is described in the presented paper.

3. Apparatus

The important terms often used in sonic inspection to describe a technique's ability to locate flaws are the wave velocity υ, frequency f, wavelength λ, attenuation coefficient α, sensitivity and resolution Δx. Sensitivity is the ability to locate small discontinuities. Sensitivity generally increases with higher frequency. Resolution is the ability of the system to locate discontinuities that are close together within the material or located near the surface. Resolution also generally gets better as the frequency increases and can be evaluated as $\Delta x \approx \lambda/2$. The attenuation coefficient α increases with frequency sufficiently rapidly as $\alpha = k_1 f + k_2 f^n$, n = 2..4. These facts lead to the conclusion that low frequency sonic waves are better to use for inspection of long multilayer pipes. Thus, frequencies equal to or higher than 1 kHz have been chosen to use in the apparatus elaborated.

The elaborated inspection system consists of several functional units, such as the pulser/receiver (home-made), transmitter and receiver transducers (home-made), display devices, analog-to-digital (ADC) and digital-to analog (DAC) converters produced by the Nationals Instruments, computer ASUS"EeePC1000H" and power supplier.

The elaborated pulser is an electronic device that can produce electrical pulses up to 3 kV of amplitude. Driven by the pulser, the transmitter transducer connected to an amplifier through the electric transformer generates sonic energy at desired frequencies in the range of 1..20 kHz. The generation of the carrier is fulfilled by the computer. The length of the pulse can be changed from two to ten cycles of a carrier. The sound energy is introduced into the pipe body through its head. The acoustic contact between the transducers and the surface of the head of a pipe is provided through the slice of alabaster (gypsum) or other contact liquid. An acoustic wave propagates through the pipe. When there is a crack or partial bond with cementation in the wave path, part of the energy will be reflected back from the flaw surface.

The receiver transducer is situated also at the head of a pipe. The reflected signal amplitude is displayed versus the time from signal generation to that when an echo was received. The signal travel time can be directly related to the distance that the signal travelled. Sound velocity in the body of steel pipes of oil wells was estimated as being 5150 m/s.

The home-made transducers were employed for measurements. Lead zirconate titanate ceramic compositions produced by "Avrora" enterprise, Volgograd, Russian Federation, were employed. The preamplifier was placed immediately into the body of transducer. The crossed diodes were used to protect receivers during the large amplitude signal of the pulser.

The usual ASUS"EeePC1000H" netbook was used to control the system and process of the data. All parts of the software were elaborated in the National Instruments LabView environment. M Series Multifunction DAQ for USB-16-bit, 250 kS/s, produced by NI, was chosen to perform analog-to-digital and digital-to-analog conversion. The software contains parts for signal acquisition, averaging, smoothing of measured values of signal amplitudes, evaluating of a "midline", approximating the midline by the exponential functions, dividing the smoothed experimental line by the midline, cut off the noise level, and other final transformations of the measured curves into the cement bond logging curves.

The batteries (accumulators) were used in the power supplier. The possibility of charging the batteries was also taken into account. The cable equipment consists of cables for power supplying, transmitting to and receiving of electric signals from the transducers. The length of the cables is 12 meters to perform measurements from the remote automobile. The inspection system is portable because being placed in the two small suitcases (40x35x20 centimeters), one of them for the processor and measurement units and other for the cables and transducers.

4. *Experimental results*

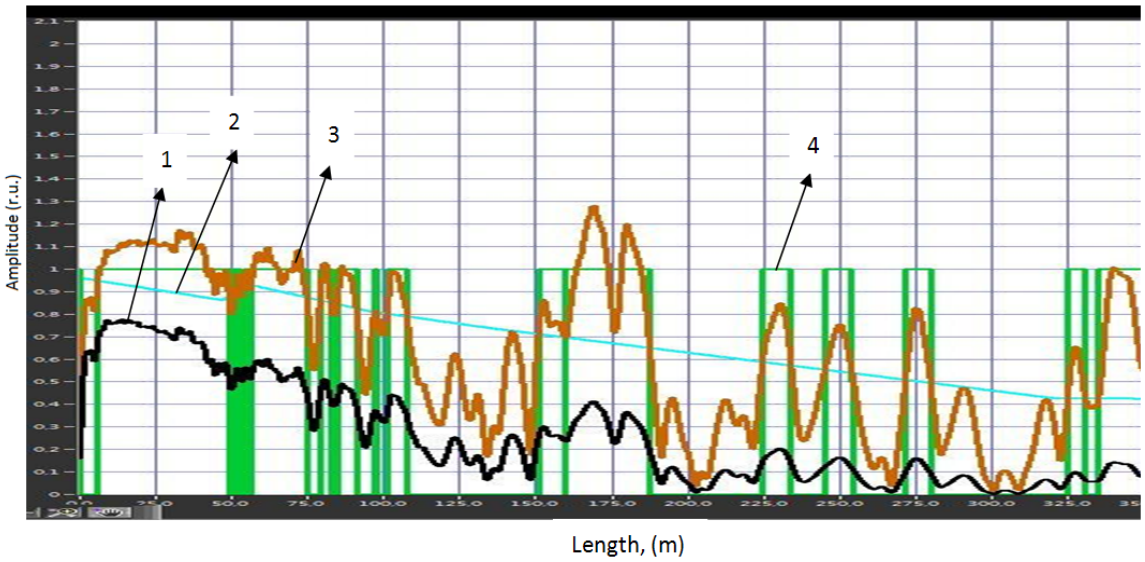

a)

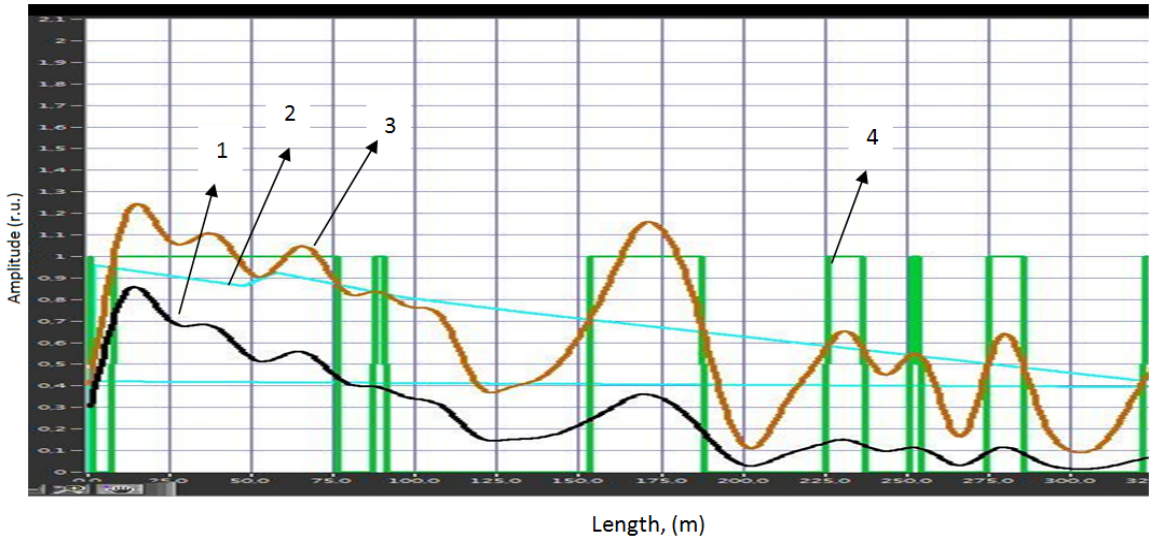

b)

Fig.1,a (top). The curve 1 is the sonic signal amplitude after the rectifier and low-pass filter versus the distance from the head of the well (length). The curve 2 is the normalized exponential approximation of the curve 1. The curve 3 is the measured curve 1 normalized by dividing point-by-point by the exponential curve. The curve 4 is the threshold curve depicted as rectangles indicating the location of defects along the well pipe detected by the other method of well logging.

Fig 1, b (bottom). The curves 1 and 3 after the procedure of calculation of moving average over given range of sampled values.

The experimental testing was performed at frequency 1 kHz for comparision at the well with the known construction and with the available results of the previous inspection by the usual sonic well logging ACC technique. The example results are presented in the figures.

5. Discussion and conclusions

The tests executed on the real oil wells shown capacity for work of the elaborated inspection system for pipe length up to 300 meters. The results of the system coincided with the results of the acoustic well logging in more than 80% of localised defects.

By our opinion, this elaborated system for vibroacoustic cementometry will be, in some cases, an alternative to the well known systems of acoustic well logging because its low price. The ACC is invasive because the inspection is carried out by equipments that are located in the inner space of oil wells filled by a liquid. The inner well equipment should be extracted before testing by the ACC technique. Therefore the ACC technique is much time more expensive than the VAC technique.

The authors recognise that much work should be done to bring the technique to perfect.

The technique has advantages that are usual inherent to all sonic echo techniques [1, 2, 3]. Here the main of them can be repeatedly listed: a) Only single-sided access is needed. b) The measurements require only short time (within 30 minutes). c) Detailed measurements can be produced with automated systems.

Sonic inspection also has its limitations, which can be here itemized: a) Surface must be accessible to transmit sound. b) Linear defects oriented parallel to the sound beam may go undetected. c) Reference standards are required for both equipment calibration and the characterization of flaws. d) Resolution is limited by half of the wave length. c) Outside sounds and noises are the serious hindrance to perform correct measurements. d) A signal-to-noise ratio exponentially decreases with the distance from transducers. This fact leads to serious problems for inspection of very long pipes.

References

[1] Schroeter J., Mehta S.K., Carter G.C. Acoustic Signal Processing: *The Electrical Engineering Handbook*. Ed. Richard C.Dorf. Boca Raton: CRC Press LLC, 2000.

[2] E. R. (Ross) Crain, P.Eng. Cement Bond Logging. Cement Integrity Logs. *Crains Perophysical Handbook.* Online Shareware Petrophysics Training and Reference Manual.

[3] http://www.ndt-ed.org/ education resources/community college/ Home – Education Resources – NDT Course Material – Ultrasound.

[4] Blizeyev A.B., Kozlov A.V., Smerkovich E.C. Acoustical diagnostics of the quality of the cement ring out of the well pipe. Russian patent 2055176, cl. IPC E 21 B 47/00. Claim 5029717 from 27.02.92, published 27.02.96. Bull. No 6.

Spectral Analysis of the Surface Topography of Cold Rolled Sheets Using Two Dimensional Fourier Transform

J. Zavadil[1,2], J. Valíček[1,3], M. Harničárová[4], M. Kušnerová[3], R. Grznárik[4]

[1]RMTVC, Faculty of Metallurgy and Materials Engineering,
[2]Department of Control Systems and Instrumentation,
Faculty of Mechanical Engineering,
[3] Institute of Physics, Faculty of Mining and Geology,
[4] Nanotechnology Centre,
VSB – Technical University of Ostrava, Ostrava – Poruba, Czech Republic
Email: jaromir.zavadil@vsb.cz

Abstract. *The paper provides an analysis of the surface topography of cold rolled sheets using the two-dimensional Fourier transform and methods based on digital image processing. Surface parameters of cold rolled sheets were measured using an optical profilometer and measured data were processed in MATLAB. The results from different samples have been compared and the influence of surface roughness on the calculated spectrum has been evaluated. The experiments which have been performed demonstrate the advantages of the use of two dimensional Fourier transform for the analysis of a surface topography of cold rolled sheets. Calculated spectral maps highlighted the periodicities which have not been apparent in the measured data.*

Keywords: Spectral Analysis, Fourier Transform, Surface Topography, Cold Rolling

1. Introduction

The Fourier transform is an important tool used for frequency analysis and signal filtering. Extension of the standard one dimensional Fourier transformation (1D FT) to the two dimensional Fourier transformation (2D FT) provided new possibilities of 2D data processing. When working with images, 2D FT is often used for image filtering. Contrary to the application in the field of image processing, this work uses 2D DFT for a frequency analysis of 2D data that represents a height roughness of a surface topography of cold rolled sheets. The surface analysis is an actual topic reflected in number of publications e.g. [1], [2], [3], [4]. Furthermore, between the years 2010 and 2012 first international standard for the analysis of 3D surface texture has been released. There have already been several publications focused on the spectral analysis of the surface topography. Most of the recently published works in this area end with displaying the calculated spectra as an image or in a 3D graph. In contrary, this work aims to find a relationship between the calculated spectrum and the surface quality to allow evaluation of surface topography using 2D DFT.

2. Measurement of the surface topography

Deep-drawn steel sheets KOHAL of the quality 697 were used for this experiment. The samples with dimensions 150 x 31 x 2.52 mm were rolled using a laboratory rolling mill Q110 (Fig. 1) which is placed at the VSB – Technical University of Ostrava. The surface topography of the samples was measured using optical profilometer MicroProf FRT (Fig. 2). This profilometer uses a principle of the chromatic aberration of the optical lenses (Fig. 1). Since this measurement is contactless, the measured surface is not affected.

Fig. 1. Q110 Laboratory Rolling Mill.

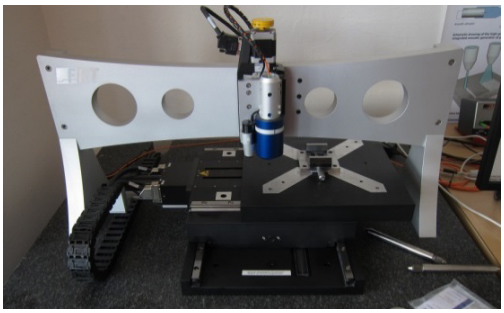

Fig. 2. MicroProf FRT.

The size of the measured surface was 5 x 5 mm and 1700 points were measured in each dimension. Data measured using this profilometer were exported and consequently processed using MATLAB. Application created in MATLAB transforms the data into a matrix consisting of height irregularities of the measured surface. These matrices are then used for spectral analysis. In the program Mark III, which is a part of the MicroProf FRT equipment, parameters *Ra*, *Rq* and *Rz* were also calculated. These parameters were compared with the results of the spectral analysis.

3. Processing of the acquired data

When performing measurements by the MicroProf profilometer, the measured head does not follow the profile of measured surface but it moves in a parallel way with the table, so the data measured can be affected by inaccurate placing of the measured sample. For this reason, it is important to calculate the mean plane. This mean plane is also suitable for reduction of the waviness of the sample after cold rolling. The Least Squares Mean Plane was used in this work. Since the samples after the cold rolling were considerably curled, the polynomial surface was used.

The n-th order polynomial surface is defined as

$$f(x,y)=\sum_{i=1}^{n}\sum_{j=1}^{i}a_{(i-j)\,j}x^{i-j}y^{i} \tag{1}$$

The sum of the surface asperity departures from this polynomial plane is

$$\varepsilon^2=\sum_{l=1}^{N}\sum_{k=1}^{M}(z(x_k,y_l)-f(x_k,y_l))^2=\sum_{l=1}^{N}\sum_{k=1}^{M}\left(z(x_k,y_l)-\sum_{i=1}^{n}\sum_{j=1}^{i}a_{(i-j)\,j}x^{i-j}y^{i}\right)^2 \tag{2}$$

Polynomial surfaces from 2. order to the 4. order were tested. The best results were achieved using the 4. order polynomial surface. From this reason and also due to adequate PC performance, the 4. order polynomial surface was used for data processing in this work. There is an example of use of the mean plane in Fig. 3.

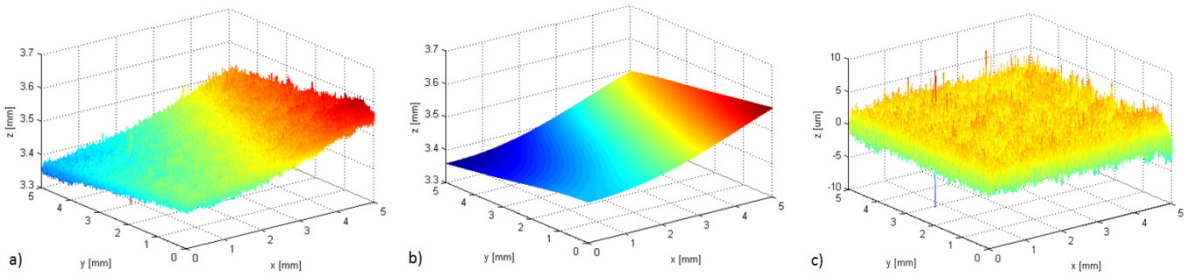

Fig. 3. An example of compensation of a surface waviness using mean plane
a) the data measured; b) 4. order polynomial mean plane; c) deviations from the mean plane

After the pre-processing of the data measured using the Least Squares Mean Plane, the frequency analysis using 2D DFT follows. The sample of data measured represented as a matrix of dimension M x N can be expressed as a function *f(x,y)* for $x = 0,1,2,...,M-1$ a $y = 0,1,2,..., N-1$. 2D DFT of this function *f(x,y)* is then

$$F(u,v) = \sum_{x=0}^{M-1}\sum_{y=0}^{N-1} f(x,y)e^{-j2\pi(u\,x/M + v\,y/N)} \tag{3}$$

for $x = 0, 1, 2, ..., M-1$ and $y = 0, 1, 2, ..., N-1$. The resulting $M \times N$ array calculated is called a frequency rectangle. The inverse 2D DFT is given by

$$f(x,y) = \frac{1}{MN}\sum_{u=0}^{M-1}\sum_{v=0}^{N-1} F(u,v)e^{j2\pi(u\,x/M + v\,y/N)} \tag{4}$$

for $u = 0, 1, 2, ..., M-1$ and $v = 0, 1, 2, ..., N-1$.

A result of the Fourier transform is complex even if *f(x,y)* is a real function. Therefore analysis of the result of the transform is based on computing the spectrum (magnitude of *F(u,v)*).

$$|F(u,v)| = \sqrt{R^2(u,v) + I^2(u,v)} \tag{5}$$

An important mathematical property of DFT is that the result of this transform is infinitely periodic. However, DFT computes only one period (array of size MxN). Fourier spectrum is symmetrical about the origin

$$|F(u,v)| = |F(-u,-v)| \tag{6}$$

4. Results

In the calculated spectra, it is possible to examine the changes in the surface topography caused by cold rolling (Fig. 4), first capture shows an image of the original surface of the sample before rolling (Fig. 4a). From the result of the Fourier transform of this data homogeneity of the surface is apparent which led to the homogeneous spectral map (Fig. 4d). In the next figure (Fig. 4b) it is possible to see a thin horizontal stripes created by rolling of the material. These periodic stripes cause stripes in the calculated spectral map (Fig. 4e). The stripes in the calculated spectral map are orthogonal to the stripes in the original image. In the spectral map periodicities in the surface topography are highlighted. Also in the Fig. 4f the change in the spectrum can be seen.

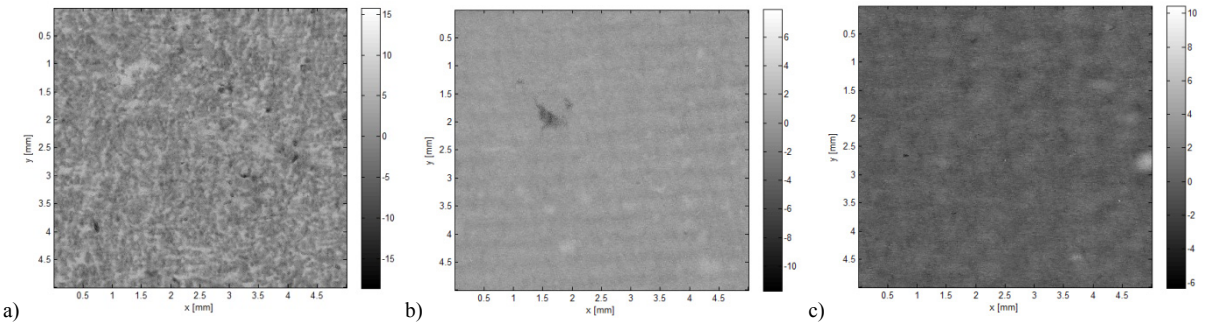

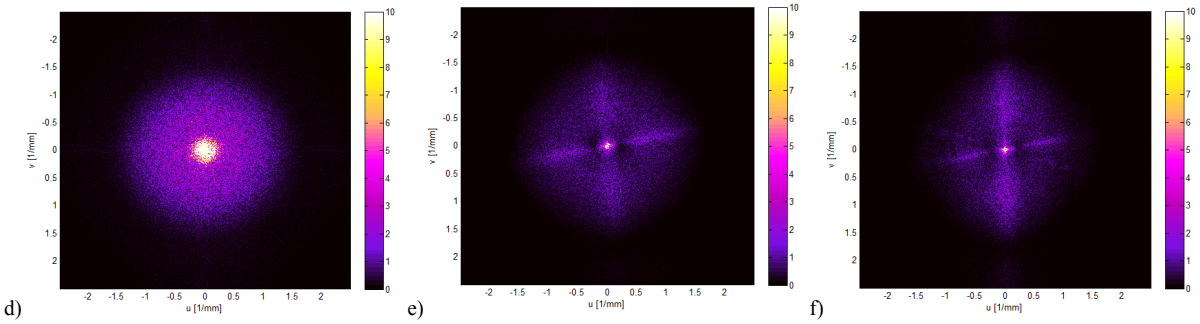

Fig. 4. An example of images of surfaces and the spectral maps calculated
a) an image of the original surface of the sample before rolling; b) the image of the surface of the sample after rolling with absolute drafting 1.2mm; c) the image of the surface of the sample after rolling with absolute drafting 1.98mm; d) the calculated spectral map of the original surface of the sample before rolling; e) the calculated spectral map of the surface of the sample after rolling with absolute drafting 1.2mm; f) the calculated spectral map of the surface of the sample after rolling with absolute drafting 1.98mm;

5. Conclusions

Experiments performed demonstrate the advantages of use of two dimensional Fourier transform for the analysis of a surface topography of cold rolled sheets. Calculated spectral maps highlighted the periodicities which were not so apparent in the measured data. Cold rolling creates marks on the surface of the material, which represent periodicities that can be effectively detected by 2D Fourier transform. Design of an algorithm for automatic evaluation of the surface quality of cold rolled sheets is the subject of the next research.

Acknowledgements

The contribution was supported by the projects RMTVC No. CZ.1.05/2.1.00/01.0040. Thanks also belong to the Moravian-Silesian Region (project RRC01569/2012).

References

[1] Valíček J, Držík M, Hryniewicz T, Harničárová M, Rokosz K, Kušnerová M, Barčová K, Bražina D. Non-contact method for surface roughness measurement after machining. *Measurement Science Review*, 12 (5): 184-188, 2012.

[2] Łukianowicz, C., Karpiński, T. Optical system for measurement of surface form and roughness. *Measurement Science Review*, 1 (1): 151-154, 2001.

[3] Kawate, E., Hain, M. New scatterometer for spatial distribution measurements of light scattering from materials. *Measurement Science Review*, 12 (2), 56-61, 2012.

[4] Senchenko, E.S., Chugui, Yu.V. Shadow inspection of 3D objects in partially coherent light. *Measurement Science Review*, 11 (4): 104-107, 2011.

Analysis of Surface Roughness Parameters in Aluminium Fine Turning with Diamond Tool

R. Horváth, Á. Drégelyi-Kiss

Bánki Donát Faculty of Mechanical and Safety Engineering, Óbuda University
Népszínház u. 8, H-1081 Budapest, Hungary
Email: horvath.richard@bgk.uni-obuda.hu

Abstract. *Machining of aluminium parts has become particularly important in recent years. Aluminium alloys are increasingly used in automotive, aerospace and defence industries due to the advantageous mechanical and chemical properties. In technology planning, the average surface roughness is as important criterion as geometrical size or tolerance. In this paper, machinability of an AlMgSi alloy with a diamond tool is examined by design of experiments. An empirical relation is established between the surface roughness and the cutting parameters.*

Keywords: Fine Turning, Surface Roughness Measurement, Design of Experiments, RSM Method

1. Introduction

Surface roughness measurements are essential in characterization of the features of a machined surface. To examine the effect of cutting parameters on surface roughness thoroughly, a huge number of experiments are needed, depending on the number of parameters. By utilizing the method of design of experiments (DoE), the number of experiments can be reduced in such a way that the effect of parameters could be assessed appropriately. If linear effects of cutting parameters are considered, then fractional factorial design is sufficient, but to examine the quadratic term, RSM method has to be utilized [1].

DoEs are often employed in cutting research. Aouchi et al. [2] and M. Y. Noordin et al.[3] examined hard turning with a CBN and hard metal tool and the resulting surface with the help of DoE. Asiltürk et al. [4] examined stainless steel turning with coated hard metal tools. Dry, wet, and MQL turning was examined with the help of DoE by Young Kug Hwang [5]. M. Harničárová et al. studied the topography of laser-cut surfaces [6]. Lazarevic, D. et al. examined the surface roughness of engineering polymers by using Taguchi method [7].

In this study, cutting parameters and surface roughness parameters were correlated to determine the relationship between them in case of aluminium fine turning. Our goal was to create a mathematical model that can be easily used in technology planning to estimate the expected values of surface roughness. In this paper, the dependence of the *Ra* parameter on cutting parameters will be described.

2. Subject and Methods

Workpiece and tool materials

Turning experiments were performed in dry conditions using CNC lathe type NCT EUROTURN 12B, with 7 kW spindle power and 6000 1/min rotation speed. The workpiece material was AS17, frequently used in automotive, aerospace and defence industries. The chemical composition (in wt.%) is: Al = 74.35 %; Si = 20.03 %; Cu = 4.57 %; Fe = 1.06%. The hardness of the workpiece was 114 $HB_{2,5/62,5/30}$. The examined part was a cylinder with a diameter of 110 mm. The experimental runs were made every 10 mm.

The standard designation of the used tool was DCGW 11T304 FN (CVD-D) and it was manufactured by TiroTool. The holder of the tool was codified as SDJCR 1616H 11. The average surface roughness value (*Ra*) was measured by a Mitutoyo SJ-301 surface roughness tester. Parameters related to surface roughness measurement were: $l=4$ mm, $\lambda_c=0.8$, $N=5$. The measurements were repeated three times at three reference lines equally positioned at 120° and the result was the average of these values.

Experimental design

Response surface methodology (RSM) is a procedure which is able to determine a relationship between independent input process parameters (e.g. cutting parameters) and output data (process response, e.g. *Ra*). In the current study, the relationship between the input parameters, as the cutting conditions (cutting speed (v_c, m/min), feed rate (f, mm), depth of cut (a, mm), and the output parameters, defined as the machinability aspect (*Ra*) which is given as:

$$Ra = \Omega(v_c, f, a) \tag{1}$$

where Ω is the response function.

The approximation of *Ra* is proposed by using the following equation which consist of linear and quadratic effects of the input parameters and their interactions as well:

$$Ra = b_0 + b_1 \cdot v_c + b_2 \cdot f + b_3 \cdot a + b_{11} \cdot v_c^2 + b_{22} \cdot f^2 + b_{33} \cdot a^2 + b_{12} \cdot v_c \cdot f + b_{13} \cdot v_c \cdot a + b_{23} \cdot f \cdot a + \varepsilon \tag{2}$$

where $b_i s$ are the calculated coefficients, v_c, f and a are input parameters, and ε is the experimental error.

In the course of design of experiments, a response surface method was chosen, the central composite design (CCD) method. CCD was set up for three controllable factors: cutting speed (v_c), feed rate (f) and depth of cut (a). Each factor had 5 different levels. The number of experimental runs was 16, in which two trials were examined in the centre of the design.

The limits of the studied cutting parameters are set so that they meet the values used by industries currently and so that they should meet the requirement of high speed cutting (HSC) applications as well. Taking these into consideration the chosen limits of cutting parameters are summarized in Table 1.

Table 1. The limits of used cutting parameters.

v_{cmin} =500 m/min	v_{cmax} = 2000 m/min
f_{min}= 0.05 mm	f_{max} = 0.12 mm
a_{min} = 0.2 mm	a_{max}= 0.8 mm

3. Results

Values of input parameters and the response factor, as a surface roughness component are shown in Table 2. Surface roughness was obtained in the range of 0.47 and 1.77 μm. The calculated standard deviation of *Ra* related to measurement error and inhomogeneity of the surface of the examined part was 0.126 μm.

Table 2. Input parameters of experimental runs and the measured surface roughness values.

	Machining parameters			Response factor			
Runs	v_c, m/min	f, mm	a, mm	Ra_1, µm	Ra_2, µm	Ra_3, µm	$Ra_{average}$, µm
1	667	0.058	0.267	0.47	0.48	0.48	0.477
2	667	0.058	0.733	0.62	0.51	0.35	0.493
3	667	0.112	0.267	1.06	1	1.03	1.030
4	667	0.112	0.733	1.55	1.44	1.54	1.510
5	1833	0.058	0.267	0.41	0.51	0.6	0.507
6	1833	0.058	0.733	0.7	0.58	0.67	0.650
7	1833	0.112	0.267	0.96	1.01	1	0.990
8	1833	0.112	0.733	1.34	1.23	1.31	1.293
9	500	0.085	0.5	0.98	1.05	1.1	1.043
10	2000	0.085	0.5	0.8	1.01	1.03	0.947
11	1250	0.05	0.5	0.55	0.48	0.49	0.507
12	1250	0.12	0.5	1.72	1.75	1.85	1.773
13	1250	0.085	0.2	0.82	0.82	0.91	0.850
14	1250	0.085	0.8	0.84	0.85	0.85	0.847
15 (C)	1250	0.085	0.5	0.76	0.9	0.86	0.840
16 (C)	1250	0.085	0.5	0.83	0.83	0.85	0.837

4. Statistical analysis

Statistical analysis was employed to determine the relation between the individual measured values of surface roughness and the cutting parameters. Results of variance analysis are shown in Table 3. In the second column, the calculated coefficient (b_is) of Eq (2) are shown. It is obvious, that several factors have a large impact on the measurement results like f^2, a^2, $v_c{\cdot}f$, and $f{\cdot}a$. The estimated model describes well the measurement points since the value of R^2 is near 90%.

Table 3. Analysis of variance of the measuring points

Term	Coef	SECoef	T	P
Constant	-0.067	0.4537	-0.147	0.884
Vc [m/perc]	0.000	0.0003	1.311	0.198
f [mm]	-5.007	8.0181	-0.624	0.536
a [mm]	1.223	0.7374	1.659	0.105
Vc [m/perc]*Vc [m/perc]	-0.000	0.0000	-0.398	0.693
f [mm]*f [mm]	102.111	43.5245	2.346	0.024
a [mm]*a [mm]	-1.862	0.5890	-3.162	0.003
Vc [m/perc]*f [mm]	-0.004	0.0017	-2.091	0.043
Vc [m/perc]*a [mm]	-0.000	0.0002	-0.236	0.815
f [mm]*a [mm]	12.385	4.2124	2.940	0.006

S = 0.129823 PRESS = 1.00648
R-Sq = 89.90% R-Sq(pred) = 84.13% R-Sq(adj) = 87.51%

The model can be simplified by only considering effects of the significant parameters. By keeping the main factors (v_c, f, a), the equation can be reduced by avoiding other non-significant parameters. This leads to the equation of the reduced model:

$$Ra_{predicted} = 0.01236 + 0.0002698 \cdot v_c - 5.023 \cdot f + 1.166 \cdot a + \\ + 102.206 \cdot f^2 - 1.862 \cdot a^2 - 0.003521 \cdot v_c \cdot f + 12.385 \cdot f \cdot a \quad (3)$$

The goodness of correlation is of the reduced model is R^2=89.84%. Residual analysis shows that the residuals are normally distributed and random, therefore the estimated model is adequate. The reduced model equation is plotted in Fig. 1. Dependence of Ra on cutting speed is quite small, but the feed rate has a great impact on the resulting roughness. With this method, a simple relationship can be established between the surface roughness and the cutting parameters within the examined parameter range, which is beneficial in planning of fine turning processes.

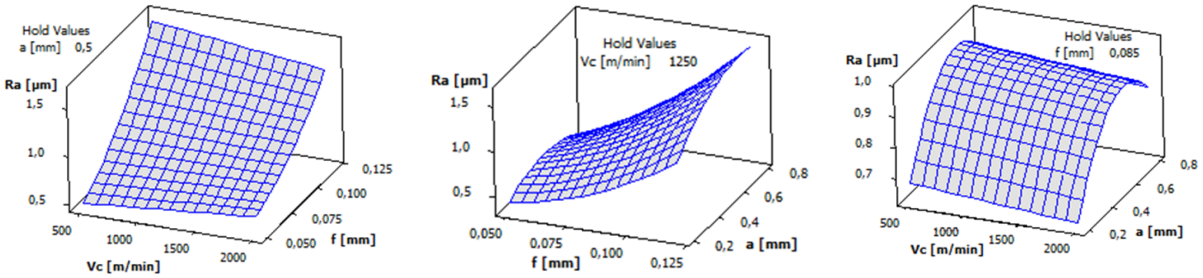

Fig. 1. Representation of built-up model plotted against cutting parameters.

5. Conclusions

In this paper, the influence of cutting parameters (v_c,f, a) were examined in case of fine turning of a cylinder of AS17 alloy with a CVD-D tool. A reduced empirical equation was built up to describe the examined function. In case of technology planning the equation obtained is suitable for estimating the required average surface roughness easily, and for specifying the ranges of optimal cutting parameters. To compare the estimated values with the measured values, it can be stated that a good agreement has been achieved. Additionally, this study shows which factors (cutting parameters) have a significant effect on average surface roughness. Further examinations of the other surface roughness parameters as well as those of different tool materials and geometries are needed to examine their machinability.

Acknowledgements

The project was realised through the assistance of the European Union, with the co-financing of the European Social Fund, TÁMOP-4.2.1.B-11/2/KMR-2011-0001 Research on Critical Infrastructure Protection.

References

[1] Drégelyi-Kiss Á, Horváth R, Mikó B.: Design of experiments (DOE) in investigation of cutting technologies; Development in Machining Technology/Scientific-Research Reports vol.3 (book chapter, in press).

[2] Hamadi Aouici, Mohamed Athmane Yallese, Kamel Chaoui, Tarek Mabrouki, Jean-François Rigal: Analysis of surface roughness and cutting force components in hard turning with CBN tool: Prediction model and cutting conditions optimization, *Measurement* 45 (2012) p. 344-353.

[3] M. Y. Noordin & D. Kurniawan & Y. C. Tang & K. Muniswaran: Feasibility of mild hard turning of stainless steel using coated carbide tool, *Int J Adv Manuf Technol* (2012) 60:853–863.

[4] Ilhan Asiltürk, Süleyman Neseli: Multi response optimisation of CNC turning parameters via Taguchi method-based response surface analysis, *Measurement* 45 (2012) 785–794.

[5] Young Kug Hwang and Choon Man Lee: Surface roughness and cutting force prediction in MQL and wet turning process of AISI 1045 using design of experiments, *Journal of Mechanical Science and Technology* 24 (8) (2010) 1669-1677.

[6] M. Harničárová, J. Valíček, M. Kušnerová, R. Grznárik, J. Petrů, L. Čepová: A New Method for the Prediction of Laser Cut SurfaceTopography, *Measurement Science Review*, Volume 12, No. 5, 2012, (p. 195.-204.).

[7] Lazarević, D., Madić, M., Janković, P. , Lazarević, A.: Surface roughness minimization of polyamide pa-6 turning by Taguchi method, *Journal of Production Engineering*, 2011.

Balanced Devices of Strain Measurements with Current Excitation

R. Masiulionis, R. Kvedaras, V. Kvedaras

Electronics faculty of Vilnius Gediminas Technical University, Vilnius, Lithuania,
Email: vygaudas.kvedaras@vgtu.lt

Abstract. *The paper analyzes the proposed three circuits of strain measurement devices using high-output-current DACs. Operating principles and capabilities of these devices are analyzed. It has been shown that the proposed designs have an advantage of being relatively simple and flexible while ensuring high linearity and wide strain measurement range.*

Keywords: Strain Measurements, Small Resistance Change Measurement, Current Excitation, High-Output-Current DACs.

1. Introduction

The strain measurements are applied to the newly designed structures and constructions for carrying out tests in order to determine durability and resistance to applied forces, identify weaknesses, and to provide means for improvement or strengthening of these constructions. It is also important to monitor different statuses of the existing buildings. In this case it can be seen that in some time deformations reaches some critical values and gives possibility to predict construction accident, and to take appropriate actions to prevent it. Such strain measurements should be applied to number of specific points of the construction while these points can be distant one from another while measurement results should acquired to central data analysis and storage centers by using wired or wireless measurement equipment [1, 2]. In this case measurement equipment should be organized in a way that there is number of measuring units that are situated in variuos places of the construction and acquiring strain measurements and after that sending the measurement information to the data analysis center. Therefore it is necessary to design simple and relatively cheap strain measurement units that are capable to operate under various external conditions. Strain gauges with balanced [1] and not balanced Wheatstone bridges [3] are widely used for this purpose. It is proposed to use bridge circuits with current excitation [4] as these have better resistance to external noise and automated balancing circuits with current balancing [5].

Integrated circuits of DACs with current output are quite common in the market nowadays (e.g. MAX5548, MAX5550, AD5510, AD8810 and many others). These DACs are 10 to 16 bits resolution with capability to generate output currents of 20–30 mA. For some of these DACs output currents can be set by software and several DACs (up to 8) can be situated in one IC. New balancing strain measurement devices designed using DACs with current output are presented and analysed in this paper.

2. New circuits of balancing strain measurement devices

A new structural design for monitoring strains of constructions using two current DACs (Fig. 1) is proposed. Two analogous current DACs are formed in one microchip MAX5550, using the same reference voltage, which allows to reduce environmental conditions on the monitoring results, as temperature changes almost equally affects both DACs' output currents and drift. This IC is designed to be used in balancing circuits in wide temperature range. The DACs' current ranges are determined before monitoring by the control code and it can be flexibly chosen for observable construction. Values of the output currents are also set by control code to any of 12 different sub-ranges starting from 1 up to 30 mA. Therefore it is possible to set the most suitable strain gauge excitation currents according to gauge specifications. Output currents of these DACs can differ one from another up to ± 2 %. Such

difference of the currents can be eliminated together with resistance differences of strain gauges and connecting wires and disbalance of measurement amplifier by applying two strain measurements for construction without load (initial value) and measurement of the strain of construction with load applied. The strain measured is the difference between these two measurements. For the initial measurement (measurement with no load applied to the construction) microcontroller DD1 (e.g. MAXQ2000) control signals switches on MOSFET transistors VT*i*1, VT*i*2. Transistors are opened and connect pair of strain gauges R_{ji1}, R_{ji2} to the outputs A and B of the current DAC. MOSFET transistors used should have a resistance of the open channel less than 0.1 Ω and does not influence strain measurement results. Strain gauges are connected to the equipment using twisted-pair 4 wire cable. Results of the experimental investigations have shown that using cable of 10 meters length measurement results are not influenced by 50 Hz mains noises and disturbances. Therefore it is possible to connect from 16 to 32 strain gauges that are located in ± 10 m range from the measuring equipment. Differences of the component values of the measuring circuit shall result in disbalance of the circuit and input voltages of DA1 shall be different. Measuring process is started. Microcontroller DD1 generates changing control code to the B DAC and therefore output current of B DAC is changing. DD1 is reading output signal of the DA1 (logic 0 or 1) and changes control code of B DAC accordingly until the circuit is very near to the balance condition. The resulting control code is stored and sent to system database if needed. All other pairs of strain gauges are measured in the same way and measurement results are stored. Construction is exposed to the load after that and measurements with balancing circuit are repeated for the desired pairs of strain gauges. Result of the strain measurement is the difference between two measurement codes – code obtained in the initial stage with no load applied to the construction and the code obtained by measuring construction under load.
The expression of dependence of code on the gauge resistance change is determined in [5]:

$$m_{\mathrm{m}} = \frac{2^n I_1}{I_{\max}} \delta R_{\mathrm{j1a}}, \qquad (1)$$

where

$$\delta R_{\mathrm{j1a}} = \Delta R_{\mathrm{j1a}} / R_{\mathrm{j2}}$$

relative changes of the active strain gauge resistance of the loaded and the nominal resistance value of the gauge.

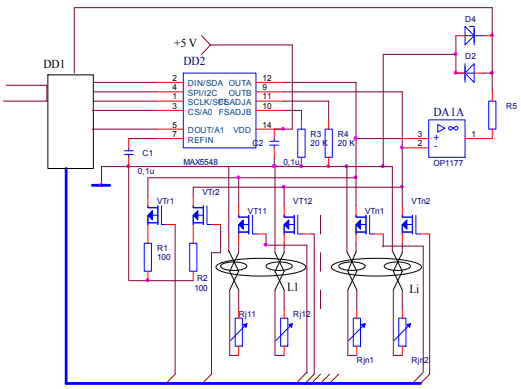

Fig. 1. Strain monitoring device using two current digital-to-analog converters.

Obtained equation indicates that the DAC control code is directly proportional to the gauge resistance change. However, the integrated current DAC (for example MAX5550) has 10 bits. In this case the full range of the strain measurement shall be

$$m_d = 2^n d$$

where

n number of DAC bits
d range of strain.

In case OUTB current is set to the value of the most significant bit, then for the steel constructions ($d = \pm 0.3$) $m_{\mathrm{d}} = 353$, concrete constructions ($d = \pm 0.06$) – $m_{\mathrm{d}} = 61$. Device resolution meets the requirements for monitoring equipment and does not meet the requirements for laboratory equipment. It is necessary to mention that in case of monitoring applications only one or several compensating strain gauges are used. In this case construction of the equipment is simpler and number of measurement points can be increased.

In order to avoid influences of external conditions to the measurement circuit high accuracy and thermally stable resistors $R1$ and $R2$ can be used in monitoring equipment that operates for long periods of time and in different temperature conditions for calibration.
In this case after some predefined time of operation VTr1 and VTr2 connects precision resistors $R1$ and $R2$ to the measurement circuit and performs balancing of the circuit. Code obtained is compared to the stored values and differences are calculated. These differences are subtracted from the measurement results to eliminate external influences.

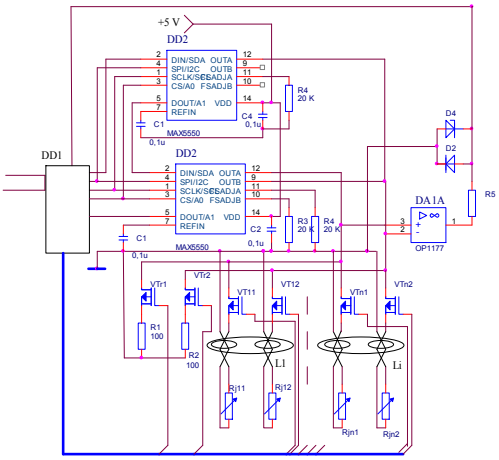

Fig. 2. Strain monitoring device using three current digital-to-analog converters.

In order to increase the resolution, structure of device with three current DACs (two MAX5550 chips) has been proposed (Fig. 2). The current of the device's second DAC output is equal to $I_B = I_A - I_d$, where I_d – the maximum readjusting current. Third current DAC (DD3) of the same type is designed to balance the current and the current output of this DAC is connected in parallel with the second DAC output. In this case, the first two DACs are constant current sources, and the third is determined by balancing the currents so that the initial and strain measurement codes is determined by the strain size and does not affect the strain measurement.

Range of the strain measurement and resolution can be changed by changing output current of A and C DACs. For instance in case concrete construction is under investigation (range $d \leq 0.06$), excitation current of DAC B is set to $I_B = 5$ mA, excitation current of DAC A is set to $I_A = 4.7$ mA and maximum output current of DAC C is set to $I_A = 1$ mA. All 10 bits of the DAC C bits are used for measurement and this setup is corresponding to the requirements of the laboratory equipment. In case steel constructions are measured with the measurement range ($d \leq 0.3$), current of DAC B is set to $I_B = 5$ mA, excitation current of DAC A is set to $I_A = 3.5$ mA and maximum output current of DAC C is set to $I_A = 3$ mA. All 10 bits of the DAC C bits are used for measurement and this setup is corresponding to the requirements of the laboratory equipment.

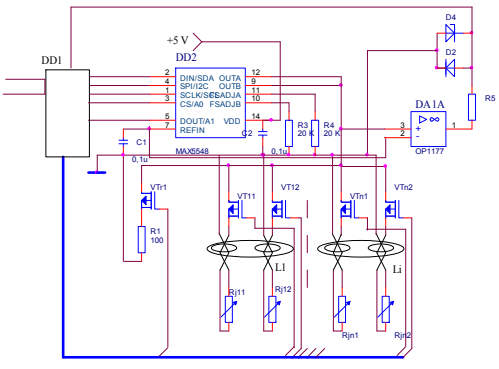

Fig. 3. Strain monitoring device using two current DAC with increased resolution.

New balancing circuit implementing two current DACs has been proposed (Fig. 3). Initial excitation current to strain gauges is generated by DAC A. Balancing of the circuit is made by the sum of the currents of DAC A and DAC B connected in parallel. Range of DAC B is set the same way as in circuit with 3 DACs. But the current is balanced in respect of constant U_a. Value of it be proportional to voltage drop on the strain gauges $U_0 \approx I_{Am} R_{jv}$ (where I_{Am} – named current value for the strain gauges, R_{jv} – named resistance value of the strain gauge).
The proposed structure is fairly universal: according to tested construction material it determines allowable excitation current for this material or gauges and it allows to eliminate the monitoring deviations caused by monitored construction properties or temperature increase of the gauge on the gauge resistance variation, it allows flexibility (software setting) to change the measurement range and resolution; it allows identification of large strains with high resolution.

Simulation using MultiSim 11 modeling software and physical model has been developed and investigated. Performing simulation of change of the strain gauge resistance R_{j11} and balancing circuit afterwards it has been found that the dependence of digital-to-analog converter control code in the decimal counting system and the change of balancing current are directly proportional to the change of the resistance of the strain gauge. Range of the measured strain (and resistance change of the strain gauge) is ± 30 %. Resistance differences of the connecting cables, open channels of MOSFET switches and gauges itself has been simulated by setting different resistance values of the compensating gauge R_{j12}. It has been found that by performing two measurements (measurement without strain applied and with strain applied) abovementioned resistance differences are eliminated from the measurement result.

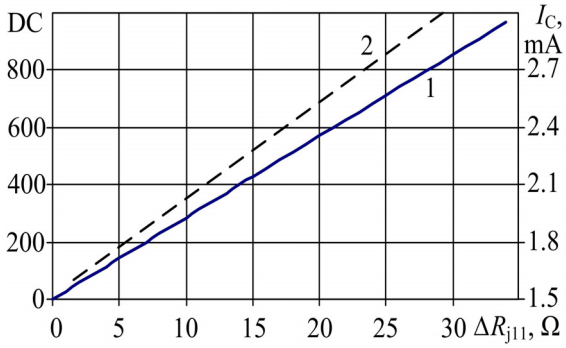

Fig.4. Dependence of control decimal code (DC) (1) and current I_C (2) on gauge resistance changes.

3. Conclusions

1. A newly designed circuit for strain measurement implementing two DACs situated in single IC and having single excitation supply is proposed. Design ensures that instabilities of two DACs are nearly identical. Resolution of the circuit and relatively simple design ensures the possibility to implement this circuit in strain monitoring applications. Strain measurement result (measurement code obtained by balancing the circuit) is directly proportional to the change of the strain gauge resistance. Differences of the DAC output current is compensated and do not influence measurement results.

2. New design of strain measurement device with three current DACs has been proposed. Third DAC is used for balancing the circuit. In this implementation it is possible to select required excitation current for the selected type of strain gauges and the material of the construction under investigation. Design allows elimination of the measurement errors caused by heating of the gauge or the construction. New design of strain measurement device implementing two current DACs connected in parallel has been proposed. The device has and advantage of simpler construction while ensuring extended resolution for laboratory type measurements. The latter two designs allows flexible (software based) change of measurement range and resolution and therefore ensures measurement of high values of strain with high resolution by setting output current of B DAC.

3. Results of computer modeling and experimental investigations have shown that the dependence of control code and balancing current on sensor resistance is linear. Device is capable of measuring strains that changes resistance of the strain gauge up to ± 30 %.

References

[1] Kvedaras V, Kvedaras R, Masiulionis R. Methods of strain measurements in construction monitoring systems. *The 25th International Symposium on Automation and Robotics in Construction (ISARC 2008)*. Vilnius, Technika, 343-349, 2008.

[2] Harms T, Sedfigh S, Bastianini F. Structural Health Monitoring of Bridges Using Wireless Sensor Networks. *IEEE Instrumentation and Measurements Magazine,* Vol. 13, No 6, 14-18, 2010.

[3] Dual, 10-Bit, Programmable, 30mA High-Output-Current DAC. Interactive http://www.maximintegrated.com/datasheet/index.mvp/id/4811.

[4] 2, Makal J, Warsza Z.L. Application of Double Current Bridge-Circuit for Simultaneous Measurements of Strain and Temperature *IEEE Instrumentation, Measurement and Technology Conference, (IMTC 2007)*. – Warsaw, Poland, May 2007. – P. 1-4.

[5] Masiulionis R, Kvedaras V, Kvedaras R. Analysis of balancing methods of measurement of small resistance changes. *Elektronika ir elektrotechnika*. 8(114), 3-6, 2011.

Isotropic Electromagnetic Sensor Measurement Error

R. Hartansky, V. Smiesko, L. Marsalka

Slovak University of Technology in Bratislava
Faculty of Electrical Engineering and Information Technology,
Institute of Electrical Engineering, Bratislava, Slovakia
Email: rene.hartansky@stuba.sk

Abstract. *This article deals with classifying and quantifying of electromagnetic field measurement errors when an isotropic sensor is used as a field probe. The focus is mainly given to the error of the measurement method resulting from the mutual interaction of the field probe sensors associated with the origin of the so-called mutual impedance.*

Keywords: Electromagnetic Field, Sensors, Measurement Error

Introduction

In many areas of electrical engineering it is required to measure the amplitude of electromagnetic field with sufficient accuracy (e.g. during electromagnetic compatibility testing of electrical devices). The measurement is in many cases performed in a far field. Then it is sufficient to measure only one component of the electromagnetic field while the other can be easily estimated. Despite this simplification, the measured component of the electromagnetic field is a vector. This means that we need to know all the vector components (x, y, z) which determine its final amplitude. To determine the mentioned components of the vector, an omnidirectional probe of the electromagnetic field must be used. In general, such a probe is made of three orthogonal sensors and the output voltage of the sensors is determined as follows:

$$U_E = \sqrt{U_x^{\,2} + U_y^{\,2} + U_z^{\,2}} \tag{1}$$

In order to ensure sufficient accuracy, the sensors have to meet a series of conditions: frequency independence [1]; sufficient output voltage [1]; sensitivity to only one component of the electric field vector [1], [2]; linearity [2], [3]; no (or negligible) interaction with surrounding objects. In the scientific literature, attention is given to the first four conditions; however the *fifth condition is not solved*. Therefore this article deals with the mutual interaction of sensors, and their effects on the error of the electromagnetic field measurement.

Mutual Impedance

If a conductive object is situated in an electromagnetic (EM) field, there is an interaction between the field and the object. This interaction is reflected by changed distribution of the EM field's geometry and origin of electric current or electromotive voltage in the conductive object. If there are other objects in the EM field, also other interactions are created; not only the interaction between the field and the object but also an interaction between the objects. This interaction is known as mutual impedance in the antenna theory, and is reflected by a change of the voltage and the current conditions in the field of the objects, similar to the theory of linear circuits. The mutual impedance may be calculated by several methods. All the methods are based on the interaction between the incident and the radiated EM fields of the studied objects (for example: two wires with lengths 2h). According to Balanis [3] the mutual impedance may be expressed as:

$$Z_{21} = -\frac{1}{I_{1i} I_{2i}} \int_{-h}^{h} I_2(z') E_{z21}(z')\, dz' \tag{2}$$

where $I_2(z)$ is the current distribution in wire 2, Ez_{21} is E-field component radiated by wire 1, which is parallel to wire 2; I_{1i}, I_{2i} are wire input currents. As mentioned above, the mutual impedance affects the induced voltage at the inputs of wire 1 and wire 2 as follows:

$$U_1 = U_{11} + Z_{21} I_2 \tag{3}$$

where U_1 is the driving point voltage of wire 1 when wire 2 is present. U_{11} is the driving point voltage of wire 1 without wire 2.

Let's return to the EM field probe which consists of three sensors. If one of the sensors captures only x-axis component of the field, its output voltage will be:

$$U_x = k_x E_x \tag{4}$$

If the two sensors for *x*-axis and *y*-axis component of the field are situated close to each other, then their output voltage will be:

$$\begin{aligned} U_{x1} &= U_x + Z_{xy} I_y \\ U_{y1} &= U_y + Z_{yx} I_x \end{aligned} \tag{5}$$

One can see that the sensors interact mutually which results in a change of the output voltage. This influence brings a systematic error to the measurement of the EM field which can be expressed [2], e.g. for x-axis sensor, in the presence of the other sensor as a percentage:

$$\delta_{U_x} = \frac{Z_{xy} I_y}{U_x}.100\% \tag{6}$$

and in the presence of the two other sensors:

$$\delta_{U_x} = \frac{Z_{xy} I_y + Z_{xz} I_z}{U_x}.100\% \tag{7}$$

Numerical calculation

Mutual impedance of the electromagnetic field sensors and its impact on the induced voltage at the sensors' terminals may be calculated analytically or numerically. However, analytical calculation is very complex and it exceeds the scope of this work. Therefore, we will rather pay attention to the numerical calculation which may be used to calculate the mutual impedance between the sensors as well as the induced voltage at their terminals.

The numerical calculation was carried out using FEKO EM field solver. First, we placed one sensor into an EM field generated by a planar wave. Our sensor is a dipole oriented to be parallel to the electric field vector – E. Next, we changed the dipole's orientation to be perpendicular to the vector E, as shown in Fig. 1. The intensity of E-field was 1 V/m.

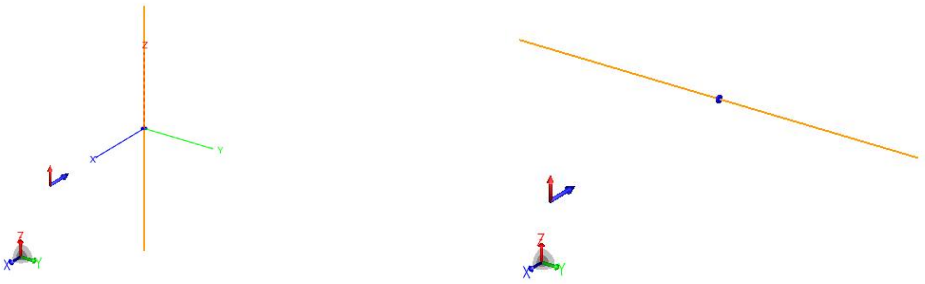

a) b)

Fig. 1. Impact of EM wave on a) tangentially oriented sensor b) normally oriented sensor.

In both cases the dipoles were loaded by impedance of 75 Ω. In the case a) current of 1.35mA flows via the mentioned impedance and in the case b) the current has zero value. The absolute value of the input impedance of the dipole a) was 70.438 Ω. In the next, the model will consist of two sensors located very close to each other, as shown in Fig. 2.

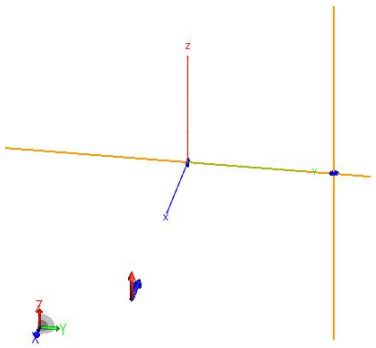

Fig. 2. Arrangement of two sensors in EM field.

It is obvious from Fig. 2 that one sensor (dipole) is located tangentially and the other normally to the electric vector component of the incident electromagnetic field.

Results

Based on the simulation models (Fig. 1 and Fig. 2.) we performed the calculation of input

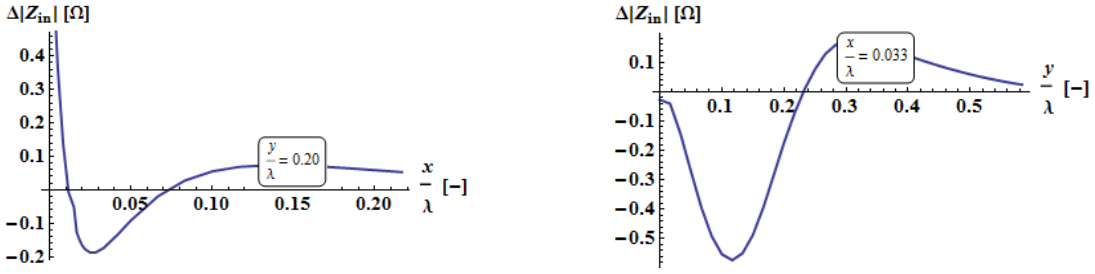

a) b)

Fig. 3. Dependence of input impedance variation of z-sensor on relative position of the sensors a) shift in x-direction b) shift in y-direction.

impedance of the sensor positioned on the *z*-axis which depends on the position of the sensor situated on the *y*-axis. Fig. 3 shows only the change of the input impedance of the *z*-dipole.

One can see that the input impedance variation of the examined dipole will be zero if the second dipole is placed at a considerable distance from the examined dipole. Similar effect may be reached by locating the second dipole near the center or at the end of the examined dipole. The design of the EM field probe has to be based on Fig. 3 to minimize the interactions between the dipoles (sensors).

Next, we focused on the calculation of the induced current in the y-dipole which is oriented normally to the vector of the incident electric field (see Fig. 4). Unlike the previous case, the induced current takes a zero value only if the examined dipoles are sufficiently far apart.

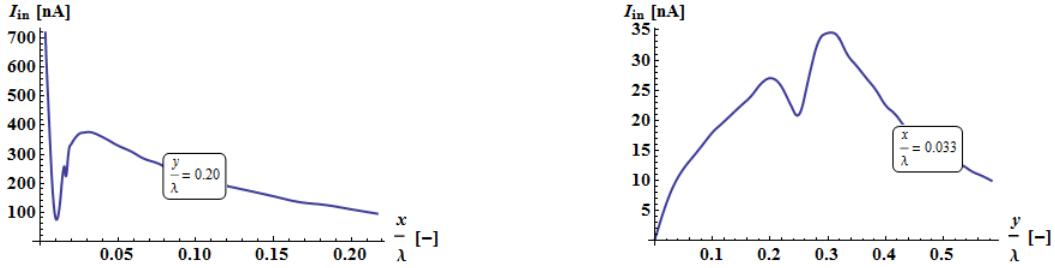

a) b)

Fig. 4. Induced current of y-sensor depending on relative position of the sensors a) shift in x-direction b) shift in y-direction.

To quantify the effect of mutual impedance on the accuracy of the EM field measurement, we have to rely on Fig. 3 and Fig. 4, and the modified equation (1). Dependence of the relative error (caused by the existence of the mutual impedance) on variation at x and y axes has the same shape as is shown in Fig. 3. In this case the y-axis value will reach values in the range from -0.2% to 0.6% in a) and from -0.8% to 0.2% in b).

Conclusions

In the case of EM field measurement with multiple sensors which are situated close to each other, there is mutual impedance between the sensors which may affect the measured results by up to 1% error, depending on relative positions of the sensors.

Acknowledgements

This work was supported by the project VEGA 1/0963/12 and by the project VEGA 2/0048/13.

References

[1] Hajach, P. – Harťanský, R. Solution of Resistive Loaded Dipoles by Hallen Method and by Moment Method. In *10 th International Scientific Conference Radioelektronika 2000*, Bratislava: FEI STU, September 2000, ISBN 80-227-1389-9, s. IV62–IV94.

[2] Harťanský, R. – Bittera, M. Assurance of non-directive pattern of electromagnetic field sensor. In *Mechatronika 2001 - 4th International Symposium Mechatronics*, Trenčianske Teplice: TnUAD, Jún 2001, ISBN 80-88914-36-1, s. 164–168.

[3] Balanis, A. C. *Antenna Theory Analysis and Design 2nd edition*. New York: John Wiley & Sons, 1982, 1997.

Proposal of Novel Sensor Applicable to Contactless Displacement Measurement

L. Marsalka, R. Hartansky

Slovak University of Technology, Faculty of Electrical Engineering and Information Technology, Institute of Electrical Engineering, Bratislava, Slovakia
Email: lukas.marsalka@stuba.sk

Abstract. *The paper deals with sensor design, which is applicable for contactless displacement measurement. Sensing principle is based on change of electromagnetic field properties. They are changed during resonance of electrical part of the sensor. In this paper there is in detail described the sensor construction. The sensor consists of the mechanical part – load cell and electrical part – parallel resonance circuit, which is implemented on load cell body. Structure of the load cell is proposed so that the value of resonance frequency is dependent on size of sensing displacement. The change of electromagnetic field properties is in turn visible in behaviour of easily measurable input parameters of the electromagnetic field radiator.*

Keywords: Electromagnetic Field, Mutual Impedance, Parallel Resonance Circuit, Load Cell

1. Introduction

Nowadays it is more popular the design of sensors applicable to micro and nano-technologies, where the mechanical parts of structures are in micrometer or nanometer dimensions. These structures are usually named MEMS. For realization of ultra-high precision systems in deep sub-micron or nano-scales one of important sensors is displacement sensor. Different methods for realization of high precision displacement sensor have been used. In this area, optical methods, ultrasound methods, methods using piezoelectric materials and new opto-mechatronics method opens new insight to sensor design.

In this paper we introduce new sensor applicable for contactless displacement sensing. The working principle of this sensor is based on measuring method making use of electromagnetic energy. This method is applicable for signal transmission and for the measurement of displacement. The advantages of this method are high sensitivity and usability in harsh environment such as ultra-high vacuum systems [1].

2. Mutual impedance between wire structure

Let us consider an electromagnetic field, which is generated by a wire structure, specifically by half-wave dipole 1. Put another dipole 2 into the vicinity of the dipole 1, as it is shown in Fig. 1. We must take into account the mutual effects between dipole 1 and dipole 2. This interaction causes the mutual impedance creation between dipole 1 and dipole 2:

$$Z_{21i} = -\frac{1}{I_{1i}I_{2i}}\int_{-h'}^{h'} E_{z21}(z')I_2(z')dz' \tag{1}$$

where

I_{1i}, I_{2i} – input current of dipole 1 and dipole 2, respectively
$E_{z21}(z')$ – component of E-field radiated by dipole 1, which is parallel to dipole 2
$I_2(z')$ – current distribution along dipole 2

Equation (1) describes the electromagnetic (EM) field $E_{z21}(z')$, which is the field radiated by dipole 1 at any point on dipole 2. This kind of EM radiation causes the change of input impedance of dipole 1 due to generation of the mutual impedance Z_{21i}. One may say that the change of this input impedance indicates a presence of the dipole 2. As it is evident from equation (1) the mutual impedance is changing together with current distribution $I_2(z')$ of the dipole 2, too. Current distribution of dipole 2 is mainly changed with its dimension (arm length – h'). It means that the input impedance change of dipole 1 contains not only information about presence of some conducting object, but also information about its basic physical dimensions [1].

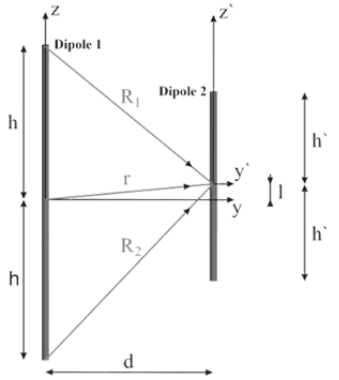

Fig.1. Dipole positioning for mutual coupling

According to [1], when dipole 2 is in the EM field, it acts as resonance circuit at some frequency. Based on this, there is possible to replace dipole 2 with a LC resonance circuit (Fig. 2 b)), whereby a relation in equation (1) is still valid [2]. The distance of the capacitor plates is in this case represented by a distance between two planar parts of load cell. The dipole 1 is need replaced by EM generator with constant amplitude-frequency characteristic at the operating frequency band. The stripline is used as convenient EM field generator [3].

3. Modelling of the sensor for numerical calculation

It is necessary to create the numerical model of designed sensor to verify the theory described above. The precise solution of the model may be obtained by numerical Method of Moments (MoM). MoM is mainly focused on solve current distribution on conducting surface. In order to calculate dielectric parts of sensor MoM is combined with Finite Element Method (FEM). This kind of solution which combines several methods is known as hybrid framework. In the computational code FEKO, several numerical techniques are used combining the MoM with high frequency asymptotic techniques, and also with mentioned FEM.
Created model of the sensor is shown in Fig. 2. The sensor structure consists of EM field generator – stripline (1.) and electrical part – parallel resonance circuit (2.). The resonance circuit with load cell [4] (3.) create coupled unit as it is shown in Fig. 2 b). Specific equivalent materials and dimensions of modelled sensor structure are stated in Table 1.

Table 1. Parameters of modelled sensor:

Used materials:	Structure parts:	Important dimensions:
Brass (σ=2,5647 S.m^{-1})	Stripline	l_S= 100 mm, h_S= 50 mm, d_s= 50 mm
Silver (σ=6,1737 S.m^{-1})	LC resonator	a= 30 mm, b= 5 mm, d=0-2 mm, n=2.5
Teflon (ε_r=2,08 F.m^{-1})	Load cell	l_{LC}= 50 mm, h_{LC}= 100 mm

n – count of inductor winding

As it was previously mentioned the sensing principle is based on resonance frequency change of sensor's electrical part, which is dependent on distance between capacitor's plates [2]. Considering this fact the shape of load cell was designed. During the sensing process specific parts of load cell (where plates of capacitor are implemented) are changed. As it was mentioned before, the behaviour of the wire structure at the resonant frequency is similar to those of resonant circuits. Therefore, it is necessary to analyse influences of such a resonant circuit on the stripline's input characteristics. We consider the scattering parameter s_{11}.

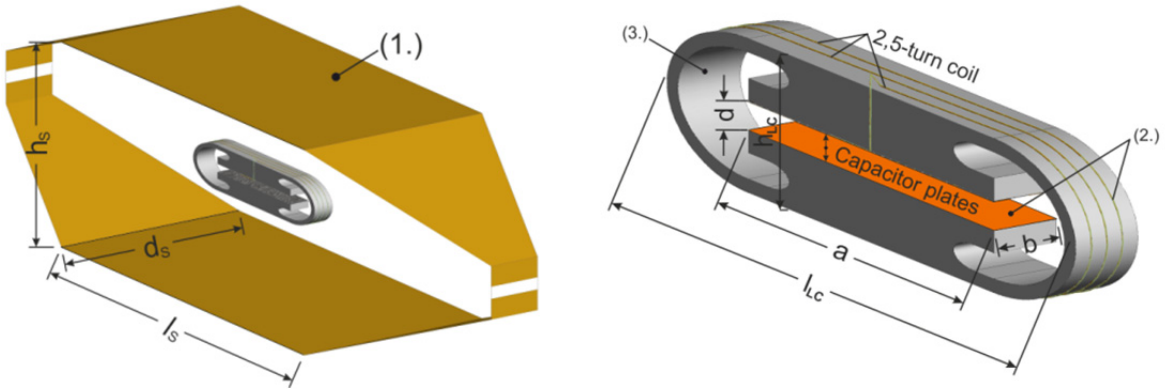

a) b)

Fig. 2 a) Full structure model in CADFEKO environment, (1.) – stripline
b) Electrical part (2.), load cell (3.)

4. Numerical simulation results

The frequency dependence of s_{11} of the stripline without sensor's structure is shown in Fig. 3a). The s_{11} curve of such a structure is not constant. Increase of the s_{11} in operating frequency band is caused by imperfect adaptation of stripline input and output parts. This is not an issue to next simulations.

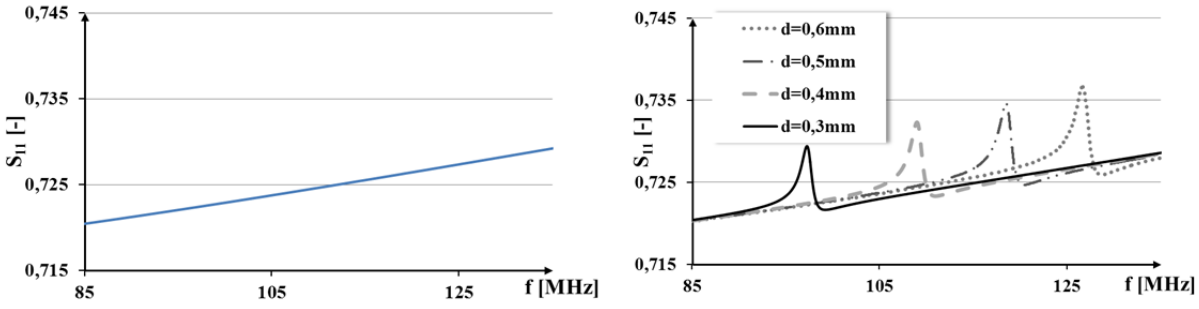

a) b)

Fig. 3 a) The s_{11} curve of stripline
b) The frequency position of s_{11} local maximum as a function of distance capacitor plates

The s_{11} curve of stripline is distorted, if the coupled unit (parallel resonance circuit with load cell) of proposed sensor is placed in the middle of the stripline, as it is shown in Fig. 3b). The deformation or peaks are manifested when the parallel resonance circuit begin to absorb the energy from EM field. Absorbed EM field energy is used for the self-resonance of the resonant circuit. The frequency position of local s_{11} maximum corresponds to resonance frequency of resonance circuit as it is investigated in detail in [1].

5. Real structure measurement

The real model of proposed sensor was created to verify results obtained by numerical calculation. The real structure of sensor we can see in Fig. 4a).The sensing distance of real sensor model was changed by micrometer screw gauge as we can see in Fig. 4a). The s_{11} measurement (Fig. 4b)) by network analyzer confirms functionality of created model of sensor. We can observe difference in amplitude course between calculated (Fig. 3b)) and measured (Fig. 4b)) s_{11} parameter. This kind of difference could be neglected because the sensing distance is represented by frequency position of local s_{11} maximum. The little frequency variations between numerical and measured results are caused by many factors like different inductance of coil, inaccurate of real model dimensions.

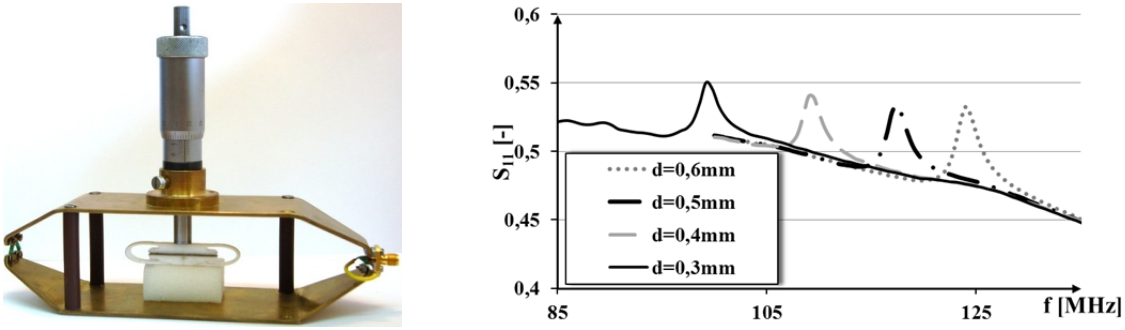

a) b)

Fig. 4 a) Real model of proposed sensor
b) The s_{11} curve obtained by measurement on real structure of sensors

6. Conclusions

Results of numerical modelling and measurement on real model confirmed that the proposed sensor is suitable for displacement measurement. The sensing principle uses a method based on change of electromagnetic field parameters. This method is described in detail in [1] and appears to be perspective measurement method applicable in micro or macro area not only for distance or displacement measurement, but also for another physical quantities measurement such as pressure, temperature and so on.

Acknowledgements

This work was supported by the Slovak Research and Development Agency under the contract no. APVV-0333-11 and by the project VEGA VG 1/0963/12.

References

[1] probodnika v elektromagnitnom pole, *Intelektualnye sistemy v proizvodstve*. No 2/2012, Naučno-praktičeskij žurnal, ISSN 1813-7911.

[2] Marsalka, L., Hartansky, R., Electromagnetic Method for Distance Measurement on MEMS Structures. MM Science Journal Special Edition, 2011, Brno, Czech Republic. s. 48. ISSN 1803-1269.

[3] Krammer Hartansky R., Marsalka L., Kocner E., Chvorenkov V. V., Karavaev Y. L. Izmerenye dliny, A., Bittera, M., Distributed Impedance as Terminating Load at GTEM Cell. In EMD'2012 : 22nd International Conference "Electromagnetic Disturbances EMD'2012". Vilnius, Lithuania, September 20-21, 2012. Vilnius Gediminas Technical University, 2012, s. 52--55. ISBN 978-609-457-260-9.

[4] Havlik S., Hricko J. The Analysis and Design Study of High Speed Robotic Devices, *Applied Mechanics and Materials*, vol. 282, 2013, p. 18-26, ISSN: 1662-7482.

Analysis of Vibration into the Scanning Area of the Open-air NMR Imager Working with a Weak Magnetic Field

J. Přibil, D. Gogola, T. Dermek, and I. Frollo

Institute of Measurement Science, SAS, Dúbravská cesta 9, Bratislava, Slovakia
Email: Jiri.Pribil@savba.sk

Abstract. *The paper analyzes of spectral properties of an acoustical noise produced by mechanical vibration of the gradient coils during scanning in the open-air Magnetic resonance imaging equipment working with a weak magnetic field up to 0.2 T. This vibration signal exhibits harmonic character, so it is suitable to analyze its properties in the spectral domain. Mapping of intensity distribution of the vibration signal is also described in this paper. Obtained results of spectral analysis will be used to suppression of a negative influence to the quality of resulting MR images of the thin layer samples tested in this device.*

Keywords: Acoustic Vibration and Noise, Spectral Analysis, NMR Imaging

1. Introduction

Magnetic resonance imaging (MRI) devices working with a weak magnetic field are used for non-invasive MR scanning of different parts of a human body in clinical practice as well as for testing of biomedical or agriculture samples. This type of MRI equipment can be also applied for analyzing of weak magnetic materials (belonging to diamagnetic and paramagnetic materials) [1] and for testing of widely used body implants or dental casting alloys. The MRI device consists of a gradient coil system that produces three orthogonal linear fields for spatial encoding of a scanned object. The noise is produced by these gradient coils due to rapidly changing Lorentz forces during fast switching inside the weak static field B_0 environment [2]. It results in significant mechanical pulses that cause secondary vibration in the MR scanning area and can also be induced to vibration of tested samples inserted in the MRI device. By this way induced vibrations can have a negative influence to the quality of resulting MR images (blur effect) especially when the thin layer samples are tested. In this case the vibration originated from a gradient coil causes movement of the tested sample lying on the undulating surface of a water solution. Due to its harmonic nature the produced vibration signal [3] can be generally treated as a voiced speech signal and it can be analyzed using similar methods as those used for spectral speech analysis [4].

The paper is focused on measurement and calculation of 3D maps of the vibration signal sensed at bottom plastic holder of the MRI equipment scanning area, where the gradient coil system is arranged. Determination and evaluation of the main spectral parameters of recorded vibration signals for basic types of 3D scanning sequences implemented in the MRI device was performed. The main motivation of our work was to obtain statistical results of spectral parameters of the vibration signal, which can be used to devise sharpening and reduction of the motion effect in the MR pictures of thin layer samples and phantoms.

2. Method of Analysis of the Vibration Signal Spectral Properties

Spectral analysis of the vibration signal is performed in the following way: from the input samples (after segmentation and weighting by a Hamming window with the length w_L) the absolute value of the N_{FFT} points fast Fourier transform $|S(k)|$ and the power spectrum $P(k)$ is calculated – see the block diagram in Fig. 1. The harmonics-to-noise ratio (HNR) provides an indication of the overall periodicity of the speech signal [5]. Specifically, it quantifies the

ratio between the periodic and aperiodic components in the signal. The HNR expressed in [dB] is computed as

$$HNR = 10\log_{10}\left(\frac{\sum_{k=N_{FB}LO}^{N_{FFT}/2}|S(k)|^2}{\sum_{k=N_{FB}HI}^{N_{FFT}/2}|S(k)|^2}\right),\quad N_{FB} = \frac{f_{\max FB}\,N_{FFT}}{f_s}, \quad (1)$$

where summation index N_{FB} depends on the chosen frequency band, f_{s} is used sampling frequency, and f_{maxFB} is the maximum frequency of the band. Determined spectrum portion of harmonic amplitudes is summed from low frequencies corresponding to the index $N_{FB}LO$ (10 ÷ 70 Hz); the noise portion is calculated from high frequencies corresponding to the index $N_{FB}HI$ (1500 ÷ 4500 Hz). The spectral centroid (SC) is a centre of gravity of the power spectrum and represents an average frequency weighted by the values of the normalized energy of each frequency component in the spectrum. The spectral flatness measure (SFM) can be used to determine the degree of periodicity in the signal. This spectral feature can be calculated as a ratio of the geometric and the arithmetic mean values of the power spectrum. The spectral entropy is a measure of spectral distribution. It quantifies a degree of randomness of spectral probability density represented by normalized frequency components of the spectrum. All mentioned spectral properties – SC in [Hz], SFM, and Shannon spectral entropy (SHE) were calculated using following formulas [5]

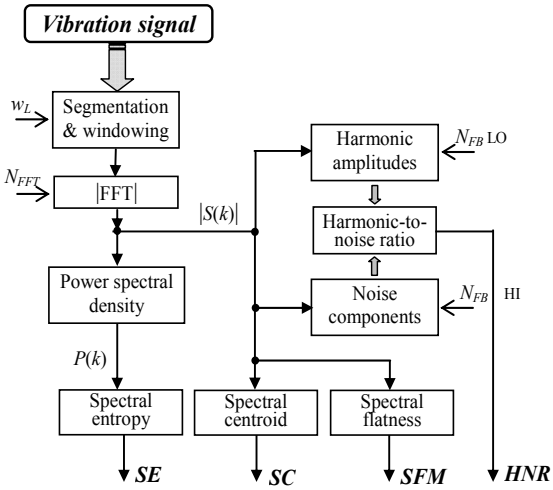

Fig. 1. Block diagram of spectral analysis of the vibration signal.

$$SC = \frac{\sum_{k=1}^{N_{FB}} k|S(k)|^2}{\sum_{k=1}^{N_{FB}}|S(k)|^2}\cdot\frac{f_s}{N_{FFT}},\qquad SFM = \frac{\left[\prod_{k=1}^{N_{FB}}|S(k)|^2\right]^{\frac{2}{N_{FFT}}}}{\frac{2}{N_{FFT}}\sum_{k=1}^{N_{FB}}|S(k)|^2},\qquad SHE = -\sum_{k=1}^{N_{FB}}P(k)\log_2 P(k)\,. \quad (2)$$

3. Experiments and Results

Our experiments with mapping of produced vibrations and analyzing of spectral properties of the vibration signal were performed in the open-air 0.178 T imaginer E-scan Esaote OPERA [6]. To prevent an interaction with the stationary magnetic field B_0 in the MRI scanning area, the vibration sensor must be totally free of ferromagnetic materials. In praxis, the piezo-electric sensors for contact measurement of vibrations on surfaces were often used. The standardized vibration sensors or accelerometers designed for professional measurement usually consist of cover sleeve from metal or ferromagnetic materials, so it is impossible to measure their usage in the MRI device. Because we principally engaged in the frequency range of <10 Hz÷5 kHz> [4] we finally decided to use the vibration sensor primary designed for sensing of musical instruments – contrabass. This sensor consists of the active piezo-electric element mounted on the circular 1“ target of brass. Tested MRI equipment has

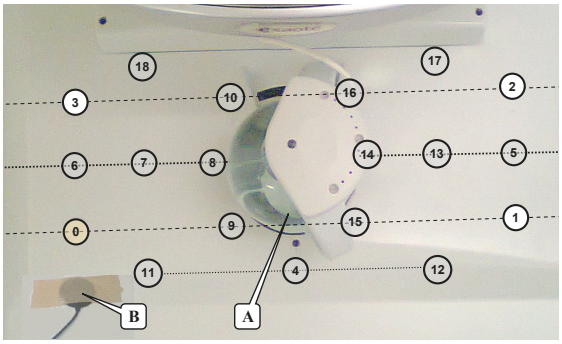

Fig. 2. Photo of distribution of 19 measuring points on the bottom scan plate of the MRI: RF knee coil with a water phantom (A), piezo-electric vibration sensor (B).

a planar arrangement of the gradient sub-system consisting of parallel combination of surface coils located on the upper and bottom part of the scanning area. For mapping of distribution of the vibration on the scan area of the MRI device, the bottom plastic plate was covered by a measuring matrix consisting of 19 points (see Fig. 2), and the spherical testing phantom filled with doped water inserting in the scanning RF knee coil were used. An electric signal from the vibration sensor was directly measured by the digital oscilloscope Tektronix TDS 210. Obtained relative peak-to-peak values were subsequently recalculated to signal levels in [dBuV]. The vibration signal was parallel recorded with the help of the Behringer PODCAST STUDIO equipment connected to a separate personal computer (originally recorded at 32 kHz, resampled to 16 kHz). The whole measurement was performed for eight different types of the 3D and Hi-Res scanning sequences (often used for MR images of the thin layer magnetic materials) in four different measuring positions – see Tab. 1.

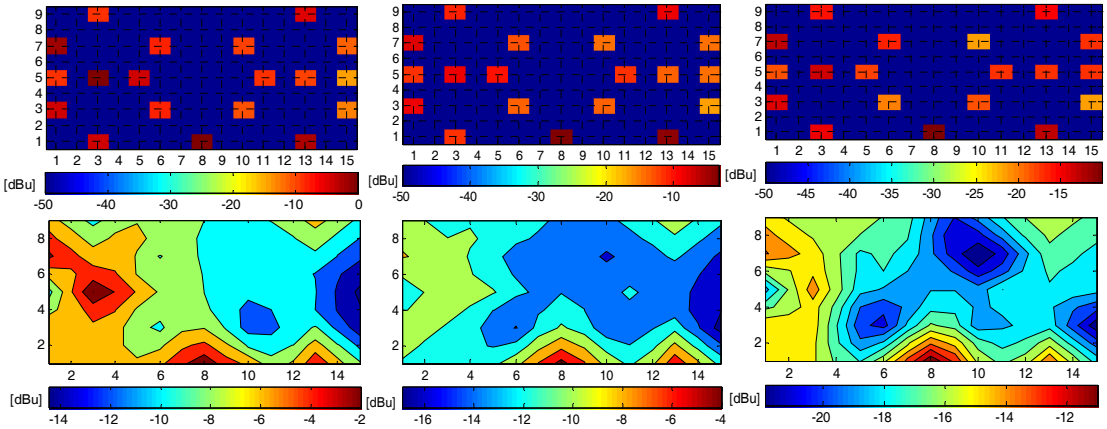

Fig. 3. Graphic representation of distribution of the vibration signal: discrete values at measuring positions of <0÷18> in the 15x9 grid (upper set) – the background level was substituted with the -50 dBuV value; calculated 2D contour map (lower set) – used scanning sequence No 1 (left), No 4 (centre), and No 8 (right).

Table 1: Parameters of tested scanning sequences together with measured vibration signal level on the basic positions (in corners of the plastic plate), and the mean values of spectral properties measured at position "0".

No	Sequence type*)	TE [ms]	TR [ms]	Signal level at positions [dBuV]**)				Mean values of spectral properties			
				0	1	2	3	HNR	SC [Hz]	SFM	SHE
1	SS 3D balanced	5	10	-4.4	-13.1	-11.6	-1.6	0.0902	876.9	0.0008	4.579
2	SSF 3D	10	40	-11.1	-18.2	-14.4	-6.4	0.1008	911.7	0.0017	5.128
3	SSF 3D rsf	10	30	-11.1	-18.8	-15.3	-6.8	0.1004	911.6	0.0018	5.115
4	SSE 3D	10	20	-8.7	-16.9	-15.1	-7.8	0.1158	945.1	0.0013	3.815
5	TURBO 3D-T1	16	40	-17.5	-21.4	-15.6	-13.6	0.1289	1012.2	0.0032	5.319
6	3D-CE	30	40	-15.3	-19.9	-19.1	-15.9	0.1181	1020.1	0.0031	5.111
7	Hi Res SE 26 HF	26	500	-13.4	-20.5	-18.0	-8.8	0.2077	1779.4	0.0675	5.606
8	Hi Res GE STIR 25	25	1000	-14.2	-21.7	-17.3	-12.9	0.2630	2091.6	0.1094	6.023

*) Auxiliary parameters: FOV 200x200x192, 10 slices, 4 mm thick, orientation sagittal. **) Background level were -48dBuV for all sequences

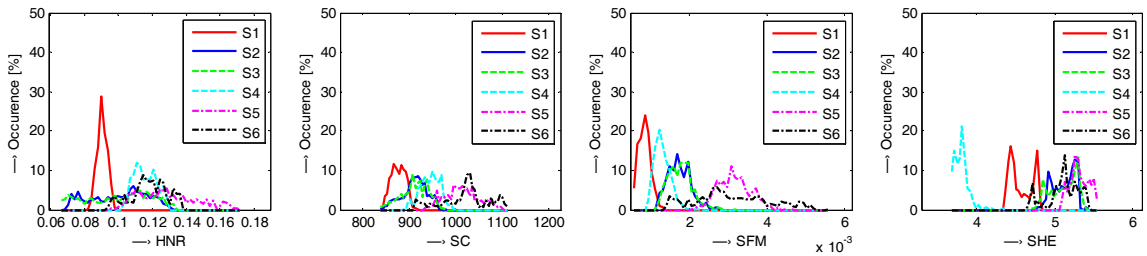

Fig. 4. Histograms of the spectral properties values measured at point "0" for the first six scanning sequences.

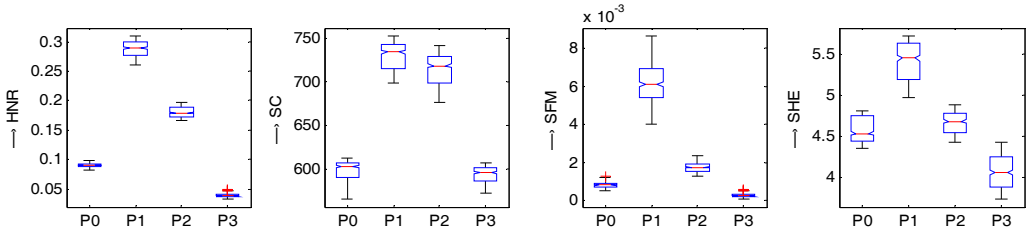

Fig. 5. Values comparison of spectral properties obtained at different measuring positions; MR sequence No 1.

4. Conclusions

Performed analysis of distribution of the vibration signal for different scanning sequences shows that the intensity on the bottom plastic plate is not consistent – see maps in Fig. 3. The maxima are located near the front edge of the scanning area and the minimum is approx. in the centre of the plate. This is a positive result instead of the fact that in the centre is placed the RF coil with the tested samples. On the other hand, not only the intensity of vibrations influences the tested thin layer samples. Realized analysis of spectral features of the vibration signal shows that different frequencies are attended – see comparison of results in Tab. 1 and graphs in Fig. 5. Obtained values of the HNR and SC parameters demonstrate that representation of the different frequencies depends first of all on the used MR sequence, and next on basic setting of the scan parameters – TE and TR time. Measurements using the scanning sequences No 2, 3 yielded similar results, because these two types differ only in the parameter TR. Given results confirm our assumption, that the TR time affects first of all the fundamental frequency of the vibration signal (like as the F0 of a speech signal [4]).

In the near future, we will to realize the mapping of the vibrations with higher precision – in more measuring points. To obtain the results in normalized vibration (pressure) level [3] our piezo-electric sensor must be calibrated with the standard one designated for this purpose. In addition, we plan to measure and analyze the time propagation delay [2] between the electrical excitation pulse of gradient coils and subsequently generated vibration wave.

Acknowledgements

The work has been supported by the Grant Agency of the SAS (VEGA 2/0090/11), the State program SPVV no. 2003SP200280203, and the State project APVV-0513-10.

References

[1] du Trémolet de Lacheisserie É, Gignoux D, Schlenker M. Magnetism: Fundamentals. Springer Science & Business Media, Inc., 2005, 0-387-23062-9, E-book.

[2] Moelker A, Wielopolski PA, Pattynama MT. Relationship between magnetic field strength and magnetic-resonance-related acoustic noise levels. Magnetic Resonance Materials in Physics, Biology and Medicine 2003;16:52–55.

[3] Yao GZ, Mechefske CK, Brian RK. Acoustic noise simulation and measurement of a gradient insert in a 4 T MRI. Applied Acoustics 2005;66:957-973.

[4] da Silva LA, Joaquim MB. Noise reduction in biomedical speech signal processing based on time and frequency Kalman filtering combined with spectral subtraction. Computers and Electrical Engineering 2008;34: 154-164.

[5] Hosseinzadeh D, Krishnan S. On the use of complementary spectral features for speaker recognition. EURASIP Journal on Advances in Signal Processing, Vol. 2008, Article ID 258184, 10 pages, doi:10.1155/2008/258144, Hindawi Publishing Corp 2008.

[6] E-scan Opera. Image Quality and Sequences manual. 830023522 Rev. A, Esaote S.p.A., Genoa, April 2008.

Receive Coil for Low-field NMR Scanner Optimized Using Inductive Coupling

P. Andris, T. Dermek, I. Frollo

Institute of Measurement Science, Slovak Academy of Sciences, Dúbravská cesta 9, 841 04 Bratislava, Slovak Republic
Email: peter.andris@savba.sk

Abstract. *The paper describes a receive coil system for low-field NMR scanner intended for cardio measurements. The coil system is based on good qualities of surface coils accommodating them to volume measurements. The active volume of the coil is widened using two inductively coupled resonators. Signal from the coil system is amplified using a high-impedance preamplifier thus no special matching is necessary. The coil can be utilized for larger samples measurements. Thanks to inductive coupling the coil system need not be retuned before every new measurement. Performed experiments confirmed good agreement between the theory and the practice but should be verified by more experiments.*

Keywords: Receive Coil, Low-Field NMR, Inductive Coupling

1. Introduction

One of the first uses of inductive coupling for nuclear magnetic resonance (NMR) receive coil systems solved balancing surface coils [1]. The purpose was reducing losses due to parasitic capacitances and increasing sensitivity in this way. Widening the frequency bandwidth in over-coupled mode motivated to experiments with coil systems not needing fine tuning before every measurement [2]. Moreover the authors used preamplifier with high input impedance and matched the coil system to receiver in the manner. The subsequent step should have been a receive system with universal coupling coil and several receive coils changed at need. The first experiments and deeper analysis showed that fulfilling the theoretical assumptions in [2] is not a simple thing. The further experiments therefore were aimed at a receive coil system with one passive and one active receive coils widening the frequency bandwidth, preserving proper tuning in sufficiently wide span. Purpose of the paper is to describe some interesting parts of the designed system.

2. Subject and Methods

Older studies revealed that surface coils can operate in smaller volume compared to volume coils but their signal-to-noise ratio (SNR) in the volume is higher than SNR of volume coils in their volume. The fact motivated to design of receive systems consisting of several surface coils. The way has been selected for solving the studied problems. Fig. 1 depicts a circuit diagram of the investigated system. The difference to usual use of such circuit and also to [2] is the fact that the signal from the excited sample is induced into both coils of the circuit. It changes behaviour of the circuit compared to known uses. The coil system can be described by the equation system

$$\begin{bmatrix} \mathrm{V}_{s1} \\ \mathrm{V}_{s2} \end{bmatrix} = \begin{bmatrix} R_1 + \mathrm{i}\left(\omega L_1 - \frac{1}{\omega C_1}\right) & \mathrm{i}\omega M \\ \mathrm{i}\omega M & R_2 + \mathrm{i}\left(\omega L_2 - \frac{1}{\omega C_2}\right) \end{bmatrix} \cdot \begin{bmatrix} \mathrm{I}_1 \\ \mathrm{I}_2 \end{bmatrix}, \tag{1}$$

where V_{s1} and V_{s2} are voltages induced into the both coils from the excited sample,

M is the mutual inductance and the other quantities are obvious from the circuit diagram.

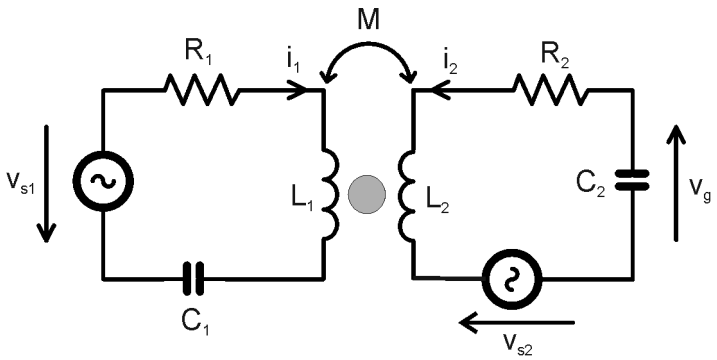

Fig. 1. Circuit diagram of the receive coil system. Voltages V_{s1} and V_{s2} are induced into the both coils from the excited sample.

The output voltage v_g is amplified using a preamplifier with high input impedance. Fig. 2 depicts a real configuration of the coil system.

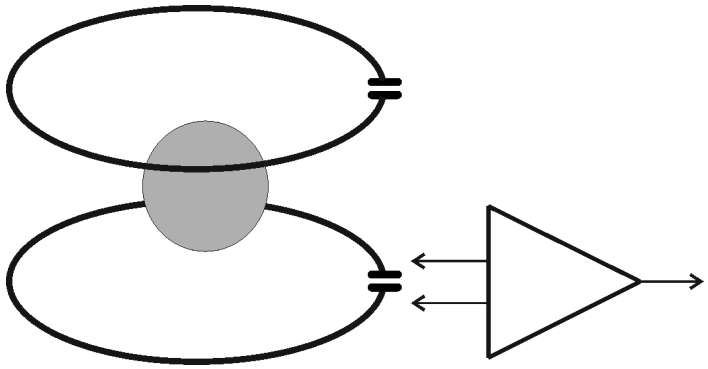

Fig. 2. A real configuration of the experiment. One of the both coils is active and its voltage is amplified using a preamplifier with high input impedance. The second coil is passive and serves to widening the active volume.

The used preamplifier must, besides the high impedance input, have also low own noise. Whereas the coil system was intended for a low-field scanner, also an appropriate operational amplifier (OA) can be used as a base for the preamplifier design. Preamplifiers using an operational amplifier are rather simple. There is a basic circuit diagram in Fig. 3 of a voltage amplifier with voltage and current noise sources. In practice the circuit diagram must be completed with protection circuits, protecting the semiconductor device from too strong signal during the excitation of the sample. The circuit with back-to-back diodes and detuning circuits are utilized. Many equations for calculation of the output noise of the OAs can be found in publications of the manufacturers, but they consider infinity voltage gain of the used operational amplifier. It can be fulfilled at acoustic frequencies, nevertheless at frequencies of MHz an infinity gain cannot be considered. The analysis of the circuit in Fig. 3 yielded the following equation for the spectral density corresponding to noise, added to output voltage V_2

$$S(\mathrm{V}_2) = \left(\frac{A \cdot (R_1 + R_2)}{R_1 + R_2 + A \cdot R_2}\right)^2 \cdot [(I_{n2} \cdot R_g)^2 + 4kTR_g + e_n^2 + \left(\frac{R_2}{R_1 + R_2}\right)^2 4kTR_1 +$$

$$+ \left(\frac{I_{n1} R_1 R_2}{R_1 + R_2}\right)^2 + \left(\frac{R_1}{R_1 + R_2}\right)^2 4kTR_2] \qquad (2)$$

RMS value of the noise voltage is given by

$$V_{2n} = \sqrt{\int_{f_0-\Delta f}^{f_0+\Delta f} S(V_2)df}, \quad (3)$$

where f_0 and Δf determine the noise bandwidth of the receiver, A is voltage gain of the used operational amplifier at the working frequency. Resistor R_g represents the real part of the coil system impedance. Sources of noise voltage e_n and noise currents I_{n1} and I_{n2} together with a noiseless operational amplifier simulate noise in the real preamplifier. The expression

$$G_v = \frac{V_2}{V_g} = \frac{A \cdot (R_1 + R_2)}{R_1 + R_2 + A \cdot R_2} \quad (4)$$

represents voltage gain of the preamplifier.

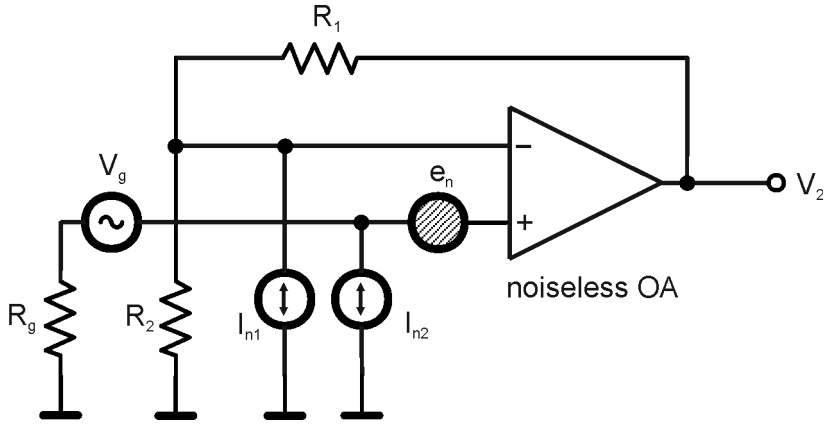

Fig. 3. Circuit diagram of the preamplifier with an operational amplifier. A noiseless operational amplifier together with voltage and current noise sources simulate the real circuit.

The amplifier is connected to the receiver using a cable, therefore output of the preamplifier must be matched to its impedance. All necessary calculations were performed using the program package Mathematica (Wolfram Research Inc., Champain IL). Verification experiments have been performed using the experimental scanner with home-made resistive magnet, equipped with the Apollo (Tecmag Inc., Houston, TX) console.

3. Results

The two one-turn square-shaped coils of the described coil system has been manufactured of copper tube with diameter of 6 mm. Dimensions of one coil is 30 cm × 30 cm. Each coil, including non-magnetic ceramic tuning capacitors is encapsulated in PVC shell. The active coil is connected to the preamplifier and the passive coil is in changeable distance from it to widen the active volume of the system. The operational amplifier for the preamplifier is ADA4817 (Analog Devices Inc., Norwood, MA, U.S.A.). It is a FET IC with very low voltage and current sources of noise. The ability of widening the volume of the coil was verified in the following experiment: the coil system was tuned to 4.45 MHz, the working frequency of the scanner and a beaker (more than 1 liter) filled with water solution of 5 nM of $NiCl_2$ and 55 nM of NaCl was measured using the spin echo measuring sequence. First the both coils were used to measurement and the SNR was calculated (Fig 4(a)) within the pixels of the sample. Subsequently only the active coil was used and the same measurement was repeated and the SNR calculated (Fig. 4(b)). Widening the active volume is evident when used the both coils in this experiment, though the SNR has been decreased. The result needs to be verified in more, different experiments.

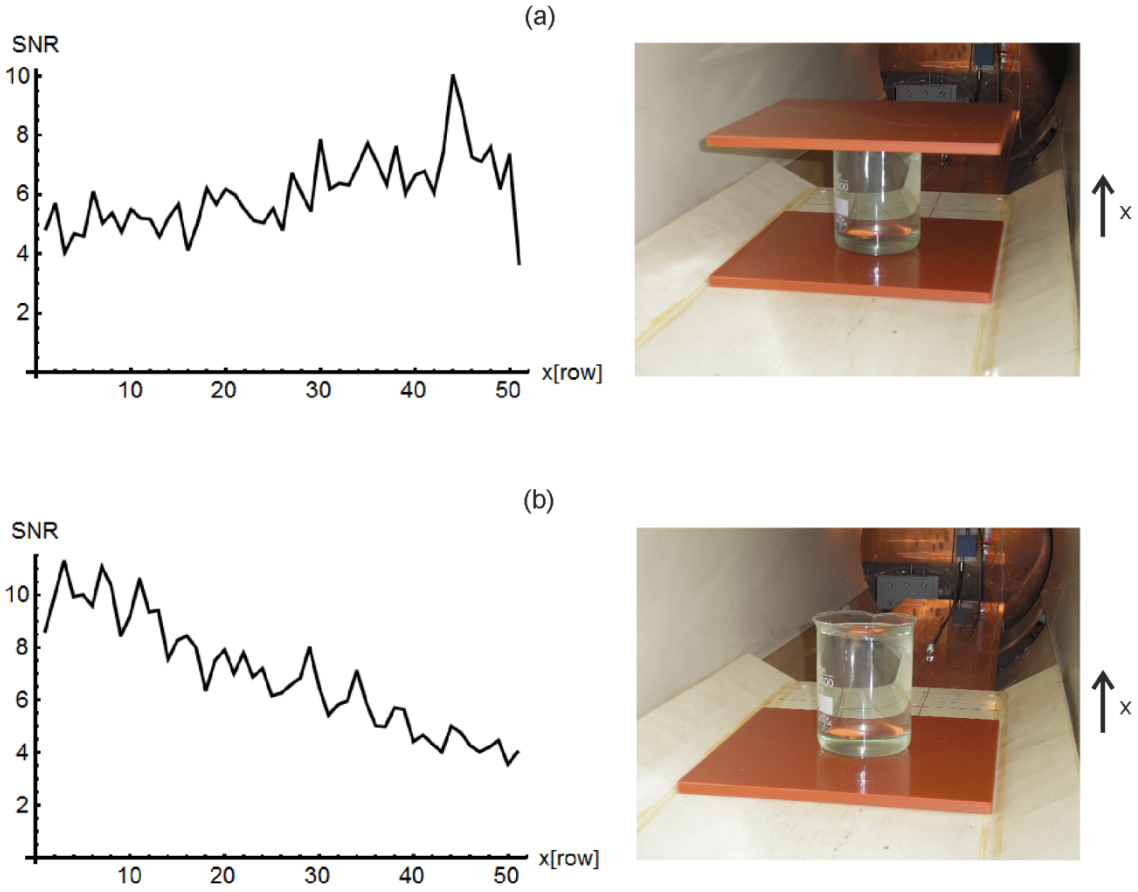

Fig. 4. Signal-to-noise ratio for experiments with double-coil system (a) or single-coil system (b). The active volume is more wide for the double-coil system. The value of the SNR depends also on parameters of the measurement and on qualities of the static magnetic field (stability, homogeneity, noise).

4. Discussion and Conclusions

Planes of the both coils are considered to be parallel. Nevertheless using the equations (1) it can be easily calculated that phase shifts between the signals induced from the sample into the both coils can change the shape of the output signal curve significantly. The best situation seems to be with the phase shift of $\pi/2$ but using such result in practice can be problematic. The width of the double-coil system active volume is larger, although its SNR is rather low. It can be increased using better filling the coil volume with the sample and also homogeneity of the static magnetic field within the coil and noise of the static magnetic field are very significant. The studies will continue in more, different experiments.

Acknowledgements

The research was sponsored by the Grant Agency of the Slovak Academy of Sciences, under Grant Number 2/0090/11 and by the Slovak Research and Development Agency, project number APVV-0513-10.

References

[1] Decorps M, Blondet P, Reutenauer H, Albrand JP, Remy C. An Inductively Coupled, Series-Tuned NMR Probe. *Journal of Magnetic Resonance, 65* (1): 100-109, 1985.

[2] Raad A, Darrasse L. Optimization of NMR Receiver Bandwidth by Inductive Coupling. *Magnetic Resonance Imaging*, 10, (1): 55-65, 1992.

Contrast Agents Based on Magnetic Nanoparticles and its Interaction with Surrounding Environment During Contrast Imaging

D. Gogola, O. Štrbák, M. Škrátek and I. Frollo

Institute of Measurement Science, SAS, Dúbravská cesta 9, Bratislava, Slovakia
Email: daniel.gogola@savba.sk

Abstract. *The paper analyzes properties of commonly used contrast agents, based on gadolinium and different types of iron oxides, like Fe_2O_3, Fe_3O_4. The goal of the study was to investigate the influence of the molecules of interest (NaCl and glucose) to the Resovist contrast agent relaxation properties.*

Keywords: Magnetic Nanoparticles, Contrast Agents, NMR Imaging

1. Introduction

Magnetic resonance imaging (MRI), like another imaging techniques, meets the challenge to distinguish tissue structures, whose signal intensity are overlapped. It is despite to the fact that MRI is currently regarded as imaging techniques with the best resolution ability for the soft tissues [1, 2]. The most commonly used contrast agents are based on particles of gadolinium or different iron oxides, like Fe_2O_3 and Fe_3O_4, which are in the form of colloidal suspension in the carrier liquid [3].
The goal of this study was to observe the influence of the molecules of interest (MOI), like NaCl and glucose, to the relaxivity of Resovist contrast agent.

2. Materials and methods

Resovist is a widely used contrast agent in clinical practice. Its active substance is the superparamagnetic iron oxide, which is coated by the carboxyl-dextran. Resovist increases the spatial resolution between tissues in T_2, T_2^* weight images. This contrast agent is highly effective and generally is a very good tolerated by the cardiovascular system. Concentration of Resovist in our in-vitro experiments was equal to the concentration of contrast agent during in-vivo imaging in humans. Images were acquired by the MR tomograph Varian 4.7 T, with "Spin-echo Multi-slices Imaging sequence" (SEMS). The parameters of imaging sequence includes repetition time TR = 2 s and twelve different echo time (TE = 8.344; 16.688; 25.032; 33.376; 41.72; 50.064; 58.408; 66.752; 75.096; 83.44; 91.784; 100.128 ms). The T_2 values were obtained by the exponential fitting of intensity decrease by the least squares method (VNMRj 2.3A software). The acquired data was compared with the data obtained by the clinical tomograph ESAOTE Opera 0.178 T. Five samples were observed (one as a reference) with the same concentration of Resovist and different concentrations of MOI (NaCl and glucose) are shown in Table 1.

Table 1: Five samples and one as a reference with different concentration of MOI .

Sample number	Basal solution	Concentration molecules of	
		c_{NaCl} [g/l]	c_{Glu} [g/l]
1	distilled water	0	0
2	distilled water + Resovist	9	0
3	distilled water + Resovist	9	0
4	distilled water + Resovist	90	0
5	distilled water + Resovist	0	1
6	distilled water + Resovist	0	10

3. Results and Discusion

In Fig. 1 are showed data obtained by the SEMS sequence at 4.7 T for twelve different echo times.

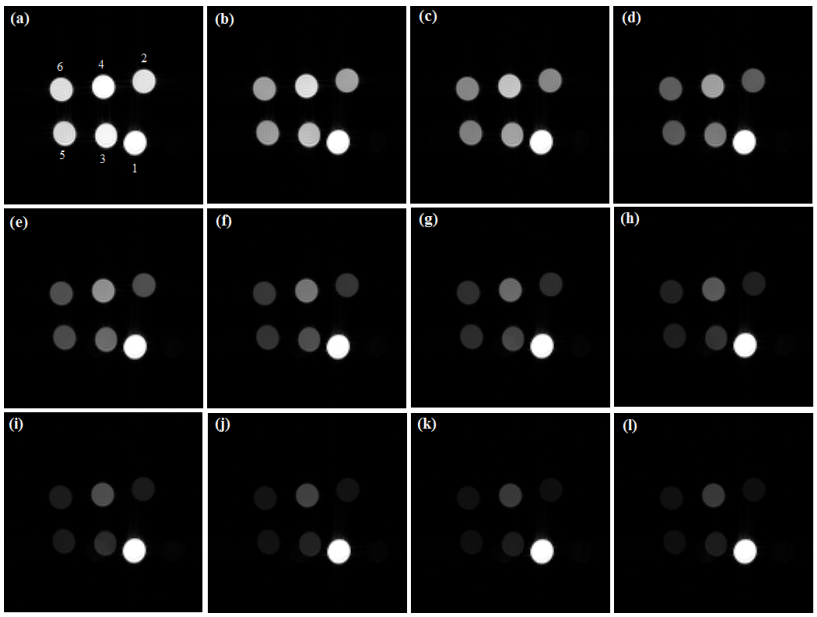

Fig. 1. Six samples with different concentration of MOI obtained by MR tomography with magnetic field strength 4.7 T, TR = 2 s.

The images show, that different MOI with a different concentration, have an influence to the relaxation times of contrast agent. Changes of T_2 relaxation time are shown in Table 2.

Table 2: T2 relaxation time values and standard deviation for each sample measured at 4.7 T, 'std' means standard deviation .

	Sample n.1	Sample n.2	Sample n.3	Sample n.4	Sample n.5	Sample n.6
T_2[s]	0.3205	0.0286	0.0348	0.0463	0.0287	0.0297
[std]+/- [s]	0.009	0.00009	0.00024	0.00017	0.00007	0.00013

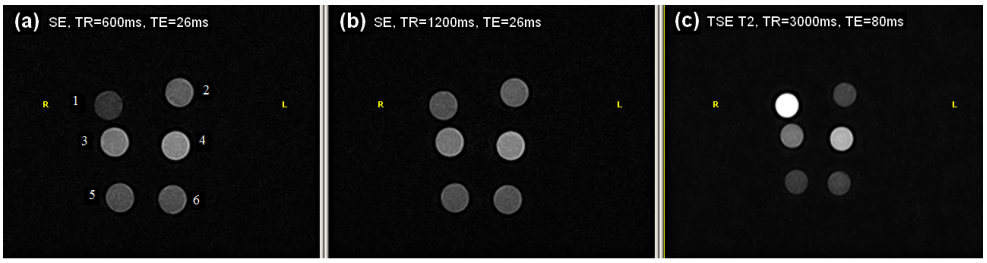

Fig. 2. MR images of six samples with different concentration of MOI, measured by clinical MR tomograph 0.178 T

To compare the influence of the MOI to the relaxation properties of the contrast agent, the samples were imaged by the clinical tomograph ESAOTE Opera 0.178 T (Fig. 2). The images show the change of the contrast for the samples number 1, 3, and 4, when the SE image sequence was used.

For quantification of signal intensity at ESAOTE E-scan Opera XQ, we used custom-made phantoms, which parameters are summarized in Table 3. Decrease in signal intensity with dependence on the concentration is shown in graph (Fig. 3)

Tab.3 Properties description of prepared samples

Sample	Concentration EMG607 [μg/ml]	Susceptibility of sample	T2 relaxation time [ms]
Distilled water	0	$-9{,}04\text{x}10^{-6}$	1800 ±20
Distilled water + EMG607	1.11	$4{,}24\text{x}10^{-5}$	31 ±0.3
	2.19	$3{,}11\text{x}10^{-5}$	15.2 ±0.2
	3.26	$5{,}58\text{x}10^{-5}$	10 ±0.079
	4.3	$1{,}28\text{x}10^{-4}$	8.8 ±0.088
	5.33	$1{,}11\text{x}10^{-4}$	6.4 ±0.073
	6.33	$1{,}33\text{x}10^{-4}$	5.2 ±0.052
	7.32	$1{,}41\text{x}10^{-4}$	4.6 ±0.053

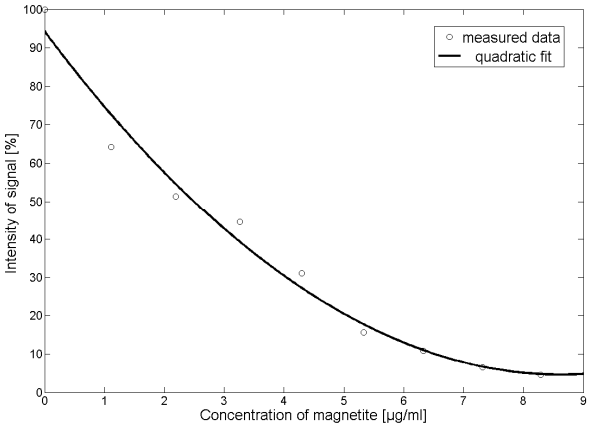

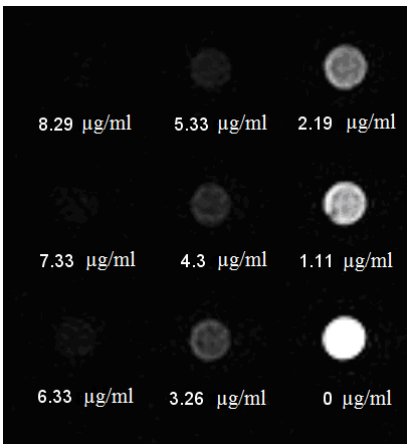

Fig. 3., **Fig. 4.** Dependence of signal intensity on the concentration of magnetite. For a reference value (maximal), the distilled water was chosen. The intensity values are in % range with regard to distilled water value.

4. Conclusions

The decrease of signal intensity in each sample with MOI, with increase of echo time, was expected. However, the changes in T_2 relaxation times for MOI samples are a little bit surprising. These changes, together with variations measured at clinical tomograph are subject of next study.

Acknowledgements

The work has been supported by the Grant Agency of the Slovak Academy of Sciences, VEGA 2/0090/11, APVV-0513-10 and by State program ŠPVV no.2003SP200280203.

References

[1] Youtaka, I. and Y. Tmohiro, "History, Present and Future of Diagnostic Imaging: Magnetic Resonance Imaging (MRI)," *Japanisch-Deutsche Medizinische Berichte*, vol.50, pp. 40-51, 2005.

[2] Berry, E. and A.J. Bulpitt, "Fundamentals of MRI: an interactive learning approach," *Series in medical physics and biomedical engineering*, Boca Raton, FL: CRC Press. XVII, p.298, 2009.

[3] Keevil, S., "Magnetic resonance imaging in medicine," *Physic Education*, vol.36, pp. 476-485, 2001.

X-ray Diagnostics of Wood Invaded by Insect

[1]P. Fiala, [1]P.Koňas, [1]M.Friedl, [1]R. Kubásek1, [2]P.Šmíra

[1]1Department of Theoretical and Experimental Electrical Engineering,
Brno University of Technology, Brno, Czech Republic
[2]Thermo Sanace s.r.o., Ostrava – Kunčičky, Czech Republic
Email: fialap@feec.vutbr.cz

Abstract. *The problem of finding a suitable diagnostic procedure for the examination of structural elements has been closely analyzed in recent years. In this connection, the main material of interest is wood as a sort of heterogeneous matter, and the diagnostic procedure is directed towards enabling industrial application in the future. A new diagnostic method based on X-ray imaging has been proposed and tested; the technique utilizes the reduction of imaging information into 2D planar projection. It allows us to image clearly the rate of material damage through displaying the weighted damage rate.*

Keywords: X-ray, Diagnostic, 2D

1. Introduction

Currently, the protection of structural elements made of wood against decay fungi and wood-destroying insects is widely realized through the thermal treatment technique, which has been known and used in Germany since 1930. The principle of this method consists in heating the related wooden structures, by means of hot air whose temperature does not exceed 120 °C, for a period of 4 - 10 hours. Heat is accumulated inside wooden components of the structure under treatment, and the temperature of these components may reach as high as 60 °C within the cross-section, Fig. 1.

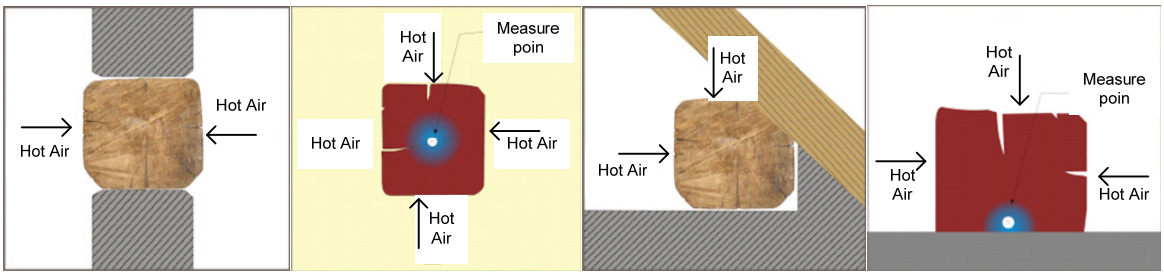

Fig. 1. Heat propagation and detection in a non-homogeneous material: wood.

At the temperature of 55 °C, all viable forms (including the ova, worm, nymph, and beetle) of wood-destroying insects perish; this temperature is the boundary value for the coagulation of proteins that nurture wood-destroying insects such as old-house borer (Hylotrupes bajulus), common house borer (Anobium punctatum), the death watch beetle (Xestobium rufovillosum), or the powder post beetle (Lyctus brunneus).

A necessary precondition for any sensible application of the method consists in diagnostics performed on damaged portions of structural elements. The diagnostics can be realized by means of non-destructive techniques or, alternatively, through destructive methods resulting in partial disruption of the examined element. This paper contains the proposal and analysis of a mobile non-destructive diagnostic method suitable for use with a damaged or disrupted structural element (Fig. 2). In connection with non-destructive diagnostics, the thermal

treatment method constitutes a well-suited approach to be applied in artefacts and buildings of great historic value.

Fig. 2. Examples of wood invaded by decay-fungi and wood-destroying insects.

2. Treatment methods

The group of basic treatment methods includes the liquidation of insect foetus, fungus, or rot through the use of hot air or chemical preparations. In all application cases, these techniques are further modified or combined, and the extent of their use is usually determined from the diagnostic results.

Diagnostics
The diagnostics in buildings or in the applied structural elements containing wood are performed both visually and acoustically within the range of audible frequencies, or within the ultrasonic band. The application of acoustic methods frequently results in partial damage of the material. Suitable types of approach to the diagnostics of temperature distribution status include optical measurement methods or destructive methods utilizing probes introduced into a section through the material.

Destructive diagnostics
The rate of a material damage in 3D imaging can be determined by means of the acoustic diagnostic method whose application nevertheless poses certain risks; generally, there are two problems involved. In this respect, the first point of interest is related to erroneous interpretation of diagnostics by the employed software, whereby a mere 10 % damage may be rendered as a large-scale problem within the material volume; this fact follows from the characteristics of acoustic waves propagation through a heterogeneous material as well as from its reconstructions and interpretations of the damaged region. The other problem as mentioned above consists in destructive character of the applied diagnostics together with certain limitations to the use of sensors (namely its repeatability). Further, the situation is made somewhat more difficult by the fact that, owing to the rate of wood heterogeneity, every diagnosed component constitutes a unique entity having no identical counterpart.

Non-destructive diagnostics
The group of non-destructive methods classifying the rate and extent of damage or inhomogeneity in wood includes various techniques that utilize, as a source of the active system, an electromagnetic wave in X-ray range. Thus, wood treatment processes may involve the use of antenna systems applied in the diagnostics of breast carcinoma [2] or utilization of the X-ray diagnostic method known in the fields of human or veterinary

medicine. With this technique, however, there occurs certain difficulty related to the evaluation of damage to the material volume. In spite of the fact, a cycle of tests using damaged material samples (Fig.3) has led to an alternative approach; this solution is based on the evaluation of the obtained shot image through a transparent X-ray method having a high rate of image resolution.

3. Solution proposal

The described method utilizes a high-quality X-ray shot of the diagnosed material as well as a very effective image processing technique. The image was segmented, with subsequent evaluation of the required mapping of damage rate realized through filtration. At this point, for example, the evaluation of shot no. 1 is represented in the resolution of damage probability shown is Fig. 3. For image processing, we applied the Otsu filter, the binary filter, and the mean filter. These filters were implemented by the help of convolution techniques [3]. While the Otsu filter automatically calculates the threshold value by the scatter maximization, the binary filter enables the user to define user value for sensitive separation of the structure from the image background [4].

The multiple Otsu filter is based on an algorithm [5], and it is capable of determining multiple threshold values in such a manner that the mutual scatter of intervals determined by these threshold values is the maximum. Threshold value of the i-th group, number of points on the i-th threshold, total number of points, total number of colour pigments, total number of threshold groups are computed.

The stages of processing (Fig. 3) represent individual steps of progressive filtration including the identification of main threshold values from the input x-ray image to the resulting interpretation composite together with the quantification of the individual image segments.

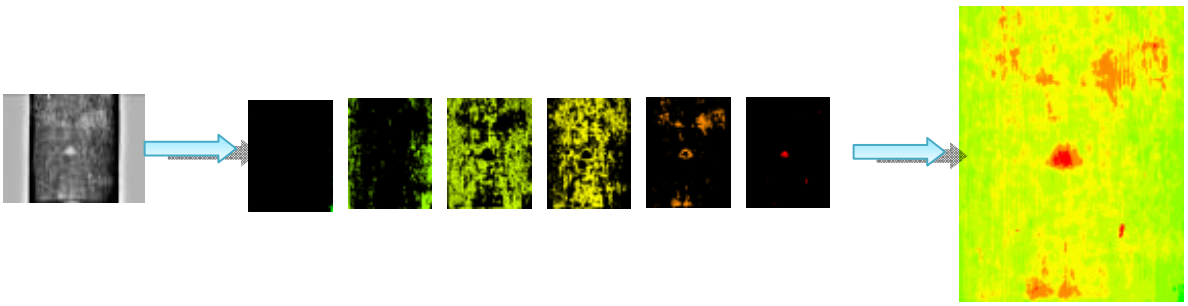

Fig. 3. Progress of filtration in X-ray images.

4. Experiments

Structural element infested wood-destroying insects such as old-house borer (Hylotrupes bajulus), common house borer (Anobium punctatum) was tested. The device used was following: X-ray source EcoRay HF1025, 40-100 kV, 0.32 – 50 mAs, focus 1.2 mm, digital radiography sensor Minolta, 87/125 mm/pixel, 500 x 400 mm, no filters was used. Scans were performed through the wall and in two orthogonal axis of wood girder for 3D evaluation. Fig. 4 shows maggot print inside wood sample acquired by X-ray shot – wood-destroying insects. Structural element infected wood-destroying insects in external location (old building) and experiment setup can be seen in Fig. 5.

Fig. 4. The X-ray images of insects localisation.

Fig. 5. The X-ray diagnostic in external location – Na mlýně Štramberk.

5. Conclusions

We designed and tested an X-ray transparent diagnostic method for 2-D imaging and 3-D quality evaluation with respect to the assigned image parameters. The parameters were set in such a manner as to enable the imaging of shot sections showing the rate of damage to the heterogeneous structure building. Experiments were carried out with the application of microwave power to eliminate wood decaying fungi and wood-destroying insects.

Acknowledgements

The research described in the paper was financially supported by a grant of the project of the BUT Foundation Agency FEKT-S-11-5, project funded by the Education for Competitiveness Operative Programme CZ.1.07.2.3.00.20.0175, and the Thermosanace Company Czech Republic. This paper also benefited from the use of the Insight Segmentation and Registration Toolkit (ITK), an open source software developed as an initiative of the U.S. National Library of Medicine.

References

[1] Prosser V. Experimentální metody biofyziky, Academia Praha, 1989.

[2] O'Halloran M., Glavin M., and Jones E., Channel-ranked beamformer for the earlydetection of breast cancer, Progress In Electromagnetics Research, Boston, USA.

[3] YOO, T. S., 2004: Insight into Images – Principles and Practice for Segmentation, Registration, and Image Analysis, A K Peters, Ltd. Wellesey, p. 393.

[4] Ibáñez, L., Schroeder, W., NG, L., Cates, J., The ITK Software Guide – Second Edition Updated for ITK version 2.4, Kitware, Inc., pages 804, ISBN 1-930934-15-7.

[5] Liao, P. S., Chen, T. S., & Chung, P. C. (2001). A fast algorithm for multilevel thresholding. *Journal of information science and engineering*, 17(5), 713–728. Institute of Information Science Academia Sinica.

Influence of Image Bit Depth for Subpixel Detection Sensitivity

L. Šroba, R. Ravas

Slovak University of Technology in Bratislava, Faculty of Electrical Engineering and Information technology, Institute of Electrical Engineering, Bratislava, Slovakia
Email: lukas.sroba@stuba.sk

Abstract. *Determination of corner point in subpixel accuracy is widely used in image processing area these days and it has high significance in many practical applications. This contribution deals with sensitivity of subpixel detection if we consider the influence of image bit depth. For this experiment there was a very accurate pointing device chosen and sets of images for every position taken. The main goal is comparison of found corner point subpixel coordinates and standard deviations for every bit depth we consider. The results are illustrated in a plot and listed in a table. This contribution answers the question if the really high bit depth can improve the subpixel detection sensitivity in case of standard brightness condition and, if the usage of these high bit depth cameras is reasonable for this purpose.*

Keywords: Subpixel Detection, Harris Detector, Bit Depth

1. Introduction

The area of corner point detection is well known and very often used in many practical tasks, for example motion tracking, object detection and recognition, 3D modelling and many others. As it is known, the smallest part of an image is a pixel. We cannot access information "between" pixel in usual. But there is a possibility to use some mathematical techniques to interpolate or approximate the brightness intensity among pixels and increase the accuracy of detected corner points. The possibility of a more accurate location can decrease costs for cameras and other hardware equipment. Be able to find the chosen image features with a better accuracy could be very useful in many practical fields. For example, the camera calibration or experimental measurement verifications for specific sensors [1] are just some of them. This paper slightly follows our previous papers [2], [3] dedicated to accuracy and sensitivity of subpixel detection. The main aim was to investigate the effect of image bit depth on detection sensitivity results we can obtain. Reference [4] deals with precision of subpixel detection for example.

2. Harris corner detector

We can imagine corner point as a point, where at least two edges are intersected, the point around which is high change of brightness intensity in all directions or the point having the smallest radius of curvature for example. Many corner detectors were invented over the years and the Harris corner detector is one of the most famous. This detector was developed by Chris Harris and Mike Stephens in 1988 [5]. The basic idea is to find the minimum of intensity difference between the chosen part of an image (marked as W) and the shifted part of image W in all directions. There is the first-order Taylor series approximation for that purpose used:

$$M(x,y) = \sum_{W} \left(\begin{bmatrix} I_x \\ I_y \end{bmatrix} \cdot \begin{bmatrix} I_x & I_y \end{bmatrix} \right) \tag{1}$$

The first step is determination of the matrix M as it is shown in Eq. 1. The variables I_x, I_y are approximations of derivations (also referred as differences) in horizontal and vertical

directions. These differences are usually computed by using suitable convolution masks. The window W has usually size 3x3, 5x5 or 7x7 pixels. The matrix M is calculated for every pixel in the image. The next step is determination of the matrix C by using Eq. 2. But there are many possible modifications of this formula. The matrix C has the same size as the original image and it contains the specific value for every pixel in the image.

$$C(x, y) = \min(\lambda_1(x, y), \lambda_2(x, y)) \tag{2}$$

The variables x and y are coordinates of a particular pixel in the corresponding directions. The symbols λ_1, λ_2 are eigenvalues of 2x2 sized matrices M and they are computed by using appropriate mathematic formulas.

The last step is looking for elements in the matrix C having the highest values. These points are marked as corner points. It is necessary to use global and local thresholding, of course. As it is obvious, this algorithm can be used to find corner points with pixel accuracy. If we want to obtain the subpixel coordinates using Harris detector, we need to interpolate the brightness intensity values among the pixels. For that reason, bilinear or bicubic interpolation is usually used. The procedure is following: Firstly, we find corner points with pixel accuracy according to the method we mentioned before. Then we choose the small window surrounding corner pixel and define the brightness intensity values among the pixels. We may use step 0.01 pixel between original pixels for example. It means that 1 pixel contains 100 subpixels in this case. So we can reach 100 times higher accuracy as initially. The rest of the procedure is exactly the same as we described before.

3. Experimental tests

The tests we have taken are very similar to the tests described in [2], [3]. We have chosen very accurate (up to 0.01 mm) pointing device. We fixed a small picture of chessboard segment (because it contains easy detectable X-corner points) to pointing device and we set small shifts on device (the orders of hundredths of millimeters) in horizontal direction. Then we took series of images with high-resolution camera and we found subpixel coordinates by the Harris corner detector from every single image from series. There were 30 images for 10 different positions taken in our measurement.

Our research is based on comparison of the found corner point subpixel coordinates and standard deviations for every bit depth. We consider 8, 7, 6, 5 and 4 bit length values. It also slightly follows our previous papers [3] and especially [2], dedicated to sensitivity of the subpixel detection. All shifts on the pointing device are recalculated in pixels, not hundredths of millimeters. It is important to notice, that we got the images under standard lighting conditions (brightness intensity changes).

4. Experimental results

There are 5 different types of values in Fig. 1 and they are marked as A, B, C, D and E in legend. It represents the average values of horizontal coordinates (based on the used pointing device shifts) for 8, 7, 6, 5 and 4 bit length in the corresponding order. This plot is illustrative example of subpixel coordinates we can obtain, if we set the different bit length. As can be seen, there is very small difference between data A and the other type of data in case of data B and C. In case of the values D and mainly E, there is a little bit more significant difference (up to 0.03 pixels).

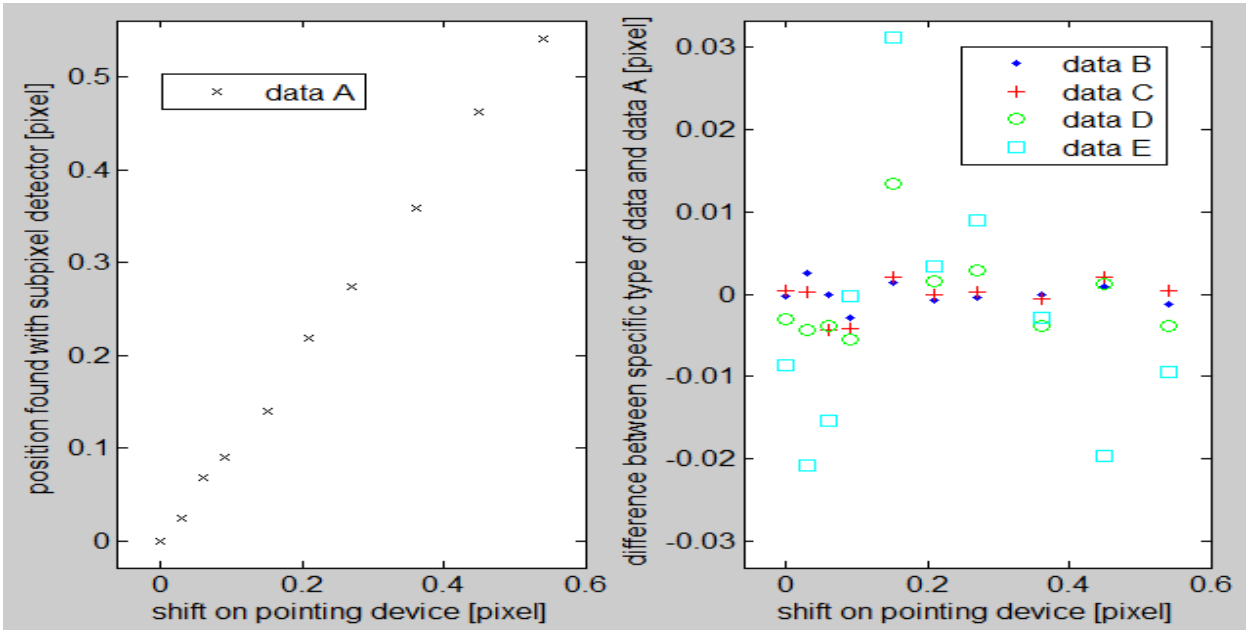

Fig. 1. Horizontal subpixel coordinates for every considered bit length

It is caused by smaller number of bits used for coding the brightness intensity value.
We determined the standard deviation for every single shift in every considered bit length. It is obvious, that average values of the corresponding data are very similar in case of 8, 7 and 6 bit length (*A*, *B* and *C*). If we compare our findings to the results published in [2], we can see that the smallest distance necessary to differentiate shift of image (shift of pointing device) for 8 bit length is around 15 hundredths of pixel. This quantity was determined by comparing 3σ limits between various positions. Because of very similar standard deviation stated for *A*, *B* and *C*, we can also assume sensitivity of subpixel detection around 15 hundredths of pixel for all of them. The standard deviations of *D* and *E* prove that, if we use only 5 or 4 bit depth, then the sensitivity and accuracy of subpixel detection decrease rapidly.

Table 1. The standard deviations for every considered bit length

data	**A (8 bits)**	**B (7 bits)**	**C (6 bits)**	**D (5 bits)**	**E (4 bits)**
shift [pixel]	*σ [pixel]*	*σ [pixel]*	*σ [pixel]*	*σ [pixel]*	*σ [pixel]*
0	0.0200	0.0198	0.0183	0.0185	0.0175
0.03	0.0174	0.0168	0.0161	0.0226	0.0306
0.06	0.0187	0.0207	0.0211	0.0239	0.0356
0.09	0.0180	0.0189	0.0216	0.0249	0.0406
0.15	0.0221	0.0218	0.0230	0.0295	0.0321
0.21	0.0180	0.0177	0.0185	0.0189	0.0279
0.27	0.0208	0.0201	0.0218	0.0236	0.0314
0.36	0.0144	0.0139	0.0135	0.0188	0.0190
0.45	0.0105	0.0121	0.0141	0.0176	0.0260
0.54	0.0159	0.0167	0.0174	0.0224	0.0394
$\bar{\sigma}$	**0.0176**	**0.0178**	**0.0185**	**0.0221**	**0.0300**

It is obvious that increasing of the bit depth (more than 8 bits) is not necessary, especially in standard brightness conditions. One of possible explanations might be that reducing of image bit length works also as a smoothing filter (Gaussian for example) and smoothing is usually the first step in subpixel detection to avoid noise in image.

5. Conclusions

This contribution deals with the sensitivity of subpixel detection considering the influence of various image bit depth values. The Harris corner detector was chosen for its very good detection qualities and a possibility to be successfully applied in real conditions. We implemented the experiments with a very accurate pointing device. Then we have been changing positions of a chessboard image fragment and we observed how obtained coordinates change. We performed statistic analysis resulting in a plot and table.

As it is shown in Fig. 1, the found absolute horizontal coordinates of our data types (8, 7 and 6 bit depth) are very similar and there is no significant difference between them. Only in case of *D* and especially *E* (5 and 4 bits), the difference is a little bit more significant. This is caused by smaller number of bits used for coding the brightness intensity value and this kind of image cannot approximate original image well enough. We determined the standard deviation for every single shift in every considered bit length. We found that sensitivity of subpixel detection for 8, 7 and 6 bit depth is around 15 hundredths of pixel. The standard deviations for *D* and *E* prove that, if we use only 5 of 4 bit depth, then the sensitivity and accuracy decrease rapidly. Increasing of the bit depth (more than 8 bits) in case of standard lighting conditions is not reasonable for that reason. It could be caused by smoothing character of decreasing bit depth. The possibility to use, e. g. 6 bit length instead of usual 8 bit length (75% of all bytes amount) is very convenient in many applications, where data compression is a goal and we can still reach very similar precision and sensitivity of detection.

Acknowledgements

This work was supported by the Slovak Research and Development Agency under the contract No. APVV-0333-11 and VG-1/0936/12.

References

[1] Marsalka L, Hartansky R. Electromagnetic method for distance measurement on MEMS structures, Modern Machinery Science Journal, ISSN 1803-1269, pp. 48-53, 2011.

[2] Sroba L, Ravas R. Sensitivity of subpixel corner detection, 23rd DAAAM International Symposium, pp 0743-0746, 2012.

[3] Sroba L, Ravas R. Comparison of 2 various approaches to determine subpixel coordinates of corner point in static scene, 2nd Theoretical and Applied Aspects of Cybernetics, 2012.

[4] Stock Ch, Muhlmann U, Chandraker M. K, Pinz A. Subpixel corner detection for tracking applications using CMOS camera technology, 26th Workshop of the AAPR/OAGM, 191-199, 2002.

[5] Harris Ch, Stephens M. A combined corner and edge detectors, In Alvey Vision Conference, pp. 147-152, 1998.

Precise Edge Detection in 1-D Images for Contactless Measurement of Object

M. Hagara, P. Kulla

Institute of Electronics and Photonics FEI STU, Bratislava, Slovakia
Email: miroslav.hagara@stuba.sk

Abstract. *In some industrial applications it is necessary to measure only a single dimension of object. In such cases 1-D camera is sufficient and non-contact measurement is mostly based on edge detection with a precision of one pixel. If we need to increase the accuracy of measurement, we have two options, either use a 1-D optical sensor with more pixels or increase the accuracy of edge detection. In this paper we present comparison of four methods for edge detection with sub-pixel accuracy in 1-D images: method based on approximation of real image function with erf function, moment-based edge operator, technique using spatial moments of the image function and the method based on wavelet transform of image. The paper presents results of simulations as well as of experiments to compare methods in terms of accuracy, the standard deviation of the edge localization error is chosen as precision criterion.*

Keywords: Edge Detection, Sub-pixel Accuracy, Image Processing

1. Introduction

Some applications, e.g. measurement of the objects with high precision, need to detect edges with sub-pixel accuracy in 1-D images. There are a lot of methods for edge detection with sub-pixel accuracy and user can have a problem, which method is most suitable for his concrete purpose. This is a reason why we present in this paper the comparison of four methods for edge detection with sub-pixel accuracy in 1-D images: method based on approximation of real image function with erf function (AEF) [1], gray level moment (GLM) edge operator [2], spatial moment (SM) edge detector [3] and edge detector [4] based on wavelet transform (WT). We used simulations as well as experiments to compare methods in terms of accuracy and we chose standard deviation of the edge localization error as precision criterion.

2. Edge Detectors with Sub-pixel Accuracy for 1-D Images

Tabatabai and Mitchel proposed grey level moment (GLM) edge operator for 1-D image [2] based on the first three moments of the input data sequence:

$$m_i = \frac{1}{n}\sum_{j=1}^{n} x_j^{\,i} \quad \ldots\ i = 1,2,3 \quad , \tag{1}$$

where $x_1, x_2, \ldots x_n$ are image samples. Let suppose that they are the samples of ideal step edge (Fig. 1a) and p_h is a number of samples with gray level h (they are the pixels on the left of the edge). If we define the densities p_1 and p_2 as:

$$p_1 = \frac{p_h}{n} \tag{2}$$

$$p_2 = \frac{n - p_h}{n} = 1 - p_1 \tag{3}$$

then solution of three equations

$$m_1 = (1-p_2)h + p_2(h+k) \tag{4}$$

$$m_2 = (1-p_2)h^2 + p_2(h+k)^2 \tag{5}$$

$$m_3 = (1-p_2)h^3 + p_2(h+k)^3 \tag{6}$$

with three unknown variables h, k, p_2 results in

$$p_2 = \frac{1}{2}\left(1 + s\sqrt{\frac{1}{4+s^2}}\right), \tag{7}$$

where

$$s = \frac{m_3 + 2m_1^3 - 3m_1m_2}{\left(m_2 - m_1^2\right)^{3/2}} . \tag{8}$$

In the case of real image, $p_h = n.p_1$ is not integer and represents sub-pixel edge location. Another sub-pixel edge detector [3] is based on spatial moments (SM) of continuous function $f(x)$ of order p, which are defined

$$M_p = \int x^p f(x)dx . \tag{9}$$

Let function $f(x)$ represents step edge and x is from –1 to +1 (Fig. 1b), to simplify calculations. Then Eq. 9 for $p = 0, 1$ and 2 can be written as

$$M_0 = h\int_{-1}^{1} dx + k\int_{l}^{1} dx = 2h + k(1-l) \tag{10}$$

$$M_1 = h\int_{-1}^{1} x\,dx + k\int_{l}^{1} x\,dx = \frac{1}{2}k(1-l^2) \tag{11}$$

$$M_2 = h\int_{-1}^{1} x^2\,dx + k\int_{l}^{1} x^2\,dx = \frac{2}{3}h + \frac{1}{3}k(1-l^3) . \tag{12}$$

The solution of these equations results in formula for edge location l

$$l = \frac{3M_2 - M_0}{2M_1} . \tag{13}$$

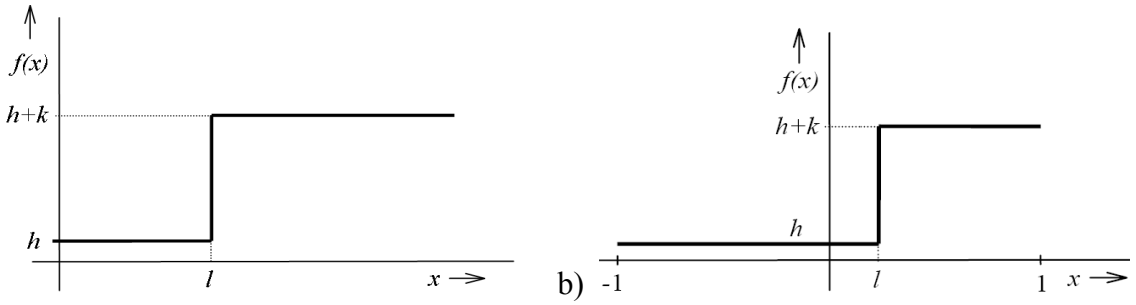

Fig. 1. a) Step edge model. b) Edge model for spatial moment edge detector.

Third edge detector used for comparison is based on wavelet transform [4]. If x_1, x_2, ... x_n are the samples of the image and $W_s(x_i)$ are values of wavelet transform, then

$$p_i = \frac{W_s(x_i)}{\sum_{j=1}^{n} W_s(x_j)} \tag{14}$$

is the probability that the sample $W_s(x_i)$ of wavelet transform is a local maximum. Position l of the edge is calculated using the formula

$$l = \sum_{i=1}^{n} i.p_i \,. \tag{15}$$

Last sub-pixel edge detector used for comparison is based on approximation of real image function $f_r(i)$ with function $f_a(x)$ [1], which is equal to

$$f_a(x) = \frac{k}{2}\left(erf\left(\frac{x-l}{\sqrt{2}\sigma} \right) + 1 \right) + h \,, \tag{16}$$

where

$$erf(x) = \frac{2}{\sqrt{\pi}} \int_0^x e^{-t^2} dt \,. \tag{17}$$

Function $f_a(x)$ has four parameters $–h$, k, l and σ. The core of this AEF edge detector is parametric fitting by minimizing a difference between the real image function $f_r(i)$ and function $f_a(i)$. This difference is defined

$$E(h,k,l,\sigma) = \sum_{i=1}^{N} \left(f_r(i) - f_a(i) \right)^2 \tag{18}$$

where N is a number of samples. Minimizing the difference $E(h,k,l,\sigma)$ gives subpixel edge location l. Edge detection algorithm based on approximation consists of three steps: edge detection with pixel accuracy, initial values estimation of parameters (h,k,l,σ) and parametric fitting by minimizing difference function $E(h,k,l,\sigma)$. First step can be done by any edge detection method with pixel accuracy. One can find how to estimate initial values σ_0, h_0 and k_0 in [1]. To minimize difference function $E(h,k,l,\sigma)$ we apply Matlab function *fminsearch*.

3. Results of Simulations and Experiments

We did all simulations in program Matlab. Let there is 1-D image sensor which consists of elements with width w and gap g between two sensor elements. Let the brightness around the edge is constant in time and varies only in the direction x according to blurring edge model [5]. Then simulated noiseless output signal $f_{rs}(i)$ is [1]

$$f_{rs}(i) = \gamma T_a \int_{i-w/2}^{i+w/2} \left(\frac{k}{2}\left(erf\left(\frac{x-l}{\sqrt{2}\sigma} \right) + 1 \right) + h \right) dx \,, \tag{19}$$

where σ represents edge blurring parameter, γ is sensor integral sensitivity and T_a is accumulation time. For simulations we can set $\gamma T_a = 1$, $w = 1$, $h = 0.1$ and $k = 1$. To add noise to signal defined in Eq. 19 we apply Matlab function *randn*, which returns a pseudorandom value with a normal distribution. We did simulations for signal-to-noise ratio $SNR = 30$dB. To get random difference c between actual position of the edge and centre of corresponding sensor element we used Matlab function *rand*, which returns pseudo-random values drawn from a uniform distribution on the unit interval, so $c = rand - 0.5$. We calculated noisy signal for different values of blurring parameter σ with random c two thousand times and for each noisy signal we used 31 samples around the edge to find sub-pixel edge location. Then we calculated edge location error for all realizations and for these errors we determined the standard deviation STD_{cn}. Results are presented in Table 1 and in Fig. 2a. For experimental verification we shot few images of car engine valve. We shot some images with manual focusing so we got unfocused images with different values of blurring parameter. Since the valve must be perfectly straight, computed sub-pixel edge positions should create a straight line, which can be represented as polynomial. Difference between the computed edge position and the value of the polynomial can be considered to be the edge location error. Obtained results are presented in Table 2 and in Fig. 2b.

Table 1. Standard deviation STD_{cn} (in px) of edge location error of simulated noisy signal.

σ[px]	0.75	1	2	3	4
AEF	0.029	0.032	0.048	0.060	0.082
GLM	0.030	0.033	0.050	0.720	0.127
SM	0.083	0.082	0.082	0.115	0.241
WT	0.093	0.087	0.097	0.122	0.234

Table 2. Standard deviation STD_e (in px) of edge location error (experiments).

σ_s [px]	0.84	1.54	2.18	3.25	4.25
AEF	0.031	0.043	0.060	0.075	0.092
GLM	0.031	0.043	0.060	0.094	0.129
SM	0.045	0.045	0.062	0.129	0.236
WT	0.054	0.047	0.063	0.144	0.265

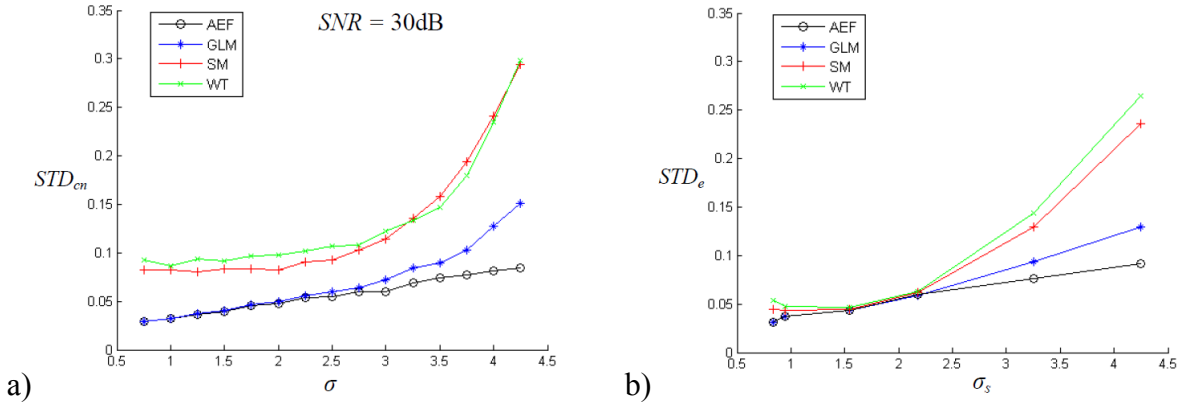

Fig. 2. Standard deviation of edge location error (in px): a) simulations, b) experiments (σ and σ_s are in px).

4. Discussion

We can conclude on the basis of simulations and experiments that for well-focused images ($\sigma < 1$) AEF and GLM methods offer highest accuracy. GLM can be preferred because it has the lowest computation time among all the compared methods. For slightly unfocused real images ($1 \leq \sigma < 2.5$) the accuracy of all methods is roughly equal. However, GLM method can be preferred because of its lowest computation time. For strongly unfocused real images ($2.5 \leq \sigma$) AEF method is most accurate. But the computational time of this method is significantly larger than computational time of the GLM method, so it can be used in the case, if computational time is not important.

Acknowledgements

This work was supported by grant No. VEGA 1/0987/12.

References

[1] Hagara M, Kulla P. Edge detection with sub-pixel accuracy based on approximation of edge with erf function. *Radioengineering*, 20 (2): 516-524, 2011.

[2] Tabatabai AJ, Mitchel OR. Edge location to subpixel values in digital imagery. *IEEE Transactions on Pattern Analysis Machine Intelligence*, 6 (2): 188-201, 1984.

[3] Lyvers EP, Mitchel OR, Akey ML, Reevs AP. Subpixel measurements using a moment-based edge operator. *IEEE Transactions on Pattern Analysis Machine Intelligence*, 11 (12): 1293-1309, 1989.

[4] Xu GS. Study on a fast method for sub-pixel edge detection. In proceedings of the 3rd International Conference on Information and Computing, 2010, 141-144.

[5] Zhang W, Bergholm F. Multi-scale blur estimation and edge type classification for scene analysis. *International Journal of Computer Vision*, 24 (3): 219-250, 1997.

The Use of Brightness Correction Improvement in Defectoscopy of Transparent Polymeric Foils

L. Syrová, R. Ravas

Slovak University of Technology in Bratislava, Faculty of Electrical Engineering and Information Technology, Institute of Electrical Engineering, Bratislava, Slovakia
Email: livia.syrova@stuba.sk

Abstract. *The contribution treats the topic of analysis of deformations sources of visualized transparent polymeric foils images by the schlieren method and by methods of image processing. The brightness deformations caused by the in-homogeneity and imperfection of tested material are visualized by schlieren system and by methods of image processing. A new method of correction of brightness distortion is presented. The method is completed by the image correction of foil based on the equalizing local mean values of greyscale to the global mean value of the image excluding pixels with outlying brightness. The described correction is applied on the detection of polymeric foils defects.*

Keywords: Schlieren, Optical Visualization, Polymeric Foil, Brightness Correction, Defectoscopy

1. Introduction

Optical visualization methods utilize changes in the absorption of photons during their transmission through mechanically loaded regions. With regard to the equipment of our optical laboratory we have chosen schlieren visualization method. Schlieren system serves to measure the amount of light deflection generated by an optical transparent phase object. A parallel light beam traverses the test object and is focused thereafter by means of a lens of spherical mirror, named the schlieren head. Optical apparatus constructed after J. Bolf [1] consists of the light source. Light beam traversing the test object is deviated along the optical path from the nominal course corresponding to the absence of variations of refractive index. The camera objective focuses the test object onto the recording plane, where a reduced intensity of light, depending on the amount of light cut off by the carefully adjusted diaphragm can be observed. Without any disturbances in the optical path the original light source will have uniform reduction in intensity due to the light cut-off by the diaphragm. When there is a disturbance in the optical path, the light rays will be deflected. The biggest advantage of Schlieren method is that it provides an illustrative and comprehensive picture of the nature of the flow, it provides useful information on the visually inaccessible objects such as optically transparent materials, especially, polymeric foils [2], [3]. Digital recording can be further processed by means of image processing methods enabling defectoscopy and classification of tested polymeric foils.

2. Brightness correction

In order to evaluate images gained by the optical visualization of polymeric foils by image processing it is necessary to correct influence of non-homogeneity of light source, influence of the optical string and the sensing device [4]. One of the possibilities is to use reference image picked up without presence of test object. The reference image can be taken as an image of errors of the whole optical system provided that we have used a virtual light source [5]. Correction of brightness errors is necessary for the further image processing. The brightness disturbances can be caused by non-colinearity of optical axes of the condenser lens and the objective lens [4], non-homogeneity of the light source and impurities in the optical

path. When we scan the image by the schlieren apparatus without presence of the tested foil brightness distortions of the obtained image represent image of distortions of the optical path and non-homogeneity of light source. Formula for corrected foil image $f_C(i,j)$

$$f_C(i,j) = \frac{c}{f_e(i,j)} . f(i,j) \tag{1}$$

where f(i,j) is distorted foil image, $f_e(i,j)$ is an image of distortions from virtual ideal homogenous light source whose image in ideal case is the image with the constant brightness c. The value c is chosen in order to have brightness value of corrected image in boundaries of display access. Correction [5] is based on the fact that in case of the foil without defects each area of image of visualized foil structure of sufficient size should have the same mean value. Image of foil I(i,j) of size NxN has been divided into square disjunctive areas J(m,n) of size KxK, where K=N/k. Coefficient of correction of radial deformation for the area centre is described by

$$C\left((m-1)K+\frac{K}{2},(n-1)K+\frac{K}{2}\right) = \frac{\frac{1}{N^2}\sum_{i=1}^{N}\sum_{j=1}^{N} I(i,j)}{\frac{1}{K^2}\sum_{i=(m-1)K}^{mK}\sum_{j=(n-1)K}^{nK} I(i,j)} \tag{2}$$

When to put $m_K = (m-1)K + \frac{K}{2}$ $n_K = (n-1)K + \frac{K}{2}$ then the coefficient (5) can be expressed by $C_{m,n} = C(m_K, n_K)$. We shall calculate value of correction for the arbitrary point of the image by the bilinear transformation of coefficients (3) of four nearest areas centres to the given point. When for i, j $i \in \langle r_K, (r+1)_K \rangle$, $j \in \langle s_K, (s+1)_K \rangle$ and when to mark A, B as

$$A = C_{r,s} + \frac{C_{r+1,s} - C_{r,s}}{K}(i - r_K) \qquad B = C_{r,s+1} + \frac{C_{r+1,s+1} - C_{r,s+1}}{K}(i - r_K)$$

Brightness values of corrected image are calculated from

$$f_{CR}(i,j) = f_C(i,j).C(i,j) \tag{3}$$

where $C(i,j) = A + \frac{B-A}{K}(j - s_K)$.

3. Experimental results

Images of visualized foils have been captured by a color still camera because of higher resolution (5 megapixels). Quantization error of brightness level with 256 levels of brightness using equation (1) causes that distortion correction towards lower values are characterized by higher relative error. This effect gives rise to the fact that greater brightness distortions are not sufficiently corrected. It can be seen that image brightness distortion are caused by the global tendency of decrement in brightness with increasing distance from the optical axis of the schlieren apparatus. Fig. 1 demonstrates the difference between results of brightness correction according to (1) and (3) on the images of foil sample KXE20.

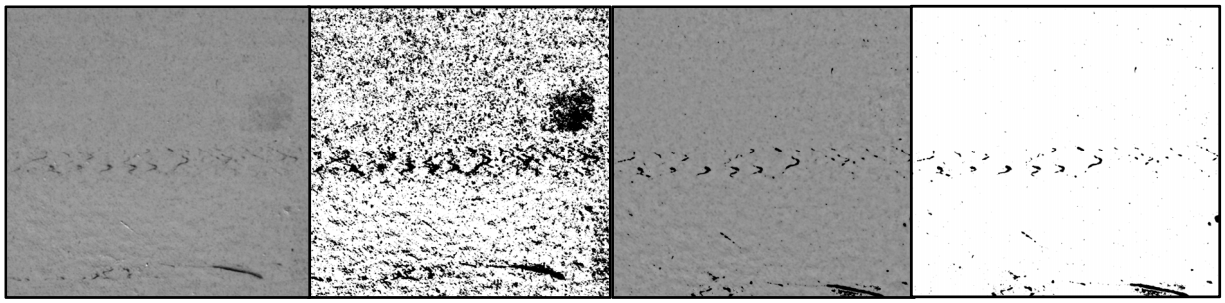

a/ b/ c/ d/

Fig. 1. Images of foil KXE20 a/ after correction according (1), b/ thresholded image corrected according (1), c/after correction according (3), d/ thresholded image corrected according (3)

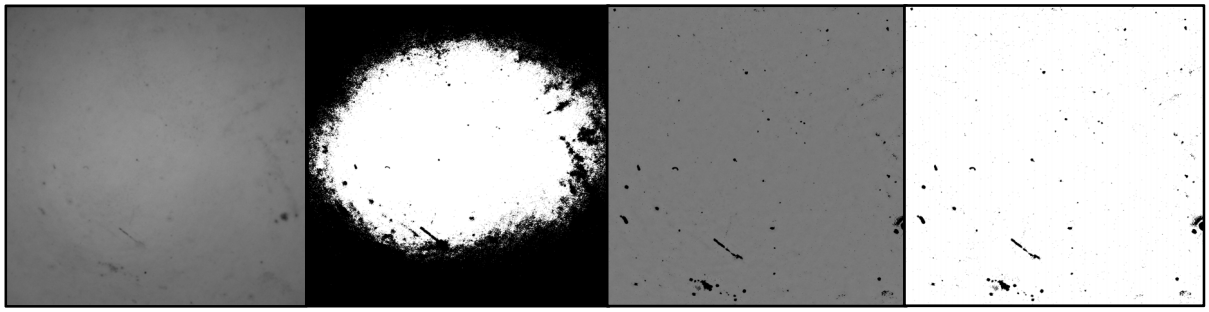

a/ b/ c/ d/

Fig. 2. Reference image a/ without foil corrected according (1), b/ thresholded image according (1), c/ after correction according (3), d/ thresholded image corrected according (3)

Imperfection of the correction is visible in Fig. 1.b created by the thresholding by the optimal global threshold (Otzu) of corrected image (Fig. 1. a) by the method (1). Good properties of correction of the image 1.c according (3) demonstrates Fig. 1.d obtained by the thresholding of the image 1.c by the same method as the image 1.b was.

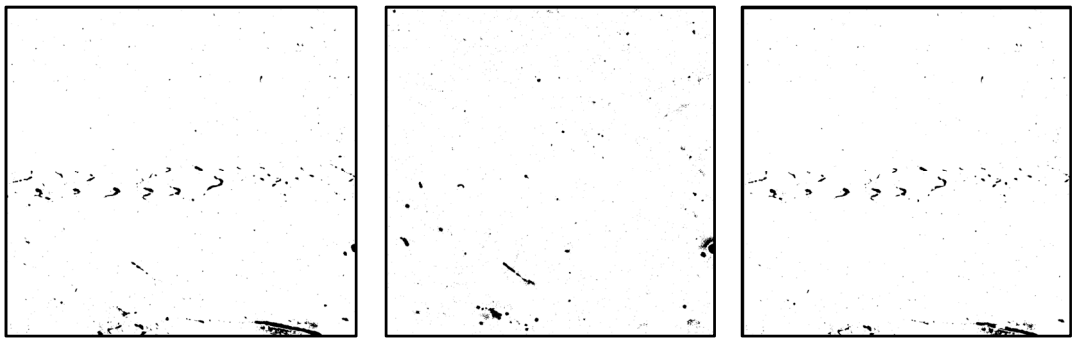

a/ b/ c/

Fig. 3. Thresholding of corrected images by method (3) a/ foil KXE20 with defects and with anomalies of optical path, b/ reference image, c/foil KXE20 with defects but without anomalies caused by the optical path.

The ability of method (3) to correct the inhomogeneity of the light source caused by the tendency of image intensity reduction with increasing distance from the optical axis demonstrates Fig. 2 for image gained by the schlieren system without foil sample. Method (3) demonstrates good properties in Fig. 2.c presenting corrected image Fig.2.a. Correction quality proves thresholded image Fig. 2.d of the image Fig. 2.c. From Fig. 1.d and Fig. 2.d it is evident that correction (3) doesn't suppress nor deform local anomalies of the image brightness level. As the significant anomalies we shall consider such areas whose brightness

level after correction exceeds k.σ (k multiple of the standard deviation from mean brightness level of all image). During the foil recognition from their images these areas are excluded from the calculation. In the case of defectoscopy marked areas in Fig. 2.d detect local anomalies of the optical path of the schlieren system that logically are areas where it is not possible to localize defects of the tested foil. In the case of foil images mentioned anomalies in the image can be caused by the foil defect. The fact enables to visualize only defects of the foil without anomalies caused by the optical path. Correction (3) gives a relatively simple representation of anomalies in the image of distorted foil. In Fig. 1.d we can see not only deformation caused by the defects of the foil but also anomalies caused by the optical path. There are only anomalies of the optical path in Fig. 2. Detection of defects is based on the extraction of optical path anomalies from images of tested foils. Described procedure demonstrates Fig. 3. There are visualized anomalies caused only by the defects of tested foil in Fig. 3.c.

4. Conclusions

The contribution presents application of a new approach concerning correction of brightness levels of visualized polymeric foils images in defectoscopy. In contrast with method [6] that was able to detect only areas with extensive defects described method localizes and distinguishes significantly smaller defects. As a result the method enables to analyse shape, frequency and distribution of defects in the image.

Acknowledgements

This work was supported by the Slovak Research and Development Agency under the contract No. APVV-0333-11 and VG-1/0936/12.

References

[1] Bolf J, Bajcsy J, Bolf P. Methods of the properties testing of optically transparent materials. *Journal of Electrical Engineering*, 44 (8): 244-247, 1993 (in Slovak).

[2] Brownlee C, Pegoraro V, Shankar S, McCormick PS, Hansen CD. Physically-based interactive flow visualization based on schlieren and interferometry experimental techniques. *IEEE Transactions on Visualization and Computer Graphics*, 17(11): 1574-1586, 2011.

[3] Castle DA, Gibbins B, Hammer PS. Physical methods for examining and comparing transparent plastic bags and cling films. *Journal of Forensic Science Society*, 34: 61-68, 1994.

[4] Ravas R, Syrová L, Grman, J. Analysis of selected factors in the diagnostic testing of optically transparent polymeric foils. *Measurement Science Rewiev.* 3: 163-167, 2003.

[5] Ravas R, Syrova L, Grman J. Correction of optical errors in the images of visualized optically transparent polymeric foils. RADIOELEKTRONIKA '09, 2009, 303-306.

[6] Syrová L, Ravas R, Grman J. Use of statistical approach for defectoscopy of visualized transparent polymeric foils. *Measurement Science Rewiev.* 1: 155-158, 2001.

Biodecorated Magnetic Nanoparticles Preparation, Modification and Properties

[1]P. Capek, [2]A. Dvurečenskij, [2]M. Majerová, [2]J. Maňka, [3]I. Capek

[1]Chemical Institute, Slovak Academy of Sciences, Bratislava, Slovakia
[2]Institute of Measurement Science, Slovak Academy of Sciences, Bratislava, Slovakia
[3]Polymer Institute, Slovak Academy of Sciences, Bratislava, Slovakia
E-mail: andrej.dvurecenskij@savba.sk

Abstract. *For the discussed biomedical applications, the vast number of known magnetic materials is strongly reduced by the demands of biocompatibility including: (i) non-toxicity; (ii) a sufficient chemical stability in bio-environment; (iii) an appropriate circulation time in the blood; and (iv) a harmless biodegradability. As a consequence investigations mainly concentrate on magnetic iron oxides Fe_3O_4 (magnetite) and γ-Fe_2O_3 (maghemite). The quality of the magnetic nanoparticles (MNPs) required for a specific biomedical application is strongly related to their structural and magnetic properties. For most biomedical applications, the particles should have intrinsically a large saturation magnetization allowing for large magnetic moments despite the small particle volumes. Due to the biocompatibility constraint, the choice of magnetic substances is, at least at the moment, concentrated on the strong magnetic iron oxides: magnetite and maghemite.*

Keywords*: Magnetic Nanoparticles, Fe_3O_4, γ-Fe_2O_3, Biotherapeutics, Magnetic Drug Targeting, Hyperthermia*

Subject and Methods

Various synthesis methods were developed and adjusted to meet the requirements for biomedical applications MNPs. The reaction mechanism of microemulsion and the size of metal particles prepared by the microemulsion (the particle diameter varies with the ratio $w = [H_2O]/[\text{surfactant}]$) are summarized in Figs. 1 and 2. At w values below ca. 10, water mobility is greatly reduced (bound water) and particles below 5 nm can be prepared. Above $w = 10$, the linear increase in the water pool diameter, d_w, with w (from 6 to 18 nm) is explained by a geometrical model that assumes a constant area per surfactant molecule and that all surfactant molecules participate in the reverse micelle interface. The volume of water added to the solution is the main parameter controlling the droplet diameter or final particle size [1].

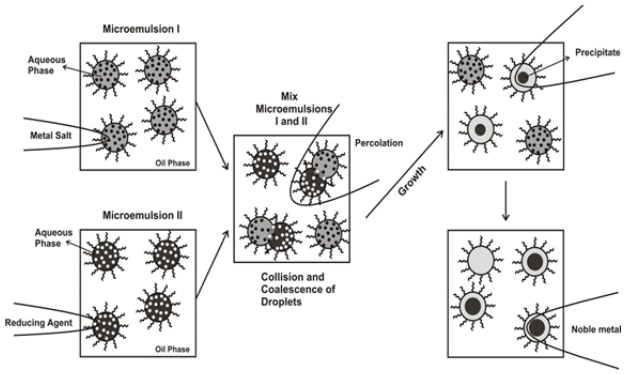

Fig. 1. Proposed mechanism for the formation of magnetic (Fe_3O_4) nanoparticles in the microemulsion.

MNPs with diameter of 8 nm were prepared using a coprecipitation method using NaOH - $FeCl_2$ - $FeCl_3$. An oxidation precipitation method in a $FeCl_2$–$NaNO_3$–NaOH aqueous system appeared

larger 24 - 400 nm MNPs. Core-shell nanoparticles with different coatings (from 10 wt% to 30 wt%) were prepared with various stabilizers such as oleic acid (OA,), sodium bis(2-ethylhexyl)sulphosuccinic acid (AOT), sodium dodecylsulfate (SDS), 2,3-dimercaptosuccinic acid (DMSA), phosphonoacetic acid (PA), dextran (Dx), aminodextran (ADx), carboxydextran (CDx) and citric acid (CA) (Fig. 3). The colloidal stability and particle size is also function of costabilizers (or solvents, such as acetone, acetonitrile,..) which passivate the particle size [1-3].

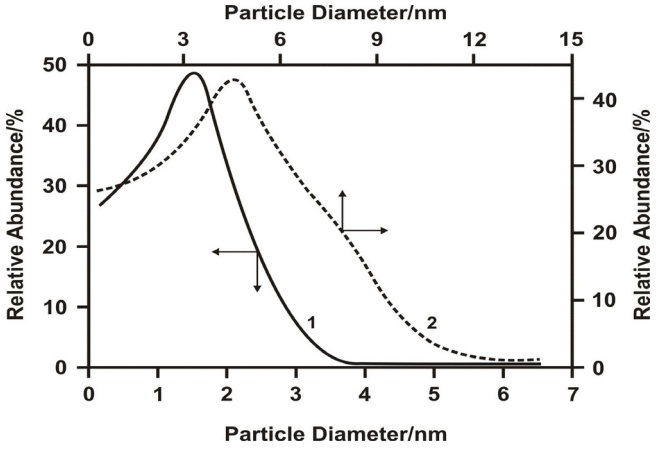

Fig. 2. Variation of particle diameter with $w = [H_2O]/[Na(AOT)]$, (1) $w = 2.5$, $d = 1.5$ nm, (2) $w = 15$, $d = 5$ nm, w determines the reverse micelle size where surfactant is adsorbed on the particle surface.

The volume of water added to the solution is the main parameter controlling the droplet diameter.

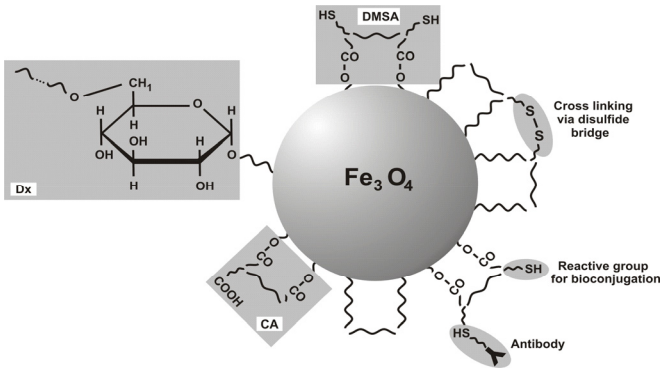

Fig. 3. Schematic picture of 2,3-dimercaptosuccinic acid (DMSA), dextran (Dx) and citric acid (CA) - coated water-soluble Fe_3O_4 where surfactants and chemisorbed on the particle surface which is passivated by solvent molecules.

Nanoparticle dispersion stability depends on charge and surface chemistry, which give rise to both steric and electrostatic repulsion. Conventionally, a zeta potential higher than ±30 mV would be considered stable, i.e., the dispersion will resist aggregation. In the case of DMSA-, PA-, Dx- and CA-coated samples, the ionizable carboxylate groups on their surfaces govern the pH dependent evolution of the Z-potential, whose high values indicate the formation of stable systems. A pure polymer-coated sample, such as dextran sample, shows lower electrostatic stabilization (lower Z-potential), due to the lack of ionizable surface groups; the steric effect helps to maintain a stable dispersion, independently of the pH. The uncoated particles show the typical Z-potential values reported for bare iron oxide nanoparticles (unstable) nanoparticles, which is ~ 0 at pH 7. All negatively charged samples had similar hydrodynamic sizes (~ 80 - 100 nm) and the highest coating (Fig. 4). On the contrary, aminodextran (ADx) has the smallest coating [2].

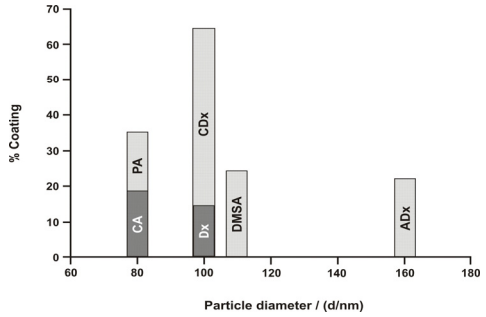

Fig. 4. Variation of % coating with the particle diameter for each surfactant.

MNPs modified with dextran or oleic acid, and functionalized with a polymer or liposome, and/or further conjugated with an anticancer therapeutic drug can also improve the colloidal stability of the magnetic fluid, affinity for the carcinoma cell, or confer a tumor-specific targeting ability. These modified magnetic particles show an improved adsorption and accumulation in the area of a tumor, and also have an improved heating efficiency on exposure to an AC magnetic field (Fig. 5). Particles modified with DMSA showed the most efficient adsorption/release capacity. Changes in synthesis method and particle coating not only altered the crystalline nature of the particles, but also modified their capacity to adsorb and release biomolecules (ligands) [3, 4].

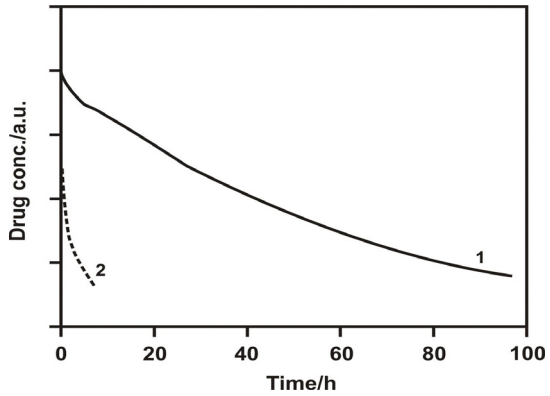

Fig. 5. Nanoparticles can have extended pharmacokinetics over the therapeutic entity alone. The data are from a nanoparticle containing drug (dox) (1) and a small-molecule drug (2) in rats.

Magnetic nanoparticles have been used, for example, for magnetic cell separation or magnetic resonance imaging (MRI). The development of biocompatible nanosized drug delivery systems for specific targeting of therapeutics is the focus of medical research, especially for the treatment of cancer and diseases of the vascular system. An important advantage of these carriers is the possibility for detecting these nanoparticles after treatment with common imaging techniques (i.e. x-ray-tomography, magnetorelaxometry, magnetic resonance imaging), which can be correlated to histology. Magnetic hyperthermia has recently attracted significant attention as a safe method for cancer therapy. It can increase the temperature in tumors to 41 - 46 °C, thereby killing the tumor cells with minimum damage to normal tissue. This method involves the introduction of ferromagnetic or superparamagnetic particles into the tumor tissue, followed by irradiation using an alternating current (AC) magnetic field. In general, magnetic particles generate heat in an external AC magnetic field from several physical mechanisms. These include relaxation loss or hysteresis loss, which strongly depends on the frequency of the external field, as well as the nature of the particles, such as the particle size and surface modifications. The dependence of the magnetization M_s and the coercivity H_c on the particle size d is in the Fig. 6 [5].

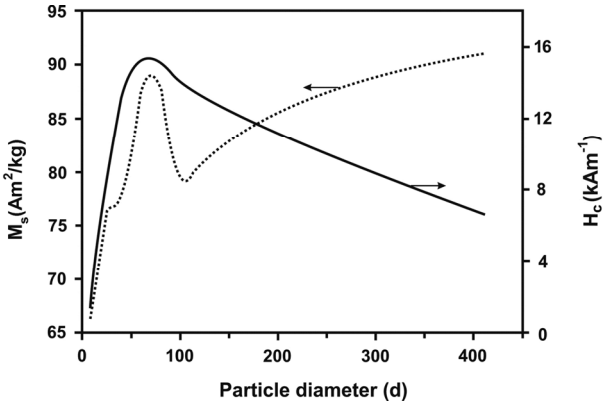

Fig. 6. Variation of the magnetization M_s and the coercivity H_c with the particle diameter d [nm].

Results

There are a variety of nanoparticle systems currently being explored for cancer therapeutics. The material properties of each nanoparticle system have been developed to enhance delivery to the tumor. For example, hydrophilic surfaces can be used to provide the nanoparticles with stealth properties for longer circulation times and positively charged surfaces can enhance endocytosis. Functionalization of nanoparticles with proteins, for example, is necessary to increase circulation times through avoidance of removal by the reticuloendothelial systems (RES). Short circulation times decrease the efficiency of the delivery of the nanoparticle to the tumor site. Incorporation of a hydrophilic groups or segments to the surface of the nanoparticle allows for a reduction in opsonization, which reduces removal by the RES. Active targeting involves the use of peripherally conjugated targeting moieties for enhanced delivery of nanoparticle systems. Although antibody targeting is regarded as a promising strategy, some groups have reported that antibody targeting might not increase tumor localization. The targeting moieties are important to the mechanism of cellular uptake. Long circulation times will allow for effective transport of the nanoparticles to the tumor site through the enhanced permeation and retention (EPR) effect, and the targeting molecule can increase endocytosis of the nanoparticles. The internalization of nanoparticle drug delivery systems has shown an increased therapeutic effect. If the nanoparticle attaches to vascular endothelial cells via a noninternalizing epitope, high local concentrations of the drug will be available on the outer surface of the target cell. Although this has a higher efficiency than free drug released into circulation, only a fraction of the released drug will be delivered to the target cell. In most cases, internalization of the nanoparticle is important for effective delivery of some anticancer drugs, especially in gene delivery, gene silencing, and other biotherapeutics [6].

Acknowledgements

This research was supported by the project APVV-0125-11 and the project 26240220073 of the Agency of the Ministry of Education of the Slovak Republic for the Structural Funds of the EU.

References

[1] Capek I, Nanocomposite structures and dispersions, Science and nanotechnology – Fundamental principles and colloidal particles, D. Mobius and R. Miller (Eds), Elsevier, London, 2006.
[2] Li Z, et al., Materials Science and Engineering C 30 (2010) 990.
[3] Mejías R, et al., J. Controlled Release 130 (2008) 168.
[4] Byrne JD, et al., Adv. Drug Deliv. Rev. 60 (2008) 1615.
[5] Jozefczak A, Skumiel A, J. Magn. Magn. Mater. 311 (2007) 193.
[6] Lee K, et al., Biomaterials 31 (2010) 6530.

Transport and Low Field Magnetic Properties of $Gd_{1+x}Ba_{2-x}Cu_3O_{7-\delta}$ Superconductors with Gadolinium Excess

A. Dvurečenskij, A. Cigáň, J. Maňka, R. Bystrický, M. Majerová, M. Škrátek

Institute of Measurement Science, Slovak Academy of Sciences, Dúbravská cesta 9
841 04 Bratislava, Slovakia
E-mail: andrej.dvurecenskij@savba.sk

Abstract. *A series of single-phase samples of $Gd_{1+x}Ba_{2-x}Cu_3O_{7-\delta}$ with slight gadolinium excess x from the stoichiometric value of 0 to 0.1 were synthesized by the solid-state reaction method and their structural, transition, and magnetic properties were studied. The samples with $x \leq 0.01$ show critical temperature T_c above 93 K. DC and AC magnetization measurements confirm the control role of the gadolinium overdoping in Gd-Ba-Cu-O compounds to tailoring temperature and magnetic field application parameters as critical current density.*

Keywords: High-T_c Superconductor, $Gd_{1+x}Ba_{2-x}Cu_3O_{7-\delta}$, Nonstoichiometry, Critical Temperature, Mass Magnetization, Paramagnetic

1. Introduction

High temperature oxide superconductors, namely of the RE-123 type, are promising materials for high-field power applications at high temperatures. The systems, where RE is represented by so-called light rare-earth element (LRE) like La, Nd, Sm, Eu or Gd, are particularly interesting. It is well known that in the LRE-123 systems, the LRE^{3+} ions can occupy the Ba^{2+} sites because the ion radius of the elements is nearest to the ion radius of Ba ion. It was reported that the increasing occupation of Ba^{2+} sites resulted in a deterioration of superconducting properties, e.g. critical transition temperature, T_c, mainly at high LRE-Ba substitution levels [1-2]. On other hand, for the melt-textured samples or single crystals, local composition fluctuations were observed, known as nanostrips or nanoclusters, consisting of the $LRE_{1+x}Ba_{2-x}Cu_3O_y$ phase. The 10-50 nm dimension nanoclusters may work as highly effective pinning centers at higher magnetic fields [3-4].

H. Shimizu at al. [5] investigated $Gd(Ba_{2-x}Gd_x)Cu_3O_{6+\delta}$ polycrystalline samples for x from 0.00 to 0.25 and refer decreasing T_c and the orthorhombicity with increasing the Gd concentration, marked for $x > 0.1$ K. Miyachi et al. [6] investigated the $Gd_{1+x}Ba_{2-x}Cu_3O_{7-\delta}$ thin film prepared by PLD using the targets with changing the composition x from 0 to 0.4.The highest T_c of 91.5 K and critical current density j_c at 77 K were measured for $x = 0.04$. C. Xu et al. [2] studied a series of compounds of melt textured samples of $Gd_{1+x}Ba_{2-x}Cu_3O_{7-\delta}$ with x ranging from -0.1 to 0.2. They show that solubility was limited to 0 - 0.1 and onset T_c decreases with increasing x.

In our former works [7, 8], we studied nonstoichiometric bulk sintered $Eu_{1+x}Ba_{2-x}Cu_3O_{7-\delta}$, and $Sm_{1+x}Ba_{2-x}Cu_3O_{7-\delta}$ compounds with x from 0 to 0.1. In this work we prepared a series of slight non-stoichiometric bulk samples of $Gd_{1+x}Ba_{2-x}Cu_3O_{7-\delta}$ and investigated composition deviation effects on their structural, superconducting and magnetic properties.

2. Subject and Methods

The $Gd_{1+x}Ba_{2-x}Cu_3O_{7-\delta}$ samples, where nominal x = 0, 0.01, 0.02, 0.04, 0.05, 0.07 and 0.1, were prepared by a standard solid-state reaction method using commercial 99.99 % purity oxide powders of Gd_2O_3, CuO, and $BaCO_3$. Prior to weighing and mixing, the Gd_2O_3, CuO, $BaCO_3$ powder was pre-annealed at 950 °C for 8 h in air to release contaminations, e.g., moisture. Thereafter, the powders were carefully weighed in appropriate weight amounts, homogenized in acetone in an agate mortar for five minutes, put into alumina crucibles and calcined at 950 °C for 40 hours in air. The precursors were then homogenized, pressed into pellets (with the diameter of 12 mm) and sintered in a horizontal tube furnace in flowing oxygen 20 ml/min) at about 1000 °C for 72 h, cooled to 450 °C and held at this temperature for 24 h, and thereafter cooled in the furnace to room temperature. The critical temperature, $T_c(R = 0)$ was determined by a standard resistance four-point method and the transition width ΔT_c was characterized by the 10-90 % criterion. The uncertainty of temperature measurements was less than 0.2 K. The phase composition was studied by X-ray diffraction measurements (CuKα radiation). AC (0.1 Hz) low field magnetization at 77 K was measured by a compensation method using the second-order SQUID gradiometer [9] and DC magnetization at the higher field and lower temperature by Quantum Design SQUID magnetometer MPMS XL-7.

3. Results

From X-ray diffraction data, it can be concluded that all samples of series are single-phase. It was impossible to identify any impurity phase within the limit of the resolution. The XRD patterns of some samples of $Gd_{1+x}Ba_{2-x}Cu_3O_{7-\delta}$ series are shown in Fig. 1.

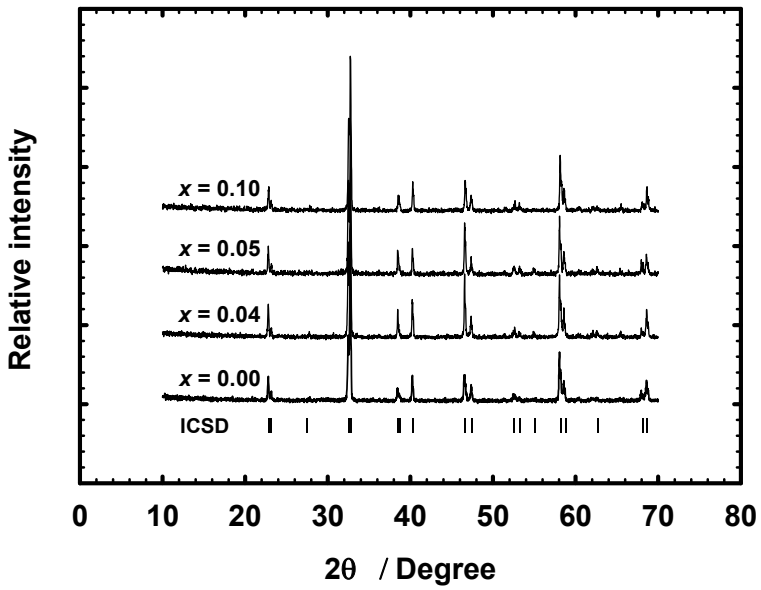

Fig. 1. Comparison of the powder X-ray diffraction patterns of four sample series $Gd_{1+x}Ba_{2-x}Cu_3O_{7-\delta}$ for shown x and position of main peaks of $Gd_1Ba_2Cu_3O_{6.99}$ of ICSD #78456.

Changes of T_c and ΔT_c of the samples vs. x are shown in Fig. 2 and Fig. 3, respectively. The values of T_c and ΔT_c of the samples change slightly except for that with x = 0.1. The results are consistent with corresponding results in [1].

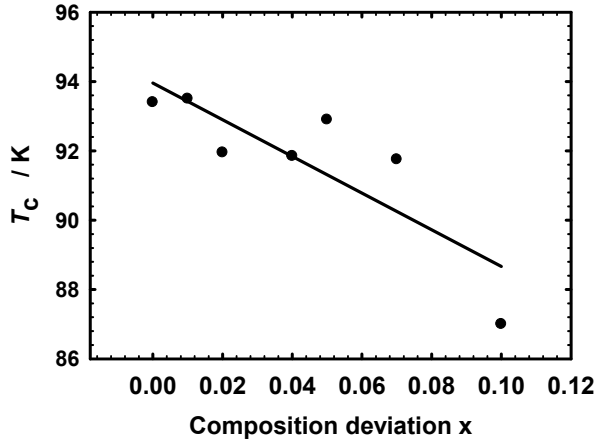

Fig. 2. T_c vs. x of the $Gd_{1+x}Ba_{2-x}Cu_3O_{7-\delta}$.

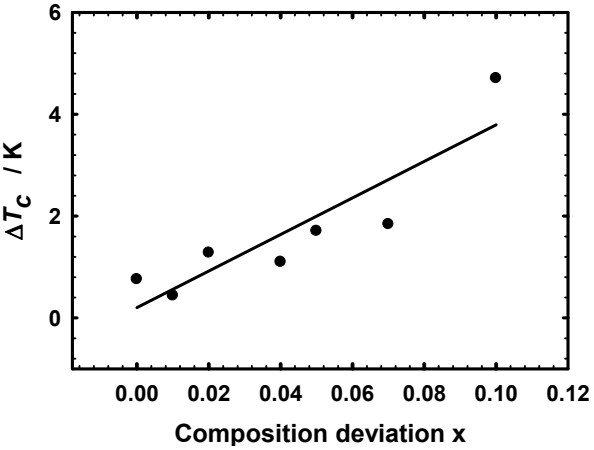

Fig. 3. ΔT_c vs. x of the $Gd_{1+x}Ba_{2-x}Cu_3O_{7-\delta}$.

We think that local structure disordering effects start to dominate at higher composition deviations of x as a result of the Gd substitution for Ba. It is in accordance with the model proposed by M. J. Kramer et al. and J. Chen et al. [10, 11], according to which the increase of the Gd content of x results in an increase of the total oxygen content and a decrease in the hole concentration in Cu-O_2 planes by donate electrons of the substitution of Gd^{3+} entering Ba^{2+} sites. The effects together determine the superconducting properties of samples, e.g. T_c, ΔT_c and their degradation for higher levels of x.

Mass magnetization hysteresis curves of M vs. H of samples at 77 and 20 K are shown in Figs. 4 and 5, respectively.

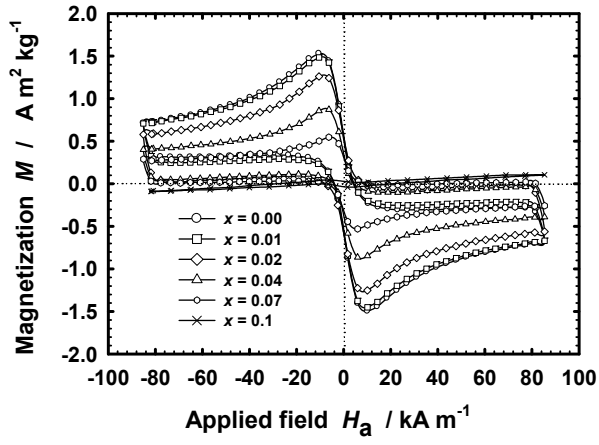

Fig. 4. M vs. H_a dependences of $Gd_{1+x}Ba_{2-x}Cu_3O_{7-\delta}$ at 77 K.

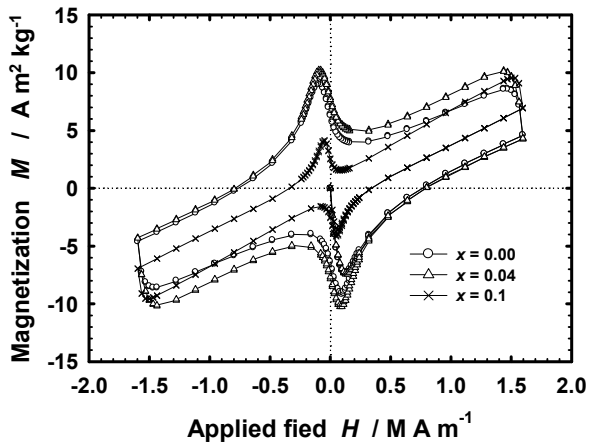

Fig. 5. The same as in Fig. 4 at 20 K.

The AC magnetization $M(H)$ curves at the low field to ~85 kA m^{-1}for the x = 0, 0.01, 0.02, 0.04, 0.07 and 0.1 (Fig. 4) show superconducting hysteresis field dependences (diamagnetic, sitting in the second and forth quadrants). The increase of the Gd content results in a decrease in magnetization except for similar curves with x = 0.01 - 0.02 with the best one, where x = 0.01. All the samples show the Z-shaped magnetization curves typical for polycrystalline samples except for that with x = 0.1. The curve with the highest Gd content shows paramagnetic behavior (sitting in the first and third quadrants).The situation is different if the effect of magnetic moment of Gd^{3+} ions is increased. It can be done by increasing temperature (considering the Curie–Weiss law) or by applied field. The result is shown in Fig. 5 where the DC mass magnetization curves with x = 0.00, 0.04 and 0.1 are shown at 20 K and at H ~ 1.59 MA m^{-1}.The curves include a superconducting component (diamagnetic behaviors at

low field and hysteresis) and paramagnetic one - slope of the curves points to the first and third quadrants. In this case, the best superconducting properties belong to composition deviation $x = 0.04$.

We believe that slight Gd/Ba non-stoichiometry x supports composition fluctuations (like nanoclusters in grains) and thus magnetic flux pinning is increased. On the other hand, the entering of Gd into Ba sites results in a certain degradation of superconductivity, e.g. T_c and ΔT_c, however at higher substitution levels. These two effects compete to each other. We note that similar results were reported for non-stoichiometric thin films too. K Miyachi et al. [6] investigated an effect of the substitution of Gd into the Ba site in $Gd_{1+x}Ba_{2-x}Cu_3O_{6+\delta}$ thin film samples ($0 \leq x \leq 0.4$). The highest values of $T_c = 91.5$ K and $j_c = 3$ MAcm^{-2} were observed for $x = 0.04$. Of course, our results have to be verified on monodomain or single crystal samples.

4. Conclusions

We studied slight Gd excess doping effects in a series of single-phase $Gd_{1+x}Ba_{2-x}Cu_3O_{7-\delta}$ samples with a composition deviation x from 0 to 0.1. The samples were synthesized by the solid-state reaction method at ~ 1000 °C for 72 h in flowing oxygen. The samples, up to $x \leq 0.07$, show values of $T_c > 91$ K and still $\Delta T_c \leq 1.8$, whereas the slight excess Gd doping x can be used for tailoring critical current density with respect to temperature and magnetic field application range.

Acknowledgements

This work was supported by the Agency of the Ministry of Education of the Slovak Republic for the Structural Funds of the EU, Operational Programme Research and Development, Project Code 26240220073.

References

[1] Wu H, Dennis KW, Kramer MJ, McCallum RW. *Appl. Superconductivity* **6**: 87, 1998.

[2] Xu C, Hu A, Sakai N, Izumi M, Hirabayashi I. *Physica C* **417**: 77, 2005.

[3] Hu A, Koblischka MR, Yao X, Zhou H, Winter M, Hartmann U, Murakami M, Supercond. *Sci. Technol*. **19**: 580, 2006.

[4] Koblischka MR, Koblischka-Veneva A, Muralidhar M, Wolf T, Babu NH, Hartmann U. *Physica C* **471**: 66, 2011.

[5] Shimizu H, Tomimatsu T, Motoya K. *Physica C* **341**: 621, 2000.

[6] Miyachi K, Sudoh K, Ichino Y, Yoshida Y, Takai Y. *Physica C* **392-396**: 1261, 2003.

[7] Cigáň A, Maňka J, Polovkova J, Majerová *M*, Kopčok *M*, Van Driessche I, Zrubec V. *J. Phys.: Conference Series* **97**: 2008. 012184.

[8] Maňka J, Cigáň A, Polovková J, Koňakovský A, Prnová A. *Meas. Sci. Rev.* **11***:* 9, 2011.

[9] Zrubec V, Cigáň A, Maňka J. *Physica C* **223**: 90, 1994.

[10] Kramer MJ, Yoo SI, McCallum RW, Yelon WB, Xie H, Allenspach P. *Physica C* **219**: 145, 1994.

[11] Chen JM, Liu RG, Chung SC, Liu RS, Kramer MJ, Dennis KW, McCallum RW. *Phys. Rev. B* **55**: 3186, 1997.

Preliminary Study of Thermal Properties of Al_2O_3-Yb_2O_3 Glass Microspheres

[2]A. Prnová, [1]K. Bodišová, [4]M. Škrátek, [2]R. Klement, [3]M. Migát [3]P. Veteška, [2]D. Galusek, [5]Els Bruneel and [5]I. Van Driessche

[1]Department of Ceramics, Institute of Inorganic Chemistry, Slovak Academy of Sciences, Dúbravská cesta 9, 841 04 Bratislava, Slovak Republic
[2] Vitrum Laugaricio – Joint Glass Center of the IIC SAS, TnU AD, FCHTP STU and Rona, a.s., Študenstská 2, SK-911 50 Trenčín, Slovak Republic
[3] Faculty of Chemical and Food Technology, Slovak University of Technology; Bratislava, Slovak Republic
[4] Department of Magnetometry, Institute of Measurement Science, Slovak Academy of Sciences, Dúbravská cesta 9, 841 04 Bratislava, Slovak Republic
[5] Department of Inorganic and Physical Chemistry, Gent University, Krijgslaan 281 (53), 9000 Gent, Belgium
Email: martin.skratek@savba.sk

Abstract. *Binary ytterbium-aluminate glass microspheres with eutectic (79.4 mol. % Al_2O_3, 20.6 mol. % Yb_2O_3) composition were prepared by flame synthesis in methan-oxygen flame. The starting powder was prepared by sol-gel method in order to obtain homogenous glass particles with a narrow interval of particle size distribution. Prepared microspheres were studied by optical microscopy, scanning electron microscopy (SEM), X-ray diffraction analysis (XRD) and differential thermal analysis (DTA). According to the XRD, small portion of YbAG, α-Al_2O_3 and non-identified phase were present in glass microspheres after flame synthesis. From DTA records, temperatures of onset of crystallization (T_c) and temperature of maxima of the exothermic crystallization peak (T_x) were determined. High temperature X-ray diffraction analysis (HT-XRD) in temperature range 750-1200 °C with 2h and 4h isothermal holding time at temperatures 933 and 1044 °C was performed for preliminary study of thermal behaviour of prepared system.*

Keywords: Ytterbium-Aluminate Glasses, Flame Synthesis, Thermal Properties

1. Introduction

Aluminate glasses with high alumina content have recently come to the attention both - technologists and researchers for their excepted excellent properties, as hardness, fracture thoughnes, chemical and thermal resistance. Due to good optical properties, these materials are also suitable for replacement of commercially used laser materials as corundum (monocrystalline α-Al_2O_3), PCA (polycrystalline alumina), YAG (yttrium-aluminium garnet), YbAG (ytterbium-aluminium garnet). However their main disadvantages are high melting temperatures, high crystallisation rates and high cooling rates required during preparation. The several works were focused on study of Re_2O_3-Al_2O_3 glasses, and various preparation method with using of splat quenching technique [1], AAL (aero-acoustic levitator), CNL (conical nozzle levitator) [2] devices and other were described. New approach was used in the work of Rosenflanz et al [3]. They prepare the glasses in form a small microspheres which were subsequently sintered by hot press technique. For successful preparation of larger pieces of glass or glassceramic materials, it is very important to know thermal behavior of aluminate glasses. In this work, ytterbium-aluminate glasses with eutectic composition were prepared by combination of sol-gel method and flame synthesis. The morphology of prepared glass

microbeads was studied by optical microscopy and SEM. DTA and HT-XRD were used for determination of phase evolution during heat treatment of prepared material.

2. Experimental

The Al_2O_3-Yb_2O_3 precursor powder with composition corresponding to the eutectics phase (AYbEM) was prepared by mixing aluminium nitrate and ytterbium nitrate solutions in deionised water. Ytterbium nitrate solution was prepared by dissolution of ytterbium oxide in diluted nitric acid. The water solution of citric acid and ethylene glycol were added to the nitrates solution (the molar ratios of citric acid and ethylene glycol to metal ions were 1:1). The solution was allowed to reflux at 85 °C for 2 hours. Polymerization was promoted by heating to 150 °C, at which the viscosity rapidly increased with accompanying solvent evaporation until aerated resins were formed. The organic compounds from the powders were removed by heating to 800 °C for several hours. Prepared powders were fed into methan-oxygen flame and molten particles were cooling by distilled water, collected, separated, dried and calcinated at 650 °C for 4h to remove of residua from flame synthesis. Prepared glass microbeads were examined by optical microscopy (Nicon ECLIPSE ME 600), SEM (Zeiss EVO 40HV at accelerating voltage 20kV) and X-ray powder diffraction analysis (Panalytical Empyrean, CuKα radiation, 2Θ range 10-80). HT-XRD in range of 750-1200 °C with step 5 °C and different isothermal dwell time was used for preliminary kinetics study of prepared glass microspheres. DTA measurements (Netzsch STA 449 F1 Jupiter) in nitrogen atmosphere, with heating rate 10 °C/min in temperature range of 35-1200 °C were performed for determination of T_c (onset of crystallization temperature) and T_x (temperature of maxima of the exothermic crystallization peak) of prepared glasses.

Table 1. The basic charasteristics of prepared system (p.c.-polycrystalline)

sample	Al_2O_3 (mol.%)	Yb_2O_3 (mol.%)	T_m (°C)	T_c (°C)	T_x (°C)	XRD
AYbEM eutectic composition	79,4	20,6	1750	929,2 1030,9 1074,3	933,8 1044,3 1089,6	p.c.

3. Results

Prepared glass microbeads were transparent, spherical and fully remelted with diameter size up to 10 μm (Fig. 1). Only small amount of fully or partially crystalline particles was observed by SEM (Fig. 2). Also XRD confirms predominantly amorphous character of prepared samples (high background in XRD patterns) with traces of YbAG, α –Al_2O_3 and non-identified phase (peaks with small intensities centered at 16,89, 28,62 and 45,23 in 2Θ range). The presence of this non-identified phase is probably associated with the transition of alumina and yttria to thermodynamically stable YbAG phase. The formation of this phase can be explained with high temperature in methan-oxygen flame and high cooling rates used in system [4] and also with existence of non-homogenous temperature field and short dwell time of particles in methan-oxygen flame during flame synthesis. One strong exothermic peak with onset at 929,2 °C and maximum at 933,8 °C; which can be attributed to the crystal growth of YbAG, and two smaller broad exothermic peaks at 1044,3 °C and 1089,6 °C (onset temperatures 1030,9 °C and 1074 °C)were observed in DTA records of prepared glass microspheres (Fig. 3). The basic characteristics of prepared sample are in Table 1.

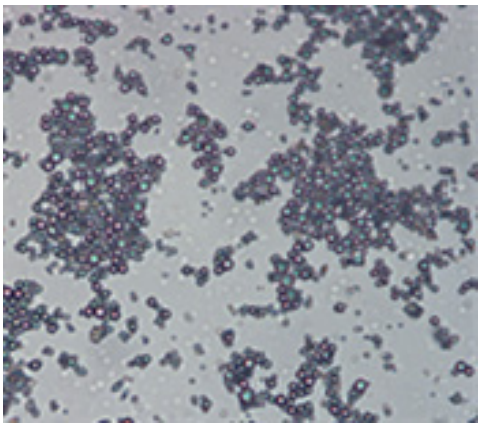

Fig. 1 The optical micrograph of sample AYbEM

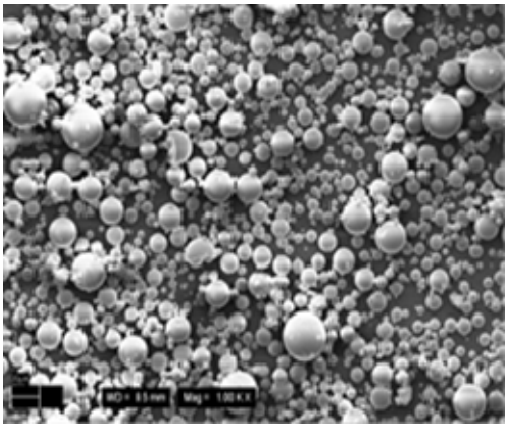

Fig. 2 SEM micrograph of sample AYbEM

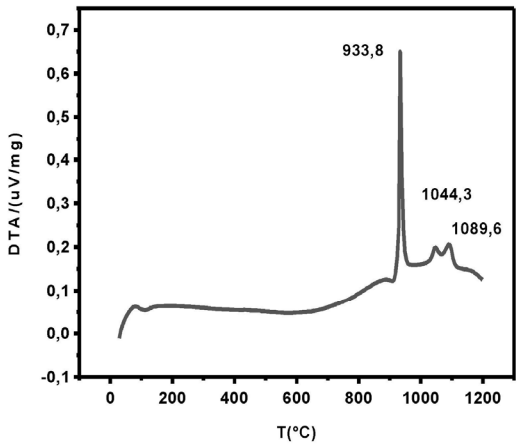

Fig. 3 DTA records of sample AYbEM

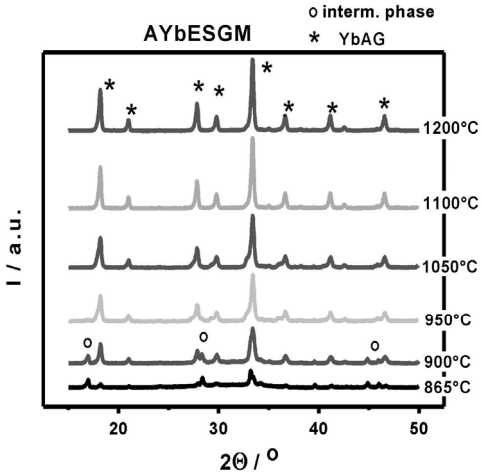

Fig. 4 HT XRD patterns of sample AYbEM in temperature range 865-1200 °C

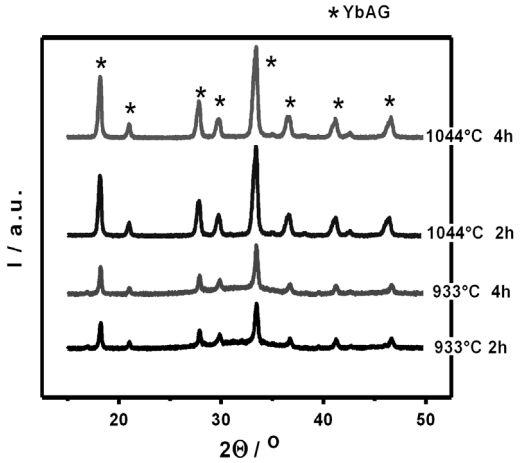

Fig. 5 The comparison of results of HT XRD after 2h and 4h dwell time at 933 °C and 1044°C.

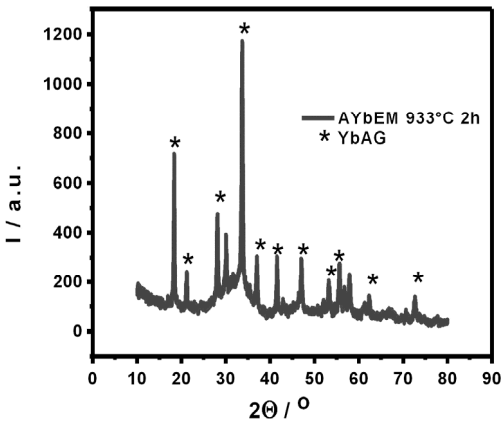

Fig. 6 HT X-ray patterns of sample AYbEM recorded after 2h dwell time at 933 °C

For better understanding of thermal behavior of prepared sample, HT-XRD was performed. From results of this HT-XRD, it is clearly seen, that traces of non-identified phase, were converted to YbAG phase in temperature range of 865-1050 °C (Fig. 4). However, with further increasing of temperature (1050-1200 °C), observed YbAG peaks become higher and sharper, which can be explained by crystal growth of YbAG phase in prepared sample. The next HT XRD experiments with isothermal hold of 2 and 4 hours at first two exothermic maxima (933 °C and 1044 °C), show only crystallisation of YbAG phase, with conversion of non-identified phase to YbAG during the first ten minutes at 933 °C and ≈ 7 minutes at 1044 °C. Higher content of YbAG crystalline phase was observed in sample held at 1044 °C after 2 hours of dwell time and fully crystalline material was obtained after 4 hours (Fig. 5). The HT XRD spectra after 2h and 4h at 933 °C with persistent amorphous background between 20-40 in 2Θ range, indicated incomplete crystallisation of eutectic glass sample (Fig. 6). This observed slow crystallization at 933 °C opens the possibility of preparation of glassceramics materials in system Al_2O_3-Yb_2O_3 by controlled crystallization of glass microspheres. The further DTA analysis and HT-XRD study focused on nucleation of prepared glass microspheres is necessary for better understanding of crystallisation behavior of prepared glass microspheres.

4. Conclusions

The partially crystalline glass microspheres with high alumina content in system Al_2O_3-Yb_2O_3 were prepared with diameter ≤ 10μm. DTA and HT-XRD for preliminary study of crystallisation behaviour of prepared glass were performed. The crystallisation of YbAG phase in prepared sample was studied at temperatures 933 °C and 1044 °C with different isothermal holding time. As shown results this work, for preparation glass-ceramics materials is interesting slowly crystallization of pure YbAG phase at 933 °C.

Acknowledgements

The financial support of this work to the project SAS-NSC JRP 2012/14, and by the APVV grant LPP 0133-09 is gratefully acknowledged. This publication was created in the frame of the project "Centre of excellence for ceramics, glass, and silicate materials" ITMS code 262 20120056, based on the Operational Program Research and Development funded from the ERDF.

References

[1] Fondeur F, Mitchell BS. Infrared studies of preparation effects in calcium aluminate glasses. *Journal of Non-Crystalline Solids*, 224, 184-190, 1998.

[2] Wallenberger FT, Weston NE, Motzfeldt K, Swartzfager DG. Inviscid Melt Spinning of Alumina Fibers: Chemical Jet Stabilization, *Journal of the American Ceramic Society*, 75 (3), 629–636, 1992.

[3] Rosenflanz A, Frey M, Endres B, Anderson T, Richards E, Schardt C. Bulk glasses and ultrahard nanoceramics based on alumina and rare-earth oxides, *Nature*, 430, 761-764, 2004.

[4] Prnová A, Galusek D, Škrátek M, Karell R, Klement R, Kraxner J. Preparation and characterization of Yb_2O_3 - Al_2O_3 glass microspheres with high alumina content. In proceedings of the Measurement 2011: 8th International Conference on Measurement, 2011, 269-273.

Evaluation of the Positional Deviation by Calibration of CNC Machines

T. Peták, P. Benkó, E. Kureková

Faculty of Mechanical Engineering STU, Bratislava, Slovakia,
Email: tomas.petak@stuba.sk

Abstract. *CNC machines are required to produce accurate and high-quality products. It is only possible to produce accurate workpieces if we have an accurate machine. This contribution deals with the evaluation of calibration of CNC measuring systems and it simultaneously presents the solution of the problem from the metrological point of view, which is different from the common practice.*

Keywords: Calibration, Positional Deviation, Uncertainty in Measurement, Covariance

1. Introduction

CNC (**C**omputer **N**umerical **C**ontrol) machines can be defined as computer-controlled machines, which also meet the classification of the measurement system, because there are measuring systems in the axes of these machines. The capability of a machine to cope with rapidly changing operating conditions is an ultimate factor for its accuracy. A transition from roughing to finishing completely changes the mechanical and thermal load on the machine. Position control is important in this context. By indirect measuring (see Fig. 1) is monitored variable position of the servomotor monitored, which made movement. The position of an NC feed axis can be measured through the ball screw in combination with a rotary encoder. Changes in the driving mechanics due to wear or temperature cannot be compensated [1].

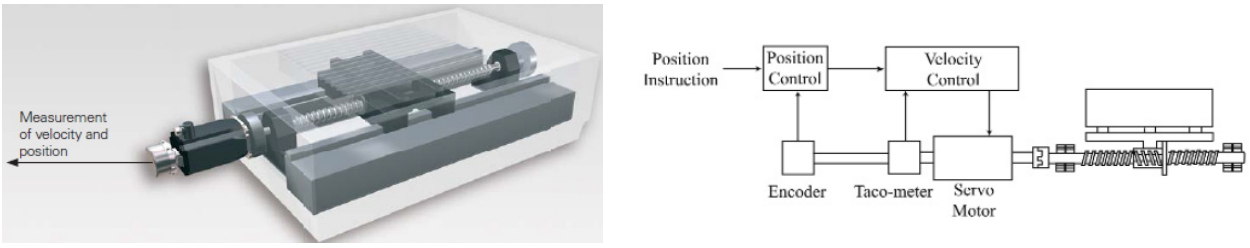

Fig. 1. The principle of indirect measuring (left) and its block diagram (right) [2]

Direct measuring systems are designed to immediately provide the information about the relative motion due to the machine frame. The target value is compared with the actual value as a result of feedback operation. The motion system of the CNC machine corrects the immediate value of the actuator of reading a linear encoder (see Fig. 2). Measurement accuracy depends solely on the precision and installation location of the linear encoder.

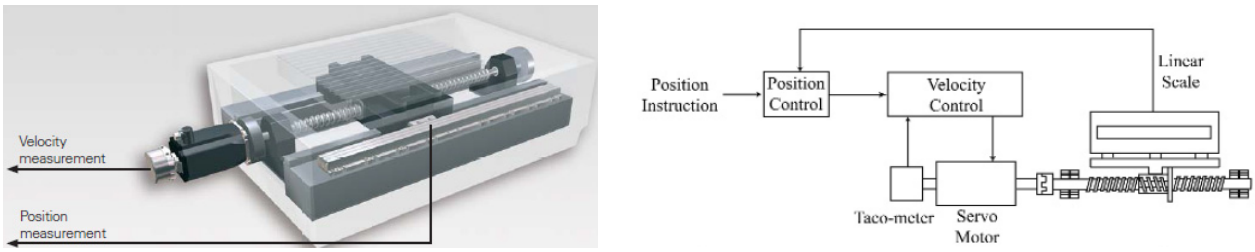

Fig. 2. The principle of direct measuring (left) and its block diagram (right) [2]

2. Calibration of the measuring systems of CNC machines

Calibration of the measuring systems of CNC machines and its evaluation is often carried out by ISO 230-2 in practise. Between the recommendations of this standard and conventional metrological approach could be found some discrepancies. According to definition of calibration by VIM 3 should be measured the measuring system of machine in first step. In the second step are measured data entered into the control system of the machine. This is subsequently used for determination of relationship for obtaining a measurement result from an indication [3]. In the metrological context we can talk about correction of systematic errors of positioning (in practice often called as compensation), which is awarded to control the CNC machine in the form of compensation map. By CNC machine calibration method called determination of accuracy and repeatability of positioning numerically controlled axes are evaluated nine standard parameters. After analysis of the above parameters and comparison with the definitions in metrological terminology is offered even easier possibility of expressing the results that characterize positioning of CNC machine. It is the expression of the average positional deviation in the axis and its uncertainty. This parameter is expressed in direct and reverse direction with the uncertainty of the measurement result, which includes the contribution of the uncertainty of determining the positional deviation of repeatability and other contributions, which appears systematically. This procedure also represents the intersection of the recommendations of the ISO 230-2 and metrological approach to the evaluation of the calibration of CNC machines. This solution corresponds to the evaluation method according to ISO GUM.

3. Evaluation of the calibration of CNC machines

Model of the measurement consists of the system of equations where number of equations is greater than number of unknown parameters of the deviation function [4]. In the model are including other influence quantities of the measurements. Therefore the right side of model will be:

$$\begin{aligned}
\overline{P}_1 - P_{\mathrm{nv}_1} + P_{\mathrm{nv}_1}\cdot\alpha\cdot\Delta t + \delta_{\cos} + \delta_{\mathrm{cc}} + \delta_{\mathrm{res}} &= a + b\overline{x}_1 + c\overline{x}_1^{2} + d\overline{x}_1^{3} \\
\overline{P}_2 - P_{\mathrm{nv}_2} + P_{\mathrm{nv}_2}\cdot\alpha\cdot\Delta t + \delta_{\cos} + \delta_{\mathrm{cc}} + \delta_{\mathrm{res}} &= a + b\overline{x}_2 + c\overline{x}_2^{2} + d\overline{x}_2^{3} \\
&\vdots \\
\underbrace{\overline{P}_n - P_{\mathrm{nv}_n} + P_{\mathrm{nv}_n}\cdot\alpha\cdot\Delta t + \delta_{\cos} + \delta_{\mathrm{cc}} + \delta_{\mathrm{res}}}_{\boldsymbol{W}=\boldsymbol{P}+\boldsymbol{C}\boldsymbol{\Delta}} &= \underbrace{a + b\overline{x}_n + c\overline{x}_n^{2} + d\overline{x}_n^{3}}_{\boldsymbol{A}\cdot\boldsymbol{y}}
\end{aligned} \tag{1}$$

where

$\overline{x}_1, \overline{x}_2 \ldots \overline{x}_n$ mean positional deviation in position

$\overline{P}_1, \overline{P}_2 \ldots \overline{P}_n$ position determined from the series of measurements (n = 5).

$P_{\mathrm{nv}_1}, P_{\mathrm{nv}_1}, \ldots P_{\mathrm{nv}_n}$ nominal value of length – position set by control unit of CNC machine

α coefficient of the thermal expansion

$\delta_{\cos}$ correction of the cosine error

δ_{cc} correction of the indication of the standard from the calibration certificate

δ_{res} correction of the resolution of the standard

$\Delta t = \left(t_{\mathrm{CNC}} - t_{20}\right)$ difference between temperature of CNC machines t_{CNC} and reference temperature t_{20} 20 °C.

The left side of the model is deviation function which represents mean positional deviation in given position. Deviation functions are polynomial. Degree of polynoms is depended from the characteristics of measured values, in our cases polynomial of third degree. Third degree polynomial was chosen after iterative estimations, where we found that it best follows the process of the measured values.

where a, b, c, d are parameters of polynoms.

Now model of measurement is described in matrix notation:

$$\underbrace{\underbrace{\begin{pmatrix} \overline{P}_1 - P_{\mathrm{nv}_1} \\ \overline{P}_2 - P_{\mathrm{nv}_2} \\ \vdots \\ \overline{P}_n - P_{\mathrm{nv}_n} \end{pmatrix}}_{\boldsymbol{P}} + \underbrace{\begin{pmatrix} P_{\mathrm{nv}_1} & 1 & 1 & 1 \\ P_{\mathrm{nv}_2} & 1 & 1 & 1 \\ \vdots & & & \\ P_{\mathrm{nv}_n} & 1 & 1 & 1 \end{pmatrix}}_{\boldsymbol{C}} \cdot \underbrace{\begin{pmatrix} \alpha\Delta t \\ \delta_{\cos} \\ \delta_{\mathrm{cc}} \\ \delta_{\mathrm{res}} \end{pmatrix}}_{\boldsymbol{\Delta}}}_{\boldsymbol{W}} = \underbrace{\begin{pmatrix} 1 & \bar{x}_1 & \bar{x}_1^2 & \bar{x}_1^3 \\ 1 & \bar{x}_2 & \bar{x}_2^2 & \bar{x}_2^3 \\ \vdots & \vdots & \vdots & \vdots \\ 1 & \bar{x}_n & \bar{x}_n^2 & \bar{x}_n^3 \end{pmatrix}}_{\boldsymbol{A}} \cdot \underbrace{\begin{pmatrix} a \\ b \\ c \\ d \end{pmatrix}}_{\boldsymbol{y}} \tag{2}$$

where

- $\boldsymbol{W}$ observation vector
- $\boldsymbol{P}$ vector of the mean positional deviations
- $\boldsymbol{C}$ matrix of the sensitivity coefficients
- $\boldsymbol{\Delta}$ vector of corrections
- $\boldsymbol{A}$ Vandermonde matrix
- $\boldsymbol{y}$ vector of the output quantities, in our case vector of unknown parameters for polynomial of third degree.

Estimation of the parameters is possible to find out by application of the least squares method. Because of corrections are considered as zeros, their influence taking into the uncertainties is described by input covariance matrix $\boldsymbol{U}_W$.

$$\hat{\boldsymbol{y}} = \left(\boldsymbol{A}^T \cdot \left(\boldsymbol{U}_A + \boldsymbol{C} \cdot \boldsymbol{U}_B \cdot \boldsymbol{C}^T\right) \cdot \boldsymbol{A}\right)^{-1} \cdot \boldsymbol{A}^T \cdot \underbrace{\left(\boldsymbol{U}_A + \boldsymbol{C} \cdot \boldsymbol{U}_B \cdot \boldsymbol{C}^T\right)^{-1}}_{\boldsymbol{U}_W} \cdot \boldsymbol{W} \tag{3}$$

where

$\boldsymbol{U}_{\mathrm{A}} = \boldsymbol{U}_{\mathrm{A}}(\boldsymbol{P}) = \mathrm{diag}\left(u_{\mathrm{A}}(\boldsymbol{P}_1); u_{\mathrm{A}}(\boldsymbol{P}_2) \ldots u_{\mathrm{A}}(\boldsymbol{P}_n)\right)$, where $\boldsymbol{P}_i = \overline{\boldsymbol{P}}_i - \boldsymbol{P}_{nv_i}$ are contributions of the repeatability in given position

$\boldsymbol{U}_{\mathrm{B}} = \boldsymbol{U}_{\mathrm{B}}(\boldsymbol{\Delta}) = \mathrm{diag}\left(u_{\mathrm{B}}(\boldsymbol{\Delta}_1); u_{\mathrm{B}}(\boldsymbol{\Delta}_2) \ldots u_{\mathrm{B}}(\boldsymbol{\Delta}_4)\right)$ is matrix contains uncertainty determined by method type B.

After multiplication of the covariance matrix $\boldsymbol{U}_{\mathrm{B}}$ with matrix $\boldsymbol{C}$ from right and left, we get covariance matrix $\boldsymbol{U}_{W\mathrm{B}}$, where out of the diagonal are covariances of influence quantities.

Uncertainty of the estimations of parameters of deviation function calculates by applying law of propagation uncertainties:

$$\boldsymbol{U}_y = \left(\boldsymbol{A}^{\mathrm{T}} \cdot \boldsymbol{U}_W \cdot \boldsymbol{A}\right)^{-1} \tag{4}$$

Uncertainty of the deviations in given position is evaluated by following expression:

$$\boldsymbol{U}_{\mathrm{A}}\left(\hat{\boldsymbol{W}}\right) = \left(\boldsymbol{A} \cdot \boldsymbol{U}_y \cdot \boldsymbol{A}^{\mathrm{T}}\right), \quad \text{where } \hat{\boldsymbol{W}} = \boldsymbol{A} \cdot \hat{\boldsymbol{y}} \tag{5}$$

Evaluation with designed algorithm allows estimating the parameters of the deviation function and their uncertainties when are considered covariances between influence quantities

in the whole range of the positioning in given axes. For verification of this algorithm was carried out the measurements on the CNC turning machine. On the Figure 3 are displayed deviation functions and their expanded uncertainties U when are considering covariance or not. Erratic function is because there are not thought the covariances, where the source of the covariance is temperature. Conversely, where we considered the covariances, it caused that the function is smoothed.

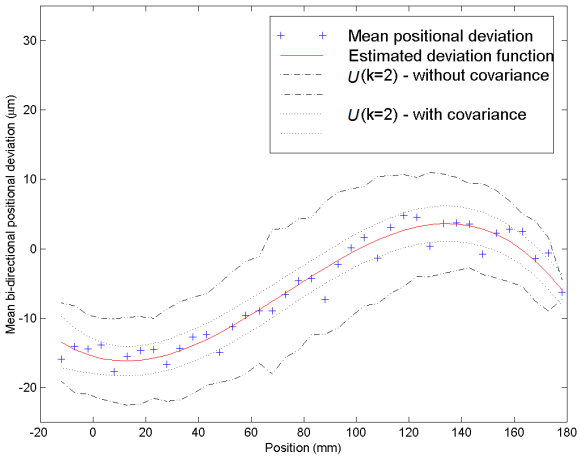

Fig. 3. Mean positional deviation of the CNC machine before compensation

When we considered covariance in evaluation, value of the expanded uncertainty U is markedly smaller. The reason is right application of the law of propagation uncertainties. By this way of evaluation is possible to uncover and quantify mutual resources of uncertainties.

4. Conclusions

By procedure described in this paper we have obtained not only a function describing the dependence of the positional deviation from the position, but also the covariance matrix of output quantities. If we know the confidence interval of the deviation function, **i.e.** we are able to determine the uncertainty for each one point, respectively position [4]. The evaluation procedure is applied for determination the equation or measurement function in direct and reverse direction.

Acknowledgements

The research work was performed to financial support Ministry of Education of the Slovak Republic, grant No. VEGA 1/0584/12.

References

[1] Marek J, a kol. Konstrukce CNC obrábacích strojů. MM publishing. ISBN 978-80-254-7980-3, 82-83, 2010.

[2] The principle and block diagram of direct and indirect measuring. Copy from http://www.heidenhain.co.uk/en_UK/products-and-applications/length/measurements/, 13.01.2013.

[3] JCGM 200:2012. International Vocabulary of Metrology – Basic and General Concepts and Associated Terms [online]. Paris: JCGM, BIPM, 2012.

[4] Palenčár R, Halaj M, Kureková E. Evaluation of the positional deviation of numerically controlled axes. *Measurement Science Rewiew*, 7 (1), 2-4, 2007.

Mobile Measurement of Ionizing Radiation

G. Války, M. Bittera

Slovak University of Technology in Bratislava, Faculty of Electrical Engineering and Information Technology, Institute of Electrical Engineering, Bratislava, Slovakia
Email: gabriel.valky@stuba.sk

Abstract. *This document describes an apparatus which can be used for monitoring of ionizing radiation and for building graphical maps representing the radiation dose rates by geographical position. Essential parts of this apparatus are a calibrated dosimeter for estimating the gamma dose rate, GPS receiver and personal computer for storing the measured values and for visualization purposes. This system generates interactive map based on Google Maps API that clearly visualizes ionizing radiation levels for easy examination and localization of radiation anomalies or radioactive contamination zones.*

Keywords: Dosimetry, GM tube, Ionizing Radiation Measurement, GPS

1. Introduction

Nuclear plant accidents and radioactive waste management is still widely discussed topic in spite of high level of security systems and regulations. Such contamination caused by radioactive materials presents a hazard because of the radioactive decay of the contaminants, which emit harmful ionising radiation. The degree of hazard is determined by the concentration of the contaminants, the energy of the radiation being emitted, the type of radiation and proximity to organs of the body. It is always important to measure the dose rates in highly populated areas to reduce the risk of exposition to radioactive substances. When dealing with radiation dosimentry we usually talk about portable radiometry devices used for measuring exposure to ionizing radiation. When it's necessary to perform the measurement on larger area, e.g. around a plant or a city, this measurement is done by personnel walking around with dosimeters and manually localizing the zones with high radiation levels. In case of natural disasters, power plant failures or huge contamination leakages, the measurement needs to be done on larger geographical scale and it's reasonable to investigate the methods for more effective monitoring of radiation leakages.

2. System overview

Calibrated dosimeter as a standalone device is used for measuring the ionizing radiation levels. This device calculates the dose rate by counting the particles registered by Geiger Muller tube (GM tube) during a selected time interval. GM tubes are gas filled at specific pressure anduse Towsend avalanche phenomenon to produce easily detectable electronic pulses from a single ionising event caused by entering a radioactive particle into the tube [1]. We modified the dosimeter to make the filtered output of GM tube available for processing by programmable oscilloscope DS203. The firmware running on this oscilloscope uses the analog input channel for measuring the impulses representing a particle hit, the count of impulses observed during defined time interval is used

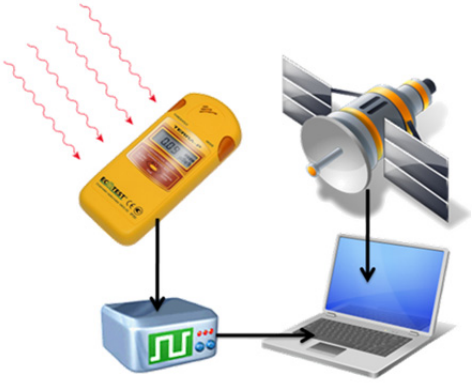

Fig. 1. Measurement system

for calculation of the dose rate. These values are further processed by personal computer by the means of storing the current dose rate value with GPS coordinates in the database. Figure 1 shows this configuration with dosimeter on top left, programmable oscilloscope on left bottom and laptop computer receiving GPS coordinates from satellites.

Software part of this apparatus consists of three components: oscilloscope firmware providing the computer immediate dose rate value through serial link, server application running on PC aggregating the dose rate values and geographic position from GPS receiver and finally a visualization application that analyses these logs, fragments measured values into a grid with fixed sized cells by geographical coordinate and calculates the average dose rate for each cell of this grid. Because there are usually multiple measured values belonging to a single cell, this application also allows the user to apply one of the detector modes on these values to get a single representative value of dose rate for each cell. It can be either calculation of the average, maximum or minimum dose rate.

3. Calculating the dose rate with programmable oscilloscope

For processing the dose rate values by the personal computer we need a device that is able to analyse the output signal of GM tube, count the impulses, calculate the dose rate and provide the result to the computer through serial link. This value is calculated from the number of impulses generated by the ionizing particles, by mutiplication of this number with tube sensitivity and by taking the dead and recovery times of the tube into account [2]. If n' counts are recorded in a time interval t with a detector of dead time d, it is necessary to compute the true number n that would have been observed with a counter of zero dead time. Since n'd is the total dead time and n/t is the true counting rate, (n/t)n'd is the total number of counts that would have occurred during the total dead time interval. Therefore (n/t)n'd = n – n'. In terms of the counting rate, R=n/t and R'=n'/t. Corrected rate is calculated rate by Eq. 1.

$$R = \frac{R'}{1 - R'd} \tag{1}$$

For this purpose we have developed an application for DS203 oscilloscope which setups the sampler to 200 mV/div at 200 ns/div and trigger to reliably capture each impulse from GM tube. Output signal voltage in idle state is 2.1 V and during the ionising event drops to 0 V for 2 µs, total recovery time for the GM tube is 4 µs, the oscilloscope requires extra 23 µs to be ready for capturing next trigger event. Constants of the calculation algorithm were finetuned to get similar reading on the oscilloscope as on the dosimeter. Next task of this application is counting the impulses during chosen time interval. Sensitivity of GM tubes are usually specified as a ratio of count of ionization events per second or minute to micro Sieverts per hour. Thus we need to calculate the count of ionization events per fixed time period. For mobile measurements we use one minute interval and for static measurement the interval of 5 minutes gives very accurate reading, providing one extra digit to the value displayed by dosimeter. Setting the length of time interval is a trade-off between the precision and sensitivity, the longer the interval, the higher accuracy we get at the expense of slow adaptation to environment changes. With short interval we can quickly identify fast changes of the radiation levels, but with lower accuracy.To get immediate reading of the dose rate levels we developed an algorithm that calculates the count of impulses during chosen time interval. Whole time interval (e.g. 1 minute) is divided into 60 time slots

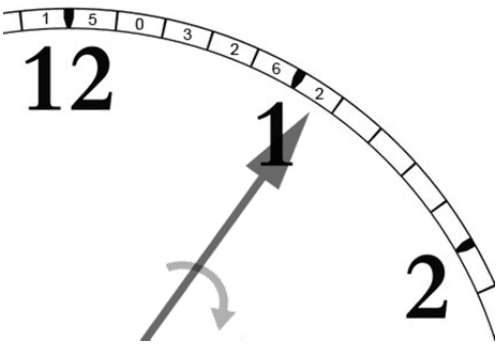

Fig. 2. Continuous filling of the time

(see Fig. 2). Every captured pulse causes an increment of the value of current slot, on the figure this slot is shown as seconds hand on clock. This is periodically moving around these 60 slots same as seconds hand does. When the hand jumps to next slot, it clears this slot to zero. Count of impulses that were captured during last minute is calculated as sum of all time slots, while for the current time slot we use it's value before clearing, because its value is still being changed. By this algorithm the calculation of pulses per minute is quick and trivial task. This algorithm was optimized for running on microcomputer with little available memory and is implemented as ring-buffer in informatics terminology [3].

When not all of the slots are filled yet, the result is calculated as the sum of the N filled slots multiplied by the correction factor that is calculated as ratio of 60 to N. When we want to achieve higher accuracy, we can increase the integration time by slowing the movement seconds hand. For example by slowing the hand 5 times, we get total integration time 5 minutes, thus getting 5 times better accuracy, while keeping the memory footprint of calculating algorithm the same. The application screen running on DS203 is shown on Fig. 3, on top we can see particle counter with calculated dose rate in micro Sieverts per hour and on the bottom there are 60 time slots with the highlighted one in center.

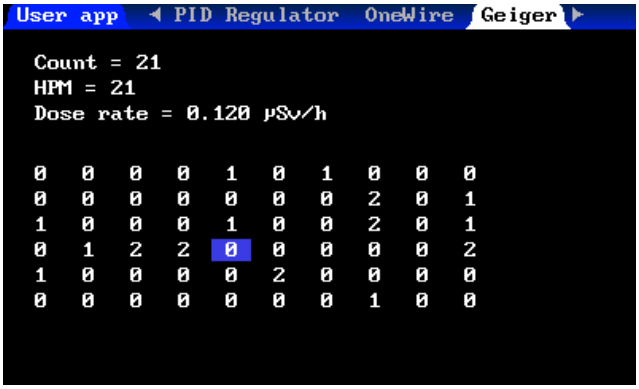

Fig. 3. Portable oscilloscope application

4. Visualization of results

For visualization purposes we have employed the Google Maps API as JavaScript component [4]. Over the road map series of semi-transparent rectangles are drawn representing the dose rate at specific position (see Fig. 4). These rectangles cover whole travelled route. For visual differentiation of the levels we use different colors or grayscale gradient, in this case the rectangles are solid black for values higher than 0.25µSv/h, lower values are drawn with higher transparency and for values below 0.05 µSv/h they are completely transparent.

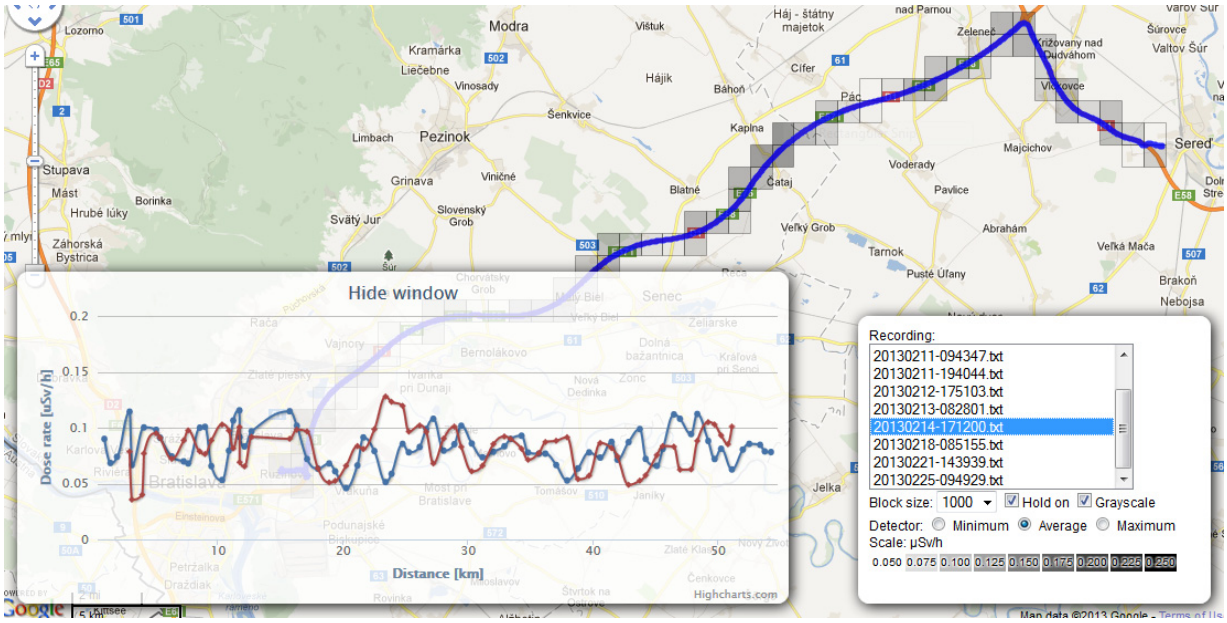

Fig. 4. Measuring while travelling between two cities (50 km).

On the bottom left part of the application window there is a graph representing the dose rate levels depending on the position relative to route. For evaulation purposes we travelled the highway between two cities multiple times on different dates and at different times of day to compare the results. Fig. 4 shows the comparison of two recording. The dimension of grid cells can be set in range from 50 meters up to 1.5 km. Smaller dimensions are suitable for measurements performed at low speeds inside city (see Fig. 5) while the higher values are good for visualizing longer routes. Whole travelled route is fragmented into series of these cells, the server application records the dose rate and GPS position in one second intervals, thus we are getting multiple dose rate values belonging to a single cell. Similarily as in other fields of electronics we apply detection mode for getting single numerical value representing the overall dose rate in single cell. It can be either calculation of the minimal value, maximal or average.

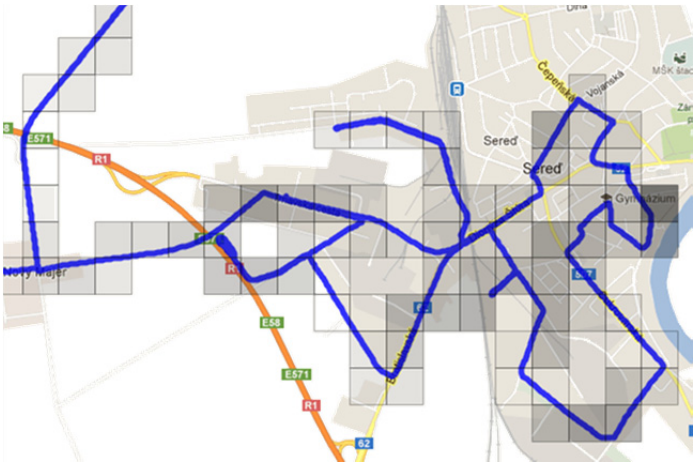

Fig. 5. Measuring inside city

5. Conclusions

Presented apparatus offers an innovative mobile method of dosimetry measurement, using Google Maps API we get flexible application allowing the operator to examine and compare measured recordings on any computer platform. We demonstrated this system by measuring the ionizing radiation on highway between two cities mutliple times as such as monitoring the dose rates around a single city helping us to localize areas with higher background radiation levels. In case of radiation emergency by having this system installed on multiple cars, this can be used for investigation of the impact of this accident. By building radiation maps, we can quickly identify the most affected areas and prepare evacuation plans for their inhabitants.

Acknowledgements

This work was supported by the project VEGA VG 1/0963/12.

References

[1] Attix, FH. Introduction to Radiological Physics and Radiation Dosimetry. John Wiley& Sons, 2008.

[2] Koori N, et al. Dead zone characteristics of SQS and GM tubes. *IEEE Transactions onNuclear Science*, 37 (2): 107-111, 1990.

[3] Oshana R. DSP Software Development Techniques for Embedded and Real-Time Systems. Newnes, 2006.

[4] Wang, A. Jun, Z. Jiang WR. Useful resources integration based on Google Maps. In proceedins of the 4th International Conference Computer Science & Education, 2009, 1044-1047.

Wi-Fi Parameter Measurements and Analysis

I. Soldo, K. Malarić

University of Zagreb, Faculty of Electrical Engineering and Computing,
Zagreb, Croatia,
Email: Ivana.Soldo@fer.hr

Abstract. *This paper describes the measurements of the Wi-Fi signal strength and measurements performed in a real-life example WLAN available in most homes today. The idea was to present how the signals were measured, analysed and conclusion was based on that analysis. The paper shows how an ordinary tablet device along with a couple of applications and the tablet's built-in Wi-Fi antenna can be used for such measurement purposes. Several measurements were conducted – showing the influence of different factors on the strength of the Wi-Fi signal and on the download and upload speed.*

Keywords: Wi-Fi Network, Signal Strength Measurement, Mobile Applications

1. Introduction

The Wi-Fi network is a wireless local area network (WLAN) which is intended to be used in local premises like a business building or on headquarters of an institution which consists of more building in a same place. The purposes of using WLAN networks are: wireless connection of computers into a network; providing mobility of computers [1]. A wireless local area network (WLAN) system is a system that includes the distribution system (DS), access points (APs), and portal entities. It is also the logical location of distribution and integration service functions of an extended service set (ESS). A WLAN system contains one or more APs and zero or more portals in addition to the DS [2]. The quality of Wi-Fi network depends on distance from the router, the used antenna and quality of the device. Wireless telecommunications networks are implemented and administered using radio communication, *(*physical layer of OSI model network structure [3]. The IEEE so far has defined nine protocols for the 802.11 technology. The used device in this paper supports Wi-Fi 802.11 b/g/n and Bluetooth. The Table 1 bellow shows an overview of the most important technical specifications of the standards 802.11 a/b/g/n [4-6].

2. Measuring device and applications

The device used for measurements was the Google Nexus 7 tablet (due to availability of device and since it is used for writing the Diploma thesis). It supports Wi-Fi 802.11 b/g/n as well as Bluetooth. It operats on 4.2 Android operating system (Jelly Bean).

Table 1. Overview of the 802.11 a/b/g/n standards.

Standard name	802.11a	802.11b	802.11g	802.11n
Standardization date	January 2000	December 1999	June 2003	June 2009
Maximum bandwidth	54 Mbps	11 Mbps	54 Mbps	600 Mbps
Modulation technique	OFDM	DSSS, CCK	DSSS, CCK, OFDM	DSSS, CCK, OFDM+
RF band	5 GHz	2.4 GHz	2.4 GHz	2.4 or 5 GHz
Channel bandwidth	20 MHz	20 MHz	20 MHz	20 or 40 MHz

Two Android applications installed on the measuring device were used, the first being the "Wi-Fi Analyzer" (Fig. 1.). It helps the user to select a better channel. Wi-Fi Analyzer scans nearby wireless access points and shows spots with best signal strength and least traffic.

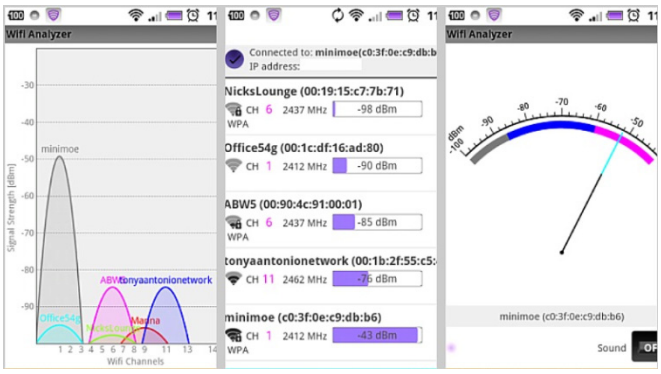

Fig. 1. Wi-Fi Analyzer application.

The second application used was the "Speedtest.net" (Fig. 2.). It measures the network download and upload speed.

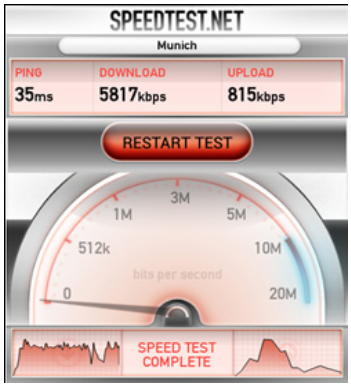

Fig. 2. Speedtest net application.

3. Results

For a more complete overview of the influence of different factors on the Wi-Fi signal, there were six measurement points. For the 1st measurement, the device was placed close to the WLAN router (30 cm away) with no obstacle or interference with the Wi-Fi signal. In the next measurement points, the distance from the router was increased, from 4 meters to 12 meters of distance. Distances of 8 and 12 meters included the concrete wall as well. Furthermore, the measurements included the interference from microwave owen and Bluetooth devices (measuring points 3 and 4).

For 2nd measurement, with distance from router of 4 m, a drop in the signal strength (of approx. 25 dB) has been noticed and a very slight drop in the upload and download speed. In the 3rd measurement, the same distance was used as in the 2nd measurement but with interference of a 500 W microwave owen. A slight drop of signal strength (approx. 3 dB) was noticed but a yet bigger drop in the speedtest than in the 2nd measurement.

In the 4th measurement, the distance from router was 4m as in the 2nd measurement, but with the Bluetooth interference (two cell-phones sending files over Bluetooth next to the measuring tablet). The results showed further drop in the Wi-Fi signal strength (approx. 3 dB), with no significant download and upload speed change. In the 5th measurement, the

distance from the WLAN router was increased to 8m. In this case there was an obstacle – a concrete wall inbetween. The results have shown further Wi-Fi signal strength drop compared to the 2nd measurement (approx. 7 dB) but a more significant download and upload speed (approx. 1.4 Mbps of download and 0.120 Mbps of upload). In the 6th measurement, the distance from the WLAN router was 12m. Compared to the 4th measurement, the Wi-Fi signal strength has slightly dropped (approx. by 6 dB). The upload and download have on the other hand showed the best results compared to other measurement points. Table 2. shows the results of the measurements.

Table 2. Power levels, upload and download speed of measured Wi-Fi network.

Measuring point	Power (dBm)	Download (Mbps)	Upload (Mbps)
30 cm from WLAN router	-30	5.745	0.797
4 m from WLAN router	-55	5.674	0.765
4 m from WLAN router with 500W microwave interference	-58	5.441	0.703
4 m distance from router with Bluetooth interference	-61	5.712	0.824
8 m from WLAN router with wall interference	-62	5.609	0.750
12 m from WLAN router with wall interference	-68	5.468	0.778

Fig. 3. shows dependence of the power (dBm) vs distance from the router (m). The measurements on 8 and 12 m include the wall barrier.

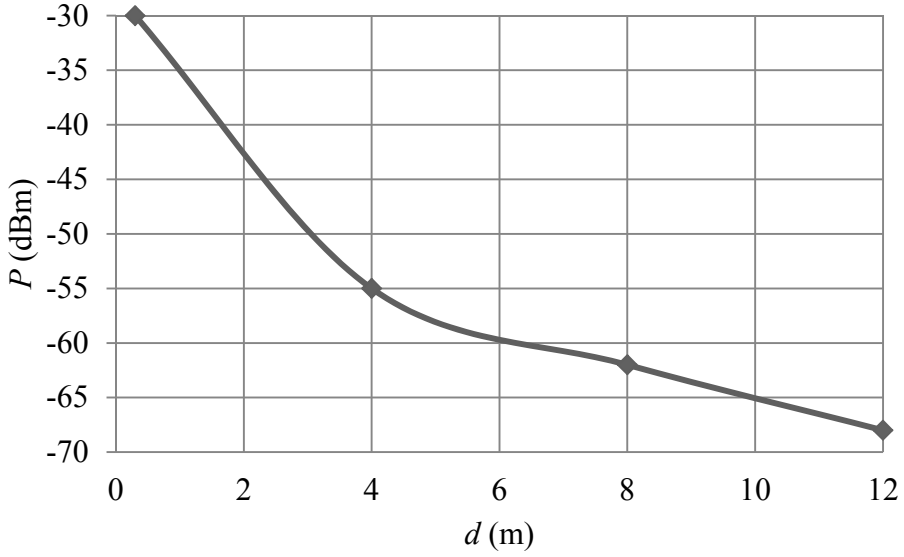

Fig. 3. Power depending on the distance from the router.

Fig.4. shows download and upload rates depending on the distance from the router. While the upload speed has remained almost the same, a slight change in the download speed has been noticed from increasing the distance to 8 m and beyond. During the testing, no other devices (other than the measuring device) were connected to that wireless access point. Therefore, no download/upload speed interference could have been caused by another device.

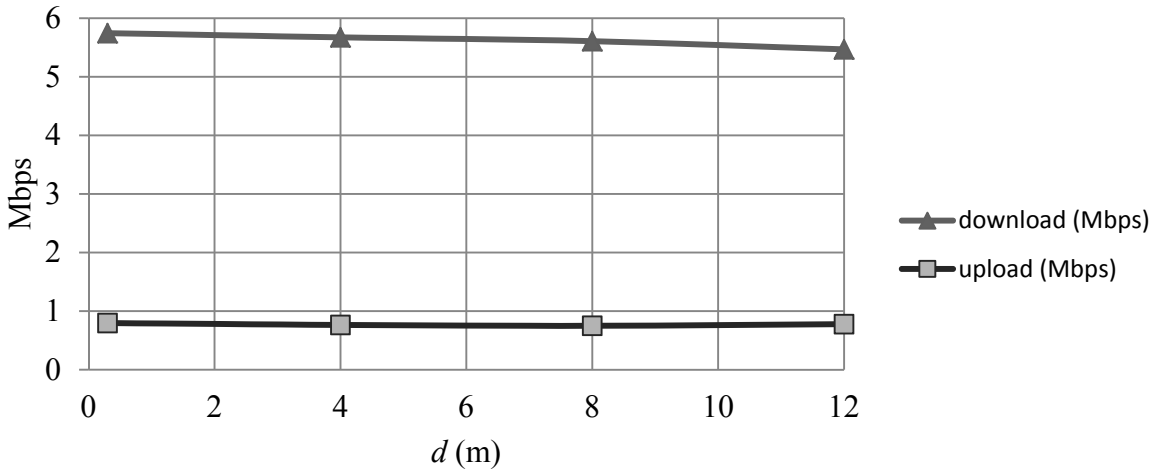

Fig. 4. Download and upload (Mbps) vs distance from the router.

4. Conclusions

Increasing the distance from the WLAN router leads to a drop in the Wi-Fi signal strength, while the download/upload remains nearly the same. The interference from microwave owen and Bluetooth device shows a drop in the Wi-Fi signal strength (the later more the the first), but the upload and download speeds remained almost the same. The interference of a wall between the measuring device and the WLAN router does cause a drop in the Wi-Fi signal strength, although the download/upload remains quite stable (except for 8 m distance where a significant drop of speed was detected). Naturally, numerous other measurements can be made to further show the influence of different objects and factors on the strength of the Wi-Fi signal and on the download/upload. They can include influence of a stronger magnetic field, influence of a stronger electric field, further increase of the distance, influence of other jamming devices (wireless phones, etc). Wi-Fi signal can also be increased by better placement of the WLAN router, replacement of the WLAN router's antenna, adding WLAN signal repeaters, changing the used channel of the WLAN signal of the WLAN router, switching to the 802.11n standard on all devices, using the same manufacturer for the WLAN cards and the router and so on.

References

[1] Radovan M. Računalne mreže. Digital Point tiskara, 2010.

[2] IEEE Std 802.11-2012. Part 11: Wireless LAN Medium Access Control (MAC) and Physical Layer (PHY) specifications.

[3] Basavarai P. et all. IP in Wireless Networks. Prentice Hall, 2003.

[4] IEEE Std 802.11b-1999 (Supplement to IEEE Std 802.11-1999). Part 11: Wireless LAN Medium Access Control (MAC) and Physical Layer (PHY) specifications: High-speed Physical Layer in the 2.4 GHz Band.

[5] IEEE Std 802.11g-2003. Part 11: Wireless LAN Medium Access Control (MAC) and Physical Layer (PHY) specifications Amendment 4: Further Higher Data Rate Extension in the 2.4 GHz Band.

[6] IEEE Std 802.11n-2008. Part 11: Wireless LAN Medium Access Control (MAC) and Physical Layer (PHY) specifications Amendment 5: Enhancement for Higher Throughput.

Improvement of Electromagnetic Field Homogeneity within EMC Immunity Testing Area

J. Hallon, K. Kováč

Slovak University of Technology, Faculty of Electrical Engineering and Information Technology, Institute of Electrical Engineering, Bratislava, Slovak Republic,
Email: jozef.hallon@stuba.sk

Abstract: *To fulfill standardized requirements for electromagnetic field uniformity by radiated immunity testing floor absorbers are obviously placed between transmitting antenna and tested device. The paper analyses possibility to establish such field without the absorbers only by moving the antenna between two heights in dependence on frequency. It shows possibility of this solution with full satisfaction of uniformity requirements.*

Keywords: Electromagnetic Compatibility, Immunity Testing, Field Uniformity

1. Introduction

Within the frame of electromagnetic compatibility (EMC) two basic radiofrequency (RF) electromagnetic field tests are included. For radiated emission measurement semianechoic chamber with reflecting floor is prescribed. For radiated immunity testing anechoic resp. modified semianechoic chamber with RF floor absorbers is required, while absorbers must be placed between source antenna and equipment under test (EUT) [1]. If test laboratory has only one semianechoic chamber at its disposal, it is necessary to rearrange the configuration of floor absorbers for fully testing of each EUT. It is cumbersome and requires additional space for storage of large absorbers. So it would be beneficial to have possibility to perform immunity test within test configuration without floor absorbers. This problem was studied by several authors. Their publications deal with comparison of test results obtained in anechoic chamber and in chambers with different characteristics [2].

In the paper [3] the authors showed by only experimental measurements, that it is possible to keep the homogeneity within test area, which is named in standard as uniform field area (UFA) in required limits also without floor absorbers by changing the antenna height within the interval $1 - 2$ m at 5 points. Their procedure needs computer control system, which performs relatively complicated calibration (5 times longer than standard) and it controls the antenna height depending upon frequency during the test procedure.

The presented paper analyses the possibility to ensure the UFA homogeneity by simpler way even by only two transmitting antenna heights. For this purpose we analysed the influence of transmitting antenna height upon UFA homogeneity at first by numerical simulation. Consequently we verified the obtained results by measurement in semianechoic chamber.

2. The uniform field area

Radiated immunity test standard [1] prescribes the calibration procedure for test space area. It defines the requirements for uniform field area (UFA) within which the EUT is placed. The electric field shall be calibrated over a volume or surface in front of the radiating antenna. The norm EN 61000-4-3 specifies a UFA, which is a hypothetical vertical plane of the field in which variations are acceptably small: at each frequency a field is considered uniform if its magnitude measured at 16 (4 x 4 uniformly spaced with 0,5 m distance) grid points is within -0/ +6 dB of the nominal value for not less than 75% of all grid points (e.g. if at least 12 of the 16 points of an 1.5m×1.5m UFA measured are within the tolerance) [4].

Moreover in the frequency range up to 1 GHz a tolerance greater than +6 dB up to +10 dB but not less than -0 dB is allowed for a maximum of 3 % of the test frequencies. In the calibration procedure specified in standard [1] it is stated that one has to measure the electric field at each one of the 16 grid points of the UFA at the selected frequencies. The forward power from the amplifier to the antenna shall be adjusted so that the field strength obtained is equal to the required calibration field strength E_u (electric field calibrated in the anechoic chamber). According to this procedure it is clear that the allowed tolerance of + 6 dB extendible to + 10 dB for 75% of all grid points permits a great variability of the electric field strength uniformity [4].

3. Problem description

Mechanism of EM field creation within semianechoic EMC chamber may be illustrated by figure 1. In all points within the UFA the field intensity is the result of the sum of two propagating waves – direct wave and the wave reflected from the floor.

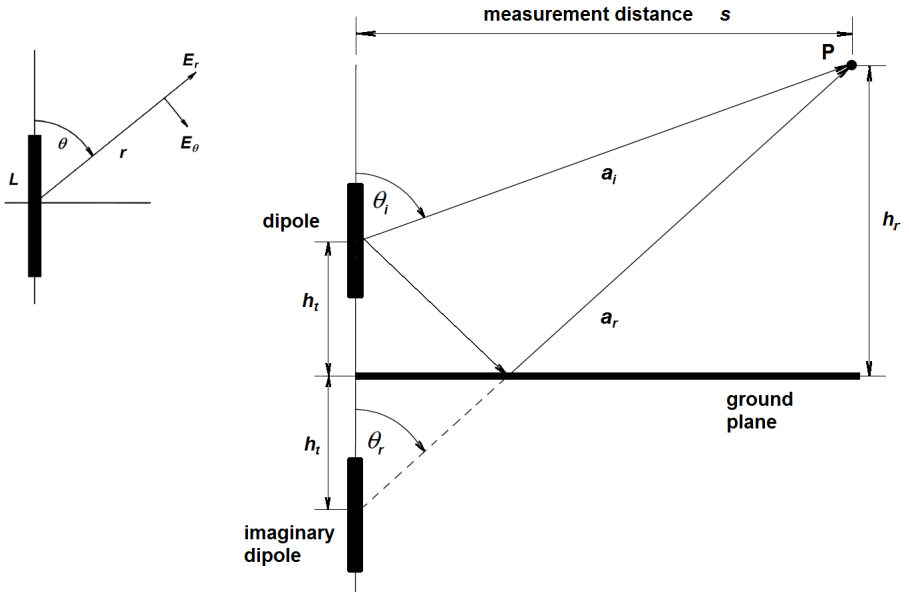

Fig. 1. Wave paths with ground plane reflection

The intensity of electric component of electromagnetic field at the observation point may be expressed as the sum of direct wave intensity and reflected wave intensity multiplied by the reflection coefficient ρ:

$$E = E_d + \rho E_r \qquad (1)$$

There are several factors influencing the resulting intensity. Generally the intensity of the wave is indirectly proportional to the length of propagation path of the wave i.e. distance between field source and observation point. So the reflected wave has significantly lower intensity than direct one. Then the reflection coefficient is negative for horizontal wave propagation and positive for vertical one. And the phase shift between waves significantly affects the resulting intensity. Two factors, propagation length and phase shift, are dependent upon antenna height. Due to the described interference of both waves the field intensity is significantly dependent upon frequency and as the propagation distance differs between UFA points, the field homogeneity is expressively changing up to more than 20dB at some frequencies.

4. Creation of simulation model

It is advantageous to use numerical simulation tools to study the influence of transmitting antenna position upon EM field homogeneity in UFA. They allow simpler analysis mainly in cases of complicated configurations. We used software system FEKO based on method of moments. The walls of chamber covered by RF absorbers where modeled by open area space border as well as the chamber ceiling, the conducting floor by perfectly conducting space border.

5. Evaluating procedure

The principle of evaluating procedure was based upon the fact that although the UFA homogeneity is rapidly changing it is possible that minimum homogeneity for all antenna heights is lower than limit value of 6 dB. So we performed homogeneity analyses by numerical simulation in frequency bands 80 - 1000 MHz and 1000 - 3000 MHz with 2 MHz frequency step. The antenna height was changing in the range 1 – 2,1 m with 10 cm step. For each antenna position and each frequency point we stored the EM field intensity values in all 16 points prescribed by the standard. Then the dependence of UFA homogeneity upon frequency was calculated for each antenna height.

On obtained data file the searching procedure could start. It takes all combinations of two antenna heights and searches the minimal homogeneity at all frequencies. Then it counts the frequency points for which the homogeneity is more then 6 and less than 10 dB. If the homogeneity is more than 10 dB, the combination is consider unacceptable.

On the basis of the result obtained by described procedure we performed verification of simulation results by measurements at chosen antenna heights within semianechoic chamber of our EMC laboratory. The measurements were executed by automatic software system fully complying standard requirements for UFA calibration and immunity test performance. The obtained results were then processed by the same procedure as the simulation results.

The results of the whole process are shown in following figures. In figure 2 the simulated and measured values of homogeneity are shown for frequency range 80-1000 MHz and horizontal antenna polarisation. It is evident from presented figures, that required homogeneity is reachable by combination of two antenna heights – 130 and 200 cm. This combination allows to reach the best UFA homogeneity, when the 6 dB limit value was excessed less than 0.7 dB only in 1,73 % of total number of frequency points. By verification measurement the 6 dB value was crossed by maximum 0.7 dB in 1,96 % of number of frequency points.

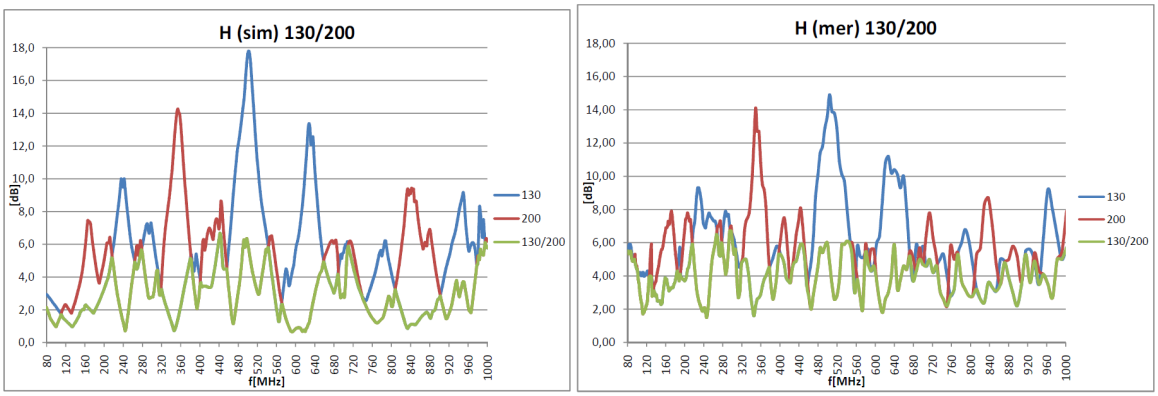

Fig.2. Simulated and measured results for frequency band 80 - 1000 MHz and horizontal antenna polarisation

Similar analysis was performed also for vertical antenna polarisation. In this case the situation is much better as the floor reflection coefficient is positive. Our simulations showed that all heights above 140 cm comply with requirements of standard. By the measurements all heights above 180 cm were conforming. Both simulated and measured results for 190 cm antenna heights are presented in figure 3.

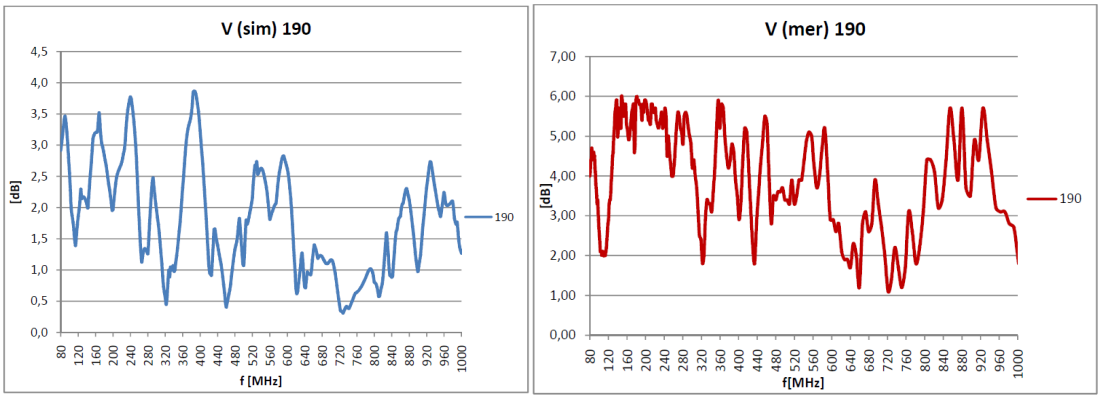

Fig.3. Simulated and measured results for frequency band 80 - 1000 MHz and vertical antenna polarisation.

The analysis in 1-3 GHz range was performed by simulation. For horizontal polarisation the homogeneity was conforming by combination of 190 and 200 cm antenna heights, when the limit values 6 dB was exceeded by maximum 1,2 dB only for 1,24 % of frequency points. For vertical polarisation all heights above 110 cm are complying.

6. Conclusions

The paper showed that it is possible to fulfill the requirements of EM field immunity test standard [1] without floor absorbers placed between transmitting antenna and EUT by using only two antenna heights. This allows to make EMC testing arrangement less time consuming so more effective. After including the algorithm for controlling the designed procedure into the whole software system the realisation of our technique does not need any additional test operator activity.

Acknowledgements

This work was supported by Slovak Ministry of Education under grant No. 2003SP200280802 and the Slovak Grant Agency VEGA under grant No. 1/0963/12.

References

[1] EN 61000-4-3:2006. Electromagnetic compatibility (EMC). Part 4: Testing and measurement techniques. Section 3: Radiated, radio frequency, electromagnetic field immunity test.

[2] Streitwolf H, Heinrich R, Behnke H, Dallwitz L, Karst U Comparison of radiated immunity tests in different EMC test facilities. *Proceedings, 18th Int. Zurich Symposium on EMC,* Munich 2007.

[3] WINDLER, M. J. – URBANSKI, S.: A Radiated Immunity Uniform Field Over a Ground Plane. In: *IEEE Int. Symp. on EMC 2003, Boston, USA, 18.-22.8.2003,* p. 669-673.

[4] Audone B, Marziali I Repeatability and Reproducibility of Radiated Immunity Tests *Proc. of the 10th Int. Symposium on Electromagnetic Compatibility (EMC Europe 2011), York, UK, September 26-30, 2011.*

Method for Validation of Antenna Calibration Measurements

[1]M. Kollár, [2]K. Kováč

[1]Seibersdorf Laboratories GmbH, RF-Engineering, A-2444 Seibersdorf Austria
[2]Slovak University of Technology in Bratislava, Faculty of Electrical Engineering and Information Technology, Institute of Electrical Engineering, Bratislava, Slovak Republic
Email: matej.kollar@seibersdorf-laboratories.at

Abstract. *Antenna calibration measurement is a specific type of multidimensional measurement with a plenty of influencing factors. In order to validate these measurements, the specialized methodology with a goal of improving the calibration procedures has been developed. The method is based on cluster analysis of existing antenna calibration measurements in a combination with tailored outlier detection method. The paper describes proposed methodology of the validation of individual measurements.*

Keywords: Antenna Calibration, Measurement Validation, Data Clustering, Outlier Detection

1. Introduction

This paper is focused on the analysis and validation of antenna calibration data. The goal is to examine about 6000 antenna calibration measurements collected in a period of last 14 years. Having access to this unique dataset, various antennas models and calibration methods combinations can be examined.
Our first task was to collect and organize the calibration data and make them ready for further processing. The preliminary analysis of the obtained data has shown that the calibration curves, associated with the same antenna model and calibration method, tend to form natural clusters in praxis. Being able to recognize these groups, it would be possible to determine if a specific antenna diverts from the others of the same model, if calibration data of a specific measurement are valid or not, and more. For the purpose of the data separation a tailored cluster analysis method has been introduced.

2. Subject and Methods

Essential part of the data processing was to obtain all the calibration information from distributed heterogeneous archives. Involving software engineering techniques, we were able to find automatically up to 75% of all calibration certificates and from 80% of them we succeeded in extracting also the quantitative calibration data. As a result we have created a database containing thousands of antenna calibrations of different antenna models, performed according to variety of calibration methods.

As proposed in [1], we have chosen the agglomerative hierarchical clustering using the Euclidean distance measure, for the purpose of separation of the antenna factor curves into distinct groups. The crucial property of this clustering approach is that the final number of clusters must be known in advance. When the number of clusters is not explicitly known, one needs to estimate this number empirically from the data. This is, however, a problem on its own for which a number of techniques could be employed. In [1], we stated that the total cluster variance criterion delivers acceptable results. Nevertheless, further experiments on larger dataset have shown limits of this approach. One of the most prominent issues was its inability to detect just a single cluster. Experiments with the real data have shown that the total cluster variance of one cluster is always larger than two smaller clusters. To be able to detect number of clusters in our data correctly, some other criterion had to be considered.

In this paper, we propose another approach how to formulate the clustering criteria based on the expert knowledge. In general, experts recognize false calibrations as those with significantly different shapes with respect to all other curves in the group or if their bias from the others is large. The cases where only small part of the curve differs cannot be considered as invalid because there is possibility that the specific antenna was calibrated in unusual frequency range on special customer request. In our proposed algorithm we attempted to transform these general rules to an autonomous method for determination of number of clusters in the data.

Fig. 1. shows an example set of multiple calibration measurements (curves) obtained for a specific antenna model and calibration method over time. One can see that an outlier in some respect does not necessarily mean an invalid calibration measurement. It can just belong to another subcluster within the given set which can still be considered as valid. This is, however, in a slight contradiction with the typical outlier scenario, where any deviation from the global model is automatically understood as an erroneous measurement. In our case, the nature of the antenna calibration allows for multiple clusters of measurements, although belonging to the same antenna model and calibration method. Thus the elements of one cluster may pose outliers to the other clusters, but still represent valid measurements.

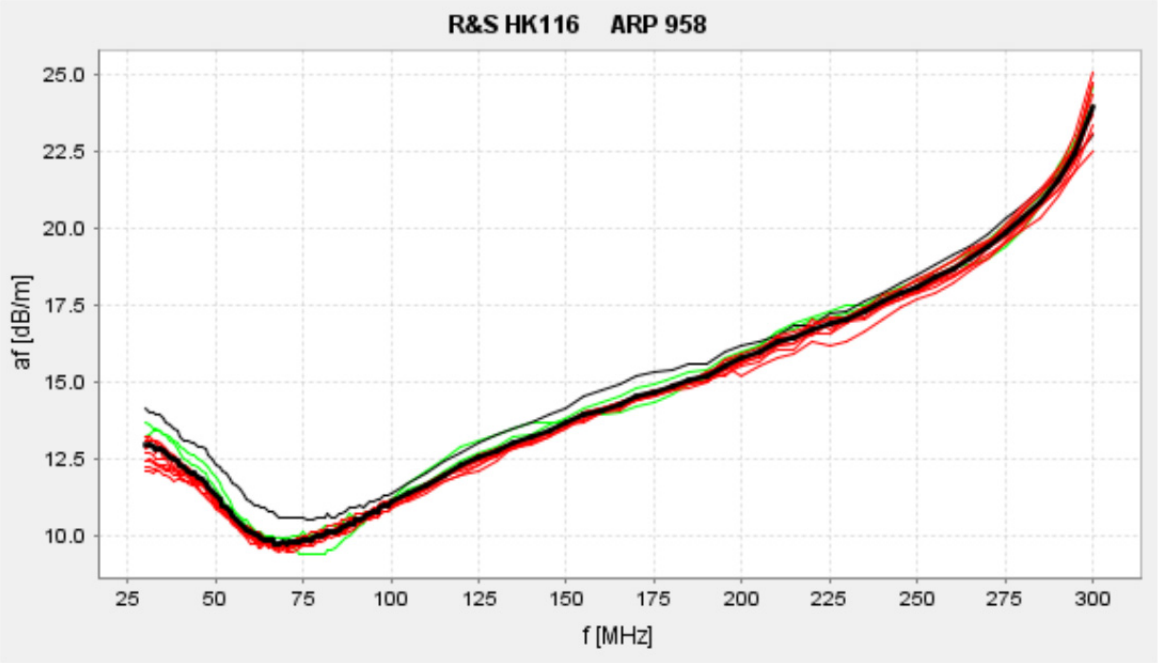

Fig. 1. Example of multiple calibration measurements (curves) obtained for a specific antenna model and calibration method over time. Color groups stand for results of the cluster analysis applied to the data.

The traditional approach to multivariate outlier detection is typically based on the Mahalanobis distance [3]:

$$D_M(x) = \sqrt{(x-\mu)'S^{-1}(x-\mu)}\,.$$

This measure gives the distance of a vector x from the data mean μ, taking into account correlations between variables reflected by the covariance matrix S. Assuming that the data follow the multivariate normal distribution, it can be shown that $D_M^2 = \chi^2(k)$, where $\chi^2(k)$ is the Chi-squared distribution with k degrees of freedom, which is equal to the dimensionality of the data. Given the vector x, comparing $D_M^2(x)$ with $(1-\alpha)$-th quantile of $\chi^2(k)$ provides an easy-to-use tool for assessing whether x complies with the model at the significance level α or not. Note that the model is fully defined by the mean vector μ and the covariance matrix S, which must be known either explicitly from an expert knowledge or via estimation from the training data.

However, in the case of antenna calibration measurements, there is always much less calibration curves in each data group than the number of measured frequencies. That causes the covariance

matrix S of the trained model to be inevitably singular and the inversion S^{-1} having no exact analytical solution. In order to resolve this issue, we have considered another regularizing assumption that the errors are independent in each measured frequency. This assumption reduces the Mahalanobis distance into the following simpler form:

$$\widehat{D}_M(x) = \sqrt{\sum_{i=1}^{k} \left(\frac{x_i - \mu_i}{\sigma_i}\right)^2},$$

where x_i is i-th element of the calibration curve x, μ_i is i-th element of the mean vector μ and σ_i is the standard deviation of the data in i-th measured frequency. Comparing $\widehat{D}_M^2(x)$ with the appropriate quantile of $\chi^2(k)$, one can discard those calibration curves which are unacceptably far from the average, taking into account variances in the individual frequencies.

One of the problems with the above approach is that the computed mean can be influenced by presence of outliers in the training data and thus the resulting outlier detection may fail. Typical solution to this issue is to substitute the mean and standard deviation with the robust statistics such as the median and median absolute deviation, as proposed by, e.g., Hampel [2]. Nevertheless, our experiments have shown that such a modification does not bring required performance improvement in our task. The reason is that our datasets contain only small numbers of elements which are moreover fragmented into multiple subclusters.

As an answer to this problem, we propose a combined approach where the agglomerative hierarchical clustering is supported by the actual outlier detection in each divisive step. As for the outlier detection, we propose to estimate means and standard deviations for sets mutual distances between individual measured curves rather than directly for the curve data. This modification provides better notion about distribution of distances within and between clusters, where those within clusters tend to be significantly smaller than between clusters. In this context, we define the outlier as the curve having unusually large distance from the others within cluster compared to the rest of within-cluster distances.

As in our antenna calibration collection it is quite usual that clustered datasets contain 4+ curves, the robustness of the outlier detection method can be further improved by removing the most extreme value from the dataset before determining the outlying observation. When the largest distance is removed from calculation of the mean and standard deviation, the estimated confidence interval better reflects valid distances within the cluster and thus the outlier is more likely to be recognized. In the limit case, when the outlier has to be determined in a group of just 3 curves, we use a heuristics approach based on the comparison of two means, where the test statistic is defined by the two-sample t statistic:

$$t = \frac{\mu_1 - \mu_2}{\sqrt{\frac{\sigma_1^2}{n_1} - \frac{\sigma_2^2}{n_2}}}.$$

In this case, the two populations are represented by frequency-wise differences between two closest and two furthest curves of the three. We assume that the significant difference is observed only when the furthest observation is the outlier.

The step-by-step process of the proposed combined approach can be explained as follows. The first iteration starts by determination of two clusters in the input dataset using the agglomerative hierarchical clustering [1]. Then the mean and standard deviation is calculated for the pair of the shortest Euclidean distances within the clusters. The shortest between-cluster distance is then compared to the 98-th percentile of the Gaussian distribution given by the mean and standard deviation estimated in the previous step. If the distance does not exceed the threshold, the clusters are merged and the resulting cluster is returned. Otherwise, the algorithm repeated for each of the two clusters recursively. In the case of 3 analyzed curves, the outlier detection is performed using the heuristic approach described earlier. Using this procedure we are able to separate curves into distinct clusters automatically, without knowing the number of clusters in advance.

Finally, having all the clusters recognized correctly, utilizing the traditional χ^2-based approach, we propose the following procedure for validating new calibration measurements:

1. estimate μ and σ vectors for the curves in each cluster,
2. given the validated curve x, calculate $\widehat{D}_M(x)$ for all the recognized clusters,
3. check if the $\widehat{D}_M$ value for any of the cluster falls behind the required quantile of the χ^2 distribution; if yes, the tested curve can be considered as valid; if no, there is strong evidence that the curve is invalid.

3. Results

In order to evaluate performance of the proposed combined clustering approach in comparison with the traditional approach using the total cluster variance criterion, an exhaustive testing on 170 groups containing 1126 calibration curves was conducted. Beforehand, all the curves within each group were manually clustered by a field expert, which provided a baseline for evaluation of the automated methods. In Tab. 1., the final results are shown. One can clearly see that our clustering method delivers approx. 2x higher success rate (with respect to the expert opinion) than the traditional approach. In absolute values, the traditional method succeeded in recognizing 37.06% of clusters, while our method succeeded in 80.59% of the cases.

Table 1. Result of a test on 170 groups containing 1126 calibration curves for both considered automatic clustering methods.

Algorithm	**Success rate w.r.t. expert opinion**
Total cluster variance criterion	37.06%
Proposed combined clustering	80.59%

4. Conclusions

During our research we have created a unique database of antenna calibrations allowing for diverse analyses according to various criterions such as antenna model, serial number, calibration method or measurement parameters.

By developing a tailored clustering method utilizing the proposed outlier detection algorithm, we were able to separate antenna factor curves into subclusters without in advance knowledge of the number of clusters. Compared to the traditional automated clustering approach, our method provided 2x higher success rate reaching up to 80.59%.

Having all the clusters recognized correctly, we proposed procedure for validating new calibration measurements utilizing the traditional χ^2-based approach to the model testing.

Acknowledgements

This work was supported by Seibersdorf Laboratories GmbH, Slovak Ministry of Education under grant No. 2003SP200280802 and the Slovak Grant Agency VEGA under grant No. 1/0963/12.

References

[1] Kollár M. , Kováč K., Application of Cluster Analysis on Antenna Factor Measurements Data. Proceedings of the 8th International Conference Measurement 2011, Smolenice, Slovakia.

[2] Hampel F. R., A general qualitative definition of robustness. Annals of Mathematics Statistics 42, 1887–1896, 1971.

[3] Penny K. I., Jolliffe I. T., A comparison of multivariate outlier detection methods for clinical laboratory safety data. The Statistician 50(3), 295–308, 2001.

Broadband Antennas Scanning Error as Contribution to Uncertainty of EMI Measurement

M. Bittera, M. Kamensky, V. Smiesko

Slovak University of Technology in Bratislava, Faculty of Electrical Engineering and Information Technology, Institute of Electrical Engineering, Bratislava, Slovakia, Email: mikulas.bittera@stuba.sk

Abstract. *Since the receiving antenna scans in range of 1 to 4 m to get the maximal interference there is no way how to make a correction to the effect of the ground plane. In this manner, error of antenna height variation and error of antenna directivity have to be included into the EMI measurement uncertainty. Based on choice of proper antenna models and numerical technique we investigated mentioned errors in this paper. We focus not only on their values but also how they vary with frequency of the received electromagnetic interference.*

Keywords: Broadband Antennas, Antenna Height Variation, Directivity, Uncertainty

1. Introduction

Broadband antennas - as log-periodic dipole arrays (LPDA) and biconical antennas are - have become very popular in electromagnetic compatibility (EMC) labs worldwide for electromagnetic interference (EMI) measurement mainly. Because there are no band breaks in given frequency ranges and test time are reduced. EMC engineers know the performance of these antennas - biconical antenna is used at lower frequency range, LPDA at higher frequencies. The question of higher measurement uncertainty due to antennas properties in such a case has opened.

During EMI measurement the receiving antenna varies its height over reference ground plane [1], which leads to another change of antenna's properties and also to another uncertainty contribution. Limited research has been conducted on the uncertainty contribution analysis of these broadband antennas [2],[3], mainly in their relation with reference ground plane. Therefore, we focus on the uncertainty contributions - errors of antenna - related to ground plane presence and varying height of antennas over the plane. The antenna height error and antenna directivity error in case of biconical antenna and LPDA are analyzed in this paper.

2. Broadband antennas and their models

To analyze the mentioned errors of broadband antennas numerical methods have to be executed – analytical methods are suitable just for simple problems, while measurement is always affected by surroundings. The most suitable method for antenna analysis are solver in frequency domain [4], method of moments was chosen to analyze the problems.

Typical representatives of the broadband antennas were examined:

- biconical antenna (see Fig. 1a) – 1300 mm long, with a cone radius of 260 mm created by 6 wires. Also a crossbar is in each cone. The frequency range of such antenna is from 30 MHz to 300 MHz;
- log-periodic dipole array (LPDA) (see Fig. 1b) - 760 mm long and 750 mm wide, with 14 pairs of dipole elements. The scale factor and the spacing factor of log-periodic dipole array elements are 0.85 and 0.126 (the longest dipole element is 750 mm long). The LPDA works in frequency range from 300 MHz to 1GHz.

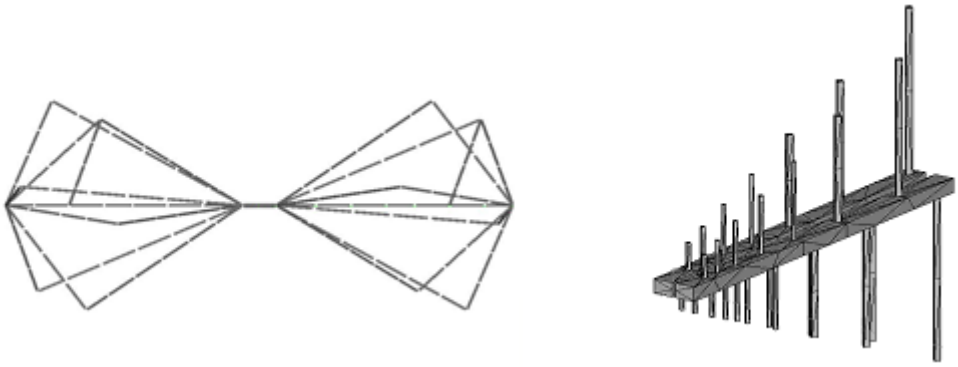

Fig. 1. Models of biconical antenna (left) and LPDA (right).

To use these models, at first we have to validate them. That means to verify if the obtained results copy sufficiently the properties of real antenna. Antenna factors (AF), input impedances, gains and directional patterns were compared in case of various models. The AF values are obtained by simulation where we placed a source of electromagnetic (EM) field e.g. short dipole antenna at adequate distance (ca. 100 m) away from the model of analyzed antenna. Then AF is given as ratio between known E field values and computed induced voltage at antenna output. Based on mentioned comparison [5] as the best model to represent real broadband antenna in simulation process is model, which consists of wire as well as surface elements (see Fig. 1).

3. Principles and methods

Antenna factor is mostly obtained when the antenna is in free space and the incident EM field is a plane wave. Such a free-space AF is an intrinsic property of the antenna which should not vary. However, the environment in which antenna is used may also affect the AF value. Since EMI measurement is performed over the conducting ground plane and actually antenna height over the plane is not constant. Hence, AF values may be changed depending on antenna polarization, height over the ground plane and also type of antenna, which may be different. Then the antenna height error relates to variable AF due to scanning the receiving antenna. AF was obtained using numerical simulation as it was mentioned above. However, conducting ground plane was replaced by a mirror image of the antenna situated in a double the distance as the height of the antenna under the original model to ensure homogenous plane wave.

The other important parameter of the antennas for our analysis is the radiation pattern. It refers to the directional dependence of radiation from the antenna. It is generally known that radiation pattern of an ideal half-wave dipole is constant in H plane, but in E plane it is a figure-of-eight pattern. So the directivity F given by sphere angles (θ,φ) can be expressed as:

$$F(\theta,\varphi)=\frac{\cos\left(\frac{kl}{2}\cos\theta\right)-\cos\left(\frac{kl}{2}\right)}{\sin\theta}=\frac{\cos\left(\frac{\pi}{2}\cos\theta\right)}{\sin\theta} \qquad (1)$$

where k is wave number (k=2π/λ) and l is the length of the dipole (in case of half-wave dipole l=λ/2). Unfortunately, the radiation patterns of broadband antennas are not known. In addition they may vary with changing frequency. The variation of radiation pattern may be expressed also as the error of AF. If the source of radiation is not situated in front of analyzed antenna in direction of maximal radiation (zero angle-wise), but it is moved so that radiation from itself affects the analyzed antenna with angles (θ, φ), we obtain the real AF of antenna AF:

$$AF(\theta,\phi) = AF(dB) + F(\theta,\phi) \quad (2)$$

where AF(dB) is known antenna factor and F is directivity of analyzed antenna. Then the error, obtained by replacing the half-wave dipole antenna by broadband antenna, may be expressed as error of antenna factor ΔAF defined as:

$$\Delta AF(dB) = AF(\theta,\phi) - AF_D(\theta,\phi) - K \quad (3)$$

where AF and AF_D are antenna factors at the same angles of incidence given by angles (θ,φ). The parameter K is a correction for neglecting the difference between the values of antenna factors of these antennas.

Since the receiving antenna varies its height from 1 to 4 m (antenna has to scan), angles of incidence of disturbing electromagnetic waves on measuring antenna vary their values as well. For example, if tested object is assumed to be in 1 m height and the measuring distance is standard [1] recommended 10 m the angle of incidence of direct wave varies from 0° to 17°. In case of shorter distances these angles may increase to higher value. If we consider not only the direct wave incident on the antenna, but also the wave reflected from the reference ground plane, angles of incidence are from 0° up to 27° for 10 m measuring distance. Hence, it is necessary to rotate the source of radiation around the analyzed measuring antenna with these angles and to record the maximal variations as compared with a zero angle of incidence. To examine the ground plane affect the model of antenna was again extended by its mirror image, as it was mentioned above.

4. Results

Exact height of the antenna and also the angle of incidence are not known, therefore, we expect a maximum error obtained for antenna scanning in a given range by 10 cm. As the antennas vary its height above the ground plane, also their AF are changing. This variation ΔAF is shown in Fig. 2. The error is strongly frequency dependent and it is more evident for biconical antenna, maximally ±0.67 dB. In both cases the worse situation occurs for horizontally polarized antennas. The maximal variation of AF is mainly in case of the lowest height of antenna h = 1 m. It is the situation when the mutual coupling between the antenna and the ground plane is maximal. The LPDA causes not so great error due to height variation.

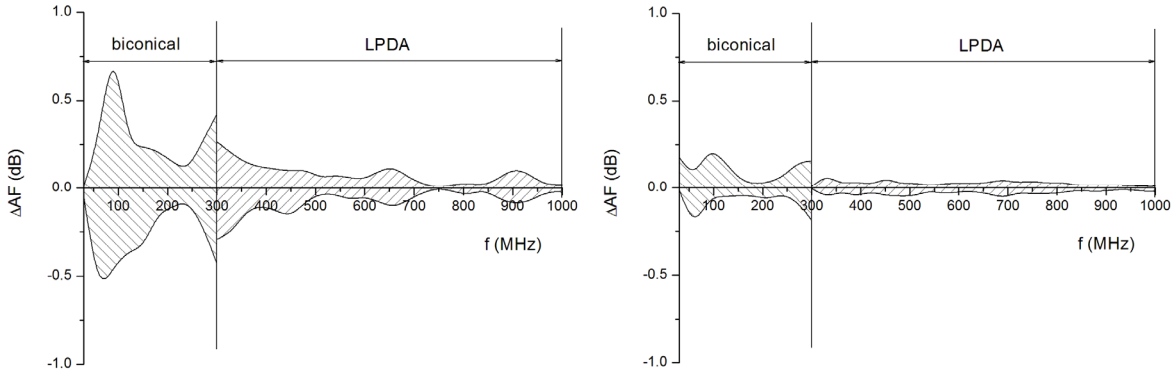

Fig. 2. Possible errors of AF for horizontally (left) and vertically (right) polarized broadband antennas caused by their antenna height variation.

The directional pattern of biconical antenna is similar to the pattern of the dipole. However, mainly in case of LPDA the main lobe of radiation pattern becomes more dominant with increasing frequency of radiation, so there is less similarity between radiation patterns of dipole and LPDA. Hence, there should be a higher probability that AF error caused is higher in case of LPDA. However, the ground plane presence nearby the antenna influences also its

directivity pattern in addition. There are evident changes in directional patterns of analyzed antennas. While in case of LPDAs the main lobe of the pattern is just crinkled at low heights of antenna, in case of the biconical antenna one can say evident change of the directional patterns, which lead to higher errors. In Fig. 3 possible directivity errors of analyzed antennas are shown. These graphs represent of course the worst case error ΔAF.

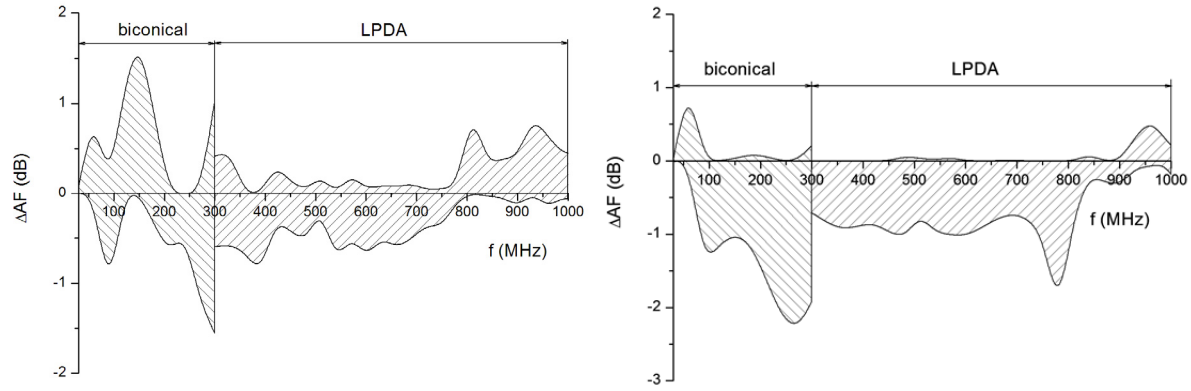

Fig. 3. Possible errors of AF for horizontally (left) and vertically (right) polarized broadband antennas caused by their directivity for distance 10 m.

It is necessary to mention that directivity error increases with the larger measuring distances because in those cases also the range of possible angles of incidence is larger.

5. Conclusions

Broadband antennas are more popular among EMC engineers in comparison with the half-wave dipole due to their benefits. On the other hand they may introduce additional errors into measurements which may lead to higher values of the measurement uncertainty because the correction is impossible due to unknown height of antenna. As it was seen above the vicinity of the ground plane impacts the AF value of broadband antennas as well as their directional patterns. In both cases biconical antenna introduces bigger error due to its bigger dimensions. The analyzed errors are strongly frequency dependent which may lead to evaluation of the frequency dependent uncertainty.

Acknowledgements

This work was supported by the project VEGA VG 1/0963/12.

References

[1] CISPR 16-1-4: Specification for radio disturbance and immunity measuring apparatus and methods - Radio disturbance and immunity measuring apparatus - Ancillary equipment - Radiated disturbances. 3rd Ed., IEC, 2010.

[2] Chen Z., Foegelle M.D., Harrington T. Analysis of log periodic dipole array antennas for site validation and radiated emission measurement. In proceedins of the IEEE International Symposium on EMC, 1999, 618-623.

[3] Van Dijk, N. Uncertainties in 3-m radiated emission measurements due to the use of different types of receive antennas. *IEEE Transaction on EMC,* 47 (1): 77-85, 2005.

[4] Hajach P., Hartansky R. Resistively loaded dipole characteristics. *Radioengineering*, 12 (1): 23-27, 2003.

[5] Bittera M., Stih M. Modelling of wire antennas. In proceedins of the 12th International Conference on Mechatronics, 2009, 73-76.

The Errors in Radar Level Gauge Calibration

P. Mikuš, R. Harťanský

Slovak University of Technology in Bratislava, Faculty of Electrical Engineering and Information Technology, Institute of Electrical Engineering, Bratislava, Slovakia
E- mail: peter.mikus@stuba.sk

Abstract. *This article deals with the verification of the radar sensors. These are very accurate devices but they are vulnerable to distortion of the measured value due to false reflections. This is an assigned measure, therefore it is necessary to ensure that the results are fixed and reproducible. It puts the request on geometry and optimalization of the environment to minimize the false reflections and in this way achieve the highest accuracy measurement.*

Keywords: *Radar Level Gauge, Verification, Reflections, High-Frequency Wave, Radiation Patterns.*

Introduction

The radar level gauge is a device which measures the distance by using indirect method in a contactless way. It consists of two basic parts: a transmitter and a reciever. The transmitter consists of a signal generator and a directional antenna. The receiver is composed of a directional antenna, an amplifier, a decoding device, a circuit with the volltage comparator and a powerline circuit. The transmitter and the receiver are integral. The latest sensors are not sensitive to the changes of temperature, pressure, density and the composition of the gas in the measuring environment. The radar sensor uses a continuous frequency modulation.

Continuous frequency modulated system

The most of the latest level sensors works through the continuous frequency modulated method. It uses a measurement of the distinction of the transmitter and receiver frequencies. The transmitted frequency is swept between two known values f_1 and f_2, and the distinction between the transmitted signal and the return signal is measured.

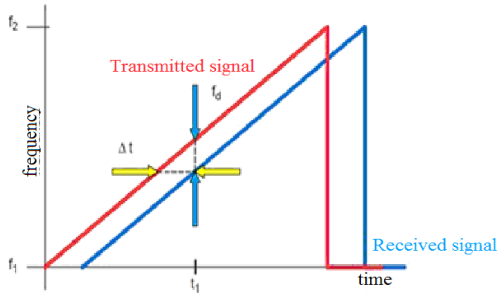

Fig. 1. The principle of the method "continuous frequency-modulated signal"

The principle of verification level gauges

Department for verification of radar sensors is located at the long corridor in the building SLM n.o. on the ground floor. Under the ceiling of the corridor (2.20 m high) are fixed beams which hold the metal guide rail. On the metal bar moves reflection board with the assistance of a toothed belt and a servo drive. This reflection board simulates water level in the tank. At one end of the hall is located a massive rack that holds the calibrated level gauge of 1.35 m above the floor and the etalon of the length - the laser interferometer XL 80. In this way of

verification occur several disturbances. Unless unlimited space is available, there appears disturbing reflection. The radiation angle of level meter is 10 °, the width of the corridor is 1.93 m and the beams are 0.85 m distant. From these data we can calculate when there appear parasitic reflections. [1]

$$tg\alpha = \frac{d}{x} \Rightarrow x = \frac{d}{tg\alpha} = \frac{0{,}85}{tg6{,}5} = \frac{0{,}85}{0{,}11394} = 7{,}46\,\text{m} \qquad (1)$$

d – distance from the ceiling

There are reflections from the beam at a distance of about 7 m in our conditions. It means that there will occur distortion of measured values if the measuring distance is longer than 7 m . We can not change the environment so we must solve this problem in another way. It is necessary to focus a ray in a way to avoid reflection from the walls of the environment where the verification is carried out. One of the solutions is to build an anechoic wall which absorbs electromagnetic waves earlier than the parasitic reflection occurs. The next problem is to provide uprightness of the reflection board towards level gauge (If the uprightness is insufficient it can cause the distinction between the rays flating on the top and bottom part of the board and thus the distance measurement error). The shape, location and the edges of the board affect the extension of radar waves and therefore it also affect the process of verifing accuracy of the level gauges.

Minimizing the false reflections

In order to avoid or to minimize the formation of false reflections, it is important to send the sharpest ray without side lobes. This will ensure that the ray will turn out just to the reflection board and there will not form the false echoes. The figure (see Fig. 2) shows two types of radiation patterns and reflections which occurs in each type.

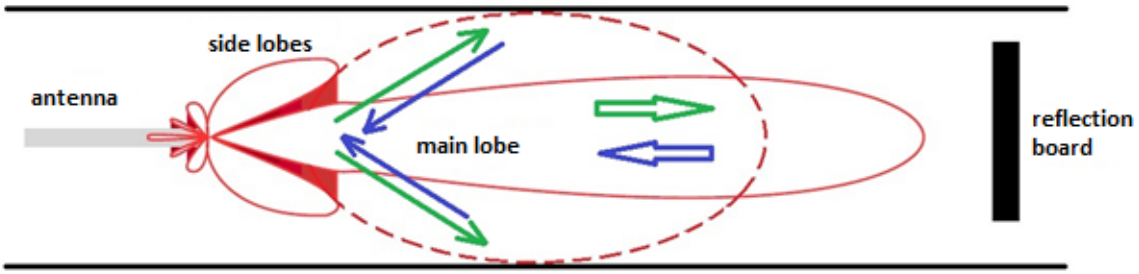

Fig. 2. Undesired reflections in the verification of level gauges

As we can see, if the ray is sharper there will occur only primary reflections on the reflection board which is desirable. If the ray is wider there will occur not only primary reflections but also false reflections of the radar signal. In this case interference of multiple signals appears which significantly change the final measured value. The borderline cases can be seen in the figure (see Fig. 3a). Another problem in the process of verification of level gauges is the formation of side lobes a directional patterns. It is caused by the reflection board itself. This phenomenon can be caused by diffraction on the edges of the reflection board. Diffraction or bending is a change of the spreading way of radiation because of the barrier. As it can be seen in the figure (see Fig. 3b) there can occur two cases. Only one side of the barrier is lightened or the both sides of the barrier are lightened. In the first case: in the area: 0 to $\pi-\varphi$ appear all the field components namely - incidental, reflected and bending fields. In the area: $\pi-\varphi$ to $\pi+\varphi$ occur reflected and bending fields. In the next area: $\pi+\varphi$ to α exists only bending field. In the second case, if the both sides are lightened we can see the following situation: In the

area 0 to π–φ and 2α–π–φ to α appear all the fields. The area π–φ to 2α–π–φ includes incidental and bending fields. [2]

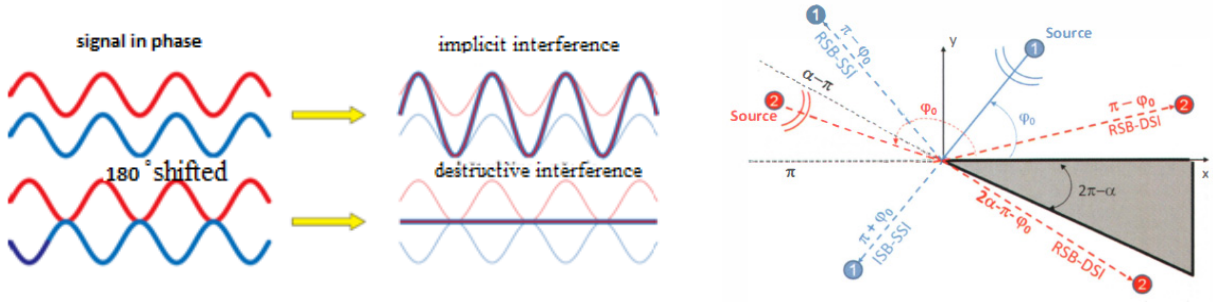

Fig. 3. a) Constructive and destructive interference, b) geometry of diffraction on the edge

In the formation of diffraction can be significantly changed the shape of the directional patterns of level gauge. This could negatively affect the results of verification.

Results

To be able to assess the effect of the environment (in this case – reflection board) in the process of verifing the radar level gauges we must simplify the situation in a way that the verification process affects only one factor. So we placed all the verification department in a fictitious, infinitely vast, homogeneous and linear space. In this space, using numerical methods, (Method of moments) we calculated radiation patterns of radar level gauge Fig. 4a. In the picture is microwave emitter, parabolic reflector (diameter: d= 441 mm) and the radiation patterns obtained at a freqency of 10 GHz and powering emitter voltage of 1 V. The width of the sheaf of the radiation patterns can be read from Fig. 5a – more thickness curve.

Fig. 4. a) Antenna of the level gauge and its radiation patterns, b) irregularly shaped absorber

In the next step, we add to the environment perfectly conducting board of finite dimensions *a* x *a* = 60 x 60 cm. On board occurred a reflection of electromagnetic wave on the face side and diffraction of waves at the edges of the board. These two physical mechanisms affect the shape of the radiation patterns. Width of the main lobe sheaf was increased to 40 ° in Fig. 6 - blue curve. This will increase the probability of parasitic reflections of electromagnetic ray and the degradation of the verification, see Fig. 2. It is important to minimize such components of the reflected waves which cause the extension of the main lobe of radiation patterns. Such components are primarily diffraction fields. In order to suppress diffraction at the edges we covered edges of the reflection board with the absorbing material [3], which followed the edges of the board. Simulation results are shown in Fig. 5b – more thickness curve. As can be seen from the figure, the main lobe of radiation patterns was not changed, and the results were not satisfactory. In the next step, we modified the outer edges of the absorber into the irregular shape (see Fig. 4b).

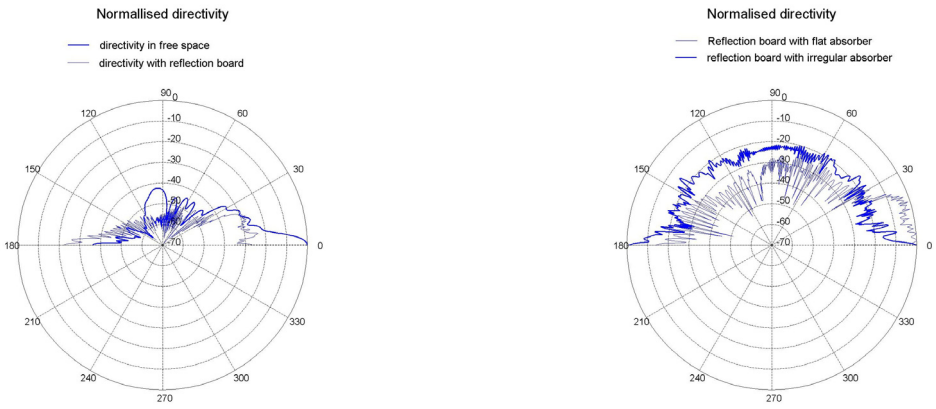

Fig. 5. a) Comparison of emitted ray with and wihtout reflection board, b) comparison of absorbers with straight and curved edge

The results can be seen in the picture (see Fig. 5b) - blue curve. Originally, the HPBW of the main lobe of the radiation patterns was 40 ° and after modification of the shape of the absorbers was this HPBW reduced to about 2 °, which is extremely satisfactory result. This means that adding of the reflection board will only reflect the electromagnetic ray, and not to change the HPBW of the sheaf. This result is for the verification of the accuracy and reproducibility of microwave level gauges very important.

Conclusions

To ensure the accuracy and reproducibility of measurements in the process of verifying microwave level gauges we need to make a number of mechanical and electrical requirements. This article focused on ensuring the narrow HPBW of the sheaf of the radiation patterns. The narrow sheaf will minimize occurrence of the parasitic reflections from the walls or the construction of the verification department. Suitable shape of the radiation patterns, in the presence of the reflection board, was provided by placing irregularly shaped absorbers are secure location on the edge of the reflection board. The type and the shape of the absorbers ensure the sheaf reduction from 40° to 2°.

Acknowledgements

This work was supported by the Slovak Research and Development Agency under the contract No. APVV-0333-11 and by the project VEGA VG 1/0963/12.

References

[1] Benkó, P – Peták, T. *Straightness measurement of linear motion guide*. In MMA 2012 – Advanced production technologies : Proceedings. 11th international scientific conference. Novi Sad, Serbia, 2012. 2 p. ISBN 978-86-7892-429-3.

[2] Hacivelioglu, F. - Uslu, M.A. - Sevgi, L. A MATLAB-Based Virtual Tool for the Electromagnetic Wave Scattering from a Perfectly Reflecting Wedge. In Antennas and Propagation Magazine, 2011, ISSN 1045-9243, 234-243.

[3] E. COX, Amanda a Michael D. JANEZIC. *Preliminary Studies of Electromagnetic Properties of Microwave Absorbing Materials used in Calibration Targets*, 4 p.

[4] PÁLENÍK, T. -- BITTERA, M. -- SMIEŠKO, V. Sub-Domain MoM Formulation for Circular and Non-Circular Loop Antenna Arrays. International Journal of Engineering Science and Technology Vol. 3, No. 5. s. 3686--3692. ISSN 0975-5462.

Analysis of Measurement Systematic Error in the Near Field Region

J. Slizik, R. Hartansky

Institute of Electrical Engineering, Faculty of Electrical Engineering and Information Technology, Slovak University of Technology in Bratislava, Slovakia
Email: jozef.slizik@stuba.sk

Abstract. *This article deals with determination of systematic error, which occurs in the measurement of near field of the source electromagnetic field. Systematic error depends on the size of a sensor. We consider inhomogeneous distribution of electromagnetic field in this paper. In article there is shown what maximum dimension of the sensor is, if we want to measure with precision ± 3 % in the near field zone. This dimension of the sensor depends on the wavelength. Electromagnetic field is created by an electrical dipole.*

Keywords: Sensor, Systematic Error, Near Field, Source Dipole

1. Introduction

Measurement of the electromagnetic field has its own specifics. The most important is the fact that it is necessary to measure two elements of the vector: electrical field $\bar{\boldsymbol{E}}$ and magnetic field $\bar{\boldsymbol{H}}$. High importance is given to the selection of the correct borders of the elements of the field in places where these elements are measured. In the case that the point of measurement is very near the source dipole, $\bar{\boldsymbol{E}}$ and $\bar{\boldsymbol{H}}$ vectors are not orthogonal to each other. Vectors contain elements of the field x*, y, z (r, Θ, Φ)*. If electric dipole is the source of electromagnetic field, then elements E_r, E_Θ and H_Φ (1), (2), (3) in its vicinity exist. If the source of electromagnetic field is electric loop or magnetic dipole respectively, then elements of the field H_r, H_Θ and E_Φ in its vicinity exist. Because the intensities of electric and magnetic field are vectors we need to measure individual elements of these vectors. Value of the elements in the vector depends on the distance from the source dipole. Based on the distance from source dipole we can subdivide the field into several regions:

- If $kr > 1$ we talk about far field region and must apply $r >> \lambda / 2\pi$ (Fig.1, dashed line).
- If $kr \equiv \lambda / 2\pi$ we talk about transient field region. All elements of the electromagnetic field are expressed in this region (Fig.1, crossed marks)
- If $kr << 1$ we talk about near field region, specifically about static region and must apply $r << \lambda / 2\pi$ (Fig.1, black dotted line)
- If $kr < 1$ we talk about near field region, specifically about inductance region and must apply $r << \lambda / 2\pi$ (Fig.1, starred line) [1]

Where: k – wave number; r – distance from source dipole; λ – wavelength

Additional distribution of this space around the antenna we can subdivide into the three regions: reactive near field, radiating near field (Fresnel) and far field (Fraunhofer) regions. More information about this distribution is in the literature [2].

In this article we deal with the error which arises from the measurement of the source of electromagnetic field $\bar{\boldsymbol{E}}$ in near region by the source. Electromagnetic field is radiated by the electric dipole which dimensions are much smaller than the wavelength λ of the RF signal input.

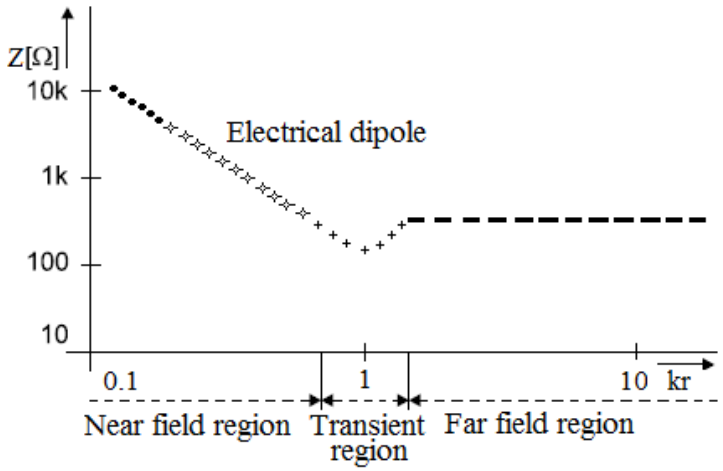

Fig. 1. Dependence of wave impedance on the distance from the source

The elements of the electromagnetic field and their amplitudes could be defined in spherical coordinate system [2]:

$$E_{\Theta} = -j\frac{LIk^3 \sin\Theta}{4\pi\omega\varepsilon}\left(\frac{1}{(kr)^3}+\frac{j}{(kr)^2}-\frac{1}{kr}\right)e^{-ikr} \tag{1}$$

$$E_{r} = -j\frac{2LIk^3 \cos\Theta}{4\pi\omega\varepsilon}\left(\frac{1}{(kr)^3}+\frac{j}{(kr)^2}\right)e^{-jkr} \tag{2}$$

$$H_{\Phi} = \frac{LIk^2 \sin\Theta}{4\pi}\left(\frac{1}{(kr)^2}+\frac{j}{kr}\right)e^{-jkr} \tag{3}$$

Where: L – length of dipole; I – electric current; ω – angular velocity; ε – permittivity

Two elements of the electrical field E_{Θ} and E_r exist in the near region of the dipole. These elements are orthogonal to each other. The element of the electrical field E_{θ} is oriented tangentially to the source dipole and element E_r is oriented radially to the source dipole [4]. If we want to measure the field in the near region of the dipole, we must measure each element of the field separately [3]. This is because sensor of the electric field is also electric dipole. Dimension of the sensor cannot be neglected in this case. Therefore, the output RF voltage from the sensor is not an amplitude of electrical field vector at the point of measurement, but average field value over the volume of the sensor „ V “. Volume of the sensor is created by the own dimension of the sensor [3].

2. Computing of measurement error

The equations (1) and (2) are used for the analytical calculation of the individual elements of the electric field E_{Θ} and E_r in the near field region. Total electric field E we get from individual elements of the electric field, see equation (4).

$$E = \sqrt{E_{\Theta}^2 + E_r^2} \tag{4}$$

The electric field reaches high value of intensity that is caused by considerable amplitude of the power supply and also by vicinity of the source dipole. Radial and tangential fields have $|Sin\ (\Theta)|$ respectively $|Cos\ (\Theta)|$ function pattern in the space. The fields are mutually shifted in $\pi/2$ in the direction Θ. In Fig.2 we can see that the radial element of the electric field

dominates in the near field region. The magnitudes of radial and tangential fields are considered to be true values of the fields.

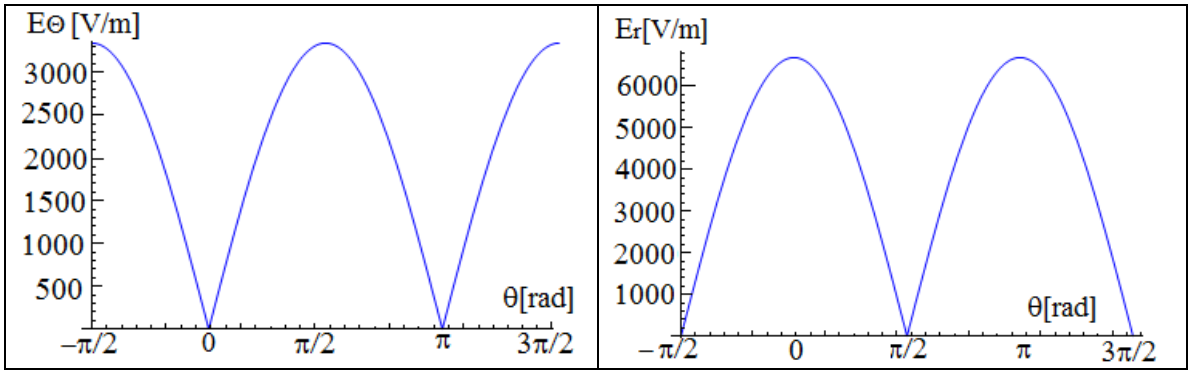

Fig. 2. Near field pattern of the electrically short dipole

If the individual elements of the electric near field are measured by the sensors, which have non-zero dimensions, we will get the results influenced by error (the sensor is averaging the measured values). Shape of the measured radiation characteristics is different in comparison to analytical model. If we want to determine relative error between ideal and measured near field, we must create near field measurement model with use of an electrically short dipole. By comparison of results from numerical near field model to value of the analytical near field model we get measurement error of the electric field in the near region of the source for each model. More about analytical model and relative error calculation of measurement near field is described in [3]. In that article systematic error for different lengths of the sensor is expressed. There is also proved that the systematic error decreases with reduces of the size of the sensor. We used the results from [3] to specify the dependency of the systematic error on the dimension of the sensor.

3. Results

We got values of maximum δ_{MAX} and minimum δ_{MIN} errors from values of systematic error. These errors are dependent on the length of the sensor. Wavelength is *30* m for this sensor.

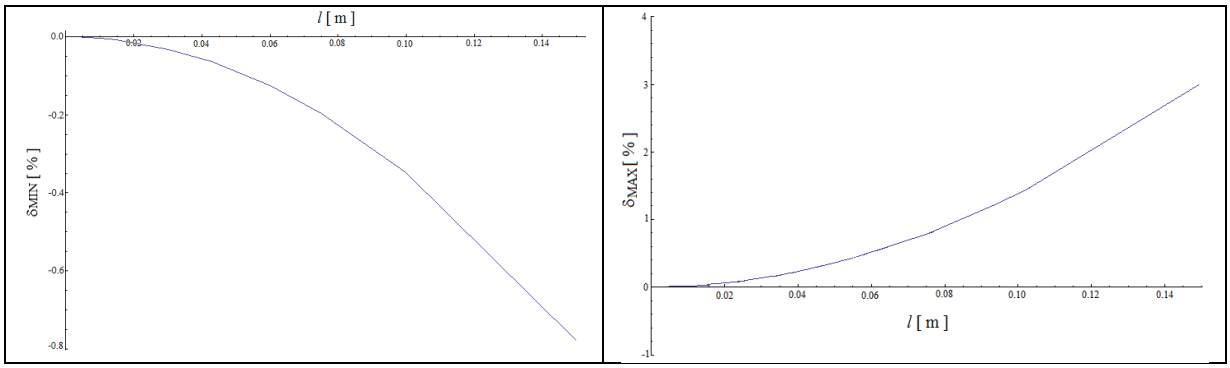

Fig. 3. a) Dependence of the error δ_{MIN} on length of the sensor for static region
b) Dependence of the error δ_{MAX} on length of sensor for static region

In Fig.3a we can see the dependence of the minimum error on the length of the sensor in the near region of the source, specifically in the static region. In Fig.3b the dependence of maximum error on the length of the sensor in the same region as a minimum error is shown. We can see that the values are changing with enlarging dimensions of the sensor, mainly with its length. If the dimension of the sensor is bigger, then the error is bigger, too. It could be proved that waveforms of δ_{MIN} and δ_{MAX} errors are changed by a function of the third order.

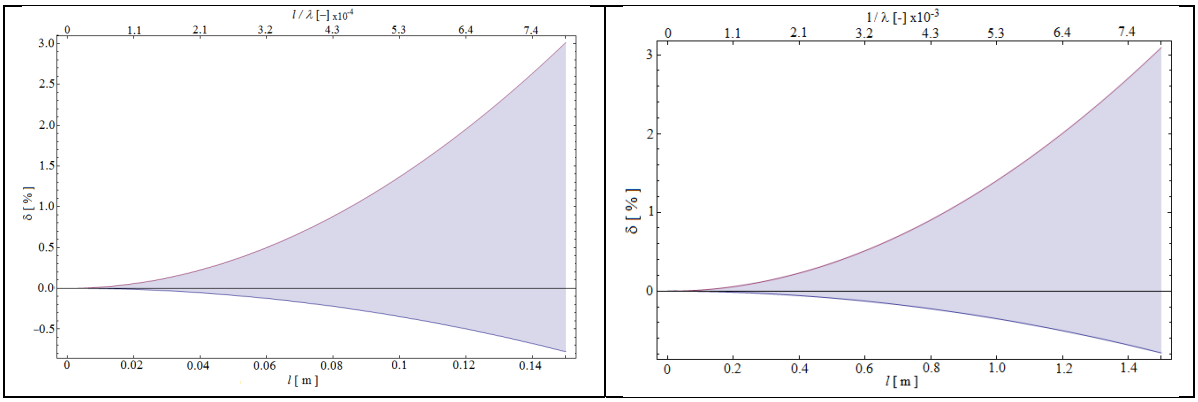

a) b)

Fig. 4. Dependence of systematic error on ratio l / λ for near region

After drawing both characteristics δ_{MAX} and δ_{MIN} into one graph (Fig.4a) we can see how the systematic error is changing with the ratio l / λ for static region. We can see that systematic error is rising with increasing the ratio sensor length to wavelength. Ratio sensor length to wavelength is on the order of 10^{-4}. In Fig.4b the change of systematic error for near field region (inductance region) is shown. Systematic error is rising with ratio sensor length to wavelength, too. But ratio sensor length to wavelength is only on the order of 10^{-3}. When we compare both figures (Fig.4a and Fig.4b), we can see that maximum length of the sensor for static region must be smaller as a maximum length of the sensor for inductance region.

4. Conclusions

In process of measurement of the near field the error of measured field changes with value of sensing elements. In this article the impact of the systematic error to the changes of sensor value was described. For examples, when we want to measure with precision ±3 % in inductance region, the sensor must have maximum length $l \leq 7\,\lambda / 1000$. However this formula is valid only for inductance region. The length of the sensor must be almost 10 times smaller than the length of sensor in the inductance region, if we want to reach similar error, in static region. In this case the maximum sensor length must be $l \leq 7\,\lambda / 10000$.

Acknowledgements

This work was supported by the project VEGA 1/0963/12.

References

[1] Bittera M, Smieško V, Kováč K, Hallon J. Directional Properties of the Bilog Antenna as a Source of Radiated Electromagnetic Interference Measurement Uncertainty. In: *IET Microwaves Antennas & Propagation*. - ISSN 1751-8725. - Vol. 4, Iss. 10 (2010), s. 1469-1474.

[2] Balanis Constantine A. *Antenna theory: analysis and design*. 3rd ed. Hoboken: Wiley-Interscience, 2005, xvii, 1117 s. ISBN 978-0-471-667282-7.

[3] Slížik J, Harťanský R. Metrology of electromagnetic intensity measurement in near field, In *Quality Innovation Prosperity Journal*. ISBN 1335-1745 (in press).

[4] Čičáková O, Szolik I, Krammer A. Complex System for EMC Immunity Tests. In: *Applied Electronics 2009: International Conference*. Pilsen, Czech Republic, 87-90 s., 2009. ISBN 978-80-7043-781-0.

AUTHORS INDEX